Physics of Atomic Nuclei, Vol. 68, No. 2, 2005, pp. 171–176. Translated from Yadernaya Fizika, Vol. 68, No. 2, 2005, pp. 195–200.
Original Russian Text Copyright © 2005 by Balabekyan, Danagulyan, Drnoyan, Demekhina, Adam, Kalinnikov, Krivopustov, Pronskikh, Stegailov, Solnishkin, Chaloun, Tsoupko-Sitnikov, Musulmanbekov.

Investigation of Spallation Reactions on ^{120}Sn and (d, xn), (d, pxn), (p, xn), and (p, pxn) Reactions on Enriched Tin Isotopes

A. R. Balabekyan[1], A. S. Danagulyan, J. R. Drnoyan, N. A. Demekhina[2], J. Adam[3], V. G. Kalinnikov[4], M. I. Krivopustov[4], V. S. Pronskikh[4], V. I. Stegailov[4], A. A. Solnishkin[4], P. Chaloun[3], V. M. Tsoupko-Sitnikov[4], and G. Musulmanbekov[4]

Yerevan State University, ul. A. Manukyana 1, Yerevan, 375049 Armenia

Received December 17, 2003; in final form, April 28, 2004

Abstract—The cross sections for (d, xn), (d, pxn), (p, xn), and (p, pxn) reactions on enriched tin isotopes are obtained at a projectile energy of 3.65 GeV per nucleon. The yields in the energy range 0.66–8.1 GeV are analyzed with resort to experimental data obtained previously. Experimental data are compared with the results of theoretical calculations performed within the cascade–evaporation model. The dependence of the yields on the number of emitted neutrons, the projectile type, and the isotopic composition of a target is investigated. The cross sections for the $(p, xpyn)$ reactions on a ^{120}Sn target are presented at a primary-proton energy of 0.66 GeV. © *2005 Pleiades Publishing, Inc.*

1. INTRODUCTION

Nuclear reactions where a target nucleus loses only a few nucleons occur much more frequently than other processes such as spallation and deep-inelastic scattering. It is assumed that such reactions proceed via a peripheral interaction and that a nuclear cascade does not play a significant role here. They were investigated predominantly at projectile energies below 1 GeV [1–4]. Such processes are also classified as simple reactions. Their mechanism can be explained either by

(i) a direct interaction in which a projectile particle interacts with a bound target neutron, knocking it out, with the result that the target nucleus acquires an excitation energy not greater than 10 MeV (knockout), or by

(ii) inelastic projectile-proton scattering on surface nucleons that is accompanied by the transfer of a moderate (10 to 20 MeV) excitation energy and which is followed by the evaporation of a small number nucleons (the class of processes described in terms of this mechanism includes charge-exchange reactions).

At high projectile-proton energies, reactions of the (p, xn), (p, pxn), and $(p, 2pxn)$ types were investigated in [5]. High energies are not expected to change the mechanism of such reactions substantially.

The objective of the present experiment was to study the cross sections for such reactions on enriched tin isotopes versus the projectile type, the number of emitted neutrons (x), and the nucleonic composition of the target and to analyze the excitation functions for (p, xn) and (p, pxn) reactions with the aid of data obtained previously at proton energies of 0.66, 1, and 8.1 GeV [6, 7].

2. EXPERIMENTAL PROCEDURE

Samples from enriched tin isotopes ^{112,118,120,124}Sn were irradiated with protons and 3.65-GeV/nucleon deuterons from the nuclotron and the synchrophasotron of the Laboratory of High Energies at the Joint Institute for Nuclear Research (JINR, Dubna). For targets, we used metallic foils, three layers of them for ^{118,120,124}Sn and one layer for ^{112}Sn. The duration of the irradiation run was 6.42 h in the case of protons and 1.083 h in the case of deuterons. The cross section of the deuteron beam had the shape of an ellipse, its axes being 3 and 2 cm. The diameter of the proton beam, which was round in shape, was 2 cm. For beam monitoring, we employed the reactions $^{27}\mathrm{Al}(d, 3p2n)^{24}\mathrm{Na}$ and $^{27}\mathrm{Al}(p, 3pn)^{24}\mathrm{Na}$, their cross sections being 14.2 ± 0.2 [8] and 10.6 ± 0.8 mb [9], respectively. On the basis of this monitoring, we obtained the

---

[1] Yerevan State University, ul. A. Manukyana 1, Yerevan, 375049 Armenia; Joint Institute for Nuclear Research, Dubna, Moscow oblast, 141980 Russia.

[2] Yerevan Institute of Physics, ul. Brat'ev Alikhanian 2, Yerevan, 375036 Armenia.

[3] Nuclear Physics Institute, AVČR, CZ-250 68 Řež, Czech Republic; Joint Institute for Nuclear Research, Dubna, Moscow oblast, 141980 Russia.

[4] Joint Institute for Nuclear Research, Dubna, Moscow oblast, 141980 Russia.

Table 1

Target	Enrichment, %	Thickness, g/cm^2	Weight, g
^{112}Sn	92.6	0.378	2.658
^{118}Sn	98.7	0.201	0.805
^{120}Sn	99.6	0.198	0.791
^{124}Sn	95.9	0.204	0.816

Integrated beam intensities

proton	deuteron
3.21×10^{13}	2.0×10^{13}

following beam intensities: 1.33×10^{13} d/h (^{112}Sn), 0.768×10^{13} d/h (^{118,120,124}Sn), 2.35×10^{13} protons (0.366×10^{13} p/h) (^{112}Sn), and 0.73×10^{13} protons (0.114×10^{13} p/h) (^{118,120,124}Sn). The features of the targets and the integrated beam intensities are given in Table 1.

The induced-activity method was used to explore the yields of radioactive residual nuclei formed in the targets. The gamma spectra of residual nuclei were measured by means of ultrapure germanium detectors at the Research and Experimental Department of Nuclear Spectroscopy and Radiochemistry at the Laboratory of High Energies at JINR. These measurements were performed within a year after the irradiation. The residual nuclei formed in the targets were identified by characteristic gamma lines and by the respective half-lives. The measured spectra were processed on the basis of the DEIMOS code [10].

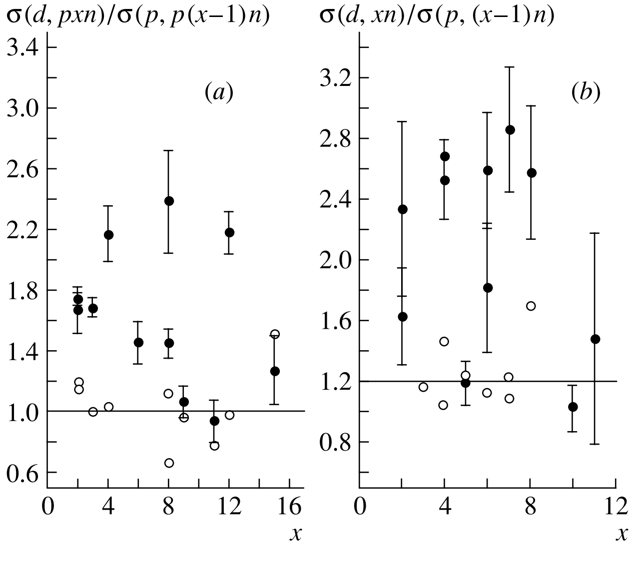

Fig. 1. Ratio of the cross sections for the formation of residual nuclei in deuteron- and proton-induced nuclear reactions versus the number of emitted neutrons: (closed circles) experimental data for all targets and (open circles) results of the calculations within the cascade–evaporation model.

3. EXPERIMENTAL RESULTS AND THEIR DISCUSSION

In the present study, we explored the formation of Sb and Sn isotopes in ^{112,118,120,124}Sn targets. Tables 2 and 3 present the cross sections for the formation of products—independent (I) and cumulative (C) ones—along with the reaction types. Data calculated on the basis of the cascade–evaporation model [11] are given parenthetically. The values quoted in Tables 2 and 3 as the errors in the respective quantities were obtained as the largest deviation of the results of various measurements from the averaged cross-section value. These errors include statistical uncertainties in determining the detector efficiencies, the numbers of particles in a beam, and the number of nuclei in a target.

The data obtained here make it possible to compare the reactions under study for two projectile types, protons and deuterons. A feature peculiar to the reactions induced by deuterons is associated with the looseness of the deuteron structure, so that the question of whether both nucleons of the projectile deuteron are involved in the nuclear interaction is of interest in studying such processes. Figure 1 displays (a) the ratio of the cross sections for the relevant (d, pxn) and $(p, p(x-1)n)$ reactions and (b) the ratio of the cross sections for the relevant (d, xn) and $(p, (x-1)n)$ reactions versus the number of emitted neutrons. In individual measurements, the yields from the reactions induced by protons and deuterons proved to be in agreement within the errors (^{115}Sb and ^{110}Sn from a ^{118}Sn target). In the majority of the reactions being studied, these ratios were on average 1.5 to 2 within the errors and exceeded the ratios obtained from the calculations within the cascade–evaporation model, which yielded values of 1 to 1.2. It can be assumed that these theoretical calculations are insensitive to the fact that the incident deuteron involves two nucleons.

Investigation of the energy dependences of the yields from (p, xn) and (p, pxn) reactions shows that these yields decrease with increasing projectile energy [12–14]. In the present study, the energy dependences of the yields from the reactions being studied are discussed with resort to the data measured previously at 0.66, 1, and 8.1 GeV [6, 7]. From Figs. 2 and 3, one can see that, at energies of a few GeV, the (p, xn) and (p, pxn) cross sections for $x \leq 3$ grow, the slope that characterizes this growth decreasing as the number of emitted neutrons increases. At a large

Table 2. Cross sections for the formation of products of (d, xn) and (d, pxn) reactions

Reaction type	Residual nucleus	Cross-section type	Cross section, mb	Reaction type	Residual nucleus	Cross-section type	Cross section, mb
$^{118}\mathrm{Sn}(d,2n)$	$^{118m}\mathrm{Sb}$	I	$1.6 \pm 0.3\ (0.03)$	$^{112}\mathrm{Sn}(d,p)$	$^{113g}\mathrm{Sn}$	C	15.7 ± 0.3
$^{120}\mathrm{Sn}(d,2n)$	$^{120m}\mathrm{Sb}$	I	1.5 ± 0.3	$^{118}\mathrm{Sn}(d,p2n)$	$^{117m}\mathrm{Sn}$	C	$46.9 \pm 3.5\ (105.2)$
$^{124}\mathrm{Sn}(d,2n)$	$^{124}\mathrm{Sb}$	I	$4.5 \pm 0.6\ (1.011)$	$^{124}\mathrm{Sn}(d,p2n)$	$^{123m}\mathrm{Sn}$	C	94.9 ± 1.0
$^{118}\mathrm{Sn}(d,3n)$	$^{116m}\mathrm{Sb}$	H	2.6 ± 0.2		$^{123g}\mathrm{Sn}$		40.6 ± 4.0
$^{120}\mathrm{Sn}(d,4n)$	$^{118m}\mathrm{Sb}$	I	$3.8 \pm 0.3\ (2.4)$	$^{112}\mathrm{Sn}(d,p3n)$	$^{110}\mathrm{Sn}$	C	$37.8 \pm 0.9\ (39.9)$
$^{124}\mathrm{Sn}(d,4n)$	$^{122}\mathrm{Sb}$	I	$10.5 \pm 1.5\ (1.75)$	$^{120}\mathrm{Sn}(d,p4n)$	$^{117m}\mathrm{Sn}$	C	$33.9 \pm 1.2\ (24.2)$
$^{118}\mathrm{Sn}(d,5n)$	$^{115}\mathrm{Sb}$	C	$5.6 \pm 0.5\ (1.10)$	$^{118}\mathrm{Sn}(d,p6n)$	$^{113g}\mathrm{Sn}$	C	22.8 ± 1.0
$^{120}\mathrm{Sn}(d,6n)$	$^{116m}\mathrm{Sb}$	I	$2 \pm 0.3\ (1.3)$	$^{124}\mathrm{Sn}(d,p8n)$	$^{117m}\mathrm{Sn}$	C	$20.8 \pm 2.4\ (8.1)$
$^{124}\mathrm{Sn}(d,6n)$	$^{120}\mathrm{Sb}$	I	$3.9 \pm 0.3\ (1.76)$	$^{120}\mathrm{Sn}(d,p8n)$	$^{113g}\mathrm{Sn}$	C	$11.3 \pm 0.6\ (10.5)$
$^{120}\mathrm{Sn}(d,7n)$	$^{115}\mathrm{Sb}$	C	$4.3 \pm 0.6\ (0.76)$	$^{118}\mathrm{Sn}(d,p9n)$	$^{110}\mathrm{Sn}$	C	$3.3 \pm 0.3\ (5.3)$
$^{124}\mathrm{Sn}(d,8n)$	$^{118m}\mathrm{Sb}$	I	$2.4 \pm 0.4\ (0.554)$	$^{120}\mathrm{Sn}(d,p11n)$	$^{110}\mathrm{Sn}$	C	$1.5 \pm 0.2\ (2.6)$
$^{124}\mathrm{Sn}(d,10n)$	$^{116m}\mathrm{Sb}$	I	$1.1 \pm 0.3\ (0.032)$	$^{124}\mathrm{Sn}(d,p12n)$	$^{113g}\mathrm{Sn}$	C	$5.9 \pm 0.3\ (6.2)$
$^{124}\mathrm{Sn}(d,11n)$	$^{115}\mathrm{Sb}$	C	$1.2 \pm 0.2\ (0.21)$	$^{124}\mathrm{Sn}(d,p15n)$	$^{110}\mathrm{Sn}$	I	$0.7 \pm 0.1\ (1.5)$

Table 3. Cross sections for the formation of products of (p, xn) and (p, pxn) reactions

Reaction type	Residual nucleus	Cross-section type	Cross section, mb	Reaction type	Residual nucleus	Cross-section type	Cross section, mb
$^{118}\mathrm{Sn}(p,n)$	$^{118m}\mathrm{Sb}$	I	$0.98 \pm 0.05\ (0.694)$	$^{124}\mathrm{Sn}(p,10n)$	$^{115}\mathrm{Sb}$	C	$0.81 \pm 0.4\ (0.125)$
$^{120}\mathrm{Sn}(p,n)$	$^{120m}\mathrm{Sb}$	I	$0.64 \pm 0.07\ (0.662)$	$^{118}\mathrm{Sn}(p,pn)$	$^{117m}\mathrm{Sn}$	C	$28.1 \pm 0.9\ (87.88)$
$^{124}\mathrm{Sn}(p,n)$	$^{124}\mathrm{Sb}$	I	$1.7 \pm 0.2\ (0.324)$	$^{124}\mathrm{Sn}(p,pn)$	$^{123g}\mathrm{Sn}$	I	$54.5 \pm 1.5\ (83.13)$
$^{120}\mathrm{Sn}(p,3n)$	$^{118m}\mathrm{Sb}$	I	$1.5 \pm 0.1\ (1.64)$	$^{112}\mathrm{Sn}(p,p2n)$	$^{110}\mathrm{Sn}$	C	$22.4 \pm 0.7\ (40.09)$
$^{124}\mathrm{Sn}(p,3n)$	$^{122}\mathrm{Sb}$	I	$3.9 \pm 0.2\ (1.94)$	$^{120}\mathrm{Sn}(p,p3n)$	$^{117m}\mathrm{Sn}$	C	$15.6 \pm 1.2\ (23.39)$
$^{118}\mathrm{Sn}(p,3n)$	$^{116m}\mathrm{Sb}$	I	2.1 ± 0.3	$^{118}\mathrm{Sn}(p,p5n)$	$^{113g}\mathrm{Sn}$	C	$15.6 \pm 1.1\ (14.3)$
$^{118}\mathrm{Sn}(p,4n)$	$^{115}\mathrm{Sb}$	C	$4.7 \pm 0.4\ (1.16)$	$^{124}\mathrm{Sn}(p,p7n)$	$^{117m}\mathrm{Sn}$	C	$8.7 \pm 0.7\ (12.29)$
$^{120}\mathrm{Sn}(p,5n)$	$^{116m}\mathrm{Sb}$	I	$1.1 \pm 0.2\ (1.152)$	$^{120}\mathrm{Sn}(p,p7n)$	$^{113g}\mathrm{Sn}$	C	$7.8 \pm 0.3\ (9.37)$
$^{124}\mathrm{Sn}(p,5n)$	$^{120m}\mathrm{Sb}$	I	$1.5 \pm 0.2\ (1.89)$	$^{118}\mathrm{Sn}(p,p8n)$	$^{110}\mathrm{Sn}$	C	$3.1 \pm 0.1\ (5.52)$
$^{120}\mathrm{Sn}(p,6n)$	$^{115}\mathrm{Sb}$	C	$1.5 \pm 0.1\ (0.613)$	$^{120}\mathrm{Sn}(p,p10n)$	$^{110}\mathrm{Sn}$	C	$1.6 \pm 0.1\ (3.36)$
$^{124}\mathrm{Sn}(p,7n)$	$^{118m}\mathrm{Sb}$	I	$0.93 \pm 0.03\ (1.52)$	$^{124}\mathrm{Sn}(p,p11n)$	$^{113g}\mathrm{Sn}$	C	$2.7 \pm 0.1\ (6.33)$
$^{124}\mathrm{Sn}(p,9n)$	$^{116m}\mathrm{Sb}$	I	$1.07 \pm 0.10\ (0.29)$	$^{124}\mathrm{Sn}(p,p14n)$	$^{110}\mathrm{Sn}$	C	$0.55 \pm 0.06\ (0.99)$

number of emitted neutrons, the respective dependences on the projectile-proton energy remain unchanged. Figure 2 displays curves that represent the energy dependences for the residual nuclei (Fig. 2a) $^{116m}\mathrm{Sb}$ and (Fig. 2b) $^{110}\mathrm{Sn}$. The slope that characterizes the growth of the cross section with energy for the residual nucleus $^{110}\mathrm{Sn}$ changes within the range 2.2 ± 0.054 for a $^{112}\mathrm{Sn}$ target and within the range -0.048 ± 0.033 for a $^{124}\mathrm{Sn}$ target. Calculations based on the cascade–evaporation model do not show a growth of the reaction yields in this energy region.

It should be noted that the activation-analysis procedure, which was applied in the present study, gave no way to distinguish between reaction channels

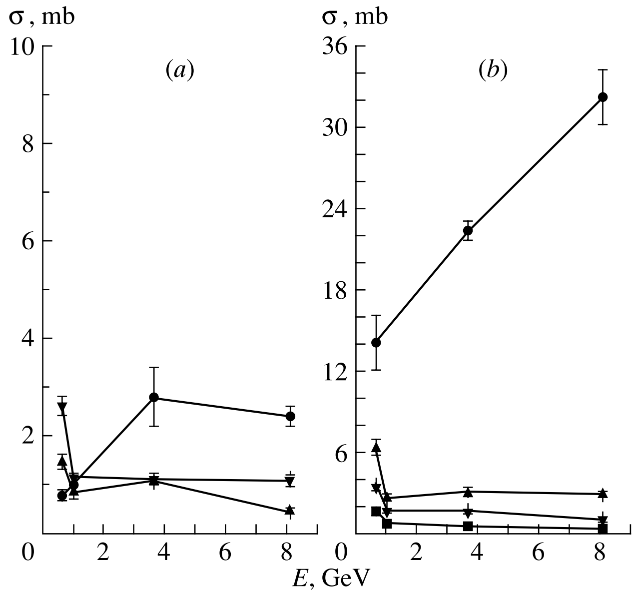

Fig. 2. Cross sections for the formation of residual nuclei versus the projectile-proton energy (a) for ^{116m}Sb from (closed circles) ^{118}Sn, (inverted closed triangles) ^{120}Sn, and (right closed triangles) ^{124}Sn targets and (b) for ^{110}Sn from (closed circles) ^{112}Sn, (right closed triangles) ^{118}Sn, (inverted closed triangles) ^{120}Sn, and (closed boxes) ^{124}Sn targets.

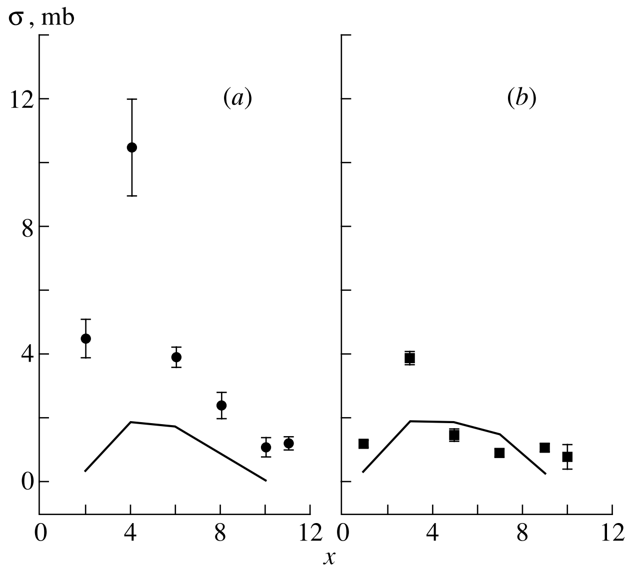

Fig. 3. Cross sections for the (a) (d, xn) and (b) (p, xn) reactions on ^{124}Sn targets versus the number of emitted neutrons. The solid line represents the results of the calculation on the basis of the cascade–evaporation model.

involving different numbers of emitted pions if these channels led to identical final nuclei. Obviously, the above growth of the cross sections can be explained by the contribution of such processes. Calculations within the cascade–evaporation model show that the contribution of meson-production processes is large at energies of 1.84, 3.2, and 6 GeV (see [11, p. 360]) for $A \sim 100$, but that there is virtually no such effect at 0.66 GeV. Our analysis revealed that, in charge-exchange reactions of the (p, n) and (p, pn) types, the contribution of these interaction channels may be significant at high energies.

The character of the dependence of the (d, xn) and (p, xn) yields on the number of emitted neutrons can be seen in Figs. 3a and 3b. The cross sections for these processes first increase and then decrease with increasing number of emitted particles. For the most part, independent yields are given in the figures, but only the isomeric-state (^{116m}Sb, ^{118m}Sb, ^{120m}Sb) yields were determined for the majority of the nuclei. The residual nuclei in the ground states are formed with substantially higher probabilities, and the deviations of the experimental points referring to the yields of ^{124}Sb, ^{122}Sb, and ^{115}Sb are explained by precisely this circumstance. A similar dependence was found in (p, xn) reactions at an energy of 0.66 GeV and in $(\gamma, \pi^{\pm} xn)$ reactions [6, 15]. That the dependences of the cross sections for these reactions on the number of emitted neutrons are similar gives sufficient grounds to assume that the mechanisms of neutron formation in the (d, xn) and (p, xn) reactions are similar. The (d, pxn) and (p, pxn) reactions are characterized by substantially larger (by more than one order of magnitude) cross sections than the (d, xn) and (p, xn) reactions, whose cross sections decrease with increasing number of emitted neutrons. As can be seen from Fig. 3 and from Tables 2 and 3, this pattern is described within the cascade–evaporation model—the shape of the experimental curve is in good qualitative agreement with the predictions of this model. In some cases, it is difficult to perform a quantitative comparison since the measured yields are cumulative in those cases and since experimental information is insufficient in the case where one measures only one state of the isomeric pair of a residual nucleus.

Data on such reactions at low energies are indicative of a pronounced mass dependence of their cross sections for light targets ($A \leq 65$). For heavier targets, the cross sections were measured with large uncertainties, which prevent the isolation of the effect of an increase in the number of nucleons in a nucleus. The set of targets used in the present experiment made it possible to refine the behavior of the cross sections for these reactions in the mass range 112–124 and to verify the effect of the nucleonic composition of the target on the probability of the emission of a few nucleons from the surface of the nucleus. Within the accuracy of our measurements, the presence of the dependence of the reaction yields

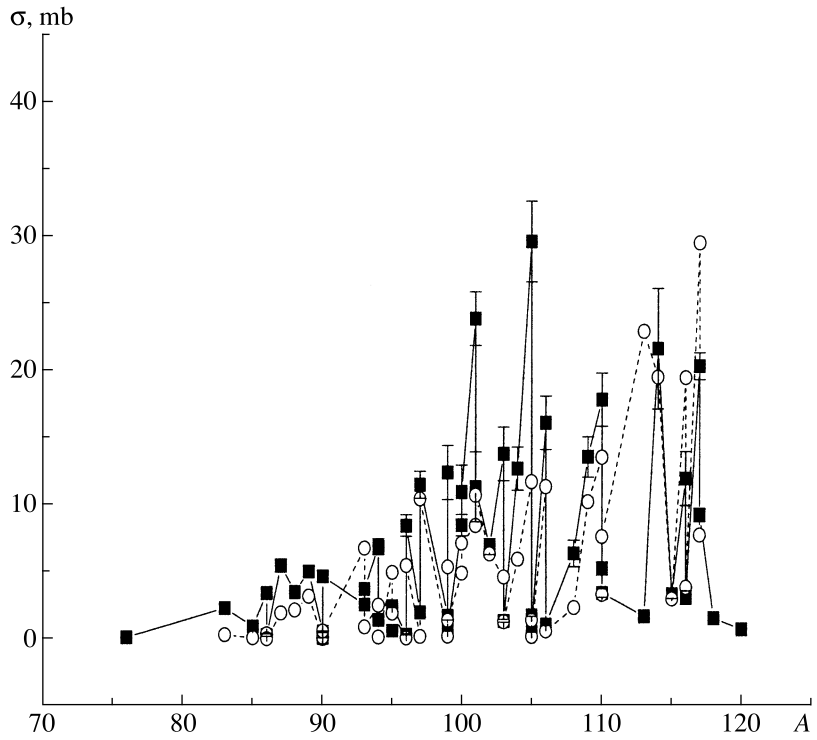

Fig. 4. Cross sections for the formation of residual nuclei versus their mass numbers for ^{120}Sn targets at a projectile-proton energy of 0.66 GeV: (closed boxes) experimental results and (open circles) results of the calculation based on the cascade–evaporation model.

on the nucleonic composition of the targets could not be established by analyzing the yields found here in the form of the ratios of the cross sections for the reactions on tin isotopes in the mass range 118–124 ($1.36 \le N/Z \le 1.48$) in various combinations: $(p, 3n)/(p, n)$, $(p, 5n)/(p, 3n)$, $(p, 5n)/(p, n)$, etc. We can assume that reactions belonging to the class under study proceed via a local interaction of a projectile particle at the target surface with a small number of target nucleons, so that the contribution of the whole target nucleus (including the neutron excess) does not have a significant effect on the yields.

The cross sections for the formation of about 60 residual nuclei have been measured for ^{120}Sn targets irradiated with a proton beam accelerated to an energy of 0.66 GeV at the phasotron of the Laboratory of Nuclear Processes at JINR. The values obtained in this way for the reaction yields were compared with their counterparts calculated within the cascade–evaporation model [11]. Figure 4 displays the reaction cross sections versus the mass number of a residual nucleus. In comparing the experimental values with the results of the calculations, use was made of the parameter [16]

$$H = 10^{\sqrt{\langle(\log(\frac{\sigma_{\text{calc } i}}{\sigma_{\text{expt } i}}))^2\rangle}},$$

whose standard deviation is $S(\langle H\rangle) = 10^{\sqrt{a}}$, where

$$a = \left\langle \left(\left| \log\left(\frac{\sigma_{\text{calc } i}}{\sigma_{\text{expt } i}}\right) \right| - \log(\langle H\rangle) \right)^2 \right\rangle.$$

Here, $\langle\ \rangle$ denotes averaging over all cases under comparison ($i = 1, \ldots, N_s$, where N_s is the number of experimental and calculated values subjected to a comparison). The resulting values of $\langle H\rangle = 3.18$ and $S(\langle H\rangle) = 2.07$ indicate that there is no satisfactory agreement between the experimental and calculated values.

4. CONCLUSIONS

New data have been obtained for the (p, xn) and (p, pxn) processes on enriched tin isotopes ^{112,118,120,124}Sn for $1 \le x \le 14$ at an energy of 3.65 GeV/nucleon.

(i) The cross sections for the (p, xn) and (p, pxn) reactions for $x \le 3$ first decrease and then increase in the energy region above 1 GeV. The character of changes in the cross sections over the range 1–8.1 GeV can be approximated by a linear dependence whose slope decreases with increasing number of emitted neutrons. The above growth of the cross sections can be explained by the presence of the contributions to the yields of measured residual products from pion-production channels.

For reactions involving the emission of more than four neutrons, the cross sections remain virtually constant over the above energy range, this being in agreement with the results of the calculations based on the cascade–evaporation model.

(ii) Changes in the reaction yields versus the number of emitted neutrons—that is, the presence of a maximum followed by a decrease—can be qualitatively described within the cascade–evaporation model.

(iii) Measured ratios of the reaction cross sections, $(d, xn)/(p,(x-1)n)$ and $(d, pxn)/(p, p(x-1)n)$, do not agree with the predictions of the model proposed in [11]—on average, the experimental values exceed their calculated counterparts by a factor of 1.5 to 2.

(iv) No pronounced dependence on the isotopic composition of the targets has been observed. This can be a consequence of a local character of the interaction, in which case only a few nucleons are emitted. The primary charge-exchange process involves a small number of neutrons, and an increase in the total number of neutrons in the target nucleus does not manifest itself in the reaction yield.

The cross sections for the spallation reactions on the ^{120}Sn isotope at a projectile-proton energy of 0.66 GeV have been obtained. Respective calculations within the cascade–evaporation model have made it possible to obtain a qualitative pattern that is consistent with the experimental dependence of the cross sections on the mass number of a residual nucleus. A quantitative comparison on the basis of the criterion proposed in [16] indicates that this description of our experimental data is unsatisfactory.

REFERENCES

1. W. J. Treytl and A. A. Caretto, Phys. Rev. **146**, 836 (1966).
2. L. B. Church and A. A. Caretto, Phys. Rev. **178**, 1732 (1969).
3. M. A. Molecke and A. A. Caretto, Phys. Rev. C **15**, 719 (1977).
4. Y. Nagame, S. Baba, and T. Saito, Appl. Radiat. Isotopes **45**, 281 (1994).
5. T. Asano, Y. Asano, Y. Iguchi, *et al.*, Phys. Rev. C **28**, 1840 (1983).
6. A. S. Danagulyan, L. G. Martirosyan, N. S. Amelin, *et al.*, Yad. Fiz. **60**, 965 (1997) [Phys. At. Nucl. **60**, 863 (1997)].
7. V. E. Aleksandryan, J. Adam, A. R. Balabekyan, *et al.*, Yad. Fiz. **65**, 810 (2002) [Phys. At. Nucl. **65**, 776 (2002)].
8. Ts. Damdinsuren, V. I. Ilyushchenko, *et al.*, Preprint No. P1-89-757, OIYaI (Joint Institute for Nuclear Research, Dubna, 1989).
9. R. Michel, M. Gloris, H.-J. Langs, *et al.*, Nucl. Instrum. Methods Phys. Res. B **103**, 183 (1995).
10. J. Frana, J. Radioanal. Nucl. Chem. **257**, 3 (2003).
11. V. S. Barashenkov and V. D. Toneev, *Interactions of High-Energy Particles and Nuclei with Nuclei* (Atomizdat, Moscow, 1972) [in Russian]; Zh. Musulmanbekov and B. Khulerbaatar, Preprint No. P2-99-59, OIYaI (Joint Institute for Nuclear Research, Dubna, 1999).
12. R. Michel, R. Bodemann, H. Busemann, *et al.*, Nucl. Instrum. Methods Phys. Res. B **129**, 153 (1997).
13. I. V. Moskalenko and S. G. Mashnik, LANL Report, LA-UR-03-3323; in *Proceedings of the 28th ICRC, Tsukuba, 2003*, p. 1969.
14. Yu. E. Titarenko, V. F. Batyaev, *et al.*, LANL Report, LA-UR-03-3403.
15. A. A. Arakelyan, A. R. Balabekyan, A. S. Danagulyan, and A. G. Khudaverdyan, Yad. Fiz. **50**, 1226 (1989) [Sov. J. Nucl. Phys. **50**, 763 (1989)].
16. R. Michel and P. Nagel, NEA/OECD, NSC/DOC(97)-1 (Paris, 1997).

Translated by A. Isaakyan

Physics of Atomic Nuclei, Vol. 68, No. 2, 2005, pp. 177–183. From Yadernaya Fizika, Vol. 68, No. 2, 2005, pp. 201–208.
Original English Text Copyright © 2005 by Pikul, Jovliev, Koblik, Khugaev, Muminov, Nasirov, Pavliy, Yuldashev.

NUCLEI
Experiment

Analysis of Fragment Mass Distribution in Asymmetric Area at Fission of ^{235}U Induced by Thermal Neutrons*

V. P. Pikul[1], U. Yu. Jovliev[2], Yu. N. Koblik[1], A. V. Khugaev[1], A. I. Muminov[2], A. K. Nasirov[2),3)], K. V. Pavliy[2], and B. S. Yuldashev[1]

Received October 10, 2003; in final form, June 26, 2004

Abstract—The fragment mass yields in fission of ^{235}U induced by thermal neutrons for $A = 145{-}160$ and $E_K = 50{-}75$ MeV were measured using a mass spectrometer. The fine structure is observed at $A = 153$, 154 and $E_K = 50{-}60$ MeV. The obtained results were described in the framework of a model based on the dinuclear system concept. The analyzed correlation between the total kinetic energy and mass distribution of fission fragments is connected with the shell structure of the formed fragments of fission. From this correlation and the time dependence of the calculated mass distribution of the binary reaction products, one can conclude that the descent time from a saddle point to a scission point for the more deformed fragments is longer than that for fragments of more compact shape. *© 2005 Pleiades Publishing, Inc.*

1. INTRODUCTION

The complete understanding of the nuclear fission mechanism and dynamics of mass distribution is yet to be achieved. Nuclear fission is one of the most complex nuclear transformations, related to a strong change of compound nucleus shape, leading to formation of two or three (ternary fission) fragments having an excitation energy that is sufficient for emission of several neutrons and γ quanta. It is difficult to obtain complete information reflecting the dynamics of fission processes during experiment. The process of fission allows us to observe a nucleus of abnormally high deformation and large surplus of neutrons, which opens opportunities of research of such properties of the nucleus as collective movement with large amplitude, strength functions of β decay, and viscosity and friction of a nuclear matter.

The exploration of mass and charge distributions of fission fragments and their kinetic energy is an important task in the analysis of the fission process. In Section 2, we present and discuss the results of measurements of mass and kinetic energy distributions of the fission products of ^{236}U. Section 3 is devoted to the calculation of the mass distribution between fragments of fission in the framework of the dinuclear system model. In Section 4, the theoretical and experimental results are compared and discussed. Conclusions are in Section 5.

2. EXPERIMENT

We carried out measurements of mass (A) and kinetic energy (E_K) distributions of the heavy fission products of ^{236}U in a region where there are not enough experimental data, namely, $A = 150{-}160$ and $E_K = 50{-}75$ MeV. Measurements were performed using an electromagnetic mass spectrometer for the unslowed fission products [1]. It was placed on the horizontal channel nuclear reactor VVR-SM of the Institute of Nuclear Physics of the Academy of Sciences of Uzbekistan. The accuracies of measurements of kinetic energy and mass of fission products were equal to 0.02 and 0.06%, respectively.

Mass distributions of the heavy products with kinetic energies $E_K = 50, 55, 60, 65, 70$, and 75 MeV, which were measured in fission of ^{235}U induced by thermal neutrons [2], are presented in Fig. 1. The structure at $A = 144{-}146$ in the range $E_K = 50{-}60$ MeV (Fig. 1) is, most likely, connected to large probability of formation of complementary light fragments with $A = 90{-}92$ [2]. The contour diagrams of the shell corrections, which are designed on the Wilkins model [3], show (Fig. 2) that there are areas with the minima of the potential energy corresponding to the small deformations of fragments with the magic numbers $Z = 50$ of protons and $N = 50, 82$ of neutrons and to the large deformations $\beta = 0.6{-}0.7$ of fragments with the proton numbers $Z = 40, 44$ and the neutron numbers $N = 66, 88$ of fission fragments.

---

*This article was submitted by the authors in English.

[1] Institute of Nuclear Physics, Tashkent, Uzbekistan.

[2] Heavy-Ion Physics Department, Institute of Nuclear Physics, Tashkent, Uzbekistan.

[3] Bogolyubov Laboratory of Theoretical Physics, Joint Institute for Nuclear Research, Dubna, Moscow oblast, 141980 Russia.

1063-7788/05/6802-0177$26.00 © 2005 Pleiades Publishing, Inc.

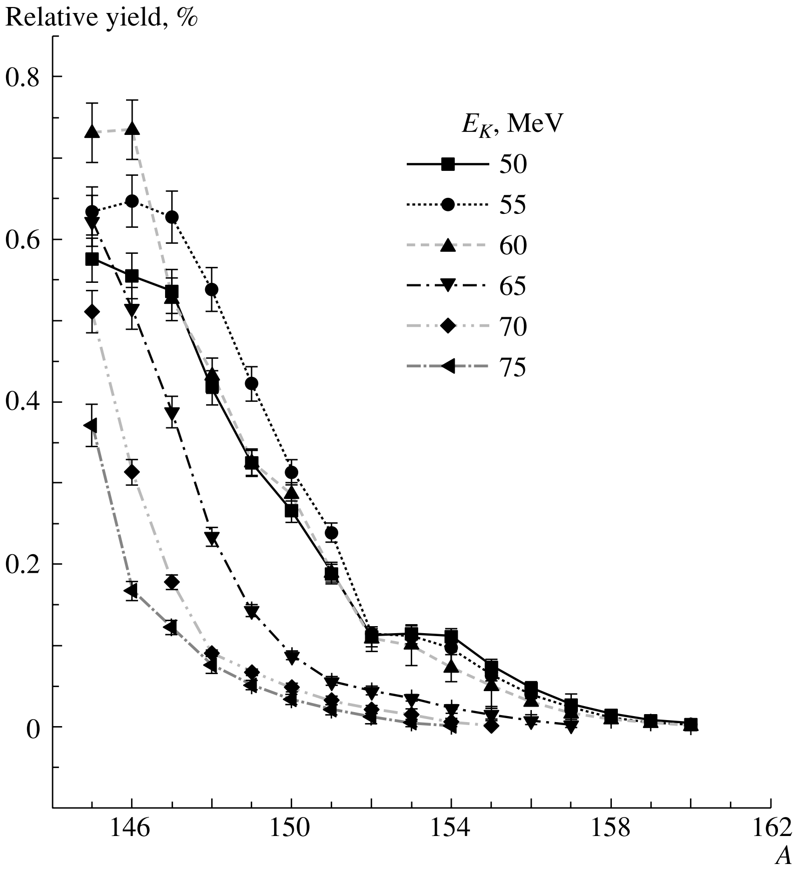

Fig. 1. Mass distributions of fragments by energies $E_K = 50{-}75$ MeV in fission of ^{235}U induced by thermal neutrons.

The distance between centers of fragments is around 15.5 fm for the small deformations of fragments and it is equal to 17 fm for the large deformations of fragments. The total kinetic energy (TKE) of the fission fragments was determined from the measured values of E_K for a heavy fragment by formula

$$\mathrm{TKE} = E_K(A_0/(A_0 - A_H - \nu_H)). \qquad (1)$$

Here, A_0 is the mass number of a compound nucleus, A_H is the mass number of a heavy fragment, E_K is the kinetic energy of a heavy fragment, and ν_H is the number of neutrons from a heavy fragment determined by the formula [4]

$$\nu_H = 0.531\nu + 0.062(A_H - 143), \qquad (2)$$

where ν is average number of neutrons emitted from a fissionable nucleus (in the case of fission of ^{235}U induced by thermal neutrons, $\nu = 2.35$). From the definition of TKE, the distance between centers of ellipses at a scission point was calculated by the formula [5]

$$D = Z^2 R_a e^2/(\mathrm{TKE}(1 + R_a)^2), \qquad (3)$$

where Z is the charge of a fissionable nucleus, R_a is the mass relation A_H/A_L, and $e^2 = 1.44$ MeV fm. Assuming $D = c_1 + c_2$, we can find the shape of fragments at the scission point. The deformation parameter of fragments was calculated using the expression

$$\beta = 1.05(c_i - a_i)/(a_i^2 c_i)^{1/3}, \qquad (4)$$

where c_i and a_i are the large and small axes of ellipse, respectively.

The mass yields of fragments in fission of ^{235}U induced by thermal neutrons were calculated in [3] as a function of the distance between centers of fission fragments at the scission point. Two-dimensional contour diagrams of these dependences have been constructed. In these contour diagrams, the correlation between the distance D and different values of TKE (Fig. 2) can be established. Rather good agreement between the mass yields measured by us and calculated using the Wilkins model [3] is observed. The large probability of formation of fission fragments with $A = 146{-}150$ with relatively low kinetic energies is connected with the increase in the shell corrections for deformation parameters $\beta = 0.6{-}0.7$, which corresponds to the distance between centers of fragments $D \approx 17$ fm (Fig. 2), because the values of TKE for the given pair of fragments are defined by their deformation parameters β at the scission

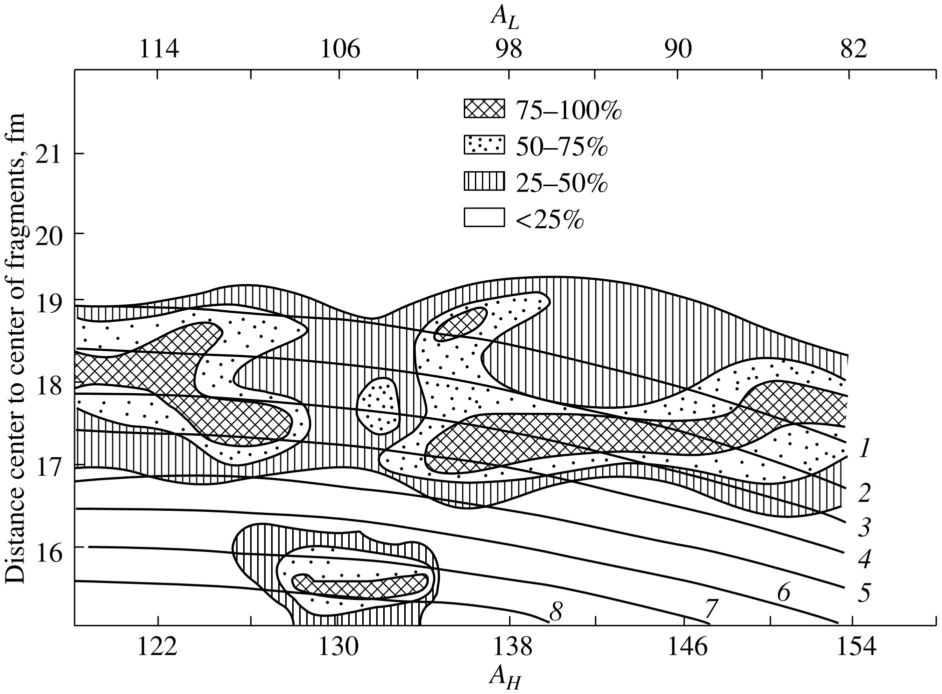

Fig. 2. The contour diagram of the fragment mass yields in fission of ^{235}U induced by thermal neutrons as a function of distance between centers at a scission point. Curves *1*–*8* show values of distance at fixed values of TKE: (*1*) 160, (*2*) 165, (*3*) 170, (*4*) 175, (*5*) 180, (*6*) 185, (*7*) 190, (*8*) 195 MeV.

point. The shell structure of a nucleus is determined by the deformation parameters and vice versa. At the scission point, the fission fragments have such values of β which correspond to minima of potential energy. The position of these minima depends strongly on the number of protons and neutrons in nuclei. It is well known that the value and shape of the potential energy surface of a fissionable nucleus determine the mean value and dispersion, respectively, of the kinetic energy of fission fragments and their mass and charge distributions.

The excitation energy on the scission point can be found using the value of TKE from measurements, the number of all the emitted neutrons by formula (2), and the Q_{gg} value obtained from the half-empirical mass formula in [6] and the tables by Milton [7]. We think that further development of this method by inclusion of the factors influencing the dynamics of the fission process (for example, friction forces) will make it possible to find a change in the form of a nucleus descending from a saddle point to a scission point.

3. MASS DISTRIBUTION OF FISSION FRAGMENTS IN THE DINUCLEAR-SYSTEM MODEL

The nuclear-physical research with heavy ions at low energies has opened a new class of nuclear processes: deep-inelastic nucleon transfer, fusion–fission, and quasi-fission reactions [8, 9]. In the dinuclear system (DNS) concept, the formation of the transient nuclear complex DNS is supposed to be a common mechanism in these processes [8, 10–12]. In heavy-ion collisions at low energies, after complete dissipation of kinetic energy of the relative motion, a DNS is formed. Such a system differs from nuclear molecules in its instability and variable mass asymmetry due to nucleon transfer from one nucleus to another. These peculiarities of the DNS carry a statistical property and proceed on the large fluctuation of the charge and mass numbers and on the dispersion of TKE of fragments at its decay. The main feature in the behavior of the DNS is the preservation of individuality of its component nuclei that is caused by their shell structure. It does not mean that nuclei are frozen. Nucleon exchange between components of the DNS occurs, while the system evolves to a configuration with the minimal surface energy. Motion of the fissioning nucleus from the saddle point up to a scission point can be considered as a slow relative motion of two fragments being formed, since its shape looks like a DNS. At this stage, the mass yields of fission fragments could be calculated in the framework of a model DNS [10–12]. This is opposite to the case of fusion of nuclei, when mass (charge) transfer between interacting nuclei causes evolution of the DNS in the direction of complete fusion (transfer of all nucleons of a light nucleus into a heavy one). In this paper, we consider fission of the ^{235}U nucleus induced by a neutron in the framework of the DNS concept. The aim is an estimation of the mass distribution between fragments during the fission process. We did not consider dynamics of elongation of the dividing system. The elongation of the system is a slow changing variable in comparison with the nucleon-exchange process between the fragments being formed. The DNS is assumed to have some initial charge asymmetry Z and $Z_{\rm CN} - Z$ ($Z_{\rm CN}$ is the charge of the dividing nucleus) after overcoming the saddle point. During slow descent of the fissioning system from the saddle point to the scission point, its mass and charge asymmetries fluctuate due to continuous nucleon exchange between the fragments being formed. This fluctuation is considered as a diffusion process and may be simulated as a nucleon transfer between fragments up to the scission point. This kind of evolution of the DNS by nucleon transfer can be calculated by the master equation of Pauli

$$dP_Z(t)/dt = \Delta^{(+)}_{Z-1} P_{Z-1}(t) \tag{5}$$
$$+ \Delta^{(-)}_{Z+1} P_{Z+1}(t) - \Delta_Z P_Z(t),$$

where $\Delta_Z = \Delta^{(+)}_Z + \Delta^{(-)}_Z$. Here, $P_Z(t)$ is the probability that one of the fragments of the DNS has the charge Z, while the other fragment has the charge $Z_{\rm CN} - Z$; the transition coefficients $\Delta^{(+)}_Z$ and $\Delta^{(-)}_Z$ are responsible for transforming the DNS from the charge-asymmetry state $\{Z; Z_{\rm CN} - Z\}$ into $\{Z+1; Z_{\rm CN} - (Z+1)\}$ and $\{Z-1; Z_{\rm CN} - (Z-1)\}$ states, respectively. $\Delta^{(+)}_Z$ and $\Delta^{(-)}_Z$ were calculated by averaging the nucleon-exchange probability between nuclei Z and $(Z_{\rm CN} - Z)$ over $\Delta t = 10^{-22}$ s:

$$\Delta^{(+)}_Z = 2\sum_{ij} \left| g^{(Z)}_{ij} \right|^2 (2l_i + 1) \tag{6}$$
$$\times (2l_j + 1) n_i^{(Z_{\rm CN}-Z)} (1 - n_j^{(Z)})$$
$$\times (E_i^{(Z_{\rm CN}-Z)} - E_j^{(Z)})^{-2} W_{ij}^{(Z)}/\Delta t,$$

$$\Delta^{(-)}_Z = 2\sum_{ij} \left| g^{(Z)}_{ij} \right|^2 (2l_i + 1)(2l_j + 1) n_j^{(Z)} \tag{7}$$
$$\times (1 - n_i^{(Z_{\rm CN}-Z)})(E_i^{(Z_{\rm CN}-Z)} - E_j^{(Z)})^{-2} W_{ij}^{(Z)}/\Delta t,$$

where

$$W_{ij}^{(Z)} = \sin^2[(E_i^{(Z_{\rm CN}-Z)} - E_j^{(Z)})\Delta t/\hbar]; \tag{8}$$

$n_i^{(Z_{\rm CN}-Z)}$, $E_i^{(Z_{\rm CN}-Z)}$, l_i and $n_j^{(Z)}$, $E_j^{(Z)}$, l_j are occupation numbers, energies, and degeneracy factors of the single-particle states in one and the other fragment of the DNS, respectively, and $g^{(Z)}_{ij}$ are the matrix elements of nucleon transition between single-particle states i and j of fragments $(Z_{\rm CN} - Z)$ and Z of the DNS, respectively. Matrix elements $g^{(Z)}_{ij}$ describe a nucleon exchange between nuclei of the DNS, and their values were calculated microscopically using the expression obtained in [13]. The relaxation of the mass asymmetry degree of freedom achieves the equilibrium value in time $\tau_{\rm mass} = 2 \times 10^{-21}$ s (see Fig. 3). The single-particle occupation numbers are found as a solution of the master equation in the framework of the model presented in [14]. Equation (5) with coefficients (6) and (7) at the initial condition $P_Z(0) = \delta_{ZZ_p}$ has been solved numerically, and the primary isotope distributions are found for a certain descent time $t_{\rm fis}$ from the saddle point to the scission point. The final result of calculations is obtained after averaging the solution of Eq. (5) with the different initial conditions for the charge asymmetry of the DNS $\{Z_p, Z_{\rm CN} - Z_p\}$ ($Z_p = 2, 4, 6, \ldots, 46$) after overcoming the saddle point of the fission path. The analysis showed that the solutions of Eq. (5) for different initial conditions starting from $Z_p > 32$ are qualitatively alike at $t_{\rm fis} > 1.5 \times 10^{-20}$ s. The quantitative description of the yield of fission products was performed in the way suggested in [10, 11], but for the matrix elements $g^{(Z)}_{ij}$, the expressions obtained in [13] have been used. To take into account decay of the DNS, the term $\Lambda^{\rm fis}_Z P_Z(t)$ was subtracted from the right side of Eq. (5),

$$dP_Z(t)/dt = \Delta^{(+)}_{Z-1} P_{Z-1}(t) \tag{9}$$
$$+ \Delta^{(-)}_{Z+1} P_{Z+1}(t) - \Delta_Z P_Z(t) - \Lambda^{\rm fis}_Z P_Z(t),$$

where $\Lambda^{\rm fis}_Z$ is "Kramer's rate" for the decay probability of the DNS to fragments with charge numbers Z and $Z_{\rm CN} - Z$ [12] and is proportional to $\exp(-B^{\rm fis}_Z/T)$ with the fission barrier $B^{\rm fis}_Z$ and DNS temperature T at formation of fragments Z and $Z_{\rm CN} - Z$. The yield of fission products with the charge Z during time $t_{\rm fis}$ is found by the expression

$$Y_Z = \Lambda^{\rm fis}_Z \int\limits_{t_0}^{t_{\rm fis}} P_Z(t)dt, \tag{10}$$

where t_0 is the start time of descent from the saddle point and it is equal to zero. The results of calculation (Fig. 3) reflect peculiarities of the experimental data (Fig. 1) for the case of superasymmetric fission of a ^{235}U nucleus induced by neutrons. There are bumps in the mass distribution of fragments at charge numbers $Z = 50$ and 54. Analyzing the evolution of mass asymmetry as a function of time, we found that, in fission induced by neutrons, the relaxation time of the degree of freedom connected with the mass (charge) asymmetry of the breaking-up dinuclear system is 10^{-20} s (Fig. 4). The time dependence of the calculated mass yield of fragments shows that, in mass distribution, the appearance of the fine structure around $A_H = 134$, 144, 150, and 154 is enhanced with increasing fission time, because large shell corrections in this region lead to an increase in the transition probability to this region of mass asymmetry from the other configurations. We should stress that the effects of shell structure are included in the expressions of the transition coefficients $\Delta_Z^{(+)}$ (6) and $\Delta_Z^{(-)}$ (7) of the master equation by means of occupation numbers, energies, and degeneracy of the single-particle states and matrix elements $g_{ij}^{(Z)}$ of nucleon transition between single-particle states i and j in fragments $(Z_{\rm CN} - Z)$ and Z. The theoretical results obtained in this paper show good agreement with the well-known behavior of the mass distribution shape of the ^{236}U fission fragments, which has two wide bumps around mass numbers $A = 102$ and 134 [15] and charge numbers $Z = 40$ and 52 [16]. We confirm that the reason for location of the bumps at these mass and charge regions is an increase in shell effects due to the neutron number $N = 82$ in the heavy fragment $A = 134$. Notice that the neutron emission is not taken into account in calculation of this mass distribution.

4. COMPARISON OF THE MEASURED AND CALCULATED MASS YIELDS FOR $A = 145$–160

Comparison of the experimental and calculated results on mass yields of the fission fragments allows us to establish a correlation between the shape of nuclei at the scission point and descent time of the nuclear complex from the saddle point to the scission point. The experimental data showed (Fig. 1) a fine structure for fission fragments with small kinetic energies in the region of masses $A = 145$–152. It was explained by the large shell corrections at larger deformation parameters of the heavy fragment (Fig. 2). The yield of fragments with low kinetic energies is several times larger than that with larger kinetic energies $E_K > 65$ MeV (see Fig. 1). In the calculations, which were performed in the framework of the presented model (Section 3), we found that the appearance of the fine structure in the yield of fission products is enhanced more strongly by an increase in descent time of fission ($t_{\rm fis}$) from the saddle point to the scission point (Fig. 4). Based on the calculated mass distribution, we assume that the hillock on the experimental curves corresponding to the yield of fragments with kinetic energies $E_K = 50$, 55, and 60 MeV is a consequence of the large shell effects in the conjugate light fragments having the mass number $A = 82$ and charge number $Z = 32$ ($N = 50$). The curves describing theoretical results have peaks around the mass numbers $A = 134$, 144, 150, 154, and 158 (Fig. 3). Three of them at the mass numbers $A = 144$, 150, 154 are seen in the measured yields of mass fragments with lower kinetic energies (Fig. 5). The theoretical results obtained for the short descent time $t_{\rm fis} \leq 2 \times 10^{-21}$ s (solid curve, Fig. 5) do not show any fine structure. Therefore, the absence of the fine structure in the curves corresponding to the yield of fragments with the kinetic energies $E_K = 65$, 70, and 75 MeV is explained by the short fission time of ^{236}U, which is too short for the appearance of shell-structure effects. The conclusion is that the fine structure in the mass yield appears more strongly if the descent time of the system from the saddle point to the scission point increases. This indicates the existence of a correlation between the shape of fragments at the scission point and formation time of mass distribution. We conclude as well that, if a formation of mass distribution occurs during the descent time from the saddle point, then the more deformed fragments are formed for a longer time than fragments of more compact shape (Fig. 4). The strong appearance of peculiarities of shell structure in one or both fragments being formed causes the fine structure

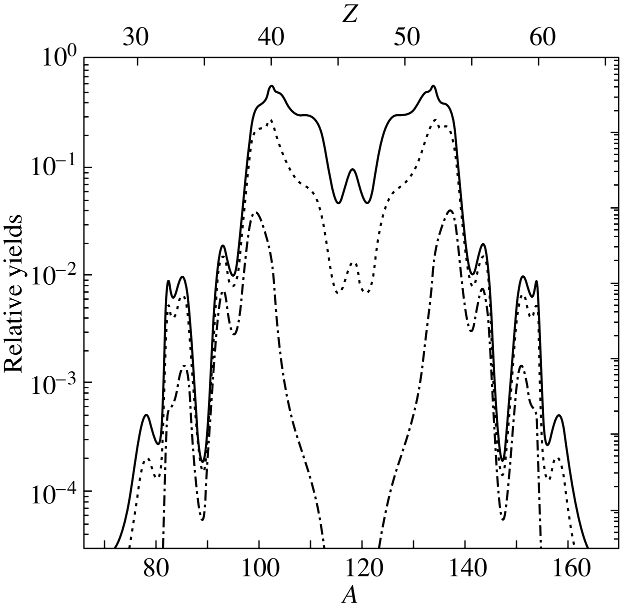

Fig. 3. The mass yields of the fragments in fission of the ^{236}U nucleus calculated in the DNS model: solid, dotted, and dash-dotted curves correspond to the descent times from a saddle point to a scission point $t_{\rm fis} = 2 \times 10^{-20}$, 10^{-20}, and 2×10^{-21} s, respectively.

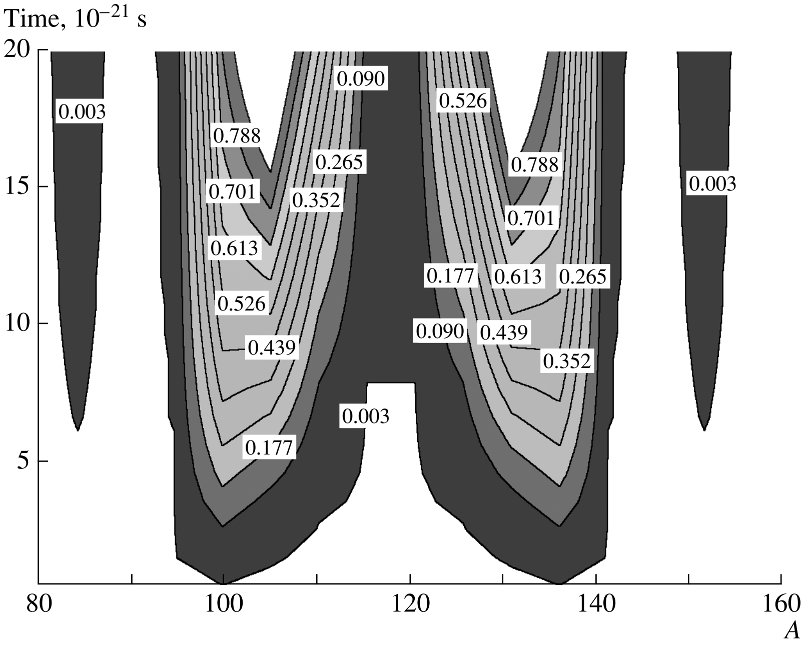

Fig. 4. Time dependence of mass yields of the fission fragments of ^{236}U calculated in this paper. The numbers show relative yield.

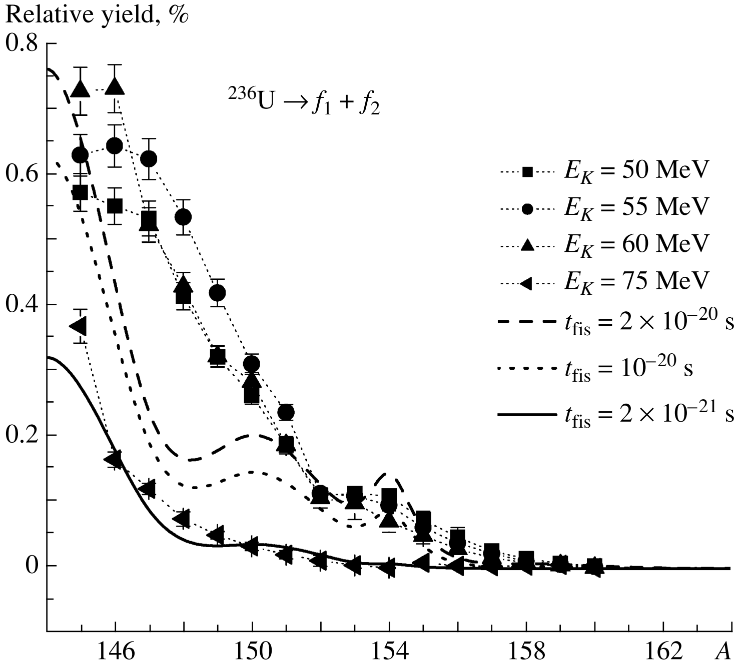

Fig. 5. Comparison of the calculated mass yields of fission fragments for the descent times from a saddle point to a scission point $t_{\text{fis}} = 2 \times 10^{-20}$, 10^{-20}, and 2×10^{-21} s (curves) with the measured data for the heavy fragments with kinetic energies $E_K = 50$, 55, 60, and 75 MeV (symbols connected by dotted lines).

even at short descent time. This is connected with the increase in nuclear shell effects for the neutron number $N = 82$ in the light fragment. Due to strong shell effects for the configuration of the nuclear system with the charge numbers $Z_1 = 40$ and $Z_2 = 52$ and atomic mass numbers $A_1 = 102$ and $A_2 = 134$ of its fragments, the main bumps in the calculated mass yield of the primary fragments in fission of ^{236}U appear even at small values of the descent time. The fission time must be greater than 1.2×10^{-21} s for the formation of this shape of mass distribution.

5. CONCLUSION

The experimental data on the mass yield of fission of ^{235}U induced by thermal neutrons for $A = 145-160$ and $E_K = 50-75$ MeV measured by a mass spectrometer are presented. The fine structure is found at $A = 153$, 154 and $E_K = 50-60$ MeV. In the $A = 145-160$ region of mass distribution, the yield of fragments with lower kinetic energies is several times higher than that with larger kinetic energies (see Fig. 1). It was explained by the increase in shell corrections at larger deformation parameters of the heavy fragment (Fig. 2). The time dependence of the mass yields of fragments was analyzed in the framework of a model based on the dinuclear system concept and using transport equations for nucleon transfer. Our theoretical results showed that the fine structure in the fragment mass distribution is pronounced more strongly with the increase in the descent time (t_{fis}) from the saddle point to the scission point. Assuming the existence of the correlation between the shape of fragments at the scission point and formation time of mass distribution, we can conclude that the formation time of the fragments with lower kinetic energies (more deformed nuclear shape) is longer than that for fragments having higher kinetic energies (more compact nuclear shape). The main maxima of the calculated mass yields of primary fragments in fission of ^{235}U induced by thermal neutrons are placed at charge numbers $Z_1 = 40$ and $Z_2 = 52$ and atomic mass numbers $A_1 = 102$ and $A_2 = 134$, which is in good agreement with the experimental data [15, 16]. The theoretical results showed peaks in the mass yield around the mass numbers $A = 134$, 144, 150, 154, and 158 (Fig. 3). Three of them at the mass numbers $A = 144$, 150, 154 are seen in the measured yields of mass fragments with lower kinetic energies (Fig. 5) in the experiment using the electromagnetic mass spectrometer at the Institute of Nuclear Physics of the Academy of Sciences of Uzbekistan. The hillock in the mass yield at $A_1 < 78$ ($A_2 > 158$) was observed in the experiment by A. Goverdovsky and his colleagues [15]. Complete analysis of experimental data demands the performance of dynamical calculations, which include the dependence of deformation parameters of nuclei on the peculiarities of shell structure.

ACKNOWLEDGMENTS

We thank Prof. R.V. Jolos and Prof. V.V. Volkov for useful discussions.

We are grateful to STCU (grant Uzb-45) for financial support; one of us, A.K.N., thanks INTAS for partial support.

REFERENCES

1. U. A. Arifov, V. A. Kogan, V. P. Pikul, *et al.*, in *Proceedings of the 8th International EMIS Conference on Low Energy Ion Accelerators and Mass Separators, Goteborg, Sweden, 1973,* p. 226; Y. N. Koblik, V. P. Pikul, and B. S. Yuldashev, in *Proceedings of the 4th International Conference "Modern Problems of Nuclear Physics", Tashkent, Sept. 25–29, 2001*, p. 102.
2. G. Siegert, H. Wollnik, J. Greif, *et al.*, Phys. Rev. C **14**, 1864 (1976).
3. B. D. Wilkins, E. P. Steinberg, and R. R. Chasman, Phys. Rev. C **14**, 1832 (1976).
4. A. C. Wahl, R. L. Ferguson, D. R. Nethaway, *et al.*, Phys. Rev. **126**, 1112 (1962).
5. S. Prakash, S. B. Manohar, S. B. Dange, *et al.*, J. Inorg. Nucl. Chem. **34**, 2685 (1972).
6. V. A. Kravtsov, *Masses and Binding Energies of Nuclei* (Atomizdat, Moscow, 1974), p. 340 [in Russian].
7. Y. C. Milton, *Fission Energy Tables and an Application to Nuclear Division* (Berkley, California, 1962).
8. V. V. Volkov, in *Proceedings of Nucleus–Nucleus Collision II, Visby, 1985*, Ed. by B. Jakobson and K. Aleclett (North Holland, Amsterdam, 1985), Vol. 1, p. 54; Izv. Akad. Nauk SSSR, Ser. Fiz. **50**, 1879 (1986); in *Proceedings of International School–Seminar on Heavy-Ion Physics, Dubna, 1986*, Preprint No. D7-87-68, JINR (Dubna, 1987), p. 528; in *Proceedings of the 6th International Conference on Nuclear Reaction Mechanisms, Varenna, 1991*, Ed. by E. Gadioli; Ricerca Scientifica ed Educazione Permanente Suppl., No. 84, 39 (1991).
9. W. U. Schroder and J. R. Huizenga, in *Treatise on Heavy-Ion Science*, Ed. by D. A. Bromley (Plenum Press, New York, 1984), Vol. 2, p. 115.
10. R. V. Jolos, A. I. Muminov, and A. K. Nasirov, Yad. Fiz. **44**, 357 (1986) [Sov. J. Nucl. Phys. **44**, 228 (1986)].
11. R. V. Jolos, S. M. Lukyanov, A. K. Nasirov, *et al.*, Yad. Fiz. **50**, 382 (1989) [Sov. J. Nucl. Phys. **50**, 239 (1989)].
12. G. Fazio *et al.*, in *Proceedings of International Symposium on New Projects and Lines of Research in Nuclear Physics, Messina, Italy, 24–26 Oct., 2002*, Ed. by G. Giardina and A. Lamberto (World Sci., Singapore, 2003), p. 258.
13. G. G. Adamian, R. V. Jolos, and A. K. Nasirov, Yad. Fiz. **55**, 660 (1992) [Sov. J. Nucl. Phys. **55**, 366 (1992)].
14. G. G. Adamian, R. V. Jolos, A. I. Muminov, and A. K. Nasirov, Phys. Rev. C **53**, 871 (1996).
15. A. A. Goverdovsky, V. F. Mitrofanov, and V. A. Khryachkov, Yad. Fiz. **58**, 1546 (1995) [Phys. At. Nucl. **58**, 1460 (1995)].
16. Arthur C. Wahl, Phys. Rev. C **32**, 184 (1985); B. F. Rider, Vallecitos Nuclear Center Report No. NEDO 12154-3(C) (1981).

Physics of Atomic Nuclei, Vol. 68, No. 2, 2005, pp. 184–190. Translated from Yadernaya Fizika, Vol. 68, No. 2, 2005, pp. 209–215.
Original Russian Text Copyright © 2005 by Kadmensky.

NUCLEI
Theory

Description of Two-Proton Radioactivity on the Basis of Methods of the Quantum Theory of Ternary Nuclear Fission

S. G. Kadmensky[*]

Voronezh State University, Universitetskaya pl. 1, Voronezh, 394693 Russia

Received November 27, 2003; in final form, March 4, 2004

Abstract—The two-proton decay of spherical nuclei is investigated on the basis of the formalism developed in constructing the quantum-mechanical theory of ternary fission. The proposed method for determining the amplitudes of partial widths with respect to two-proton decay and the asymptotic behavior of the wave function for a decaying nucleus makes it possible to solve the problem of describing two-proton radioactivity without recourse to the traditionally used (in R-matrix approaches) cumbersome procedure of matching the internal and the external wave function for the decaying nucleus within the three-body formulation. In the diagonal approximation and with allowance for the properties of the potential describing the interaction of the products of two-proton decay, the structure of the wave function for the Cooper pair of two protons bound in the parent nucleus is analyzed, along with the behavior of the wave function describing the potential scattering of the products of binary decay, the coupling of decay channels being taken into account in this analysis. *© 2005 Pleiades Publishing, Inc.*

1. INTRODUCTION

The phenomenon of two-proton radioactivity was predicted in [1] and was analyzed in detail in the monograph of Baz' *et al.* [2]. This phenomenon consists in the simultaneous emission of two protons that accompanies the deep-subbarrier decay of the ground state of a parent nucleus that is even in Z and which lies in the vicinity of the proton-drip line determining the stability boundary of the region of proton-rich nuclei in nature. In principle, two protons can be emitted by a nucleus sequentially, but, in this case, two-proton decay reduces to the one-proton decays of a parent and the respective intermediate nucleus. Such a situation is realized, with an overwhelming probability, for nuclei like ^{6}Be and ^{12}O. For true two-proton radioactivity to be observable experimentally, it is necessary that the channel of sequential proton emission be strongly suppressed because of a deep-subbarrier character of one-proton decay and a negative or a small positive energy Q_{1p} of proton separation from a parent nucleus.

The first case of two-proton radioactivity was discovered in 2002 for the ^{45}Fe nucleus [3, 4]. In that case, the energy Q_{2p} required for the separation of two protons proved to be 1.1 ± 0.1 MeV [3] and 1.14 ± 0.05 MeV [4], while the half-life $T_{1/2}$ of the ^{45}Fe nucleus took values of $3.2^{+2.6}_{-1.0}$ ms [3] and $4.7^{+3.4}_{-1.4}$ ms [4]. The branching fraction of the two-proton decay of this nucleus ranged between 70 and 80% [4]. The experimental energy Q_{2p} proved to be in fairly good agreement with the predictions of a number of systematics: $Q_{2p} = 1.15 \pm 0.09$ MeV [5], $Q_{2p} = 1.28 \pm 0.18$ MeV [6], and $Q_{2p} = 1.22 \pm 0.05$ MeV [7]. At the same time, the proton-separation energy Q_{1p} in these systematics takes values in the range between -24 and 10 keV, this leading to times of the one-proton decay of the ^{45}Fe nucleus in excess of one hour, which are considerably longer that the observed half-life of this nucleus. Therefore, the mechanism involving the sequential two-proton decay of the ^{45}Fe nucleus can be disregarded.

Two theoretical approaches are presently used to describe two-proton radioactivity. Within the first approach [8, 9], two emitted protons are considered to be strongly correlated. Also, they are assumed to occur, on the energy scale, in the vicinity of their s-resonance state at an energy of about 0.55 MeV, this corresponding to the two-body diproton decay mode, in which case two particles (a diproton and a daughter nucleus) are considered in the asymptotic region of the wave function for the decaying nucleus. In order to describe this decay mode, the authors of [8, 9] used R-matrix theory [10].

The second approach treats the two-proton decay of nuclei in a more consistent way, via a three-body formulation [11, 12] where three particles (two protons and a daughter nucleus) appear in the asymptotic region of the wave function for the decaying nucleus and where use is made of the formalism of

---

[*] e-mail: `kadmensky@phys.vsu.ru`

three-particle nuclear reactions, the method of hyperspherical functions [13–15], which is natural for describing such reactions, being applied in this case. The calculations performed in [16] for rather heavy parent nuclei ($A \geq 40$) revealed that the two-proton-decay widths obtained within the diproton approach are more than one order of magnitude larger than the analogous widths calculated within the three-body approach. This means that, if the calculations reported in [16] are correct, then the role of the diproton decay mode is likely to be strongly exaggerated in [8, 9].

Unfortunately, significant uncertainties in experimentally measured energies Q_{2p} of separation of two protons [3, 4] and the more so in their counterparts predicted by the systematics in [5–7] hinder the verification of validity of these two approaches via a comparison of the two-proton widths obtained within them with respective experimental values for the ^{45}Fe nucleus, for example. Indeed, a deep-subbarier character of two-proton decay results in that the diproton width changes by a factor of about 20 in response to a change of 100 keV in the separation energy Q_{2p} from 1.09 to 1.19 MeV.

Within the three-particle approach, the multiparticle problem of describing two-proton radioactivity reduces [11, 12] to solving the three-body problem of finding the wave function for two interacting protons in the field of a daughter nucleus. The method used in [11, 12] to solve this problem is based on matching two functions in a multidimensional configuration space, the internal wave function that describes the bound state of two protons in the parent nucleus with allowance for pairing effects and the external wave function that describes the motion of two interacting protons in the field of the daughter nucleus in the region of the continuous spectrum. This procedure is extremely cumbersome and generates a number of uncertainties in its practical implementation.

In order to describe the two-proton decay of nuclei, it is therefore natural to invoke the results obtained within the quantum-mechanical theory of ternary fission [17, 18], since this theory also deals with the problem of the three-body decay of nuclei. The theory in question is based on methods used in the multiparticle theory of nuclear reactions [10] (including the theory of three-particle nuclear reactions [13–15]), on the unified theory of the nucleus [19], and on the theory of open Fermi systems [20]. Within the theory of the ternary fission of nuclei [17, 18], the aforementioned difficulty associated with the need for matching the internal and the external component of the wave function for the decaying nucleus can be sidestepped owing to the use of the projection-operator method and the integral formula for the amplitude of the partial width with respect to the three-particle decay of nuclei [19, 20]. The formalism of the quantum-mechanical theory of ternary nuclear fission can be generalized to the case of the two-proton decay of nuclei, and this is the objective of the present study.

2. WAVE FUNCTION FOR A NUCLEUS UNDERGOING TWO-PROTON DECAY

A further consideration will be performed for the case where a spherical parent nucleus of atomic weight A and charge number Z decays to two interacting protons and a daughter nucleus $(A-2, Z-2)$. The wave function $\Psi_\sigma^{JM}(\xi)$ describing an isolated quasistationary parent-nucleus state characterized by a spin J, its projection M onto the z axis of the laboratory frame, other quantum numbers σ, and a full set of intrinsic coordinates ξ satisfies the Schrödinger equation

$$(H_A - \bar{E}_\sigma^J)\Psi_\sigma^{JM}(\xi) = 0, \qquad (1)$$

where H_A is the Hamiltonian for the parent nucleus A in the c.m. frame and $\bar{E}_\sigma^J = (E_\sigma^J - i\Gamma_\sigma^J/2)$ is a complex-valued energy whose real part E_σ^J coincides with the sign-reversed binding energy of the nucleus and whose imaginary part is related to the total width Γ_σ^J with respect to the decay of nucleus A through all open channels. Following the ideas developed in the unified theory of the nucleus [19] and in the theory of open Fermi systems [20], we can represent the wave function $\Psi_\sigma^{JM}(\xi)$ in the form

$$\Psi_\sigma^{JM}(\xi) = \hat{P}\Psi_\sigma^{JM}(\xi) + \hat{Q}\Psi_\sigma^{JM}(\xi). \qquad (2)$$

The operator $\hat{P}$ projects states of nucleus A onto the internal (shell) region of the configuration space defined by the full set of coordinates of nucleons forming nucleus A, its center-of-mass coordinates being excluded from this set. In this region, nucleus A is simply connected and can be described in terms of an orthonormalized basis $\Psi_n^{JM}(\xi)$ of multiparticle shell functions that are constructed with allowance for normal and superfluid nucleon–nucleon correlations and collective modes of nuclear motion, where the index n runs through a discrete and finite set of values. The operator $\hat{P}$ can then be represented in the form

$$\hat{P} = \sum_n |\Psi_n^{JM}\rangle\langle\Psi_n^{JM}|.$$

The operator $\hat{Q} = 1 - \hat{P}$ projects the decaying-nucleus state onto the configuration-space region (cluster region) where the products of two-proton decay have already been formed. In the cluster region, the parent-nucleus wave function $\hat{Q}\Psi_\sigma^{JM}$ can be represented in the form [19, 20]

$$\hat{Q}\Psi_\sigma^{JM}(\xi) = \langle G^{JM}(\xi,\xi')|\hat{Q}(H_A - E_\sigma^J)\hat{P}|\Psi_\sigma^{JM}(\xi')\rangle, \qquad (3)$$

where $G^{JM}(\xi,\xi')$ is the multiparticle Green's function in the cluster region; it satisfies the equation

$$\hat{Q}(H_A - E^J_\sigma)\hat{Q}G^{JM}(\xi,\xi') = \delta(\xi - \xi'). \quad (4)$$

In order to describe the relative motion of two-proton-decay products in the cluster region, it is natural to employ the relative coordinates $\mathbf{R} = \mathbf{R}_1 - \mathbf{R}_2$ and $\mathbf{r} = \mathbf{R}_3 - (\mathbf{R}_1 + \mathbf{R}_2)/2$, where $\mathbf{R}_1$, $\mathbf{R}_2$, and $\mathbf{R}_3$ are the center-of-mass coordinates of the two protons and the daughter nucleus. The solid angles $\Omega_\mathbf{r}$ and $\Omega_\mathbf{R}$ specify the directions of the radius vectors $\mathbf{r}$ and $\mathbf{R}$ in the laboratory frame. In order to describe three-particle decay channels, it is natural to use [13, 14], instead of the variables R and r, the variables ρ and ε,

$$r = \left(\frac{M_a}{M_b}\right)^{1/4}\rho\sin\varepsilon, \quad R = \left(\frac{M_b}{M_a}\right)^{1/4}\rho\cos\varepsilon, \quad (5)$$

where the reduced masses M_a and M_b are defined as $M_a = m/2$ and $M_b = 2(A-2)m/A$, with m being the proton mass, while the phase-space element R^2dRr^2dr is transformed as $\rho^5\sin^2\varepsilon\cos^2\varepsilon\, d\rho d\varepsilon$. In formula (5), the angle ε lies in the interval $0 \le \varepsilon \le \pi/2$ and specifies [13] the asymptotic kinetic energies of the emitted protons and the daughter nucleus. In the cluster region, one can then introduce [17, 18] the channel function $U^{JM}_\alpha(x)$ possessing correct transformation properties under time inversion [10]; that is,

$$U^{JM}_\alpha(x) = \{\{\Psi^{J'M'}_{\sigma'}(\xi')\{\chi_{1/2m_1}\chi_{1/2m_2}\}_{SM_S}\}_{IM_I} \quad (6)$$

$$\times \{i^L Y_{LM_L}(\Omega_\mathbf{R}) i^l Y_{lM_l}(\Omega_\mathbf{r})\}_{L_0M_0}\}_{JM}\frac{R(L,l,\lambda,\varepsilon)}{\sin\varepsilon\cos\varepsilon},$$

where $\alpha \equiv c\beta Ll\lambda$; $c = J'\sigma'$; $\beta \equiv SIL_0$; and the set x of coordinates includes all coordinates ξ of the parent nucleus, with the exception of the hyperradius ρ. In (6), $\Psi^{J'M'}_{\sigma'}(\xi')$ is the daughter-nucleus wave function, for which one can take, to a high accuracy, its shell component $\hat{P}\Psi^{J'M'}_{\sigma'}(\xi')$; $\chi_{1/2m_i}$ is the spin function for the ith proton ($i = 1,\ 2$); $Y_{LM_L}(\Omega_\mathbf{R})$ and $Y_{lM_l}(\Omega_\mathbf{r})$ are spherical harmonics that describe the relative angular motions of decay products, the respective orbital angular momenta being L and l; and braces denote the vector composition of angular momenta. The normalized functions $R(L,l,\lambda,\varepsilon)/(\sin\varepsilon\cos\varepsilon)$ [13] are solutions to the three-particle Schrödinger equation in the asymptotic region, where the Coulomb interactions of ternary-decay products are screened. The functions $R(L,l,\lambda,\varepsilon)$ coincide with Jacobi polynomials [13], since the quantity λ takes integral values of $\lambda = 0$, 1, …. The channel functions in (6) are generalizations of six-dimensional hyperspherical functions characterized by the grand-orbital momentum $K = L + l + 2\lambda$ and used in [11, 12] to a multidimensional case. The energy of the relative motion of two-proton-decay products in the channel c is given by $Q_c = E^J_\sigma - E^{J'}_{\sigma'}$. At the same time, the asymptotic kinetic energy E_3 of the daughter nucleus is related to the quantity ε by the equation $E_3 = 2Q_c/A\cos^2\varepsilon$ [14].

In order to find the Green's function (4), we can introduce the wave function $\Psi^{JM}_\alpha(\xi)$ that describes, in the cluster region, the potential scattering of two-proton-decay products and which satisfies the Schrödinger equation

$$\hat{Q}(H_A - E)\hat{Q}\Psi^{JM}_\alpha(\xi) = 0. \quad (7)$$

By using the orthogonal-projection method [21], we can go over from the operator $\hat{Q}(H_A - E)\hat{Q}$ to the operator $(\tilde{H}_A - E)$, where $\tilde{H}_A = H^0_A + \tilde{V} = H^0_A + V + \chi\hat{P}$, with H^0_A and V being, respectively, the Hamiltonian of noninteracting two-proton-decay products and the potential of interaction of these products. The quantity χ is taken in the limit $\chi \to \infty$, which ensures the orthogonality of the functions $\Psi^{JM}_\alpha(\xi)$ to the set of shell functions $\Psi^{JM}_n(\xi)$ specifying the projection operator $\hat{P}$. Owing to the presence of the term $\chi\hat{P}$ in the effective Hamiltonian $\tilde{H}_A$, the function $\Psi^{JM}_\alpha(\xi)$ describes the potential scattering of two-proton-decay products without the formation of multiparticle resonances corresponding to the shell structure of the parent nucleus. The function $\Psi^{JM}_\alpha(\xi)$ can be sought in the form of the expansion [18]

$$\Psi^{JM}_{\alpha E}(\xi) = \sum_{\alpha'} U^{JM}_{\alpha'}(x)\frac{f^J_{\alpha'\alpha}(\rho)}{\rho^{5/2}}. \quad (8)$$

Here, the form factor $f^J_{\alpha'\alpha}(\rho)$, normalized to a delta function of energy, satisfies a set of coupled equations of the form

$$\left(\frac{d^2}{d\rho^2} - \frac{\bar{L}'_0(\bar{L}'_0+1)}{\rho^2} + k^2_{c'}\right)f^J_{\alpha'\alpha}(\rho) \quad (9)$$

$$- \frac{2M}{\hbar^2}\sum_{\alpha''}\tilde{V}^J_{\alpha'\alpha''}(\rho)f^J_{\alpha''\alpha}(\rho) = 0,$$

where $\bar{L}_0 = L + l + 2\lambda + 3/2$ for the channel α and $\tilde{V}_{\alpha'\alpha''}(R) = \langle U^{JM}_{\alpha'}|\tilde{V}|U^{JM}_{\alpha''}\rangle$, with boundary conditions corresponding to a regular solution to the set of Eqs. (9); that is,

$$f^J_{\alpha'\alpha}(\rho) \xrightarrow[\rho\to 0]{} 0; \quad (10)$$

$$f^J_{\alpha'\alpha}(\rho) \xrightarrow[\rho\to\infty]{} -\frac{1}{2i}\sqrt{\frac{2}{\pi\hbar v_{c'}}}\left\{\exp\left[-i\left(k_c\rho - \frac{L_0\pi}{2}\right)\right]\right.$$

$$\left.\times\,\delta_{\alpha'\alpha} - S^J_{\alpha'\alpha}\exp\left[i\left(k_{c'}\rho - \frac{L'_0\pi}{2}\right)\right]\right\}.$$

In (10), $S^J_{\alpha'\alpha}$ is an element of the S matrix, $k_c = \sqrt{2MQ_c/\hbar^2}$, $v_c = \hbar k_c/M$ for the channel α, and $M = m\sqrt{(A-2)/A}$. By using the representations specified by Eqs. (2) and (3) and finding the asymptotic behavior of the Green's function $G^{JM}(\xi,\xi')$ (4) for $\rho \to \infty$, we can obtain [18, 22] an asymptotic expression for the decaying-nucleus wave function Ψ^{JM}_σ in the form

$$\Psi^{JM}_\sigma \xrightarrow[\rho\to\infty]{} \sum_\alpha \frac{U^{JM}_\alpha}{\rho^{5/2}} \tag{11}$$

$$\times \exp\left[i\left(k_c\rho - \frac{\bar{L}_0\pi}{2} + \delta^J_\alpha\right)\right]\sqrt{\frac{\Gamma^J_{\sigma\alpha}}{\hbar v_c}},$$

where the potential-scattering phase shift δ^J_α and the real amplitude $\sqrt{\Gamma^J_{\sigma\alpha}}$ of the partial width with respect to the two-proton decay of the parent nucleus through the channel α are determined by the integral formula [18, 22]

$$\sqrt{\Gamma^J_{\sigma\alpha}}e^{i\delta^J_\alpha} \tag{12}$$

$$= \sqrt{2\pi}\sum_{\alpha'}\left\langle U^{JM}_{\alpha'}\frac{f^{J(-)}_{\alpha'\alpha}(\rho)}{\rho^{5/2}}\left|H_A - E^J_\sigma\right|\hat{P}\Psi^{JM}_\sigma\right\rangle,$$

where $f^{J(-)}_{\alpha'\alpha}(\rho)$ is the time-inversed form factor $f^J_{\alpha'\alpha}(\rho)$,

$$f^{J(-)}_{\alpha'\alpha}(\rho) = (-1)^{\bar{L}_0}[f^J_{\alpha'\alpha}(\rho)]^*. \tag{13}$$

We note that, for deep-subbarrier two-proton decay, the potential-scattering phase shift δ^J_α is very close to the phase shift $(\delta^J_\alpha)^{\mathrm{Coul}}$, which is determined exclusively by the Coulomb interactions of two-proton-decay products.

In [23], the integral formula that was obtained previously in [24] for the case of deep-subbarrier two-body decays of nuclei and which was widely used to describe two-proton alpha decay [25, 26], the protonic decay of spherical [27, 28] and deformed [29] nuclei, and cluster radioactivity [30] was generalized to the case of three-body decays in order to describe the amplitude $\sqrt{\Gamma^J_{\sigma\alpha}}$ of the partial width with respect to two-proton decay. Unfortunately, the generalized formula from [23] possesses serious drawbacks. First, it is valid only in the case of deep subbarrier decays. Second, it can be employed only upon determining the parent-nucleus wave function not only in the shell region, where the structure of this function can be reconstructed quite reliably, but also in the transition region between the shell and cluster regions. But in the transition region, two-proton-decay products undergo not only Coulomb but also intense nuclear interaction, so that this determination of the parent-nucleus wave function requires applying the aforementioned (see Introduction) cumbersome procedure of matching the internal and the external component of the decaying-nucleus wave function.

We note that the integral formula (12) does not possess the above drawbacks. Indeed, the method of its derivation proves to be valid not only for deep-subbarrier but also for above-barrier two-proton decays. But what is of greatest importance in calculating the amplitudes of two-proton-decay partial widths by formula (12) is that the procedure for matching the internal and external components of the parent-nucleus wave function is not invoked at all. The determination of the partial width by formula (12) reduces to three successive operations. First, it is necessary to find the parent- and the daughter-nucleus wave function [$\hat{P}\Psi^{JM}_\sigma(\xi)$ and $\hat{P}\Psi^{J'M'}_{\sigma'}(\xi')$, respectively] in the shell region by using the multiparticle shell model with allowance for normal and superfluid nucleon–nucleon correlations. This is not a difficult challenge since, at the present time, there exist quite elaborate methods for constructing such wave functions for a broad range nuclei [31, 32]. Second, it is necessary to calculate the form factors $f^{J(-)}_{\alpha'\alpha}(\rho)$, which are determined by Eqs. (9)–(13) and which are appropriate for describing the three-body potential scattering of two-proton-decay products with allowance for both nuclear and long-range Coulomb forces. This is a difficult problem, but one can employ, in solving it, experience gained in [11, 12], where the authors actually solved the problem of reconstructing form factors of the type $f^J_{\alpha'\alpha}(\rho)$ over the entire external region. Finally, the use of the results obtained for the shell parent- and daughter-nucleus wave functions and for the form factors $f^{J(-)}_{\alpha''\alpha'}(\rho)$ makes it possible to calculate, by the integral formula (12), the amplitudes of two-proton-decay partial widths.

With the aid of the asymptotic expression (11) for the parent-nucleus wave function, we can calculate the multipaticle current density j_p in the direction of the hyperradius $\boldsymbol{\rho}$:

$$j_p = \frac{i\hbar}{2M}\left[\Psi^{JM}_\sigma\frac{d}{d\rho}(\Psi^{JM}_\sigma)^* - (\Psi^{JM}_\sigma)^*\frac{d}{d\rho}\Psi^{JM}_\sigma\right]. \tag{14}$$

Multiplying this current density by $\rho^5\sin^2\varepsilon\cos^2\varepsilon\, d\varepsilon d\Omega_{\mathbf{r}} d\Omega_{\mathbf{R}}$ and performing integration with respect to the spin coordinates of the protons and with respect to the internal coordinates ξ' of the daughter nucleus, we can obtain the triple-differential total two-proton-decay width, which characterizes the angular distribution of two-proton-radioactivity, in the form

$$\frac{d^3\Gamma^J_\sigma}{d\Omega_{\mathbf r}\, d\Omega_{\mathbf R}\, d\varepsilon} = \sum_{cSIM_I}\ \sum_{L_0Ll\lambda M_0}\ \sum_{L'_0L'l'\lambda'M'_0} \{Y^*_{lm_l}(\Omega_{\mathbf r}) \tag{15}$$

$$\times Y^*_{LM_L}(\Omega_{\mathbf R})\}_{L_0M_0} C^{JM}_{L_0IM_0M_I} \{Y_{l'm_{l'}}(\Omega_{\mathbf r})$$

$$\times Y_{L'M_{L'}}(\Omega_{\mathbf R})\}_{L'_0M'_0} C^{JM}_{L'_0IM'_0M_I} R(L,l,\lambda,\varepsilon)$$

$$\times R(L',l',\lambda',\varepsilon)(-1)^{\lambda-\lambda'}$$

$$\times \exp[i(\delta^J_{cSIL_0Ll\lambda} - \delta^J_{cSIL'_0L'l'\lambda'})]$$

$$\times \sqrt{\Gamma^J_{\sigma cSIL_0Ll\lambda}}\sqrt{\Gamma^J_{\sigma cSIL'_0L'l'\lambda'}}.$$

3. TWO-PROTON DECAY OF SPHERICAL NUCLEI IN THE DIAGONAL APPROXIMATION

In pursuing further our investigation into the two-proton decay of rather heavy spherical nuclei, we will restrict ourselves to the diagonal approximation, which was previously used to classify alpha-particle [25, 26] and protonic [27, 28] transitions. This approximation, which is aimed at describing a favored transition where only one parent-nucleus state σ'_0 whose shell wave function has a structure close to that of the shell wave function for the parent-nucleus core is predominantly populated in the two-proton decay of the ground state of the daughter nucleus, is valid if matrix elements of the $\tilde V^J_{\alpha'\alpha''}$ type for the multiparticle potentials $V_{1\ A-2}$ and $V_{2\ A-2}$ simulating the interaction of the first and the second emitted proton with the daughter nucleus [such matrix elements are used in (9)] are diagonal in the channel indices c and c'. In this approximation, the multiparticle problem of two-proton decay reduces to the three-particle problem of the interaction of two protons and the daughter nucleus occurring in a specific $\sigma' = \sigma'_0$, $J' = J'_0$ state. As a matter of fact, the approximation in question was employed in describing two-proton radioactivity in [1, 2, 8, 9, 11, 12].

In this approximation, the multiparticle potentials $V_{1\ A-2}$ and $V_{2\ A-2}$ can be replaced by their diagonal matrix elements for the daughter-nucleus shell wave function $\hat P\Psi^{J'_0M'}_{\sigma'_0}(\xi')$, which coincide with the real parts of the optical potentials of proton interactions with the daughter nucleus, $\mathrm{Re}V^{\mathrm{opt}}_{1\ A-2}(\mathbf R + \mathbf r/2)$ and $\mathrm{Re}V^{\mathrm{opt}}_{2\ A-2}(\mathbf R - \mathbf r/2)$, and which depend only on the relative coordinates $\mathbf R$ and $\mathbf r$. At the same time, one can perform integration with respect to all internal variables ξ' of the daughter nucleus in formula (12), which determines the amplitude of the partial width with respect to favored two-proton decay through the $c_0 = J'_0, \sigma'_0$ channel, and express this formula in terms of an integral with respect to six variables, $d\mathbf r d\mathbf R = d\Omega_{\mathbf r} d\Omega_{\mathbf R} \rho^5 d\rho \sin^2\varepsilon \cos^2\varepsilon\, d\varepsilon$, upon the substitution of the potentials $\mathrm{Re}V^{\mathrm{opt}}_{1\ A-2}$ and $\mathrm{Re}V^{\mathrm{opt}}_{2\ A-2}$ for the potentials $V_{1\ A-2}$ and $V_{2\ A-2}$ and upon introducing an effective shell wave function $\varphi(1, 2)$ for two protons bound in the parent nucleus, this function being given by

$$\varphi(1,2) = \langle \hat P\Psi^{J'_0M'}_{\sigma'_0} | \hat P\Psi^{JM}_\sigma\rangle. \tag{16}$$

The form factors $f^{J(-)}_{\alpha'\alpha}(\rho)$, which describe the potential scattering of two-proton-decay products and which are determined by Eqs. (9)–(13), then become diagonal in the channel indices c and c' and do not vanish at $c = c' = c_0 = J'_0, \sigma'_0$.

In order to construct the shell wave function $\hat P\Psi^{JM}_\sigma$ for the ground state of a rather heavy spherical parent nucleus even in Z, one can use the superfluid model of the nucleus [30, 31], where

$$\hat P\Psi^{JM}_\sigma = \Psi^{00}_Z \Psi^{JM}_N. \tag{17}$$

Here, Ψ^{JM}_N and Ψ^{00}_Z are the wave functions for, respectively, the neutron subsystem of the parent nucleus and its proton subsystem, which is even in Z. For a diagonal favored two-proton decay, the daughter-nucleus shell wave function can be represented in the form

$$\hat P\Psi^{J'M'}_{\sigma'_0} = \Psi^{00}_{Z-2}\Psi^{JM}_N \delta_{J'J}\delta_{M'M} \tag{18}$$

for the case where the neutron subsystem of the parent nucleus appears to be a spectator for favored two-proton decay.

Within the superfluid model of the nucleus, the shell wave function Ψ^{00}_Z is represented as [26]

$$\Psi^{00}_Z = \prod_{\nu, m>0} (u^{(Z)}_\nu + v^{(Z)}_\nu (-1)^{j-m+l} a^+_{\nu m} a^+_{\nu -m})|0\rangle, \tag{19}$$

where $a^+_{\nu m}$ is the operator of proton creation in the $nljm \equiv \nu m$ shell state characterized by the wave function $\varphi_{\nu m}(1)$, while $u^{(Z)}_\nu$ and $v^{(Z)}_\nu$ are the coefficients of the Bogolyubov u–v transformation. The shell wave function Ψ^{00}_{Z-2} for the proton subsystem of the daughter nucleus is given by the analogous formula where the index Z is replaced by the index $(Z-2)$. For the effective wave function $\varphi(1, 2)$ (16), which describes the system of two protons, we can then obtain the expression [26]

$$\varphi(1,2) = \sum_\nu \sqrt{\frac{2j+1}{2}} (-1)^l u^{(Z-2)}_\nu v^{(Z)}_\nu \tag{20}$$

$$\times \{\varphi_{\nu m}(1)\varphi_{\nu-m}(2)\}_{00},$$

which in fact represents the wave function for a Cooper pair of two protons having zero spin and a positive parity. The wave function $\varphi(1,2)$ (20) can be represented as a superposition of two terms for which the total spin of two protons is $S = 0$ and $S = 1$, with the total orbital angular momentum being $L_0 = S$. By using the generalized Talmi transformation [25], we can go over from the proton coordinates $\mathbf{r}_1$ and $\mathbf{r}_2$ reckoned from the center of mass of the daughter nucleus to the relative coordinates $\mathbf{r}$ and $\mathbf{R}$. The specific calculations performed in [33] revealed that, because of coherent superfluid mixing, the $S = 0$, $L_0 = 0$ spin-singlet component, where states of orbital angular momenta l and L equal to zero are the most significant, plays the main role in the function $\varphi(1,2)$ (20). This result is confirmed by the calculations of Grigorenko *et al.* [16], who relied on the SU_3-symmetry scheme. Since the potentials $\mathrm{Re}V^{\mathrm{opt}}_{1\,A-2}(\mathbf{R}+\mathbf{r}/2)$ and $\mathrm{Re}V^{\mathrm{opt}}_{2\,A-2}(\mathbf{R}-\mathbf{r}/2)$ and the potential $V_{12}(\mathbf{r})$ of the interaction of two outgoing protons are scalar, their effect on the wave functions for two-proton-decay products cannot change the total relative orbital angular momentum $\mathbf{L}_0 = \mathbf{L}+\mathbf{l}$ of these products. At the same time, the potentials in question can change the relative orbital angular momenta $\mathbf{l}$ and $\mathbf{L}$ of two-proton-decay products individually by, respectively, $\Delta\mathbf{l}$ and $\Delta\mathbf{L}$—but in such a way that $\Delta\mathbf{l}+\Delta\mathbf{L} = 0$—since these potentials are nonspherical, depending on the angle $\theta_{\mathbf{rR}}$ between the vectors $\mathbf{r}$ and $\mathbf{R}$. Because of the properties of the integrand in (12), one can therefore expect that the partial widths for the $S = 0$, $L_0 = 0$, and $l = L$ two-proton-decay channels will play a dominant role for favored two-proton decay, the quantities l and L taking only even values owing to the structure of the potentials simulating the interaction of decay products.

In this case, the triple-differential two-proton-decay width (15) assumes a simpler form,

$$\frac{d^3\Gamma^J_\sigma}{d\Omega_{\mathbf{r}}d\Omega_{\mathbf{R}}d\varepsilon} = \sum_{l\lambda l'\lambda'} \{Y^*_{lm_l}(\Omega_{\mathbf{r}})Y^*_{lM_L}(\Omega_{\mathbf{R}})\}_{00} \quad (21)$$
$$\times \{Y_{l'm_{l'}}(\Omega_{\mathbf{r}})Y_{l'M_{L'}}(\Omega_{\mathbf{R}})\}_{00}R(l,l,\lambda,\varepsilon)$$
$$\times R(l',l',\lambda',\varepsilon)(-1)^{\lambda-\lambda'}$$
$$\times \exp[i(\delta^J_{l\lambda}-\delta^J_{l'\lambda'})]\sqrt{\Gamma^J_{l\lambda}}\sqrt{\Gamma^J_{l'\lambda'}},$$

where, in the notation used above, $\Gamma^J_{l\lambda}$ and $\delta^J_{l\lambda}$ coincide with $\Gamma^J_{\sigma J\sigma'_0 0J0ll\lambda}$ and $\delta^J_{\sigma J\sigma'_0 0J0ll\lambda}$, respectively. If we use the formula

$$\{Y_{lm_l}(\Omega_{\mathbf{r}})Y_{lM_L}(\Omega_{\mathbf{R}})\}_{00} = Y_{l0}(\theta_{\mathbf{rR}})\frac{1}{4\pi} \quad (22)$$

and integrate formula (21) with respect to ε, the angular distribution of products originating from the favored two-proton decay of nuclei takes the form

$$\frac{d^2\Gamma^J_\sigma}{d\Omega_{\mathbf{r}}d\Omega_{\mathbf{R}}} = \sum_{\lambda ll'} Y_{l0}(\theta_{\mathbf{rR}})Y_{l'0}(\theta_{\mathbf{rR}}) \quad (23)$$
$$\times \sqrt{\Gamma^J_{l\lambda}}\sqrt{\Gamma^J_{l'\lambda}}[\delta_{ll'}+2\cos(\delta^J_{l\lambda}-\delta^J_{l'\lambda})(1-\delta_{ll'})].$$

At the same time, integration of formula (21) over all directions of proton emission yields the energy distribution for these products; that is,

$$\frac{d\Gamma^J_\sigma}{d\varepsilon} = \sum_{l\lambda\lambda'}\sqrt{\Gamma^J_{l\lambda}}\sqrt{\Gamma^J_{l\lambda'}}R(l,l,\lambda,\varepsilon)R(l,l,\lambda',\varepsilon) \quad (24)$$
$$\times [\delta_{\lambda\lambda'}+2\cos(\delta^J_{l\lambda}-\delta^J_{l\lambda'})(1-\delta_{\lambda\lambda'})].$$

4. CONCLUSION

By using methods employed in studying protonic [29] and alpha [30] decays and the binary and ternary fission of deformed nuclei [17, 18], the formalism developed above for describing the two-proton decay of spherical nuclei can readily be generalized to the case of the two-proton decay of deformed nuclei.

ACKNOWLEDGMENTS

I am grateful to B.V. Danilin, L.V. Grigorenko, and V.E. Bunakov for stimulating discussions.

This work was supported in part by the program Universities of Russia (grant no. 02.01.003).

REFERENCES

1. V. I. Goldansky, Nucl. Phys. **19**, 482 (1960).
2. A. I. Baz', V. I. Goldansky, *et al.*, *Light and Medium-Mass Nuclei in the Vicinity of the Nuclear Drip Line* (Nauka, Moscow, 1972).
3. M. Pfützner *et al.*, Eur. Phys. J. A **14**, 279 (2002).
4. J. Giovinazzo *et al.*, Phys. Rev. Lett. **89**, 102501 (2002).
5. B. A. Brown, Phys. Rev. C **43**, 2568 (1991).
6. W. E. Ormand, Phys. Rev. C **53**, 214 (1996).
7. B. J. Cole, Phys. Rev. C **54**, 1240 (1996).
8. F. C. Barker, Phys. Rev. C **63**, 047303 (2001).
9. B. A. Brown and F. C. Barker, Phys. Rev. C **67**, 041304 (2003).
10. A. M. Lane and R. G. Thomas, Rev. Mod. Phys. **30**, 257 (1958).
11. L. V. Grigorenko *et al.*, Phys. Rev. Lett. **85**, 22 (2000).
12. L. V. Grigorenko *et al.*, Phys. Rev. C **64**, 054002 (2001).
13. L. M. Delves, Nucl. Phys. **9**, 391 (1958).
14. N. F. Mott and H. S. W. Massey, *The Theory of Atomic Collisions* (Clarendon, Oxford, 1965; Mir, Moscow, 1969).

15. A. I. Baz' *et al.*, Yad. Fiz. **25**, 281 (1977) [Sov. J. Nucl. Phys. **25**, 153 (1977)].
16. L. V. Grigorenko, I. G. Mukha, and M. V. Zhukov, Nucl. Phys. A **714**, 425 (2003).
17. S. G. Kadmensky, Yad. Fiz. **65**, 1833 (2002) [Phys. At. Nucl. **65**, 1785 (2002)].
18. S. G. Kadmensky, Yad. Fiz. **67**, 167 (2004) [Phys. At. Nucl. **67**, 170 (2004)].
19. K. Wildermuth and Y. C. Tang, *A Unified Theory of the Nucleus* (Vieweg, Braunschweig, 1977).
20. S. G. Kadmensky, Yad. Fiz. **62**, 639 (1999) [Phys. At. Nucl. **62**, 592 (1999)]; **64**, 478 (2001) [**64**, 423 (2001)].
21. V. I. Kukulin, V. G. Neudatchin, and Yu. F. Smirnov, Fiz. Élem. Chastits At. Yadra **10**, 1236 (1979) [Sov. J. Part. Nucl. **10**, 492 (1979)].
22. S. G. Kadmensky, Yad. Fiz. (in press).
23. B. V. Danilin and M. V. Zhukov, Yad. Fiz. **56** (4), 67 (1993) [Phys. At. Nucl. **56** (4), 460 (1993)].
24. S. G. Kadmenskiĭ and V. E. Kalechits, Yad. Fiz. **12**, 70 (1970) [Sov. J. Nucl. Phys. **12**, 37 (1970)].
25. S. G. Kadmensky and W. I. Furman, *Alpha Decay and Related Nuclear Reactions* (Énergoatomizdat, Moscow, 1985).
26. S. G. Kadmenskiĭ, V. E. Kalechits, and A. A. Martynov, Yad. Fiz. **14**, 343 (1971) [Sov. J. Nucl. Phys. **14**, 193 (1971)].
27. V. P. Bugrov, S. G. Kadmenskiĭ, V. I. Furman, and V. G. Khlebostroev, Yad. Fiz. **41**, 1123 (1985) [Sov. J. Nucl. Phys. **41**, 717 (1985)].
28. S. G. Kadmensky, Yad. Fiz. **63**, 613 (2000) [Phys. At. Nucl. **63**, 551 (2000)].
29. V. P. Bugrov and S. G. Kadmenskiĭ, Yad. Fiz. **49**, 1562 (1989) [Sov. J. Nucl. Phys. **49**, 967 (1989)].
30. S. G. Kadmenskiĭ, V. I. Furman, and Yu. M. Chuvil'skiĭ, Izv. Akad. Nauk SSSR, Ser. Fiz. **50**, 1786 (1986).
31. A. Bohr and B. R. Mottelson, *Nuclear Structure* (Benjamin, New York, 1969, 1975; Mir, Moscow, 1971, 1977), Vols. 1, 2.
32. V. G. Solov'ev, *Theory of Atomic Nuclei: Nuclear Models* (Énergoatomizdat, Moscow, 1981).
33. S. G. Kadmenskiĭ, K. S. Rybak, and V. I. Furman, Yad. Fiz. **24**, 501 (1976) [Sov. J. Nucl. Phys. **24**, 260 (1976)].

Translated by A. Isaakyan

Physics of Atomic Nuclei, Vol. 68, No. 2, 2005, pp. 191–207. Translated from Yadernaya Fizika, Vol. 68, No. 2, 2005, pp. 216–232.

Investigation of the Neutron Shell Structure of the Even–Even Isotopes $^{40-56}$Ca within the Dispersive Optical Model

O. V. Bespalova*, **I. N. Boboshin**, **V. V. Varlamov**, **T. A. Ermakova**,
B. S. Ishkhanov, **E. A. Romanovsky**, **T. I. Spasskaya**, and **T. P. Timokhina**

Institute of Nuclear Physics,
Moscow State University, Vorob'evy gory, Moscow, 119899 Russia

Received December 3, 2003; in final form, May 1, 2004

Abstract—Within the method of matching experimental data obtained in the neutron-stripping and neutron-pickup reactions on ^{40,42,44,46,48}Ca isotopes, the single-particle energies and probabilities that neutron states are filled are obtained for the even–even calcium isotopes. These data are analyzed within the dispersive optical model, and good agreement between the calculated and experimental values of the energies of states is obtained. The dispersive optical potential is extrapolated to the region of the unstable ^{50,52,54,56}Ca nuclei. The calculated single-particle energies of bound states in these isotopes are compared with the results of the calculations within the multiparticle shell model, the latter predicting a new magic number $N = 34$ for $Z = 20$ nuclei. *© 2005 Pleiades Publishing, Inc.*

1. INTRODUCTION

Searches for and investigation of new magic nuclei form one of the most important lines of experimental and theoretical studies stimulated by advances in the realms of obtaining and accelerating radioactive nuclei and by the development of new computational procedures in nuclear-structure theory.

In the past years, a full set of parameters of effective interaction for pf-shell nuclei has been determined on the basis of experimental information about the energies of single-particle states and matrix elements of two-particle interactions for the doubly magic nuclei $^{40}_{20}$Ca$_{20}$ and $^{48}_{20}$Ca$_{28}$ and nuclei closest to them. By using the new set of effective-interaction parameters, the energies of 2_1^+ states in the even–even calcium isotopes from ^{42}Ca to ^{56}Ca inclusive were calculated in [1] on the basis of the multiparticle shell model (MSM).

For the even–even calcium isotopes from the mass-number range $42 \leq A \leq 52$, the calculated energies of 2_1^+ states are in good agreement with their experimental counterparts. For ^{54}Ca, the calculated energy of the 2_1^+ state is identical to that in the ^{48}Ca nucleus, while its counterpart in ^{56}Ca is close to the energies of the 2_1^+ states in ^{42,44,46}Ca. Also, the single-particle energies of the $1f$ and $2p$ neutron states were calculated in [1] for the even–even nuclei $^{42-56}$Ca. It was shown that the energy gap between the $1f_{5/2}$ and $2p_{1/2}$ states increases as the mass number A grows from 50 to 54, reaching a value of about 4 MeV—that is, this gap proves to be commensurate with the gap between the $1f_{7/2}$ and $2p_{3/2}$ states in the doubly magic nucleus $^{48}_{20}$Ca$_{28}$. On the basis of the fact that the gap between the $1f_{5/2}$ and $2p_{1/2}$ states is correlated with the energy of the 2_1^+ level in ^{54}Ca, it was assumed in [1] that, in the ^{54}Ca nucleus, the $2p_{3/2}$ and $2p_{1/2}$ subshells are completely filled; therefore, $N = 34$ is a new magic number for $Z = 20$ isotopes, and the $^{54}_{20}$Ca$_{34}$ nucleus is a candidate for a doubly magic nucleus.

In order to test the assumption that the number $N = 34$ is magic, it is important to determine experimentally the energy of the first 2_1^+ level in the ^{54}Ca nucleus and to calculate the energy gap between the $1f_{5/2}$ and $2p_{1/2}$ states in the ^{50,52,54,56}Ca nuclei on the basis of a model that is different from the multiparticle shell model and which would make it possible to obtain reliable data on the single-particle energies E_{nlj} of neutron states specified by the quantum numbers n, l, and j.

However, it is necessary to assess the reliability of the experimental values of single-particle energies before proceeding to compare the results of respective calculations with them. We address this issue in the second section of this article. Our analysis of experimental data has made it possible to find, for the ^{40,42,44,46,48}Ca nuclei, sets of reliable experimental values of energies for single-particle states.

---

*e-mail: `besp@monet.npi.msu.ru`

In the third section of the article, the refined experimental data on the single-particle energies of states are compared with the results obtained by other authors on the basis of various models. For the ^{40}Ca nucleus, we analyze the quantities

$$\chi^2 = \sum_{nlj} \left(\frac{E^{\rm theor}_{nlj} - {\rm E}^{\rm expt}_{nlj}}{\Delta^{\rm expt}_{nlj}} \right)^2 ,$$

where $\Delta^{\rm expt}_{nlj}$ is the error in determining $E^{\rm expt}_{nlj}$ for states in the vicinity of the Fermi energy $E_{\rm F}$. It is shown that minimum values of χ^2 correspond to the $E^{\rm DOM}_{nlj}$ values calculated within the dispersive optical model (DOM).

In the fourth section of the article, it is shown that the use of the traditional version of the dispersive optical model in calculating the energies of levels in the stable even–even isotopes $^{42-48}$Ca runs into serious difficulties because of scarcity of experimental data on neutron-scattering cross sections. In order to describe experimental information obtained for the single-particle properties of states of the ^{42,44,46,48}Ca nuclei, we therefore employ a new version of the dispersive optical model.

In the fifth section, we investigate the accuracy to which it is possible to match the single-particle energies calculated for neutron states in the ^{42,44,46,48}Ca nuclei on the basis of the new version of the dispersive optical model with their experimental counterparts. It is shown that, for valence states, the calculated and experimental values of the energies E_{nlj} agree within the experimental errors.

In the sixth section, we discuss issues associated with extrapolating some parameters of the dispersive optical potential from the region of stable nuclei to the region of unstable nuclei, present the results obtained by calculating the single-particle energies of neutron states for the ^{50,52,54,56}Ca nuclei, and explore the possible magicity of the number $N = 34$ in $Z = 20$ nuclei.

2. SINGLE-PARTICLE ENERGIES AND PROBABILITIES OF THE FILLING OF NEUTRON STATES IN ^{40,42,44,46,48}Ca

The parameters of the neutron shell structure of the ^{40,42,44,46,48}Ca nuclei in the vicinity of $E_{\rm F}$ were determined by the method based on matching the data obtained in stripping and pickup reactions on the same nucleus. The single-particle energies E_{nlj} of subshells characterized by the quantum numbers n, l, and j and their occupation numbers N_{nlj} were calculated with allowance for the spectroscopic factors S_{nlj}. A detailed description of this method is given in [2]. Below, we only present the formulas for calculating N_{nlj} and E_{nlj}.

For levels characterized by the energy E_x and the quantum numbers n, l, and j, we denote by $S^{\mp}_{nlj}(E_x)$ the spectroscopic factors determined from data on pickup $(-)$ and stripping $(+)$ reactions and by $S^{\mp}_{nlj}$ the total spectroscopic factors:

$$S^-_{nlj} = \sum_x S^-_{nlj}(E_x), \quad S^+_{nlj} = \sum_x S^+_{nlj}(E_x). \quad (1)$$

In Eq. (1), the quantity $S^-_{nlj}(E_x)$ is proportional to the number of particles in the respective subshell (in the case of a pickup reaction), while $S^+_{nlj}(E_x)$ is proportional to the number of vacancies in the subshell (in the case of a stripping reaction).

From the energies E_x of the levels and the quantities $S^{\mp}_{nlj}(E_x)$, one determines the energies of the centroids of single-particle levels in final nuclei:

$$e^-_{nlj} = \frac{\sum\limits_x E_x S^-_{nlj}(E_x)}{S^-_{nlj}}, \quad e^+_{nlj} = \frac{\sum\limits_x E_x S^+_{nlj}(E_x)}{S^+_{nlj}}. \quad (2)$$

A transition from the energies e^-_{nlj} and e^+_{nlj} reckoned from the ground-state energies of the final nuclei $(A-1)$ and $(A+1)$ to the energies E^-_{nlj} and E^+_{nlj} reckoned from the ground-state energy of the nucleus A is accomplished by the formulas

$$E^-_{nlj}(A) = -B(A) - e^-_{nlj}, \quad (3)$$

$$E^+_{nlj}(A+1) = -B(A+1) + e^+_{nlj}, \quad (4)$$

where $B(A)$ and $B(A+1)$ are the neutron-separation energies in the nuclei whose mass numbers are A and $A+1$, respectively.

For each nucleus, experimental information about the stripping and pickup of neutrons was recast into a mutually consistent form by renormalizing the spectroscopic factors in such a way that respective sum rules were valid for them. The renormalized values of $\mathbf{S}^{\mp}_{nlj}$ were used to calculate the average occupation numbers for single-particle states by the formula

$$N_{nlj} = \frac{[\mathbf{S}^-_{nlj} + (2j+1-\mathbf{S}^+_{nlj})]}{2(2j+1)}. \quad (5)$$

The single-particle energies E_{nlj} of states were determined from the relation

$$E_{nlj} = \frac{\mathbf{S}^-_{nlj}E^-_{nlj} + \mathbf{S}^+_{nlj}E^+_{nlj}}{\mathbf{S}^-_{nlj} + \mathbf{S}^+_{nlj}}. \quad (6)$$

From Eqs. (3)–(6), we obtain

$$-E_{nlj} = (1 - N_{nlj})[B(A+1) - e^{+}_{nlj}] \qquad (7)$$
$$+ N_{nlj}[B(A) + e^{-}_{nlj}].$$

In order to determine N_{nlj} and E_{nlj}, we used the experimental data on the reactions of neutron stripping and pickup from [3–6; 7–10; 4, 8, 11, 12; 13–17; 18–22] for ^{40}Ca, ^{42}Ca, ^{44}Ca, ^{46}Ca, and ^{48}Ca, respectively.

The spins of the levels in the $^{A-1}$Ca and $^{A+1}$Ca nuclei were borrowed from the "Adopted Levels" section of the ENSDF international database of nuclear properties [23]. For a large number of levels excited in $^{A-1}$Ca and $^{A+1}$Ca nuclei in the pickup and stripping reactions, the spin values are ambiguous or unknown; therefore, the calculation was performed for each possible spin value. For the sake of brevity, the set of E_{nlj} values found from such calculations will be referred to as a "solution." An analysis of all solutions makes it possible to determine the total range of energies and occupation numbers for each single-particle state.

It is well known that $S_{nlj}(E_x)$ values calculated by the distorted-wave method involve an uncertainty not less than 20%, which contains both a systematic and a statistical component. The first is caused by the method used to derive spectroscopic factors as the coefficients of proportionality between the experimental values of the cross sections and their counterparts calculated by the distorted-wave method. Calculations within the distorted-wave method are based on the use of standard codes, the geometric parameters of the real and spin–orbit potentials being fixed, as a rule. The depth of the real potential is determined for each state. The calculations reveal that a 1% variation in the range parameter of the Woods–Saxon (WS) real potential for the $n + A$ system leads to a change of 10% in the calculated differential cross section for the stripping or pickup reaction. The systematic uncertainty in $S_{nlj}(E_x)$ also receives contributions from the ambiguities in the parameters of the optical potentials for projectile and emitted particles, uncertainties in the effective nucleon–nucleus interaction, and uncertainties in the sum rule. The application of the method based on matching data on stripping and pickup reactions makes it possible to remove, to a considerable extent, these sources of systematic uncertainties, the remaining statistical uncertainty in determining the individual values of renormalized $\mathbf{S}_{nlj}(E_x)$ being estimated at a value not greater than 10%. The errors in N_{nlj} values are about 0.05 near their boundaries of 0 and 1, falling to about 0.1 between their boundaries [2]. The use of the sums of the spectroscopic factors in our calculations creates a new source of uncertainties, since the quantum number j is unknown for many spectroscopic factors, so that the inclusion of such a spectroscopic factor in the sum in (1) or (2) or the disregard of this form factor would change the value of the respective sum. The method used in our analysis makes it possible to estimate these uncertainties by sampling all of the acceptable values of j. Therefore, the total error in determining $\mathbf{S}_{nlj}$ and N_{nlj} is taken here to be a root-mean-square value that takes into account the error because of the uncertainty in the spins of states and an error of about 10% in determining the individual values of renormalized $\mathbf{S}_{nlj}$. The errors in the single-particle energies are determined in a similar way.

The N_{nlj} and E_{nlj} values found for ^{40,42,44,46,48}Ca are given in Table 1, along with their total errors in parentheses. One can see that, because of incompleteness of experimental data, we were unable to determine the features of some states. The values N^{expt}_{nlj} and E^{expt}_{nlj} quoted in Table 1 for single-particle states in the vicinity of E_{F} for the ^{40,42,44,46,48}Ca isotopes were determined by using a unified method for all nuclei and are the most complete data. We note that, here, we define single-particle energies with allowance for coupling to collective degrees of freedom, which affect the occupation numbers for single-particle states and the energy centroids appearing in Eq. (7).

Figure 1 shows, according to data in Table 1, the energy positions of single-particle neutron orbits in calcium nuclei. From this figure, one can see that an increase in the number of neutrons in the $1f_{7/2}$ subshell leads to an increase in the absolute value of the energy of the $1f_{7/2}$ state and to a modest decrease in the absolute value of the energy of the $2\text{p}_{3/2}$ state, with the result that an individual shell in $^{48}_{20}\text{Ca}_{28}$ and the magic number $N = 28$ appear.

The single-particle energy E_{nl} of the state characterized by the quantum numbers n and l can be expressed in terms of spin–orbit splitting $\Delta_{\text{so}}(nl) = E_{nlj=l-1/2} - E_{nlj=l+1/2}$ as

$$E_{nl} = E_{nlj=l-1/2} - \Delta_{\text{so}}(nl)\frac{l+1}{2l+1}, \qquad (8)$$
$$E_{nl} = E_{nlj=l+1/2} + \Delta_{\text{so}}(nl)\frac{l}{2l+1}.$$

According to the data in Table 1, the values of E_{nl} for the $1f$ states in ^{40}Ca, ^{46}Ca, and ^{48}Ca are −4.92, −6.70, and −6.44 MeV, respectively, while the corresponding values for the $2p$ states are −5.49, −5.09, and −4.08 MeV. With increasing number of neutrons in calcium isotopes, the energy gap between the p and f states proves to be approximately four times larger in ^{48}Ca than in ^{40}Ca. As N increases from 20 to 28, the energy gap between the $2\text{p}_{3/2}$ and $1f_{7/2}$ subshells increases approximately in the same proportion.

Table 1. Mean neutron occupation numbers N_{nlj} for subshells in the ^{40,42,44,46,48}Ca nuclei and their single-particle energies $-E_{nlj}$ (in MeV)

Subshell	N_{nlj}	$-E_{nlj}$	N_{nlj}	$-E_{nlj}$	N_{nlj}	$-E_{nlj}$	N_{nlj}	$-E_{nlj}$	N_{nlj}	$-E_{nlj}$
	^{40}Ca		^{42}Ca		^{44}Ca		^{46}Ca		^{48}Ca	
$2s_{1/2}$	>0.92	17.2(18)	0.93(4)	15.44(154)					1.00(0)	15.07(152)
$1d_{3/2}$	0.83(3)	15.2(20)	0.91(4)	13.03(184)	0.94(6)	13.91(159)			0.99(1)	15.22(179)
$1f_{7/2}$	0.02(2)	7.52(75)	0.20(4)	7.70(107)	0.49(8)	9.23(112)	0.77(7)	10.07(100)	1.00(0)	10.10(101)
$2p_{3/2}$	0.02(2)	6.10(67)	0.01(0)	5.73(57)	0.07(3)	5.92(75)	0.10(5)	5.84(60)	0.01(1)	4.68(47)
$2p_{1/2}$	0.01(1)	4.27(43)	0.00(0)	4.10(41)	0.01(0)	3.63(36)	0.04(4)	3.58(39)	0.00(0)	2.87(28)
$1f_{5/2}$	0.02(2)	1.46(20)					0.06(5)	2.20(45)	0.03(3)	1.57(40)

On the basis of data quoted in Table 1, one can trace variations in the particle–hole gap $\Delta^{\text{expt}} = E_{1f_{7/2}} - E_{1d_{3/2}}$ for the ^{40,42,44,46}Ca nuclei. The gap value of $\Delta^{\text{expt}} = E_{2p3/2} - E_{1f7/2} = 5.42(111)$ MeV for ^{48}Ca is smaller than Δ^{expt} for ^{40}Ca approximately by 2 MeV.

From the data in Table 1, it follows that, for ^{40,42}Ca, the sequence of the levels is $2s_{1/2}$–$1d_{3/2}$, while, for ^{48}Ca, there is an experimental indication that the sequence of the levels changes to become $1d_{3/2}$–$2s_{1/2}$, but the uncertainties in E^{expt}_{nlj} give no way to draw a definitive conclusion. Calculations on the basis of the relativistic mean-field approximation (RMFA) [24, 25] predict the sequence $1d_{3/2}$–$2s_{1/2}$, while the results reported in [26–28] favor the inverse sequence $2s_{1/2}$–$1d_{3/2}$.

It seems necessary to compare the data on E^{expt}_{nlj} for $^{40-48}$Ca in Table 1 with those that are available in the literature. In Table 2, we quote data on E^{expt}_{nlj} for the $2s_{1/2}$, $1d_{3/2}$, $1f$, and $2p$ states in the ^{40,48}Ca nuclei from articles in which the compiled values of E^{expt}_{nlj} are contrasted against E^{theor}_{nlj}.

From an analysis of the data on E^{expt}_{nlj} (see Tables 1, 2) for ^{40}Ca, it follows that the average value found in the present study for the energy of the $2s_{1/2}$ state is smaller in absolute value than its counterpart quoted in [5, 29–33] approximately by 1 MeV. It should be noted that, in those studies, only the ^{39}Ca state at $E_x = 2.463$ MeV, which possesses the highest spectroscopic factor, was taken into account in determining the energy of the $2s_{1/2}$ level. A modest distinction between the average energy of the $1d_{3/2}$ state and that which is given in [5, 29, 31–33] is explained in a similar way. From Table 2, it can be seen that, according to data from [5, 29–33], the spacing between the $1f_{7/2}$ and $2p_{3/2}$ levels lies in the range 1.9–2.5 MeV; according to our data, it is as small as 1.4 MeV. It is noteworthy that our result for the central value of the single-particle energy of the $1f_{7/2}$ state in the ^{40}Ca nucleus is approximately 0.8 MeV less than its counterparts in other studies. This is explained by taking here into account the fragmentation of the stripping strength for the $1f_{7/2}$ state and its distribution over various states of the ^{41}Ca nucleus. The use of full arrays of data on the spin–parities of the ^{41}Ca nucleus made it possible to conclude that the $1f_{7/2}$ spectroscopic strength is distributed among several states, including, in addition to the ground state, at least three more states of ^{41}Ca at 6567.4, 6686.2, and 6748.1 keV. Because of the fragmentation of the $1f_{7/2}$ state, the centroids of the $1f_{7/2}$ and $2p_{3/2}$ states prove to be quite close to each other, so that the corresponding occupation numbers are identical (see Table 1). We also note that our result for the energy of the $1f_{5/2}$ state is consistent with the data from [5], but that it is two times less in absolute value than the result quoted in [31] and 2.5 times less than its counterpart in [32].

Table 2 presents the values E^{expt}_{nlj} for ^{48}Ca from [29, 33]. We note that, within the errors, the energies of the $1f$ and $2p$ states from [29, 33] agree with our results, but that the energies of the $2s_{1/2}$ and $1d_{3/2}$ states according to our data are much greater in absolute value than their counterparts in those studies. With allowance for what will be said in the next section, the data on E^{theor}_{nlj} in the vicinity of E_{F} that were calculated for $^{40-48}$Ca by different authors within various theoretical approaches will be compared with the values E^{theor}_{nlj} obtained in the present study.

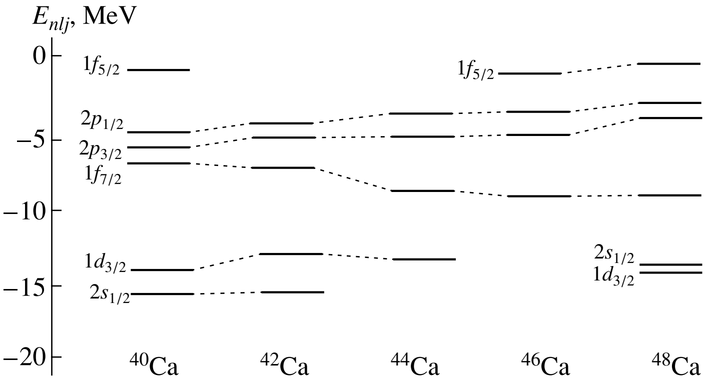

Fig. 1. Experimental values of the energies of neutron single-particle states in ^{40,42,44,46,48}Ca.

3. COMPARISON OF THE SINGLE-PARTICLE ENERGIES $E_{nlj}^{\rm expt}$ OF NEUTRON STATES IN ^{40,42,44,46,48}Ca WITH THE CALCULATED ENERGIES $E_{nlj}^{\rm theor}$

In [34], information about $E_{nlj}^{\rm expt}$ for deep hole levels was obtained from an analysis of the quasielastic-deuteron-knockout reaction $^{40}{\rm Ca}(p, np)^{39}{\rm Ca}$ at $E_p =$ 1.0 GeV. Data from [34] on $E_{nlj}^{\rm expt}$ for deep levels and our present data on $E_{nlj}^{\rm expt}$ in the vicinity of $E_{\rm F}$ (from Table 1) are contrasted against $E_{nlj}^{\rm theor}$ for ^{40}Ca in Table 3. In a great number of studies, the theoretical values $E_{nlj}^{\rm theor}$ were calculated either for deep hole or for valence states. The number of studies where calculations were performed for all bound states of ^{40}Ca is relatively small. Some comments on the arrangement of data in Table 3 are in order here.

In column 4, we present the values $E_{nlj}^{\rm theor}$ calculated with the standard Woods–Saxon (WS) potential of the shell model. The depth of the neutron–nucleus interaction potential was chosen by fitting $E_{nlj}^{\rm theor}$ to $E_{nlj}^{\rm expt}$ for states in the vicinity of the Fermi energy [35].

The energies $E_{nlj}^{\rm DOM}$ calculated on the basis of the dispersive optical model are given in columns 5 and 6 [31, 36]. By and large, the agreement between $E_{nlj}^{\rm DOM}$ and $E_{nlj}^{\rm expt}$ is quite good. At the same time, the value of $E_{nlj}^{\rm DOM} = -2.73$ MeV [31] for the $1f_{5/2}$ state is in sharp contradiction with the experimental value of $E_{nlj}^{\rm expt} = -1.46$ MeV; for the $1s_{1/2}$ state, $E_{nlj}^{\rm DOM} =$ -66.12 MeV [36], which is greater in absolute value than $E_{nlj}^{\rm expt} = -61.5(10)$ MeV [34] by approximately 5 MeV.

Columns 7–10 display the $E_{nlj}^{\rm theor}$ values calculated by the Hartree–Fock (HF) method with a phenomenological effective interaction between intranuclear nucleons. This interaction differs from the interaction of two free nucleons and depends strongly on the intranuclear density. In [37], use was made of the effective Skyrme interaction (HFS). In [38], Hartree–Fock calculations were performed with a potential whose density dependence is nonlinear, while, in [39], a new set of Skyrme interaction parameters that was proposed for calculating $E_{nlj}^{\rm theor}$ in conventional and exotic nuclei was employed. The calculations in [28] were performed with a density-dependent effective Gogny interaction.

In column 11, we give the results of the calculations performed within the self-consistent theory of finite Fermi systems (TFFS) [40]. The effective interaction of quasiparticles was introduced there phenomenologically as well (the quoted values $E_{nlj}^{\rm theor}$ were calculated in [40] by using set no. 5 of the parameters of the quasiparticle Lagrangian). From a comparison of the values $E_{nlj}^{\rm theor}$ from [40] with the analogous values from [28, 37–39], one can see that the values $E_{nlj}^{\rm theor}$ calculated within the self-consistent theory of finite Fermi systems are in better agreement with $E_{nlj}^{\rm expt}$ than their counterparts calculated within the Hartree–Fock method by using various versions of effective density-dependent interaction. This is associated in part with the energy and velocity dependence of the effective quasiparticle interaction used in the self-consistent theory of finite Fermi systems; as a result, the mean field acting on a quasiparticle also depends on its energy and velocity within this theory.

In [24, 25, 27], the energies of single-particle levels in some spherical nuclei, including ^{40}Ca, were calculated within the relativistic mean-field approximation (RMFA). Column 12 of Table 3 gives the values $E_{nlj}^{\rm theor}$ from [24], since only in that study did

Table 2. Experimental values $-E^{\mathrm{expt}}_{nlj}$ (in MeV) for ^{40,48}Ca

$2s_{1/2}$	$1d_{3/2}$	$1f_{7/2}$	$2p_{3/2}$	$2p_{1/2}$	$1f_{5/2}$	References
			^{40}Ca			
17.2(18)	15.2(20)	7.52(75)	6.10(67)	4.27(43)	1.46(20)	Our study
18.2	15.6	8.4	6.3	4.3	2.9	[29]
		8.364	6.264	4.464	1.864	[30]
18.19	15.64	8.36	6.29	4.23	2.86	[31]
18.29	15.64	8.36	5.86	4.20	1.38	[5]
18.11	15.64	8.36	6.42	4.75	3.48	[32]
18.11	15.64	8.36	6.42			[33]
			^{48}Ca			
15.07(152)	15.22(179)	10.10(101)	4.68(47)	2.87(28)	1.57(40)	Our study
12.4	12.4	9.9	5.1	3.1	1.2	[29]
12.55	12.53	9.95	5.15	3.13	1.56	[33]

Table 3. Experimental energies E^{expt}_{nlj} of single-particle neutron states along with their calculated counterparts E^{theor}_{nlj} for ^{40}Ca

Subshell	$-E^{\mathrm{expt}}_{nlj}$, MeV		$-E^{\mathrm{theor}}_{nlj}$, MeV								
	[34]	our study	WS [35]	DOM [36]	DOM [31]	HFS [37]	HF [38]	HFS [39]	HF [28]	TFFS [40]	RMFA [24]
1	2	3	4	5	6	7	8	9	10	11	12
$1s_{1/2}$	61.5(10)		45.61	66.12	61.00	55.33	62.20				58.15
$1p_{3/2}$	42.1(4)		33.65	43.8	41.00	39.22	42.80				40.73
$1p_{1/2}$	37.5(8)		30.84	39.12	37.00	36.08	39.00				36.01
$1d_{5/2}$	23.6(1)		21.80	22.48	22.25	23.26	24.50		23.00	19.50	23.98
$2s_{1/2}$	18.2(1)	17.2(18)	18.14	17.53	17.49	17.08	18.00	15.70	18.00	16.00	17.29
$1d_{3/2}$	15.6(1)	15.2(20)	15.64	15.79	16.08	17.53	17.70	14.60	16.00	14.60	16.36
$1f_{7/2}$		7.52(75)	8.35	8.54	8.30	8.34	8.00	9.90	9.00	9.10	8.57
$2p_{3/2}$		6.10(67)	6.44	5.59	5.65	3.02		5.50	3.90	6.80	3.74
$2p_{1/2}$		4.27(43)	4.29	4.19	4.43	1.56		3.80	1.50	4.50	2.02
$1f_{5/2}$		1.46(20)	2.72	1.50	2.73	1.21		2.60	0.30	2.40	0.23

the calculations cover all bound states of the ^{40}Ca nucleus. Only the conclusion that there is qualitative agreement between E^{RMFA}_{nlj} and E^{expt}_{nlj} can be drawn from a global analysis of the values E^{theor}_{nlj} from [24, 25, 27]. According to [41], all versions of the relativistic mean-field approximation that have been developed thus far are based on the use of energy-independent scalar and vector potentials. Therefore, the relativistic mean-field approximation provides a good description of the ground-state properties of nuclei and of the order of single-particle levels, but it is unable to describe their density in the vicinity of the Fermi energy.

In summary, we can state that, at the present time,

Table 4. Experimental energies E_{nlj}^{expt} of single-particle neutron states according to the present study along with the calculated energies E_{nlj}^{theor} for ^{42,44,46,48}Ca

$-E_{nlj}$, MeV						References
$2s_{1/2}$	$1d_{3/2}$	$1f_{7/2}$	$2p_{3/2}$	$2p_{1/2}$	$1f_{5/2}$	
		^{42}Ca				
15.44(154)	13.03(184)	7.70(107)	5.73(57)	4.10(41)		Our study
17.44	16.85	8.81	3.86	2.19	1.80	[24]
17.80	16.40	9.00	4.00	1.80	0.40	[28]
18.10	15.40	7.80	6.30	1.80	0.30	[42]
		8.80	5.60	5.60	4.00	[1]
		^{44}Ca				
17.61	13.91(159)	9.23(112)	5.92(75)	3.63(36)		Our study
	17.39	9.10	3.97	2.34	0.64	[24]
17.80	16.70	9.00	4.10	2.00	0.60	[28]
		9.00	5.20	3.70	1.00	[1]
		^{46}Ca				
17.81		10.00(100)	5.85(60)	3.58(39)	3.20(45)	Our study
	17.97	9.43	4.10	2.50	0.90	[24]
		9.20	4.30	2.20	0.80	[28]
		9.30	5.00	3.20	1.00	[1]
		^{48}Ca				
15.07(152)	15.22(179)	10.10(101)	4.68(47)	2.87(28)	1.57(40)	Our study
12.59	12.51	9.90	5.14	3.09	1.15	[37]
18.10	18.95	9.10	4.13	2.60	2.02	[39]
20.50	20.70	10.40	5.10			[35]
15.10	13.60	8.80	5.80	4.20	1.90	[38]
18.20	17.60	9.50	4.60	2.50	1.10	[28]
13.70	13.00	8.30	6.50	4.00	1.50	[40]
18.02	18.69	9.83	4.19	2.64	1.15	[24]
		9.80	5.00	3.00	1.00	[1]

the calculations within the dispersive optical model and within the self-consistent theory of finite Fermi systems lead to the best agreement between E_{nlj}^{theor} and E_{nlj}^{expt} for ^{40}Ca.

For ^{42,44,46,48}Ca, there are no data on E_{nlj}^{expt} for deep hole states. In Table 4, data available in the literature for E_{nlj}^{theor} are therefore contrasted only against the values E_{nlj}^{expt} in the vicinity of E_{F} that were found in the present study.

From the experimental and theoretical values of E_{nlj} that are presented in Table 4 for ^{42,44,46}Ca, one can see that the values E_{nlj}^{MSM} calculated in [1] exhibit

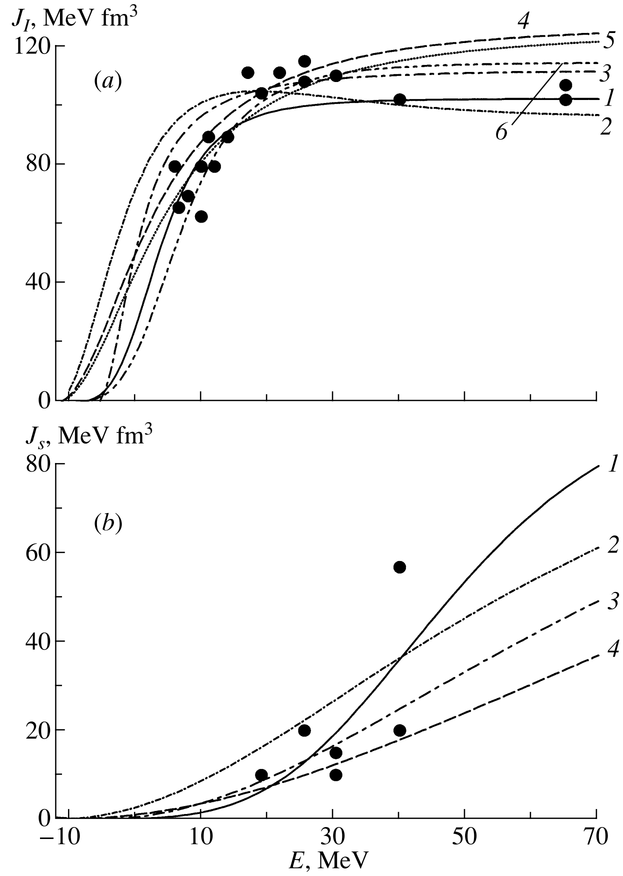

Fig. 2. (a) Volume integral J_I of the imaginary part of the optical potential and (b) volume integral J_s of the volume component of the imaginary optical potential for the $n\ +\ ^{40}$Ca system versus energy: (points) experimental values of $J_I(E_k)$ and $J_s(E_k)$ and (curves) parametrizations of $J_I(E)$ and $J_s(E)$ (see explanations in the main body of the text).

smaller deviations from E_{nlj}^{expt} than the values E_{nlj}^{theor} from [24, 28, 42].

The values E_{nlj}^{theor} for ^{48}Ca in Table 4 were borrowed from the same articles as those for ^{40}Ca. The calculated values E_{nlj}^{TFFS} [40] and E_{nlj}^{MSM} [1] show the smallest deviations from E_{nlj}^{expt}.

Since the best agreement between E_{nlj}^{theor} and E_{nlj}^{expt} for ^{40}Ca was obtained in the case of the calculations within the dispersive optical model, it is of importance to address the following issues: the application of the dispersive optical model to describing E_{nlj}^{expt} for the ^{42,44,46,48}Ca nuclei and the investigation of the possibility of employing the dispersive optical model to calculate the single-particle energies of the bound states of neutrons in neutron-rich calcium isotopes. This is done in the sections of this article that follow.

4. ANALYSIS OF THE SINGLE-PARTICLE FEATURES OF NEUTRON STATES IN ^{40}Ca WITHIN THE DISPERSIVE OPTICAL MODEL

The method of a dispersive optical-model analysis is based on the idea to employ information about neutron (proton) scattering on a nucleus to calculate the single-particle features of neutron (proton) bound states in this nucleus. The method for calculating single-particle features of levels in spherical nuclei on the basis of the dispersive optical model was described in detail in a number of studies (see [43] and references therein).

For the $n + A$ system, the dispersive optical potential can be represented in the form

$$U(r, E) = -U_n(r, E) - U_{\text{so}}(r, E), \tag{9}$$

where $U_n(r, E)$ is a complex-valued central potential and $U_{\text{so}}(r, E)$ is a spin–orbit potential. The central potential is the sum of three components of the real part and two components of the imaginary part; that is,

$$U_n(r, E) = V_{\text{HF}}(r, E) + \Delta V_s(r, E) \tag{10}$$
$$+ \Delta V_d(r, E) + i[W_s(r, E) + W_d(r, E)].$$

In (10), V_{HF} is the Hartree–Fock component; $\Delta V_{s,d}$ and $W_{s,d}$ are, respectively, the dispersive and imaginary parts of the dispersive optical potential; and the indices s and d label, respectively, the volume and surface parts. Within the dispersive optical model, $\Delta V_s(r, E)$ and $\Delta V_d(r, E)$ are calculated with the aid of dispersion relations where $W_s(r, E)$ and $W_d(r, E)$ appear as integrands. The dispersion relations are also valid for the volume integrals of the corresponding parts of the dispersive optical potential.

Within the traditional version of the dispersive optical model, one analyzes experimental data on the differential cross sections $\sigma^{\text{expt}}(\theta)$ for the respective scattering process and on the corresponding polarization $P^{\text{expt}}(\theta)$ at a specific energy value E_k. Data on the volume integrals per nucleon of the resulting imaginary potentials $J_s(E_k)$, $J_d(E_k)$, and $J_I(E_k) = J_s(E_k) + J_d(E_k)$ are parametrized by analytic dependences $J_s(E)$, $J_d(E)$, and $J_I(E)$ that are symmetric with respect to E_{F}. These dependences are then used to calculate the volume integrals of the dispersive components of the dispersive optical potential.

In order to determine the parameters of the dispersive optical potential, the experimental values $\sigma^{\text{expt}}(\theta)$ and $P^{\text{expt}}(\theta)$ for the $n\ +\ ^{40}$Ca system were analyzed in [44] for $9.9 \leq E_n \leq 40$ MeV, in [36] for $5.3 \leq E_n \leq 40$ MeV, and in [31] for $11 \leq E_n \leq 40$ MeV. By using the optical-potential parameters found previously by other authors, $J_s(E_k)$, $J_d(E_k)$, and $J_I(E_k)$ were determined in [31, 36, 44]; of these, $J_s(E_k)$ and $J_I(E_k)$ are shown in Fig. 2, and they are seen to have the largest scatter.

In [44], the dependences $J_I(E_k)$ and $J_s(E_k)$ were parametrized by means of the Brown–Rho formula,

$$J_I(E) = \frac{\alpha_I}{1 + \left(\dfrac{\beta_I}{E - E_{\mathrm{F}}}\right)^2}, \quad (11)$$

$$J_s(E) = \frac{\alpha_I}{1 + \left(\dfrac{\beta_s}{E - E_{\mathrm{F}}}\right)^2},$$

where α_I, β_I, and β_s are parameters.

In [31], use was made of a parametrization where E_0 was substituted for E_{F} in (11). It is assumed that, in the interval from E_{F} to E_0 and in the interval from $(2E_{\mathrm{F}} - E_0)$ to E_{F}, the imaginary potential vanishes, so that single-particle states are not fragmented.

In Fig. 2*a*, curve *3* was calculated by formula (11) with the parameters set to the values of $\alpha_I = 113.6$ MeV fm^3, $\beta_I = 6.46$ MeV, and $E_0 = -5.86$ MeV [31]; also, the parameter values used in this figure were $\alpha_I = 130$ MeV fm^3, $\beta_I = 15$ MeV, and $E_{\mathrm{F}} = -12.0$ MeV [36] for curve *4* and $\alpha_I = 128$ MeV fm^3, $\beta_I = 16.5$ MeV, and $E_{\mathrm{F}} = -12$ MeV [44] for curve *5*.

In [44], use was made of the Jeukenne–Mahaux approximating formula,

$$J_I(E) = \frac{\alpha_I}{1 + \left(\dfrac{\beta_I}{E - E_{\mathrm{F}}}\right)^4}, \quad (12)$$

$$J_s(E) = \frac{\alpha_I}{1 + \left(\dfrac{\beta_s}{E - E_{\mathrm{F}}}\right)^4}.$$

Curve *6* in Fig. 2*a* was calculated by formula (12) with the parameter values of $\alpha_I = 116$ MeV fm^3, $\beta_I = 18.8$ MeV, and $E_{\mathrm{F}} = -12.0$ MeV [44].

In Fig. 2*a*, the point at $E_k = 65$ MeV was borrowed from data reported in [45]. This value of $J_I(E_k)$ was not taken into account in determining the parameters α_I and β_I in [31, 36, 44]. From the above list of values of the parameters α_I and β_I, one can see that they have a considerable scatter for a specific approximating dependence.

In Fig. 2*b*, curves *4* and *3* were calculated by formula (11) with the parameter values of $\alpha_I = 130$ MeV fm^3, $\beta_s = 130$ MeV, and $E_{\mathrm{F}} = -12.0$ MeV [36] for the former and the parameter values of $\alpha_I = 113.6$ MeV fm^3, $\beta_s = 86.5$ MeV, and $E_0 = -5.86$ MeV [31] for the latter.

In practice, the application of the above version of the dispersive optical model involves considerable difficulties because of the absence of information about $\sigma^{\mathrm{expt}}(\theta)$ and $P^{\mathrm{expt}}(\theta)$ at various values of E_k for many nuclei. This comment applies perfectly to the ^{42,44,46,48}Ca nuclei. This explains the fact that, in various studies, an analysis within the dispersive optical model was performed only for a few nuclei. The version of the dispersive optical model where the parameter α_I for the $p + A$ and $n + A$ systems is determined by the method described below was proposed in [43, 46] in order to overcome these difficulties.

In [47], the CH89 systematics of the average (global) parameters of a traditional (nondispersive) optical potential was proposed on the basis of an analysis of information about $\sigma^{\mathrm{expt}}(\theta)$ and $P^{\mathrm{expt}}(\theta)$ for $p + A$ systems in the range $16 \le E \le 65$ MeV and $n + A$ systems in the range $10 \le E \le 26$ MeV for nuclei in the mass-number range $40 \le A \le 209$. In this systematics, the strength parameters depend on E and A, the range parameters depend on A, and the diffuseness parameters of the real and imaginary potentials are fixed at $a_V = a_s = a_d = 0.69$ fm. The CH89 systematics was composed without including experimental data on the total reaction cross sections $\sigma_r(E)$. Later on, $\sigma_r(E)$ was measured for some $p + A$ systems to a precision of about 3% [48]. The $\sigma_r^{\mathrm{CH89}}(E_k)$ values calculated with the CH89 parameters agree with $\sigma_r^{\mathrm{expt}}(E_k)$ [43] to within about 15%. In [49], it was shown that, for each $p + A$ system, one can determine individual values of the parameters $a_s^* = a_d^*$ for each nucleus such that the use of these values, together with the remaining parameter values of the CH89 systematics, leads to the cross sections $\sigma_r^{\mathrm{CH89}}(E_k)$ that are consistent with $\sigma_r^{\mathrm{expt}}(E_k)$ to within 3%. The version of the CH89 systematics where, instead of the average value of $a_s = a_d = 0.69$ fm, use is made of individual parameters $a_s^* = a_d^*$ for each nucleus was denoted by CH89* in [49]. The use of individual values of $a_s^* = a_d^*$ reduces the root-mean-square deviations χ^2 of $\sigma^{\mathrm{CH89}^*}(\theta)$ and $P^{\mathrm{CH89}^*}(\theta)$ from $\sigma^{\mathrm{expt}}(\theta)$ and $P^{\mathrm{expt}}(\theta)$ to values close to those found by freely varying all parameters of the potential of the traditional optical model. The average parameters of the CH89 systematics make it possible to describe well the positions of the maxima and minima of the experimental differential cross sections for elastic scattering and of the respective polarization, but the results for their absolute values prove to be inadequate. The description of the absolute cross-section and polarization values depends predominantly on the imaginary part of the optical potential; in order to improve this description, it is necessary to go over from the average values of the geometric parameters of the imaginary part of the optical potential for all nuclei to individual parameters for each nucleus. It turned out that this individualization can be implemented by varying only the parameters $a_s = a_d$. The use of the CH89* systematics of parameters underlies the dispersive-optical-model version developed in [43]. Within this version, a subsequent determination of the parameters of the dispersive optical potential is based on analyzing the model dependences $\sigma^{\mathrm{CH89}^*}(\theta)$ and $P^{\mathrm{CH89}^*}(\theta)$ instead of $\sigma^{\mathrm{expt}}(\theta)$ and $P^{\mathrm{expt}}(\theta)$. In [43, 46], it was shown that, for $p+A$ systems, the procedure for determining the average parameters of the dispersive optical potential is simplified considerably within this version without loss of accuracy.

In the CH89 systematics, the geometric parameters of the optical potential are identical for $p+A$ and $n+A$ systems. In the CH89* systematics, the parameters $a_s^* = a_d^*$ take individual values for each $p+A$ system. There arises the question of whether the parameters $a_s^* = a_d^*$ found for $p+A$ systems are appropriate for $n+A$ systems. In [50], it was shown that the values of $a_s^* = a_d^*$ make it possible to describe experimental data on $\sigma(\theta)$, the total reaction cross sections σ_r, and the total interaction cross sections σ_t for $n+A$ systems as well.

A new global systematics of the parameters of the traditional optical potential was proposed in [51], and individual (local) parameters were determined there for some nuclei. The values of the parameter α_I that were obtained from an analysis of the model cross sections $\sigma^{\mathrm{CH89}^*}(\theta)$ and $\sigma^{[51]}(\theta)$ for calcium isotopes differ from one another within 2 to 3%. In the present study, the volume integrals $J_s^{\mathrm{CH89}^*}(E)$ and $J_I^{\mathrm{CH89}^*}(E)$ are approximated by the expressions in (12), where $\alpha_I = J_I^{\mathrm{CH89}^*}(E_k)$ for $E_k \approx$ 50–60 MeV.

In order to determine the parameter β_I, one needs experimental information about $\sigma^{\mathrm{expt}}(\theta)$ and $P^{\mathrm{expt}}(\theta)$ at low energies. Since there are no such data for even–even calcium isotopes, with the exception of ^{40}Ca, it would be reasonable to determine β_I in (12) as an adjustable parameter that corresponds to the minimum deviation of the energies E_{nlj}^{DOM} calculated within the dispersive optical model from E_{nlj}^{expt} in the vicinity of E_{F}.

In order to determine β_s within the traditional version of the dispersive optical model, it is necessary to have information about the values of $J_s(E_k)$ for $E_k \approx$ 30–60 MeV. Because of the aforementioned scarcity of experimental information, the parameter β_s was found here on the basis of data on $J_s(E_k = E_{\mathrm{F}} - E_{1s1/2})$ from the systematics presented in [47, 51]. In doing this, it was assumed that $E_{1s1/2} \approx -60$ MeV.

For ^{40}Ca, the parameter α_I, which appears in (12), was determined in this study to be 103.5 MeV fm^3. Curve *1* in Fig. 2*a* was calculated by using this value of the parameter α_I, $E_{\mathrm{F}}^{\mathrm{expt}} = -11.36$ MeV, and $\beta_I =$ 18 MeV. From Fig. 2*a*, one can see that curve *1* is consistent with the empirical values of $J_I(E_k)$ at $E_k \leq 10$ MeV and $E_k = 40$ and 65 MeV. In the region of low energies, the dependence $J_I(E)$ calculated with the parameters of the systematics from [51] (curve *2*) agrees poorly with $J_I(E_k)$.

In Fig. 2*b*, curve *1* was calculated by formula (12) with the parameter values of $\alpha_I = 103.5$ MeV fm^3, $\beta_s = 65$ MeV, and $E_{\mathrm{F}}^{\mathrm{expt}} = -11.36$ MeV; for curve *2*, use was made of the parameters from [51].

Within the traditional version of the dispersive optical model, the geometric parameters $r_{s,d}(E_k)$ and $a_{s,d}(E_k)$ are found from an analysis of $\sigma^{\mathrm{expt}}(\theta)$ and $P^{\mathrm{expt}}(\theta)$ under the condition that the volume integrals $J_{s,d}(E_k)$ are fixed in accordance with an analytic dependence chosen for them (in the Jeukenne–Mahaux, the Brown–Rho, or some other form). After that, the parameters $r_{s,d}(E_k)$ and $a_{s,d}(E_k)$ are averaged over energy. In [43, 46], it was shown that the parameters of the CH89* systematics can be taken for the average parameters r_s, r_d, a_s, and a_d.

A method for determining the energy dependence of the strength parameter of the Hartree–Fock component $V_{\mathrm{HF}}(E)$ was proposed in [43, 46]. As in [43], the dependence $V_{\mathrm{HF}}(E)$ was represented here as

$$V_{\mathrm{HF}}(E) = V_{\mathrm{HF}}^{(1)}(E_{\mathrm{F}}) + V_{\mathrm{HF}}^{(2)}(E_{\mathrm{F}})\exp\left[\frac{-\lambda(E-E_{\mathrm{F}})}{V_{\mathrm{HF}}^{(2)}(E_{\mathrm{F}})}\right] \text{ for } E > E_{\mathrm{F}} \tag{13}$$

and as

$$V_{\mathrm{HF}}(E) = V_{\mathrm{HF}}(E_{\mathrm{F}}) - \lambda(E - E_{\mathrm{F}}) \text{ for } E < E_{\mathrm{F}}, \tag{14}$$

where

$$V_{\mathrm{HF}}(E_{\mathrm{F}}) = V_{\mathrm{HF}}^{(1)}(E_{\mathrm{F}}) + V_{\mathrm{HF}}^{(2)}(E_{\mathrm{F}}). \tag{15}$$

The parameters $V_{\mathrm{HF}}(E_{\mathrm{F}})$, λ, r_{HF}, and a_{HF} were determined according to the following procedure. The dispersive components of the real part of the dispersive optical potential (10), $\Delta V_s(r,E)$ and $\Delta V_d(r,E)$, were calculated with the parameters α_I, β_I, β_s, r_s, r_d, a_s, and a_d fixed at the values found for them. The parameters r_{so} and a_{so} were taken in accordance with [47] or [51], while the parameter V_{so} was varied.

It turned out that, to within 3%, the $J_{\mathrm{HF}}(E_{\mathrm{F}})$ and $V_{\mathrm{HF}}(E_{\mathrm{F}})$ values determined within various versions

Table 5. Parameters of the dispersive optical potential for the $n\ +\ ^{40-56}$Ca systems

A	$r_d = r_s$, fm	$a_d = a_s$, fm	α_I, MeV fm^3	β_s, MeV	β_I, MeV	$r_{\rm so}$, fm	$a_{\rm so}$, fm	$r_{\rm HF}$, fm	$a_{\rm HF}$, fm	λ	$-E_{\rm F}$, MeV	$V_{\rm so}$, MeV fm^3
40	1.207	0.600	103.5	60	18	0.989	0.63	1.179	0.79	0.580	11.36	5.9
42	1.209	0.605	88	60	9	0.995	0.63	1.160	0.760	0.561	10.36	6.2
44	1.211	0.610	90	60	12	1.000	0.63	1.190	0.667	0.572	11.57	6.5
46	1.213	0.615	90	60	12	1.005	0.63	1.200	0.636	0.577	12.3	6.8
48	1.214	0.540	83	54	15	1.010	0.63	1.205	0.619	0.557	7.4	7.0
50	1.216	0.53	80	53	18	1.014	0.63	1.170	0.760	0.576	7.2	7.2
52	1.217	0.54	80	53	18	1.018	0.63	1.150	0.850	0.563	2.2	7.5
54	1.217	0.54	80	53	18	1.018	0.63	1.150	0.850	0.579	2.2	8.0
56	1.220	0.53	80	53	15	1.026	0.63	1.150	0.850	0.573	2.3	8.0

of the dispersive optical model for various $n + A$ and $p + A$ systems agree with the $J_V^{[51]}(E_{\rm F})$ and $V^{[51]}(E_{\rm F})$ values calculated by the formulas from [51]. We note that the identity $J_{\rm HF}(E_{\rm F}) \equiv J_V(E_{\rm F})$ holds by definition of the dispersion relations (see [52]). This made it possible to determine, for each trial value of $r_{\rm HF}$, the corresponding diffuseness parameter $a_{\rm HF}$ from the equality $g_{\rm HF} = g_V^{[51]}$, where

$$g_{\rm HF} = \int f(r, r_{\rm HF}, a_{\rm HF})d\mathbf{r}, \qquad (16)$$

$$g_V^{[51]} = \int f(r, r_V^{[51]}, a_V^{[51]})d\mathbf{r}.$$

For several fixed values of $V_{\rm so}$ and trial pairs of $r_{\rm HF}$ and $a_{\rm HF}$, the values of $V_{\rm HF}(E_{nlj})$ were found from a fit to $E^{\rm expt}_{1s1/2}$, $E^{\rm expt}_{1d3/2}$, and $E^{\rm expt}_{1f7/2}$ in solving the Schrödinger equation for bound states. The parameters $V_{\rm HF}(E_{\rm F})$ and λ, which appear in (13) and (14), were determined for ^{40}Ca by the formulas

$$V_{\rm HF}(E_{\rm F}) = \frac{V_{\rm HF}(E^{\rm expt}_{1d3/2}) + V_{\rm HF}(E^{\rm expt}_{1f7/2})}{2}, \qquad (17)$$

$$\lambda = \frac{V_{\rm HF}(E^{\rm expt}_{1s1/2}) - V_{\rm HF}(E_{\rm F})}{E^{\rm expt}_{1s1/2} - E^{\rm expt}_{\rm F}}. \qquad (18)$$

The energies $E^{\rm DOM}_{nlj}$ for the $2s_{1/2}$, $1d_{3/2}$, $1f$, and $2p$ states in the vicinity of $E_{\rm F}$ were calculated by the iteration method (for details of the relevant calculation, the interested reader is referred to [43]) in solving the Schrödinger equation at fixed values of the dispersive-optical-potential parameters $V_{\rm so}$, $r_{\rm so}$, $a_{\rm so}$, $V_{\rm HF}(E_{\rm F})$, λ, $r_{\rm HF}$, and $a_{\rm HF}$. The optimum set of trial parameters was determined by minimizing the functional

$$\chi^2 = \sum_{nlj}\left(\frac{E^{\rm DOM}_{nlj} - E^{\rm expt}_{nlj}}{\Delta^{\rm expt}_{nlj}}\right)^2.$$

The values found in this way for the parameters of the dispersive optical potential are given in Table 5.

The criterion according to which the parameters of the dispersive optical potential are self-consistent if, in the energy range $E_{\rm F} - 10$ MeV $< E < E_{\rm F} +$ 10 MeV, the volume integral ΔJ_I of the sum of the dispersive corrections ΔV_s and ΔV_d is a nearly linear function of energy was discussed in [41]. Figure 3 displays the dependences $\Delta J_{I,s,d}$, which illustrate self-consistency according to this criterion for the dispersive-optical-potential parameters given in Table 5.

The calculated values of single-particle energies E_{nlj} of states and their occupation numbers N_{nlj} (the formulas for calculating N_{nlj} can be found in [5]) are given in Table 6. Column 2 there contains the experimental values $E^{\rm expt}_{nlj}$ obtained in [34] for the $1s_{1/2}$–$1d_{5/2}$ states and in the present study for the $2s_{1/2}$–$1f_{5/2}$ states; columns 3 and 4 present the values $E^{\rm DOM}_{nlj}$ and $N^{\rm DOM}_{nlj}$, respectively, calculated in the present study; and column 5 gives the values $N^{\rm expt}_{nlj}$ determined in the present study. In order to demonstrate the dependence of the energies $E^{\rm DOM}_{nlj}$ on the choice of the parameter β_I, the values $E^{\rm DOM}_{nlj}$ calculated at $\beta_I = 15$ MeV are quoted in column 6. The results calculated in the present study with $\beta_I =$ 18 MeV correspond to the minimum of the sum of the squared deviations of $E^{\rm DOM}_{nlj}$ calculated in [31, 36] (see

Table 6. Experimental values of the single-particle energies E_{nlj} and of the respective occupation numbers N_{nlj} in ^{40}Ca along with their counterparts calculated on the basis of the dispersive optical model

Subshell	$-E_{nlj}^{\rm expt}$, MeV	$-E_{nlj}^{\rm DOM}$, MeV	$N_{nlj}^{\rm DOM}$	$N_{nlj}^{\rm expt}$	$-E_{nlj}^{\rm DOM}$, MeV ($\beta_I = 15$ MeV)
1	2	3	4	5	6
$1s_{1/2}$	61.5(10)	61.47	0.934		61.35
$1p_{3/2}$	42.1(4)	40.53	0.921		40.36
$1p_{1/2}$	37.5(8)	35.30	0.915		35.00
$1d_{5/2}$	23.6(1)	21.24	0.894		20.23
$2s_{1/2}$	17.2(18)	17.61	0.891	0.67–0.79	16.80
$1d_{3/2}$	15.2(20)	15.01	0.874	0.81–0.85	14.25
$1f_{7/2}$	7.52(75)	7.72	0.113	0.02–0.04	7.36
$2p_{3/2}$	6.10(67)	5.63	0.072	0.00–0.04	5.39
$2p_{1/2}$	4.27(43)	4.08	0.060	0.00–0.06	3.93
$1f_{5/2}$	1.46(20)	1.46	0.072	0.00–0.02	1.48

Note: The values $E_{nlj}^{\rm expt}$ for the $1s_{1/2}$–$1d_{5/2}$ and $2s_{1/2}$–$1f_{5/2}$ states were obtained in [34] and in the present study, respectively.

Table 3, columns 6, 5) from $E_{nlj}^{\rm expt}$ for the $2s_{1/2}$–$1f_{5/2}$ states. We note that the values $N_{nlj}^{\rm DOM}$ calculated on the basis of the dispersive optical model in the present study and in [31, 36] for the $1f_{7/2}$, $2p_{3/2}$, and $1f_{5/2}$ states exceed their experimental counterparts. In [8], it was shown that the calculated values $N_{nlj}^{\rm DOM}$ for states in the vicinity of $E_{\rm F}$ can be reduced upon considering that the imaginary potential is nonlocal, which violates the symmetry of absorption with respect to $E_{\rm F}$ at high $|E|$.

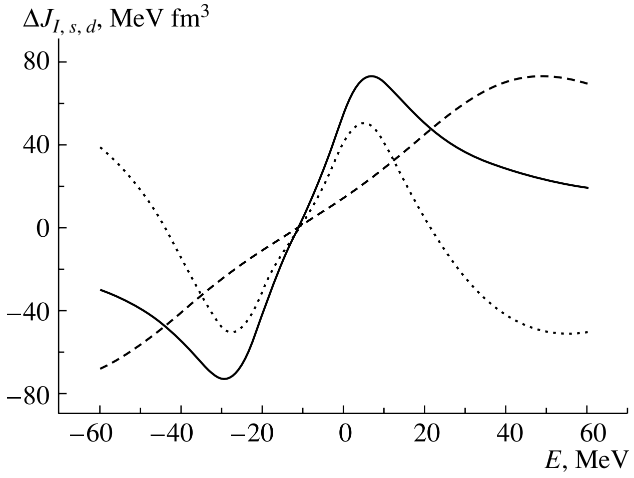

Fig. 3. Energy dependences of the volume integrals (solid curve) ΔJ_I, (dashed curve) ΔJ_s, and (dotted curve) ΔJ_d of the dispersive components of the dispersive optical potential for the $n + {}^{40}$Ca system.

The results obtained in this section provide grounds to employ the proposed version of the dispersive optical model to describe the features of single-particle states in the ^{42,44,46,48}Ca nuclei. This is done in the next section.

5. COMPARISON OF EXPERIMENTAL SINGLE-PARTICLE FEATURES OF NEUTRON STATES IN ^{42,44,46,48}Ca WITH THEIR COUNTERPARTS CALCULATED ON THE BASIS OF THE DISPERSIVE OPTICAL MODEL

In the even–even isotopes ^{42,44,46}Ca, there occurs the successive filling of the $1f$ and $2p$ subshells. In describing nuclei that involve open shells, it is necessary to take into account superfluid correlations. We assume that nucleon-pairing effects can be taken into account by selecting individual parameters of the dispersive optical potential for each nucleus. According to [53], the experimental values of the ground-state spins and parities are $7/2^-$ in ^{43,45,47}Ca and $3/2^-$ in ^{49}Ca. If use is made of the values $E_{nlj}^{\rm expt}$ for the $1d_{3/2}$ and $1f_{7/2}$ states in ^{42,44}Ca (see Table 1), then the average values of the Fermi energy for these two nuclei are $E_{\rm F} = -10.36$ and -11.57 MeV, respectively. For ^{46}Ca, there are no data on the energy of the $1d_{3/2}$ state. Assuming that the average value of the energy of the $1d_{3/2}$ state in ^{46}Ca is equal to the half-sum of the energies of the analogous states in ^{44}Ca and ^{48}Ca, we obtain, for ^{46}Ca, the average value of $E_{\rm F} = -12.3$ MeV estimated on the basis of the data in Table 1. For ^{48}Ca, the data in Table 1 lead to the average value of $E_{\rm F} = -7.4$ MeV, which is in good agreement with the value of -7.55 MeV found from data on the binding energies. The deviation of the $E_{\rm F}$ values calculated for ^{42,44,46}Ca by using data on the binding energies (-9.70, -9.27, and -8.84 MeV, respectively) from those determined on the basis of information about $E_{nlj}^{\rm expt}$ indicates that the structure of levels in these nuclei differs from the single-particle structure.

In order to determine the parameters of the dispersive optical potential for ^{42,44,46,48}Ca, we employed the dispersive-optical-model version described in the preceding section, slightly changing the procedure for evaluating the parameter $V_{\rm so}$.

For a large number of magic nuclei and nuclei close to magic ones, Koura and Yamada [33] presented a compilation of the single-particle energies $E_{nlj}^{\rm expt}$ of proton and neutron states in a tabular form. They compared the experimental values of E_{nlj} with the theoretical results found within the relativistic mean-field approximation. The shell potential was written in the standard form by using the Woods–Saxon form factors. Expressions for calculating the parameters of the shell potential and tables of these parameters were also given in that article. We used the tables of the parameters from [33] and calculated the volume integrals of the spin–orbit potentials for ^{40}Ca and ^{48}Ca. It turned out that the volume integral for ^{48}Ca is approximately 15 to 20% greater than that for ^{40}Ca.

At the present time, the isospin dependence of the spin–orbit potential is being studied in detail by many authors. Interest in this problem was stimulated by the development of studies within the relativistic mean-field approximation (see [54–56] and references therein). However, there is no unambiguous solution here because of the scarcity of relevant experimental data.

If the geometric parameters of the spin–orbit potential are fixed, for example, in accordance with the CH89 systematics, then an increase in the volume integral for ^{48}Ca can be associated with an increase in the strength parameter $V_{\rm so}$. A slight increase in $V_{\rm so}$ in response to a change in A from 40 to 48 can be described by using the formulas proposed in [57],

$$V_{\rm so}^{n} = \frac{(NV_{nn} + ZV_{np})}{A} K \ \ [\text{MeV fm}^2], \tag{19}$$

where

$$K = 0.263 \left[1 + 2\frac{N-Z}{A}\right], \tag{20}$$

$$V_{pp} = V_{nn} = 19.7, \quad V_{pn} = V_{np} = 87. \tag{21}$$

It can readily be shown that, for the $n\ +\ ^{42,44,46,48}$Ca systems, the quantity $V_{\rm so}^{n}$ can be represented in the form

$$V_{\rm so}^{n}(A) = V_{\rm so}^{n}(A = 40)\xi, \tag{22}$$

where

$$\xi = 1 + 0.018(A - 40). \tag{23}$$

For each calcium isotope, we have calculated $V_{\rm so}^{n}(A)$ by formulas (22) and (23) at the fixed value of $V_{\rm so}^{n}(A = 40) = 5.9$ MeV fm^2.

The parameters α_I for the $n\ +\ ^{42,44,46,48}$Ca systems were determined by the method applied to the $n\ +\ ^{40}$Ca system. By using data on σ_r from [48] for the $p\ +\ ^{42,44,48}$Ca systems and the values of σ_r for ^{46}Ca that were estimated on the basis of data from [48], we determined the CH89* parameters for the $n\ +\ ^{42,44,46,48}$Ca systems by the method proposed in [50] and found that $\alpha_I = 88$, 90, 90, and 83 MeV fm^3, respectively. If one employs data from [51], the values of the parameter α_I for these systems appear to be 93, 92, 90, and 88 MeV fm^3, respectively. The maximum distinction between the values of α_I that were determined with the parameters from [51] and from the CH89* systematics was 5%. The error of 5% in determining α_I does not have a significant effect on the accuracy in determining $E_{nlj}^{\rm DOM}$. In the following, we will use the values of α_I that were calculated on the basis of the CH89* parameters.

The values of the parameters β_s were calculated, while the values of β_I, $r_{\rm HF}$, and $a_{\rm HF}$ were selected for each $n + A$ system by using the same procedure as that which was described for the $n\ +\ ^{40}$Ca system in Section 3. The resulting set of dispersive-optical-potential parameters for the ^{42,44,46,48}Ca nuclei is given in Table 5.

The values $E_{nlj}^{\rm DOM}$ calculated with the parameters from Table 5 are given in Table 7. Comparing the values $E_{nlj}^{\rm DOM}$ for the $2s_{1/2}$–$1f_{5/2}$ states in the ^{42,44,46,48}Ca nuclei with the data in Table 1, we can conclude that these results agree within the experimental errors. The agreement between $N_{nlj}^{\rm DOM}$ and $N_{nlj}^{\rm expt}$ for the ^{42,44,46,48}Ca nuclei is of approximately the same character as in the case of ^{40}Ca. For the $1f$ and $2p$ states, the values $E_{nlj}^{\rm DOM}$ agree well with the values $E_{nlj}^{\rm MSM}$ from [1]. For the ^{42,44,46,48}Ca isotopes, the spin–orbit splitting $\Delta_{1p}^{\rm DOM}$ calculated on the basis of the dispersive optical model changes within the range 5.1–5.8 MeV, which is in agreement with the value of $\Delta_{1p}^{\rm expt} = 4.6(9)$ MeV for ^{40}Ca. For the 1d state, the values $\Delta_{d}^{\rm DOM}$ range between 6.3 and 8.3 MeV, this being in agreement with the value of $\Delta_{d}^{\rm expt} = 8.0(2)$ MeV for ^{40}Ca. The values $\Delta_{1f}^{\rm DOM}$ and $\Delta_{2p}^{\rm DOM}$ agree with $\Delta_{1f}^{\rm expt}$ and $\Delta_{2\rm p}^{\rm expt}$, respectively, within the errors in the experimental values.

Figure 1 clearly demonstrates that, in ^{48}Ca, the filling of the $1f_{7/2}$ subshell leads to an increase in the absolute values of the energies of the respective states and that the Fermi energy $E_{\rm F}$ undergoes a jump upon going over from ^{46}Ca to ^{48}Ca. From Table 5, one can see that, for the $n + {}^{40,42,44,46,48}$Ca systems, all of the dispersive-optical-potential parameters, with the exception of $E_{\rm F}$, take close values and that the parameter $V_{\rm so}$ increases smoothly. If, in calculating $E_{nlj}^{\rm DOM}$ for ^{48}Ca, one employs, for $E_{\rm F}$, the average value for the ^{40,42,44,46}Ca isotopes, there will be no agreement between $E_{nlj}^{\rm DOM}$ and $E_{nlj}^{\rm expt}$.

On the basis of a comparison of the results of calculations and experimental data, we can conclude that the proposed version of the dispersive optical model provides a fairly accurate description of experimental single-particle energies of bound states in calcium isotopes both for doubly magic nuclei and for nuclei featuring unfilled shells. Good agreement between $E_{nlj}^{\rm DOM}$ and $E_{nlj}^{\rm expt}$ for ^{40,42,44,46,48}Ca gives sufficient grounds to apply this version of the dispersive optical model to calculating the positions of single-particle 1f and 2p levels in ^{50,52,54,56}Ca. It would then be reasonable to compare the results derived in this way with their counterparts obtained in [1] on the basis of the multiparticle shell model. Questions associated with these calculations and comparison are considered in the next section.

6. CALCULATION OF THE SINGLE-PARTICLE ENERGIES OF NEUTRON LEVELS IN THE NEUTRON-RICH NUCLEI ^{50,52,54,56}Ca

The neutron-rich nuclei ^{50,52,54,56}Ca are unstable. They undergo beta decay, with the half-lives $T_{1/2}$ [53] being 14 s for ^{50}Ca, 4.6 s for ^{52}Ca, and 10 ms for ^{56}Ca (there are presently no data on $T_{1/2}$ for ^{54}Ca). The ground-state spin–parities determined experimentally for the ^{51}Ca and ^{53}Ca nuclei in [53] involve ambiguities, $(3/2^-)$ and $(3/2^-, 5/2^-)$, respectively. There are no data on the spins of the ^{55,57}Ca nuclei. If the spin–parity of ^{51}Ca is $3/2^-$, then $E_{\rm F} = -7.2$ MeV according to data from [1] on $E_{1f7/2}^{\rm MSM}$ and $E_{2p3/2}^{\rm MSM}$. If the spin–parity of ^{53}Ca is $3/2^-$, $E_{\rm F} = -7.35$ MeV, but, if it is $5/2^-$, then $E_{\rm F} = -2.2$ MeV. According to data from [1], $E_{\rm F}$ takes nearly identical values for ^{54}Ca and ^{56}Ca—they are approximately equal to -2.2 MeV.

The Δ_{1f} and Δ_{2p} values estimated for the ^{50,52,54,56}Ca nuclei on the basis of data from [1] do not decrease with increasing A, remaining approximately identical to those for ^{48}Ca. The calculations that were performed in [24] and which were based on the relativistic mean-field approximation yield, for $\Delta_{1f}^{\rm RMFA}$, values that decrease slightly with increasing A and, for $\Delta_{2\rm p}^{\rm RMFA}$, values that, on the contrary, increase slightly with increasing A. In this connection, we calculated the values of $V_{\rm so}$ by formulas (22) and (23) as in the case of ^{42,44,46,48}Ca.

In order to determine λ by formula (18), it is necessary to estimate the energy of the $1s_{1/2}$ state for ^{50,52,54,56}Ca. According to [24], the values $E_{1s1/2}^{\rm RMFA}$ for ^{50,52,54,56}Ca range between -58.7 and -57.4 MeV. For the ^{40}Ca nucleus, $E_{1s1/2}^{\rm RMFA} = -58.15$ MeV, but $E_{1s1/2}^{\rm expt} = -61.5(10)$ MeV. Since the average energy of this state for the ^{50,52,54,56}Ca isotopes is $E_{1s1/2}^{\rm RMFA} = -58.0$ MeV (that is, it is equal to $E_{1s1/2}^{\rm RMFA}$ for ^{40}Ca), we estimated the respective energy for them at $E_{1s1/2}^{\rm est} = -61.5(10)$ MeV. The parameters of the dispersive optical potential for ^{50,52,54,56}Ca are given in Table 5.

The calculated values $E_{nlj}^{\rm DOM}$ for ^{50,52,54,56}Ca are presented in Table 8. For the sake of comparison, we also quote there the respective energies calculated within the relativistic mean-field approximation [24], on the basis of the Hartree–Fock model with Skyrme forces [58], and within the multiparticle shell model [1] ($E_{nlj}^{\rm RMFA}$, $E_{nlj}^{\rm HFS}$, and $E_{nlj}^{\rm MSM}$, respectively).

The last five columns of Table 8 display the results of the calculations based on the data of this table and performed for the energies Δ_p, Δ_d, Δ_f, and Δ_{2p} of the spin–orbit splitting of the 1p, 1d, 1f, and 2p states and for the energy gap $\Delta = E_{1f5/2} - E_{2p1/2}$ between the $1f_{5/2}$ and $2p_{1/2}$ states.

For ^{52}Ca, Table 8 gives the calculated values $E_{nlj}^{\rm DOM}$ corresponding to the presumed spin–parity of the ^{53}Ca ground state, $5/2^-$.

From Table 8, one can see that the aforementioned models predict approximately identical results for the

Table 7. Single-particle neutron-state energies $-E_{nlj}^{\mathrm{DOM}}$ (in MeV) calculated for ^{42,44,46,48}Ca on the basis of the dispersive optical model with the parameter values from Table 5

A	$1s_{1/2}$	$1p_{3/2}$	$1p_{1/2}$	$1d_{5/2}$	$2s_{1/2}$	$1d_{3/2}$	$1f_{7/2}$	$2p_{3/2}$	$2p_{1/2}$	$1f_{5/2}$
42	61.55	41.31	36.16	19.79	15.69	13.52	7.59	5.52	4.06	1.52
44	61.50	42.25	36.64	21.34	16.54	14.73	8.53	5.13	3.51	1.69
46	61.63	43.07	37.28	22.37	17.05	15.40	9.52	5.46	3.72	2.18
48	61.55	43.12	37.54	24.11	17.36	15.83	9.47	5.18	3.27	1.65

Table 8. Calculated values $-E_{nlj}^{\mathrm{theor}}$ (in MeV) for ^{50,52,54,56}Ca

Subshell	DOM	RMFA	HFS	MSM	DOM	RMFA	HFS	MSM	DOM	RMFA	HFS	MSM	DOM	RMFA	HFS	MSM
	^{50}Ca				^{52}Ca				^{54}Ca				^{56}Ca			
$1s_{1/2}$	61.52	58.69			61.50	58.58			62.20	58.15			61.00	57.44		
$1p_{3/2}$	41.22	42.09			40.50	41.99			40.91	41.78			40.65	41.40		
$1p_{1/2}$	35.97	38.34			35.43	38.14			35.54	37.99			35.57	37.88		
$1d_{5/2}$	22.64	25.45			22.50	25.50			22.96	25.53			23.30	25.57		
$2s_{1/2}$	17.57	18.43			17.48	18.78			17.58	19.01			17.49	19.24		
$1d_{3/2}$	15.07	18.62			14.30	18.71			14.18	18.92			14.16	19.26		
$1f_{7/2}$	8.72	9.96	8.90	9.50	8.43	10.14	9.00	9.20	8.81	10.41	9.20	9.00	8.77	10.70	9.00	9.00
$2p_{3/2}$	5.64	4.63	5.40	5.00	5.80	5.01	5.00	5.50	5.89	5.36	4.60	6.00	5.91	5.68	4.80	6.00
$2p_{1/2}$	3.70	2.95	3.60	3.50	3.86	3.25	3.20	4.00	3.81	3.56	3.00	4.20	3.92	3.88	3.20	4.20
$1f_{5/2}$	0.90	1.53	2.00	0.70	0.67	1.92	2.20	0.50	0.50	2.37	2.50	0.30	0.84	2.90	2.60	0.50
Δ_p	5.25	3.75			5.07	3.85			5.37	3.79			5.08	3.52		
Δ_d	7.57	6.83			8.20	6.79			8.78	6.61			9.14	7.31		
Δ_f	7.82	8.43	6.90	8.80	7.76	8.22	6.80	8.70	8.31	8.04	6.70	8.70	7.93	7.80	6.40	8.50
Δ_{2p}	1.94	1.68	1.80	1.50	1.94	1.76	1.80	1.50	2.08	1.80	1.60	1.80	1.99	1.80	1.60	1.80

spin–orbit splitting of the $1f$ and $2p$ states in the ^{50,52,54,56}Ca nuclei. The predictions are substantially different for Δ. Only the values Δ^{DOM} calculated in the present study agree with Δ^{MSM} [1].

Studying in detail the question of which parameters of the dispersive optical potential are responsible above all for the agreement of E_{nlj}^{DOM} with E_{nlj}^{MSM} and of Δ^{DOM} with Δ^{MSM}, we found that, within the dispersive-optical-model version used here, these are the parameters E_{F}, r_{HF}, a_{HF}, and V_{so}. We note that this agreement takes place only at the E_{F} value from Table 5. If we fix the parameters r_{HF} and a_{HF}, then Δ^{DOM} increases with increasing V_{so}. The calculations that we performed for E_{nlj}^{DOM} at fixed values of V_{so} and various trial pairs of r_{HF} and a_{HF} (see the procedure described in Section 4) revealed that an increase in a_{HF} (accompanied by the respective slight decrease in r_{HF}) leads to the growth of Δ^{DOM}. This increase in a_{HF} (see Table 5) is consistent with the idea of the growth of the surface diffuseness of nuclei as the number N of neutrons in them increases (see, for example, [59] and articles quoted therein).

We note that, within the relativistic mean-field approximation, the energies Δ_{so} of the spin–orbit splitting of states decrease with increasing number of neutrons in neutron-rich nuclei [54–56]. Within nonrelativistic mean-field models, a spin–orbit potential is introduced as an additional parameter, and it would be natural to expect a decrease in V_{so} with increasing number of neutrons. However, it follows from the results of the present study that the dependence of V_{so} on N has some special features that call for a dedicated investigation. That such an investigation is necessary is also suggested by the results reported in [41], which show that an additional term that takes into account the coupling between single-particle motion and collective degrees of freedom of a nucleus at energies in the vicinity of E_F must be included in the computational scheme of the relativistic mean-field approximation. In [41], this was done phenomenologically by introducing an additional potential that changes linearly with E. The introduction of such a potential leads to a change in the spin–orbit splitting of states.

Thus, the prediction of the multiparticle shell model [1] that the energy gap between the $1f_{5/2}$ and $2p_{1/2}$ levels in neutron-excess calcium isotopes must increase as the number N of neutrons increases from 28 to 34 is reproduced by the calculations within the dispersive optical model. This reproduction within a model that is different from the multiparticle shell model is an additional argument in support of the assumption put forth in [1] that the number $N = 34$ can be magic for $Z = 20$ nuclei.

7. CONCLUSIONS

(i) By using the method of matching data obtained in neutron-stripping and neutron-pickup reactions on the same nucleus, the neutron single-particle energies of valence states in the even–even isotopes $^{40-48}$Ca and their occupation numbers have been determined in the present study. The regularities of changes in the particle–hole energy gap between the $1f$ and $2p$ states of these nuclei and in the energies of their spin–orbit splitting have been investigated.

(ii) A new version of the dispersive optical model has been proposed. This version is appropriate for determining the parameters of the dispersive optical potential for $n + A$ systems, information about $p + A$ systems being partly used for this. The potential of this version of the dispersive optical model has been tested by comparing the results that it yields for the energies of single-particle neutron states in ^{40}Ca and for their occupation numbers with their experimental counterparts. It has been shown that the calculated values of these quantities are in good agreement with corresponding experimental data for the valence states of this nucleus.

(iii) On the basis of the proposed version of the dispersive optical model, we have calculated the single-particle energies of neutron states in the ^{42,44,46,48}Ca nuclei. For the valence states, the energy values calculated with the dispersive-optical-potential parameters determined individually for each nucleus have been found to agree, within the experimental errors, with the respective experimental results. This example illustrates advantages of this version of the dispersive optical model over the traditional version.

(iv) Problems associated with extrapolating the dispersive optical potential from the region of stable to the region of unstable nuclei have been investigated. The parameters of the dispersive optical potential for calculating the spectra of single-particle neutron states in the ^{50,52,54,56}Ca nuclei have been determined.

(v) Single-particle energies of neutron states in the ^{50,52,54,56}Ca nuclei have been calculated on the basis of the dispersive optical model. It has been shown that the values E_{nlj}^{DOM} for the $1f$ and $2p$ states are consistent with the values E_{nlj}^{MSM}. This result is the consequence of a slight increase in the diffuseness parameter a_{HF} (this is accompanied by a slight reduction of r_{HF}) and the strength parameter V_{so}. With increasing number of neutrons in nuclei, the energy gap Δ between the $2p_{1/2}$ and $1f_{5/2}$ states increases, reaching a maximum value at $N = 34$, this being in accord with the assumption put forth in [1] that the number $N = 34$ is magic for $Z = 20$ nuclei.

ACKNOWLEDGMENTS

This work was supported by a presidential grant (no. 1619.2003.2) for support of leading scientific schools.

REFERENCES

1. M. Honmu *et al.*, Phys. Rev. C **65**, 061301 (2002).
2. I. N. Boboshin *et al.*, Nucl. Phys. A **496**, 93 (1989).
3. M. Matoba *et al.*, Phys. Rev. C **48**, 95 (1993).
4. P. Doll *et al.*, Nucl. Phys. A **263**, 210 (1976).
5. Y. Uozumi *et al.*, Phys. Rev. C **50**, 263 (1994).
6. F. J. Eckle *et al.,* Nucl. Phys. A **506**, 159 (1990).
7. P. Martin *et al.,* Nucl. Phys. A **185**, 465 (1972).
8. G. Brown, A. Denning, and J. G. B. Haigh, Nucl. Phys. A **225**, 267 (1974).
9. T. A. Belote, W. E. Dorenbusch, and J. Rapaport, Nucl. Phys. A **120**, 401 (1968).
10. W. E. Dorenbusch, T. A. Belote, and O. Hansen, Phys. Rev. **146**, 734 (1966).
11. H. Schar, D. Trautmann, and E. Baumgartner, Helv. Phys. Acta **50**, 29 (1977).
12. J. Rapaport, W. E. Dorenbusch, and T. A. Belote, Phys. Rev. **156**, 1255 (1967).
13. J. L. Yntema, Phys. Rev. C **4**, 1621 (1971).
14. J. H. Bjerregaard, O. Hansen, and G. R. Satchler, Phys. Rev. **160**, 889 (1967).
15. J. Rapaport, W. E. Dorenbusch, and T. A. Belote, Nucl. Phys. A **177**, 307 (1971).
16. T. A. Belote *et al.,* Phys. Rev. **142**, 624 (1966).
17. J. H. Bjerregaard, O. Hansen, and G. Sidenius, Phys. Rev. **138**, 1097 (1965).
18. R. Abegg, J. D. Hutton, and M. E. Williams-Norton, Nucl. Phys. A **303**, 121 (1978).
19. W. D. Metz, W. D. Callender, and C. K. Bockelman, Phys. Rev. C **12**, 827 (1975).

20. J. S. Hanspal *et al.*, Nucl. Phys. A **436**, 236 (1985).
21. S. Fortier, E. Hourani, M. N. Rao, and S. Gales, Nucl. Phys. A **311**, 324 (1978).
22. Y. Uozumi *et al.*, Nucl. Phys. A **576**, 123 (1994).
23. T. W. Burrows, Nucl. Instrum. Methods Phys. Res. A **286**, 5953 (1990).
24. S. Typel and H. H. Wolter, Nucl. Phys. A **656**, 331 (1999).
25. M. Rashdan, Phys. Rev. C **63**, 044303 (2001).
26. B. F. Gibson and K. J. Van Oostum, Nucl. Phys. A **90**, 159 (1967).
27. K. Rutz *et al.*, Nucl. Phys. A **634**, 67 (1998).
28. M. Kleban *et al.*, Phys. Rev. C **65**, 024309 (2002).
29. X. Campi and D. W. Sprung, Nucl. Phys. A **194**, 401 (1972).
30. V. K. B. Kota and V. Potbhare, Nucl. Phys. A **331**, 93 (1979).
31. C. Mahaux and R. Sartor, Nucl. Phys. A **528**, 253 (1991).
32. L. Corradi *et al.*, Phys. Rev. C **61**, 024609 (2000).
33. H. Koura and M. Yamada, Nucl. Phys. A **671**, 96 (2000).
34. S. S. Volkov *et al.*, Yad. Fiz. **52**, 1339 (1990) [Sov. J. Nucl. Phys. **52**, 848 (1990)].
35. S. Kamerdzhiev, J. Speth, and G. Tertychny, Nucl. Phys. A **624**, 328 (1997).
36. C. H. Johnson and C. Mahaux, Phys. Rev. C **38**, 2589 (1988).
37. D. Vautherin and D. M. Brink, Phys. Rev. C **5**, 626 (1972).
38. J. W. Enlers and S. A. Moszkowski, Phys. Rev. C **6**, 217 (1972).
39. B. A. Brown, Phys. Rev. C **58**, 220 (1998).
40. V. A. Khodel and E. E. Saperstein, Phys. Rep. **92**, 183 (1982).
41. D. Vretenar, T. Nikšić, and P. Ring, Phys. Rev. C **65**, 024321 (2002).
42. P. Von Neumann-Cosel *et al.*, Nucl. Phys. A **516**, 385 (1990).
43. E. A. Romanovsky *et al.*, Yad. Fiz. **63**, 468 (2000) [Phys. At. Nucl. **63**, 399 (2000)].
44. C. Mahaux and R. Sartor, Nucl. Phys. A **484**, 205 (1988).
45. E. L. Hjort *et al.*, Phys. Rev. C **50**, 275 (1994).
46. O. V. Bespalova *et al.*, Yad. Fiz. **66**, 673 (2003) [Phys. At. Nucl. **66**, 644 (2003)].
47. R. L. Varner *et al.*, Phys. Rep. **201**, 57 (1991).
48. R. F. Carlson, At. Data Nucl. Data Tables **63**, 93 (1996).
49. E. A. Romanovsky *et al.*, Yad. Fiz. **61**, 37 (1998) [Phys. At. Nucl. **61**, 32 (1998)].
50. O. V. Bespalova *et al.*, Izv. Akad. Nauk, Ser. Fiz. **67**, 62 (2003).
51. A. J. Koning and J. P. Delaroche, Nucl. Phys. A **713**, 231 (2003).
52. C. Mahaux and R. Sartor, Adv. Nucl. Phys. **20**, 1 (1991).
53. Nuclear Wallet Cards (Jan. 2000).
54. H. Sagawa and S. Yoshida, Nucl. Phys. A **688**, 755 (2001).
55. F. Hofmann, C. M. Keil, and H. Lenske, Phys. Rev. C **64**, 034314 (2001).
56. N. Kaiser, Nucl. Phys. A **720**, 157 (2003).
57. V. A. Chepurnov, Yad. Fiz. **6**, 955 (1967) [Sov. J. Nucl. Phys. **6**, 696 (1967)].
58. B. A. Brown and W. A. Richter, Phys. Rev. C **58**, 2099 (1998).
59. J. Dobaczewski *et al.*, Phys. Rev. Lett. **72**, 981 (1994).

Translated by A. Isaakyan

Physics of Atomic Nuclei, Vol. 68, No. 2, 2005, pp. 208–218. Translated from Yadernaya Fizika, Vol. 68, No. 2, 2005, pp. 233–243.

NUCLEI
Theory

Nucleon–Nucleus Optical Potential at Finite Temperatures within a Semimicroscopic Approach for the Case of Skyrme Forces

V. I. Kuprikov, V. V. Pilipenko, and A. P. Soznik[1]

Kharkov Institute for Physics and Technology, Akademicheskaya ul. 1, Kharkov, 61108 Ukraine

Received June 20, 2003; in final form, January 14, 2004

Abstract—Within the nuclear-matter approximation, the local-density approximation, and perturbation theory, an approach to constructing a microscopic nucleon–nucleus optical potential at finite nuclear temperatures is developed on the basis of effective density-dependent nucleon–nucleon forces. The real and the imaginary part of the neutron–nucleus optical potential and the mean free paths of neutrons in nuclear matter are calculated at various neutron energies and various nuclear temperatures. The effect of the inclusion of the rearrangement potential on the quantities under consideration is studied, and its importance is demonstrated. *© 2005 Pleiades Publishing, Inc.*

1. Optical models underlie many important theoretical approaches to analyzing nucleon–nucleus and nucleus–nucleus collisions. Although a phenomenological approach that relies on parametrizing a complex-valued optical potential is quite elaborate and makes it possible to describe experimental data successfully, the problem of constructing microscopic nucleon–nucleus and nucleus–nucleus optical potentials on the basis of a preset nucleon–nucleon interaction still remains a problem of importance in nuclear physics.

According to the formal microscopic theory developed for optical potentials long ago in [1], an optical potential can be represented as the sum of the main term, where the interaction between a projectile particle and a target nucleus is averaged over their ground state, and the polarization term, which is caused by intermediate excitations of colliding nuclei. Because of the presence of the polarization term, the problem of calculating an optical potential is extremely difficult. In view of this, specific calculations are always performed within some approximations, where the first term in the formal expression for the optical potential actually plays a dominant role, the contributions from the polarization term being taken into account either approximately or phenomenologically.

Folding models for nucleon–nucleus collisions and double-folding models for nucleus–nucleus collisions (see, for example, [2–10]) have been used most extensively in constructing microscopic optical potentials that are intended for quantitatively describing experimental data on angular distributions in nuclear scattering. These models are based on calculating an optical potential in the form of the folding of an effective nucleon–nucleon interaction with single-nucleon densities of colliding nuclei. Among the proposed versions of effective nucleon–nucleon forces, the *M3Y* forces from [11] and the *DDM3Y* forces, which are a generalization [12] of the *M3Y* forces to the case where nucleon–nucleon interaction is explicitly dependent on the nuclear density, have become the most popular. Since the effective forces being considered are real-valued, the folding model only yields the real part of an optical potential, the imaginary part, which is associated in this case with the polarization term exclusively, usually either being chosen in a standard phenomenological form (see, for example, [2, 4]) or being constructed on the basis of the calculated real part of the optical potential by introducing the minimum necessary number of parameters [5–7]. The use of a complex-valued nucleon–nucleon interaction—this makes it possible to include part of the polarization-term effects in the main (folded) term—is yet another method [8–10] for deriving the imaginary part of the optical potential within the folding model.

In [13], it was shown that, from the point of view of many-body theory, a nucleon–nucleus optical potential can be identified with the mass operator in the single-particle Green's function, specific calculations being performed, in particular, within the nuclear-matter approximation with a subsequent application of the local-density approximation [14]. In [15], an optical potential for nuclear matter was determined from leading terms of the expansion of the mass operator under the assumption of a low nucleon density by using the Brueckner–Hartree–Fock method and the complex reaction matrix, which is similar to the

---

[1] Academy of Fire Safety of Ukraine, Kharkov, Ukraine.

Brueckner G matrix. A conceptually similar approach was proposed in [16], where the Bethe–Goldstone equation was solved with the Hamada–Johnston and hard-core Reid potentials.

It is well known (see, for example, [17, 18]) that many properties of nuclei can be described satisfactorily on the basis of Hartree–Fock theory by using effective nuclear-density-dependent nucleon–nucleon forces of the Skyrme type, which have a rather simple form convenient for calculations. It seems quite tempting to make an attempt at constructing a microscopic nucleon–nucleus optical potential on the basis of Skyrme forces. Previously, it was shown in [19] that the Hartree–Fock potential calculated by using Skyrme forces makes it possible to take into account general properties of the real part of an optical potential and to reproduce data on elastic nucleon scattering on nuclei, at least for energies in the region $E < 50$ MeV.

In the present study, we consider a nucleon–nucleus optical potential at finite target-nucleus temperatures in the nuclear-matter approximation. An expression for the optical potential is obtained here by calculating the mass operator in the single-particle Green's function [13, 20] on the basis of an effective nuclear-density-dependent Skyrme nucleon–nucleon interaction [21–24]. We note that the concept of a microscopic potential presumes, from the outset, a calculation with exact wave functions for finite nuclei. Therefore, the potential that is calculated here within the aforementioned approximations can be referred to as a semimicroscopic potential.

Theoretical investigations of the properties of hot nuclei (for $T > 0$) have become ever more important in the past years in connection with the development of the physics of heavy-ion collisions. Prior to the present time, calculations of a microscopic nucleon–nucleus optical potential both at $T = 0$ and at finite nuclear temperatures were performed within the aforementioned approach in a number of studies (see [25–27]) by using Skyrme nucleon–nucleon forces. Indicating that nucleon absorption by nuclei, which is characterized by the nucleon mean free path in a nucleus, l, can be described in terms of the imaginary part of an optical potential, the authors of [25–27] gave much attention, among other things, to the temperature dependence of l. This interest was motivated by the fact that the mean free path in question is directly determined by the intranuclear-nucleon density and by the cross section for nucleon–nucleon interaction.

Taking into account nuclear temperature, the authors of [26, 27] did not include, however, the rearrangement (saturation) potential in their calculations, which arises because of the nuclear-density dependence of the effective forces used and which plays an important role in describing the structure of nuclei within Hartree–Fock theory and within nuclear-matter theory [28–30]. The effect of the rearrangement potential on the real and imaginary parts of an optical potential at $T = 0$ was investigated in [31–33], and it was shown there that its inclusion is of importance for describing nucleon–nucleus scattering, since this suppresses, to a considerable extent, the intensity of nucleon attraction to nuclei, reducing nucleon absorption significantly, and leads to better agreement between calculated optical potentials and their phenomenological counterparts determined for finite nuclei.

In the present study, the approach developed in [25–27, 31–33] is generalized to the case of calculating optical potentials for nucleon scattering on hot nuclei ($T > 0$) with allowance for the rearrangement potential. A nucleon–nucleus optical potential is constructed here by calculating the mass operator in the nuclear-matter approximation within perturbation theory to the second order inclusive, the Fermi distribution being taken into account for occupation numbers at finite temperatures. By employing the local-density approximation, we then derive an optical potential for finite nuclei from the resulting potential for nuclear matter. We have calculated optical potentials for symmetric and for asymmetric nuclear matter and for the finite nuclei ^{40}Ca and ^{208}Pb. We have also investigated the effect of the rearrangement potential and of finite temperatures on the properties of optical potentials and on the nucleon mean free path in nuclear matter and in finite nuclei.

2. In microscopically calculating a nucleon–nucleus optical potential, we rely on an effective two-particle nucleon–nucleon interaction in the form of density-dependent generalized Skyrme forces, which, according to [21–24], can be represented as

$$v \equiv v_{ij} = v_1(\mathbf{r}) + v_2(\mathbf{r}, \rho), \tag{1}$$

where i and j are the numbers of interacting nucleons and the quantities $v_1(\mathbf{r})$ and $v_2(\mathbf{r}, \rho)$ defined as the interaction components that are, respectively, independent of and dependent on the nuclear density $\rho = \rho_n + \rho_p$ are given by

$$\begin{aligned} v_1(\mathbf{r}) = t_0(1 + x_0 P_\sigma)\delta(\mathbf{r}) + \frac{1}{2}t_1(1 + x_1 P_\sigma) \\ \times [\mathbf{k}'^2\delta(\mathbf{r}) + \delta(\mathbf{r})\mathbf{k}^2] + t_2(1 + x_2 P_\sigma)\mathbf{k}' \cdot \delta(\mathbf{r})\mathbf{k} \\ + iW_0(\boldsymbol{\sigma}_i + \boldsymbol{\sigma}_j) \cdot [\mathbf{k}' \times \delta(\mathbf{r})\mathbf{k}], \end{aligned} \tag{2}$$

$$\begin{aligned} v_2(\mathbf{r}, \rho) = \frac{1}{6}t_3(1 + x_3 P_\sigma)\rho^\gamma(\mathbf{R})\delta(\mathbf{r}) \\ + \frac{1}{2}t_4(1 + x_4 P_\sigma)[\mathbf{k}'^2\rho(\mathbf{R})\delta(\mathbf{r}) + \delta(\mathbf{r})\rho(\mathbf{R})\mathbf{k}^2] \\ + t_5(1 + x_5 P_\sigma)\mathbf{k}' \cdot \rho(\mathbf{R})\delta(\mathbf{r})\mathbf{k}. \end{aligned} \tag{3}$$

Here, $\mathbf{r} = \mathbf{r}_i - \mathbf{r}_j$; $\mathbf{R} = (\mathbf{r}_i + \mathbf{r}_j)/2$; $P_\sigma = (1 + \boldsymbol{\sigma}_i \boldsymbol{\sigma}_j)/2$ is the spin-permutation operator; and $\mathbf{k} = -i\partial/\partial\mathbf{r}$ and $\mathbf{k}' = i\partial/\partial\mathbf{r}'$ are the momentum operators for the relative motion of nucleons in, respectively, the initial and the final state. The rest of the notation is identical to that in [21–24].

Since a nucleon–nucleus optical potential can be identified with the mass operator $M_{\alpha\beta} = \langle\alpha|M|\beta\rangle$ (α and β are the indices of final and initial single-particle states) in the single-particle Green's function, we construct the potential in question by calculating this mass operator in the nuclear-matter approximation by perturbation theory (to the second order inclusive). The fact that the success of such calculation within the perturbation theory used depends greatly on the effective inclusion of contributions from some of higher order diagrams (see, for example, [34]) is an important special feature of the calculations to be performed here. An appropriate choice of zero-order approximation is of importance for correctly taking into account such contributions. In view of this, we choose the mean self-consistent Hartree–Fock potential for a zero-order approximation to the mass operator. Since the nucleon–nucleon interaction is density-dependent, fulfillment of the self-consistency condition in varying the Hartree–Fock potential requires taking into account, in addition to standard direct and exchange Hartree–Fock terms, the so-called rearrangement (saturation) term that arises in varying the effective forces proper with respect to density. Various effects associated with nucleon correlations are included through the density dependence of effective nucleon–nucleon forces in nuclear matter. Changes in the nuclear density lead to the rearrangement of a multinucleon system (that is, to changes in the distribution of nucleons over single-particle levels). As a result, the effective interaction itself changes, which is reflected in the emergence of the rearrangement potential. In the zero-order approximation, the required mass operator $M^{(0)}_{\alpha\beta}$ can therefore be represented in the form

$$M^{(0)}_{\alpha\beta} = U^{(\mathrm{HF})}_{\alpha\beta} = U^{(0)}_{\alpha\beta} + U^{(R)}_{\alpha\beta}, \tag{4}$$

where the standard Hartree–Fock potential $U^{(0)}_{\alpha\beta}$ and the rearrangement potential $U^{(R)}_{\alpha\beta}$ are given by

$$U^{(0)}_{\alpha\beta} = \sum_{\lambda} [\langle\alpha\lambda|v|\beta\lambda\rangle - \langle\alpha\lambda|v|\lambda\beta\rangle] n_\lambda \tag{5}$$
$$= \sum_{\lambda} \langle\alpha\lambda|v(1 - P_{12})|\beta\lambda\rangle n_\lambda,$$

$$U^{(R)}_{\alpha\beta} = \sum_{\lambda\mu} \langle\alpha| \left\langle \lambda\mu \left| \frac{1}{2}\delta(\mathbf{r} - \mathbf{R}) \right.\right. \tag{6}$$
$$\left.\left. \times \frac{\partial v}{\partial \rho}(1 - P_{12}) \right| \lambda\mu \right\rangle n_\lambda n_\mu |\beta\rangle.$$

Here, n_λ are the occupation numbers for the eigenstates φ_λ of the single-particle Hartree–Fock Hamiltonian,

$$(\hat{t} + U^{(\mathrm{HF})})\varphi_\lambda = \varepsilon_\lambda \varphi_\lambda, \tag{7}$$

while P_{12} is the particle-permutation operator. In (6), it is implied that the states $|\alpha\rangle$ and $|\beta\rangle$ depend on $\mathbf{r}$ and that $|\lambda\rangle$ and $|\mu\rangle$ depend on $\mathbf{r}_1$ and $\mathbf{r}_2$; also, we have $\mathbf{R} = (\mathbf{r}_1 + \mathbf{r}_2)/2$ [35].

As is well known, a certain class of diagrams is canceled in all orders of perturbation theory upon taking into account, in the zero-order approximation, the mean field in the form of the standard Hartree–Fock potential $U^{(0)}_{\lambda\mu}$ (see, for example, [36]). In particular, this annihilates first-order diagrams in the interaction in (1) for the mass operator $M^{(1)}_{\alpha\beta}$. As to the rearrangement (saturation) potential $U^{(R)}_{\alpha\beta}$, its inclusion in the zero-order approximation corresponds to taking into account a number of higher order diagrams (specifically, from the third order) inducing corrections to the occupation probabilities for single-particle states in the exact multiparticle wave function (see [29, 30, 34]). The standard Hartree–Fock term in (5) describes the interaction of a nucleon with medium nucleons in the occupied states λ, the occupation numbers for these states at $T = 0$ being equal to unity. The above higher order diagrams take into account the interaction of a nucleon in an occupied state λ with particle–hole excitations, this interaction leading to a decrease in the occupation numbers for the original (standard) Hartree–Fock set of states. It was precisely the corresponding corrections to the potential of nucleon interaction with a medium that were referred to as the rearrangement (saturation) potential in [28–30]. The rearrangement term in (6) also describes similar effects of a change in the occupation probabilities for states λ [34], redefining the chosen set of single-particle states. The rearrangement potential arising from the variational principle is closely related to rearrangement corrections induced by Goldstone diagrams (see [29, 30, 34]). In connection with the aforesaid, we will assume that the real part of the sought microscopic nucleon–nucleus optical potential is determined by the chosen zero-order approximation for the mass operator in the form of the Hartree–Fock field with allowance for the rearrangement potential.

In the case of the effective interaction specified by Eqs. (1)–(3), the first nonvanishing contribution to the imaginary part of the optical potential arises in the second order of perturbation theory, and we will restrict ourselves to this contribution. We disregard the contribution of the second-order diagrams to the real part of the optical potential, since estimations demonstrate its smallness [25]. Considering that density-dependent effective forces simulate the reaction matrix, we can assume that the main part of the second-order Goldstone contribution has already been taken into account in the canceled first-order diagrams. The contribution of the second-order diagrams to the imaginary part of the mass operator (that is, to the imaginary part of the optical potential) has the form (see [25–27, 32, 33])

$$\begin{aligned}\mathrm{Im}M^{(2)}_{\alpha\beta} \equiv W_{\alpha\beta} = -\frac{\pi}{2}\sum_{\lambda\mu\nu}\langle\alpha\mu|v \\ \times (1-P_{12})|\lambda\nu\rangle\langle\lambda\nu|v(1-P_{12})|\beta\mu\rangle \\ \times [n_\mu(1-n_\lambda)(1-n_\nu) + n_\lambda n_\nu(1-n_\mu)] \\ \times \delta(\varepsilon_\alpha + \varepsilon_\mu - \varepsilon_\lambda - \varepsilon_\nu).\end{aligned} \tag{8}$$

The occupation numbers for single-particle states at finite temperatures ($T > 0$) are determined by the Fermi distribution

$$n_\lambda = \left\{1 + \exp\left[\frac{1}{T}(\varepsilon_\lambda - \mu)\right]\right\}^{-1}, \tag{9}$$

where μ is the chemical potential.

The first term in the bracketed expression on the right-hand side of (8) yields the retarded part of the mass operator and is the main one. The second term yields the advanced part and can make a significant contribution only at rather low energies and high temperatures [26, 27]. At $T = 0$, this term makes no contribution at all.

As in [25–27, 31–33], we consider the nuclear-matter approximation in deriving specific expressions for a nucleon–nucleus optical potential. In this case, the functions φ_α, which satisfy Eq. (7), have the form of plane waves,

$$\varphi_\alpha = \Omega^{-1/2}\exp(i\mathbf{k}_\alpha\cdot\mathbf{r})\chi_{\sigma_\alpha}\chi_{\tau_\alpha}, \tag{10}$$

where χ_σ and χ_τ are, respectively, the spin and isospin functions; Ω is the normalization volume; and the wave vector $\mathbf{k}_\alpha$ obeys the dispersion relation

$$k_\alpha^2 = \frac{2m_{\tau_\alpha}}{\hbar^2}[\varepsilon_\alpha - U^{(\mathrm{HF})}_{\alpha\alpha}]. \tag{11}$$

The chemical potential μ_{τ_α} at a given temperature T and a given density ρ_{τ_α} of nucleons belonging to the type τ_α ($\tau_\alpha = n, p$) is determined from the equation

$$\rho_{\tau_\alpha} = \frac{1}{\pi^2}\int_0^\infty dk_\alpha k_\alpha^2\{1 + \exp[(\varepsilon_{\tau_\alpha}(k_\alpha) - \mu_{\tau_\alpha})/T]\}^{-1}. \tag{12}$$

Taking into account relations (1)–(3), we derive the quantity $U^{(\mathrm{HF})}_{\alpha\beta}$ from (5) and (6) in the form

$$U^{(\mathrm{HF})}_{\alpha\beta} = \delta(\mathbf{k}_\alpha - \mathbf{k}_\beta)\delta_{\sigma_\alpha\sigma_\beta}\delta_{\tau_\alpha\tau_\beta}U_\alpha, \tag{13}$$

where the real part U_α of the optical potential is

$$U_\alpha = \frac{\hbar^2}{2m_{\tau_\alpha}}\left(\frac{m_{\tau_\alpha}}{m^*_{\tau_\alpha}} - 1\right)k_\alpha^2 + U^{(0)}_{\tau_\alpha} + U^{(R)}, \tag{14}$$

$$\begin{aligned}U^{(0)}_{\tau_\alpha} = \rho g_0 - \rho_{\tau_\alpha}h_0 + \frac{1}{4\pi^2}[g_1 + g_2 \\ + \rho(g_4 + g_5)](J_n + J_p) + \frac{1}{4\pi^2}[-h_1 + h_2 \\ + \rho(-h_4 + h_5)]J_{\tau_\alpha} + \frac{1}{6}\rho^\gamma(\rho g_3 - \rho_{\tau_\alpha}h_3),\end{aligned} \tag{15}$$

$$\begin{aligned}U^{(R)} = \frac{1}{12}\gamma\rho^{\gamma-1}[\rho^2 g_3 - (\rho_n^2 + \rho_p^2)h_3] \\ + \frac{1}{4\pi^2}[\rho(g_4 + g_5)(J_n + J_p) \\ + (-h_4 + h_5)(\rho_n J_n + \rho_p J_p)],\end{aligned} \tag{16}$$

$$\begin{aligned}\frac{m_{\tau_\alpha}}{m^*_{\tau_\alpha}} = 1 + \frac{m_{\tau_\alpha}}{2\hbar^2}\{\rho[g_1 + g_2 + \rho(g_4 + g_5)] \\ + \rho_{\tau_\alpha}[-h_1 + h_2 + \rho(-h_4 + h_5)]\},\end{aligned} \tag{17}$$

$$J_{\tau_\alpha} = \int_0^\infty dk k^4\{1 + \exp[(\varepsilon_{\tau_\alpha}(k) - \mu_{\tau_\alpha})/T]\}^{-1}, \tag{18}$$

$$g_i = t_i\left(1 + \frac{1}{2}x_i\right), \quad h_i = t_i\left(\frac{1}{2} + x_i\right). \tag{19}$$

In (14), the term $U^{(0)}_{\tau_\alpha}$ stems from the standard Hartree–Fock potential, while $U^{(R)}$ emerges from the rearrangement potential; also, we have introduced an effective nucleon mass $m^*_{\tau_\alpha}$. The dispersion relation (11) can be recast into the form

$$k_\alpha^2 = \frac{2m^*_{\tau_\alpha}}{\hbar^2}[\varepsilon_\alpha - U^{(0)}_{\tau_\alpha} - U^{(R)} - V_\mathrm{C}]. \tag{20}$$

Here, we have also taken into account the Coulomb potential V_C for the case of proton scattering (for neutrons, $V_\mathrm{C} = 0$). Employing relations (14) and (20), we eventually obtain the following expression for the real part of the optical potential at a nucleon energy E:

$$\begin{aligned}V = V_{\tau_\alpha}(E) \\ = \frac{m^*_{\tau_\alpha}}{m_{\tau_\alpha}}\left[\left(\frac{m_{\tau_\alpha}}{m^*_{\tau_\alpha}} - 1\right)(E - V_\mathrm{C}) + U^{(0)}_{\tau_\alpha} + U^{(R)}\right].\end{aligned} \tag{21}$$

Knowing the dispersion relation (20) and using Eq. (8), we can now obtain an expression for the imaginary part of the mass operator. The result is similar to that presented in [26, 27] and has the form

$$W_{\alpha\beta} = \delta(\mathbf{k}_\alpha - \mathbf{k}_\beta)\delta_{\sigma_\alpha\sigma_\beta}\delta_{\tau_\alpha\tau_\beta}W_{\tau_\alpha}(E), \tag{22}$$

where the sought imaginary part $W_{\tau_\alpha}(E)$ of the optical potential at a nucleon energy E is given by

$$W = W_{\tau_\alpha}(E) = -\frac{1}{64\pi^5}\sum_{i=1}^{7} W_i, \tag{23}$$

$$\begin{aligned} W_1 = {} & \left(2g_{00} + \frac{1}{18}g_{33}\rho^{2\gamma} + \frac{2}{3}g_{03}\rho^\gamma\right) \\ & \times [I_1(\tau_\alpha, n) + I_1(\tau_\alpha, p)] \\ & - \left(2h_{00} + \frac{1}{18}h_{33}\rho^{2\gamma} + \frac{2}{3}h_{03}\rho^\gamma\right) I_1(\tau_\alpha, \tau_\alpha), \end{aligned}$$

$$\begin{aligned} W_2 = {} & \left[2(g_{01} + g_{04}\rho) + \frac{\rho^\gamma}{3}(g_{13} + g_{34}\rho)\right] [I_2(\tau_\alpha, n) \\ & + I_2(\tau_\alpha, p)] - \Bigg[2(h_{01} + h_{04}\rho) \\ & + \frac{\rho^\gamma}{3}(h_{13} + h_{34}\rho)\Bigg] I_2(\tau_\alpha, \tau_\alpha), \end{aligned}$$

$$\begin{aligned} W_3 = {} & \left(\frac{1}{2}g_{11} + \frac{1}{2}g_{44}\rho^2 + g_{14}\rho\right) [I_3(\tau_\alpha, n) \\ & + I_3(\tau_\alpha, p)] - \left(\frac{1}{2}h_{11} + \frac{1}{2}h_{44}\rho^2 + h_{14}\rho^\gamma\right) I_3(\tau_\alpha, \tau_\alpha), \end{aligned}$$

$$\begin{aligned} W_4 = {} & 2\left[2(g_{02} + g_{05}\rho) + \frac{\rho^\gamma}{3}(g_{23} + g_{35}\rho)\right] \\ & \times [I_4(\tau_\alpha, n) + I_4(\tau_\alpha, p)], \end{aligned} \tag{24}$$

$$\begin{aligned} W_5 = {} & 2[g_{12} + \rho(g_{15} + g_{24}) + g_{45}\rho^2] \\ & \times [I_5(\tau_\alpha, n) + I_5(\tau_\alpha, p)], \end{aligned}$$

$$\begin{aligned} W_6 = {} & 2(g_{22} + g_{55}\rho + 2g_{25}\rho)[I_6(\tau_\alpha, n) + I_6(\tau_\alpha, p)] \\ & - 2(h_{22} + h_{55}\rho + 2h_{25}\rho)I_6(\tau_\alpha, \tau_\alpha), \end{aligned}$$

$$W_7 = 4W_0^2[I_7(\tau_\alpha, n) + I_7(\tau_\alpha, p) + I_7(\tau_\alpha, \tau_\alpha)],$$

where $g_{ij} = t_i t_j[1 + x_i x_j + (x_i + x_j)/2]$, $h_{ij} = t_i t_j \times [x_i + x_j + (1 + x_i x_j)/2]$, and we have also introduced the integrals (which were considered in [26, 27])

$$\begin{aligned} I_i(\tau_\alpha, \tau_\mu) = {} & \int d\mathbf{k}_\mu d\mathbf{k}_\lambda d\mathbf{k}_\nu f_i(\mathbf{K}_{\alpha\mu}, \mathbf{K}_{\lambda\nu}) \\ & \times [n_\mu(1 - n_\lambda)(1 - n_\nu) + n_\lambda n_\nu(1 - n_\mu)] \\ & \times \delta(E + \varepsilon_\mu - \varepsilon_\lambda - \varepsilon_\nu)\delta(\mathbf{k}_\alpha + \mathbf{k}_\mu - \mathbf{k}_\lambda - \mathbf{k}_\nu). \end{aligned} \tag{25}$$

In the above expressions, we have also used the following notation: $\tau_\lambda = \tau_\alpha$, $\tau_\nu = \tau_\mu$, $\mathbf{K}_{\alpha\mu} = (\mathbf{k}_\alpha - \mathbf{k}_\mu)/2$, $\mathbf{K}_{\lambda\nu} = (\mathbf{k}_\lambda - \mathbf{k}_\nu)/2$, and

$$\begin{gathered} f_1 = 1, \quad f_2 = K_{\alpha\mu}^2 + K_{\lambda\nu}^2, \\ f_3 = (K_{\alpha\mu}^2 + K_{\lambda\nu}^2)^2, \quad f_4 = \mathbf{K}_{\alpha\mu} \cdot \mathbf{K}_{\lambda\nu}, \\ f_5 = (K_{\alpha\mu}^2 + K_{\lambda\nu}^2)(\mathbf{K}_{\alpha\mu} \cdot \mathbf{K}_{\lambda\nu}), \\ f_6 = (\mathbf{K}_{\alpha\mu} \cdot \mathbf{K}_{\lambda\nu})^2, \quad f_7 = (\mathbf{K}_{\alpha\mu} \times \mathbf{K}_{\lambda\nu})^2. \end{gathered} \tag{26}$$

It should be noted that a method for calculating the integrals in (25) for the case where the occupation numbers n_λ are given by (9) is described in [26].

In the above formulas, the rearrangement potential does not appear directly in the imaginary part of the optical potential, but our calculations reveal that its inclusion affects the imaginary part significantly because of the change in the dispersion relation. This circumstance was also indicated in [32, 33] for the case of cold nuclei ($T = 0$).

Within the approach being considered, the formulas obtained above for the case of infinite nuclear matter and the local-density approximation are used to calculate a microscopic optical potential for nucleon scattering on finite nuclei. In the local-density approximation, the local values of the nuclear densities $\rho(r)$ and $\rho_{\tau_\alpha}(r)$ for the point being considered are substituted into formulas (15), (16), (21), and (23)–(26) in calculating the required quantities. Concurrently, the chemical potential $\mu_{\tau_\alpha}(r)$ is also treated as a function of r and is calculated according to Eq. (12) for local values of the density. In the case of nucleon scattering on finite nuclei, the energy E is related to the laboratory energy E_{lab} by the equation $E = AE_{\text{lab}}/(A+1)$. As in [25, 26, 31–33], the semiempirical Negele formulas [14] for the proton and neutron densities are used here in the calculations for finite nuclei.

On the basis of the complex-valued nucleon–nucleus optical potentials found here, we have also calculated the nucleon mean free path l in nuclear matter and finite nuclei in order to study the effect of the rearrangement potential on this feature at various values of energy and temperature. The neutron mean free path is related to the optical potential by the equation (see, for example, [26])

$$l = \frac{\hbar}{2m_{\tau_\alpha}^*|W_{\tau_\alpha}(E)|}\{2m_{\tau_\alpha}[E - V_{\tau_\alpha}(E)]\}^{1/2}. \tag{27}$$

3. On the basis of the approach outlined above, the real (V) and the imaginary (W) part of the nucleon–nucleus optical potential have been calculated here both for symmetric and asymmetric (for $Z/A = 82/208$) nuclear matter and for finite nuclei at various values of the neutron energy and temperature in the ranges $0 \leq E \leq 50$ MeV and $0 \leq T \leq 15$ MeV, respectively. The calculations were performed by using various parameter sets known from the literature for generalized Skyrme forces. For basic versions of the effective interaction, we took the *Ska* forces [23] and the *SGI* forces [24], since, as became clear from our calculations, they provide the best description of the experimental energy dependence of the volume integrals J_V and J_W for the real and imaginary parts of the optical potential for finite nuclei.

Our calculations revealed a significant effect of the rearrangement potential on the calculated real (V) and imaginary (W) parts of the optical potential and on the neutron mean free path l at finite temperatures. For nuclear matter, the results of the calculations with the *Ska* forces [23] are displayed in Fig. 1. These results are similar for symmetric and asymmetric nuclear matter. From Fig. 1, one can see that the real part of the optical potential depends on temperature only slightly, but that the effect of the rearrangement potential $U^{(R)}$ is much more significant: as T changes from 0 to 15 MeV, V changes by not more than 10%, while the inclusion of $U^{(R)}$ reduces $|V|$ by approximately 25% both at $T = 0$ and at $T = 15$ MeV. We note that, in all cases, the slope of the curve that represents the E dependence of V undergoes no changes, since it depends on the effective mass $m^*_{\tau_\alpha}$, whose value is determined exclusively by the chosen version of Skyrme forces (for the case of the *Ska* forces, we have $m^*_{\tau_\alpha} = 0.588 m_{\tau_\alpha}$). The imaginary part of the optical potential features a significant dependence both on T and on the inclusion of $U^{(R)}$. By way of example, we indicate that, as T increases from 0 to 15 MeV, the value of $|W|$ for symmetric nuclear matter at $E = 40$ MeV increases by a factor of about 1.6, while the inclusion of $U^{(R)}$ leads to a sizable decrease in the quantity $|W|$ at all values of E and T and to a moderation of its growth with increasing E.

The inclusion of the rearrangement potential has the most significant effect on the neutron mean free path at low temperatures of nuclear matter, but this effect decreases with increasing E. At $T = 15$ MeV, the effect in question becomes rather small over the entire range of energies E considered here. From our calculations, it also follows that l decreases with increasing T and E, this being due to a reduction of the effect of the Pauli exclusion principle for final states of colliding nucleons. For the same reasons, the influence of temperature effects on l becomes less pronounced with increasing E. We note that the mean free paths for symmetric and asymmetric nuclear matter differ significantly at low temperatures and that, at high temperatures ($T = 15$ MeV), they are weakly dependent on the energy E and are virtually identical in the two cases in question ($l = 3$–7 fm).

The effect of the rearrangement potential on the radial dependences $V(r)$, $W(r)$, and $l(r)$ for n^{40}Ca scattering at various values of temperature and energy is illustrated in Fig. 2. The inclusion of $U^{(R)}$ in the calculation of the real part of the optical potential leads to the same effect at all values of E: the depth of the real-valued potential well decreases significantly, the absolute value of this change being nearly identical (approximately 20–40%) for different values of E. This conclusion is valid for all T values considered here, since the radial dependence $V(r)$ is weakly dependent on temperature. With increasing E, the value of $|V|$ at $r = 0$ (the potential-well depth) decreases. A change in E and T and the inclusion of the potential $U^{(R)}$ have a significant effect on the value of the imaginary part of the optical potential, especially in the interior of a nucleus. The disregard of the rearrangement potential leads to an increase in the depth of $W(r)$, so that, at $E \leq 30$ MeV, for example, the potential $W(r)$ ceases to be superficial, acquiring a volume character. An increase in E and T leads to the same effect. For example, the potential $W(r)$ calculated at $E = 10$ MeV and $T = 15$ MeV is nearly coincident with that calculated at $E = 30$ MeV and $T = 10$ MeV.

This dependence of the potentials $V(r)$ and $W(r)$ on E and T determines the character of the energy and temperature dependence of the mean free path l: with increasing E and T, the value of l in the interior of the nucleus decreases—by way of example, we indicate that, at $E = 50$ MeV, the value of l at the center of the ^{40}Ca nucleus changes from 6 fm at $T = 0$ to 3.5 fm at $T = 15$ MeV.

We note that, in the case of neutron scattering on ^{208}Pb nuclei, the calculations of the quantities $V(r)$, $W(r)$, and $l(r)$ lead to a pattern similar to that obtained for ^{40}Ca nuclei, the results differing only in absolute value. At $r = 0$ and $E = 50$ MeV, we have $l = 7.5$ fm at $T = 0$ and $l = 4$ fm at $T = 15$ MeV. It is noteworthy that the above values of l are close for ^{40}Ca and ^{208}Pb nuclei, as well as for nuclear matter.

In the energy and temperature ranges being considered, the mean free path l in finite nuclei is longer at the center of a nucleus; as r increases up to the nuclear surface, l decreases smoothly to some value, whereupon it increases sharply at r values exceeding the nuclear radius R. This behavior of $l(r)$ differs significantly from that predicted in [27], where, even at $E = 40$ MeV, l assumes a constant value over the entire region within the nucleus, $r \leq R$. This difference in the behavior of $l(r)$ as a function of radius

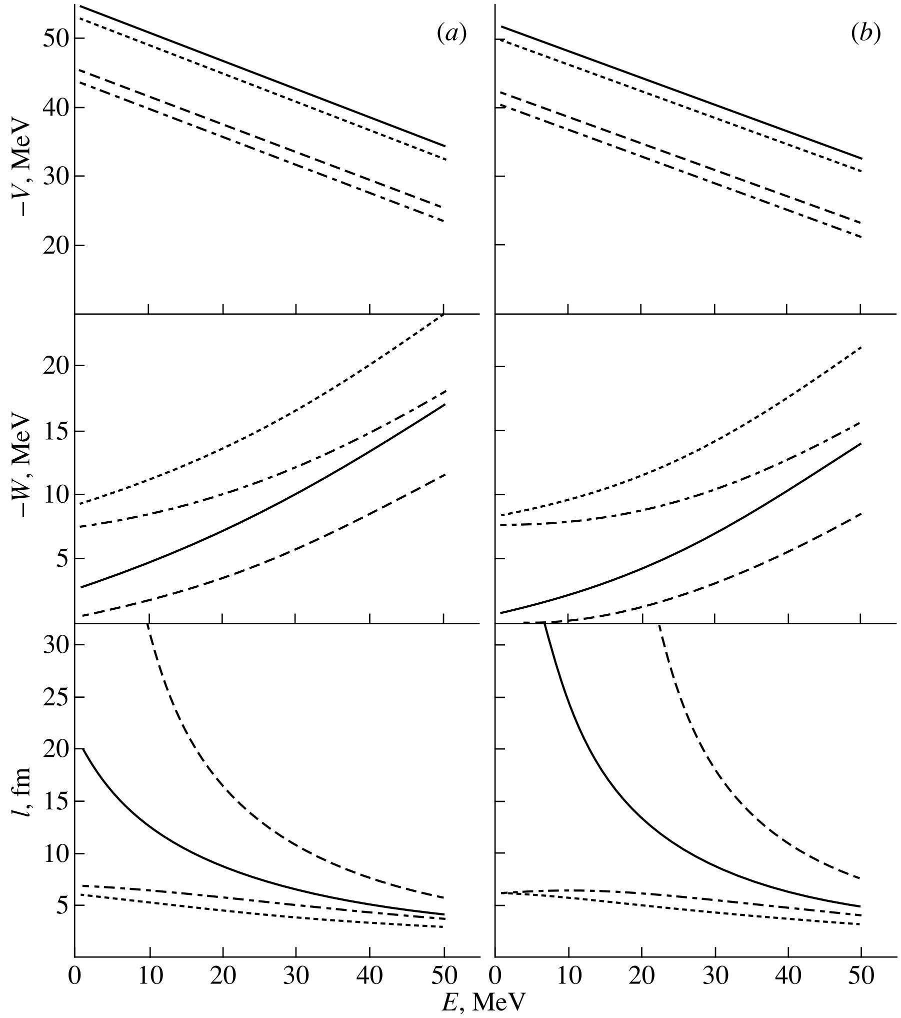

Fig. 1. Dependences of the real (V) and imaginary (W) parts of the optical potential and of the neutron mean free path l on the incident-neutron energy E for (a) symmetric and (b) asymmetric nuclear matter at $T = 0$ (the solid and dashed curves were calculated, respectively, without and with allowance for the rearrangement potential) and at $T = 15$ MeV (the dotted and dash-dotted curves were calculated, respectively, without and with allowance for the rearrangement potential). The calculations were performed with the Ska forces.

is due to the circumstance that the inclusion of the rearrangement potential leads, as can be seen from Fig. 2, to the emergence of at least a modest surface hump in the potential $W(r)$ for $E \leq 50$ MeV, while the disregard of the potential $U^{(R)}$ results in a purely volume behavior of the potential $W(r)$ even at $E = 40$ MeV. The presence of a surface hump in the radial dependence of the imaginary part of the optical potential leads to a decrease in l as r increases from 0 to R. It is interesting to note that, at each value of the nuclear temperature, the curves representing $l(r)$ for different values of the energy E (see Fig. 2) intersect at $r \approx R$ irrespective of whether one takes into account $U^{(R)}$.

For the sake of comparison, we present in Fig. 3 the results obtained by calculating the optical potentials for asymmetric nuclear matter and for n^{208}Pb scattering by using the Ska forces and SGI forces; as a matter of fact, the latter are an improved version of the former (see [24]). The results for the real part of the optical potential for nuclear matter (see Fig. 3a) differ only slightly for these two versions of nucleon—nucleon forces, the main distinction consisting in different slopes of the curves representing $V(E)$ (because of different effective-mass values). The distinctions between the calculated imaginary parts $W(E)$ of the optical potential are more pronounced, but they are relatively small as well. The growth of the depth of the potential $|W|$ with increasing energy E is slower for the Ska than for the SGI forces. At low temperatures, there are some distinctions between the values of the mean free path for the Ska and SGI forces, but they decrease with increasing energy; at

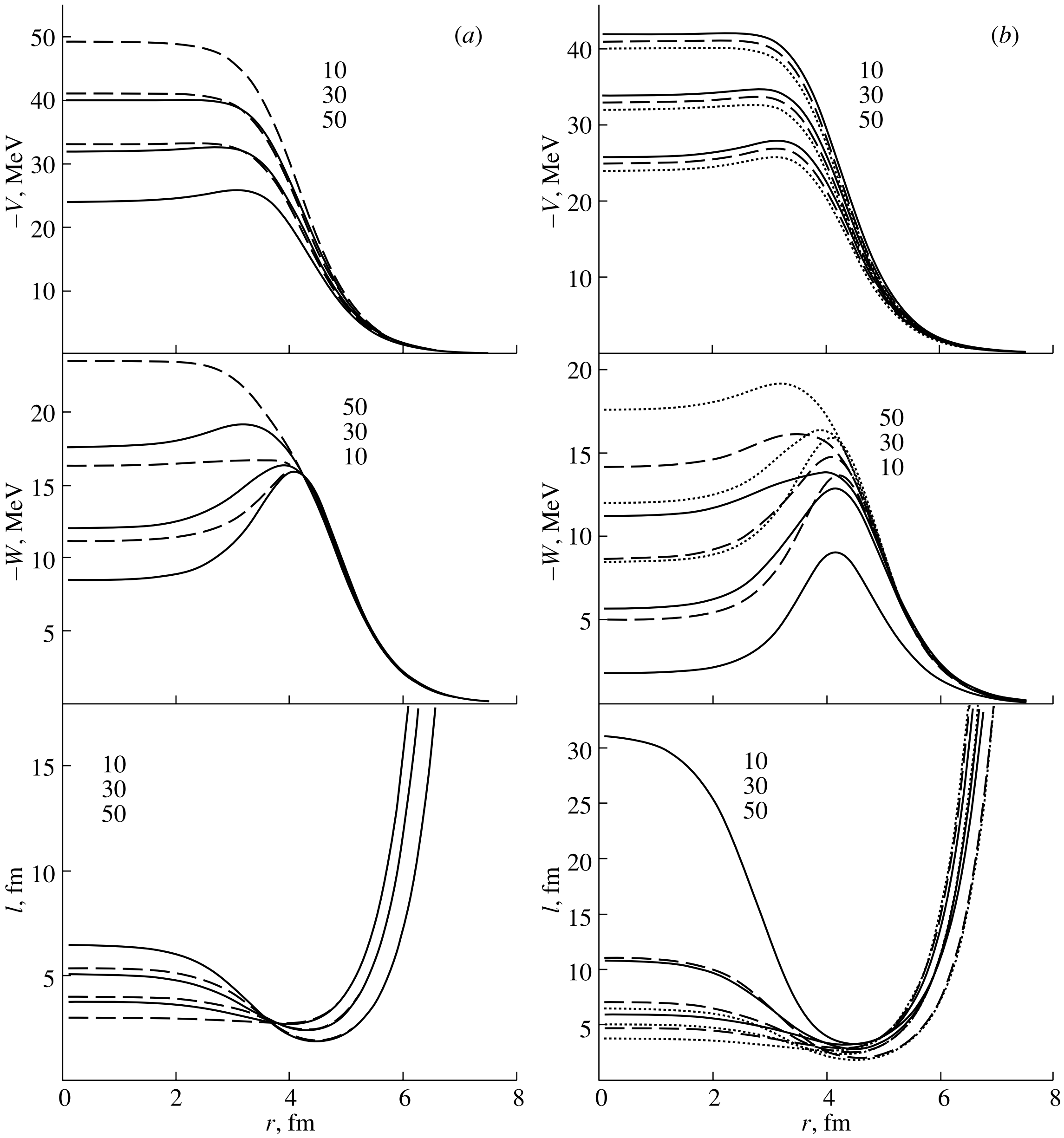

Fig. 2. Dependences of the optical potential $V + iW$ and of the mean free path l on the radius r for n^{40}Ca scattering at $E = 10$, 30, and 50 MeV (curves from top to bottom for V and l and from bottom to top for W) for various temperatures: (a) results obtained at $T = 15$ MeV (solid curves) with and (dashed curves) without allowance for the rearrangement potential and (b) results obtained at (solid curves) $T = 0$, (dashed curves) $T = 10$ MeV, and (dotted curves) $T = 15$ MeV with allowance for the rearrangement potential. All calculations were performed with the Ska forces.

rather high temperatures, the distinctions in question are very small. Figure 3b shows that the use of the Ska and SGI forces leads to close results for the radial dependence $V(r)$; at the same time, the function $W(r)$ exhibits some distinctions in the nuclear interior (the SGI forces yield a deeper imaginary part of the optical potential). The mean free paths $l(r)$ also differ somewhat in the nuclear interior: the Ska forces yield greater values for l.

We have also performed calculations with temperature-dependent generalized Skyrme forces, whose parameters were determined in [37] from calculations of the Brueckner reaction matrix. Even at $T = 0$, these forces yielded results that differ drastically from those obtained with phenomenological forces. At the same time, the inclusion of a temperature dependence in these forces has but a slight effect on the behavior of the quantities under study. In view of this, we do not

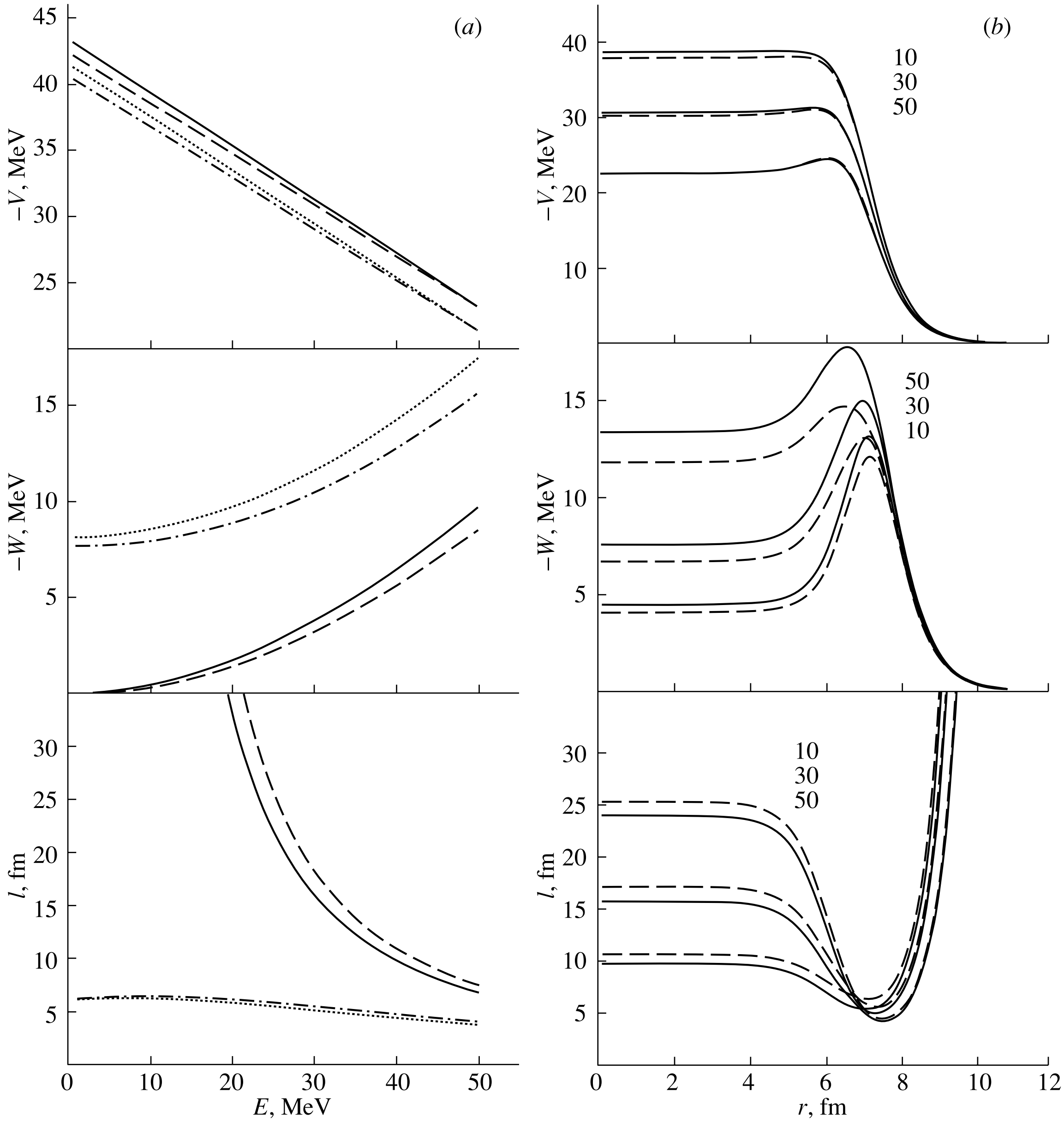

Fig. 3. (a) Dependences of the real (V) and imaginary (W) parts of the optical potential and of the neutron mean free path l on energy for asymmetric nuclear matter with allowance for the rearrangement potential in the cases of the SGI and Ska forces (solid and dashed curves, respectively, at $T = 0$ and dotted and dash-dotted curves, respectively, at $T = 15$ MeV). (b) Dependences of the real (V) and imaginary (W) parts of the optical potential and of the neutron mean free path l on r for n^{208}Pb scattering at $T = 10$ MeV and $E = 10$, 30, and 50 MeV (curves from top to bottom for V and l and from bottom to top for W) in the cases of the SGI and Ska forces (solid and dashed curves, respectively).

quote here the results of the calculations with such forces.

Let us finally consider Fig. 4, where, for the real $[J_V(E)]$ and imaginary $[J_W(E)]$ volume integrals of the optical potential for neutron scattering on ^{40}Ca and ^{208}Pb nuclei,

$$J_V = -\frac{1}{A}\int d^3rV(r), \quad J_W = -\frac{1}{A}\int d^3rW(r), \quad (28)$$

where A is the mass number of the target nucleus, we present the energy dependences calculated with the Ska forces. It should be recalled that these volume integrals are important features of not only the radial distribution of the optical potential but also the scattering processes being studied. The results of the calculations reveal that the inclusion of the rearrangement potential has a significant effect on both volume integrals. For the integral J_V, this effect is stronger than the effect of the change in tempera-

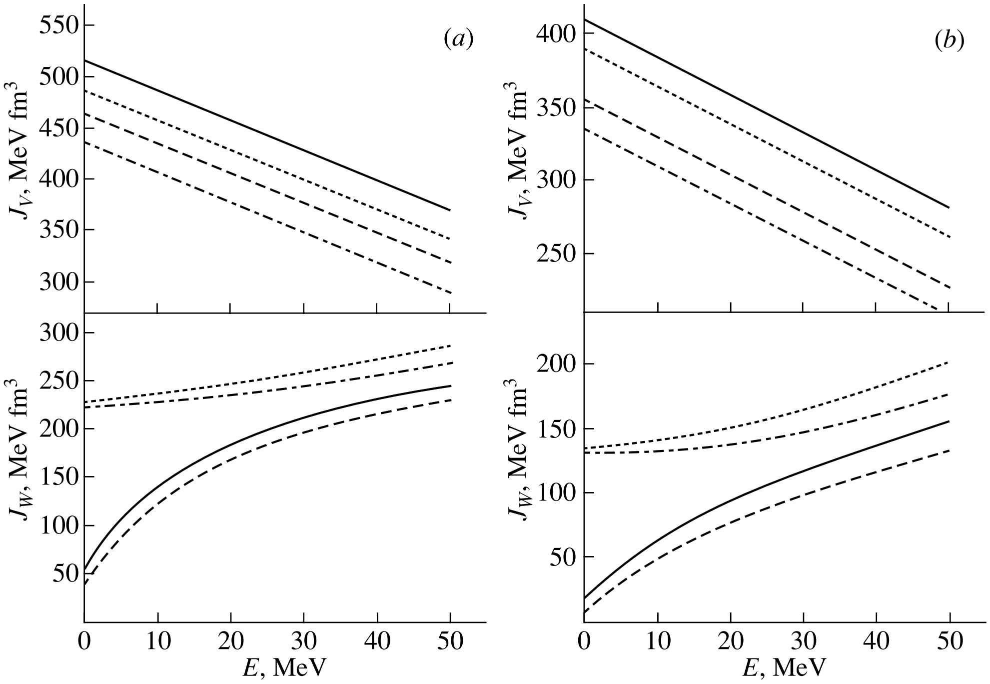

Fig. 4. Volume integrals of the real (V) and imaginary (W) parts of the optical potential for (a) n^{40}Ca and (b) n^{208}Pb scattering versus the neutron energy E for the cases where the rearrangement potential is disregarded or taken into account (solid or dashed curves, respectively, at $T = 0$ and dotted or dash-dotted curves, respectively, at $T = 15$ MeV). The calculations were performed with the Ska forces.

ture in the range $T = 0$–15 MeV, which is considered here. For the integral J_W, the growth of energy leads to a decrease in the effect of a change in temperature and to an increase in the effect of the inclusion of the rearrangement potential.

4. In the present study, a microscopic neutron–nucleus optical potential and neutron mean free paths in nuclear matter have been calculated at finite nuclear temperatures and various values of energy by using the nuclear-matter approximation. The calculations have relied on perturbation theory with allowance for the rearrangement potential in the zero-order approximation and have employed density-dependent effective nucleon–nucleon forces of the Skyrme type. The calculations have been performed both for infinite symmetric and asymmetric nuclear matter and for the finite nuclei ^{40}Ca and ^{208}Pb in the local-density approximation. The effect of the rearrangement potential on the features being considered has been investigated at various values of energy and temperature, and the importance of taking this potential into account has been demonstrated. The energy, temperature, and radial dependences of the real and imaginary parts of the neutron–nucleus optical potential and of the neutron mean free paths have been studied.

Our results for symmetric and asymmetric nuclear matter and for ^{40}Ca and ^{208}Pb are qualitatively similar. It has been found that the real part of the optical potential is weakly dependent on T, so that the effect of the rearrangement potential is much stronger than the temperature effect. A strong temperature dependence is characteristic of the imaginary part of the optical potential. Even in this case, however, the effect of the rearrangement potential is quite significant (on the order of changes in the imaginary part of the optical potential in the temperature interval being considered), this effect increasing with energy, in contrast to what we have in the case of the real part. The effect of the rearrangement potential on the mean free paths is especially pronounced at low temperatures, but it decreases with increasing energy. At high temperatures, this effect is moderate, slowly changing with energy. The neutron mean free paths in symmetric and asymmetric nuclear matter differ sizably at low temperatures, but they are close at high temperatures.

REFERENCES

1. H. Feshbach, Ann. Phys. (N.Y.) **5**, 357 (1958); **19**, 287 (1962).
2. G. R. Satchler, *Direct Nuclear Reactions* (Clarendon Press, Oxford, 1983).
3. K. Amos, P. J. Dortmans, H. V. von Geramb, *et al.*, Adv. Nucl. Phys. **25**, 275 (2000).
4. M. E. Brandan and G. R. Satchler, Phys. Rep. **285**, 143 (1997).

5. S. A. Fayans, O. M. Knyazkov, I. N. Kuchtina, *et al.*, Phys. Lett. B **357**, 509 (1995).
6. O. M. Knyazkov, A. A. Kolozhvari, I. N. Kukhtina, and S. A. Fayans, Yad. Fiz. **59**, 466 (1996) [Phys. At. Nucl. **59**, 439 (1996)].
7. D. V. Bolotov, A. A. Kolozhvari, I. N. Kukhtina, and S. A. Fayans, Yad. Fiz. **63**, 1631 (2000) [Phys. At. Nucl. **63**, 1546 (2000)].
8. I. Pecina, R. Anne, D. Bazin, *et al.*, Phys. Rev. C **52**, 191 (1995).
9. A. Hogenbirk, H. P. Block, F. A. Jansen, and J. J. A. Zalmastra, Phys. Lett. B **223**, 282 (1989).
10. S. A. E. Khallaf, A. M. A. Amry, and S. R. Mokhtar, Phys. Rev. C **56**, 2093 (1997).
11. G. Bertsch, J. Borysovicz, H. McManus, *et al.*, Nucl. Phys. A **284**, 399 (1977).
12. A. M. Kobos *et al.*, Nucl. Phys. A **384**, 65 (1982); **417**, 256 (1984).
13. J. S. Bell and E. J. Squires, Phys. Rev. Lett. **3**, 96 (1959).
14. J. W. Negele, Phys. Rev. C **1**, 1260 (1970).
15. J. P. Jeukenne, A. Lejeune, and C. Mahaux, Phys. Rep. **25C**, 83 (1976); Phys. Rev. C **16**, 80 (1977).
16. F. A. Brieva and J. R. Rook, Nucl. Phys. A **291**, 317 (1977).
17. D. Vautherin and D. M. Brink, Phys. Rev. C **5**, 626 (1972).
18. B. I. Barts, Yu. L. Bolotin, E. V. Inopin, and V. Yu. Gonchar, *Hartree—Fock's Method in the Nuclear Theory* (Naukova Dumka, Kiev, 1982) [in Russian].
19. C. B. Dover and Nguyen Van Giai, Nucl. Phys. A **190**, 373 (1972).
20. D. A. Kirzhnits, *Field Theoretical Methods in Many-Body Systems* (Gosatomizdat, Moscow, 1963; Pergamon Press, Oxford, 1967).
21. T. H. R. Skyrme, Nucl. Phys. **9**, 615 (1959).
22. S. Krewald, V. Klemt, J. Speth, and A. Faessler, Nucl. Phys. A **281**, 166 (1977).
23. H. S. Köhler, Nucl. Phys. A **258**, 301 (1976).
24. Nguyen Van Giai and H. Sagawa, Phys. Lett. B **106B**, 379 (1981).
25. Shen Qingbiao, Zhang Jingshang, Tian Ye, *et al.*, Z. Phys. A **303**, 69 (1981).
26. Ge Lingxiao, Zhuo Yizhong, and W. Nörenberg, Nucl. Phys. A **459**, 77 (1986).
27. Li Guo-Qiang, Shi Jiang-Qing, and Gao Qin, Nucl. Phys. A **515**, 273 (1990).
28. K. A. Brueckner, *The Many-Body Problem* (Wiley, New York, 1959).
29. B. H. Brandow, Phys. Rev. **152**, 863 (1966).
30. B. H. Brandow, Rev. Mod. Phys. **39**, 771 (1967).
31. V. I. Kuprikov and A. P. Soznik, Yad. Fiz. **56** (1), 84 (1993) [Phys. At. Nucl. **56**, 49 (1993)].
32. S. M. Kravchenko, V. I. Kuprikov, and A. P. Soznik, Yad. Fiz. **61**, 461 (1998) [Phys. At. Nucl. **61**, 400 (1998)].
33. S. M. Kravchenko, V. I. Kuprikov, and A. P. Soznik, Int. J. Mod. Phys. E **7**, 465 (1998).
34. H. A. Bethe, *Theory of Nuclear Matter* (Mir, Moscow, 1974); Annu. Rev. Nucl. Sci. **21**, 93 (1971).
35. K. Kumar, *Perturbation Theory and the Nuclear Many Body Problem* (North-Holland, Amsterdam, 1962; Mir, Moscow, 1964).
36. D. J. Thouless, *The Quantum Mechanics of Many-Body Systems* (Academic, New York, 1972; Mir, Moscow, 1975).
37. J. Cugnon, A. Lejeune, M. Baldo, and U. Lombardo, Nucl. Phys. A **492**, 173 (1989).

Translated by A. Isaakyan

Physics of Atomic Nuclei, Vol. 68, No. 2, 2005, pp. 219–233. Translated from Yadernaya Fizika, Vol. 68, No. 2, 2005, pp. 244–258.
Original Russian Text Copyright © 2005 by Babenko, Petrov.

NUCLEI
Theory

Description of Scattering and of a Bound State in the Two-Nucleon System on the Basis of the Bargmann Representation of the S Matrix

V. A. Babenko and N. M. Petrov[*]

Bogolyubov Institute for Theoretical Physics, National Academy of Sciences of Ukraine,
Metrologicheskaya ul. 14b, Kiev, 03143 Ukraine

Received June 20, 2003; in final form, November 11, 2003

Abstract—For the effective-range function $k\cot\delta$, a pole approximation that involves a small number of parameters is derived on the basis of the Bargmann representation of the S matrix. The parameters of this representation, which have a clear physical meaning, are related to the parameters of the Bargmann S matrix by simple equations. By using a polynomial least squares fit to the function $k\cot\delta$ at low energies, the triplet low-energy parameters of neutron–proton scattering are obtained for the latest experimental data of Arndt's group on phase shifts. The results are $a_t = 5.4030$ fm, $r_t = 1.7494$ fm, and $v_2 = 0.163$ fm^3. With allowance for the values found for the low-energy parameters and for the pole parameter, the pole approximation of the function $k\cot\delta$ provides an excellent description of the triplet phase shift for neutron–proton scattering over a wide energy range ($T_{\rm lab} \lesssim 1000$ MeV), substantially improving the description at low energies as well. For the experimental phase shifts of Arndt's group, the triplet shape parameters v_n of the effective-range expansion are obtained by using the pole approximation. It turns out that they are positive and decrease with increasing n. The description of the phase shift by means of the effective-range expansion featuring values found for the low-energy parameters of scattering proves to be fairly accurate over a broad energy region extending to energy values approximately equal to the energy at which this phase shift changes sign, this being indicative of a high accuracy and a considerable value of the effective-range expansion in describing experimental data on nucleon–nucleon scattering. The properties of the deuteron that were calculated by using various approximations of the effective-range function comply well with their experimental values. *© 2005 Pleiades Publishing, Inc.*

1. INTRODUCTION

The S matrix [1], which was first introduced by Heisenberg [2], is a fundamental quantity in scattering theory. At a fixed value of the orbital angular momentum ℓ, the S matrix is a function of the wave number k related to the energy E of two colliding particles in the c.m. frame by the equation $E = \hbar^2k^2/2m$, where m is the reduced mass of the system and $\hbar$ is Planck's constant. In the following, we restrict our consideration to the case of zero orbital angular momentum (in order to avoid encumbering formulas given below, we omit the index $\ell = 0$). The fact that a unified description of both scattering and bound states in two-particle systems can be constructed on the basis of the respective S matrix is an important consequence of the analytic properties of this matrix. In general, the analytic properties of the S matrix in the k plane are rather complicated; however, a number of important results can be obtained in considering specific physical systems by using an S matrix whose analytic properties are simple. In the k plane, the S matrix satisfies the relation [1]

$$S^*(k^*) \cdot S(k) = 1. \qquad (1)$$

At real k values, this relation coincides with the unitarity condition.

In potential-scattering theory, the S matrix $S(k)$ is expressed in terms of the Jost function $F(k)$ as [3, 4]

$$S(k) = F(-k)/F(k). \qquad (2)$$

At complex values of k, the Jost function $F(k)$ satisfies the condition

$$F^*(-k^*) = F(k). \qquad (3)$$

The S-matrix property (1) immediately follows from this condition with allowance for (2). The behavior of the Jost function at high energies is determined by the relation

$$\lim_{k\to\infty} F(k) = 1. \qquad (4)$$

The behavior of the S matrix at high energies directly follows from (2) and (4):

$$\lim_{k\to\infty} S(k) = 1. \qquad (5)$$

---

[*] e-mail: `pet@online.com.ua`

1063-7788/05/6802-0219$26.00 © 2005 Pleiades Publishing, Inc.

In the case of elastic scattering, the S matrix can be expressed in terms of the phase shift $\delta(k)$ as

$$S(k) = e^{2i\delta(k)}. \qquad (6)$$

Using relation (6) and considering that the S matrix possesses the symmetry property [1]

$$S(-k) = S^{-1}(k), \qquad (7)$$

one can easily see that, at real values of k, the phase shift $\delta(k)$ is an odd function of k; that is,

$$\delta(-k) = -\delta(k). \qquad (8)$$

From relations (5) and (6), one readily establishes the asymptotic behavior of the phase shift at high energies:

$$\lim_{k\to\infty} \delta(k) = 0. \qquad (9)$$

In practice, it is very useful to introduce the effective-range function

$$k\cot\delta = ik\frac{S(k)+1}{S(k)-1}. \qquad (10)$$

In the physical region, the function $k\cot\delta$ is real by virtue of the unitarity of the S matrix, while, in the k plane, this function is analytic everywhere, with the exception of the points where $S(k) = 1$, where it has poles. The introduction of the function $k\cot\delta$ simplifies the investigation of the analytic properties of the S matrix. It follows from (8) that the function $k\cot\delta$ is an even function of k.

In studying nucleon–nucleon scattering at low energies, it is useful to employ the well-known effective-range expansion

$$k\cot\delta = -\frac{1}{a} + \frac{1}{2}r_0k^2 + v_2k^4 + v_3k^6 + \ldots, \qquad (11)$$

which involves only even powers of k. The effective-range approximation corresponds to retaining only the first two terms in (11). In expansion (11), the quantities a and r_0 are, respectively, the scattering length and the effective range, while the quantities v_n are related to the potential shape. It should be noted that the quantity r_0 is a measure of the effective-interaction region. In the case of nucleon–nucleon interaction, the effective range r_0 is approximately equal to the range of nuclear forces (R). If, however, one deals with the doublet neutron–deuteron (nd) interaction, the effective range is anomalously large ($r_0 \sim 500$ fm), so that the statement that it is approximately equal to the range of nuclear forces ($R \sim 2$ fm) does not hold here. This is because, for nd interaction, the function $k\cot\delta$ has a pole in the vicinity of the point $k^2 = 0$ owing to the existence of a low-energy virtual triton state [5].

In a number of studies (see, for example, [6–8]), the authors approximated the S matrix by rational functions, this leading to so-called Bargmann potentials [4, 9]. The use of a Bargmann S matrix makes it possible to find explicit solutions to the direct and inverse scattering problems. Of particular importance are special cases where the Bargmann S matrix is determined by a small number of parameters such that physical observables are directly expressed in terms of these parameters. In [5], we showed that the use of the Bargmann S matrix corresponding to the presence of two states in the system being considered leads to the pole structure of the effective-range function (van Oers–Seagrave formula [10]). At low energies, this structure makes it possible to describe well doublet nd scattering on the basis of parameters that characterize the bound and the virtual state of the triton.

In the present study, we use the Bargmann representation of the S matrix to construct the pole approximation of the effective-range function, bearing in mind that the pole approximation is the most optimal for describing nucleon–nucleon scattering and that it involves a small number of parameters. The pole-approximation parameters have a clear physical meaning, and the values found for these parameters from an analysis of low-energy experimental data make it possible to obtain an excellent unified description of a bound state in the two-nucleon system (deuteron) and the triplet phase shift for neutron–proton scattering over a very wide energy range (0–1000 MeV).

2. BARGMANN REPRESENTATION OF THE S MATRIX AND POLE APPROXIMATION OF THE EFFECTIVE-RANGE FUNCTION

In order to investigate the interaction in the system of two particles, we will use the corresponding Bargmann S matrix [4, 9], which possesses simple analytic properties in the k plane. In this case, the Jost function $F(k)$ can be chosen in the simplest way in the form of a rational function,

$$F(k) = \prod_{n=1}^{N} \frac{k - i\alpha_n}{k + i\lambda_n}. \qquad (12)$$

It has N simple zeros at the points $k = i\alpha_n$ and N simple poles at the points $k = -i\lambda_n$ and exhibits the correct asymptotic behavior (4) at high energies.

As a simple example of a Bargmann S matrix, one can consider the S matrix corresponding to the Hulthén potential

$$V(r) = -V_0(e^{r/R} - 1)^{-1}, \qquad (13)$$

for which we have

$$\alpha_n = \frac{g - n^2}{2nR}, \lambda_n = \frac{n}{2R}, \tag{14}$$

where

$$g = \frac{2m}{\hbar^2} V_0 R^2, \tag{15}$$

and $N \to \infty$.

The scattering matrix

$$S(k) = \prod_{n=1}^{N} \frac{k + i\alpha_n}{k - i\alpha_n} \frac{k + i\lambda_n}{k - i\lambda_n}, \tag{16}$$

which corresponds to the Jost function (12), has N simple "physical" poles at $k = i\alpha_n$ in the k plane. The poles lying on the imaginary axis in the upper half-plane ($\alpha_n > 0$) correspond to bound states, while the poles in the lower half-plane correspond to resonances or virtual states. The resonances in the lower half-plane are grouped in pairs symmetric with respect to the imaginary axis, while the virtual states are on the imaginary axis ($\alpha_n < 0$). In addition to the physical poles corresponding to resonances and bound and virtual states, the Bargmann S matrix (16) has N so-called extra poles at $k = i\lambda_n$ in the upper half-plane, which do not correspond to any physical states. The presence of the same number of redundant poles serves as some kind of a compensation factor, ensuring the correct asymptotic behavior [see Eq. (4)] of the Jost function at infinity.

With allowance for Eqs. (2) and (3), the effective-range function (10) at real values of k can be expressed in terms of the real and the imaginary part of the Jost function as

$$k \cot \delta = -k \frac{\mathrm{Re} F(k)}{\mathrm{Im} F(k)}. \tag{17}$$

From the Bargmann representation (16) of the S matrix, it immediately follows that the effective-range function $k \cot \delta$ can then be written in the form of a rational function of k^2,

$$k \cot \delta = \frac{P_N(k^2)}{Q_{N-1}(k^2)}, \tag{18}$$

where the degrees of the polynomials $P_N(k^2)$ and $Q_{N-1}(k^2)$ of k^2 are N and $N - 1$, respectively, and where the coefficients in these polynomials are completely determined by the quantities α_n and λ_n.

The representation in (18) for the function $k \cot \delta$ can be considered as a Padé approximation of this function [11] if the expansion of the function $P_N(k^2)/Q_{N-1}(k^2) \equiv [N/(N-1)]$ in a Taylor–Maclauren series coincides with the effective-range expansion (11) up to terms of order $2N - 1$. In other words, the coefficients of $1, k^2, \ldots, k^{2(2N-1)}$ in the Taylor expansion of the function $[N/(N-1)]$ must coincide with the corresponding coefficients in the series in (11). The Padé approximation method was used by various authors to study nucleon–nucleon scattering (see, for example, [12–15]). It is of importance in our case that, from the Bargmann representation (16) of the S matrix, it automatically follows that the degree of the polynomial P in the numerator of the Padé approximant (18) must be greater by unity than the degree of the polynomial Q in its denominator, this being in accord with the condition of the theorem [12] on the solvability of the inverse scattering problem. In addition, one can see that, in the majority of cases, the condition $L = M + 1$ for the Padé approximant $[L/M]$ of the function $k \cot \delta$ is optimal for specific fits [13–15].

Let us now consider in detail the important particular case where the Bargmann S matrix corresponds to the presence of two physical states ($N = 2$) in the system. This is so, for example, in the doublet scattering of a neutron on a deuteron [5], in which case there are two triton states in the system, a bound and a virtual one. The scattering matrix corresponding to the presence of two states in the system can also be used to describe triplet neutron–proton scattering. Since the second state has not yet been observed experimentally in that case, the energy of this state must be considerably higher than the deuteron binding energy. If, in this case, the second state is a bound state of two nucleons, such a situation corresponds to the phenomenology of nodes that is described by a short-range deep attractive potential involving forbidden states [16–18].

If the system has two physical states, the rational Jost function and the Bargmann S matrix corresponding to it are given by

$$F(k) = \frac{k - i\alpha}{k + i\lambda} \frac{k - i\beta}{k + i\mu}, \tag{19}$$

$$S(k) = \frac{k + i\alpha}{k - i\alpha} \frac{k + i\beta}{k - i\beta} \frac{k + i\lambda}{k - i\lambda} \frac{k + i\mu}{k - i\mu}. \tag{20}$$

The first and second factors in the S-matrix representation (20) correspond to either bound or virtual states of the system, while the third and fourth factors correspond to redundant poles of the S matrix. The negative energies of the bound and virtual states of the system are

$$E_\alpha = -\hbar^2 \alpha^2/(2m), \tag{21}$$

$$E_\beta = -\hbar^2 \beta^2/(2m). \tag{22}$$

The expression describing the effective-range function $k \cot \delta$ and corresponding to the presence of two states in the system immediately follows from (17) and (19). The result is

$$k\cot\delta = -\frac{1}{a}\frac{1-c_2k^2+c_4k^4}{1+Dk^2}, \qquad (23)$$

where, for the sake of convenience, we have explicitly isolated the scattering length a. The parameters appearing in the pole representation (23) of the function $k\cot\delta$ and the parameters α, β, λ, and μ of the Bargmann S matrix (20) are related by the equations

$$a = \frac{1}{\alpha}+\frac{1}{\beta}+\frac{1}{\lambda}+\frac{1}{\mu}, \qquad (24)$$

$$c_2 = \frac{1}{\alpha\beta}+\frac{1}{\alpha\lambda}+\frac{1}{\alpha\mu}+\frac{1}{\beta\lambda}+\frac{1}{\beta\mu}+\frac{1}{\lambda\mu}, \qquad (25)$$

$$c_4 = 1/(\alpha\beta\lambda\mu), \qquad (26)$$

$$D = -\frac{1}{a}\frac{\alpha+\beta+\lambda+\mu}{\alpha\beta\lambda\mu}. \qquad (27)$$

The parameter D appearing in (23) determines the pole of the effective-range function k_0^2:

$$k_0^2 = -1/D. \qquad (28)$$

Expression (23), which was obtained for the function $k\cot\delta$ by the above method from the Bargmann representation of the S matrix, is a one-pole representation and involves four independent parameters. It can easily be shown that, apart from the form of presentation, the pole expression (23) coincides with the well-known empirical formulas that were given by van Oears and Seagrave [10] and by Cini, Fubini, and Stanghellini [19] and which are applied to describe, respectively, neutron–deuteron and nucleon–nucleon scattering. It is worth noting that various forms of the pole structure of the effective-range function $k\cot\delta$ have been repeatedly discussed for a rather long time and have been successfully used to describe neutron–deuteron [5, 10, 20–30] and nucleon–nucleon interactions [19, 31–35]. In the majority of cases, however, the formulas for $k\cot\delta$ were obtained empirically. But in our case, the pole formula for the function $k\cot\delta$ immediately follows from the Bargmann S matrix, which possesses simple properties and which takes into account basic physical properties of the interaction in the system being considered.

In [5], we showed that, in the case of neutron–deuteron interaction, the presence of the pole of the function $k\cot\delta$ is a direct consequence of the existence of a virtual triton state at a low energy. In the present study, the effective-range function having a pole structure will be used to describe neutron–proton interaction in the triplet (t) spin state $^3S_1$. In this case, the neutron–proton system has one bound state (deuteron), the scattering of a neutron on a proton at low energies (up to energies of about 10 MeV) being well described in the effective-range approximation. In this connection, it is convenient to recast the pole-approximation formula (23) into the form

$$k\cot\delta = -\frac{1}{a_t}+\frac{1}{2}r_tk^2+\frac{v_2k^4}{1+Dk^2}, \qquad (29)$$

where a_t and r_t are, respectively, the scattering length and the effective range, while the parameter v_2 determines the dimensionless shape parameter P_t, which is widely used in the literature, according to the relation

$$P_t = -v_2/r_t^3. \qquad (30)$$

The first two terms of the representation in (29) correspond to the effective-range approximation, while the last, pole, term describes the deviation from this approximation. The presence of this pole term makes it possible to improve, with the aid of only two additional parameters, the description of the phase shift significantly and to extend the range of applicability of this description greatly. Thus, the pole approximation (29), which was derived from the Bargmann representation of the S matrix, is a direct generalization of the effective-range approximation to the case where there are two physical states in the system. We note that the form (29) of the pole formula is more convenient for describing nucleon–nucleon scattering than that in (23), since, in (29), the low-energy scattering parameters a_t, r_t, and v_2 are isolated explicitly.

The parameters a_t and D appearing in (29) are related to the parameters of the Bargmann S matrix (20) by Eqs. (24) and (27), while the effective range r_t and the shape parameter v_2 are given by

$$r_t = \frac{2}{a_t}(D+c_2), \qquad (31)$$

$$v_2 = -\left(\frac{1}{2}Dr_t+\frac{c_4}{a_t}\right), \qquad (32)$$

where c_2 and c_4 are related to the S-matrix parameters by Eqs. (25) and (26).

Let us now consider the specific case where the S matrix in (20) for the case of two states reduces to the S matrix for one state,

$$S(k) = \frac{k+i\alpha}{k-i\alpha}\frac{k+i\lambda}{k-i\lambda}. \qquad (33)$$

In this case, the second state goes to infinity: $\beta\to\infty$ and $\mu\to\infty$. It can easily be seen that the coefficients D and v_2 then vanish in formula (29), which reduces, after that, to the effective-range-approximation formula

$$k\cot\delta = -\frac{1}{a_t}+\frac{1}{2}r_tk^2, \qquad (34)$$

where the scattering length a_t and the effective range r_t are given by

$$a_t = \frac{1}{\alpha} + \frac{1}{\lambda}, \tag{35}$$

$$r_t = \frac{2}{\alpha + \lambda}. \tag{36}$$

The dimensionless asymptotic normalization factor C_d characterizing the bound state of the two-nucleon system (deuteron) can be expressed in terms of the residue of the S matrix at the pole $k = i\alpha$ as

$$C_d^2 = \frac{i}{2\alpha} \operatorname*{Res}_{k=i\alpha} S(k). \tag{37}$$

In the case of the S matrix for one state, C_d is given by

$$C_d^2 = \frac{\lambda + \alpha}{\lambda - \alpha}. \tag{38}$$

Upon expressing λ in terms of α and C_d^2, formulas (35) and (36) for the scattering length a_t and the effective range r_t, respectively, can be recast into the form [36]

$$a_t = \frac{2}{\alpha} \frac{C_d^2}{1 + C_d^2}, \tag{39}$$

$$r_t = \frac{1}{\alpha}\left(1 - \frac{1}{C_d^2}\right). \tag{40}$$

Thus, formulas (39) and (40) give explicit expressions for the low-energy scattering parameters a_t and r_t in terms of parameters that characterize the bound state of the two-nucleon system (deuteron) in the case where the interaction in the system is described by the S matrix for one state. The inverse statement is also valid—namely, the parameters characterizing the deuteron can be expressed, in this case, in terms of the scattering parameters a_t and r_t as

$$\alpha = \frac{1}{r_t}\left[1 - \left(1 - \frac{2r_t}{a_t}\right)^{1/2}\right], \tag{41}$$

$$C_d^2 = \frac{1}{(1 - 2r_t/a_t)^{1/2}}. \tag{42}$$

The case where, at finite values of β and μ, the coefficient D vanishes, while the parameter v_2 differs from zero, is yet another important specific case of formula (29). This is so if the system has a virtual state whose wave number β is given by

$$\beta = -(\alpha + \lambda + \mu). \tag{43}$$

It can be seen from (27) that, in this case, the parameter D is equal to zero, while expression (29) for the effective-range function reduces to the expression corresponding to the shape-parameter approximation,

$$k \cot \delta = -\frac{1}{a_t} + \frac{1}{2} r_t k^2 + v_2 k^4, \tag{44}$$

where

$$r_t = 2c_2/a_t, \tag{45}$$

$$v_2 = -P_t r_t^3 = -c_4/a_t, \tag{46}$$

with a_t, c_2, and c_4 being given by (24)–(26). The effective-range approximation (34) and the shape-parameter approximation (44) are among the most popular and important methods for parametrizing data on nucleon–nucleon scattering at low energies [37, 38].

In the triplet spin state, the neutron–proton scattering length a_t is positive. It follows that, in the approximation specified by Eq. (44), the sign of the shape parameter P_t is determined by the sign of the parameter c_4 in accordance with (46). Since the redundant poles $k = i\lambda$ and $k = i\mu$ of the S matrix lie in the upper half-plane and since $\alpha > 0$ and $\beta < 0$, it follows from (26) that c_4 is negative. Therefore, the dimensionless shape parameter P_t is also negative in this approximation:

$$P_t < 0. \tag{47}$$

The authors of [37, 38] studied the relation between the parameters a, r, and P for a great number of regular potentials. It was established, among other things, that the shape parameter P takes values in the range between -0.05 and $+0.15$. However, the introduction of a hard core reduces the shape parameter P significantly—in fact, the parameter P is negative for the majority of potentials that involve a hard core. This agrees with the estimate in (47), which was derived on the basis of the Bargmann representation of the S matrix.

Thus, we have shown that the shape-parameter approximation (44) directly follows from the Bargmann representation of the S matrix in the case where the system has two physical states of which at least one is virtual. If the system has two virtual states ($\alpha < 0$, $\beta < 0$), the shape-parameter approximation (44) follows from the Bargmann representation of the S matrix under the condition

$$(\alpha + \beta) = -(\lambda + \mu) \tag{48}$$

and corresponds to the description of the neutron–proton interaction in the singlet spin state.

Table 1. Triplet phase shift for np scattering as a function of the laboratory energy $T_{\rm lab}$ according to calculations within the effective-range (ER) approximation, the shape-parameter (SP) approximation, and the pole (P1 and P2) approximations (for the shape-parameter values $v_2 = 0.163$ and $v_2 = 0.168$ fm^3, respectively)

$T_{\rm lab}$, MeV	Phase shift δ_t, deg				
	ER	SP	P1	P2	experiment [39]
1	147.84	147.83	147.83	147.83	147.83
5	118.34	118.23	118.23	118.23	118.23
10	102.93	102.56	102.55	102.54	102.55
25	81.87	80.36	80.26	80.20	80.26
40	71.19	68.44	68.11	68.01	68.11
50	66.23	62.68	62.14	62.01	62.11
75	57.51	52.16	50.90	50.70	50.77
100	51.64	44.80	42.60	42.34	42.34
125	47.30	39.25	35.95	35.66	35.58
150	43.93	34.89	30.37	30.05	29.94
175	41.19	31.35	25.53	25.19	25.09
200	38.92	28.42	21.23	20.90	20.84
225	36.99	25.95	17.36	17.04	17.03
250	35.32	23.84	13.81	13.53	13.57
275	33.86	22.01	10.53	10.29	10.37
300	32.57	20.42	7.47	7.28	7.38
325	31.41	19.02	4.60	4.47	4.56
350	30.38	17.78	1.88	1.82	1.87
375	29.44	16.68	−0.71	−0.69	−0.71
400	28.58	15.69	−3.18	−3.07	−3.20
425	27.79	14.79	−5.54	−5.34	−5.61
450	27.06	13.99	−7.82	−7.51	−7.94
475	26.39	13.25	−10.02	−9.59	−10.21
500	25.77	12.58	−12.14	−11.60	−12.41

3. CHOICE OF PARAMETERS AND DESCRIPTION OF SCATTERING IN THE TWO-NUCLEON SYSTEM

An investigation of the phase shift δ as function of energy plays a fundamental role in an analysis of data on nucleon–nucleon scattering. A traditional way to study this dependence at low energies consists in applying the effective-range approximation (34) and the shape-parameter approximation (44) [37, 38]. In order to determine the parameters a_t, r_t, and P_t, one employs experimental data on scattering and also the experimental value of the deuteron binding energy ε_d. It was shown in [38] that, in this case, the determination of the parameters a_t, r_t, and P_t involved ambiguities, and this is at odds with the meaning of the effective-range expansion (11). The ambiguity in the determination of the low-energy parameters was due primarily to an insufficient accuracy of experimental data at low energies. At the present time, the accuracy of experimental data is such that the ambiguity in the determination of the scattering length a_t, the effective range r_t, and the shape parameter P_t is quite removable.

By using the least squares method to construct a polynomial fit to the function $k\cot\delta$ at low energies ($T_{\rm lab} \lesssim 10$ MeV) and relying on the latest experimental data of Arndt's group on nucleon–nucleon phase shifts [39], we obtain the following values of the triplet low-energy scattering parameters a_t, r_t, and v_2:

$$a_t = 5.4030 \pm 0.0001\ \text{fm}, \tag{49}$$

$$r_t = 1.7494 \pm 0.0003\ \text{fm}, \tag{50}$$

$$v_2 = 0.163 \pm 0.002\ \text{fm}^3. \tag{51}$$

Here, we have also given our theoretical estimates of the respective errors in determining the low-energy parameters. The resulting dimensionless shape parameter, $P_t = -v_2/r_t^3 = -0.0304$, proved to be negative. This is in agreement with the estimate in (47), which was obtained on the basis of the Bargmann representation of the S matrix.

In order to describe triplet scattering and the bound state in the two-nucleon system, we will use the pole approximation of the effective-range function (29). In doing this, we set the low-energy parameters a_t, r_t, and v_2 to the values in (49)–(51) and choose the value of the pole parameter D to be

$$D = -0.225526\ \text{fm}^2. \tag{52}$$

With allowance for (28), this corresponds to the laboratory energy

$$T_0 = 368.026\ \text{MeV}, \tag{53}$$

at which the experimental value of the triplet phase shift [39] changes sign. Thus, it can be seen that, if the pole parameter D is fixed by using the experimental point $\delta(T_0) = 0$, the quantity D can be considered as an experimental parameter directly determined to a rather high degree of accuracy.

If one uses the parameter values in (49)–(52), then, as can be seen from the results of phase-shift calculations in Table 1 (the pole approximation P1), the pole approximation (29) describes the experimental triplet phase shift [39] up to laboratory energies of about 500 MeV with an absolute error not exceeding 0.5°. For the sake of comparison, the results obtained by calculating the phase shift within the effective-range approximation (ER) and within the shape-parameter approximation (SP) with the low-energy parameters set to the values in (49)–(51) are also presented in Table 1. As might have been expected, the effective-range approximation (34) describes well the phase shift only in the region of very low energies ($T_{\mathrm{lab}} \lesssim 10$ MeV). The shape-parameter approximation (44) describes well the experimental phase shift up to energies of about 50 MeV (to within about 0.5°). At the same time, the pole approximation (29) provides an excellent description of the phase shift within a broad energy range, considerably improving the description in the low-energy region—for example, the experimental phase shift in the energy range $T_{\mathrm{lab}} \leqslant 40$ MeV is described by formula (29) with an error not exceeding 0.01°. In the above energy range, one can therefore consider the parametrization of the phase shift by the pole formula (29) as an alternative to the data of a partial-wave analysis (PWA). As a matter of fact, the approximation specified by Eq. (29) with the parameters given in (49)–(52) provides an excellent description of the phase shift in much wider energy interval than that which was used to find the parameters of this approximation. As can be seen from Fig. 1, the accuracy of the description of the phase shift undergoes virtually no deterioration up to an energy of 900 MeV, being 0.6° for laboratory energies of $T_{\mathrm{lab}} \leqslant 900$ MeV. Along with the phase shift corresponding to the pole approximation (29), the phase shift calculated within the effective-range approximation (34) and that calculated within the shape-parameter approximation (44) are also displayed in Fig. 1 for the sake of comparison.

By slightly varying the shape parameter v_2 and leaving the parameters a_t, r_t, and D unchanged, one can improve further the quality of description of the phase shift in the energy range $T_{\mathrm{lab}} \lesssim 400$ MeV. The minimum absolute error of description of the phase shift in this energy range is attained at

$$v_2 = 0.168 \ \mathrm{fm}^3 \qquad (54)$$

and is about 0.1°, as can be seen in Table 1 (pole approximation P2). Thus, the pole approximation (29) makes it possible to describe, by using a small number of parameters, the phase shift over a wide energy range to a precision close to that in determining experimental data.

It should be noted that the value of the pole parameter D is very well determined by the experimental phase shift even at low energies and is close to the above value in (52). This can be shown most clearly by analyzing the dependence of the absolute error of the description of the phase shift,

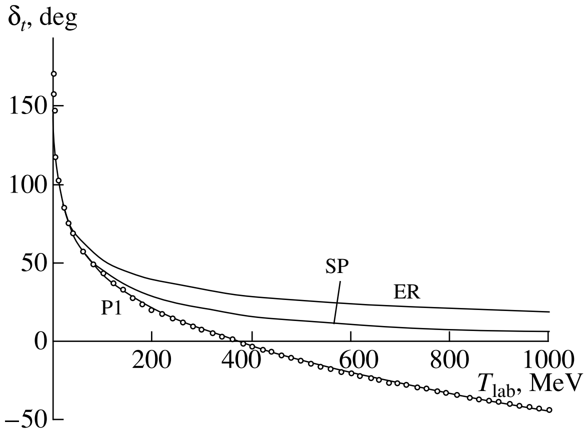

Fig. 1. Triplet phase shift for neutron–proton scattering as a function of the laboratory energy according to calculations within the effective-range (ER), the shape-parameter (SP), and the pole (P1) approximation. The points represent experimental data borrowed from [39].

$$\Delta = \max_{0 \leqslant T \leqslant T_{\max}} |\delta_{\mathrm{expt}}(T) - \delta_{\mathrm{theor}}(T)|, \qquad (55)$$

on the parameter D in a given range $0 \leqslant T \leqslant T_{\max}$. Our calculations reveal that the minimum error is achieved at negative values of D that are close to the value in (52), the dependence $\Delta(D)$ having quite a sharp character in the vicinity of the minimum, so that any significant deviation of the parameter D from the point of the minimum leads to a considerable deterioration of the quality of phase-shift description. We note that the value of $D = 0$ corresponds to the shape-parameter approximation and that, for $D \to \infty$, we obtain the effective-range approximation. The calculations also show that, at the value of $D = -0.2147$ fm^2, which corresponds to the minimal deviation Δ, the absolute error of the description of the phase shift on the basis of (29) does not exceed 0.006° in the energy range being considered. At the same time, Δ takes values of 1.16° and 0.064° for, respectively, the effective-range and the shape-parameter approximation. Thus, we see that, even at low energies, the quality of the description of the phase shift by the pole formula is an order of magnitude higher than the quality of the description within the shape-parameter approximation, the value of the parameter D being negative and close to that in (52). We emphasize that the energy of $T_0 = 386.6$ MeV, at which the calculated phase shift changes sign and which is in good agreement with the experimental value in (53), corresponds to the value of $D = -0.2147$ fm^2. The analysis revealed that the pole parameter D is a quantity that admits an unambiguous determination yielding results that are rather weakly dependent on the interval of fitting. In fact, any fit to the phase shift leads, even at low energies, to negative values of the parameter D that are close to the value in (52). Thus, we see that, in just the same way as the parameters a_t, r_t, and v_2, D is a low-energy parameter that can be determined reliably and to a high precision.

The pole formula (29) for the function $k\cot\delta$ coincides in form with the well-known empirical Cini–Fubini–Stanghellini (CFS) formula [19], which was used to describe nucleon–nucleon scattering [19, 31–35] and which is generally written as

$$k\cot\delta = -\frac{1}{a_t} + \frac{1}{2}r_t k^2 - \frac{pk^4}{1+qk^2}. \qquad (56)$$

A distinctive feature of the Cini–Fubini–Stanghellini approach is that the parameters $p \equiv -v_2$ and $q \equiv D$ in formula (56) are not independent—they are determined on the basis of the one-pion-exchange theory of nucleon–nucleon interaction. Thus, the quantities p and q in (56) are rather complicated functions of the scattering length a_t, the effective range r_t, the pion mass m_π, and the pion–nucleon coupling constant G^2. According to one-pion-exchange theory, the expressions for the parameters q and p can be written in the form [32, 33]

$$q = \lambdabar_\pi^2 \frac{2 - f^2M(3/\sqrt{2} - 4\lambdabar_\pi/a_t - r_t/2\lambdabar_\pi)}{1 - f^2M(1/2\sqrt{2} - \lambdabar_\pi/a_t)}, \qquad (57)$$

$$p = (\lambdabar_\pi^2 - q/2)(2\sqrt{2}\lambdabar_\pi - r_t - 4\lambdabar_\pi^2/a_t), \qquad (58)$$

where $M \equiv m_N/m_\pi$ is the ratio of the nucleon mass to the pion mass, $\lambdabar_\pi \equiv \hbar/m_\pi c$ is the pion Compton wave length, and $f^2 \equiv (m_\pi/2m_N)^2G^2$. For the low-energy scattering parameters a_t and r_t, we will use, in the following, the values obtained above and quoted in (49) and (50). On this basis, one can readily calculate the shape parameter v_2 and the pole parameter D within the Cini–Fubini–Stanghellini approach. The results are

$$v_2^{\mathrm{CFS}} = -0.121 \text{ fm}^3, \qquad (59)$$

$$D^{\mathrm{CFS}} = 3.777 \text{ fm}^2. \qquad (60)$$

It can be seen that the parameters v_2 and D calculated within the Cini–Fubini–Stanghellini approach differ considerably from the "experimental" values that are quoted in (51) and (52) and which are determined quite reliably from present-day data on the triplet phase shift [39]. It should be noted that the distinction is not only quantitative but also qualitative since the parameters v_2 and D have opposite signs within the Cini–Fubini–Stanghellini approach. The phase shift is described poorly with the Cini–Fubini–Stanghellini parameters. The explanation for so sharp a discrepancy with experimental data is likely to be the following. It has been firmly established that one-pion exchange is not the only mechanism and even is not the main mechanism of nucleon–nucleon interaction—the contribution of other mechanisms to nucleon–nucleon interaction is much more significant. Therefore, it comes as no surprise that the oversimplified one-pion-exchange scheme predicts erroneous values for the parameters v_2 and D. For want of a theory that would make it possible to calculate the low-energy parameters of nucleon–nucleon interaction on the basis of a microscopic approach (QCD), one has to treat them as adjustable parameters that are determined directly from experimental data.

Along with the aforesaid, we note that the recent calculation of the shape parameter v_2 within effective field theory (EFT) in [40, 41] also yielded an incorrect sign of v_2, $v_2^{\mathrm{EFT}} = -0.95$ fm^3, although calculations within this theory generally led to good agreement with experimental data for many computed features of the nucleon–nucleon and neutron–deuteron systems (see references quoted in [39, 40]). These discrepancies indicate that the shape parameter v_2 and the higher order parameters v_n are rather subtle and sensitive characteristics of the nucleon–nucleon interaction. In [40, 41], it was also indicated that the contribution to the nucleon–nucleon interaction from more "short-range" mechanisms than the one-pion-exchange mechanism is of importance.

4. LOW-ENERGY PARAMETERS OF THE EFFECTIVE-RANGE EXPANSION

Much attention has permanently been given to studying the low-energy parameters of the effective-range expansion (11) [12–15, 32–35, 37, 38, 40–50]. It should be noted that, while the scattering length a and the effective range r_0 can be determined directly from experimental data to a fairly high degree of precision [42–45], the higher order parameters v_n ($n = 2, 3, 4, \ldots$) are less convenient for an experimental determination, their theoretical calculation becoming more involved as the parameter order increases. At the same time, the shape parameters v_n, along with the scattering length a and the effective range r_0, are of particular importance for constructing and comparing various realistic models of nucleon–nucleon interaction and for describing nucleon–nucleon scattering. Moreover, the shape parameters are of importance for investigating the physical properties of the bound state in the two-nucleon system (deuteron)—in particular, their role in the useful expansion for the root-mean-square radius of the deuteron was demonstrated in [51–55]. The correlations between the properties of the deuteron and the parameters of nucleon–nucleon scattering that are determined by the expansion in (11) are also studied [51–56]. It should be noted that, in the past years, the parameters v_n were discussed and calculated in considering nucleon–nucleon interaction within effective field theory [40, 41].

In connection with the aforesaid, the determination of the parameters of the effective-range expansion (11) is of great importance. An explicit expansion of the function $k \cot \delta$ in a power series in k^2 follows directly from the pole representation (29):

$$k \cot \delta = -\frac{1}{a_t} + \frac{1}{2} r_t k^2 + \sum_{n=2}^{\infty} v_2 (-D)^{n-2} k^{2n}. \quad (61)$$

Therefore, all of the shape parameters v_n can also be obtained explicitly for this case. We have

$$v_n = (-1)^n v_2 D^{n-2}, \quad n \geqslant 3. \quad (62)$$

Thus, we see that, in the pole approximation, all parameters v_n $(n = 3, 4, 5, \ldots)$ of the effective-range expansion are determined explicitly in terms of the shape parameter v_2 and the pole parameter D according to the simple formula (62) and can easily be calculated to any order n. In our case, the parameter D is negative by virtue of (52). In view of this, it is convenient to recast formula (62) into the form

$$v_n = v_2 |D|^{n-2}, \quad n \geqslant 3. \quad (63)$$

Since we also have $v_2 > 0$ and $|D| < 1$, one can easily see that all of the parameters v_n are positive and decrease in absolute value; that is,

$$v_2 > v_3 > \ldots > v_n > v_{n+1} > \ldots > 0. \quad (64)$$

In Table 2, the low-energy scattering parameters a_t, r_t, and v_2 are presented along with the parameters v_3 and v_4 calculated by formula (63) at the experimental value of $D = -0.225526$ fm^2 and the shape-parameter value of $v_2 = 0.163$ fm^3 (approximation P1). For the sake of comparison, the parameters of the expansion in (11) that were found in [50] by using the partial-wave-analysis data on nucleon–nucleon scattering that were obtained by the Nijmegen group [57] (Nijm version) are also given in Table 2. We note that, at the present time, the partial-wave-analysis data obtained by Arndt's group [39] and the Nijmegen group [57] are the most accurate and frequently used data on the phase shifts for nucleon–nucleon scattering. The values found here for the shape parameters v_n $(n = 3, 4)$ on the basis of the pole approximation of the effective-range function are rather stable with respect to the variations in the shape parameter v_2. It can easily be shown that the parameters v_n are also rather weakly sensitive to the variation in the pole parameter D. Thus, formula (62) ensures a stable determination of the parameters v_n.

Table 2. Triplet low-energy scattering parameters obtained by using the data of the partial-wave analysis performed by Arndt's group (version P1 corresponds to the pole approximation at the shape-parameter value of $v_2 = 0.163$ fm^3) and the data of the partial-wave analysis performed by the Nijmegen group [50, 57] (Nijm version)

Version	a_t, fm	r_t, fm	v_2, fm^3	v_3, fm^5	v_4, fm^7
P1	5.4030	1.7494	0.163	0.037	0.0083
Nijm	5.420	1.753	0.040	0.672	−3.96

The following important comment concerning the applicability and accuracy of the simple one-pole approximation (29) for determining the parameters v_n is in order. Since the smooth interpolation curve specified by (29) provides an excellent description of experimental data of Arndt's group on the phase shift [39] over a wide energy range (in particular, to a precision not poorer than 0.01° for energies up to $T_{\text{lab}} = 40$ MeV), this curve determines the parameters v_n with the degree of reliability and stability as high as that to which they can in principle be determined by present-day experimental data on the phase shift, the error in these data being $\gtrsim 0.01°$. This means that, if a different interpolation curve also described well the experimental phase shift and, for some parameters v_n, gave values considerably differing from those obtained here, one could conclude that these parameters v_n are not determined by experimental data. As a matter of fact, the calculations show that only the parameters to v_4 inclusive are determined more or less reliably.

Table 2 shows that the results obtained here for the partial-wave-analysis data presented by Arndt's group [39] are radically different from the results of the calculations performed in [50] for the partial-wave-analysis data of the Nijmegen group [57], the distinction being not only quantitative but also qualitative—that is, all shape parameters v_n calculated here on the basis of the phase shifts of Arndt's group are positive and decrease, while the analogous parameters v_n calculated for the phase shifts of the Nijmegen group increase in absolute value and include a negative parameter (v_4).

A detailed investigation of the parameters of the effective-range expansion (11) will be given in our future publications. Here, we restrict ourselves to mentioning briefly the following: in order to reveal possible reasons behind such a discrepancy between the results, we have studied the stability of the calculation of the shape parameters v_n to variations in the scattering length a_t. We have shown that their

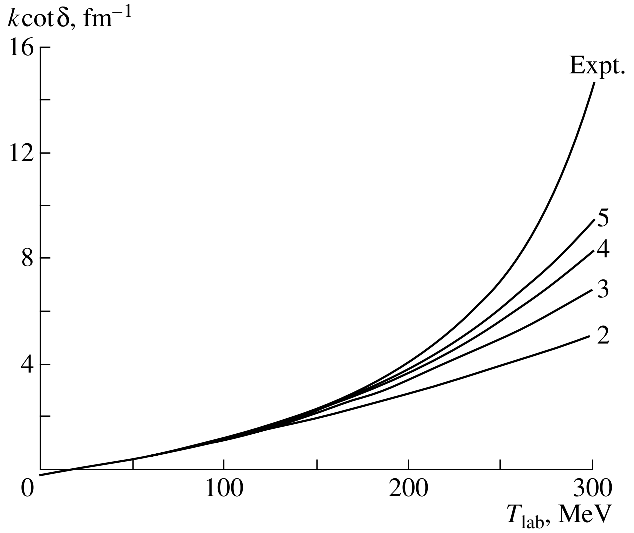

Fig. 2. Triplet effective-range function $k\cot\delta$ versus the laboratory energy for various approximations of the effective-range expansion (11). The figures on the curves indicate the order of approximation. The upper curve corresponds to experimental data borrowed from [39].

sensitivity to variations in this quantity is extremely high. In particular, a change in the scattering length a_t as small as a few tenths of a percent can lead to a severalfold change in the shape parameter v_2. This is in accord with the comment in the preceding section that the shape parameter v_2, as well as the higher order parameters v_n, is a rather subtle and sensitive characteristic of nucleon–nucleon interaction. Thus, so sharp a distinction between the shape parameters v_n for Arndt's and the Nijmegen phase shifts is due to a significant difference in the scattering length: the value of $a_t^{\rm Arndt} = 5.4030$ fm, which was obtained in the present study, differs from $a_t^{\rm Nijm} = 5.420$ fm more than by 0.3%. This difference in the values of the scattering length leads to a decrease in the shape parameter v_2 by a factor of 4 for the phase shifts of the Nijmegen group in relation to the phase shifts of Arndt's group—that is, from the value of $v_2^{\rm Arndt} = 0.163$ fm^3 to the value of $v_2^{\rm Nijm} = 0.040$ fm^3. The discrepancy between the corresponding higher order parameters v_n is still larger. At the same time, Table 2 shows that the values of the effective range r_t for Arndt's and Nijmegen phase shifts are close to each other. It should also be noted that our results on the shape parameter v_2 are close to the results of some earlier studies. In particular, the value of $v_2 = 0.137$ fm^3 corresponding to $P_t = -0.027$ for the soft-core Reid potential [58] agrees well with the value of $v_2 = 0.163$ fm^3, which was obtained in the present study.

We note that the Nijmegen value of the triplet scattering length $a_t^{\rm Nijm}$ is rather close to the presently recommended experimental value [59]

$$a_t^{\rm expt} = 5.424 \text{ fm}, \tag{65}$$

while the value calculated here on the basis of Arndt's phase shifts, $a_t^{\rm Arndt} = 5.4030$ fm, is close to some of the experimental values obtained previously for the triplet scattering length [32, 42, 43]. It should be emphasized that, for the experimental values of the triplet scattering length a_t, various authors [32–35, 38, 39, 42–46, 58–61] present values changing within a broad range—from 5.37 [38, 60] to 5.44 fm [45, 61]. We also note that the present-day experimental value of the triplet scattering length in (65) leads to exaggerated (in relation to experimental data) values of the root-mean-square radius r_d of the deuteron [52, 53, 56] and the asymptotic normalization constant A_S for it [56]. From all of the aforesaid, we can therefore draw the following important conclusion: in order to remove the existing discrepancies between the current experimental value of a_t in (65), on one hand, and the present-day values of the quantities r_d and A_S for the deuteron and the partial-wave-analysis data of Arndt's group, which lead to the value of $a_t^{\rm Arndt} = 5.4030$ fm, on the other hand, it is of paramount importance to refine the experimental value of the triplet scattering length a_t. The value of the triplet scattering length a_t is of particular importance since it is often used as one of the input values in fitting the parameters of realistic potentials of nucleon–nucleon interaction. We note that the value of $a_t^{\rm Arndt} = 5.4030$ fm, which corresponds to the partial-wave analysis performed by Arndt's group, is in perfect agreement with the experimental values of the quantities r_d and A_S for the deuteron [56].

In a wide energy range [approximately to the energy corresponding to the pole of the function $k\cot\delta(53)$], the experimental phase shift [39] is well described by the effective-range expansion (11) with the low-energy scattering parameters a_t, r_t, v_2, v_3, $\ldots$ set to the values determined here. This is a direct corollary of the fact that, for the phase shift borrowed from [39], all of the shape parameters v_n appear to be decreasing in absolute value. For example, a fifth-degree polynomial in k^2 describes the experimental phase shift in the energy range $T_{\rm lab} \leqslant 200$ MeV to within about $\sim 1°$ and in the energy range $T_{\rm lab} \leqslant 50$ MeV to within about $0.02°$. The description of the function $k\cot\delta$ by various-degree polynomials corresponding to various approximations of the effective-range expansion (11) is shown in Fig. 2. We see that a successive increase in the degree of a polynomial leads to an improved description of the function $k\cot\delta$ (and, accordingly, of the phase shift) and to the extension of the interval where this description is valid. Thus, the use of the effective-range expansion with a small number of terms provides a good description of the phase shift over a wide energy range (0–250 MeV) if the low-energy parameters are set to the values found here. This indicates that, in contrast to statements advocated in some articles (see, for example, [50]), the effective-range expansion is highly accurate and very useful in describing nucleon–nucleon scattering.

The potential of the effective-range expansion (11) is directly related to the radius of its convergence. The function $k\cot\delta$ considered in the complex plane of k^2 is an analytic function of k^2 within some region near the origin of coordinates; therefore, it can be expanded in a Taylor–Maclaurin series (11) in powers of k^2 in the vicinity of the point $k^2 = 0$. Thus, a particular importance of the function $k\cot\delta$ is associated with its analyticity near the point $k^2 = 0$. Noyes and Wong [62] showed that the one-pion-exchange model for nucleon–nucleon interaction leads to the appearance of a cut in the scattering amplitude on the negative axis of energy for $k^2 \leqslant -m_\pi^2 c^2/4\hbar^2$; therefore, the radius of convergence of the series in (11) is extremely small in the one-pion-exchange model, $T_0 = m_\pi^2/2m_N = 9.7$ MeV. This contradicts the fact that the experimental phase shift [39] is well described by the pole formula (29) with the parameters set to the values in (49)–(52), since, for the radius of convergence of the series in (11), formula (29) gives the value of $T_0 = 368.026$ MeV, which we chose on the basis of the "experimental" condition $\delta(T_0) = 0$ (the circle of convergence is determined by the condition $|k^2| < 1/|D|$). In connection with this contradiction, we recall the comments at the end of the preceding section that concern the limited applicability of the one-pion-exchange mechanism. As was indicated by Noyes himself [33], there is no a priori method for estimating the accuracy or the region of applicability of the phenomenological expansion (11), so that this question must be solved on the basis of experimental data.

Numerical values of the shape parameters v_n provide direct information about the radius of convergence of the series in (11). In the case under consideration, the increase in the parameters v_n in absolute value indicates, as is the case for the phase shift of the Nijmegen group, that the effective-range expansion (11) has a small radius of convergence, so that it is not very useful [50]. On the contrary, the decrease in the shape parameters v_n for the phase shift of Arndt's group suggests that the radius of convergence of the series in (11) is large and that this expansion is very useful in this case. This is corroborated by a high quality of the description of the phase shift in the case where the function $k\cot\delta$ is approximated by polynomials of relatively low degrees. Thus, the present-day data from the partial-wave analyses performed by the two main groups in [39] and [57] do not agree with each other both in what is concerned with the low-energy scattering parameters calculated on their basis and in what is concerned with the applicability of the effective-range expansion to them. At the same time, it is important to note that the numerical values obtained for the phase shifts by Arndt's and the Nijmegen group are rather close to each other. This indicates once again that the low-energy parameters are subtle and sensitive characteristics of nucleon–nucleon scattering.

5. DESCRIPTION OF THE PROPERTIES OF THE DEUTERON

Following the same line of reasoning as in the case of constructing the effective-range expansion (11), one can write an expansion of the function $k\cot\delta$ in a power series at the point $k^2 = -\alpha^2$—that is, at the energy equal to the deuteron binding energy $\varepsilon_d = \hbar^2\alpha^2/m_N$. This expansion has the form

$$k\cot\delta = -\alpha + \frac{1}{2}\rho_d(k^2+\alpha^2) + w_2(k^2 + \alpha^2)^2 + \ldots, \qquad (66)$$

where $\rho_d \equiv \rho(-\varepsilon_d, -\varepsilon_d)$ is the effective deuteron radius corresponding to S-wave interaction. The definition and the properties of the effective deuteron radius ρ_d and of the function $\rho(E_1, E_2)$ are discussed in detail elsewhere [38]. Using Eqs. (29) and (66), we can easily establish that the quantities α and ρ_d for the deuteron are related to the parameters of the pole representation of the effective-range function as

$$\alpha = \frac{1}{a_t} + \frac{1}{2}r_t\alpha^2 - \frac{v_2\alpha^4}{1 - D\alpha^2}, \qquad (67)$$

$$\rho_d = \rho_m - \frac{2v_2\alpha^2}{(1 - D\alpha^2)^2}, \qquad (68)$$

where $\rho_m \equiv \rho(0, -\varepsilon_d)$ is the so-called mixed effective radius given by

$$\rho_m = \frac{2}{\alpha}\left(1 - \frac{1}{\alpha a_t}\right). \qquad (69)$$

Using formulas (67) and (69), we can recast the expression for the mixed effective radius ρ_m into the form

$$\rho_m = r_t - \frac{2v_2\alpha^2}{1 - D\alpha^2}. \qquad (70)$$

From formulas (70) and (68), one can easily obtain expansions of the effective range r_t for scattering and

Table 3. Features of the deuteron according to calculations within various approximations of the effective-range expansion (ER, SP) and in the pole approximation P1

Version	ε_d, MeV	ρ_d, fm	C_d	A_S, fm$^{-1/2}$
ER	2.2387	1.7494	1.2979	0.8846
SP	2.2236	1.7145	1.2876	0.8761
P1	2.2237	1.7151	1.2878	0.8763
Experiment	2.224589	1.7251	1.2904	0.8781

the effective deuteron radius ρ_d in power series in α^2. We have

$$r_t = \rho_m - 2\sum_{n=1}^{\infty}(-1)^n v_{n+1}\alpha^{2n}, \qquad (71)$$

$$\rho_d = \rho_m + 2\sum_{n=1}^{\infty}(-1)^n n v_{n+1}\alpha^{2n}, \qquad (72)$$

where the parameters v_n are given by (62). The dimensionless asymptotic normalization factor C_d for the deuteron is expressed in terms of the effective deuteron radius ρ_d as

$$C_d^2 = (1 - \alpha\rho_d)^{-1}. \qquad (73)$$

The constant C_d and the asymptotic normalization factor A_S, which is widely used in the literature [47, 63], are related by the equation

$$A_S^2 = 2\alpha C_d^2. \qquad (74)$$

For various approximations of the effective-range function, we have calculated the following parameters characterizing the deuteron: the binding energy ε_d, the effective radius ρ_d, and the asymptotic normalization factors C_d and A_S. In Table 3, the results of these calculations are given along with their experimental counterparts from [64, 65]. We note that the deuteron binding energy was calculated by using a relativistic formula, which is more accurate than (21). It can be seen from Table 3 that the features of the deuteron that were calculated in the pole approximation (29) with the parameter values from (49)–(52) are in good agreement with their experimental values. The results obtained in the shape-parameter approximation (SP) differ insignificantly from their counterparts in the pole approximation, while the results of the calculations that take into account the cubic term in energy in the effective-range expansion are nearly coincident with those in the pole approximation. It can be seen from Table 3 that the convergence of the calculated features of the deuteron versus the number of terms that are taken into account in the effective-range expansion is very fast—the shape-parameter approximation yields a highly precise result, the inclusion of higher order terms in energy introducing virtually no changes in this result. This is a consequence of the fact that the shape parameters v_n are decreasing quantities in this case. It should be emphasized that, the features of the deuteron were calculated on the basis of the scattering-parameter values in (49)–(52), which correspond to the phase shifts of Arndt's group, and this means that we have very good agreement between the experimental data of Arndt's group on scattering [39] and the experimental data on the bound state (deuteron) from [64, 65].

The values found for the features of the deuteron in the effective-range approximation (ER) are somewhat exaggerated in relation to their experimental counterparts and the results obtained in the pole approximation. This is due primarily to an insufficiently accurate determination of the deuteron binding energy in the effective-range approximation with the low-energy parameters $a_t = 5.4030$ fm and $r_t = 1.7494$ fm. If one uses the experimental values for the deuteron binding energy and for the triplet scattering length ($\varepsilon_d = 2.224589$ MeV and $a_t = 5.4030$ fm, respectively), the effective-range approximation yields the following values for the effective radius of the deuteron ρ_d and for the asymptotic normalization factor A_S: $\rho_d = 1.7331$ fm and $A_S = 0.8795$ fm$^{-1/2}$, these results being in good agreement with the corresponding experimental values and with the results of the calculations in the pole approximation. This is in accord with the results obtained in [56], where it was established that the asymptotic normalization factor A_S depends only slightly on the model of nucleon–nucleon interaction; at the experimental value of the deuteron binding energy ε_d, 99.7% of it is determined by the triplet scattering length a_t.

6. PARAMETERS OF THE BARGMANN *S* MATRIX

The parameters α, β, λ, and μ of the Bargmann S matrix (20), which corresponds to the presence of two physical states in the system, are unambiguously related to the parameters of the pole approximation of the effective-range function (29) and, as can easily be seen, are the roots of the fourth-degree algebraic equation

$$v_2 x^4 - (1 - Dx^2)\left(\frac{1}{a_t} + \frac{1}{2}r_t x^2 - x\right) = 0. \qquad (75)$$

Solving Eq. (75) with the parameters set to the values in (49)–(52), we obtain the following values for the parameters of the Bargmann S matrix (in fm^{-1}):

$$\alpha = 0.2315, \quad \beta = 1.2293, \qquad (76)$$
$$\lambda = 2.5603 + i3.5248, \quad \mu = 2.5603 - i3.5248.$$

In the case being considered, the two-nucleon system has two bound states. In accordance with the phenomenology of nodes that employs potentials involving forbidden states [16–18], the lowest, deeply lying, state, characterized by the energy

$$\varepsilon_0 = 63.7555 \text{ MeV}, \tag{77}$$

is unobservable, while the excited state of binding energy

$$\varepsilon_d = 2.2237 \text{ MeV} \tag{78}$$

corresponds to the deuteron.

Thus, the use of the pole approximation in describing triplet neutron–proton scattering automatically leads to considering deep potentials involving forbidden states.

In the shape-parameter approximation (44) ($D = 0$), we have the following values for the parameters of the Bargmann S matrix (20) (in fm^{-1}):

$$\alpha = 0.2315, \quad \beta = -2.7787, \tag{79}$$
$$\lambda = 1.2736 + i0.3784, \quad \mu = 1.2736 - i0.3784.$$

In this case, the second state is a virtual state at the energy

$$\varepsilon_v = 353.4732 \text{ MeV}, \tag{80}$$

while the ground state, whose binding energy is

$$\varepsilon_d = 2.2236 \text{ MeV} \tag{81}$$

[in fact, it coincides with that in (78)], corresponds to the deuteron. As might have been expected, the parameters in (79) satisfy relation (43).

7. CONCLUSION

Our basic results and conclusions can be formulated as follows. Relying on the Bargmann representation of the S matrix, we have formulated the pole approximation for the effective-range function $k \cot \delta$. At specific values of the S-matrix parameters, the effective-range approximation and the shape-parameter approximation immediately follow from this approximation. The pole approximation of the function $k \cot \delta$ is optimal for describing nucleon–nucleon scattering and involves a few parameters. The parameters of this approximation have a clear physical meaning. They are related to the parameters of the Bargmann S matrix by simple equations. It has been shown that the pole approximation deduced from the Bargmann representation of the S matrix is a direct generalization of the effective-range approximation to the case where there are two physical states in the system. The presence of the pole term makes it possible to improve significantly, by using only two additional parameters, the description of the phase shift and to expand sizably the applicability range of this description. In the shape-parameter approximation corresponding to the Bargmann representation of the S matrix, one can obtain an important constraint on the shape parameter, $P < 0$—that is, the shape parameter is negative.

By using a least squares polynomial fit to the function $k\cot\delta$ at low energies, we have obtained, on the basis of the analysis of the latest experimental data on phase shifts that was performed by Arndt's group, the triplet low-energy parameters of neutron–proton scattering: $a_t = 5.4030$ fm, $r_t = 1.7494$ fm, and $v_2 = 0.163\ \text{fm}^3$. With these values of a_t, r_t, and v_2 and the pole parameter D, the pole approximation of the function $k \cot \delta$ provides an excellent description of the triplet phase shift for neutron–proton scattering over a wide energy range ($T_{\text{lab}} \lesssim 1000$ MeV), the description in the low-energy region also being improved considerably.

For the experimental phase shifts of Arndt's group, the values that we have obtained in the pole approximation for the triplet shape parameters v_n of the effective-range expansion are positive and decrease with increasing n. On the basis of the effective-range expansion with the values found for the low-energy scattering parameters $a_t, r_t, v_2, v_3, \ldots$, the phase shift is described well over a wide energy range extending approximately to the energy at which the phase shift changes sign, this being a direct consequence of a decrease in the shape parameters v_n with increasing n. This circumstance is indicative of a high precision of the effective-range expansion and its high potential for describing experimental data on nucleon–nucleon scattering, in contrast to the statements of some authors (see, for example, [50]).

The results obtained here for the shape parameters by using the data of the partial-wave analysis performed by Arndt's group differ drastically from the results of the calculations in [50] for the data of the partial-wave analysis performed by the Nijmegen group, this distinction being not only quantitative but also qualitative—that is, all of the shape parameters v_n calculated here by using the phase shifts of Arndt's group are positive and decrease, while the analogous parameters v_n calculated for the Nijmegen phase shifts increase in absolute value and include a negative parameter (v_4). In our opinion, so sharp a discrepancy between the shape parameters v_n for Arndt's and the Nijmegen phase shifts is due to quite a significant difference in the scattering length: the value $a_t^{\text{Arndt}} = 5.4030$ fm obtained here differs from $a_t^{\text{Nijm}} = 5.420$ fm by more than 0.3%. This difference in the scattering length leads to the decrease in the shape parameter v_2 by a factor of 4 for the Nijmegen phase shifts in relation to the phase shifts obtained by Arndt's group—that is, from the value $v_2^{\text{Arndt}} =$

$0.163\ \text{fm}^3$ to the value of $v_2^{\text{Nijm}} = 0.040\ \text{fm}^3$—the discrepancy between the corresponding values of the higher order parameters v_n being still greater. This confirms that the shape parameter v_2, as well as the higher order parameters v_n, is a rather subtle and sensitive characteristic of nucleon–nucleon interaction. The aforesaid leads to the important conclusion that an experimental refinement of the triplet scattering length a_t is of paramount importance since it is necessary to remove the existing discrepancies between the current experimental value of $a_t^{\text{expt}} = 5.424$ fm, on one hand, and the present-day values of r_d and A_S for the deuteron [56] and the present-day data of the partial-wave analysis performed by Arndt's group, which lead to the value of $a_t^{\text{Arndt}} = 5.4030$ fm, on the other hand. It should be emphasized that the value of the triplet scattering length a_t is of particular importance because a_t is often used as one of the input quantities in fitting the parameters of realistic potentials of nucleon–nucleon interaction.

For various approximations of the effective-range function, we have calculated the main features of the deuteron—the binding energy ε_d, the effective radius ρ_d, and the asymptotic normalization factors C_d and A_S. The results obtained for them in the pole approximation agree very well with their experimental counterparts. The results in the shape-parameter approximation differ insignificantly from those in the pole approximation. We have found that the convergence of the calculated features of the deuteron versus the number of terms that are taken into account in the effective-range expansion is very fast—the shape-parameter approximation gives a nearly precise result, which undergoes virtually no changes upon taking into account higher order terms in energy. Thus, we can state that, on the basis of the Bargmann representation of the S matrix, a good unified description has been obtained for the bound state of the two-nucleon system and the triplet phase shift for neutron–proton scattering up to energies of about 1000 MeV.

REFERENCES

1. A. G. Sitenko, *Scattering Theory* (Springer-Verlag, Berlin, 1991).
2. W. Heisenberg, Z. Phys. **120**, 513 (1943).
3. R. Jost, Helv. Phys. Acta **20**, 256 (1947).
4. R. G. Newton, *Scattering Theory of Waves and Particles*, 2nd ed. (Springer-Verlag, New York, 1982; Mir, Moscow, 1969).
5. V. A. Babenko and N. M. Petrov, Yad. Fiz. **63**, 1798 (2000) [Phys. At. Nucl. **63**, 1709 (2000)].
6. V. V. Malyarov and M. N. Popushoĭ, Yad. Fiz. **18**, 1140 (1973) [Sov. J. Nucl. Phys. **18**, 586 (1973)].
7. B. N. Zakhar'ev, V. N. Pivovarchik, E. B. Plekhanov, and A. A. Suz'ko, Fiz. Élem. Chastits At. Yadra **13**, 1284 (1982) [Sov. J. Part. Nucl. **13**, 535 (1982)].
8. B. N. Zakhar'ev, Yu. P. Nikishov, and E. B. Plekhanov, Yad. Fiz. **38**, 95 (1983) [Sov. J. Nucl. Phys. **38**, 54 (1983)].
9. V. Bargmann, Rev. Mod. Phys. **21**, 488 (1949).
10. W. T. H. van Oers and J. D. Seagrave, Phys. Lett. B **24B**, 562 (1967).
11. G. A. Baker, Jr. and P. Graves-Morris, *Padé Approximants* (Addison-Wesley, London, 1981).
12. F. Lambert, O. Corbella, and Z. D. Thome, Nucl. Phys. B **90**, 267 (1975).
13. K. Hartt, Phys. Rev. C **22**, 1377 (1980).
14. K. Hartt, Phys. Rev. C **23**, 2399 (1981).
15. K. Hartt, Bull. Am. Phys. Soc. **23**, 630 (1978).
16. V. G. Neudatchin, I. T. Obukhovsky, V. I. Kukulin, and N. F. Golovanova, Phys. Rev. C **11**, 128 (1975).
17. V. G. Neudatchin, I. T. Obukhovsky, and Yu. F. Smirnov, Fiz. Élem. Chastits At. Yadra **15**, 1165 (1984) [Sov. J. Part. Nucl. **15**, 519 (1984)].
18. V. I. Kukulin, V. M. Krasnopol'skiĭ, V. N. Pomerantsev, and P. B. Sazonov, Yad. Fiz. **43**, 559 (1986) [Sov. J. Nucl. Phys. **43**, 355 (1986)].
19. M. Cini, S. Fubini, and A. Stanghellini, Phys. Rev. **114**, 1633 (1959).
20. R. S. Christian and J. L. Gammel, Phys. Rev. **91**, 100 (1953).
21. L. M. Delves, Phys. Rev. **118**, 1318 (1960).
22. A. S. Reiner, Phys. Lett. B **28B**, 387 (1969).
23. J. S. Whiting and M. G. Fuda, Phys. Rev. C **14**, 18 (1976).
24. V. E. Kuz'michev, Ukr. Fiz. Zh. (Russ. Ed.) **23**, 188 (1978).
25. B. A. Girard and M. G. Fuda, Phys. Rev. C **19**, 579 (1979).
26. S. A. Adhikari and J. R. A. Torreao, Phys. Lett. B **132B**, 257 (1983).
27. I. V. Simenog, A. I. Sitnichenko, and D. V. Shapoval, Yad. Fiz. **45**, 60 (1987) [Sov. J. Nucl. Phys. **45**, 37 (1987)].
28. C. R. Chen, G. L. Payne, J. L. Friar, and B. F. Gibson, Phys. Rev. C **39**, 1261 (1989).
29. Yu. V. Orlov and L. I. Nikitina, Yad. Fiz. **61**, 833 (1998) [Phys. At. Nucl. **61**, 750 (1998)].
30. Yu. V. Orlov, Yu. P. Orevkov, and L. I. Nikitina, Yad. Fiz. **65**, 396 (2002) [Phys. At. Nucl. **65**, 371 (2002)].
31. D. Y. Wong and H. P. Noyes, Phys. Rev. **126**, 1866 (1962).
32. H. P. Noyes, Phys. Rev. **130**, 2025 (1963).
33. H. P. Noyes, Annu. Rev. Nucl. Sci. **22**, 465 (1972).
34. L. Mathelitsch and B. J. VerWest, Phys. Rev. C **29**, 739 (1984).
35. J. R. Bergervoet, P. C. van Campen, W. A. van der Sanden, and J. J. de Swart, Phys. Rev. C **38**, 15 (1988).
36. V. M. Galitsky, B. M. Karnakov, and V. I. Kogan, *Problems in Quantum Mechanics* (Nauka, Moscow, 1992) [in Russian].
37. J. M. Blatt and J. D. Jackson, Phys. Rev. **76**, 18 (1949).

38. L. Hulthén and M. Sugawara, in *Handbuch der Physik*, Ed. by S. Flügge (Springer-Verlag, New York, Berlin, 1957), p. 1.
39. R. A. Arndt, W. J. Briscoe, R. L. Workman, and I. I. Strakovsky, *Partial-Wave Analysis Facility SAID* [http://gwdac.phys.gwu.edu].
40. T. D. Cohen and J. M. Hansen, Phys. Rev. C **59**, 13 (1999).
41. T. D. Cohen and J. M. Hansen, Phys. Rev. C **59**, 3047 (1999).
42. R. Wilson, *The Nucleon–Nucleon Interaction* (Interscience, New York, 1963).
43. T. L. Houk and R. Wilson, Rev. Mod. Phys. **39**, 546 (1967).
44. T. L. Houk, Phys. Rev. C **3**, 1886 (1971).
45. E. L. Lomon and R. Wilson, Phys. Rev. C **9**, 1329 (1974).
46. W. Dilg, Phys. Rev. C **11**, 103 (1975).
47. M. W. Kermode, A. McKerrell, J. P. McTavish, and L. J. Allen, Z. Phys. A **303**, 167 (1981).
48. C. W. Wong, Nucl. Phys. A **536**, 269 (1992).
49. W. van Dijk, M. W. Kermode, and D.-C. Zheng, Phys. Rev. C **47**, 1898 (1993).
50. J. J. de Swart, C. P. F. Terheggen, and V. G. J. Stoks, *Invited Talk at the 3rd International Symposium "Dubna Deuteron 95," Dubna, Russia, July 4–7, 1995*; nucl-th/9509032.
51. M. W. Kermode, S. A. Moszkowski, M. M. Mustafa, and W. van Dijk, Phys. Rev. C **43**, 416 (1991).
52. D. W. L. Sprung, in *Proceedings of IX European Conference on Few-Body Problems in Physics, Tbilisi, Georgia, USSR, Aug. 1984* (World Sci., Singapore, Philadelphia, 1984), p. 234.
53. S. Klarsfeld, J. Martorell, J. A. Oteo, *et al.*, Nucl. Phys. A **456**, 373 (1986).
54. D. W. L. Sprung, H. Wu, and J. Martorell, Phys. Rev. C **42**, 863 (1990).
55. R. K. Bhaduri, W. Leidemann, G. Orlandini, and E. L. Tomusiak, Phys. Rev. C **42**, 1867 (1990).
56. V. A. Babenko and N. M. Petrov, Yad. Fiz. **66**, 1359 (2003) [Phys. At. Nucl. **66**, 1319 (2003)].
57. http://nn-online.sci.kun.nl
58. R. V. Reid, Jr., Ann. Phys. (N.Y.) **50**, 411 (1968).
59. O. Dumbrajs, R. Koch, H. Pilkuhn, *et al.*, Nucl. Phys. B **216**, 277 (1983).
60. G. L. Squires and A. T. Stewart, Proc. R. Soc. London, Ser. A **230**, 19 (1955).
61. G. E. Brown and A. D. Jackson, *The Nucleon–Nucleon Interaction* (North-Holland, Amsterdam, 1976).
62. H. P. Noyes and D. Y. Wong, Phys. Rev. Lett. **3**, 191 (1959).
63. T. E. O. Ericson, Nucl. Phys. A **416**, 281 (1984).
64. G. L. Greene, E. G. Kessler, Jr., R. D. Deslattes, and H. Boerner, Phys. Rev. Lett. **56**, 819 (1986).
65. I. Borbély, W. Grüebler, V. König, *et al.*, Phys. Lett. B **160B**, 17 (1985).

Translated by A. Isaakyan

Physics of Atomic Nuclei, Vol. 68, No. 2, 2005, pp. 234–236. Translated from Yadernaya Fizika, Vol. 68, No. 2, 2005, pp. 259–261.

ELEMENTARY PARTICLES AND FIELDS
Experiment

Inverse-Beta-Decay Reaction in the Antineutrino Flux from the Fragments of ^{232}Th and ^{233}U Fission

G. V. Domogatsky[1], V. I. Kopeikin[2], L. A. Mikaelyan[2], and V. V. Sinev[2]*

Received May 20, 2004

Abstract—The energy spectra of antineutrinos produced in the beta decay of fragments originating from ^{233}U and ^{232}Th fission induced by neutrons are calculated. The relevant cross sections and the spectra of positrons produced in inverse beta decay are found. This study was motivated by the hypothesis (discussed over the past decade) that a self-sustained chain reaction proceeds at the center of the Earth ("georeactor"). According to the author of this hypothesis, the georeactor provides energy necessary for maintaining the Earth's magnetic field. It is ^{235}U and, probably, ^{232}Th and ^{233}U that serve as a nuclear fuel in this reactor. Data obtained in the present study can be guidelines in future experiments aimed at testing the hypothesis of the georeactor and at estimating the composition of its nuclear fuel within the development of geophysical and astrophysical investigations based on the observation of antineutrino fluxes in nature.

INTRODUCTION

Owing to advances demonstrated by the KamLAND Collaboration in refining methods for detecting low-energy electron antineutrinos [1], it becomes feasible to study $\bar{\nu}_e$ fluxes in nature, which carry information about the properties of their sources, which is otherwise inaccessible.

The underground Baksan neutrino observatory of the Institute for Nuclear Research (Russian Academy of Sciences) is one of the laboratories most convenient for constructing a massive scintillation spectrometer for detecting antineutrinos and for performing investigations in this field (see the discussion in [2]). Their program could involve the following:

(i) determination of uranium and thorium concentrations in the Earth by detecting $\bar{\nu}_e$ from the beta decay of their daughter products (geoneutrinos) (this problem has been discussed since the early 1960s [3] and more intensively in recent years [4]);

(ii) investigation of the frequency of gravitational collapses in the Universe by detecting an isotropic electron-antineutrino flux [5].

Along with these studies, one can use the same spectrometer at the Baksan neutrino observatory to test the hypothesis [6] of the possible self-sustained chain reaction (georeactor) proceeding at the center of the Earth. In this hypothetical reactor, ^{235}U and, probably, ^{232}Th and ^{233}U serve as a nuclear fuel. In this article, we present the results obtained by calculating the spectra of antineutrinos produced in the beta decay of fragments originating from ^{233}U and ^{232}Th fission and find the cross sections for the inverse-beta-decay reaction and the spectra of positrons from this reaction. These data can be useful in planning future experiments aimed at discovering the georeactor and at estimating its power and the composition of its nuclear fuel by means of neutrino spectroscopy.

Below, we briefly describe the procedure for calculating the spectra of antineutrinos originating from the fragments of ^{232}Th and ^{233}U fission, present the relevant $\bar{\nu}_e$ and positron spectra in the detected reaction

$$\bar{\nu}_e + p \to e^+ + n, \qquad (1)$$

and compare them with known spectra for ^{235}U.

ANTINEUTRINO AND POSITRON SPECTRA

1. For each of the fissile nuclei considered here, the antineutrino spectra $\rho^i_{\text{calc}}(E)$ were calculated by summing about 550 beta-decay spectra of individual fission fragments with allowance for their fission yields. The fragment yields and decay diagrams were taken from, respectively, the compilation presented in [7] and the library of data accumulated at the Kurchatov Institute over the past two decades.

2. Previously, the neutrino group at the Kurchatov Institute and many other authors repeatedly calculated the spectra of antineutrinos produced in ^{235}U,

---

[1] Institute for Nuclear Research, Russian Academy of Sciences, pr. Shestidesyatiletiya Oktyabrya 7a, Moscow, 117312 Russia.

[2] Russian Research Centre Kurchatov Institute, pl. Kurchatova 1, Moscow, 123182 Russia.

*e-mail: `sinev@polyn.kiae.su`

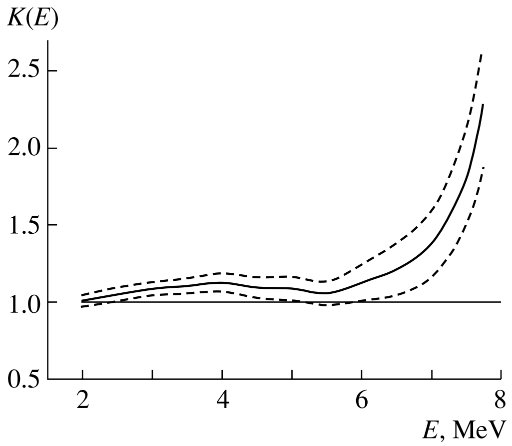

Fig. 1. Average ratio $K(E)$ of the calculated antineutrino spectra and the spectra obtained at the Laue–Langevin Institute (solid line). The dashed lines represent uncertainties found from the scatter of the $K_i(E)$ values [see Eq. (2) in the main body of the text].

^{239}Pu, ^{241}Pu, and ^{238}U fission (for a brief list of relevant references, see, for example, [8]). As a result, it was found that

(a) the antineutrino spectra of different fissile nuclei differ significantly from one another;

(b) the calculated spectra involve large uncertainties caused by imperfect knowledge of decay diagrams for many short-lived fission fragments;

(c) the ratios of the spectra of antineutrinos from different fissile isotopes are calculated with a smaller uncertainty than the spectra themselves.

The last circumstance enables us to correct the antineutrino spectra calculated for ^{232}Th and ^{233}U fission.

The correction procedure is as follows. We use the "true" ρ_{ILL} spectra found for ^{235}U, ^{239}Pu, and ^{241}Pu isotopes at the Laue–Langevin Institute by reconstructing the measured spectra of beta-decay electrons for the set of fission fragments of each of these isotopes [9]. For each isotope, we find the energy-dependent ratio $K_i(E)$ of the calculated spectrum ρ^i_{calc} and the spectrum ρ^i_{ILL},

$$K_i(E) = \rho^i_{\text{calc}}/\rho^i_{\text{ILL}}. \quad (2)$$

Averaged over the ^{235}U, ^{239}Pu, and ^{241}Pu isotopes, the ratio $K(E)$ (Fig. 1) is used to obtain the corrected spectra $\rho(E)^i_{\text{corr}}$; that is,

$$\rho(E)^i_{\text{corr}} = \rho(E)^i_{\text{calc}}/K(E), \quad (3)$$

where $i = 2$ and 3 refer to ^{232}Th and ^{233}U, respectively.

3. The antineutrino spectra derived by means of this procedure for ^{232}Th and ^{233}U fission are presented in Table 1, along with the spectrum obtained for ^{235}U at the Laue–Langevin Institute. The uncertainties in these spectra involve those of the correction procedure—that is, the uncertainty in $K(E)$ (Fig. 1)—and the uncertainties in the spectra ρ_{ILL}. The resulting uncertainty estimated here amounts to 7–10% (at a 68% C.L.) in the antineutrino-energy range 1.8–6 MeV and increases to about 15% in the range 6–8 MeV.

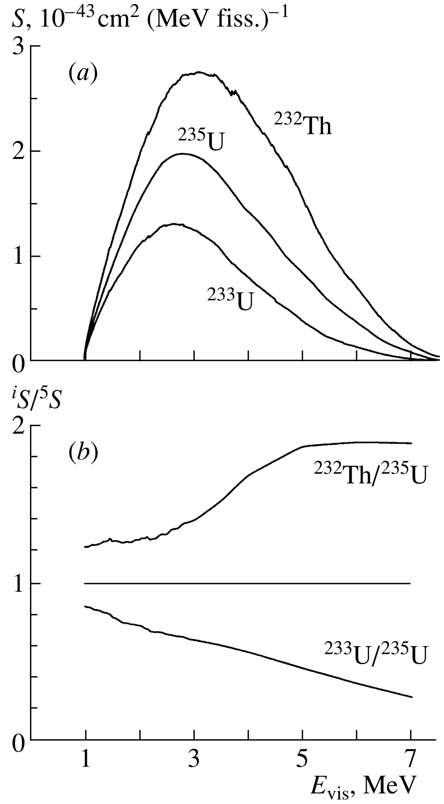

Fig. 2. (a) Spectra $S(E_{\text{vis}})$ of positrons from the inverse-beta-decay reactions for ^{232}Th, ^{233}U, and ^{235}U and (b) ratios of the positron spectra for ^{232}Th and ^{233}U to the respective spectrum for ^{235}U.

The calculated spectra $S(E_{\text{vis}})$ of positrons from inverse-beta-decay reactions in the case of ^{232}Th, ^{233}U, and ^{235}U are shown in Fig. 2 versus the energy deposited upon positron absorption in the scintillator. This energy is $E_{\text{vis}} \approx E - (1.80 - 1.02)$ MeV $\approx E - 0.8$ MeV, where E is the absorbed-antineutrino energy and 1.80 MeV is the threshold for the reaction (1). The total cross sections σ_f obtained for this reaction upon averaging over these spectra are given in Table 2.

It follows from these results that the antineutrino and positron spectra for ^{232}Th are much harder than the spectra for ^{235}U, which in turn are harder than the spectra for ^{233}U. This fact might have been expected from qualitative considerations about the relationship

Table 1. Spectra of antineutrinos from ^{232}Th, ^{233}U, and ^{235}U fission [in (MeV fission)$^{-1}$ units]

E, MeV	^{235}U	^{233}U	^{232}Th
1.75	–	1.27	1.82
2	1.30	1.08	1.61
2.5	0.900	0.675	1.13
3	0.637	0.443	0.812
3.5	0.437	0.290	0.587
4	0.283	0.177	0.405
4.5	0.172	0.992(−1)	0.268
5	0.105	0.564(−1)	0.176
5.5	0.617(−1)	0.314(−1)	0.114
6	0.370(−1)	0.159(−1)	0.672(−1)
6.5	0.203(−1)	0.778(−2)	0.372(−1)
7	0.105(−1)	0.374(−2)	0.201(−1)
7.5	0.429(−2)	0.137(−2)	0.861(−2)
8	0.136(−2)	0.403(−3)	0.272(−2)

Note: For ^{235}U, the spectra obtained at the Laue–Langevin Institute were borrowed from [9].

Table 2. Inverse-beta-decay total cross sections σ_f (in units of 10^{-43} cm^2/fission) averaged over the fission-antineutrino spectra for ^{232}Th, ^{233}U, and ^{235}U

^{235}U	^{233}U	^{232}Th
$6.39 \pm 2.7\%^*$	$3.87 \pm 10\%$	$9.70 \pm 10\%$

* The value calculated on the basis of the spectrum obtained at the Laue–Langevin Institute and presented in [9].

between the numbers of neutrons and protons in the fissile nuclei under study.

CONCLUSION

The spectra of antineutrinos emitted from fragments originating from ^{233}U and ^{232}Th fission induced by neutrons have been calculated for the first time, and the cross sections for the relevant inverse-beta-decay reactions and the spectra of positrons produced in these reactions have been found. These data can serve as a guideline for future experiments aimed at discovering the georeactor and at estimating its power and composition of its nuclear fuel within the general program of development of neutrino geophysics and astrophysics.

ACKNOWLEDGMENTS

This work was supported by a presidential grant (no. 1246.2003.2) for support of leading scientific schools and by the Russian Foundation for Basic Research (project no. 03-02-16055).

REFERENCES

1. KamLAND Collab., Phys. Rev. Lett. **90**, 021802 (2003); hep-ex/0212021; hep-ex/0310047.
2. G. Domogatsky, V. Kopeikin, L. Mikaelyan, and V. Sinev, hep-ph/0409069; Yad. Fiz. **68**, 70 (2005) [Phys. At. Nucl. **68**, 69 (2005)].
3. G. Marx and N. Menyhard, *Mitteilungen der Sternwarte* (Budapest, 1960), No. 48; G. Marx, Czech. J. Phys. B **19**, 1471 (1969); G. Eder, Nucl. Phys. **78**, 657 (1966); M. A. Markov, *The Neutrino* (Nauka, Moscow, 1964).
4. R. Raghavan, S. Schoenert, S. Emonto, *et al.*, Phys. Rev. Lett. **80**, 635 (1998); F. Mantovani, L. Carmignani, G. Fiorentini, and M. Lissia, Phys. Rev. D **69**, 013001 (2004).
5. G. V. Domogatsky, Astron. Zh. **61**, 51 (1984) [Sov. Astron. **28**, 30 (1984)].
6. J. M. Herndon, Proc. Natl. Acad. Sci. USA **100**, 3047 (2003); D. F. Hollenbach and J. M. Herndon, Proc. Natl. Acad. Sci. USA **98**, 11085 (2001); J. M. Herndon, J. Geomagn. Geoelectr. **45**, 423 (1993).
7. T. R. England and B. F. Rider, LA-UR-94-3106. ENDF-349 (LANL, Oct., 1994) (http://ie.lbl.gov/fission.html).
8. V. Kopeikin, L. Mikaelyan, and V. Sinev, hep-ph/0308186; Yad. Fiz. **67**, 1987 (2004) [Phys. At. Nucl. **67**, 1963 (2004)].
9. K. Schreckenbach *et al.*, Phys. Lett. B **160B**, 325 (1985); A. A. Hahn *et al.*, Phys. Lett. B **218**, 365 (1989).

Translated by V. Bukhanov

Physics of Atomic Nuclei, Vol. 68, No. 2, 2005, pp. 237–258. Translated from Yadernaya Fizika, Vol. 68, No. 2, 2005, pp. 262–282.

ELEMENTARY PARTICLES AND FIELDS
Experiment

Quasars as Sources of Ultrahigh-Energy Cosmic Rays

A. V. Glushkov*

Institute of Cosmophysical Research and Aeronomy, Yakutsk Research Center, Siberian Division,
Russian Academy of Sciences, pr. Lenina 31, Yakutsk, 677891 Russia

Received February 19, 2004

Abstract—The results are presented that were obtained by analyzing arrival directions for cosmic rays that the Yakutsk array for studying extensive air showers recorded between 1974 and 2002 in the energy region $E_0 \geq 5 \times 10^{17}$ eV for zenith angles in the region $\theta \leq 60°$. It is shown that quasars for which the redshift lies in the region $z \leq 2.5$ can be sources of these cosmic rays. Ordered structures are observed in the disposition of quasars and in the cosmic-ray arrival directions. These structures can be associated in one way or another with the large-scale structure of the Universe. © *2005 Pleiades Publishing, Inc.*

1. INTRODUCTION

Searches for sources of primary cosmic rays are among the most difficult problems in studying the structure of the Universe. Primary cosmic rays of ultrahigh energy ($E_0 \geq 10^{17}$ eV) are investigated by exploring extensive air showers. In recent years, there appeared reports [1–4] suggesting that quasars characterized by redshifts of the spectral lines of their radiation in the region $z \leq 0.3$ may be sources of ultrahigh-energy cosmic rays.

Quasars are the most puzzling objects in the Universe and the most powerful sources of radiation there. For the overwhelming majority of quasars, the redshifts exceed 0.1, but, for some of them, the redshifts are as large as about 4 to 5 [5]! This suggests that they occur at cosmological distances exceeding many hundred megaparsecs. It is assumed that quasars characterized by the largest redshifts are the most remote from us and belong to the group of the very first galaxies formed upon the beginning of the Big Bang in the expanding Universe [6].

A periodicity in the argument $\log(1+z)$ was discovered in the distribution of quasars [7]; later on, this periodicity was repeatedly confirmed and refined (see, for example, [8, 9]). In the spectra of quasars, Ryabinkov *et al.* [9] observed cosmological variations of the spacetime distribution of 847 absorptive systems. These variations manifest themselves as a successive appearance of maxima and minima of functions in the arguments $\ln(1+z)$ and $(1+z)^{-1/2}$. It is believed that this structure is due to the alternation of distinguished and depressive eras in the course of a cosmological evolution that are separated by a characteristic time interval in the range 520 ± 160 million years, its specific duration being dependent on the choice of cosmological model.

Presented below are experimental results obtained from an analysis of correlations between the arrival directions of cosmic rays having energies in the region $E_0 \geq 5 \times 10^{17}$ eV and the disposition of quasars characterized by redshifts not exceeding $z = 2.5$. These results reveal some new features of ultrahigh-energy primary cosmic rays and provide the possibility for studying, along these lines, the large-scale structure of the Universe.

2. METHOD OF ANALYSIS

In the present study, we consider extensive air showers characterized by zenith angles in range $\theta \leq 60°$ and recorded by the Yakutsk array over the period between 1974 and 2002. Our analysis covers showers whose arrival directions were found on the basis of data from four or more stations and whose axes fell within the central circle of the array with a radius of 1700 m. The primary-particle energy E_0 was determined from the relations

$$E_0 = (4.8 \pm 1.6) \times 10^{17}(\rho_{s,600}(0°))^{1.0\pm0.02}\ [\text{eV}], \quad (1)$$

$$\rho_{s,600}(0°) = \rho_{s,600}(\theta)\exp((\sec\theta - 1) \times 1020/\lambda_\rho)\ [\text{m}^{-2}], \quad (2)$$

$$\lambda_\rho = (450 \pm 44) + (32 \pm 15) \times \log(\rho_{s,600}(0°))\ [\text{g/cm}^2], \quad (3)$$

where $\rho_{s,600}(\theta)$ is the charged-particle density measured by ground-based scintillation detectors at a distance of $R = 600$ m from the shower axis.

---

[*] e-mail: `a.v.glushkov@ikfia.ysn.ru`

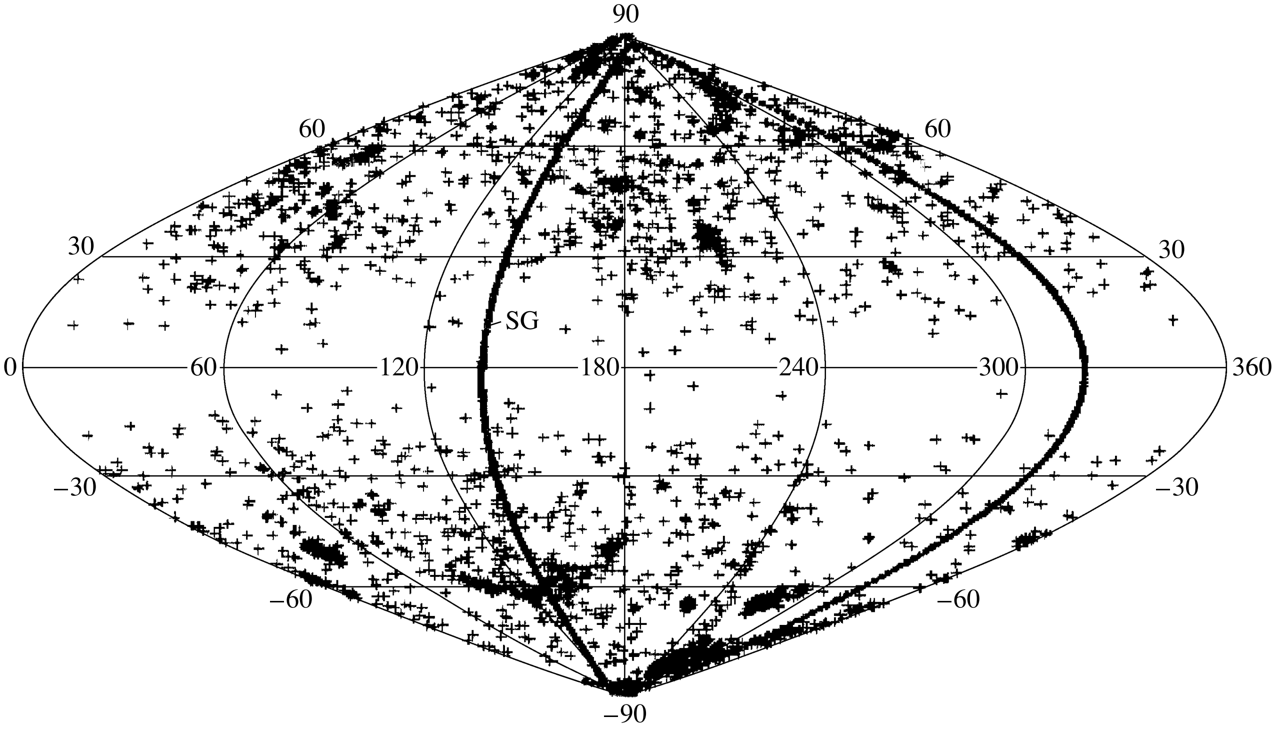

Fig. 1. Distribution of 3594 quasars from the catalog of Hewitt and Burbidge [5] in terms of galactic coordinates. The SG curve represents the Supergalaxy disk.

In [3, 4], it was shown that quasars characterized by a redshift satisfying the condition $z \leq 0.3$ may be sources of primary cosmic rays whose energies lie in the region $E_0 \geq 10^{17}$ eV. The present study is devoted to pursuing further the analysis of correlations between the disposition of more distant quasars and arrival directions of primary cosmic rays. The analysis relies on the catalog of Hewitt and Burbidge [5], which contains 3594 objects. A more comprehensive catalog presented by M.-P. Veron-Cetty and P. Veron-Cetty [10], which includes 13 214 quasars, was not quite convenient for solving this problem because of an enhanced nonuniformity of the distribution of quasars over the celestial sphere. An increase in the number of objects in it was achieved owing primarily to a deeper survey of individual areas having moderate dimensions.

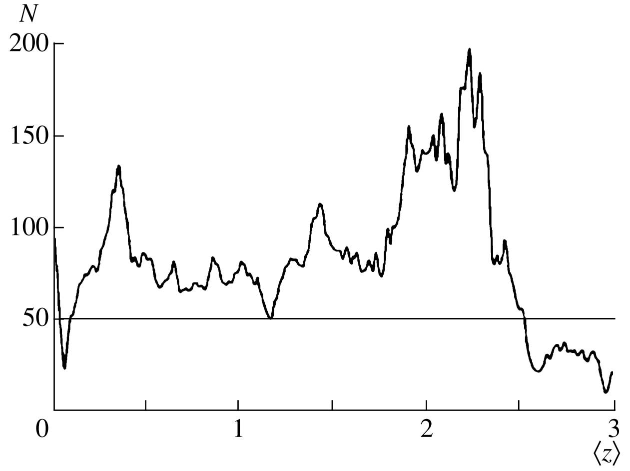

Fig. 2. Distribution of the number of quasars, N, from the catalog of Hewitt and Burbidge [5] versus the mean redshift in a bin (with a step $\Delta z = 0.07$) upon successive shifts along the z axis by 0.01. The horizontal line represents the level of 50 events.

Figure 1 shows the distribution of quasars from the catalog of Hewitt and Burbidge [5] in terms of galactic coordinates. The SG curve represents the Supergalaxy disk (local supercluster of galaxes). In the vicinity of the Galaxy disk, there are virtually no objects because of a strong light absorption. In some individual places, one can see local regions of a relatively high density of quasars, which frequently form groups characterized by different redshift values. Two such regions that are situated near the north and south pole of the Galaxy and which are associated in all probability with the large-scale structure of the distribution of matter in the Universe are especially distinct.

Figure 2 shows the distribution of the number of quasars with respect to the redshift. This distribution reflects the change in the number of objects in the

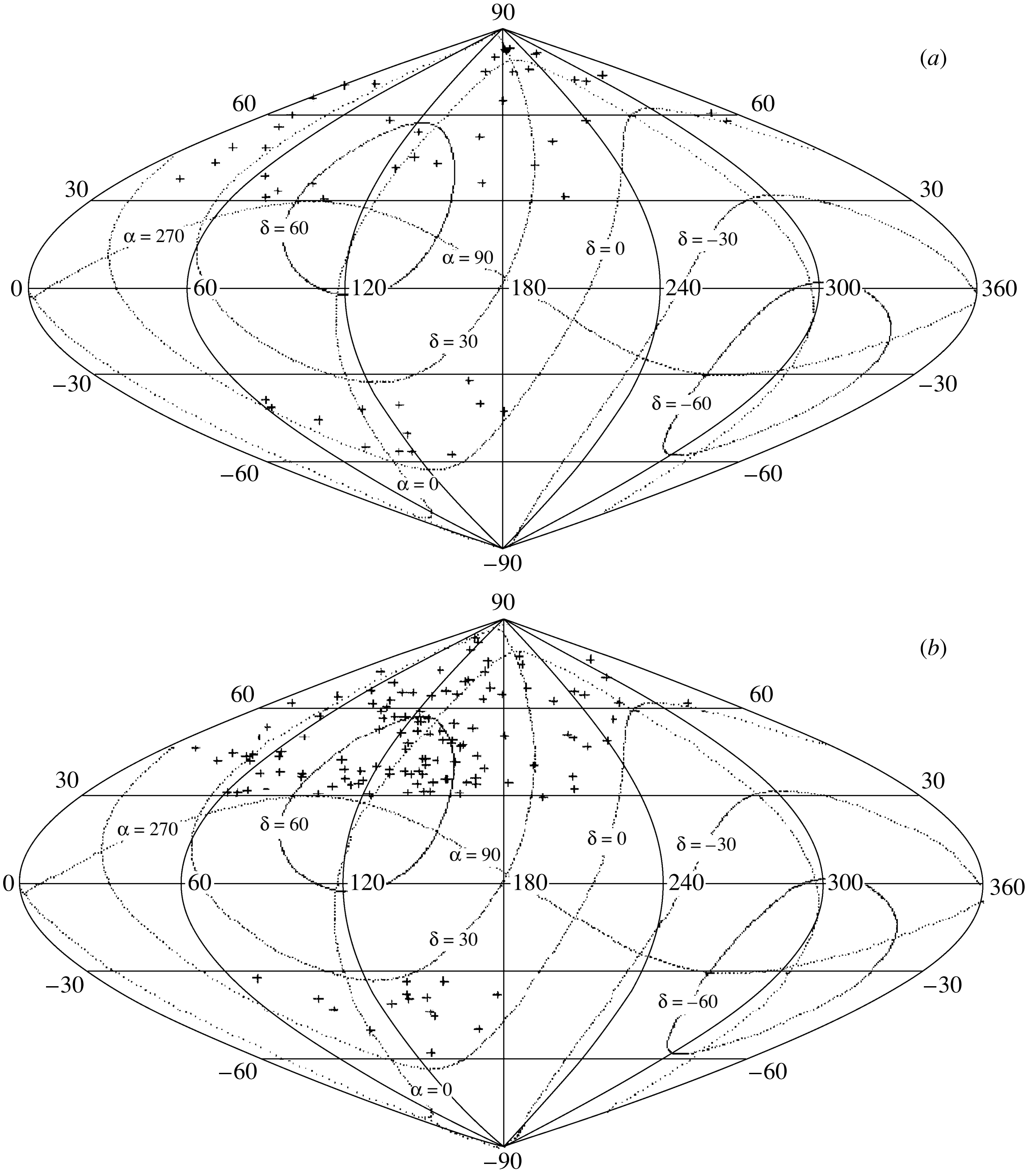

Fig. 3. Maps of the disposition (in terms of galactic coordinates) of (*a*) 50 quasars characterized by redshift values in the range $z \leq 0.08$ [5] and (*b*) 138 showers of energy in the region $E_0 \geq 8 \times 10^{18}$ eV that were recorded by the Yakutsk array at zenith angles in the range $\theta \leq 60°$. The equatorial coordinates are also shown in this figure.

range (bin) $\Delta z = 0.07$ upon successively shifting this bin along the z axis by 0.01. The horizontal line corresponds to the level of 50 events. We have set it as an upper limit for samples of quasars at any position of the bin on the z axis in order that the maximum possible number of the objects being considered would have the same value throughout the ensuing analysis. In other words, only 50 quasars chosen at random were used in all cases. One can see that this condition always holds for $z \leq 2.5$.

3. CORRELATIONS BETWEEN THE ARRIVAL DIRECTIONS OF PRIMARY COSMIC RAYS AND THE DISPOSITION OF QUASARS

Let us first consider the correlation between the disposition of quasars for which redshift values lie

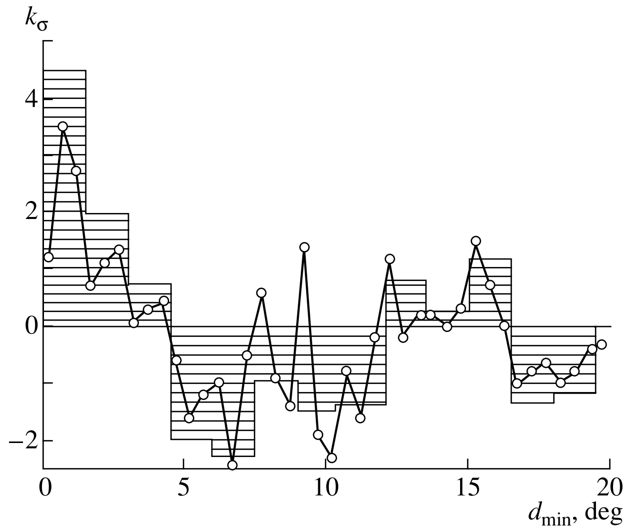

Fig. 4. Function k_σ (4) characterizing full correlations of the minimum angular distances $d_{\min} \leq 1.5°$ between the arrival directions of 138 showers of energy in the region $E_0 \geq 8 \times 10^{18}$ eV (Fig. 3*b*) with samples of 50 quasars (Fig. 3*a*) in independent bins with a step of $\Delta z = 0.05$ upon successively shifting the beginning of the bin from $z = 0$ to 2.5 by 0.05. The histogram and circles correspond to the partition of $d_{\min}$ with a step of 1.5° and 0.5°, respectively.

in the range $z \leq 2.5$ and the arrival directions of 138 showers whose energies do not fall below 8×10^{18} eV. Figure 3*a* shows, in terms of galactic coordinates, the disposition of 50 quasars characterized by redshift values not exceeding 0.08. For the presentation to be clearer, the equatorial coordinates are also indicated in this figure. The objects were taken with inclinations of $\delta \geq 0°$, in which case they are visible from the Yakutsk array. Since, in the catalog of Hewitt and Burbidge [5], there are virtually no data concerning the equatorial region of the Galaxy ($|b_G| \leq 30°$), we eliminated, from the ensuing analysis, all quasars (and showers—see Fig. 3*b*) from this region of the sky. This is a typical distribution of input data, where only samples of 50 quasars were changed in accordance with the position of a bin on the z axis.

Figure 4 shows the function

$$k_\sigma = (N_{\text{obs}} - N_{\text{ran}})/\sqrt{N_{\text{ran}}}, \qquad (4)$$

which characterizes the correlation of the minimum angular distances $d_{\min}$ between the arrival directions of 138 showers (see Fig. 3*b*) with the disposition of 50 quasars in independent bins with a step of $\Delta z = 0.05$. The measured distributions (N_{obs}) and those that are expected for random events (N_{ran}) were obtained as sums of 50 input distributions ($= 2.5/0.05$ for successive shifts of a bin by 0.05). The expected distributions for random quantities were obtained by replacing right ascensions for 138 actual showers by those generated by the Monte Carlo method from 0° to 360°. In doing this, all events characterized by a galactic latitude in the range $|b_G| \leq 30°$ were eliminated from the analysis, and they were generated anew. The results for the partition of $d_{\min}$ with a step of 1.5° (0.5°) are shown by a histogram (circles).

It can be seen that, within the angular range $d_{\min} \leq 1.5°$, there is a statistically significant (4.5σ, where σ is a standard deviation) excess of the measured number of events over their expected number. Over a broader angular interval of $d_{\min} \leq 3.0°$, the respective excess is $(1312 - 1168)/\sqrt{1168} \approx 4.2\sigma$. The probability of a random outcome on this order of magnitude is about 10^{-5}, which means that quasars can indeed be sources of primary cosmic rays having the energies indicated above.

However, Fig. 4 gives no indication of z values at which this result was obtained. To disentangle this situation, we considered individual values of k_σ versus the positions of the bins (with a step of $\Delta z = 0.07$) subjected to successive shifts by 0.01. They are represented by closed circles in Fig. 5*a*. The dashed curve shows the behavior k_σ on average upon smoothing the original distribution over 30 neighboring points.

In Fig. 5*a*, the following details of importance are worthy of note. First, one can clearly see here a peak for $z \leq 0.3$, which was previously reported in [3, 4]. Second, there is a series of other peaks, which, for $1.0 \leq z \leq 2.5$, yield a total positive effect of correlations between quasars and the arrival directions of primary cosmic rays for angular distances in the range $d_{\min} \leq 1.5°$. Although the significance of these peaks is 1.5 to 2.5 standard deviations, their total effect is about 4.5σ (see Fig. 4). This means that primary cosmic rays of ultrahigh energy may originate from not only closely lying but also more remote quasars.

The complicated shape of the distribution in Fig. 5*a* raises new questions—for example, the question of whether the positions of these peaks are random; if no, there arises the question of their origin. In seeking an answer to these questions, we considered two more samples of showers that have substantially different energies, $E_0 = 10^{18.4}$–$10^{18.6}$ and $10^{17.7}$–$10^{17.8}$ eV.[1] For the input conditions under which the results are obtained to be identical, we took, in each of these samples, only 138 events chosen at random and treated them in just the same way as in the preceding case. The results are shown in Figs. 5*b* and 5*c*, where use is made of the same notation as in Fig. 5*a*. It can be seen that, for $E_0 = 10^{18.4-18.6}$ eV, there is a positive effect of the correlations in question

---

[1] In the following, we use the notation $E_0 = 10^{18.4-18.6}$ and $10^{17.7-17.8}$ eV.

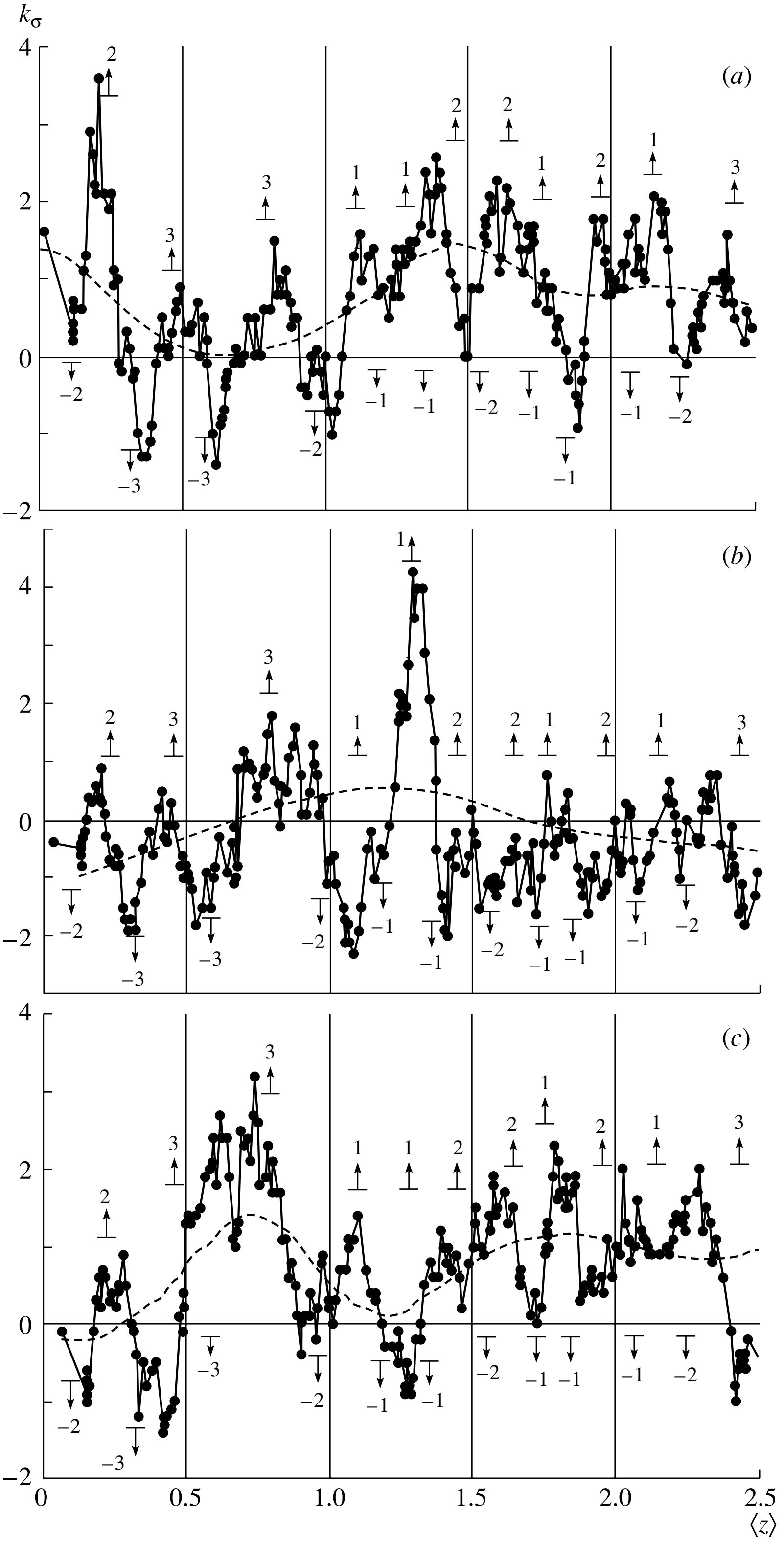

Fig. 5. Distributions of the function k_σ (4) characterizing angular correlations (for $d_{\min} \leq 1.5°$) between the arrival directions of 138 to 163 showers of energy satisfying the conditions $E_0 \geq (a)\ 8 \times 10^{18}$, $(b)\ 10^{18.4-18.6}$, and $(c)\ 10^{17.7-17.8}$ eV and the disposition of 50 quasars (in bins with a step of $\Delta z = 0.07$) with respect to the mean redshift associated with quasars. The dashed curves represent the behavior of k_σ on average. The arrows directed upward and downward point to, respectively, peaks and dips in the spacetime distribution of 847 absorptive systems in the spectra of quasars [9].

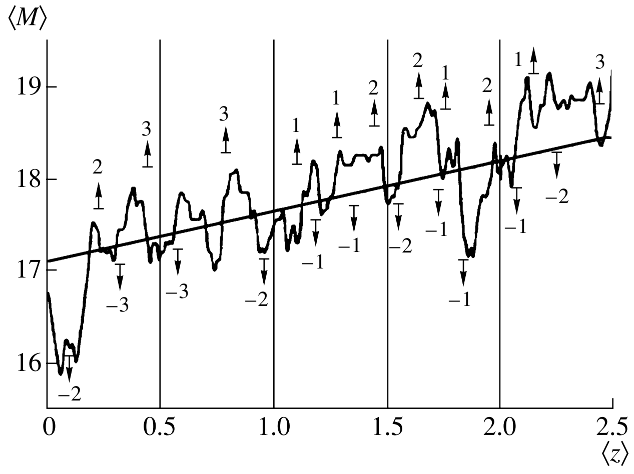

Fig. 6. Changes in the mean absolute stellar quantities of quasars (from the catalog of Hewitt and Burbidge [5]) versus their mean redshifts (in bins with a step of $\Delta z = 0.07$). The straight line represents relation (5). The meaning of the arrows is identical to that in Fig. 5.

for the interval $0.7 \leq z \leq 1.4$ (dashed curve), but that this effect is of the highest significance (about 4σ) in the interval $1.2 \leq z \leq 1.4$. Showers of energy in the range $E_0 = 10^{17.7-17.8}$ eV also reveal a trend toward the arrival from the loci of quasars. This suggests that quasars may be sources of primary cosmic rays even in the region of their lower energies. A weaker effect of the correlations in Figs. 5*b* and 5*c* is likely to be due to a smaller fraction of extragalactic particles in the respective samples of showers. The authors of [1–4, 11–13] believe that, for $E_0 \geq 8 \times 10^{18}$ eV, the sources of primary cosmic rays are predominantly extragalactic, but that, at lower energies, the fraction of galactic cosmic rays is significant. A comparison of the distributions in Fig. 5 gives sufficient grounds to assume that the effective contribution of quasars featuring various redshift values is different in different regions of primary-cosmic-ray energy.

However, almost perfect agreement between the positions of the peaks and dips in Figs. 5*a*–5*c* is the most surprising circumstance. In turn, they are at approximately the same positions as the analogous peaks (arrows upward) and dips (arrows downward) observed in the spacetime distribution of 847 absorptive systems in the spectra of quasars [9]. [The figures and horizontal dashes near the arrows indicate, respectively, their statistical significance (in units of standard deviation σ) and the uncertainty in their localization.] It is the opinion of the present author that this circumstance is indicative of a nonrandom character of the appearance of the peaks and dips in Fig. 5. Ryabinkov *et al.* [9] explain their results by a periodic alternation of eras of a high quasar luminosity and phases within which the activity of quasars is relatively low. They referred to this hypothesis as that of a cosmological variation of the activity of quasars.

We note that absorption lines arise if cold clouds of a gas consisting of atoms and molecules in low-lying states occur on the the path of light from a quasar. These atoms and molecules "eat out" (absorb), from the continuous spectrum of a quasar, those waves whose energies correspond to transitions in excited states [6]. Families of absorption lines are likely to arise as light from a quasar traverses galaxies that lie on the ray of sight from an observer to this quasar. Since the redshift in absorptive systems frequently reaches z values characteristic of quasars themselves, there are galaxies at distances where they can no longer be observed by radiation.

In all probability, changes in the correlation function k_σ reflect the actual trend of primary cosmic rays toward grouping in the vicinity of quasars at the maximum of their cosmological activity. On the contrary, a relatively low frequency of the appearance of primary cosmic rays in the vicinity of quasars (for $d_{\min} \leq 1.5°$) is observed within in the region of the dips. Within this hypothesis, it appears that cosmic rays having energies indicated above were generated with different intensities in different cosmological eras of the activity of quasars. A dominant fraction of these rays is associated with periods within which the luminosity of quasars was high. Within the phases of their reduced activity, the rate of primary-cosmic-ray production was likely to be substantially lower.

The data in Fig. 6, which shows the measured mean absolute stellar quantities of quasars in bins of width $\Delta z = 0.07$, support the hypothesis of a cosmological variation of the luminosity of quasars. The straight line corresponds to the dependence

$$\langle M \rangle = 17.14 + 0.55 \langle z \rangle, \tag{5}$$

which reflects the increase in the luminosity of quasars with increasing redshift. The arrows indicate the peaks and dips that are shown in Fig. 5. Here, one can clearly see periodic variations in the absolute brightness of quasars, these variations correlating with our data.

In [1–4, 11–14], it was shown that primary cosmic rays of ultrahigh energy consist of two components. Of these, one is characterized by an isotropic distribution and is likely to be associated with the diffusion propagation of charged particles through the Galaxy, its fraction being dominant for $E_0 \leq (2\text{–}5) \times 10^{18}$ eV. The other component has an extragalactic origin. It forms a number of clusters within solid angles of 3° and consists, in all probability, of stable neutral particles—otherwise, these particles would lose, because of the motion in the magnetic fields of the galaxy, the memory of the directions in which they are emitted by the sources and could not disclose the aforementioned structure of the distribution of matter in the Universe.

Let us revisit showers of energy in the range $E_0 = 10^{17.7-17.8}$ eV. The isotropic and the cluster component contribute about, respectively, 75 and 25% to their flux [13, 14]. We consider the correlations of each of these components with quasars. We found clusters in the following way. We partitioned all showers into seven samples, each featuring about 1000 events. The only difference between these samples was that the axes of showers belonging to different samples were within different annular areas of the central circle of the array. Each of the seven samples was analyzed for the presence of local groups of showers on the celestial sphere. To do this, all neighbors within the angular distance of $d \leq 3°$ were found around the arrival direction of any shower. If there were three or more showers within this circle, their coordinates were averaged and were used in the following as new points (below they are referred to as nodes). The nodes were additionally analyzed for the presence of not less than two intersections within each of the seven samples (the condition of intersection was that their centers were within the angular distance of $d \leq 3°$). If there were such nodes, then the arrival direction of all showers belonging to them were averaged anew, and the resulting larger node (cluster) was used for a further analysis.

For angular distances of $d_{\min} \leq 1.5°$, the closed circles in Fig. 7*a* show the factor (4) characterizing correlations between 50 quasars in various bins with a step of $\Delta z = 0.07$ and the positions of actual and generated clusters. The generated clusters were found in just the same way as actual ones. In Fig. 7*b*, the open circles represent the version for the isotropic component. It corresponds to samples of actual showers distributed at random in the sky that do not enter into clusters. The rest of the notation is analogous to that in Fig. 5.

One can see that, within different redshift intervals, clusters correlate with quasars at a level of six to eight standard deviations, the peaks and dips in Fig. 7*a* being in agreement, as before, with the hypothesis of a cosmological variation of the activity of quasars. As to showers not belonging to clusters (Fig. 7*b*), they do not produce such a pattern—here, the angular-correlation factor k_σ exhibits virtually no outliers beyond approximately two standard deviations and takes values that are close to random ones. In all probability, some kind of correlation between the positions of the peaks and dips in Figs. 7*a* and 7*b* is due to the presence of a small number of showers generated by quasars in the samples featuring no clusters.

4. ORDERED STRUCTURE IN THE DISTRIBUTION OF QUASARS

The majority of modern cosmological models are based on the assumption that all points of space are equivalent; therefore, the Universe is on average uniform and isotropic. This hypothesis is confirmed by the observations of isotropic cosmic microwave background radiation [6]. However, the distribution of matter is extremely nonuniform in the close vicinity of the Galaxy; moreover, there is a distinct hierarchy on a larger scale (from a few hundred kpc to a few hundred Mpc). Galaxies enter into the composition of clusters and superclusters, which in turn form a cellular structure of the Universe, with the characteristic size of nonhomogeneities being 100 to 130 Mpc (see, for example, [15, 16]). The cellular structure of the Universe was reliably established on the basis of the statistical analysis of the distribution of galaxies for moderate redshift values of $z \leq 0.5$. Cosmic rays of ultrahigh energy also confirm the existence of such a structure [1–4].

The above results suggest that an ordered structure of matter might exist over much larger scales of the Universe. We will now present some experimental facts in support of this point of view. In Fig. 8, the closed circles represent the angular-correlation factor (4) for the minimal angular distances $d_{\min}$ between 50 quasars in independent bins with a step of $\Delta z = 0.07$ and the arrival directions of 138 showers having energies in the range $\mathrm{E}_0 = 10^{17.7-17.8}$ eV and belonging to the clusters in Fig. 7*a*. The measured distributions and those that are expected for random quantities were derived as the sum of 35 original distributions (this number is obtained as the ratio 2.5/0.07 in the case of successively shifting the bin by 0.07). In constructing the distributions in question, all events characterized by galactic latitudes in the range $|b_{\mathrm{G}}| \leq 30°$ and inclinations satisfying the condition $\delta \geq 30°$ were excluded each time from this analysis.

In Fig. 8, a series of alternating peaks and dips at a level of about two to four standard deviations is noteworthy. In my opinion, there is some kind of interrelation in their arrangement. This can be seen from the example of a simulation whose results are shown by open circles in Fig. 8. We have considered angular distances between two nodes of a square lattice of edge length about 2.23° on a spherical surface that were chosen at random. A version where the lattice constant is about 4.48° is also quite realistic. In all probability, this means that quasars may belong to some large-scale ordered structure of the matter distribution in the Universe.

From the results of the simulation, it follows, among other things, that quasars may form a structure that roughly resembles a cubed-sphere grid.

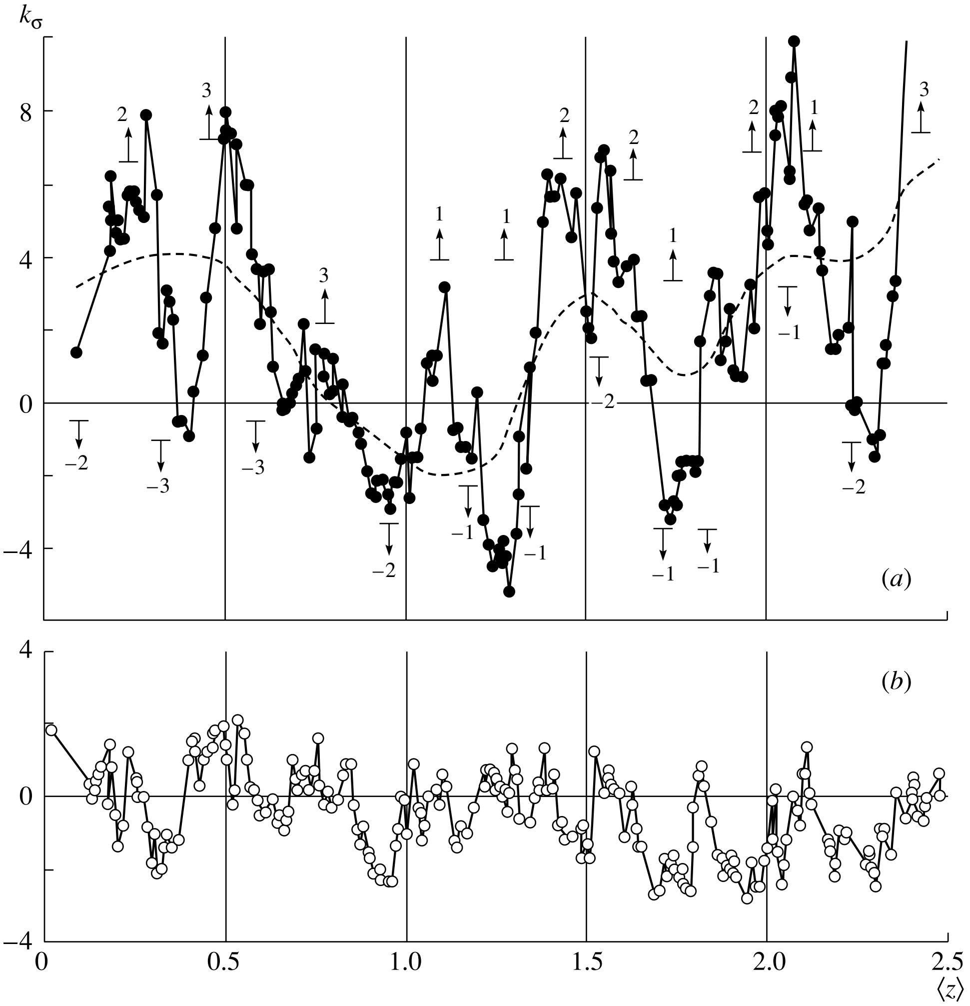

Fig. 7. Distributions of the factors k_σ (4) characterizing angular correlations (with $d_{\min} \le 1.5°$) between the positions of 50 quasars (in bins with a step of $\Delta z = 0.07$) characterized by various redshift values and the arrival directions of showers of energy in the range $E_0 = 10^{17.7-17.8}$ eV that (*a*) form clusters or (*b*) do not belong to clusters. The rest of the notation is similar to that in Fig. 5.

This three-dimensional lattice consists of a series of concentric spheres, their radii being

$$r_i = r_0 q^{i-1}, \tag{6}$$

where $q = \text{const}$ and i is the ordinal number of a sphere. Since $(r_{i+1} - r_i)/r_i = q - 1 = \text{const}$, the shape a volume element of the lattice is approximately cubic, irrespective of r_i. All of its nodes are projected along the radii onto one point; that is, they form a planar square network considered above (see Fig. 8).

From the structure of the type in (6), it follows that, for any redshift values, the number of quasars must be constant in a spherical layer of any fixed width. The actual distribution of objects in Fig. 2 confirms this roughly for $z \le 1.8$. The catalog of M.-P. Veron-Cetty and P. Veron-Cetty [10] yields the same pattern. In all probability, the peak in Fig. 2 for $1.8 \le z \le 2.4$ is associated with an individual structural feature.

Let us now consider the small-scale anisotropy of quasars. In Fig. 9, the closed circles represent the distribution of minimal angular distances $d_{\min}$ between the objects from the catalog of Hewitt and Burbidge [5] in bins with a step of $\Delta z = 0.1$. The measured distribution and that which was expected for random quantities were derived as sums of 25 independent distributions (this number is obtained as the ratio 2.5/0.1 in the case of successively shifting the bin by 0.1). The expected distribution was found with allowance for a decrease in the number of events in the region of the Galaxy disk (see Fig. 1). This distribution was derived by "smearing," with the aid of the Monte Carlo method, the actual coordinates of each quasar over the adjacent part of the sky ($\Delta\alpha = \pm 20°$ and $\Delta\delta = \pm 5°$). Figure 9 displays

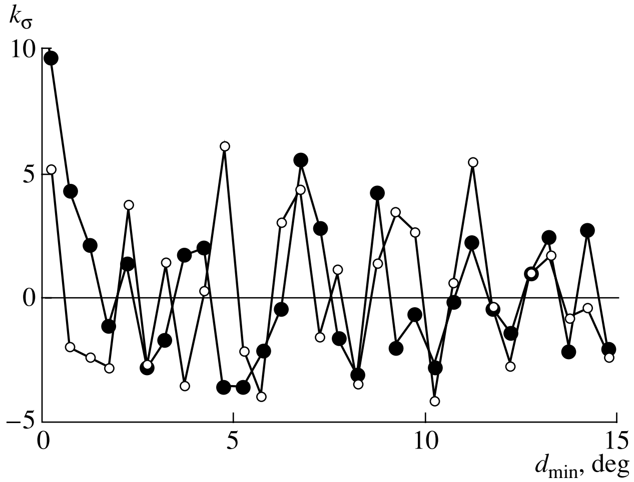

Fig. 8. Angular correlation factor k_σ (4) for the minimum angular distance $d_{\min}$ between 50 quasars in independent bins with a step of $\Delta z = 0.07$ and the arrival directions of 138 showers having energies in the range $E_0 = 10^{17.7-17.8}$ eV and belonging to the clusters in Fig. 7*a* (closed circles). The open circles in the figure correspond to the distances $d_{\min}$ between the nodes of a square lattice of edge length 2.23° on the surface of a sphere.

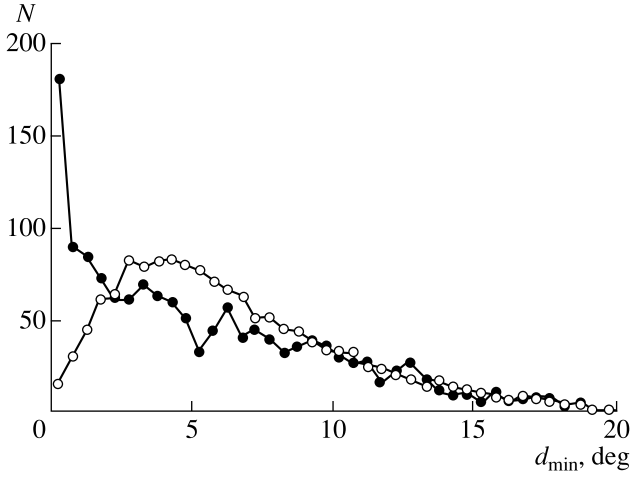

Fig. 9. Distribution of minimal angular distances $d_{\min}$ between 1436 objects from the catalog of Hewitt and Burbidge [5] within the latitude band $30° \le b_G \le 75°$ and in bins with a step of $\Delta z = 0.1$ (closed circles). The open circles represent the expected distribution for random events.

data for 1436 objects within the latitude band $30° \le b_G \le 75°$ (in the northern hemisphere of the Galaxy). One can see that quasars form a number of dense groups (nodes), which are characterized by angular distances of $d_{\min} \le 1.5°$. Within this angular interval, the fraction of their excess over random events with respect to the entire sample is $(354-90)/1436 \approx 0.18$. In the angular interval $d_{\min} \approx 3°-6°$, there is, on the contrary, a deficit of actual events, which is indicative of the presence of voids between the nodes of quasars.

In Fig. 10, the closed circles represent the distribution of 580 quasars (without objects for which $|b_G| \ge 75°$) in nodes with $d_{\min} \le 1.5°$ versus the bin position (with a step of $\Delta z = 0.07$). The open circles there show the analogous distribution for the sample of 1974 quasars that does not contain the aforementioned events entering into nodes. The arrows indicate the data from [9], which were considered above (see Figs. 5–7).

The distributions in Fig. 10 exhibit a certain resemblance. Both distributions develop peaks and dips that frequently correlate with each other; somewhere, they have a negative correlation. By and large, all of them correlate with the analogous peaks and dips associated with absorptive systems in the spectra of quasars [9]. However, there are also distinctions between the two samples in Fig. 10. For example, the mean numbers of the majority of quasars ($1974/2554 \approx 0.77$) not belonging to nodes undergo virtually no changes over the entire redshift range considered here (dashed line); as to quasars entering into nodes, they are likely to have a different spatial structure.

5. ANISOTROPY OF QUASARS

5.1. Harmonic Analysis

Let us additionally consider some special features of the spatial distribution of quasars. We will analyze their global distribution over the celestial sphere in terms of galactic coordinates by means of the harmonic-analysis method [17], which is extensively used to study the arrival directions of primary cosmic rays (see, for example, [13, 14]). The method consists in choosing the best values of the amplitude A_1 and the phase l_1 of the function

$$f(l_G) = f_0(1 + A_1 \cos(l_G - l_1)) \qquad (7)$$

by minimizing the quantity

$$\chi^2 = \sum_{i=1}^{n} (f_i - N_i)^2 / f_i, \qquad (8)$$

where N_i is the number of quasars in the ith sector $(\Delta l_G)_i$,

$$f_0 = \left(\sum_{i=1}^{n} N_i \right) / n = N/n,$$

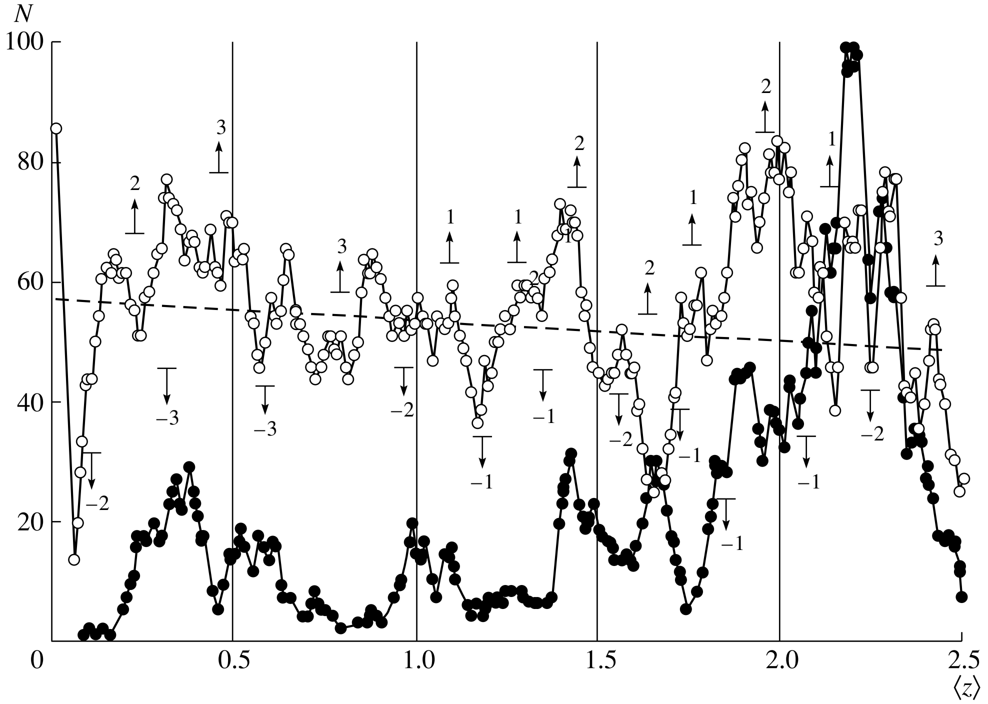

Fig. 10. Distribution of 580 quasars (without objects for which $|b_{\rm G}| \geq 75°$) in nodes with $d_{\min} \leq 1.5°$ versus the mean redshifts in bins with a step of $\Delta z = 0.07$ (closed circles). The dashed line represents the behavior of this quantity on average, and the arrows indicate the data from [9] (see Fig. 5). The open circles correspond to the analogous distribution for the set of 1974 quasars that does not contain events entering into nodes.

and

$$A_1 = (f_{\max} - f_{\min})/(2f_0) \qquad (9)$$
$$= (f_{\max} - f_{\min})/(f_{\max} + f_{\min}).$$

In Fig. 11, the phases l_1 of the first harmonic for the samples of quasars from Fig. 10 are shown versus the mean redshifts in bins with a step of $\Delta z = 0.1$. We partitioned the sky into 36 spherical sectors. Here, we also excluded, from the analysis, all objects such that $|b_{\rm G}| \geq 75°$ for them, which produce anomalously high concentrations in the directions to the Galaxy poles (Fig. 1). One can see that quasars not belonging to nodes (open circles) have a stable phase of the first harmonic for all $z \leq 2.5$, the maximum of events being within the galactic sector $\Delta l_{\rm G} \approx 100°$–$150°$. We note that this sector intersects the Supergalaxy plane at $l_{\rm G} \approx 137°$ (see Fig. 1). Previously, it was indicated in [1, 2] that enhanced fluxes of ultrahigh-energy primary cosmic rays come from the Supergalaxy plane and from the regions symmetrically adjacent to it at angles of $\pm b_{\rm SG} \approx 6.5°$. In these regions, one observes relatively high concentrations of galaxy and quasar clusters. In [3, 4], it was assumed that this may be associated with a cubic structure of the distribution of matter in the Universe, in which case the Supergalaxy plane is likely to be aligned with one of the three main planes of the hypothetical lattice.

Quasars entering into nodes with angular distances of $d_{\min} \leq 1.5°$ also show a significant anisotropy (closed circles in Fig. 11). Here, the phases of the first harmonic are frequently different from the phases l_1 of the preceding sample; they have relatively stable values of about 45° and 225°, which are indicated by dashed lines in Fig. 11.

Figure 12*a* shows the distributions of 580 and 1974 $z \leq 2.5$ quasars (which are presented in Fig. 10) in galactic spherical sectors with a step of $\Delta l_{\rm G} = 10°$ in longitude. The horizontal lines there correspond to mean values. The dashed curves represent approximations of the data in terms of the function in (7). Here, anisotropy can be seen even more distinctly in either case. For example, quasars in nodes (closed circles) yield a first-harmonic phase of $l_1 = 39° \pm 17°$ and an amplitude of $A_1 = 0.35 \pm 0.07$, while quasars not belonging to nodes (open circles) yield $l_1 = 129° \pm 11°$ and $A_1 = 0.27 \pm 0.04$ for these two quantities. The two amplitudes proved to be in agreement within the errors, while the phases are shifted by about 90°.

Within a harmonic analysis, the amplitude A_1 measures a global anisotropy. If its excess over the amplitude ΔA_1 of an equivalent isotropic flux producing the same number N of events is above three standard deviations, then it is assumed that the phase

l_1 reflects actual anisotropy. The amplitude ΔA_1 can be found by means of a Monte Carlo simulation or analytically as [17]

$$\Delta A_1 \cong 1.25\sqrt{2/N}. \tag{10}$$

From relation (10), it follows that, even in the absence of an actual anisotropy, nonzero amplitudes will always be observed in an experiment, their values becoming greater as the number N of events decreases. This means that a random distribution can mimic the anisotropy expected on the basis of some physical considerations.

The distribution of the parameters of the observed vector of anisotropy that arises because of a bounded character of a sample of N events was considered by Linsley [17], who introduced the coefficient $\eta = N(A_1/2)^2$ and a formula for estimating the probability of obtaining the observed (or a greater) value of A_1 in the case of an isotropic flux,

$$p(\geq A_1) = \exp(-\eta). \tag{11}$$

For the distributions of quasars in Fig. 12*a* in nodes and beyond them, we have $\eta = 17.9$ and 25.2, respectively, the probability (11) of such random outcomes being below 10^{-7}. It is noteworthy that, in both distributions, there are individual peaks deviating from the approximations in terms of the functions in (7) by more than three standard deviations. The majority of them correlate with one another and form an intriguing sequence (see below).

Let us now consider values of the mean redshifts for quasars in individual spherical sectors in Fig. 12*a*. They are shown in Fig. 12*b* (the notation is similar). The horizontal lines correspond to values of $\langle z \rangle = 1.64 \pm 0.04$ and 1.24 ± 0.02, which were obtained by means of averaging over all data. The dashed curves represent the best approximations in terms of the function in (7). Here, we also observe systematic changes in the mean redshifts (dashed curves) versus the galactic longitude, the minimum being at $l_G \approx 150°$. These anomalies confirm the presence of anisotropy in the global distribution of quasars, but they yield less significant values. The amplitudes of the first harmonic for quasars in nodes and beyond them are $A_1 = 0.18 \pm 0.06$ and 0.06 ± 0.03, respectively.

The anisotropy in Figs. 11 and 12 is not caused by low statistics of the objects considered above. A similar pattern is also observed for the data from the catalog presented by M.-P. Veron-Cetty and P. Veron-Cetty [10], which is more comprehensive. The absorption of light from quasars in the Galaxy disk does not have a significant effect on the results either, since the influence of this factor is approximately identical in all of the sectors.

5.2. Central Asymmetry of Quasars

We will now try to obtain deeper insight into the results obtained above. In the ensuing discussion, we will distinguish between the concept of the Universe and the concept of the Metagalaxy. We will assume that the Metagalaxy is smaller than the Universe and is only one of its objects (in all probability, it is the largest object presently accessible to observation). As any other object, it then has a finite dimension and a finite mass. Within a different approach, the Universe and the Metagalaxy are the same, in which case there is nothing else in the world. However, it is well known that matter is structured from the micro- to the macrocosm. From general considerations, it is clear that very grave causes are required for the structural staircase of matter to be completed in the region of either small or large masses—for example, the self-closure of space around an enormously large mass. But if there is one closed world, we can also imagine yet another one, identical to it, since it is unlikely that nature produces only one specimen of anything. In view of this, we will assume that there are no reasons to restrict our world, so that the Metagalaxy is only part of the large Universe, which is infinite, in all probability. Within this approach, we now associate all that was said above about the Universe with the Metagalaxy.

The idea of the Metagalaxy itself is not new and is sometimes developed by researchers (see, for example, [18–21]). In [20, 21], it was proposed to consider the Universe as that which consists of a number of "miniuniverses"; possibly, one of such miniuniverses" is precisely our Metagalaxy. In any case, this idea makes it possible, in my opinion, to develop a schematic pattern that enables one to interpret, in one way or another, the results obtained above, especially those that concern the anisotropy of the space distribution of quasars.

Let us consider once again the distributions in Fig. 12*a* and plot them in terms of polar coordinates (see Fig. 13); this system of coordinates is arranged here in the Galaxy plane. We also introduce a system of Cartesian coordinates xyz in such a way that the north pole of the Galaxy forms the third axis z, which passes approximately through the center of the Supergalaxy. The y axis points to the north pole of the Supergalaxy, while the x axis coincides with the line of intersection of the Galaxy and Supergalaxy planes. The numbers in Fig. 13 indicate the galactic longitudes in the real three-dimensional space.

The open and closed circles represent the numbers N_i of quasars in the ith sector (with a step of $\Delta l_G = 10°$ in galactic altitude) that are presented in Fig. 12*a*. The solid-line circle corresponds to the mean value of $f_0 = 55$ for the sample of quasars beyond the nodes.

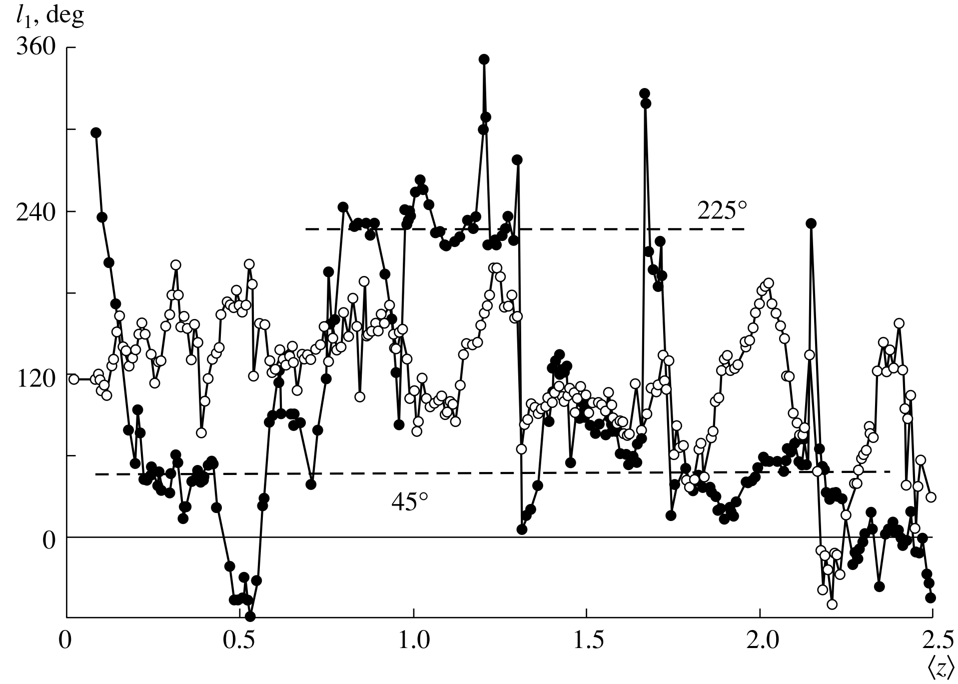

Fig. 11. Phases l_1 of the first harmonic for two samples of quasars (from Fig. 10) versus the mean redshifts in bins with a step of $\Delta z = 0.1$. The notation is identical to that in Fig. 10.

One can see there a distinct anisotropy, with the center being displaced in the direction of the x axis. As to the dashed-line circle, it is the solid-line circle whose center is shifted in direction $l_G = 129°$ by $\Delta_{XY} = A_1 f_0 = 0.27 \cdot 55 \approx 14.8$. The dashed-line circle corresponds to the dashed curve in Fig. 12*a*. The dash-dotted curve represents the version closest to the observed distribution of quasars—this is an ellipse characterized by a contraction coefficient of $k \approx 0.75$. Its center (O') coincides with the center of the dashed-line circle, and its major axis y' forms an angle of about 26° with the y axis.

This distribution of quasars can be interpreted as an indication of the possible spherical (or ellipsoidal) structure of the Metagalaxy, a structure that is similar to elliptic galaxies or spherically symmetric superclusters of galaxies. If this is so, then our Galaxy is likely to be not far off the Metagalaxy center. It does not undergo the effect of giant gravitational forces that arise in the external regions of the Metagalaxy, since the force of gravity vanishes at the center of a spherically symmetric system. One cannot rule out the possibility that there is some interplay between the growth of the luminosity of quasars and the growth of the gravitational force as the distance from the Metagalaxy center increases.

The shaded region in Fig. 13 reflects the distribution of quasars in the nodes (see Fig. 10). Here, one can see narrow peaks, and the analogous peaks in the opposite direction correspond to them. The peaks are rotated with respect to one another through an angle of about 30° (or are discrete with this pitch) and frequently correlate with the peaks of the preceding sample of quasars. It can be conjectured that all of this is associated in one way or another with the presumed cubed-sphere grid specified by Eq. (6).

In Fig. 14, the distributions of $\langle z\rangle$ that are presented in Fig. 12*b* are given in polar coordinates (the notation here is similar to that in Fig. 13). If use is made of the Hubble law

$$r = v/H_0 = \beta R_0\ [\mathrm{Mpc}], \qquad (12)$$

where r is the distance to the object being considered, $\beta = v/c$ (here, v and c are, respectively, the speed of the object and the speed of light), and $H_0 \approx$ 75 km/s Mpc is the Hubble constant, then these results can be treated as the distances $\langle r\rangle$ from the observation point (O) to a "mean quasar" in preset galactic sectors. A value of $R_0 \approx cT \approx 10^{26}$ m $\approx$ 4000 Mpc characterizes the limiting dimensions of the Metagalaxy ($T \approx 1/H_0 \approx 13$ billion years is the age of the Metalaxy since the beginning of the Big Bang [6]). In the relativistic case, the quantity β is related to the Doppler redshift z by the equation [6]

$$\beta = ((1+z)^2 - 1)/((1+z)^2 + 1), \qquad (13)$$

which will be used below in estimating the distances r.

Circles *1* and *2* in Fig. 14 correspond to the central cuts of the spheres having radii of $\langle r\rangle_1 \approx$

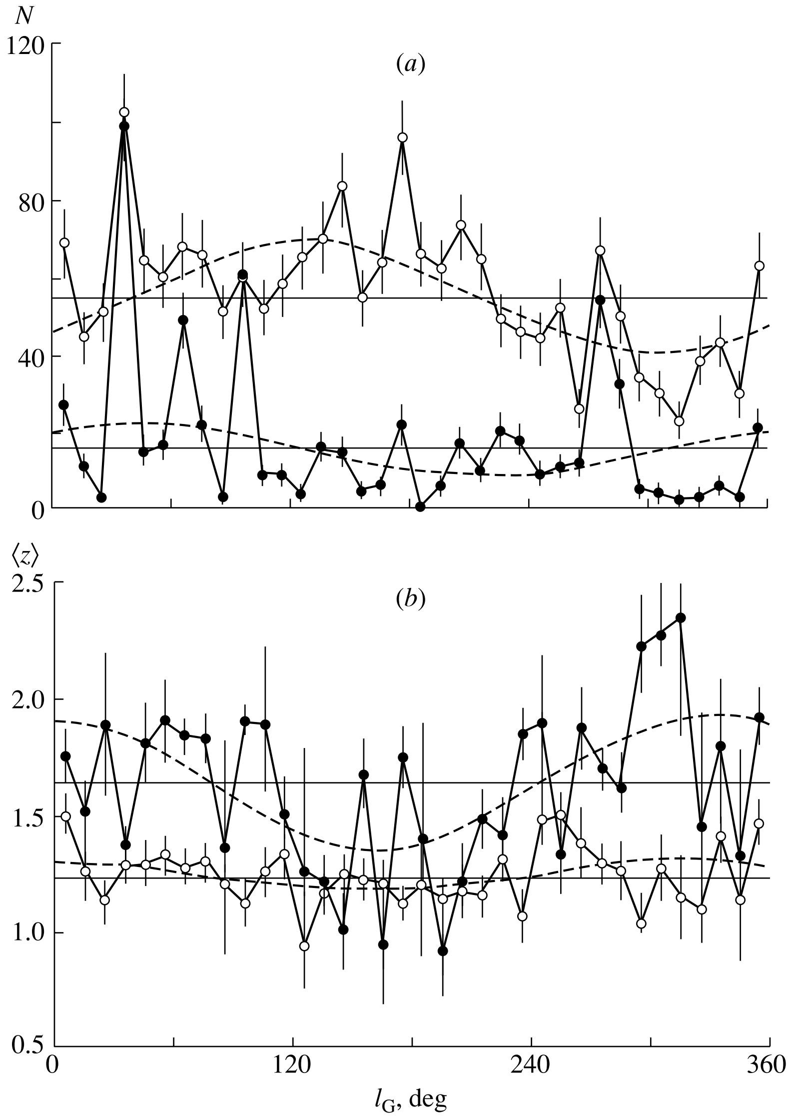

Fig. 12. Distributions of (closed circles) 580 and (open circles) 1974 $z \leq 2.5$ quasars (presented in Fig. 10) in galactic spherical coordinates: (*a*) distributions in the number of events and (*b*) distributions of mean redshifts in individual spherical sectors. The horizontal lines correspond to mean values, while the dashed curves represent the best approximations of the data in terms of the function in (7).

$0.67 \times 4000 \approx 2670$ Mpc ($\langle z \rangle \approx 1.24$) and $\langle r \rangle_2 = 0.75 \times 4000 \approx 3000$ Mpc ($\langle z \rangle \approx 1.64$), respectively, by a plane parallel to the Galaxy plane. For the sake of comparison, the region corresponding to $r_3 \approx 1026$ Mpc ($z \approx 0.3$) and housing the majority of the observed superclusters of galaxies is shown by circle *3*. It can be seen that a spherical distribution of quasars beyond the nodes (open circles) is roughly compatible with circle *1*. A more realistic approximation (dashed curve in Fig. 12*b*) corresponds to circle *1* whose center is shifted by $\Delta_{XY} = -A_1 \langle r \rangle_1 = -0.06 \times 2670 \approx -160$ Mpc (it is not shown in order to avoid encumbering the figure).

The closed circles in Fig. 14 represent the distribution of quasars in the nodes. They proved to be farther from the observation point and reveal a sizable anisotropy, which decreases with respect to the dashed-line circle centered at O', this circle being nothing but circle *2* shifted by $\Delta_{XY} = -A_1 \langle r \rangle_2 = -0.18 \times 3000 \approx -540$ Mpc in the direction $l_G \approx 330°$. However, an ellipse whose axes are denoted by x' and y' that is characterized by a contraction factor of $k \approx 0.78$ yields the best central symmetry. Its major axis y' forms an angle of about 28° with the y axis. For the total sample of quasars characterized by redshifts

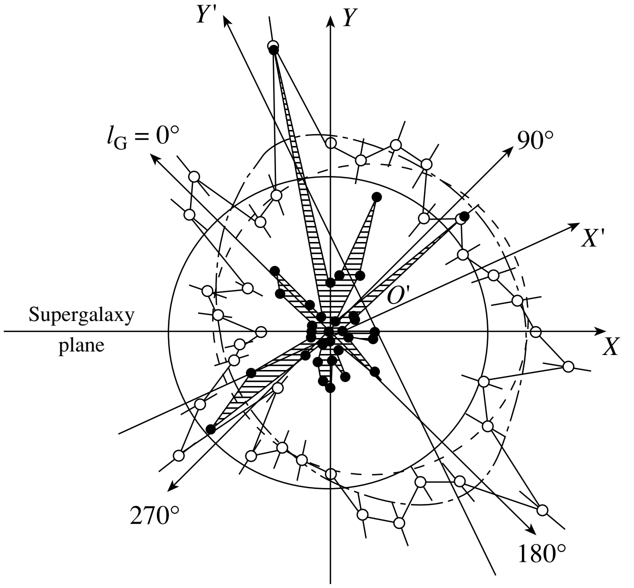

Fig. 13. Distributions of (closed circles) 580 and (open circles) 1974 $z \leq 2.5$ quasars (which are presented in Fig. 12*a*) in polar coordinates. The figures indicate the longitude in galactic coordinates. The solid-line circle corresponds to the mean values for the sample of quasars beyond the nodes (open circles), the dashed-line surface represents an approximation of these data (open circles) in terms of the function in (7), and the dash-dotted-line ellipse shows the best approximation of these data (open circles).

in the range $z \leq 2.5$, we have $\langle r \rangle_{XY} = 2770$ Mpc and $\Delta_{XY} = 0.08\langle r \rangle_{XY} \approx 220$ Mpc.

In this representation, the anisotropy of redshifts for quasars becomes more comprehensible from the physical point of view. From the distributions in Fig. 14, it can be seen that the Galaxy is shifted, in all probability, with respect to the center O' of the presumed Metagalaxy in the direction $l_G \approx 150°$. Since the Metagalaxy has a finite size R_0, this shift is in fact reflected in the mean values of the redshifts in Fig. 12–14—namely, the closer an observer to quasars, the greater the number of weak objects (that is, those that are characterized by smaller values of $\langle z \rangle$) that he sees.

Let us now estimate the possible asymmetry of $z \leq 2.5$ quasars along the z axis. Since this axis is orthogonal to the Galaxy plane, we consider the mean redshifts for quasars in solid angles for which $|b_G| \geq 75°$. For the north and the south pole of the Galaxy, we have $\langle z \rangle_N = 1.376 \pm 0.048$ and $\langle z \rangle_S = 1.665 \pm 0.038$, respectively. By employing Eqs. (12) and (13) and the relation

$$\langle r \rangle_N / \langle r \rangle_S \approx (\langle r \rangle_Z - \Delta_Z)/(\langle r \rangle_Z + \Delta_Z) \approx 0.928, \tag{14}$$

we obtain $\Delta_Z / \langle r \rangle_Z \approx 0.037$. For the total sample of quasars in both pole cones specified by the inequality

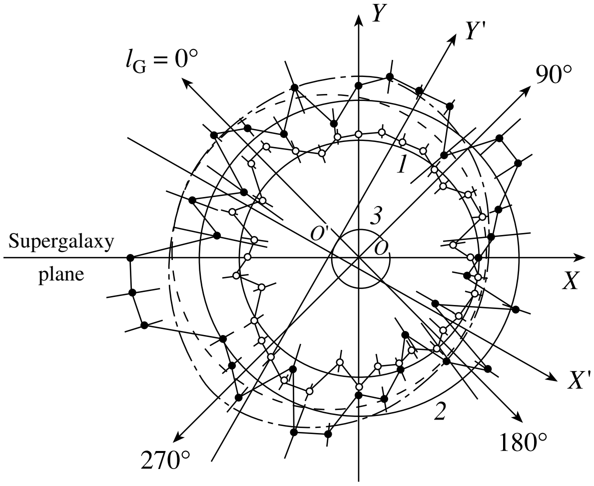

Fig. 14. Distribution of the mean redshifts for (closed circles) 580 and (open circles) 1974 $z \leq 2.5$ quasars (which are presented in Fig. 12*b*) in polar coordinates. The figures indicate longitudes in galactic coordinates. The solid-line circles correspond to various values of the mean redshift: $\langle z \rangle =$ (*1*) 1.24, (*2*) 1.64, and (*3*) 0.3. The dashed-line circle represents an approximation of the data on quasars in the nodes (closed circles) in terms of the function in (7), while the dash-dotted-line ellipse corresponds to the best approximation of these data (closed circles).

$|b_G| \geq 75°$, the mean redshift is $\langle z \rangle = 1.545 \pm 0.03$. This corresponds to $\langle r \rangle_Z = 2930$ Mpc and to the shift of $\Delta_Z \approx 108$ Mpc with respect to the symmetry center of this sample in the direction to the north pole of the Galaxy.

From the ratio $\langle r \rangle_{XY}/\langle r \rangle_Z = 2770/2930 \approx 0.94$, it follows that, in all probability, the projection of "average quasars" from the $z \leq 2.5$ sample onto the xz plane also has the shape of an ellipse. The total absolute shift of the observation point with respect to the presumed center of symmetry of the volume distribution of average quasars is

$$\Delta = \sqrt{(\Delta_{XY})^2 + (\Delta_Z)^2} \approx 245 \text{ Mpc}. \tag{15}$$

This point is nearly in the Supergalaxy plane, its coordinates being $l_{SG} \approx 116° \pm 21°$ and $b_{SG} \approx 0° \pm 5°$ (the respective equatorial coordinates are $\alpha \approx 79°$ and $\delta \approx 74°$). Within our hypothesis of the Metagalaxy, the direction opposite to it in the Supergalaxy plane ($l_{SG} \approx 296°$) points to the Metagalaxy center in a rough approximation.

6. ANISOTROPY OF $E_0 \geq 8 \times 10^{18}$ eV PRIMARY COSMIC RAYS

Let us now return to ultrahigh-energy cosmic rays. We would like to emphasize one intriguing detail in their anisotropy. In [13, 14], it was indicated that, in the energy regions $E_0 \approx 10^{17.7-17.8}$ eV and $E_0 \geq 8 \times 10^{18}$ eV, the global primary-cosmic-ray fluxes as expressed in terms of equatorial coordinates have a pronounced anisotropy, the phase of the first harmonic being $l_1 \approx 40°$, which indicates, in supergalactic coordinates, the intersection of the Galaxy and the Supergalaxy plane at $l_{SG} \approx 93°$. This direction is roughly compatible with the aforementioned anisotropy of the space distribution of quasars.

Let us consider the anisotropy of giant air showers of energy in the region $E_0 \geq 10^{19}$ eV, which have aroused particular interest since the detection of the first events at the largest arrays worldwide, such as Volcano Ranch (USA) [22], Haverah Park (United Kingdom) [23], SUGAR (Sydney University Giant Airshower Recorder, Australia) [24], and the Yakutsk array [25]. To a considerable extent, this interest is motivated by the fact that a sharp change in the shape of the energy spectrum of primary cosmic rays toward a slower decrease with increasing energy was observed at all arrays in the above energy region. However, primary particles of limiting energy in the region $E_0 \geq 10^{20}$ eV are the most puzzling. It is still unclear whether they exist in nature [26]. A great many experimental and theoretical studies have been devoted to solving the problem of the origin of giant air showers, but it still remains one of the most complicated and contradictory problems.

Recently, a local region in the arrival directions of primary cosmic rays of energy in the range $E_0 \approx (1-2) \times 10^{19}$ eV was found at a significance level of 0.007 on the basis of data from the Yakutsk array by using the wavelet-analysis method [27]. Its pole featuring the maximum number of events has equatorial coordinates of $\alpha_{\max} \approx 35° \pm 20°$ and $\delta_{\max} \approx 52.5° \pm 7.5°$ and lies in the Supergalaxy plane. This supports our hypothesis of an extragalactic origin of the bulk of primary cosmic rays that have energies in the region $E_0 \geq 10^{19}$ eV. However, Mikhailov [28–31], who also relied on an analysis of data from the Yakutsk array, arrived at a drastically different conclusion; according to Mikhailov, primary cosmic rays of energy in the range $E_0 \leq 4 \times 10^{19}$ eV are predominantly of a galactic origin. He states that a few pulsars closest to the Earth that occur at the side of the inlet of a local arm of the Galaxy and which generate predominantly iron nuclei are sources of this radiation.

In order to disentangle this contradiction, we revisit the anisotropy of arrival directions for giant air showers of energy in the region $E_0 \geq 8 \times 10^{18}$ eV that were recorded by the Yakutsk array over the period between 1974 and 2002 for zenith angles satisfying the condition $\theta \leq 60°$. For our analysis, we select only those events for which the arrival directions were found on the basis of data from four or more stations and in which the shower cores were within the perimeter of the array. The primary-particle energy E_0 was determined from relations (1)–(3). In all, we selected 559 showers in this way.

In addition, we use 522 events from the catalog presented in [32] that were recorded by the SUGAR array. These showers predominantly refer to the southern hemisphere of the Earth. Together with the data from the Yakutsk array, they provide a rather comprehensive pattern of the anisotropy of giant air showers in the surrounding space. The accuracy in determining the arrival directions of showers in [32] was about 5°.

We have investigated the deviations of the observed number of events, N_1, from the expected mean number $\langle N \rangle = N_2(\Omega_1/\Omega_2)$ in units of a standard deviation $\sigma = \sqrt{\langle N \rangle}$,

$$n_\sigma = (N_1 - \langle N \rangle)/\sigma, \qquad (16)$$

where N_1 and N_2 are the numbers of showers in the solid angles $\Omega_1 = 1 - \cos\theta_1$ and $\Omega_2 = 1 - \cos\theta_2$ ($\theta_1 = 8°$, $\theta_2 = 45°$), respectively. The values of the deviation in (16) were found upon successively shifting a 1° × 1° area over the entire sphere.

Figure 15 shows the distribution of the quantities in (16) over the developed celestial sphere in terms of (*a*) galactic and (*b*) supergalactic coordinates. Circles *1* and *2* represent, respectively, the pole of a local excess of primary cosmic rays [27] and the outlet of a local arm of the Galaxy. The range of n_σ is shown at the bottom of the figure by the shaded scale. The darkest and the lightest regions correspond to the deviation of the giant-air-shower flux from the mean value by $|n_\sigma| \geq 3\sigma$.

A few interesting and important features immediately attract attention in Fig. 15. First, numerous local regions where the fluxes of giant air showers are relatively high or low are seen over the entire sphere. Second, there is virtually no excess of radiation in the Galaxy disk, apart from the locus of intersection of the Galaxy and Supergalaxy planes at $l_G \approx 137°$. There is no indication of excess radiation even from the center of the Galaxy, where there occur the most vigorous processes of matter transformation. Nonetheless, a significant anisotropy is observed in this region according to AGASA (Akeno Giant Air Shower Array) [33] and SUGAR [34] data in the energy range $E_0 \approx (8-20) \times 10^{17}$ eV. One cannot see excess radiation of giant air showers at the outlet of the local arm of the Galaxy (circle *2*) either. In his studies, Mikhailov erroneously interpreted, as this excess, radiation from neighboring regions occurring approximately in the Galaxy disk, but $\Delta l_G \approx 25°-45°$ aside. The error resulted from a very rough partition of the

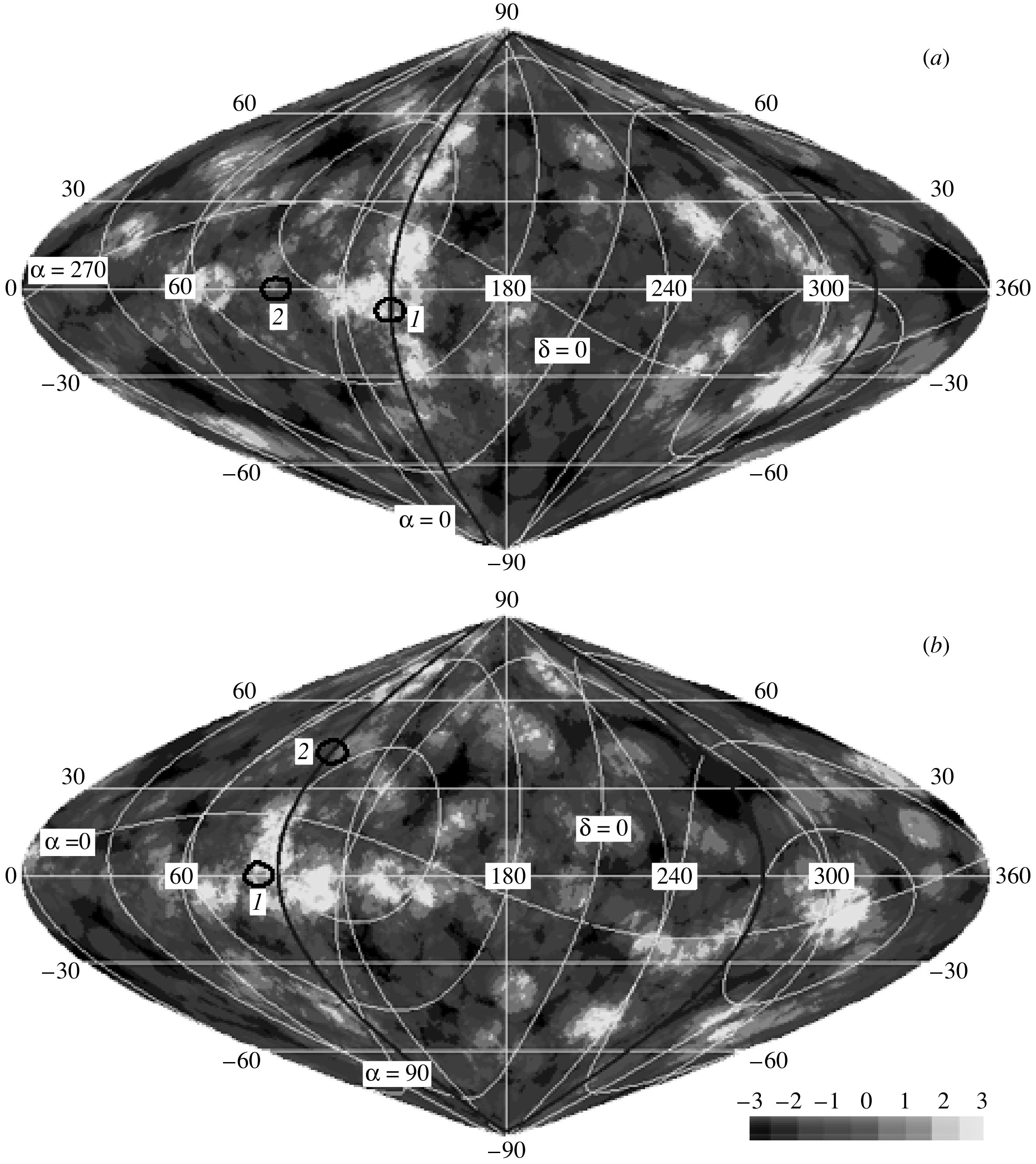

Fig. 15. Deviations of the observed number N_1 of showers from the expected mean number $\langle N\rangle$ in $n_\sigma = (N_1 - \langle N\rangle)/\sqrt{\langle N\rangle}$ units over the developed celestial sphere in (*a*) galactic and (*b*) supergalactic coordinates for giant air showers of energy in the region $E_0 \geq 8 \times 10^{18}$ eV and zenith angles in the range $\cos\theta \leq 60^\circ$ according to data from the Yakutsk array and SUGAR [32]. Circles *1* and *2* represent, respectively, the pole of a local excess of primary cosmic rays [27] and the outlet of a local arm of the Galaxy; the dark curves correspond to the (*a*) Supergalaxy and (*b*) Galaxy planes; and the shaded scale shows the range of n_σ.

sphere into plates of dimensions $\Delta l_G \times \Delta b_G = 30^\circ \times 10^\circ$ (see, for example, [31]).

There is yet another argument against the point of view advocated in [28–31]. It is provided by the distribution of pulsars in the Galaxy itself. This distribution is shown in Fig. 16 for 450 objects [35] in galactic coordinates. There, one can see a high concentration of pulsars in the vicinity of the Galaxy plane, but their concentration at the inlet of the local arm of the Galaxy ($l_G \approx 90^\circ$, $b_G \approx 0^\circ$) is rather low. If these objects had indeed been sources of ultrahigh-energy primary cosmic rays, they would have determined, to a considerable extent, the anisotropy of the arrival directions of giant air showers. However, a totally different pattern emerges in fact from observations. In Fig. 15, a correlation between the arrival directions of giant air showers and the Supergalaxy plane is clearly seen in the northern hemisphere of the Earth. This correlation can be characterized by the average values

$$\langle n_\sigma \rangle = \left(\sum_{i=1}^{k} (n_\sigma)_i \right) / k, \qquad (17)$$

which are shown in Fig. 17. These values were obtained by averaging all n_σ for $\delta \geq 0^\circ$ in intervals of width $\Delta b_{\mathrm{SG}} = 1^\circ$. At $b_{\mathrm{SG}} \approx -3^\circ$, a pronounced peak can be seen here, which was reported previously in [11, 12].

Figure 18*a* shows the changes in the quantity defined by Eq. (16) in response to successively shifting the scanning solid angles Ω_1 and Ω_2 along the latitude of $b_{\mathrm{SG}} \approx -3^\circ$. The dashed curve reflects the behavior of this distribution (versus the supergalactic longitude) on average after smoothing it over 30 neighboring points. Here, one can also see a very strong peak in the sector $\Delta l_{\mathrm{SG}} \approx 0^\circ$–$210^\circ$, its maximum being at $l_{\mathrm{SG}} \approx 120^\circ$. However, there is no such pronounced correlation in the southern hemisphere, with the exception of an excess of giant air showers in a local sky region around the point whose coordinates are $\alpha \approx 0^\circ$ and $\delta \approx -85^\circ$ (Fig. 15*b*). It is interesting to note that this excess occurs near the Supergalaxy plane in the direction nearly opposite to the region where one observes the most pronounced excess of primary cosmic rays in the northern hemisphere. Maybe, this coincidence is not purely accidental.

For the sake of comparison, the changes in the quantity defined in (16) as the result of scanning the Galaxy disk (within the latitude band $|b_{\mathrm{G}}| \leq 8^\circ$) are shown in Fig. 18*b*. It can be seen that the averaged distribution (dashed curve) peaks at $l_{\mathrm{G}} \approx 137^\circ$, where the Supergalaxy plane passes (see Fig. 15). Its magnitude (about one standard deviation) is approximately one-half as large as the analogous maximum in Fig. 18*a* at $l_{\mathrm{SG}} \approx 120^\circ$, this suggesting a predominant role of the Supergalaxy in the formation of the excess flux of primary cosmic rays in the region of intersection of the Galaxy and Supergalaxy planes.

7. DISCUSSION OF THE RESULTS

The results presented in Figs. 15–18 unambiguously indicate that the overwhelming majority of primary particles whose energies lie in the region $E_0 \geq 8 \times 10^{18}$ eV are of an extragalactic origin. However, these results contradict, at first glance, the results displayed in Fig. 5*a* and our hypothesis that quasars may be sources of primary cosmic rays in this energy region. Indeed, there immediately arises the question of the relation between quasars and the Supergalaxy, which are separated by enormous (cosmological) distances.

Nevertheless, such a relation is likely to exist. In my opinion, this is suggested by the shape of the distribution in Fig. 18*a*. As was emphasized above, it is not the whole the Supergalaxy plane but only some sectors of it that are regions of an enhanced flux of giant air showers. The central region ($l_{\mathrm{G}} \approx 192^\circ$), which features the superdense Virgo cluster of galaxies, manifests itself only slightly. All of this suggests that, in all probability, the sources of giant air showers are beyond the Supergalaxy, the Supergalaxy itself playing the role of a target where there occur some nuclear interactions at ultrahigh energies.

The meaning of this assumption is reflected in Fig. 19. Of course, this is a very rough scheme, where many proportions have been violated because of the incommensurability of the scale of the Supergalaxy and the scale of the Galaxy; nevertheless, it enables us to develop some specific pattern within the ideas outlined above. We have denoted by R_0 the outer boundary of the Metagalaxy, whose mass M_0 is approximately

$$M_0 \approx (4\pi/3)(R_0)^3 \rho \approx 4 \times 10^{52}\ [\mathrm{kg}], \qquad (18)$$

where $\rho \approx 10^{-26}$ kg/m^3 is the average matter density in the Metagalaxy [6]. The shaded region includes quasars. In all probability, lacertides (BL Lac objects) and Seifert galaxies, which are likely to be other sources of giant air showers [36, 37], may also appear there. Objects of all three types form so-called active-core galaxies, which are among the most powerful sources in the Metagalaxy.

The position of our Solar System in the Metagalaxy is denoted by S. As was shown above (see Figs. 12–14), it is shifted from the center O in the direction of the vector A—that is, toward the closest region of quasars. The numbers in Fig. 19 indicate supergalactic longitudes. The dashed line BC represents the Galaxy plane. The Supergalaxy is depicted in the form of a circle centered at D. We assume that the Supergalaxy plane is oriented in such a way that its edge faces the Supergalaxy center. By and large, this picture gives an idea of the relative positions of the objects in which we are interested. This view arises upon cutting the Metagagalaxy by the plane that is parallel to the Galaxy plane and which traverses the Metagalaxy center.

If this scheme, which is quite rough, is correct, then one can easily understand the physical meaning of the results given in Fig. 18*a*. It is obvious that particle fluxes going from external regions of the Metagalaxy to its center (arrows in Fig. 19) will "radiate" different sectors of the Supergalaxy disk differently.

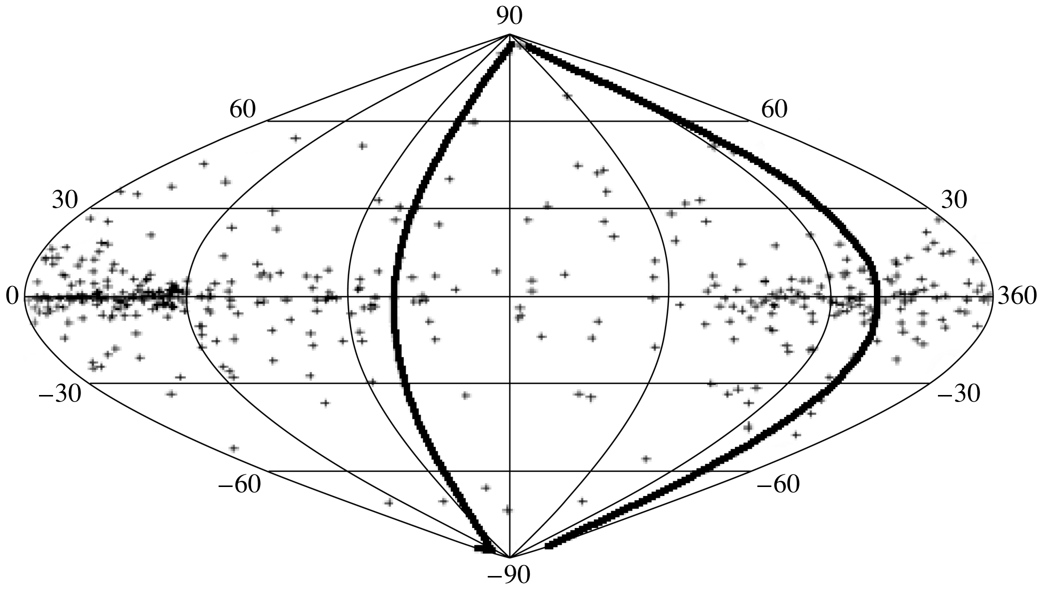

Fig. 16. Distribution of 450 pulsars [35] over the developed celestial sphere in galactic coordinates. The thick curve represents the Supergalaxy plane.

The flux from the $l_{\rm SG} \approx 120°$ direction arrives within a much wider angular sector than the flux from the $l_{\rm SG} \approx 300°$ direction, which is opposite to the former. Moreover, these fluxes will differ markedly in intensity, because, on their way to the Supergalaxy, they are attenuated by the Metagalaxy matter to drastically different degrees. As to the Galaxy, the orientation of its disk with respect to this particle flux is likely to be less pronounced. In all probability, all of these factors are reflected in the distribution of the giant-air-shower flux in Fig. 18.

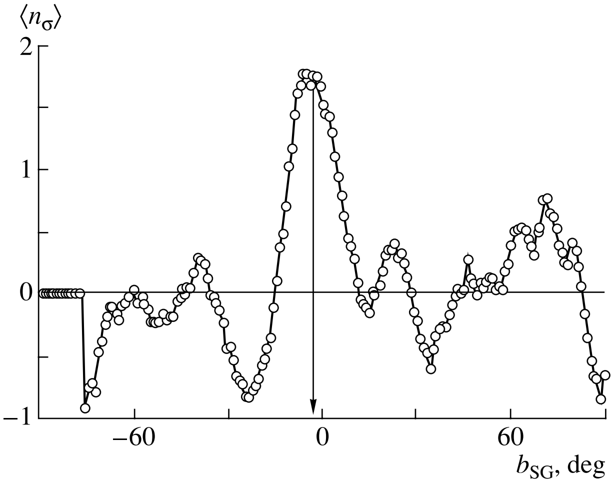

Fig. 17. Distribution of $E_0 \geq 8 \times 10^{18}$ eV showers in units of $\langle n_\sigma \rangle$ values obtained by averaging all n_σ in Fig. 15 over the intervals $\Delta b_{\rm SG} = 1°$ for $\delta \geq 0°$ (in the northern hemisphere of the Earth) versus the supergalactic latitude.

Further, we consider some interesting facts from astronomy that, in my opinion, favor the existence of a finite Metagalaxy. It is well known that Seifert galaxies are, as a rule, spiral galaxies, but that they are characterized by an enhanced growth of luminosity toward the center. With respect to ordinary spiral galaxies, their number is about 1% [6]. It is astounding that the overwhelming majority of Seifert galaxies are oriented flatwise with respect to a terrestrial observer [6]. This fact has so far remained unexplained. However, the answer is clear within the hypothesis of a Metagalaxy: the axes of rotation of Seifert galaxies are aligned with the force lines of the gravitational field directed to the Metagalaxy center. In this case, periodic oscillations of the energy of gravitational coupling between the rotating parts of Seifert galaxies and the gravitational field of the Metagalaxy are minimal. Moreover, the fact that the axes of rotation of Seifert galaxies are directed toward us is yet another piece of evidence that our Galaxy is not far off the Metagalaxy center.

At the present time, there are indications [38, 39] of some formidable structures in space. For example, the measurements of the peculiar velocities of 400 elliptic galaxies in [38] exhibit the presence of an "enormous motion" of matter. All clusters and superclusters occurring in the vicinity of our Galaxy move toward the point whose equatorial coordinates are $\alpha = 208.1°$ and $\delta = -55.5°$—this is the so-called Grand Unification point. A simulation of this gravitating mass yields an estimate of $M_{\rm A} \sim 5 \times 10^{16} M_\odot \approx 10^{47}$ kg, where $M_\odot$ is the mass of the Sun. The radius $R_{\rm A}$ of the sphere of this attractor can

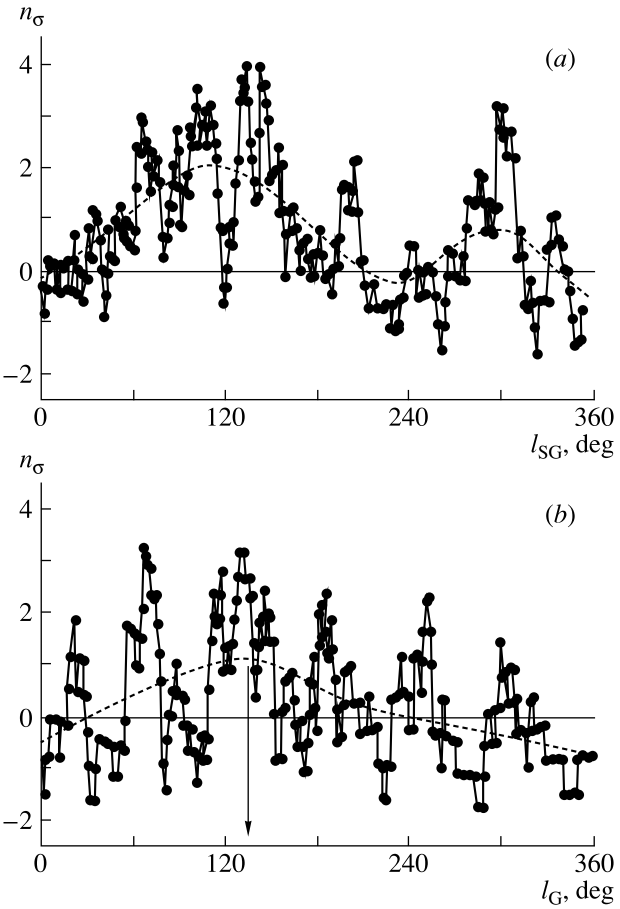

Fig. 18. Changes in the n_σ values given in Fig. 15 upon scanning along the (a) Supergalaxy and (b) Galaxy disks. The dashed curves represent the behavior on average after smoothing over 30 neighboring points.

be estimated by using the relation

$$R_{\mathrm{A}} = R_0(M_{\mathrm{A}}/M_0)^{1/3} \approx 56\ \mathrm{Mpc}.$$

One can see that this radius is quite commensurate with the shift of the observation point with respect to the presumed center of symmetry of the volume distribution of "average quasars" [see Eq. (15)]. The attractor itself is situated approximately in the same direction (the supergalactic coordinates of its center are $l_{\mathrm{SG}} \approx 269°$ and $b_{\mathrm{SG}} \approx -5°$) as the Metagalaxy center. Thus, we see that the motion of matter now becomes more comprehensible—it is a motion in the field of metagalactic gravitational forces.

In this connection, the magnitude and the spatial distribution of the gravitational potential of the Metagalaxy are of considerable interest. In regions beyond the Metagalaxy (for $r \geq R_0$), it is given by the well-known Newton formula

$$\varphi(r) = -GM_0/r, \qquad (19)$$

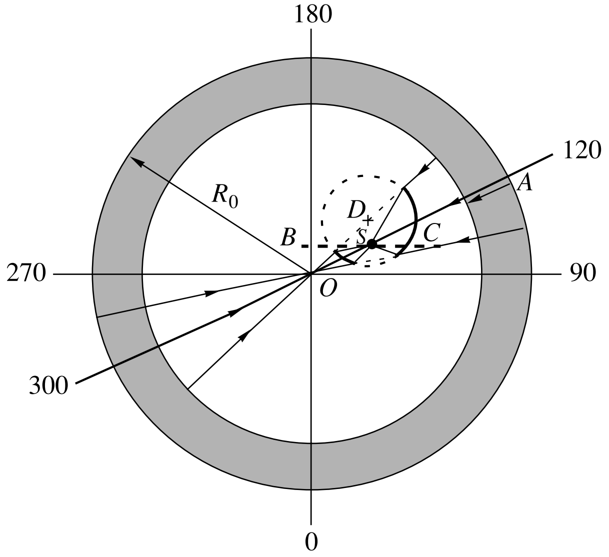

Fig. 19. Schematic disposition of the Supergalaxy (circle centered at D), the Galaxy (dashed line BC), and an observer on the Earth (S) in the Metagalaxy whose center is at the point O, the radius of the outer boundary of the Metagalaxy being R_0. The shaded region corresponds to the sphere of quasars; figures indicate supergalactic longitudes; the vector A points to region of quasars that is the closest to the observer; and arrows point to the sectors in which the maximum fluxes of $E_0 \geq 8 \times 10^{18}$ eV giant air showers are observed in Fig. 18a.

where $G = 6.67 \times 10^{-11}\ \mathrm{kg}^{-1}\ \mathrm{m}^3\ \mathrm{s}^{-2}$ is the gravitational constant. The question of the distribution of the gravitational potential within the Metagalaxy is more involved. Within a uniform sphere, it is given by [6]

$$\varphi(r) = -GM_0(3 - (r/R_0)^2)/2. \qquad (20)$$

At $r = R_0$, the two formulas match each other, yielding the same result, $\varphi_0 = \varphi(R_0) \approx 3 \times 10^{16}\ \mathrm{m}^2/\mathrm{s}^2$. At the Metagalaxy center, this potential is 1.5 times greater, the gravitational field itself vanishing there. The gravitational potential is the work that must be performed to remove a unit mass from a given gravitational field. In order to escape from the gravitational field of the Metagalaxy, a body of mass m must perform the work $A = -m\varphi_0$. For this, it must have the kinetic energy $K = mv^2/2 = -A$ and, hence, the speed $v = \sqrt{-2\varphi_0} \approx 2.5 \times 10^8$ m/s, which is close to the speed of light.

The following intriguing fact is noteworthy. The square of the speed of light, $c^2 = 9 \times 10^{16}\ \mathrm{m}^2/\mathrm{s}^2$, is nearly equal to the Metagalaxy potential within the errors in the estimate of φ_0. The Einstein mass—energy relation states that the total energy of a body is $E = mc^2$. It appears that this energy is approximately equal to the gravitational potential created by the entire mass of the Metagalaxy. Yanchilin [40] considered some surprising consequences from this circumstance, but we will not dwell on them here.

Particles forming primary cosmic rays of ultrahigh energy are of great interest. It was stated above—and previously in [1–4, 11–14]—that, in all probability, these particles must be neutral and stable. At the present time, it is difficult to determine their sort, but some of their properties are already known. These cannot be photons, since, according to various model estimates, photons initiate extensive air showers where the number of muons is approximately ten times smaller than in showers from primary cosmic rays of ordinary composition—in experiments, there were no such deviations of the muon fraction in the overwhelming majority of events.

We cannot rule out the possibility that these are neutrinos. The calculations performed in [41] revealed that, under certain conditions on the growth of the cross section for neutrino–nucleon interaction ($\sigma_{\nu N}$) in the region of ultrahigh energies, there can arise extensive air showers that are similar in many respects to showers initiated by primary cosmic rays of ordinary composition. The hypothesis of ultrahigh-energy neutrinos interacting with relic neutrinos in the vicinity of the Earth and generating "Z-boson" showers was considered in [42, 43].

According to [44], neutral pions can also appear as the presumed neutral particles of primary cosmic rays. It was shown there that stable pions can exist in the composition of cosmic rays whose energy lies in the region $E_0 \geq 10^{19}$ eV. The respective calculations relied on the model of quark–gluon strings [45] with allowance for the Landau–Pomeranchuk–Migdal effect [46] and admitted a very weak violation of Lorentz invariance in accordance with the Coleman–Glashow hypothesis. It is of paramount importance that, within this hypothesis, pion interaction with relic photons is kinematically forbidden, which makes it possible to resolve the Greisen–Zatsepin–Kuz'min paradox [47, 48]. The calculations performed in [44] revealed that neutral pions and protons lead to patterns of giant-air-shower development that are similar in many respects, although there are some distinctions between them.

Possibly, neutral pions are produced not only in local sources characterized by a vigorous energy release but also in collisions of ultrahigh-energy primary cosmic rays with a metagalactic gas. In my opinion, such processes in the Supergalaxy and in other large-scale structures of the Metagalaxy could lead to the results displayed in Figs. 17 and 18a. In this connection, a further development of the hypothesis that long-lived neutral pions can be present in primary cosmic rays seems quite promising.

However, we will assume that extragalactic primary cosmic rays can also involve other neutral particles generated by active-core galaxies. An attempt at experimentally estimating the nuclear-interaction range of puzzling neutral particles at an energy of $E_0 \sim 10^{17}$ eV was made in [4]. It turned out to be about (3–4) $\times 10^{-2}$ g/cm^2, which is approximately 1000 times smaller than the nuclear-interaction range of ultrahigh-energy protons. Therefore, these particles initiate the development of extensive air showers much earlier than primary cosmic rays of ordinary composition. But after the first interaction event, they are likely to disappear, giving way, in the development of extensive air showers, to a normal cascade of secondary particles; otherwise, showers generated by them would differ considerably from conventional showers and would be readily identifiable.

Because of so short a range to the first nuclear interaction, showers from the presumed neutral particles are expected to cause an enhanced development of extensive air showers, with the cascade-curve maximum lying higher in that case than in the case of primary protons. In view of this, showers from iron nuclei can mimic showers from puzzling neutral particles. The point is that the majority of the methods for determining the composition of primary cosmic rays are indirect: they rely on a comparison of observed features of extensive air showers with their calculated counterparts that are found on the basis of model concepts of the development of extensive air showers for one preset composition of primary cosmic rays or another. Here, one cannot rule out the situation where effects of any primary particles having very short ranges can be misinterpreted by researchers as those which are associated with an increase in the fraction of heavy nuclei.

8. CONCLUSION

The above results can be partitioned into two groups that are independent to some extent. The first group has some bearing on the origin of ultrahigh-energy primary cosmic rays. The results presented in Figs. 4–9 can be interpreted as the indication that quasars characterized by redshift values satisfying the condition $z \leq 2.5$ may be among the probable sources of cosmic rays whose energies lie in the region $E_0 \geq 5 \times 10^{17}$ eV. On the basis of a comparison of the distributions in Fig. 5, it can be assumed that the effective contributions of quasars for which z takes different values are different in different regions of the energy of primary cosmic rays. That quasars forming clusters play a more important role in the formation of primary cosmic rays than the remaining events not entering into these clusters can most clearly be seen (at a significance level not lower than five standard deviations) from the example of the data in Fig. 7.

Our results are consistent with the hypothesis [9] that the activity of quasars can undergo variations—that is, there are periods of their high and low luminosity. The angular correlations between the arrival directions of primary cosmic rays and the positions of quasars are the most pronounced in those redshift intervals that are associated with the high-activity periods.

The results presented in Figs. 1, 2, and 8–14 reflect the spatial structure of quasars. It is hardly consistent with the hypothesis of a uniform and isotropic universe on a scale where $z \leq 2.5$. For example, the data in Fig. 8 are indicative of the possible existence of an ordered structure belonging to the cubed-sphere-grid type. The total distribution of quasars over the celestial sphere (Fig. 1) is characterized by a small-scale anisotropy accompanied by the presence of a large number of nodes (see Fig. 9). Objects forming nodes and those that do not enter into them are likely to have different spatial structures (Figs. 10–12).

The results displayed in Fig. 12 indicate that there can exist a global anisotropy of quasars. This anisotropy is characterized by a central asymmetry of the spatial distribution of quasars (see Figs. 13 and 14). Its structure does not rule out the existence of a Metagalaxy, a gravitationally bound set of matter in the Universe within which we live and beyond which our sight cannot penetrate in principle. In my opinion, the hypothesis that the Supergalaxy is situated near the center of the Metagalaxy (see Fig. 19) makes it possible to obtain deeper insight into the results concerning the anisotropy of the spatial distribution of quasars and the anisotropy of the arrival directions of the global flux of giant air showers.

The results in Figs. 15–18 evince an extragalactic origin of primary cosmic rays whose energies lie in the region $E_0 \geq 8 \times 10^{18}$ eV. Some of these particles (possibly neutral pions [44]) are formed in the Supergalaxy. It can be assumed that they are formed in collisions of neutral particles generated by quasars with a supergalactic gas. Here, further investigations are required, and they are under way now.

ACKNOWLEDGMENTS

The financial support extended by the Ministry of Science of the Russian Federation to the Yakutsk multipurpose array for studying extensive air showers (grant no. 01-30), which was included in the list of unique experimental facilities of national importance, is gratefully acknowledged.

REFERENCES

1. A. V. Glushkov, Pis'ma Zh. Éksp. Teor. Fiz. **73**, 355 (2001) [JETP Lett. **73**, 313 (2001)].
2. A. V. Glushkov and M. I. Pravdin, Pis'ma Astron. Zh. **28**, 341 (2002) [Astron. Lett. **28**, 296 (2002)].
3. A. V. Glushkov, Izv. Akad. Nauk, Ser. Fiz. **66**, 1599 (2002).
4. A. V. Glushkov, Yad. Fiz. **66**, 1292 (2003) [Phys. At. Nucl. **66**, 1252 (2003)].
5. A. Hewitt and G. Burbidge, Astrophys. J., Suppl. Ser. **63**, 1 (1987).
6. *Physics of Space: Small Encyclopedia*, Ed. by R. A. Syunyaev (Sov. Encyclopedia, Moscow, 1986) [in Russian].
7. K. G. Karlsson, Astron. Astrophys. **13**, 333 (1971).
8. M. F. Khodyachikh, Astron. Zh. **73**, 11 (1996) [Astron. Rep. **40**, 6 (1996)].
9. A. I. Ryabinkov, A. D. Kaminker, and D. A. Varshalovich, Pis'ma Astron. Zh. **27**, 643 (2001) [Astron. Lett. **27**, 549 (2001)].
10. M.-P. Veron-Cetty and P. Veron-Cetty, *A Catalogue of Quasars and Active Nuclei*, 9th ed. (ESO Scientific Report, 2000).
11. A. V. Glushkov and M. I. Pravdin, Zh. Éksp. Teor. Fiz. **119**, 1029 (2001) [JETP **92**, 887 (2001)].
12. A. V. Glushkov and M. I. Pravdin, Pis'ma Astron. Zh. **27**, 577 (2001) [Astron. Lett. **27**, 493 (2001)].
13. A. V. Glushkov, Pis'ma Astron. Zh. **29**, 172 (2003) [Astron. Lett. **29**, 142 (2003)].
14. A. V. Glushkov and M. I. Pravdin, Yad. Fiz. **66**, 886 (2003) [Phys. At. Nucl. **66**, 854 (2003)].
15. B. A. Vorontsov-Vel'yaminov, I. D. Karachentsev, E. Turner, *et al.*, *Large-Scale Structure of the Universe* (Mir, Moscow, 1981) [in Russian].
16. A. V. Gurevich and K. P. Zybin, Usp. Fiz. Nauk **165**, 3 (1995) [Phys. Usp. **38**, 1 (1995)].
17. J. Linsley, Phys. Rev. Lett. **34**, 1530 (1975).
18. A. D. Chernin, *Stars and Physics* (Nauka, Moscow, 1984) [in Russian].
19. I. D. Novikov, *How the Universe Have Been Explored* (Nauka, Moscow, 1988) [in Russian].
20. A. D. Linde, Usp. Fiz. Nauk **144**, 177 (1984) [Sov. Phys. Usp. **27**, 81 (1984)].
21. A. D. Linde, Phys. Lett. B **175**, 395 (1986).
22. J. Linsley, Phys. Rev. Lett. **10**, 146 (1963).
23. D. M. Edge, A. C. Evans, H. J. Garmston, *et al.*, J. Phys. A **6**, 1612 (1973).
24. C. J. Bell *et al.*, J. Phys. A **7**, 990 (1974).
25. D. D. Krasilnikov, A. I. Kuzmin, J. Linsley, *et al.*, J. Phys. A **7**, 176 (1974).
26. A. V. Glushkov, Pis'ma Zh. Éksp. Teor. Fiz. **78**, 1265 (2003) [JETP Lett. **78**, 745 (2003)].
27. A. A. Ivanov, A. D. Krasilnikov, and M. I. Pravdin, in *Proc. 28th ICRC, Tsukuba, 2003*, Vol. 1, p. 341.
28. A. A. Mikhaĭlov, Izv. Akad. Nauk, Ser. Fiz. **63**, 557 (1999).
29. A. A. Mikhaĭlov, Pis'ma Zh. Éksp. Teor. Fiz. **72**, 233 (2000) [JETP Lett. **72**, 160 (2000)].
30. A. A. Mikhaĭlov, Izv. Akad. Nauk, Ser. Fiz. **66**, 1596 (2002).

31. A. Mikhailov and G. Nikolayeva, in *Proc. 28th ICRC, Tsukuba*, 2003, Vol. 1, p. 417.
32. M. M. Winn *et al.*, *Catalog of Highest Energy Cosmic Rays. Giant Extensive Air Showers* (World Data Center C2 for Cosmic Rays, Mito, Japan, 1986), No. 2.
33. N. Hayashida, M. Nagano, D. Nishikawa, *et al.*, Astropart. Phys. **10**, 303 (1999).
34. J. A. Bellido, B. W. Clay, R. B. Dawson, and M. Johnston-Hollitt, astro-ph/0009039.
35. A. G. Lyne and F. Graham-Smith, *Pulsar Astronomy* (Cambridge University Press, Cambridge, 1990).
36. P. G. Tinyakov and I. I. Tkachov, Pis'ma Zh. Éksp. Teor. Fiz. **74**, 499 (2001) [JETP Lett. **74**, 445 (2001)].
37. A. V. Uryson, Zh. Éksp. Teor. Fiz. **116**, 1121 (1999) [JETP **89**, 597 (1999)].
38. A. Dressler, Nature **350**, 391 (1991).
39. H. F. Klapdor-Kleingrothaus and K. Zuber, *Particle Astrophysics* (Usp. Fiz. Nauk, Moscow, 2000).
40. V. L. Yanchilin, *Uncertainty, Gravitation, Space* (Editorial URSS, Moscow, 2003) [in Russian].
41. L. Anchordoqui, H. Goldberg, T. McCauley, *et al.*, hep-ph/0011097.
42. D. Fargion, B. Mele, and A. Salis, Astrophys. J. **517**, 725 (1999).
43. T. J. Weiler, Astropart. Phys. **11**, 303 (1999).
44. L. G. Dedenko, T. M. Roganova, G. F. Fedorova, and E. Yu. Fedunin, Pis'ma Zh. Éksp. Teor. Fiz. **78**, 131 (2003) [JETP Lett. **78**, 101 (2003)].
45. A. B. Kaĭdalov, K. A. Ter-Martirosyan, and Yu. M. Shabel'skiĭ, Yad. Fiz. **43**, 1282 (1986) [Sov. J. Nucl. Phys. **43**, 822 (1986)].
46. A. B. Migdal, Phys. Rev. **103**, 1811 (1956).
47. K. Greisen, Phys. Rev. Lett. **16**, 748 (1966).
48. G. T. Zatsepin and V. A. Kuz'min, Pis'ma Zh. Éksp. Teor. Fiz. **4**, 78 (1966) [JETP Lett. **4**, 53 (1966)].

Translated by A. Isaakyan

Physics of Atomic Nuclei, Vol. 68, No. 2, 2005, pp. 259–266. Translated from Yadernaya Fizika, Vol. 68, No. 2, 2005, pp. 283–291.

ELEMENTARY PARTICLES AND FIELDS
Experiment

Direct Observation of Muon-Pair Production by High-Energy Muons in the Liquid-Argon Calorimeter BARS

V. B. Anikeev[1], S. N. Gurzhiev[1], S. P. Denisov[1], O. S. Zolina[2], S. R. Kelner[2], T. M. Kirina[2], R. P. Kokoulin[2], V. V. Lipaev[1], A. A. Petrukhin[2], A. M. Rybin[1], F. Sergiampietri[3], and E. E. Yanson[2]

Received May 27, 2004

Abstract—Experimental data accumulated over a long-term exposure of the big liquid-argon spectrometer BARS at the Institute for High Energy Physics (IHEP, Protvino) in a horizontal flux of cosmic rays are analyzed with the aim of selecting events that correspond to muon-pair production by muons in the sensitive volume of the detector. The results obtained in this way make it possible to perform, for the first time, a direct experimental test of various theoretical estimates of the total cross section for electromagnetic muon-pair production by high-energy muons. *© 2005 Pleiades Publishing, Inc.*

1. INTRODUCTION

The production of muon pairs is a relatively rare process of the electromagnetic interaction of high-energy muons. In relation to the production of electron—positron pairs, muon pairs are generated at much shorter distances from the nucleus involved; therefore, the cross section for this process depends greatly on nuclear form factors and can serve as an additional source of information about their behavior. On the other hand, this process leads to the formation of narrow muon groups, which may be a source of a heavy background in various experiments performed at accelerators and in cosmic rays—such as those that are aimed at studying particles that decay to muons, seeking new muon-generation processes, and investigating inelastic muon scattering and multimuon events in extensive air showers.

The beginning of theoretical and experimental investigations into muon-pair production by muons dates back to the late 1960s, when it became possible technically to perform cumbersome calculations and when there appeared muon beams at accelerators and cosmic-ray muon detectors reaching dimensions that ensure the accumulation of fairly high statistics within a reasonable time interval. The first calculations of the cross sections for prompt muon-pair production by muons [1—4] were performed by numerically integrating the squared matrix element corresponding to the sum of dominant Feynman diagrams for this process. From the results obtained in this way, it was deduced that the respective total cross section is determined primarily by elastic muon interaction with the nucleus involved [4], quasielastic (noncoherent interaction with target protons) and inelastic interactions with nuclei playing a less significant role. It was also shown [1] that, at moderate muon energies, it is necessary to take into account exchange effects caused by the presence of identical particles in the final state. However, investigations conducted in [1—4] were aimed, by and large, at analyzing data from specific accelerator experiments, so that the calculations there were performed for concrete primary muon energies and target nuclei and for fixed energy thresholds for final-state particles.

The first attempt at deriving the cross section for muon-pair production by muons in a convenient analytic form was undertaken by Bugaev, Kotov, and Rosental' (BKR) [5]. The BKR formula for the cross section in question was obtained from the corresponding cross section for the production of electron—positron pairs [6] by merely replacing the electron mass by the muon mass. In doing this, use was made of the formula for the limiting case of complete screening, which is realized for muon pairs only at very high energies; also, the aforementioned effect of nuclear form factors was disregarded in [5]. As a result, the BKR formula yielded overestimated (sometimes by an order of magnitude) cross-section values, this leading to misinterpretation of relevant experimental data. Nonetheless, the BKR formula had been widely used for a long time [7—12].

For any degree of screening, the cross section with allowance for nuclear and atomic form factors was

---

[1] Institute for High Energy Physics, Protvino, Moscow oblast, 142284 Russia.

[2] Moscow Engineering Physics Institute (State University), Kashirskoe sh. 31, Moscow, 115409 Russia.

[3] Istituto Nazionale di Fisica Nucleare, Sezione di Pisa, via Livornese 1291, S. Pietro a Grado (PI), I-56010 Pisa, Italy.

obtained by Kelner, Kokoulin, and Petrukhin (KKP) in [13, 14] in the form of an analytic expression for the differential distribution with respect to muon energies. A comparison of the results based on this expression with the results of a numerical integration for specific energies and target nuclei [1, 3, 4] showed good agreement.

The first attempt at experimentally recording muon-pair production by muons was made in the experiment that was reported in [15] and which was performed in cosmic rays at large zenith angles; 33 events interpreted as muon triples formed in an iron target were found in that experiment. This number of events led to an exaggerated estimate of the cross section (approximately two orders of magnitude larger than the expected value). A much smaller upper limit on the cross section was obtained in [16] on the basis of underground measurements with a facility formed by a set of lead plates interspersed with a scintillator. The contradiction between the results of the two experiments in question stems from serious difficulties in reliably identifying muon pairs. The possible reason behind the misinterpretation of the data in [15] consisted in significantly underestimating the background of spurious tracks from electromagnetic showers generated by a muon—in particular, in disregarding correlations between the actuations of the detectors in different coordinate planes.

The cross section for muon-pair production was first measured in an accelerator experiment with a beam of 10.5-GeV muons incident on an iron target, the energy threshold for each final-state particle being 1.5 GeV [17]. The results of this experiment proved to be in good agreement with their counterparts obtained from numerical calculations by the Monte Carlo method, but it should be noted that the selection criteria used corresponded to a relatively small fraction of the total cross section (about 13% according to the estimate of the authors). Under similar conditions, the results of that experiment were confirmed by later measurements reported in [18]. Unfortunately, only the region of high transverse momenta (which is the most interesting from the point of view of studying the structure of the nucleons), where it is difficult to distinguish between trimuons originating from an electromagnetic process and the background associated with deep-inelastic processes (see, for example, [19]), was explored in accelerator experiments at higher muon energies.

An attempt at studying the production of muon pairs at an intermediate incident-muon energy of about 200 GeV was undertaken in experiments reported in [11, 12]. An excess above the value expected from muons in extensive air showers was observed in the MACRO experiment (which was performed in the Gran Sasso underground laboratory at a mean depth of 3800 g/cm^2) for pairs of muons (a third muon could be stopped in rock, or its trajectory could not be covered by the detector used) flying short distances (smaller than 1.6 m) apart. Quantitative agreement between this excess and the results of the calculations by the BKR formula was interpreted by the researchers who performed this experiment as evidence that they observed muon pairs. However, the calculations by the KKP formula in [13, 14, 20] revealed that the flux of muon couples and triples that is expected for the Gran Sasso depth is three times smaller. Obviously, it is necessary to seek other reasons for the excess of narrow muon pairs in the MACRO experiment (for example, an admixture of penetrating particles, including muons and hadrons formed via the photonuclear interaction of muons in the rock above the detector).

Thus, no reliable experimental data on the production of muon pairs by high-energy muons (of energy about 100 GeV) have been obtained so far. The main reason for this was that the experimental facilities used were inadequate to this task. In the present article, we analyze muon triples generated by muons from the horizontal cosmic-ray flux in the Big liquid-ARgon Spectrometer (BARS) at the Institute for High Energy Physics (IHEP, Protvino). The structure of this apparatus guarantees an efficient and unambiguous selection of events corresponding to muon-pair production within the sensitive volume of the spectrometer. Preliminary results of this investigation were presented at the conferences reported in [21, 22].

2. EXPERIMENTAL DATA

The BARS facility [23, 24] is a finely structured large-volume detector constructed for the tagged-neutrino facility at IHEP. The detector consists of two identical calorimeters, BARS-1 and BARS-2, filled with liquid argon. Each calorimeter contains 216 t of liquid argon, 154 t of it being in the sensitive volume. Two types of detecting elements—sections of ionization chambers and scintillation planes—are placed in cryostats. The layout of the detector is shown in Fig. 1.

The ionization chambers are formed by alternating grounded and signal aluminum plates, the latter being segmented into 48 strips of width 61 mm each that are separated by 2-mm gaps. The signal and grounded plates have a thickness of 3 and 6 mm, respectively. The signal strips in neighboring planes of the chambers are successively rotated through an angle of 120°, whereby a system of three coordinates in the cross section of the detector is formed. In each cell, the thickness of the liquid-argon layer is 2×24 mm; in each section of the chambers, there are 12 such two-gap structures (288 in the whole cryostat). Electronics for measuring ionization signals include low-noise preamplifiers, bipolar amplifying pulse shapers characterized by a pulse maximum at 2 μs and recovery time of 15 μs, and 12-bit analog-to-digital converters (ADC). The total number of spectrometric channels in each calorimeter is 13 824; a typical signal-to-noise ratio in recording a single muon in a calorimeter cell is about 4 : 1.

The triggering system of a calorimeter consists of 24 planes of scintillation counters based on polymethylmethacrylate (PMMA) and installed in front of the sections of the ionization chambers. Each plane consists of eight counters 22 mm thick and 334 mm wide. Scintillation light is collected by shifter bars placed between the counters to photomultiplier tubes positioned on the two sides. The time resolution of the triggering plane is about 5 ns (FWHM), while a typical efficiency of the detection of a single particle is 90 to 95%.

The outer diameter of the system of electrodes of the ionization chambers is approximately 3 m, while the total length of the detector is 18 m. The thickness of the calorimeter along the axis of the apparatus is 2880 g/cm^2 (138 radiation-length units, which is about 25 units of the hadron-interaction length). The mean matter density within the sensitive volume is 1.60 g/cm^3, while the mass content corresponds to 70.4% argon + 27.4% aluminum + 2.2% PMMA, with $Z/A = 0.461$ and $Z^2/A = 7.50$ being the respective mean values. The spectrometer energy resolution for electromagnetic cascades that was measured with a prototype is 4% at 1 GeV [25]. Good spectrometric properties of the detector are due to the fact that more than 65% of ionizing-cascade-particle energy is released in the working substance (liquid argon).

Since 1996, one of the BARS calorimeters (BARS-2) has been used to study muons in the horizontal flux of cosmic rays. The main objective of those experiments was to measure the energy spectrum of muons by the new muon-spectroscopy method based on employing the energy dependence of the cross section for the direct production of electron–positron pairs by muons (pairmeter method). Some preliminary results concerning the pairmeter method were presented in [26, 27]. Owing to a large target thickness, a low threshold, good tracking properties of the detector, and high statistics of events, the accumulated experimental data make it possible to perform simultaneously investigations into the interactions of high-energy muons and searches for rare events in cosmic rays.

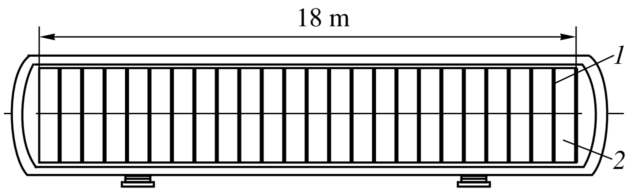

Fig. 1. Layout of the BARS calorimeter: (*1*) triggering scintillation counters and (*2*) sections of the ionization chambers.

In order to select muons arriving in a nearly horizontal direction, we used triple coincidences of signals from three groups of scintillation planes occurring at the beginning (2–4 planes), at the middle (12–14 planes), and at the end (18–20 planes) of the calorimeter. Triggering electronics were tuned in such a way as to ensure the detection of muons arriving from both sides of the facility. For events selected by triggering logic, the amplitudes of signals in calorimeter cells in excess of some threshold value (approximately 0.8 of the probable ionization generated by a single muon, or 28 counts of the ADC) were recorded. We processed data accumulated within the period from December 1996 to June 1998. Over 5480 hours of the "live" time of facility operation, 3.07 million muons arriving in the nearly horizontal direction were detected. For a physical analysis, we used 1.914 million tracks that traversed the third and the nineteenth plane of the scintillation counters (that is, at least two planes in each group of triggering planes). Under such selection conditions, the efficiency of the trigger for single muons exceeds 97%, the geometric factor of the detector is about 0.22 m^2 sr, and the track length within the sensitive volume is not shorter than 1900 g/cm^2. The interval of zenith angles is 75°–90°, with the mean value being 84°; the evaluated average energy of a muon is close to 70 GeV.

3. SELECTION OF MUON TRIDENTS

The selection of events corresponding to muon-pair production by muons is based on analyzing the longitudinal ionization profile within a ±40-cm corridor around a reconstructed muon track. For each event, ionization was measured at 200 to 288 points. For the resulting quantitative estimates to be justifiable, particular attention was given to reliability in identifying trimuons and to the possibility of measuring the parameters of an event. Therefore, we bounded the sensitive volume for the possible interaction vertex in the following way: on one hand, the interaction must occur not earlier than an incident particle reaches the 24th plane of ionization chambers after it had entered the internal volume of the calorimeter, in which case it is clear that a single muon was observed before the interaction event being considered; on the other hand, the residual path of the particles in the detector after the interaction event must not be shorter than 90 planes (900 g/cm^2, which is approximately equal to eight units of the hadron-interaction length, or more than 40 radiation-length units). The last condition specifies the minimum energy of each of the three muons in the final state (1.5 GeV). Since the expected number of muon tridents is very small (about 10^{-5} of the total number of events), the search for muon pairs was organized in two steps: a fast computer-aided selection aimed predominantly at reducing the number of candidates to an acceptable level was followed by a visual analysis of the remaining events.

The following criterion was used in the computer-aided selection. An event was considered as a candidate for muon pair if it involved a track segment of length 90 successive chamber planes where the measured ionization exceeded the threshold of 60 ADC counts (that is, more than approximately 1.7 of the probable ionization generated by a single muon) in 70 planes. The choice of the minimum number of planes (70) where signals were in excess of the threshold and the choice of the threshold value itself were optimized in such a way as to preserve a high efficiency of the selection of useful events and, at the same time, to ensure the maximum possible factor characterizing the rejection of the background (single muons). In order to verify the efficiency of the computer-aided selection, artificial trimuon profiles were formed from the measured longitudinal profiles of ionization caused by actual single muon events. In the most unfavorable case where the interaction vertex occurs in the vicinity of the end of a track in the detector (90 planes before leaving the detector) and where the trajectories of final particles diverge widely, the efficiency is close to 95% for the chosen selection parameters; it is improved fast for longer secondary tracks and for smaller angles of divergence. At these parameters, the background-rejection factor amounts to about 400. In all, 4816 candidate events were selected among the total number of 1.914 million muons.

Events selected by the computer code used involved predominantly "ordinary" muon interactions: single high-energy electromagnetic cascades (about 17%), chains of a few low-energy cascades initiated by delta electrons and electron–positron pairs from high-energy muons (about 69%), and nuclear showers resulting from inelastic muon interactions with target nuclei (about 14%). Of course, this classification is arbitrary to some extent since the boundaries between the classes (especially between the first two) are rather vague. However, it is important to emphasize that, owing to a characteristic shape of electromagnetic cascades (with dips between them to the level of ionization generated by a single particle) and to a "loose" structure of nuclear showers, which are often accompanied by short hadron tracks at large emission angles, these events differ strongly, as a rule, from the cases of muon-pair production by muons. We also note that the fraction of nuclear cascades in this sample is markedly greater than the ratio of nuclear and electromagnetic cascades at a commensurate energy that are initiated by cosmic-ray muons (about 5 to 10%), this being due to a long range of hadronic showers.

All 4816 events were independently viewed by three experts. In all cases, this resulted in selecting the same 22 events containing three genetically related muon tracks. These events can be partitioned into the following four groups:

(i) The first group includes seven events where the muon-interaction vertex is within the bounded sensitive volume of the calorimeter and where one observes ionization from a single muon before the interaction event and tripled ionization after it, all three particles emerging after the interaction event traverse more than 90 detector planes (900 g/cm^2). In all of these cases, one distinctly sees spatially separated particle tracks (at least in one of the three projections of the detector). It is of importance to emphasize, however, that the last feature was not crucial in selecting events—first of all, we applied criteria based on measuring the ionization profile. These seven events are cases of prompt muon-pair production by muons. In one of the events, the secondary muons originate from the region of an electromagnetic cascade whose energy is about 30 GeV. In principle, this muon pair could be produced by a cascade photon. The probability of such a process, as well as the probabilities of processes occurring in nuclear cascades and mimicking the reaction under study, is estimated in Appendices A and B.

(ii) The second group contains two events where the interaction vertex is also within the sensitive volume, but where the length of one (in one event) or both (in another event) secondary tracks (500–700 g/cm^2) is less than the threshold value. We did not include these events in the ultimate statistics, since the estimate of the efficiency of their selection is less reliable; moreover, the background level becomes higher for short secondary tracks.

(iii) Further, there are twelve narrow muon groups that traversed the detector and which admit interpretation in terms of cases in which muon-pair production by muons occurs in surrounding matter (neutrino-channel absorber, steel toroids of the magnetic spectrometer, other parts of the facility,

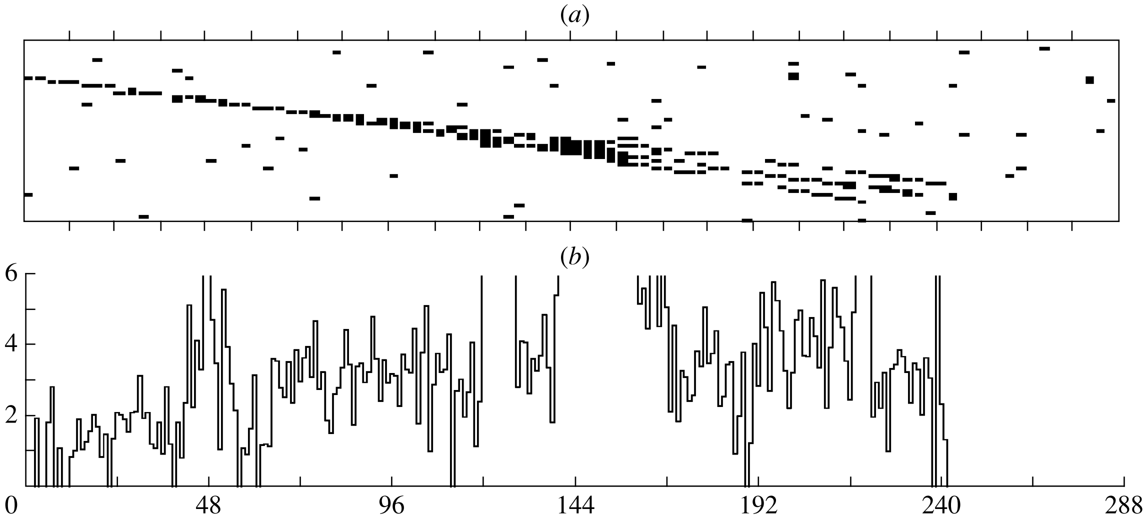

Fig. 2. Muon-pair production by a cosmic-ray muon in the BARS volume: (*a*) one of the three projections of the detector (points correspond to calorimeter cells where signals are in excess of the threshold) and (*b*) ionization (in "muon-peak" units) measured along a reconstructed muon track (the number of an ionization-chamber plane is plotted along the abscissa).

etc.). These events are characterized by diverging tracks, a typical spacing between the tracks being less than 50 cm at the inlet of the facility; the angles between the tracks range between 5 and 100 mrad. Some of these tracks end in the calorimeter. In such cases, the interaction vertex is not observed, and the respective events can be interpreted in different ways (for example, in terms of muons from hadron decays in nuclear showers formed beyond the detector). Since the reconstruction of the interaction vertex—and, hence, the determination of the substance in which the interaction event in question occurred—is ambiguous and since the estimation of the detection probability and of the efficiency of selection is rather difficult for such events, we did not use them in the ensuing quantitative analysis.

(iv) Finally, one event involves a group of three muons formed in the atmosphere. In this case, the particle tracks are parallel to one another within the errors of the measurements (less than 3 mrad). The distance between two muons is about 30 cm, the third track being 2 m apart. The zenith angle for this event is 81°. It is interesting to note that all three muons are accompanied by a few secondary electromagnetic cascades, which are indicative of high particle energies (about a few TeV).

An example of an event from the first group is given in Fig. 2. The interaction vertex where there occurs muon-pair production is near the 65th plane of the ionization chamber, and this is reflected in the transition from ionization typical of a single particle to the three-particle level. Individual narrow peaks against the background of the longitudinal profile correspond to low-energy electromagnetic cascades initiated by muons.

4. COMPARISON WITH THE RESULTS OF THE CALCULATIONS

At a specific energy threshold for secondary particles, the number of muon triples that is expected in the case where the interaction vertex is within the sensitive volume of the facility can be calculated by the formula

$$N_{\text{exp}} = \int \sigma(E, E_{\text{thr}}) R(E) dE, \qquad (1)$$

where $\sigma(E, E_{\text{thr}})$ is the total cross section (in cm^2/g) for muon-pair production by a muon of primary energy E in a target material, the energies of all final-state particles being in excess of E_{thr}, and $R(E)dE$ is the total range of muons (in g/cm^2 units) that traversed the facility and which have energies in the range between E and $E + dE$ within the sensitive volume of the detector. In the calculation of $R(E)$, we employed the formulas from [28] for the energy and angular distributions of muons produced in the decays of pions and kaons in the upper layers of the atmosphere, setting the exponent of the integrated spectrum of parent mesons to $\gamma = 1.70$ and the ratio of the generation spectra to $K/\pi = 0.15$. At these parameter values, the muon spectrum describes well the results of the measurements with a magnetic spectrometer from [29] at a zenith angle of $\theta = 85°$ for muon energies in the region $E > 50$ GeV; the majority of other data on the muon spectrum in the range from a few GeV to a few TeV are also in agreement with this model of the spectrum at γ values from 1.6 to 1.8.

In the calculations, we used two different analytic expressions (from [5] and from [14]) for the muon-

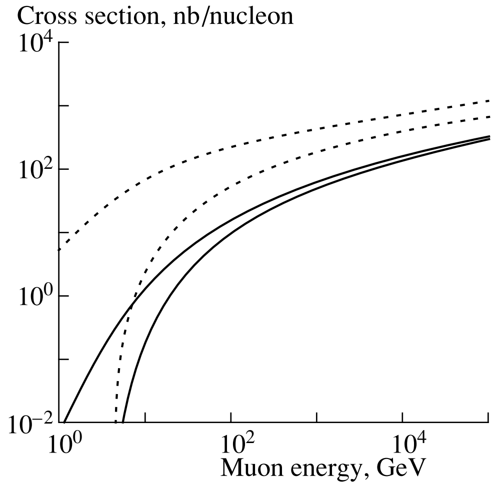

Fig. 3. Cross section for muon-pair production by a muon in the BARS material according to calculations by the formulas from (dashed curves) [5] and (solid curves) [14]. The upper curves represent the total cross-section value ($E_{\text{thr}} = \mu$), while the lower curves correspond to the muon threshold energy of $E_{\text{thr}} = 1.5$ GeV.

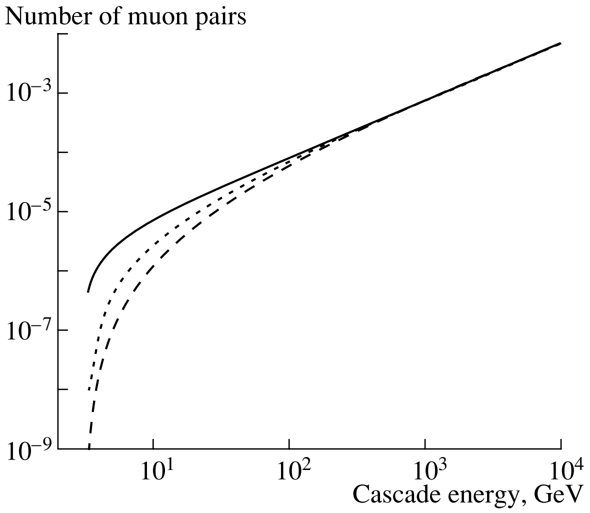

Fig. 4. Average number of muon pairs formed by cascade photons for (solid curve) a primary photon, (dotted curve) a primary electron, and (dashed curve) a primary electron–positron pair. The minimum muon energy E_{thr} is 1.5 GeV for each particle from a pair.

pair-production cross section. The total cross section obtained on the basis of these formulas for the process in the BARS material (about 70% argon and 30% aluminum) for two values of the minimal energy of final particles [$E_{\text{thr}} = \mu$ (muon mass) and 1.5 GeV] is given in Fig. 3. From this figure, one can see that the difference of the two theoretical cross sections is very large in the vicinity of the threshold and that it decreases slowly with increasing muon energy, remaining rather large (within a factor of 3 to 5) in the TeV energy range.

As was indicated above, the average muon energy was about 70 GeV in our experiment. Owing to a fast increase in the cross section near the threshold, the average energy of muons producing muon pairs was, however, much higher, about 270 GeV at $E_{\text{thr}} =$ 1.5 GeV. At such energies, the cross section at $E_{\text{thr}} =$ 1.5 GeV is about 70% of the total cross section.

The expected number of events involving muon-pair production by muons is given in the first and the second column of the table according to the calculations by the theoretical formulas from [5] and [14], respectively. A variation of 0.10 in the exponent γ of the parent-meson spectrum changes the expected number of events by 10%, while a change of 0.05 in the K/π ratio has virtually no effect on the results of the calculations. The estimated number of background events associated with electromagnetic and hadronic showers is also presented in the table. The observed number (seven) of events satisfying the above selection criteria agrees well with the results of the calculations based on the KKP formula.

Expected and observed number of muon triples

Direct muon-pair production		Mimicking in showers		Observed number
[5]	[14]	electro-magnetic	nuclear	
48	8.9	0.3	<0.94	7

5. CONCLUSION

With the aid of the liquid-argon spectrometer BARS, we have studied the rare process of muon-pair production by muons. The unique properties of the BARS detector—a combination of large dimensions (in nuclear and radiation-length units) with a fine segmentation in the longitudinal and the transverse dimension, a good energy resolution for electromagnetic showers, and a high efficiency of detection of particles producing a minimal ionization—has made it possible to single out reliably, for the first time, events involving the electromagnetic production of muon pairs by cosmic-ray muons of energy as high as a few hundred GeV. A comparison of the results obtained in this way with theoretical estimates has revealed that the KKP approximation is consistent with experimental data, but that the BKR formula leads to markedly exaggerated values for the total cross section.

ACKNOWLEDGMENTS

We are grateful to the directorate and the technical staff of IHEP for support of our investigations during

the long-term exposure of the BARS spectrometer to cosmic rays.

This work was supported by the Russian Foundation for Basic Research (project nos. 99-02-18353, 02-02-17018), the federal targeted program "Integration," and a presidential grant (no. 1305.2003.2).

APPENDIX A

Production of Muon Pairs by Photons in Electromagnetic Showers

Apart from being directly produced by muons, muon pairs may also be generated by secondary processes in electromagnetic cascades initiated by muons propagating in a target material. First of all, this is the process of muon-pair production by real photons of a cascade. In order to estimate the probability of such imitations, we applied the computational procedure employed in [30].

The average number of muon pairs produced in a cascade with an energy ε can be estimated as the convolution of the total cross section $\sigma_{\mu\mu}(\omega, E_{\text{thr}})$ for the process with the equilibrium range $g(\varepsilon, \omega)$ of photons in a cascade, where ω is the photon energy and E_{thr} is the minimum energy of muons that is determined by selection criteria. Only high-energy photons are of importance for the formation of muon pairs; therefore, one can employ approximation A of cascade theory. Since the high-energy section of the photon spectrum depends on the sort of particle that initiated the cascade being considered, the average number of muon pairs takes different values for a primary photon, a primary electron, or a primary electron–positron pair (and, accordingly, for cascades initiated in different muon-interaction processes such as bremsstrahlung, the production of delta electrons, and the generation of electron–positron pairs).

Simple formulas for approximating the spectra of cascade photons are given in [30]. We took from [31] the analytic expression that describes the cross section for muon-pair production by a photon and which is valid for any degree of screening with allowance for a nuclear form factor. Figure 4 displays the average number of muon pairs that was calculated as a function of the cascade energy (for the minimum muon energy of $E_{\text{thr}} = 1.5$ GeV, in accordance with the selection criteria used in our analysis). The probability of muon-pair production grows almost linearly with the cascade energy everywhere, with the exception of the threshold region. However, it is always small in the energy range being considered. For the statistics subjected to the analysis here, integration over the energy spectrum of cascades initiated by electromagnetic muon interactions in the sensitive volume of the BARS spectrometer yields a value of 0.3 for the average number of background events, this being much less than the observed number of muon triples. On the other hand, the above value does not rule out the possibility that one of the selected events (featuring secondary muons that issue from the region of an electron–photon shower—see the respective discussion in Section 3) was due to the production of a muon pair by a cascade photon.

The contribution of other electromagnetic processes—for example, the prompt muon-pair production by cascade electrons—is small and is disregarded, since the total range of high-energy cascade electrons is commensurate with the photon range and since the cross section for this process is much smaller than the cross section for pair production by a photon (next order in the fine-structure constant α).

APPENDIX B

Upper Limit on Imitations from Nuclear Showers

Yet another possible source that could mimic muon triples in the experiment being discussed is associated with hadrons in nuclear–electromagnetic showers that are initiated upon the inelastic interaction of muons in a target. It should be emphasized, however, that, within the scheme used here to analyze data, such imitations are possible only in the case where the energy transfer and the hadron multiplicity are low in the interaction event, so that it is difficult to recognize the respective nuclear shower.

The probability that two hadrons from a shower traverse, without being involved in secondary interactions, a thickness of 900 g/cm^3, which is specified by the selection criteria used, is very small. Hadron decays involving the production of muons in flight are more hazardous. For example, the probability of the decay of a 2-GeV pion within the BARS spectrometer (the average matter density of its material is 1.6 g/cm^3) is about 1%. Nuclear showers featuring one long-range secondary particle were observed both in experimental data and in the results of simulations.

In order to estimate the background associated with muon-pair production by secondary hadrons, we used simulated events. A total Monte Carlo simulation of the BARS response was performed on the basis of a modified version of the GEANT 3.21 package. Since the cross section for the photonuclear interaction of a muon was considerably underestimated in the original code [32], the formulas for the inelastic-muon-interaction cross section from [33], which involve the energy-dependent parametrization of the photon–nucleon cross section [34] and the corrections for the screening of a nucleus within the vector-meson-dominance model [35], were used to describe this process. A more detailed description of the simulation procedure can be found in [36].

We have analyzed 4.72 million simulated events (this number is approximately 2.5 times greater than the number of experimental events). Of these, approximately 16 000 contain inelastic muon interactions involving an energy transfer in excess of 3 GeV. In the latter sample, 1503 events passed the criteria of the preliminary computer-aided selection (see Section 3) of candidates for muon pairs. We note that the frequency of such events is in reasonable agreement with that observed experimentally (approximately 670 candidates featuring nuclear showers per 1.9 million recorded muons). No event that could be associated with the case of muon-pair production by a muon was found at the stage of visual inspection. This means that the upper limit on the average number of such imitations in the experimental-data sample analyzed here is 0.94 at a 90% confidence level.

REFERENCES

1. M. J. Tannenbaum, Phys. Rev. **167**, 1308 (1968).
2. M. N. Kobrinskiĭ and F. F. Tichonin, Yad. Fiz. **15**, 1238 (1972) [Sov. J. Nucl. Phys. **15**, 685 (1972)].
3. V. Barger, W. Y. Keung, and R. J. N. Phillips, Phys. Rev. D **20**, 630 (1979).
4. A. A. Akhundov *et al.*, Yad. Fiz. **31**, 241 (1980) [Sov. J. Nucl. Phys. **31**, 127 (1980)].
5. É. V. Bugaev, Yu. D. Kotov, and I. L. Rozental', *Cosmic Muons and Neutrinos* (Atomizdat, Moscow, 1970), p. 38 [in Russian].
6. S. R. Kel'ner, Yad. Fiz. **5**, 1092 (1967) [Sov. J. Nucl. Phys. **5**, 778 (1967)].
7. S. R. Kelner, Yu. D. Kotov, and V. M. Logunov, in *Proceedings of the 11th International Conference on Cosmic Rays, Budapest, 1969*, Ed. by A. Somogiy; Acta Phys. Acad. Sci. Hung. **29** (Suppl. 4), 299 (1970).
8. S. R. Kel'ner, Yu. D. Kotov, and V. M. Logunov, Yad. Fiz. **21**, 763 (1975) [Sov. J. Nucl. Phys. **21**, 394 (1975)].
9. V. A. Kudryavtsev and O. G. Ryazhskaya, in *Proceedings of the 25th International Cosmic Ray Conference, Durban, 1997*, Ed. by M. S. Potgieter *et al.*, Vol. 6, p. 405.
10. V. A. Kudryavtsev and O. G. Ryazhskaya, Nuovo Cimento C **21**, 171 (1998).
11. MACRO Collab. (G. Battistoni *et al.*), Nucl. Phys. B (Proc. Suppl.) **75A**, 394 (1999).
12. M. Ambrosio *et al.*, Phys. Rev. D **60**, 032001 (1999).
13. S. R. Kelner, R. P. Kokoulin, and A. A. Petrukhin, in *Proceedings of the 26th International Cosmic Ray Conference, Salt Lake City, 1999*, Ed. by D. Kieda *et al.*, Vol. 2, p. 20.
14. S. R. Kelner, R. P. Kokoulin, and A. A. Petrukhin, Yad. Fiz. **63**, 1690 (2000) [Phys. At. Nucl. **63**, 1603 (2000)].
15. M. L. Morris and R. O. Stenerson, Nuovo Cimento B **53**, 494 (1968).
16. J. C. Barton and I. W. Rogers, in *Proceedings of the 11th International Conference on Cosmic Rays, Budapest, 1969*, Ed. by A. Somogiy; Acta Phys. Acad. Sci. Hung. **29** (Suppl. 4), 259 (1970).
17. J. J. Russel *et al.*, Phys. Rev. Lett. **26**, 46 (1971).
18. J. LeBritton *et al.*, Phys. Rev. D **23**, 1 (1981).
19. D. Bollini *et al.*, Nucl. Phys. B **199**, 27 (1982).
20. V. V. Kudryavtsev, E. V. Korolkova, and N. J. C. Spooner, Phys. Lett. B **471**, 251 (1999).
21. V. B. Anikeev, S. P. Denisov, S. N. Gurzhiev, *et al.*, in *Proceedings of the 27th International Cosmic Ray Conference, Hamburg, 2001*, Ed. by K.-H. Kampert *et al.* (Copernicus Gesellschaft, Hamburg, 2001), Vol. 3, p. 962.
22. V. B. Anikeev, S. N. Gurzhiev, S. P. Denisov, *et al.*, Izv. Akad. Nauk, Ser. Fiz. **65**, 1649 (2001).
23. F. Sergiampietri *et al.* (Pisa—Serpukhov Collab.), in *Proceedings of the 4th International Conference on Calorimetry in High Energy Physics, La Biodola, Italy, 1993*, Ed. by A. Menzione and A. Scribano (World Sci., Singapore, 1994), p. 357.
24. V. B. Anikeev *et al.*, Nucl. Instrum. Methods Phys. Res. A **419**, 596 (1998).
25. C. Cerri *et al.*, Nucl. Instrum. Methods Phys. Res. A **227**, 227 (1984).
26. V. B. Anikeev, S. P. Denisov, G. Gennaro, *et al.*, in *Proceedings of the 27th International Cosmic Rays Conference, Hamburg, 2001*, Ed. by K.-H. Kampert *et al.* (Copernicus Gesellschaft, Hamburg, 2001), Vol. 3, p. 958.
27. V. B. Anikeev, S. N. Gurzhiev, A. G. Denisov, *et al.*, Izv. Akad. Nauk, Ser. Fiz. **65**, 1646 (2001).
28. L. V. Volkova, Preprint No. 72, FIAN (Lebedev Institute of Physics, USSR Academy of Sciences, Moscow, 1969).
29. O. C. Allkofer *et al.*, Nucl. Phys. B **259**, 1 (1985).
30. V. M. Aynutdinov *et al.*, Astropart. Phys. **14**, 49 (2000).
31. V. P. Kokoulin and A. A. Petrukhin, in *Cosmophysics*, Ed. by V. V. Dmitrienko (Energoatomizdat, Moscow, 1987), p. 76.
32. *GEANT—Detector Description and Simulation Tool. CERN Program Library Long Writeup*, W5013 (Geneva, 1994).
33. V. V. Borog and A. A. Petrukhin, in *Proceedings of the 14th International Cosmic Ray Conference, Munich, 1975*, Ed. by K. Pinkau *et al.*, Vol. 6, p. 1949.
34. D. O. Caldwell *et al.*, Phys. Rev. Lett. **42**, 553 (1979).
35. S. J. Brodsky, F. E. Close, and J. F. Gunion, Phys. Rev. D **6**, 177 (1972).
36. V. B. Anikeev *et al.*, Izv. Akad. Nauk, Ser. Fiz. **63**, 577 (1999).

Translated by A. Isaakyan

Physics of Atomic Nuclei, Vol. 68, No. 2, 2005, pp. 267–278. Translated from Yadernaya Fizika, Vol. 68, No. 2, 2005, pp. 292–303.
Original Russian Text Copyright © 2005 by Paston, Prokhvatilov, Franke.

ELEMENTARY PARTICLES AND FIELDS
Theory

Calculation of the Mass Spectrum of QED-2 in Light-Front Coordinates

S. A. Paston[*], **E. V. Prokhvatilov, and V. A. Franke**

Institute of Physics, St. Petersburg State University, Ul'yanovskaya ul. 1, St. Petersburg, 198904 Russia

Received January 12, 2004; in final form, July 14, 2004

Abstract—With the aim of a further investigation of the nonperturbative Hamiltonian approach in gauge field theories, the mass spectrum of QED-2 is calculated numerically by using the corrected Hamiltonian that was constructed previously for this theory on the light front. The calculations are performed for a wide range of the ratio of the fermion mass to the fermion charge at all values of the parameter $\hat{\theta}$ related to the vacuum angle θ. The results obtained in this way are compared with the results of known numerical calculations on a lattice in Lorentz coordinates. A method is proposed for extrapolating the values obtained within the infrared-regularized theory to the limit where the regularization is removed. The resulting spectrum agrees well with the known results in the case of $\theta = 0$; in the case of $\theta = \pi$, there is agreement at small values of the fermion mass (below the phase-transition point). *© 2005 Pleiades Publishing, Inc.*

1. INTRODUCTION

The Hamiltonian approach to quantum-field theory in light-front coordinates $x^{\pm} = (x^0 \pm x^3)/\sqrt{2}$, $x^{\perp} = (x^1, x^2)$, where x^+ plays the role of time [1], is one of the nonperturbative methods for solving the problem of strong interaction [2, 3]. Within this approach, the quantization is performed in the $x^+ = 0$ plane, the generator P_+ of a shift along the x^+ axis playing the role of the Hamiltonian. The generator P_- of a shift along the x^- axis does not displace the quantization surface; therefore, it is a kinematical generator (according to Dirac's terminology) in contrast to the dynamical generator P_+. As a result, the momentum operator P_- appears to be quadratic in fields and does not depend on interaction. At the same time, the operator P_- is nonnegative and has zero eigenvalue only on the physical vacuum. This results in that the field Fourier modes corresponding to positive and negative values of p_- play the role of, respectively, creation and annihilation operators over the physical vacuum and can be used to construct the Fock space. Thus, we see that, in light-front coordinates, the physical vacuum formally coincides with the mathematical vacuum.

The spectrum of bound states in the theory can be sought by solving the Schrödinger equation

$$P_+|\Psi\rangle = p_+|\Psi\rangle \tag{1}$$

in the subspace specified by fixed p_- and $p_\perp$ and by employing the expression $m^2 = 2p_+p_- - p_\perp^2$ for the mass. This search for bound states can be performed beyond perturbation theory—for example, with the aid of the so-called method of discrete light-cone quantization [2, 4].

However, the light-front Hamiltonian formalism involves a specific divergence at $p_- = 0$ [2, 3], and it must be regularized. The introduction of a cutoff $|p_-| \geq \varepsilon > 0$, which violates Lorentz and gauge invariance, is one of the methods for its regularization. A cutoff $|x^-| \leq L$ that involves imposing (anti)periodic boundary conditions in x^- (discrete light-cone quantization method, which respects gauge invariance) is yet another possible regularization. In this case, the lightlike momentum p_- becomes discrete ($p_- = p_n = \pi n/L$, where n is an integer), the field zero mode corresponding to $n = 0$ being separated explicitly. In principle, the canonical formalism makes it possible to express this zero mode in terms of other modes by solving the constraint equation, but this is difficult as a rule [5, 6].

The regularization of the above divergence usually renders a theory in light-front coordinates nonequivalent to its conventional formulation in Lorentz coordinates [7–9]. This can be revealed even in the lowest orders of perturbation theory [10]. As a result, there arises the problem of correcting the canonical light-front Hamiltonian (which is the result of a "naive" canonical quantization in light-front coordinates)—that is, the problem of seeking counterterms to it that compensate for the above distinctions between the Hamiltonians. If this problem can be solved for a specific theory in all orders of perturbation theory, the resulting corrected light-front Hamiltonian can then be used to perform nonperturbative calculations.

The aforementioned formal coincidence of the physical and the mathematical vacuum becomes

---

[*] e-mail: `paston@pobox.spbu.ru`

rigorous only after the introduction of regularization, upon which the vicinity of the point $p_- = 0$ is eliminated—for example, after the introduction of the cutoff $|p_-| \geq \varepsilon > 0$. If the corrected light-front Hamiltonian can be constructed for a theory regularized in this way, then vacuum effects inherent in the original theory in Lorentz coordinates must be taken into account with the aid of additional terms of this Hamiltonian.

The problem of constructing the corrected canonical light-front Hamiltonian was successfully solved both for nongauge field theories of the Yukawa model type [11] and for QCD in the gauge $A_- = 0$ [12]. In the last case, however, the corrected light-front Hamiltonian was constructed only for specific ultraviolet and infrared regularizations violating gauge invariance. As a result, it appears that the corrected Hamiltonian involves a large number of indeterminate coefficients; only for some, a priori unknown, dependence of these coefficients on the regularization parameter does it reproduce, in the limit where the regularization is removed, the results of the Lorentz-covariant theory in all orders of perturbation theory. The practical calculations with the resulting Hamiltonian are very cumbersome because of the presence of unknown coefficients and because of a complicated structure of regularization (the regularized Hamiltonian involves a large number of additional fields).

In view of these circumstances, it is desirable to seek alternative methods for constructing the correct light-front Hamiltonian for gauge theories. In this connection, it is of interest to study the simplest models that admit a nonperturbative approach—in particular, those where one can study the behavior of infinite series of perturbation theory in all orders. Two-dimensional QED (QED-2) featuring a nonzero fermion mass (it is also known as the massive Schwinger model) is one of such models. In recent years, this two-dimensional model has attracted attention as an object of application of new methods for studying QCD, since it possesses many properties similar to those of QCD: confinement, chiral-symmetry breaking, and a topological θ vacuum (see [13] and references therein, as well as [14–16]). Information obtained in analyzing QED-2 can also be used in developing new methods that take into account nonperturbative vacuum effects and which are appropriate for constructing the light-front Hamiltonian for four-dimensional gauge theories. It should be noted that attempts at extracting information about four-dimensional gauge theories on the light front from an analysis of QED-2 were undertaken earlier [17].

For QED-2, there exists the possibility of going over to an equivalent scalar theory [18] (belonging to the type of the sine-Gordon model). This can be done by means of the bosonization procedure—that is, by going over from the fermion variables to boson ones [9, 19]. Upon this transition, the mass term of the fermion field in the QED-2 Hamiltonian becomes the interaction term for a scalar field, while the fermion mass M becomes the interaction constant in the boson theory. In the boson theory, the fact that the quantum vacuum in QED-2 has a nontrivial character associated with instantons (θ vacuum) [18, 15] is taken explicitly into account with the aid of the parameter θ in the interaction term. At $M = 0$, QED-2 reduces to the Schwinger model, while the equivalent boson theory appears to be free.

Perturbation theory for a boson theory (perturbation theory in the fermion mass) is usually referred to as chiral perturbation theory. For this kind of perturbation theory, ultraviolet finiteness was proven in [20, 21]. By analyzing perturbation theory in all orders of M, one can construct a corrected light-front Hamiltonian in terms of bosons and, after this, return to the fermion variables [21, 22]. It should be noted that boson perturbation theory differs radically from perturbation theory in the coupling constant of the original theory involving fermions (in QED-2, the latter perturbation theory does not exist at all because of infrared divergences, and this was the reason for introducing bosonization). Therefore, the resulting light-front Hamiltonian can take into account nonperturbative (in the conventional coupling constant) effects. But at the same time, it can fail to describe effects that are nonperturbative in the fermion mass—for example, phase transitions.

It is well known that, at least at the vacuum-angle value of $\theta = \pi$, there is a phase transition in QED-2 at some value of the fermion mass M (see, for example, [13]). It should be expected that, in the presence of a phase transition, which is accompanied by the appearance of nonzero vacuum expectation values of some operators, the correct light-front Hamiltonian must have different form for different phases, since the light-front vacuum itself is always trivial. Therefore, the results of calculations performed with a specific Hamiltonian must be valid only within one phase. The calculations performed in the present study corroborate these considerations and make it possible to determine the presence and an approximated position of the phase-transition point. A similar phenomenon was discovered previously in the simple two-dimensional $\lambda\varphi^4$ scalar-field model (see [9, 23], where an approximate method was proposed for going over to the Hamiltonian describing a different phase).

In this study, we perform a numerical nonperturbative calculation of the mass spectrum of the corrected light-front QED-2 Hamiltonian constructed in [21, 22]. The results obtained in this way are compared with the results of numerical calculations on a lattice in Lorentz coordinates from [13, 14].

2. CORRECTED LIGHT-FRONT HAMILTONIAN FOR QED-2

The QED-2 Lagrangian density in Lorentz coordinates has the form

$$L = -\frac{1}{4}F_{\mu\nu}F^{\mu\nu} + \bar{\Psi}(i\gamma^\mu D_\mu - M)\Psi, \qquad (2)$$

where $F_{\mu\nu} = \partial_\mu A_\nu - \partial_\nu A_\mu$, $D_\mu = \partial_\mu - ieA_\mu$, $A_\mu(x)$ is an Abelian gauge field, Ψ and $\bar{\Psi} = \Psi^+\gamma^0$ are two-component fermion fields of mass M, e is the coupling constant, and the matrices γ^μ are chosen in the form

$$\gamma^0 = \begin{pmatrix} 0 & -i \\ i & 0 \end{pmatrix}, \quad \gamma^1 = \begin{pmatrix} 0 & i \\ i & 0 \end{pmatrix}. \qquad (3)$$

In terms of Lorentz coordinates, the Lagrangian density for the boson theory equivalent to QED-2 can be written in the form [21]

$$L = \frac{1}{8\pi}\left(\partial_\mu\varphi\partial^\mu\varphi - m^2\varphi^2\right) + \frac{\gamma}{2}e^{i\theta} : e^{i\varphi} : + \frac{\gamma}{2}e^{-i\theta} : e^{-i\varphi} :, \qquad (4)$$

$$\gamma = \frac{Mme^C}{2\pi}, \qquad m = \frac{e}{\sqrt{\pi}},$$

where $C = 0.577\,216$ is the Euler constant, θ is a quantity that parametrizes the θ vacuum of the fermion formulation of the theory, and the normal-ordering symbol means that diagrams with connected lines are excluded in perturbation theory in γ (this corresponds to the usual meaning of the normal-ordering symbol in the Hamiltonian)—it is equivalent to perturbation theory in M.

In [21, 22], the light-front Hamiltonian generating a theory that describes a one-component fermion field ψ and which, in the limit where the regularization is removed, is equivalent in all orders in γ to the Lorentz-covariant theory specified by the Lagrangian density (4) was found by using the method described in the Introduction. The theory defined by this Hamiltonian was regularized by the discrete-light-cone-quantization method mentioned in the Introduction: the cutoff $|x^-| \le L$ and the antiperiodic boundary conditions in x^- were introduced for the field ψ. The resulting corrected light-front Hamiltonian has the form

$$H = \int\limits_{-L}^{L} dx^- \left(\frac{e^2}{2}\left(\partial_-^{-1}[\psi^+\psi]\right)^2 \qquad (5)\right.$$

$$- \frac{eMe^C}{4\pi^{3/2}}\left(e^{-i\hat{\theta}(M/e,\theta)}e^{i\omega}d_0^+ + \text{h.c.}\right)$$

$$\left. - \frac{iM^2}{2}\psi^+\partial_-^{-1}\psi\right),$$

where brackets denote the omission of the zero mode in x^-. The field ψ is expanded in terms of creation and annihilation operators as

$$\psi(x) = \frac{1}{\sqrt{2L}} \qquad (6)$$

$$\times \left(\sum_{n\ge1} b_n e^{-i\frac{\pi}{L}\left(n-\frac{1}{2}\right)x^-} + \sum_{n\ge0} d_n^+ e^{i\frac{\pi}{L}\left(n+\frac{1}{2}\right)x^-}\right),$$

$$\{b_n, b_{n'}^+\} = \{d_n, d_{n'}^+\} = \delta_{nn'}, \quad b_n|0\rangle = d_n|0\rangle = 0. \qquad (7)$$

The operator ω is the quantity canonically conjugate to the charge operator Q,

$$Q = \sum_{n\ge1} b_n^+ b_n - \sum_{n\ge0} d_n^+ d_n, \qquad (8)$$

which specifies the physical subspace of states, $|\text{phys}\rangle$:

$$Q|\text{phys}\rangle = 0. \qquad (9)$$

The operator ω possesses the properties that completely define it [9, 19],

$$e^{i\omega}|0\rangle = b_1^+|0\rangle, \quad e^{-i\omega}|0\rangle = d_0^+|0\rangle, \qquad (10)$$

and

$$e^{i\omega}\psi(x)e^{-i\omega} = e^{i\frac{\pi}{L}x^-}\psi(x), \qquad (11)$$

whence it follows that

$$e^{i\omega}b_n e^{-i\omega} = b_{n+1}, \quad e^{i\omega}d_n^+ e^{-i\omega} = d_{n-1}^+, \qquad (12)$$

$$n \ge 1, \qquad e^{i\omega}d_0^+ e^{-i\omega} = b_1.$$

The parameter $\hat{\theta}$ appearing in the Hamiltonian in (5) is a function of the ratio M/e and the vacuum angle θ. This function is defined as a perturbation-theory series in M; therefore, its explicit form remains unknown. Details concerning the appearance of the parameter $\hat{\theta}$ in the Hamiltonian are considered in the Appendix. Among other things, it is established there that, in the first-order in M, we have $\hat{\theta} = \theta$ and that, at any value of M, the parameter $\hat{\theta}$ is an odd function of θ and takes the value of $\hat{\theta} = \pi$ at $\theta = \pi$. In particular, it follows from the oddness of the function $\hat{\theta}(\theta)$ that $\hat{\theta} = 0$ at $\theta = 0$. It should be noted that the parameter $\hat{\theta}$ can be related to the values of the vacuum condensates in the Lorentz-covariant theory [21, 22].

In calculating the mass spectrum of bound states, the quantity $\hat{\theta}$ is an independent parameter of the theory, along with M and e; the relation between $\hat{\theta}$ and θ for $\theta \neq 0, \pi$ can in principle be found by comparing the results obtained by calculating the mass spectrum of the theory in Lorentz coordinates and the theory on the light front. We note that expression (5) for the corrected light-front Hamiltonian and the expression obtained upon the naive canonical quantization of the original fermion theory (2) in the light-front coordinates differ only by the addition of the second term, which is linear in the field operators and which depends on $\hat{\theta}$ and, hence, on the vacuum angle θ. Thus, we see that the naive canonical quantization does not take into account vacuum effects.

The lightlike-momentum operator P_- has the form

$$P_- = \sum_{n\geq 1} b_n^+ b_n \frac{\pi}{L}\left(n - \frac{1}{2}\right) + \sum_{n\geq 0} d_n^+ d_n \frac{\pi}{L}\left(n + \frac{1}{2}\right). \tag{13}$$

This expression is used to calculate the mass spectrum of bound states.

3. CALCULATION OF THE MASS SPECTRUM OF BOUND STATES

In order to find the mass spectrum of bound states of the theory, we will seek the eigenvalues E_i of the fermion light-front Hamiltonian (5) (the subscript i numbers eigenvalues in ascending order),

$$H|\Psi_i\rangle = E_i|\Psi_i\rangle, \tag{14}$$

in the subspace of physical states at a fixed value of the lightlike momentum (13). This subspace is specified by the conditions

$$Q|\Psi\rangle = 0, \qquad P_-|\Psi\rangle = p_-|\Psi\rangle. \tag{15}$$

In view of the antiperiodic boundary conditions and the first of the equalities in (15), the eigenvalue p_- has the form

$$p_- = \frac{\pi}{L}N, \tag{16}$$

where N is a nonnegative integer. The bound-state masses M_i are given by

$$M_i^2 = 2p_- E_i = \frac{2\pi}{L} N E_i. \tag{17}$$

If, in expression (5) for the Hamiltonian, one performs the change of integration variable $x^- = (L/\pi)\,z$ and uses expansion (6), the operator $(2\pi/L)NH$, which determines the quantities M_i^2, does not involve the regularization parameter L explicitly, but it depends on N. The quantity L affects the mass spectrum only through relation (16). Since p_- does not depend on L, one can deduce from (16) that the limit $N\to\infty$ corresponds to the limit where the regularization is removed, $L\to\infty$.

Since we use the antiperiodic boundary conditions, the subspace specified by the conditions in (15) appears to be finite. This occurs because there exists a minimum positive value of the lightlike momentum p_- $(\pi/(2L))$ and because the creation operators correspond only to positive values of p_-. An arbitrary state satisfying the conditions in (15) has the form

$$|\Psi\rangle = d_{N-1}^{+\,l_{2N}} \dots d_0^{+\,l_{N+1}} b_1^{+\,l_N} \dots b_N^{+\,l_1} \Big|0\Big\rangle, \tag{18}$$
$$l_i = 0, 1;$$
$$\sum_{i=1}^{2N} \operatorname{sgn}\left(N - i + \frac{1}{2}\right) l_i = 0,$$
$$\sum_{i=1}^{2N} \left|N - i + \frac{1}{2}\right| l_i = N,$$

where sgn is the signum function. The exponents l_i take here only the values of 0 or 1 by virtue of the anticommutation relations (7).

The finiteness of the subspace that is specified by formulas (18) and where it is necessary to solve Eq. (14) reduces the problem to finding the eigenvalues of an $N_{\text{mat}} \times N_{\text{mat}}$ finite matrix whose elements are specified by the matrix elements of the operator $(2\pi/L)NH$ between the states in (18). A precise solution to this problem can be found numerically. The resulting eigenvalues will determine the squares M_i^2 of bound-state masses. It should be noted that the dimension of the matrix, N_{mat}, grows fast as the parameter N increases—this is reflected in Table 1. In this study, the maximum achieved values of N are $N = 30$ for the cases of $\hat{\theta} = \theta = 0$ and $\hat{\theta} = \theta = \pi$ and $N = 28$ for the remaining cases.

As was mentioned above, the limit $N\to\infty$ corresponds to the removal of the regularization. For this reason, it is not sufficient to calculate the mass spectrum M_i^2 at the maximum accessible value of N—it is necessary to analyze the behavior of the spectrum as a function of N and to find a way to extrapolate the calculated values to the region of $N\to\infty$. We propose the following method of extrapolation. We introduce the quantity $u = 1/N$ and consider the function $M_i^2(u)$. It is necessary to extrapolate the values of this function to zero. Our calculations reveal that the bound-state masses are sensitive to the parity of N—that is, there can occur a sharp change in M_i^2 in response to the reversal of the parity of N. Therefore, it is reasonable to extrapolate the function

Table 1. Relation between the parameter N and the dimensionality N_{mat} of the space of states

N	9	10	12	14	16	18	20	22	24	26	28	29	30
N_{mat}	31	43	78	136	232	386	628	1003	1576	2437	3719	4566	5605

$M_i^2(u)$ to zero by two methods, individually in even and in odd values of N.

In order to extrapolate the function $M_i^2(u)$ to zero, we approximate the dimensionless ratio $M_i^2(u)/e^2$ by polynomials of various degrees by the least squares method. We denote by $P_i(n)$ the value of a polynomial of degree n at zero. It is obvious that the maximum degree n that can be used is less by unity than the number of points at which the approximated function is known. In the present study, this degree is equal to ten for the cases of $\hat{\theta} = \theta = 0$ and $\hat{\theta} = \theta = \pi$ and to nine in the remaining cases (as the minimum value of N, we adopt $N = 9$ in our calculations).

At different values of the ratio M/e and the parameter $\hat{\theta}$, there arise different types of behavior of $P_i(n)$ as a function of n. In some cases, the function $P_i(n)$ tends to a saturation and changes slowly with increasing n (see Fig. 1*a*). In these cases, the value at which the saturation occurs will be considered as the result of extrapolating the function $M_i^2(u)/e^2$ to zero.

Sometimes, there arise oscillations against the background of a saturation (see Fig. 1*b*). This occurs if the error with which one calculates $M_i^2(u)$ becomes sizable. In this case, a function that involves a noticeable random noise is approximated by a polynomial of high degree. This usually takes place at large values of the ratio M/e, in which case the coefficients of various terms of the Hamiltonian in (5) differ from one another considerably. Conceptually, this situation does not differ from the preceding one. The value obtained by averaging the oscillations in the region of saturation will then be treated as the result of the extrapolation of the function $M_i^2(u)/e^2$ to zero. It is obvious that the value found in this way will have an error larger than that in the preceding situation.

In the remaining cases, there arises the situation where the saturation cannot be seen—the function $P_i(n)$ strongly changes with increasing n (see Fig. 1*c*). In order to discriminate between this case and the two preceding versions of behavior of the function $P_i(n)$, we introduce the measure of its relative variation in response to a considerable variation in the degree n of the polynomial (in the region of accessible values), for example, in the form

$$\xi = \sqrt{\frac{(P_i(4) - P_i(9))^2}{(P_i(4)^2 + P_i(9)^2)/2}}. \qquad (19)$$

This quantity characterizes the error with which the calculated values of the mass spectrum M_i^2 describe its limiting value. We will assume that, if $\xi < 0.1$, the saturation takes place for the function $P_i(n)$, so that its value obtained at accessible n describes well the limiting value of the bound-state mass. But if $\xi > 0.1$, the calculated values of $P_i(n)$ do not characterize the behavior of M_i^2 in the limit $N \to \infty$. Moreover, the most frequently occurring form of the dependence $P_i(n)$ suggests its linearly decreasing character (Fig. 1*c*). The same applies to the original dependence of the quantity M_i^2 on the parameter N (see Fig. 1*d*). This gives sufficient grounds to assume that, at these values of the ratio M/e and the parameter $\hat{\theta}$, the quantity M_i^2 tends to $-\infty$ in the limit $N \to \infty$. The possible reasons behind this effect are discussed in the next section.

It should be noted that the choice of the value of 0.1 as a boundary one for the error in ξ and the specific choice of formula (19) are arbitrary to a considerable extent, but, unfortunately, our calculations could not provide a more rigorous way to discriminate between the situations where the limit of the quantity M_i^2 for $N \to \infty$ exists and where M_i^2 tends to $-\infty$ in the same limit.

4. RESULTS OF THE CALCULATIONS

4.1. Case of $\hat{\theta} = \theta = 0$

In the case of $\theta = 0$, the mass spectrum of the massive Schwinger model in Lorentz coordinates has received quite an adequate study (see [13, 16] and references therein). Usually, one studies the masses M_1 and M_2 of the first two bound states, which are referred to as a vector and a scalar state, respectively. The most accurate results were obtained in [14] with the aid of lattice calculations. Table 2 presents the values of $(M_1 - 2M)/e$ and $(M_2 - 2M)/e$ (it is precisely these quantities that were calculated in [14]) that were found by the method proposed here (with the aid of an extrapolation to the limit $N \to \infty$) and the values of these quantities from [14]. In the case of $\theta = 0$, the error ξ does not exceed the threshold of 0.1 at any values of the ratio M/e that were considered here (more specifically, $\xi < 0.01$ for M_1 and $\xi < 0.03$ for M_2)—that is, the above procedure of extrapolation to the limit $N \to \infty$ provides quite reliable results.

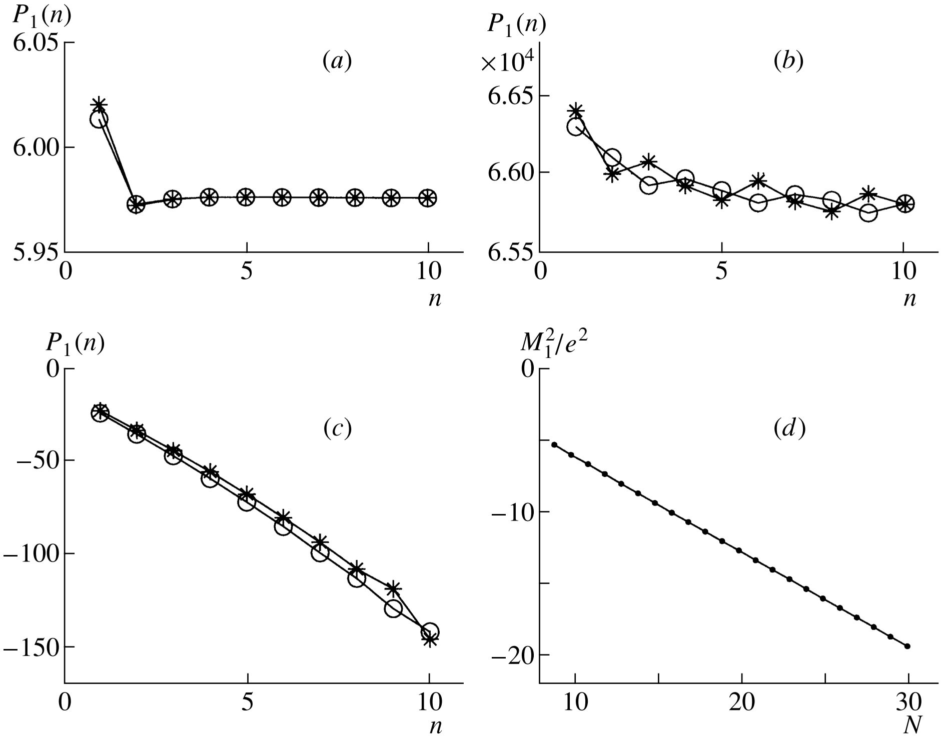

Fig. 1. Examples of the dependence of the extrapolated value of $P_1(n)$ on the degree n of the approximating polynomial (a–c) and example of the dependence of the mass of the lowest bound state on N (d) for the following parameter values: (a) $\hat{\theta} = \theta = 0$ and $M/e = 1$, (b) $\hat{\theta} = \theta = 0$ and $M/e = 2^7$, and (c, d) $\hat{\theta} = \theta = \pi$ and $M/e = 0.5$. The open circles and asterisks represent the results of the extrapolation in, respectively, even and odd values of N.

Figure 2a gives the extrapolated values of $(M_1 - 2M)/e$ along with the results obtained in [14]. The displayed errors were found from the corresponding values of the relative error ξ. In this figure, we also present the results corresponding to the maximum accessible value of $N = 30$—that is, the results obtained without extrapolation. It can be seen that these results are accurate only at small values of M/e; at the same time, the extrapolated values give a very good result up to $M/e = 8$. For $M/e > 8$, the extrapolated values reproduce a correct result within the error, which begins growing fast in this region. This is because the ratio M/e becomes large in this region, with the result that the absolute error of the difference $(M_1 - 2M)/e$ appears to be large even at a small relative error in the calculated quantity M_1^2/e^2. In order to depict the calculated results over the entire wide region of M/e, it is convenient to plot the normalized values

$$M_i^{\text{norm}} = \frac{M_i}{\sqrt{m^2 + (2M)^2}} \tag{20}$$

as was proposed in [16]. These normalized values possess the property that $M_1^{\text{norm}} \to 1$ both in the limit $M \to 0$ and in the limit $e \to 0$. In Fig. 2b, we show the curves for M_1^{norm} that correspond to those in Fig. 2a. One can see that the extrapolated values agree with the results from [14] to a high precision over the entire range of M/e.

In Fig. 3, the extrapolated values of M_1^{norm} that were calculated on the basis of the corrected Hamiltonian (5) are contrasted against the analogous values corresponding to the Hamiltonian obtained upon the naive light-front canonical quantization of the fermion theory specified by Eq. (2) {that is, to expression (5), where one discards the second term [see the comment before formula (13)]} and those corresponding to the Hamiltonian obtained upon the naive light-front canonical quantization of the boson theory specified by Eq. (4) {that is, to expression (5)} where one discards the third term and replaces $\hat{\theta}$ by θ, as was shown in [21, 22]. One can see from this figure that the naive light-front canonical quantization of the fermion formulation of the theory gives good results at large values of the ratio M/e—that is, in the region of weak coupling—while the analogous quantization of the boson formulation of the theories gives good results at small values of this ratio—that is, in the region of strong coupling. In order to obtain a light-front Hamiltonian that would provide good results at any values of the ratio M/e, it is necessary to implement the procedure of correcting the naive Hamiltonian, as was done in [21, 22].

In Fig. 4, we give the curves that represent the mass M_2 of the scalar bound state and which are analogous to those in Fig. 2a for the mass M_1 of the vector bound state. The behavior of the curves is identical to that in the case of the vector state: the values corresponding to $N = 30$ give good results only at small values of M/e, while the extrapolated values give very good results up to $M/e = 4$ and reproduce the correct result within the error for $M/e > 4$.

4.2. Case of $\hat{\theta} = \theta = \pi$.

The value of $\theta = \pi$ is of particular importance in the theory. It was predicted in [18] that, at $\theta = \pi$, a phase transition occurs in the theory at some value of the ratio M/e, so-called semiasymptotic fermions appearing in the region below the phase transition. In the region above the phase transition, as well as in the case where $\theta \neq \pi$, confinement takes place. More recent calculations, performed for $\theta = \pi$, revealed (see, for example, [13]) that the phase transition occurs at $M/e = 0.33$.

By means of lattice calculations, the mass of the lowest state in the electron—positron (two-particle) sector as a function of M/e at $\theta = \pi$ was studied in [13]. Within our approach, this mass corresponds to the quantity M_1.

In Fig. 5, the extrapolated values of M_1/e are given along with the results reported in [13]. One can see that, at small values of the ratio M/e, these results agree well, but that this agreement deteriorates as the ratio M/e grows. For $M/e > 0.14$, the extrapolation error ξ [see formula (19)] exceeds 0.1; therefore, the corresponding points on the graph are not quite reliable. For $M/e > 0.21$, there sharply appear very large oscillations in the behavior of the corresponding functions $P_1(n)$ describing the dependence of the extrapolated values on the degree of the approximating polynomial [see Section 3, the text before Eq. (19)]. At $M/e = 0.4$, the oscillations virtually disappear, whereupon the dependence begins displaying a linearly decreasing character. By way of example, this dependence at $M/e = 0.5$ is depicted in Fig. 1c, while the corresponding dependence of the quantity M_1^2/e^2 on N (it is also manifestly linear) is shown in Fig. 1d. For $M/e > 0.2$, the extrapolation error ξ exceeds 0.5.

The linear decrease in M_1^2/e^2 with increasing N gives sufficient grounds to assume that this quantity tends to $-\infty$ in the limit $N \to \infty$. This means that, at the above values of the ratio M/e and the parameter $\hat{\theta}$, the spectrum of the Hamiltonian in (5) upon the removal of the regularization appears to be not bounded from below, so that the theory specified by this Hamiltonian is incorrect. This situation is possible in the case where there arise effects that are purely nonperturbative from the point of view of perturbation theory in the fermion mass M since the Hamiltonian in (5) was constructed by analyzing such a perturbation theory (in all orders). Obviously, the presence of the aforementioned phase transition is a nonperturbative effect in this case. One can conclude that above the phase-transition point ($M/e = 0.33$), the theory generated by the light-front Hamiltonian (5) becomes incorrect; at the same time, the original theory in Lorentz coordinates, which is specified by Eq. (2), remains correct, this being corroborated by the results reported in [13] for the region above the phase-transition point.

Table 2. Masses of the vector (M_1) and scalar (M_2) bound states according to the calculations performed in the present study and in [14] at $\hat{\theta} = \theta = 0$ and various values of the ratio M/e

M/e	$(M_1 - 2M)/e$		$(M_2 - 2M)/e$	
	our study	[14]	our study	[14]
2^{-10}	0.564		1.13	
2^{-9}	0.564		1.13	
2^{-8}	0.563		1.13	
2^{-7}	0.563		1.14	
2^{-6}	0.561		1.15	
2^{-5}	0.559		1.17	
2^{-4}	0.554		1.20	
2^{-3}	0.545	0.543	1.23	1.22
2^{-2}	0.524	0.519	1.24	1.24
2^{-1}	0.489	0.485	1.20	1.20
2^{0}	0.445	0.448	1.12	1.12
2^{1}	0.393	0.394	0.99	1.00
2^{2}	0.339	0.345	0.84	0.85
2^{3}	0.295	0.295	0.75	0.68
2^{4}	0.279	0.243	0.74	0.56
2^{5}	0.302	0.198	0.84	0.45
2^{6}	0.368		1.08	
2^{7}	0.497		1.41	
2^{8}	0.619			

The appearance of the aforementioned strong oscillations of the functions $P_1(n)$ in the range $0.2 <$

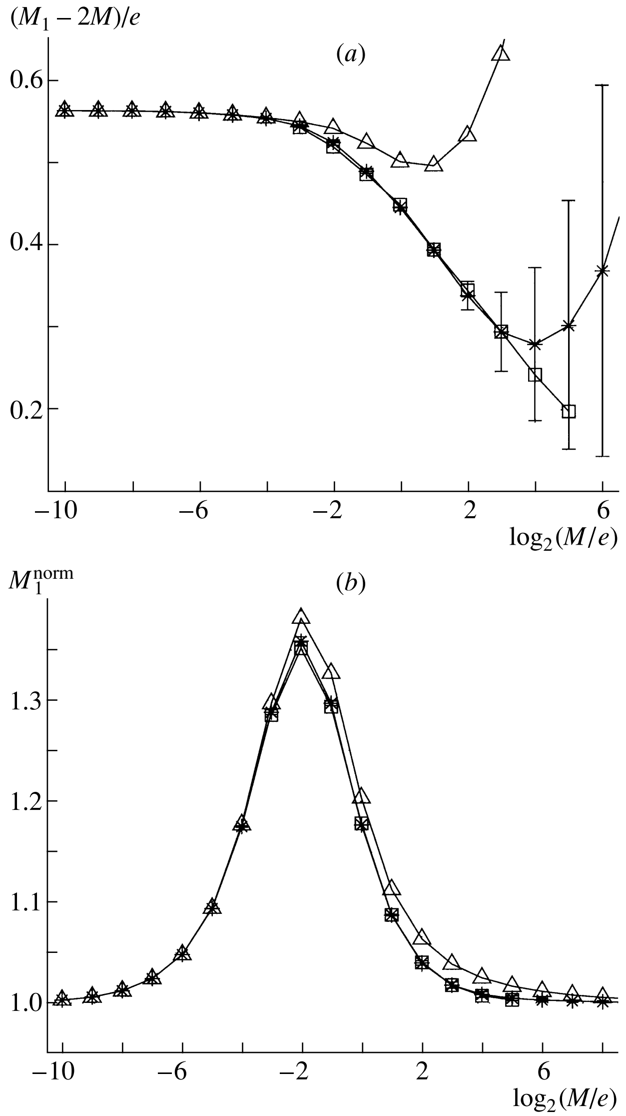

Fig. 2. Calculated mass M_1 of the vector bound state at $\hat{\theta} = \theta = 0$: (asterisks) results obtained by extrapolation to the limit $N \to \infty$, (open triangles) results of the calculation at $N = 30$, and (open boxes) results borrowed from [14].

$M/e < 0.4$ is likely to be associated with the proximity of the phase-transition point, where the regularization, which is parametrized by the number N, can distort the theory more strongly than as usual. It can also be conjectured that a sizable deviation of the extrapolated values of M_1/e from the results of Byrnes *et al.* [13] in the upper part of the region $M/e < 0.2$ is due to the same factor.

4.3. Case of Intermediate Values of $\hat{\theta}$

As was indicated above, the quantity $\hat{\theta}$ is a function of the ratio M/e and the parameter θ, this function being specified in the form of an infinite series in M. Therefore, the relation between $\hat{\theta}$ and θ is a priori unknown [this is not so only in the particular cases of $\theta = 0, \pi$ (see above)]. In principle, this relation can be sought by comparing the mass spectrum calculated on the basis of the light-front Hamiltonian (5), which depends on $\hat{\theta}$, and the spectrum calculated in Lorentz coordinates at a specific vacuum angle θ.

It can be shown that the mass spectrum of the theory is invariant under the reversal of the sign of the quantities $\hat{\theta}$ and θ (it should be recalled that $\hat{\theta}$ is an odd function θ). This can be seen most straightforwardly in the boson form of the theory [see Eq (4)], where the reversal of the sign of θ is equivalent to the replacement of φ by $-\varphi$, which does not change the mass spectrum. However, this invariance can be directly seen from the Hamiltonian in (5). One can show that it does not change if we reverse the sign of $\hat{\theta}$ and simultaneously interchange the operators d_n and b_{n+1} (in this case, ω is replaced by $-\omega$). This is a unitary transformation and does not change the mass spectrum. Thus, it is sufficient to perform calculations of the mass spectrum for the case where the parameter $\hat{\theta}$ lies between 0 and π.

For the lowest bound state, the mass M_1 calculated in this way and normalized according to (20) is displayed in Fig. 6. Each curve corresponds to a fixed value of the quantity $\hat{\theta}$ from the set $0, 0.05\pi, 0.1\pi, \ldots, \pi$. Each successive curve (for increasing $\hat{\theta}$) lies below the preceding one. In the cases of $\hat{\theta}/\pi = 0$ and $\hat{\theta}/\pi = 0.05$ (the first and the second curve from above), the extrapolation error ξ [see (19)] does not exceed 0.1 at any values of M/e.

In the case of $\hat{\theta}/\pi = 0.1$, $\xi > 0.1$ at M/e values in the range between 2 and 2^4; therefore, it is meaningless to plot the corresponding points on the graph, so that the curves decompose into two parts. In this region, the corresponding functions $P_1(n)$ (used in the extrapolation) display a manifest linearly decreasing character. This situation is similar to that considered in Subsection 4.2 for the case of $\theta = \pi$. It can be concluded that, in the region being considered, the theory specified by the Hamiltonian in (5) becomes incorrect upon the removal of the regularization, and it can be assumed that, in the vicinity of the point $M/e = 2$, there exists some nonperturbative effect as in the case of $\theta = \pi$ (see Subsection 4.2).

In principle, it can be assumed that a nonperturbative effect exists in the vicinity of the point $M/e = 2^4$ as well, above which the error ξ again falls below 0.1. However, it seems more probable that, in the region of large values of M/e, the Hamiltonian remains unbounded from below upon the removal of the regularization, but the decrease in the mass of the lowest

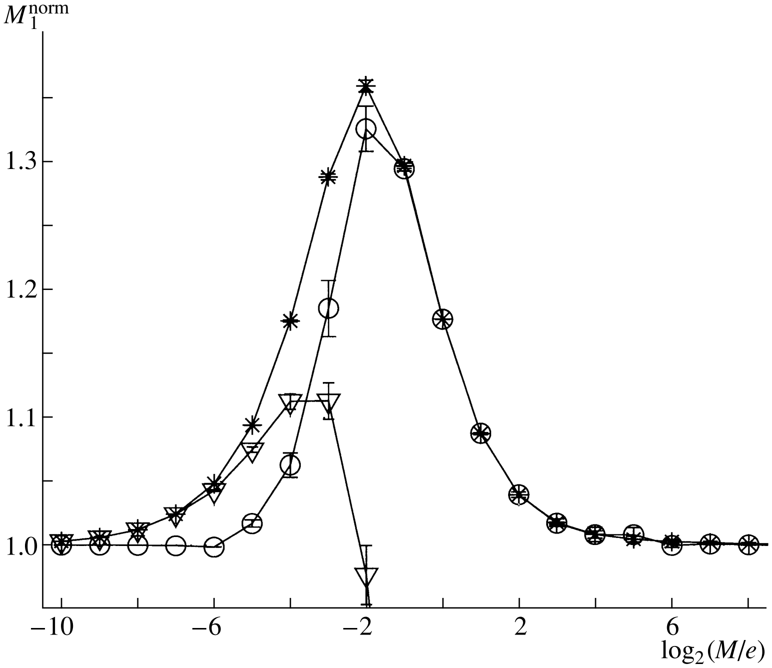

Fig. 3. Calculated mass M_1 of the vector bound state at $\hat{\theta} = \theta = 0$: (asterisks) results obtained with the aid of the corrected light-front Hamiltonian and (open circles and open inverted triangles) result obtained by means of the naive light-front quantization of, respectively, the fermion and the boson formulation of the theory.

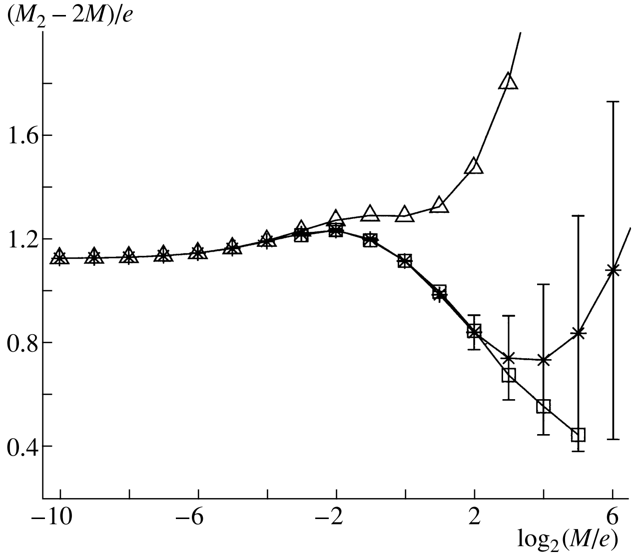

Fig. 4. Calculated mass M_2 of the scalar bound state at $\hat{\theta} = \theta = 0$: (asterisks) results obtained by means of an extrapolation to the limit $N \to \infty$, (open triangles) results corresponding to $N = 30$, and (open boxes) results borrowed from [14].

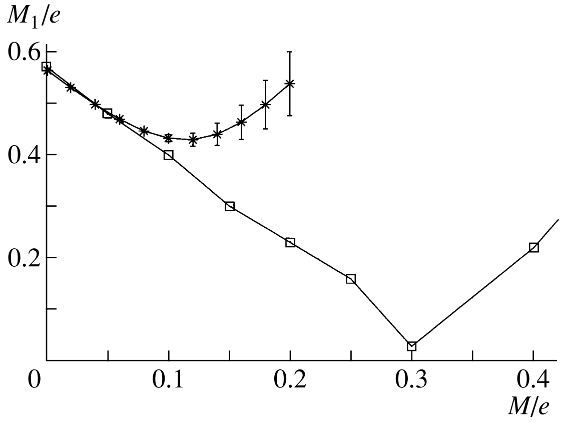

Fig. 5. Calculated mass M_1 of the lowest bound state at $\hat{\theta} = \theta = \pi$: (asterisks) results obtained by means of an extrapolation to the limit $N \to \infty$ and (open boxes) results borrowed from [13].

state with increasing regularization parameter N is so slow that ξ appears to be less than 0.1. This is favored by the dependence $P_1(n)$, which, at large values of M/e, has the form of a linear function with a moderate slope that yields $\xi < 0.1$. As was discussed at the end of Section 3, there is unfortunately no method for discriminating between the situations where, in the limit $N \to \infty$, there exists the limit of the mass of the lowest state and where this mass tends to $-\infty$.

In the cases of $\hat{\theta}/\pi = 0.15, \ldots, 0.3$, the situation is perfectly analogous to that in the case of $\hat{\theta}/\pi = 0.1$ (only the width of the region where $\xi > 0.1$ changes),

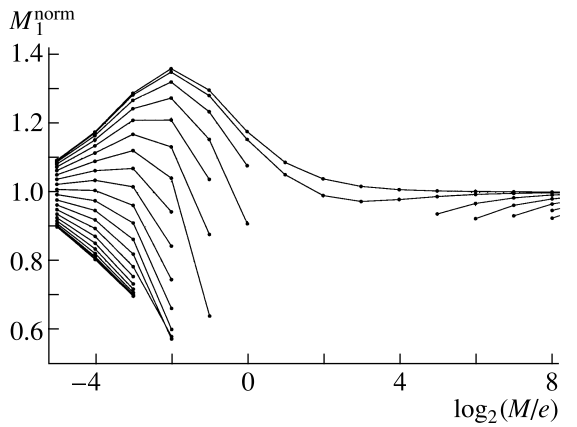

Fig. 6. Calculated mass M_1 of the lowest bound state as a function of M/e at various values of the parameter $\hat{\theta}$: $0, 0.05\pi, 0.1\pi, \ldots, \pi$. As the parameter $\hat{\theta}$ is increased, the curve is shifted downward.

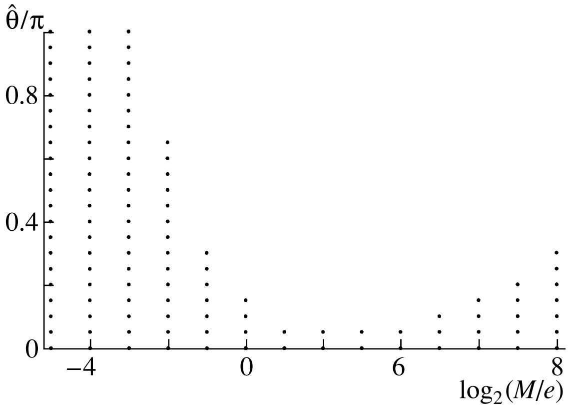

Fig. 7. Set of pairs of M/e and $\hat{\theta}$ values at which the extrapolation error ξ is less than 0.1.

which was considered immediately above, while, at $\hat{\theta}/\pi = 0.35, \ldots, 1$, the difference consists in that the region where $\xi < 0.1$ at large values of M/e is not reached at the M/e values considered here.

In Fig. 7, the points where the extrapolation error ξ is less than 0.1 are shown in the plane spanned by the parameters M/e and $\hat{\theta}$. It is natural to assume that, in the region where there are no points in the figure, the light-front Hamiltonian (5) is unbounded from below upon the removal of the regularization, $N \to \infty$.

5. CONCLUSION

A numerical nonperturbative calculation of the mass spectrum of QED-2 (massive Schwinger model) has been performed by the method of discrete light-cone quantization. In doing this, use has been made of the corrected light-front Hamiltonian (that is, that which generates a theory that is equivalent in all orders of perturbation theory in the fermion mass M to the Lorentz-covariant formulation of QED-2) constructed in [21, 22]. The results obtained in this way have been compared with the results of the numerical calculations on a lattice in Lorentz coordinates from [13, 14].

Since actual calculations are performed at a finite value of the infrared-regularization parameter N, a method has been proposed for extrapolating the results of these calculations to the region of N tending to infinity, this corresponding to the removal of this regularization. As the result of this extrapolation, it becomes clear that, at some values of the parameters of the theory, its mass spectrum is not bounded from below in the limit where the regularization is removed. This occurs only at rather large values of the fermion mass M; therefore, it is natural to assume that, in this region, the Hamiltonian used becomes incorrect, since it was constructed via an analysis of perturbation theory in M.

The calculations have been performed over a wide range of the fermion mass M for all values of the Hamiltonian parameter $\hat{\theta}$, which is a function of the ratio M/e and the vacuum angle θ. This function, which is a priori unknown, possesses the property that it vanishes at $\theta = 0$ and is equal to π at $\theta = \pi$.

At zero value of the vacuum angle θ, the resulting spectrum is bounded from below at any value of M, and the values obtained in this case for the two lowest bound states reproduce well the results reported in [14].

At the vacuum-angle value of $\theta = \pi$, which is special for the theory being considered, the masses found here for the lowest bound state agree well with the results of Byrnes *et al.* [13] for rather low values of M; as the mass M increases, there first arises a discrepancy, whereupon the spectrum of the theory become unbounded from below. Since the M value at which this takes place is approximately equal to that at which there occurs a phase transition in the theory (see, for example, [13]), it would be reasonable to assume that, at M values above the phase-transition point, the light-front Hamiltonian used here, which was constructed on the basis of an analysis of perturbation theory in M, becomes incorrect.

Our calculations have revealed that, in the case of QED-2, the procedure employed in [21, 22] to construct the corrected light-front Hamiltonian leads to a Hamiltonian that yields good results in nonperturbative calculations. By exploring the question of how the spectrum of the Hamiltonian changes in response to changes in the parameters of the theory from the perturbative region of their values, one can determine the boundaries of the applicability region of this Hamiltonian—that is, one can find the region where it is necessary to take additionally into account nonperturbative (for example, vacuum) effects. This may be of use in studying more realistic gauge field theories.

ACKNOWLEDGMENTS

The work of S.A. Paston was supported by the administration of St. Petersburg and the Ministry of Education of the Russian Federation (grant no. PD03-1.2-35).

APPENDIX

Let us find out how the parameter $\hat{\theta}$, which is a function of the ratio M/e and the vacuum angle θ, appears in the light-front Hamiltonian (5). It was shown in [21, 22] that the coefficient of the operator $e^{i\omega}d_0^+$ in the integrand on the right-hand side of (5) is the limit of the quantity $-B^*$ ($*$ denotes the operation of complex conjugation) in the limit $w \to \infty$ (which corresponds to removing the intermediate ultraviolet regularization), where B is given by

$$B = -\frac{1}{2w} + \sqrt{\frac{1}{4w^2} + \frac{A'}{w} - A''^2} + iA''. \quad \text{(A.1)}$$

Here, A' and A'' are, respectively, the real and the imaginary part of the sum (calculated in terms of Lorentz coordinates and in all orders in γ, including the first order)

$$A = \frac{\gamma}{2}e^{i\theta} + \sum_{k=2}^{\infty} A_k \gamma^k \quad \text{(A.2)}$$

of all connected diagrams of the boson theory specified by the Lagrangian in Eq. (4) that are obtained by connecting the external lines with the vertex $(\gamma/2)e^{i\theta}$ [the propagators of the external lines and a common factor that depends on their number are not included in the definition of A, as can be seen from the first term in (A.2)]. In [21], it was established that, in the limit $w \to \infty$, the quantities A_k for $k \neq 2$ are finite, while A_2 behaves as

$$A_2 = \frac{\gamma^2}{4}w + \text{const}. \quad \text{(A.3)}$$

Expression (A.1) was deduced from an analysis of perturbation theory in γ (in all orders). As a matter of fact, the series that can be obtained by substituting expansion (A.2) into (A.1) provides the definition of the quantity B. One can see that the first term of this series is linear in γ and, at large w, its radius of convergence varies in proportion to $1/w$. As was mentioned above, it is necessary to find the limit of the quantity B for $w \to \infty$. Since the aforementioned radius of convergence tends to zero in this limit, it is obvious that, before going to the limit, the quantity B must be continued analytically in γ to the region of positive γ values, which lie beyond the disk determined by this radius of convergence. For this, we determine the behavior of the radicand on the right-hand side of (A.1) at large w and γ of about $1/w$. Taking into account (A.3), we obtain

$$\sqrt{\frac{1}{4w^2} + \frac{A'}{w} - A''2} \quad \text{(A.4)}$$
$$= \frac{1}{2w}\sqrt{(1 + w\gamma\cos\theta)^2 + O\left(\frac{1}{w}\right)}.$$

From here, we find that there exist two branch points, whose positions are given by the formula

$$\gamma_{1,2} = -\frac{1}{w\cos\theta} + O\left(\frac{1}{w^{3/2}}\right). \quad \text{(A.5)}$$

It can be concluded from formulas (A.4) and (A.5) that, in the limit $w \to \infty$, the sought analytic continuation of the quantity B has the form

$$B = \operatorname{sgn}(\cos\theta)\sqrt{\frac{\gamma^2}{4} - A''^2} + iA'' = \frac{\gamma}{2}e^{i\hat{\theta}}. \quad \text{(A.6)}$$

The form of this expression corresponds to the form of the coefficient of the operator $e^{i\omega}d_0^+$ in Hamiltonian (5). Expression (A.6) differs by the presence of the signum function $\operatorname{sgn}(\cos\theta)$ from the corresponding expression presented in [21, 22], where the singularities of the analytic continuation of B were not taken into account. In the first order in γ (and, hence, in M), we find from (A.6), with the aid of expansion (A.2), that $\hat{\theta} = \theta$.

Upon the Euclidean rotation in the diagrams determining the quantity A, it becomes clear that A is a real-valued function of m, γ, $e^{i\theta}$, and $e^{-i\theta}$. It follows from here that the reversal of the sign of the parameter θ is equivalent to the complex conjugation of the quantity A, this quantity being real-valued at $\theta = \pi$. By using these facts and formula (A.6), one can easily see that $\hat{\theta}$ is an odd function of θ and, in addition, that $\hat{\theta} = \pi$ at $\theta = \pi$.

REFERENCES

1. P. A. M. Dirac, Rev. Mod. Phys. **21**, 392 (1949).
2. S. J. Brodsky, H.-C. Pauli, and S. S. Pinsky, Phys. Rep. **301**, 299 (1998); hep-ph/9705477.
3. V. A. Franke, Yu. V. Novozhilov, S. A. Paston, and E. V. Prokhvatilov, in *Quantum Theory in Honour of Vladimir A. Fock* (Unesco, St. Petersburg University, Euro-Asian Physical Society, 1998), Part 1, p. 38; hep-th/9901029.

4. A. M. Annenkova, E. V. Prokhvatilov, and V. A. Franke, Vestn. LGU, No. 4, 80 (1985).
5. V. A. Franke, Yu. V. Novozhilov, and E. V. Prokhvatilov, Lett. Math. Phys. **5**, 239 (1981).
6. V. A. Franke, Yu. V. Novozhilov, and E. V. Prokhvatilov, Lett. Math. Phys. **5**, 437 (1981).
7. A. M. Annenkova, E. V. Prokhvatilov, and V. A. Franke, Yad. Fiz. **56** (6), 179 (1993) [Phys. At. Nucl. **56**, 813 (1993)].
8. E. V. Prokhvatilov and V. A. Franke, Yad. Fiz. **49**, 1109 (1989) [Sov. J. Nucl. Phys. **49**, 688 (1989)].
9. E. V. Prokhvatilov, H. W. L. Naus, and H.-J. Pirner, Phys. Rev. D **51**, 2933 (1995); hep-ph/9406275.
10. M. Burkardt and A. Langnau, Phys. Rev. D **44**, 1187 (1991); **44**, 3857 (1991).
11. S. A. Paston and V. A. Franke, Teor. Mat. Fiz. **112**, 399 (1997); hep-th/9901110.
12. S. A. Paston, E. V. Prokhvatilov, and V. A. Franke, Teor. Mat. Fiz. **120**, 417 (1999); hep-th/0002062.
13. T. Byrnes, P. Sriganesh, R. J. Bursill, and C. J. Hamer, Phys. Rev. D **66**, 013002 (2002); hep-lat/0202014.
14. P. Sriganesh, C. J. Hamer, and R. J. Bursill, Phys. Rev. D **62**, 034508 (2000); hep-lat/9911021.
15. C. Adam, Ann. Phys. (N.Y.) **259**, 1 (1997); hep-th/9704064.
16. C. Adam, Phys. Lett. B **555**, 132 (2003); hep-th/0212171.
17. G. McCartor, Phys. Rev. D **60**, 105004 (1999).
18. S. Coleman, Ann. Phys. (N.Y.) **101**, 239 (1976).
19. E. V. Prokhvatilov, Teor. Mat. Fiz. **88**, 685 (1991).
20. S. A. Paston, E. V. Prokhvatilov, and V. A. Franke, Teor. Mat. Fiz. **136**, 69 (2003); hep-th/0310053.
21. S. A. Paston, E. V. Prokhvatilov, and V. A. Franke, hep-th/0011224.
22. S. A. Paston, E. V. Prokhvatilov, and V. A. Franke, Teor. Mat. Fiz. **131**, 84 (2002); hep-th/0302016.
23. E. V. Prokhvatilov and V. A. Franke, Yad. Fiz. **59**, 2105 (1996) [Phys. At. Nucl. **59**, 2030 (1996)].

Translated by A. Isaakyan

Physics of Atomic Nuclei, Vol. 68, No. 2, 2005, pp. 279–285. Translated from Yadernaya Fizika, Vol. 68, No. 2, 2005, pp. 304–310.
Original Russian Text Copyright © 2005 by Zamiralov, Özpineci, Yakovlev.

ELEMENTARY PARTICLES AND FIELDS
Theory

New Relations between Borel Sum Rules for the Magnetic Moments of the Σ^0 and Λ Hyperons

V. S. Zamiralov[1], A. Özpineci[2], and S. B. Yakovlev[3]

Received February 27, 2004

Abstract—New relations between the Borel sum rules in QCD for the magnetic moments of the Σ^0 and Λ hyperons are derived. It is shown that, on the basis of the sum rule for the magnetic moment of the Σ^0 hyperon, one can directly obtain the corresponding sum rule for the magnetic moment of the Λ hyperon, and vice versa, as well as the corresponding sum rule for the $\Sigma^0 \to \Lambda\gamma$ transition. *© 2005 Pleiades Publishing, Inc.*

1. INTRODUCTION

QCD sum rules for the masses and magnetic moments of baryons were first derived more than twenty years ago [1]. This resulted in calculating the masses of the nucleons [1, 2] and strange baryons [3] and the magnetic moments of the proton and neutron [2]. Later on, this analysis was extended to the strange hyperons $\Sigma^\pm$ and $\Xi^{0,-}$ and to the $\Sigma^0 \to \Lambda\gamma$ transition [3–6]. Also, the magnetic moment of Λ was calculated in some approximations [5]. This formalism was somewhat modified in [7, 8], where Borel sum rules were constructed for the neutron-beta-decay and leptonic-hyperon-decay axial-vector constants and for the magnetic moments of the octet baryons p, n, $\Sigma^\pm$, and $\Xi^{0,-}$. Difficulties in calculating the magnetic moment of Λ were overcome in [9, 10]. Recently, these sum rules and their modifications were used to calculate the magnetic moments of Σ, $\Sigma_{c,b}$, Λ, and $\Lambda_{c,b}$ baryons and the corresponding transitions $\Sigma \to \Lambda\gamma$ [11–18], the calculations for Σ- and Λ-like baryons and for transitions of the $\Sigma \to \Lambda\gamma$ type being performed independently.

Within QCD sum rules, the properties of the Λ and Σ hyperons [19, 20] and the $\Sigma \to \Lambda$ transition [21] in nuclear matter were also investigated independently, which seemed natural since the corresponding wave functions have different structures.

However, the calculations with Λ-like baryons involve difficulties indicated back in [5]. Moreover, the results of rather complicated and cumbersome calculations for the masses, the magnetic moments, and other properties of Σ- and Λ-like baryons can hardly be compared with one another. In view of all this, it is necessary to seek relations between the corresponding Borel sum rules.

The objective of the present study is to construct relations between the Borel sum rules for the Σ^0 and Λ hyperons. They are based on the relations between the wave functions for baryons characterized by specific isospins and U and V spins.

At first, we construct the sought relations within the simple nonrelativistic quark model, where they are trivial. Further, we construct similar relations for polarization operators and analyze them with the aid of the Borel sum rules for the masses and magnetic moments of the Σ^0 and Λ hyperons and for the $\Sigma^0 \to \Lambda\gamma$ transition.

2. RELATION BETWEEN THE MAGNETIC MOMENTS OF Σ^0 AND Λ WITHIN THE NONRELATIVISTIC QUARK MODEL

Let us write the magnetic moments of the Σ^0 and Λ hyperons of the baryon octet within the nonrelativistic quark model as [22]

$$\mu(\Sigma^0(ud,s)) = \frac{2}{3}\mu_u + \frac{2}{3}\mu_d - \frac{1}{3}\mu_s, \qquad (1)$$
$$\mu(\Lambda) = \mu_s.$$

The magnetic moment of any octet baryon, with the exception of Λ, can immediately be obtained by means of the corresponding substitutions for the quark symbols in the expression for $\mu(\Sigma^0(ud,s))$. It turns out, however, that the magnetic moment of Λ can also be obtained from $\mu(\Sigma^0(ud,s))$ by means of a nonlinear transformation.

---

[1] Institute of Nuclear Physics, Moscow State University, Vorob'evy gory, Moscow, 119899 Russia; e-mail: `zamir@depni.npi.msu.ru`

[2] International Centre for Theoretical Physics, Strada Costiera 11, PO Box 586, I-34014 Trieste, Italy.

[3] Faculty of Physics, Moscow State University, Vorob'evy gory, Moscow, 119899 Russia.

1063-7788/05/6802-0279$26.00 © 2005 Pleiades Publishing, Inc.

Upon performing the formal substitutions $d \leftrightarrow s$ and $u \leftrightarrow s$ in (1), we obtain the auxiliary quantities

$$\mu(\tilde{\Sigma}^0_{d\leftrightarrow s}) = \frac{2}{3}\mu_u + \frac{2}{3}\mu_s - \frac{1}{3}\mu_d, \qquad (2)$$
$$\mu(\tilde{\Lambda}_{d\leftrightarrow s}) = \mu_d,$$

$$\mu(\tilde{\Sigma}^0_{u\leftrightarrow s}) = \frac{2}{3}\mu_d + \frac{2}{3}\mu_s - \frac{1}{3}\mu_u, \qquad (3)$$
$$\mu(\tilde{\Lambda}_{u\leftrightarrow s}) = \mu_u.$$

The following relations hold:

$$2(\mu(\tilde{\Sigma}^0_{d\leftrightarrow s}) + \mu(\tilde{\Sigma}^0_{u\leftrightarrow s})) - \mu(\Sigma^0) = 3\mu(\Lambda), \qquad (4)$$
$$2(\mu(\tilde{\Lambda}_{d\leftrightarrow s}) + \mu(\tilde{\Lambda}_{u\leftrightarrow s})) - \mu(\Lambda) = 3\mu(\Sigma^0).$$

Similarly, one can obtain

$$\mu(\tilde{\Sigma}^0_{d\leftrightarrow s}) - \mu(\tilde{\Sigma}^0_{u\leftrightarrow s}) = \sqrt{3}\mu(\Sigma^0\Lambda), \qquad (5)$$
$$\mu(\tilde{\Lambda}_{d\leftrightarrow s}) - \mu(\tilde{\Lambda}_{u\leftrightarrow s}) = -\sqrt{3}\mu(\Sigma^0\Lambda).$$

The existence of these relations is due to the structure of the nonrelativistic-quark-model wave functions for the baryons of isospin $I = 1, 0$ and its third projection equal to zero, $I_3 = 0$; that is,

$$2\sqrt{3}|\Sigma^0(ud, s)\rangle_\uparrow = |2u_\uparrow d_\uparrow s_\downarrow + 2d_\uparrow u_\uparrow s_\downarrow \qquad (6)$$
$$- u_\uparrow s_\uparrow d_\downarrow - s_\uparrow u_\uparrow d_\downarrow - d_\uparrow s_\uparrow u_\downarrow - s_\uparrow d_\uparrow u_\downarrow\rangle,$$
$$2|\Lambda\rangle_\uparrow = |d_\uparrow s_\uparrow u_\downarrow + s_\uparrow d_\uparrow u_\downarrow - u_\uparrow s_\uparrow d_\downarrow - s_\uparrow u_\uparrow d_\downarrow\rangle,$$

where $q_\uparrow$ ($q_\downarrow$) is the wave function for a quark q (here, $q = u, d, s$) of helicity +1/2 (−1/2). It can be verified that the substitutions $d \leftrightarrow s$ and $u \leftrightarrow s$ lead to baryon states corresponding to states characterized by specific U and V spins. For example, the substitution $d \leftrightarrow s$ leads to the $U = 1, 0$ and $U_3 = 0$ baryon wave functions

$$-2|\tilde{\Sigma}^0_{d\leftrightarrow s}(us, d)\rangle = |\Sigma^0(ud, s)\rangle + \sqrt{3}|\Lambda\rangle,$$
$$-2|\tilde{\Lambda}_{d\leftrightarrow s}\rangle = -\sqrt{3}|\Sigma^0(ud, s)\rangle + |\Lambda\rangle,$$

while the substitution $u \leftrightarrow s$ leads to the $V = 1$, $V_3 = 0$, and $V = 0$ baryon wave functions

$$-2\tilde{\Sigma}^0_{u\leftrightarrow s}(ds, u) = |\Sigma^0(ud, s)\rangle - \sqrt{3}|\Lambda\rangle,$$
$$2|\tilde{\Lambda}_{u\leftrightarrow s}\rangle = \sqrt{3}|\Sigma^0(ud, s)\rangle + |\Lambda\rangle.$$

It can be seen that relations (4) and (5) are obtained with the aid of these expressions. In the quark model, these relations are trivial, but, in QCD, they make it possible to construct essentially nonlinear relations between Borel sum rules.

3. RELATIONS BETWEEN THE POLARIZATION OPERATORS FOR THE Σ^0 and Λ CURRENTS IN QCD

By using the Borel sum rules for the masses and magnetic moments of baryons as an example, we will now show how the above considerations can be applied to QCD sum rules.

As a starting point, we employ the polarization operators for the Σ^0 and Λ hyperons of the baryon octet. They are given by [1]

$$\Pi^{\Sigma^0,\Lambda} = i\int d^4x e^{ipx}\langle 0|T\{\eta^{\Sigma^0,\Lambda}(x), \eta^{\Sigma^0,\Lambda}(0)\}|0\rangle, \qquad (7)$$

where the baryon-current operators—an isovector one with $I_3 = 0$ (for Σ^0) and an isoscalar one (for Λ)—can be chosen in the form [14, 23]

$$\eta^{\Sigma^0} = \frac{1}{\sqrt{2}}\epsilon_{abc}[(u^{aT}Cs^b)\gamma_5 d^c \qquad (8)$$
$$+ (d^{aT}Cs^b)\gamma_5 u^c - t(u^{aT}C\gamma_5 s^b)d^c$$
$$-t(d^{aT}C\gamma_5 s^b)u^c],$$
$$\eta^{\Lambda} = \frac{1}{\sqrt{6}}\epsilon_{abc}[2(u^{aT}Cd^b)\gamma_5 s^c + (u^{aT}Cs^b)\gamma_5 d^c$$
$$- (d^{aT}Cs^b)\gamma_5 u^c + 2t'(u^{aT}C\gamma_5 d^b)s^c$$
$$+ t'(u^{aT}C\gamma_5 s^b)d^c - t'(d^{aT}C\gamma_5 s^b)u^c].$$

Here, a, b, and c are color indices; u, d, and s are the quark wave functions; C is the charge-conjugation matrix; and the index T denotes the transposition operation. At $t = t' = -1$, we return to the current obtained in [1]. By the way, currents characterized by t, $t' \neq -1$ were analyzed in [1], but it was concluded there that their use in the sum rules is not advisable.

In order to obtain the sought relations, we will specify, along with the above isospin operators, the corresponding U- and V-spin operators.

First, we introduce field operators transforming as a U vector (with $U_3 = 0$) and a U scalar by making the formal substitution $d \leftrightarrow s$ in (8). We have

$$\tilde{\eta}^{\Sigma^0(d\leftrightarrow s)} = \frac{1}{\sqrt{2}}\epsilon_{abc}\{(u^{aT}Cd^b)\gamma_5 s^c \qquad (9)$$
$$+ (s^{aT}Cd^b)\gamma_5 u^c - t(u^{aT}C\gamma_5 d^b)s^c$$
$$- t(s^{aT}C\gamma_5 d^b)u^c\},$$
$$\tilde{\eta}^{\Lambda(d\leftrightarrow s)} = \frac{1}{\sqrt{6}}\epsilon_{abc}[2(u^{aT}Cs^b)\gamma_5 d^c$$
$$+ (u^{aT}Cd^b)\gamma_5 s^c - (s^{aT}Cd^b)\gamma_5 u^c$$
$$+ 2t'(u^{aT}C\gamma_5 s^b)d^c + t'(u^{aT}C\gamma_5 d^b)s^c$$
$$- t'(s^{aT}C\gamma_5 d^b)u^c].$$

Similarly, we introduce a V vector (with $V_3 = 0$) and a V scalar by means of the substitution $u \leftrightarrow s$ in (8):

$$\tilde{\eta}^{\Sigma^0(u\leftrightarrow s)} = \frac{1}{\sqrt{2}}\epsilon_{abc}[(s^{aT}Cu^b)\gamma_5 d^c \qquad (10)$$
$$+ (d^{aT}Cu^b)\gamma_5 s^c - t(s^{aT}C\gamma_5 u^b)d^c - t(d^{aT}C\gamma_5 u^b)s^c],$$

$$\begin{aligned}\tilde{\eta}^{\Lambda(u\leftrightarrow s)} &= \frac{1}{\sqrt{6}}\epsilon_{abc}[2(s^{aT}Cd^b)\gamma_5 u^c \\ &+ (s^{aT}Cu^b)\gamma_5 d^c - (d^{aT}Cu^b)\gamma_5 s^c \\ &+ 2t'(s^{aT}C\gamma_5 d^b)u^c + t'(s^{aT}C\gamma_5 u^b)d^c \\ &- t'(d^{aT}C\gamma_5 u^b)s^c].\end{aligned}$$

At $t = t'$, the field operators (9) and (10) are related by the equations

$$\begin{aligned}-2\tilde{\eta}^{\Lambda(d\leftrightarrow s)} &= \sqrt{3}\eta^{\Sigma^0} - \eta^{\Lambda}, \qquad (11)\\ -2\tilde{\eta}^{\Sigma^0(d\leftrightarrow s)} &= \eta^{\Sigma^0} + \sqrt{3}\eta^{\Lambda}, \\ 2\tilde{\eta}^{\Lambda(u\leftrightarrow s)} &= \sqrt{3}\eta^{\Sigma^0} + \eta^{\Lambda}, \\ 2\tilde{\eta}^{\Sigma^0(u\leftrightarrow s)} &= \eta^{\Sigma^0} - \sqrt{3}\eta^{\Lambda}.\end{aligned}$$

By using the equalities in (9)–(11), we can relate, under the condition $t = t'$, the polarization operators (7) for the Σ^0 and Λ hyperons as follows:

$$2[\tilde{\Pi}^{\Sigma^0(d\leftrightarrow s)} + \tilde{\Pi}^{\Sigma^0(u\leftrightarrow s)}] - \Pi^{\Sigma^0} = 3\Pi^{\Lambda}, \qquad (12)$$

$$2[\tilde{\Pi}^{\Lambda(d\leftrightarrow s)} + \Pi^{\tilde{\Lambda}(u\leftrightarrow s)}] - \Pi^{\Lambda} = 3\Pi^{\Sigma^0}. \qquad (13)$$

These relations show that, if we obtain, for example, the sum rule for a Σ-like baryon, we can go over to the sum rule for the corresponding Λ-like baryon by merely replacing the quark fields (this is an essentially nonlinear operation), and vice versa.

Moreover, we can obtain the sum rules for the transition $\Sigma^0 \to \Lambda\gamma$ by using the relations

$$2[\tilde{\Pi}^{\Sigma^0(d\leftrightarrow s)} - \tilde{\Pi}^{\Sigma^0(u\leftrightarrow s)}] = \sqrt{3}[\Pi^{\Lambda\Sigma^0} + \Pi^{\Sigma^0\Lambda}], \qquad (14)$$

$$2[\tilde{\Pi}^{\Lambda(d\leftrightarrow s)} - \Pi^{\tilde{\Lambda}(u\leftrightarrow s)}] = -\sqrt{3}[\Pi^{\Lambda\Sigma^0} + \Pi^{\Sigma^0\Lambda}]. \qquad (15)$$

The above is valid for the pairs of charm and beauty baryons: $\Sigma_c^+(udc)$ and $\Lambda_c^+(udc)$, $\Sigma_b^0(udb)$ and $\Lambda_b^0(udb)$, $\Xi_c'^+(usc)$ and $\Xi_c^+(usc)$, and so on.

4. RELATIONS BETWEEN THE BOREL SUM RULES FOR THE MASSES OF THE Σ^0 AND Λ HYPERONS

We tested the above relations for the example of the light cone QCD sum rules derived in [14, 15] for the masses and magnetic moments. Here, we write in detail only the sum rule for the Σ^0-hyperon mass at $t = t'$, retaining terms proportional to m_u and m_d. We have

$$\begin{aligned}\mathrm{SR}(\Sigma^0) &= \frac{M^6 E_2(x)}{256\pi^4}(5 + 2t + 5t^2) \qquad (16)\\ &- \frac{m_0^2}{24M^2}[6(-1+t^2)(\langle\bar{u}u\rangle + \langle\bar{d}d\rangle)\langle\bar{s}s\rangle \\ &+ (-1+t)^2\langle\bar{u}u\rangle\langle\bar{d}d\rangle] - \frac{m_0^2}{192\pi^2}(2(2+2t+2t^2) \\ &\times[-2m_s\langle\bar{s}s\rangle + m_d\langle\bar{d}d\rangle + m_u\langle\bar{u}u\rangle] \\ &- 39(-1+t^2)m_s(\langle\bar{d}d\rangle + \langle\bar{u}u\rangle) - 3(-1+t)^2 \\ &\times(m_u\langle\bar{d}d\rangle + m_d\langle\bar{u}u\rangle) + 33(-1+t^2) \\ &\times(m_u + m_d)\langle\bar{s}s\rangle) + \frac{M^2E_0}{32\pi^2}((5+2t+5t^2) \\ &\times[m_s\langle\bar{s}s\rangle + m_d\langle\bar{d}d\rangle + m_u\langle\bar{u}u\rangle] - 6(-1+t^2) \\ &\times m_s(\langle\bar{d}d\rangle + \langle\bar{u}u\rangle) - 2(-1+t)^2 \\ &\times(m_u\langle\bar{d}d\rangle + m_d\langle\bar{u}u\rangle) - 6(-1+t^2) \\ &\times(m_u + m_d)\langle\bar{s}s\rangle) + \frac{1}{6}[3(-1+t^2) \\ &\times((\langle\bar{u}u\rangle + \langle\bar{d}d\rangle)\langle\bar{s}s\rangle + (-1+t)^2\langle\bar{u}u\rangle\langle\bar{d}d\rangle] \\ &- \frac{3m_0^2}{32\pi^2}(-1+t^2)[m_s(\langle\bar{u}u\rangle + \langle\bar{d}d\rangle) \\ &+ (m_d + m_u)\langle\bar{s}s\rangle]\left(\gamma_{\mathrm{EM}} - \ln\frac{M^2}{\Lambda^2}\right) = \lambda_\Sigma^2 e^{-M_\Sigma^2/M^2}.\end{aligned}$$

Here, $\langle\bar{q}q\rangle$ $(q = u, d, s)$ are the vacuum expectation values of the quark fields; λ_Σ is the Borel residue for the Σ hyperon; M^2 is the Borel parameter; Λ is the QCD characteristic scale; γ_{EM} is the Euler–Mascheroni constant; and $E_n(x)$ is the factor introduced to suppress the continuum contributions [1],

$$E_n(x) = 1 - e^{-x}(1 + x + \ldots + x^n/n!),$$
$$x = W_B^2/M^2, \quad B = \Sigma^0, \Lambda.$$

The quantity m_0^2, which is given by the formula

$$\langle\bar{q}q\rangle m_{0(q)}^2 = -\langle g_c\bar{q}\sigma\cdot Gq\rangle, \quad q = u, d, s,$$

is assumed to be degenerate (although this constraint can be removed). At $m_d = m_u = 0$, expression (16) can be reduced to that presented in [14].

For $\Sigma^0_{s\leftrightarrow d}$, we will now construct the auxiliary expression $\mathrm{SR}(\Sigma^0_{s\leftrightarrow d})$ corresponding to the $U = 1$, $U_3 = 0$ state by performing the substitution $s \leftrightarrow d$. We have

$$\begin{aligned}\mathrm{SR}(\Sigma^0_{s\leftrightarrow d}) &= \frac{M^6 E_2(x)}{256\pi^4}(5 + 2t + 5t^2) \qquad (17)\\ &- \frac{m_0^2}{24M^2}[6(-1+t^2)(\langle\bar{u}u\rangle + \langle\bar{s}s\rangle)\langle\bar{d}d\rangle \\ &+ (-1+t)^2\langle\bar{u}u\rangle\langle\bar{s}s\rangle] - \frac{m_0^2}{192\pi^2}(2(2+2t+2t^2) \\ &\times[-2m_d\langle\bar{d}d\rangle + m_s\langle\bar{s}s\rangle + m_u\langle\bar{u}u\rangle] \\ &- 39(-1+t^2)m_d(\langle\bar{s}s\rangle + \langle\bar{u}u\rangle) - 3(-1+t)^2 \\ &\times(m_u\langle\bar{s}s\rangle + m_s\langle\bar{u}u\rangle) + 33(-1+t^2) \\ &\times(m_u + m_s)\langle\bar{d}d\rangle) + \frac{M^2E_0}{32\pi^2}((5+2t+5t^2)\end{aligned}$$

$$\times [m_s\langle\bar{s}s\rangle + m_d\langle\bar{d}d\rangle + m_u\langle\bar{u}u\rangle]$$
$$- 6(-1+t^2)m_d(\langle\bar{s}s\rangle + \langle\bar{u}u\rangle) - 2(-1+t)^2$$
$$\times (m_u\langle\bar{s}s\rangle + m_s\langle\bar{u}u\rangle) - 6(-1+t^2)$$
$$\times (m_u + m_s)\langle\bar{d}d\rangle) + \frac{1}{6}[3(-1+t^2)$$
$$\times (\langle\bar{u}u\rangle + \langle\bar{s}s\rangle)\langle\bar{d}d\rangle + (-1+t)^2\langle\bar{u}u\rangle\langle\bar{s}s\rangle]$$
$$- \frac{3m_0^2}{32\pi^2}(-1+t^2)[m_d(\langle\bar{u}u\rangle + \langle\bar{s}s\rangle)$$
$$+ (m_s + m_u)\langle\bar{d}d\rangle]\left(\gamma_{\rm EM} - \ln\frac{M^2}{\Lambda^2}\right).$$

For $\Sigma^0_{s\leftrightarrow u}$, we similarly construct the auxiliary expression $\mathrm{SR}(\Sigma^0_{(s\leftrightarrow u)})$ corresponding to the $V = 1$, $V_3 = 0$ state by performing the substitution $s \leftrightarrow u$. On the basis of (12), we can now obtain the following nonlinear relation for the Λ-hyperon mass:

$$2[\mathrm{SR}(\Sigma^0_{s\leftrightarrow d}) + \mathrm{SR}(\Sigma^0_{s\leftrightarrow u})] - \mathrm{SR}(\Sigma^0) = 3\mathrm{SR}(\Lambda). \tag{18}$$

After some algebra, we have

$$\mathrm{SR}(\Lambda) = \frac{M^6 E_2(x)}{256\pi^4}(5 + 2t + 5t^2) \tag{19}$$
$$+ \frac{m_0^2}{72M^2}(-1+t)[4(2+t)(\langle\bar{u}u\rangle + \langle\bar{d}d\rangle)\langle\bar{s}s\rangle$$
$$+ (23 + 25t)\langle\bar{u}u\rangle\langle\bar{d}d\rangle] - \frac{m_0^2}{192\pi^2}\{-2(2 + 2t$$
$$+ 2t^2)[-2m_s\langle\bar{s}s\rangle + m_d\langle\bar{d}d\rangle + m_u\langle\bar{u}u\rangle]$$
$$- (-1+t)^2[-(m_u\langle\bar{d}d\rangle + m_d\langle\bar{u}u\rangle) + 2m_s(\langle\bar{d}d\rangle$$
$$+ \langle\bar{u}u\rangle) + 2(m_u + m_d)\langle\bar{s}s\rangle] + (-1+t)^2$$
$$\times [-4(m_u\langle\bar{d}d\rangle + m_d\langle\bar{u}u\rangle) + 35m_s(\langle\bar{u}u\rangle + \langle\bar{d}d\rangle)$$
$$- 37(m_u + m_d)\langle\bar{s}s\rangle]\} - \frac{1}{18}(-1+t)$$
$$\times [(11 + 13t)\langle\bar{u}u\rangle\langle\bar{d}d\rangle + (5 + t)$$
$$\times (\langle\bar{u}u\rangle + \langle\bar{d}d\rangle)\langle\bar{s}s\rangle] - \frac{m_0^2}{32\pi^2}(-1+t^2)$$
$$\times [m_s(\langle\bar{u}u\rangle + \langle\bar{d}d\rangle) + (m_u + m_d)\langle\bar{s}s\rangle$$
$$+ 4(m_u\langle\bar{d}d\rangle + m_d\langle\bar{u}u\rangle)]\left(\gamma_{\rm EM} - \ln\frac{M^2}{\Lambda^2}\right)$$
$$= \lambda_\Lambda^2 e^{-M_\Lambda^2/M^2}.$$

This relation exactly reproduces the sum rule for the Λ-hyperon mass from [14]. Similar relations between the sum rules for the magnetic moments from [14, 17] also hold exactly. Since they are much more cumbersome, we do not present them here.

Thus, relations (12)–(15) hold exactly, which proves their validity for the Borel sum rules, on one hand, and the self-consistency of our calculations, on the other hand. However, it would be more interesting and more compelling to verify our relations by considering examples from other studies, because this would mean independent tests.

We will begin by considering the Borel sum rules for the Σ^0- and Λ-hyperon masses. We will repeat the calculation of the first of the sum rules for the Σ^0-hyperon mass in [11], keeping the features of the u and d quarks nondegenerate; that is,

$$\frac{M^6}{8}L^{-4/9}E_2 + \frac{bM^2}{32}L^{-4/9}E_0 + \frac{a_u a_d}{6}L^{-4/9} \tag{20}$$
$$- \frac{a_u a_d(m^2_{0(u)} + m^2_{0(d)})}{48M^2}L^{-2/27}$$
$$- \frac{1}{4}[a_s m_s - (a_u - a_d)(m_d - m_u)]M^2 L^{-4/9}E_0$$
$$- \frac{1}{48}[3m_u a_d m^2_{0(d)} + 3m_d a_u m^2_{0(u)} - m_u a_u m^2_{0(u)}$$
$$- m_d a_d m^2_{0(d)}]L^{-26/27} - \frac{a_u a_d m^2_{0(s)}}{24}L^{-26/27}$$
$$= \beta^2_{\Sigma^0} e^{-(M^2_{\Sigma^0}/M^2)},$$

where a_q, b, and $a_q m^2_{0(q)}$ are defined in a standard way [1, 12],

$$a_q = -(2\pi)^2\langle\bar{q}q\rangle, \quad b = \langle g_c G^2\rangle, \tag{21}$$
$$a_q m^2_{0(q)} = (2\pi)^2\langle g_c\bar{q}\sigma\cdot Gq\rangle,$$
$$q = u, d, s, \quad L = \ln(M^2/\Lambda^2)/\ln(\mu^2/\Lambda^2),$$

μ being the normalization point for the operator-product expansion. At $m^2_{0(u)} = m^2_{0(d)}$, we return to the Borel sum rule given by Eq. (21) in [11]. In order to obtain $\mathrm{SR}(\bar{\Sigma}^0_{d\leftrightarrow s})$ and $\mathrm{SR}(\bar{\Sigma}^0_{u\leftrightarrow s})$, we perform the substitutions $d \leftrightarrow s$ and $u \leftrightarrow s$, respectively, in the expression on the left-hand side of Eq. (21) from [11] for the mass of Σ^0; employing relations (12) and (18), we then represent the Borel sum rules for the Λ-hyperon mass in the form

$$\frac{M^6}{8}L^{-4/9}E_2 + \frac{bM^2}{32}L^{-4/9}E_0 + \frac{2a_s(a_u + a_d) - a_u a_d}{18}L^{-4/9} \tag{22}$$
$$- \frac{(a_u + a_d)a_s(2m^2_{0(s)} + m^2_{0(u)} + m_{0(d)}) - a_u a_d(m^2_{0(u)} + m^2_{0(d)})}{144M^2}L^{-2/27}$$

$$- \frac{M^2}{12} L^{-4/9} E_0 m_s [3a_s - 2(a_u + a_d)] - \frac{M^2}{12} L^{-4/9} E_0 [3(m_u a_u + m_d a_d) + m_d a_u + m_u a_d$$
$$- 2(m_u + m_d) a_s] - \frac{1}{48} [2m_s (a_u m^2_{0(u)} + a_d m^2_{0(d)}) - (a_u m^2_{0(u)} - a_d m^2_{0(d)})(a_u - a_d)] L^{-26/27}$$
$$- \frac{1}{24} (m_u + m_d - m_s) a_s m^2_{0(s)} L^{-26/27} = \beta^2_\Lambda e^{-(M^2_\Lambda / M^2)}.$$

It exactly coincides with the Borel sum rule (22) from [11] at $m^2_{0(u)} = m^2_{0(d)}$. These relations do not require resort to the Gell-Mann–Okubo mass formula and fulfillment of the conditions of linearity in m_s, $a_{0(s)}/a_{0(u,d)}$, etc., which were used in the pioneering study of Belyaev and Ioffe [3] in constructing the sum rules for the Λ-hyperon mass. Relying on the Borel sum rules for the Λ-hyperon mass Eq. (24) in [11] with nondegenerate values of $m^2_{0(u)}$ and $m^2_{0(d)}$,

$$\frac{(2a_u + 2a_d - a_s) M^4}{12} E_1 \tag{23}$$
$$- \frac{(2a_u + 2a_d - a_s) b}{216} + \frac{\alpha_s}{\pi} \frac{L^{-1/9}}{243 M^2} [108 a_u a_d a_s$$
$$+ a_s (a_u^2 + a_d^2) - 2(a_u a_d + a_s^2)(a_u + a_d)]$$
$$+ \frac{M^6}{12} L^{-8/9} E_2 (2m_u + 2m_d - m_s) - \frac{b M^2}{96} L^{-8/9}$$
$$\times E_0 (2m_u + 2m_d - m_s) + \frac{1}{36} [12 m_s a_u a_d$$
$$- 2m_s a_s (a_u + a_d) + 12 a_s (m_u a_d + m_d a_u)]$$
$$+ \frac{1}{36} [a_s (m_u a_u + m_d a_d) - 2(m_u + m_d) a_u a_d]$$
$$= \beta^2_\Lambda M_\Lambda e^{-(M^2_\Lambda / M^2)},$$

and performing calculations that are similar to those described above, but which now involve relation (13), we obtain the Borel sum rule for the Σ^0-hyperon mass:

$$\frac{a_s M^4}{4} E_1 - \frac{a_s b}{72} + \frac{\alpha_s}{\pi} \tag{24}$$
$$\times \frac{[-(a_u^2 + a_d^2) + 36 a_u a_d] a_s}{81 M^2} L^{-1/9}$$
$$+ \frac{m_s M^6}{4} L^{-8/9} E_2 - \frac{m_s b M^2}{32} L^{-8/9} E_0$$
$$+ \frac{m_s a_u a_d}{3}$$
$$+ \frac{a_s (4 m_u a_d + 4 m_d a_u - m_u a_u - m_d a_d)}{12}$$
$$= \beta^2_{\Sigma^0} M_{\Sigma^0} e^{-(M^2_{\Sigma^0} / M^2)}.$$

It coincides with Eq. (23) in [11]. If we additionally set $a_{0(u)} = a_{0(d)} = a$ and $m_u = m_d = 0$, this formula reduces to the Borel sum rules for masses from [1] in the form given in Eq. (3) from [8].

Thus, we have demonstrated the validity of relations (12) and (13) for the example of the Borel sum rules for the Σ^0- and Λ-hyperon masses—specifically, we exactly reproduced formulas (22) and (23) from [11], employing formulas (21) and (24) from the same article as a starting point.

5. RELATIONS BETWEEN THE BOREL SUM RULES FOR THE MAGNETIC MOMENTS OF THE Σ^0 AND Λ HYPERONS

Let us now consider the more complicated problem of constructing Borel sum rules for baryon magnetic moments.

In the Borel sum rules for the magnetic moments, we will use, in addition to the quantities a_q, b, and $a_q m^2_{0(q)}$ defined by formulas (21), the quantities [1, 8]

$$\langle \bar{q} \sigma_{\mu\nu} q \rangle_F = e_q \chi_q \langle \bar{q} q \rangle F_{\mu\nu}, \tag{25}$$
$$\langle \bar{q} g_s G_{\mu\nu} q \rangle_F = e_q \kappa_q \langle \bar{q} q \rangle F_{\mu\nu},$$
$$\epsilon_{\alpha\beta\mu\nu} \langle \bar{q} g_s G^{\mu\nu} \gamma_5 q \rangle_F = i e_q \xi_q \langle \bar{q} q \rangle F_{\alpha\beta}.$$

We will repeat the calculations for the first of the Borel sum rules for the magnetic moments of the octet baryons from [8], relying on the results from [1]; following [8]; and taking the masses, the vacuum expectation values, and other properties of the u, d, and s quarks to be nondegenerate. We do not present the derivation of these Borel sum rules but focus on the transition from the Borel sum rules for the Σ^0 hyperon to the Borel sum rules for the Λ hyperon and to the Borel sum rules for the magnetic moment of the $\Sigma^0 \to \Lambda$ transition, using relations (12) and (14) as a basis. We have

$$2\mathrm{SR}(\Sigma^0) = \frac{M^6}{4 L^{4/9}} \cdot 2(e_u + e_d) \tag{26}$$
$$- \frac{L^{4/9}}{18 M^2} a_u a_d \times 2(e_u + e_d + 3e_s) + \frac{M^2 b}{24 L^{4/9}} (2e_u$$
$$+ 2e_d + e_s) - \frac{M^2 b}{144 L^{4/9}} \left[\ln\left(\frac{M^2}{\Lambda^2} \right) - 1 - \gamma_{\mathrm{EM}} \right]$$
$$\times 2(e_u + e_d + 2e_s) - \frac{M^2 b}{36 L^{4/9}} \left[\ln\left(\frac{M^2}{\Lambda^2} \right) \right.$$
$$\left. - \gamma_{\mathrm{EM}} - \frac{M^2}{2\Lambda^2} \right] \times 2(e_u + e_d) - \frac{1}{3 L^{4/27}}$$

$$\times \left[\left(M^2 - \frac{m^2_{(d)0}}{8L^{4/9}}\right)e_u(\chi_u a_u)a_d + \left(M^2 - \frac{m^2_{(u)0}}{8L^{4/9}}\right)e_d(\chi_d a_d)a_u\right] + \frac{L^{4/9}}{18}$$
$$\times [e_u(2\kappa_u - \xi_u)a_u a_d + e_d(2\kappa_d - \xi_d)a_d a_u]$$
$$- \frac{M^2}{8L^{4/9}} \cdot 4[2(e_u a_u + e_d a_d)m_s - (e_u a_d + e_d a_u)m_s + 2e_s(m_u + m_d)a_s + (e_u m_d + e_d m_u)a_s] + \frac{M^2}{2L^{4/9}}\left[\ln\left(\frac{M^2}{\Lambda^2}\right) - 1 - \gamma_{\rm EM}\right]$$
$$\times 2(e_u m_u + e_d m_d)a_s - \frac{M^2}{4L^{28/27}}$$
$$\times [2(e_u a_u \chi_u m_d + e_d a_d \chi_d m_u) - 2(e_u a_u \chi_u m_u + e_d a_d \chi_d m_d)] + \left[\frac{1}{6}(2\kappa_u - \xi_u)M^2 - \frac{M^2}{2}\kappa_u\right.$$
$$\times \left.\left[\ln\left(\frac{M^2}{\Lambda^2}\right) - 1 - \gamma_{\rm EM}\right]\right]e_u a_u m_d$$
$$+ \left[\frac{1}{6}(2\kappa_d - \xi_d)M^2 - \frac{M^2}{2}\kappa_d\left[\ln\left(\frac{M^2}{\Lambda^2}\right) - 1 - \gamma_{\rm EM}\right]\right]e_d a_d m_u = 2\beta^2_{\Sigma^0}\mu_{\Sigma^0}(1 + AM^2)$$
$$\times e^{(-M^2_{\Sigma^0}/M^2)} + \ldots.$$

Following our method, we will first construct the auxiliary quantities $\mathrm{SR}(\tilde{\Sigma}^0_{s\leftrightarrow d})$ and $\mathrm{SR}(\tilde{\Sigma}^0_{s\leftrightarrow u})$ and then, with the aid of relation (12), obtain the sum rule for the magnetic moment of the Λ hyperon. We have

$$2[\mathrm{SR}(\tilde{\Sigma}^0_{s\leftrightarrow d}) + \mathrm{SR}(\tilde{\Sigma}^0_{s\leftrightarrow u})] - \mathrm{SR}(\Sigma^0) = 3\mathrm{SR}(\Lambda). \tag{27}$$

Finally, we arrive at the Borel QCD sum rule for the magnetic moment of the Λ hyperon. For the sake of a direct comparison, we present it in the same approximations as in [9]—namely, at $m_u = m_d = 0$, $a_u = a_d = a$, $a_s = (1 + f)a$, $a_u\chi_u = a_d\chi_d = a\chi$, and $a_s\chi_s = a\chi\phi$:

$$\mathrm{SR}(\Lambda) = \frac{M^6}{12L^{4/9}}(e_u + e_d + 4e_s) \tag{28}$$
$$+ \frac{M^2 b}{144L^{4/9}}(4e_u + 4e_d + 7e_s) - \frac{L^{4/9}}{108M^2}[2(7e_u + 7e_d + e_s) + 8f(2e_u + 2e_d + e_s)]a^2 - \frac{M^2 b}{192L^{4/9}}$$
$$\times \left[\ln\left(\frac{M^2}{\Lambda^2}\right) - 1 - \gamma_{\rm EM}\right](5e_u + 5e_d + 2e_s)$$
$$- \frac{M^2 b}{108L^{4/9}}\left[\ln\left(\frac{M^2}{\Lambda^2}\right) - \gamma_{\rm EM} - \frac{M^2}{2\Lambda^2}\right]$$
$$\times (e_u + e_d + 4e_s) + \left\{\frac{-\chi a^2}{18L^{4/27}}\left(M^2 - \frac{m^2_{(s)0}}{8L^{4/9}}\right) + \frac{L^{4/9}}{108}(2\kappa - \xi)a^2\right\}\{(e_u + e_d)(1 + 2f) + 4e_s\phi\}$$
$$- \frac{15M^2}{36L^{4/9}}m_s(e_u + e_d)a + \frac{2m_s a e_s M^2}{3L^{4/9}}$$
$$\times \left[\ln\left(\frac{M^2}{\Lambda^2}\right) - 1 - \gamma_{\rm EM}\right] + (e_u + e_d)$$
$$\times \left[\frac{1}{18}(2\kappa - \xi)M^2 - \frac{M^2}{6}\kappa\left[\ln\left(\frac{M^2}{\Lambda^2}\right) - 1 - \gamma_{\rm EM}\right]\right]am_s - \frac{M^2}{6L^{28/27}}(e_u + e_d$$
$$- 2e_s\phi)m_s a\chi = \beta^2_\Lambda\mu_\Lambda e^{-(M^2_\Lambda/M^2)}(1 + A_\Lambda M^2) + \ldots.$$

This is in perfect agreement with the result presented in [9], apart from the coefficient 15/36 (instead of 19/36 in [9]) of the seventh term.

By using Eq. (14), we construct the sum rule for the $\Sigma^0 \to \Lambda\gamma$ transition. The result is

$$\mathrm{SR}(\tilde{\Sigma}^0_{s\leftrightarrow d}) - \mathrm{SR}(\tilde{\Sigma}^0_{s\leftrightarrow u}) = \sqrt{3}\mathrm{SR}(\Sigma^0\Lambda). \tag{29}$$

Finally, we obtain the QCD Borel sum rule for the $\Sigma^0 \to \Lambda\gamma$ transition in the same approximation,

$$\mathrm{SR}(\Sigma^0\Lambda) = (e_u - e_d)\left\{\frac{M^6}{4L^{4/9}} + \frac{L^{4/9}}{9M^2}a_s a\right. \tag{30}$$
$$+ \frac{M^2 b}{24L^{4/9}} - \frac{M^2 b}{144L^{4/9}}\left[\left[\ln\left(\frac{M^2}{\Lambda^2}\right) - 1 - \gamma_{\rm EM}\right] + 4\left[\ln\left(\frac{M^2}{\Lambda^2}\right) - \gamma_{\rm EM} - \frac{M^2}{2\Lambda^2}\right]\right] + \left[\frac{-\chi}{6L^{4/27}}\right.$$
$$\times \left.\left(M^2 - \frac{m^2_{0(s)}}{8L^{4/9}}\right) + \frac{L^{4/9}}{36}(2\kappa - \xi)\right]aa_s$$
$$+ \frac{M^2}{L^{4/9}}\frac{1}{4}m_s a - \frac{M^4}{4L^{28/27}}m_s a\chi + \left[\frac{1}{18}(2\kappa - \xi)M^2\right.$$
$$\left.\left. - \frac{M^2}{6}\kappa\left[\ln\left(\frac{M^2}{\Lambda^2}\right) - 1 - \gamma_{\rm EM}\right]\right]m_s a\right\}$$
$$= \beta_{\Sigma^0}\beta_\Lambda\sqrt{3}\mu_{\Sigma^0\Lambda}e^{-(\bar{m}^2/M^2)}(1 + A_{\Sigma^0\Lambda}M^2) + \ldots,$$
$$\bar{m} = (M_\Sigma + M_\Lambda)/2.$$

This formula agrees with the result obtained in [13], apart from the coefficient of the seventh term as before—we have 1/4 instead of 1/3 in [13].

At present, we are unable to disclose the reason behind this discrepancy because the contribution from the corresponding group of diagrams to the magnetic moment of the Σ^0 hyperon was not given in [9, 13] in sufficient detail. Anyway, this reason cannot be associated with our relations.

In order to test our relations additionally, we have constructed a series of sum rules for magnetic moments that is associated with the Λ hyperon and verified that we exactly reproduce the sum rule (26) for Σ^0, relying on the sum rule obtained for Λ in the form (28) and employing relations (13) and (15).

6. CONCLUSION

We have obtained nonlinear equations that relate the QCD sum rules for the Σ^0 and Λ hyperons.

First, we have considered relations (12) and (13) for the example of the light-cone QCD sum rules proposed in [15]. It has been shown that they hold exactly. (The sum rules written within this formalism for magnetic moments also hold exactly. These results will be presented in a separate publication because of their unwieldiness.) We assumed that it would be more compelling to verify the validity of the proposed relations for the known sum rules previously obtained by other authors. For the example of the Borel QCD sum rules for the masses and magnetic moments of the Σ^0 and Λ hyperons, we have shown that, relying on the sum rules for the Σ hyperon, one can directly obtain the corresponding sum rules for the Λ hyperon with the aid of relation (12). At the same time, relation (14) makes it possible to derive straightforwardly the sum rule for the $\Lambda \to \Sigma^0\gamma$ transition (the only discrepancy with the results presented in [9, 13] was discussed above).

We have tested the validity of the inverse relation (13) for the example of the Borel sum rules for the hyperon masses and verified, without explicitly presenting the results, that, from the sum rule for the magnetic moment of the Λ hyperon, one can obtain, with the aid of relation (13), the original sum rule for the magnetic moment of the Σ^0 hyperon.

Relations (12)–(15) can be used to obtain various sum rules for Λ-like baryons from the corresponding sum rules for Σ-like baryons, and vice versa; also, these relations can be used to perform a crosscheck of expressions for them, which are frequently very cumbersome and complicated.

ACKNOWLEDGMENTS

We are grateful to B.L. Ioffe for a stimulating discussion and to T. Aliev, F. Hussain, and G. Thompson for interest in this study. V.S. Zamiralov is grateful to S.Randjbar-Daemi for the hospitality extended to him at the International Centre for Theoretical Physics (Trieste, Italy), where a part of this work was performed.

This work was supported in part by a presidential grant (no. 1619.2003.2) for support of leading scientific schools. The work of V.S. Zamiralov was financially supported by the International Centre for Theoretical Physics.

Note added in proof. Apart from a change in the notation, our formula (12) coincides with formula (2.26) from [24].

REFERENCES

1. B. L. Ioffe, Nucl. Phys. B **188**, 317 (1981); **191**, 591(E) (1981).
2. V. M. Belyaev and B. L. Ioffe, Zh. Éksp. Teor. Fiz. **83**, 876 (1982) [Sov. Phys. JETP **56**, 493 (1982)].
3. V. M. Belyaev and B. L. Ioffe, Zh. Éksp. Teor. Fiz. **84**, 1236 (1983) [Sov. Phys. JETP **57**, 716 (1983)].
4. B. L. Ioffe and A. V. Smilga, Nucl. Phys. B **232**, 109 (1984).
5. B. L. Ioffe and A. V. Smilga, Phys. Lett. B **133B**, 436 (1983).
6. I. I. Balitsky and A. V. Yung, Phys. Lett. B **129B**, 328 (1983).
7. Ch. B. Chiu, J. Pasupathy, and S. L. Wilson, Phys. Rev. D **32**, 1786 (1985).
8. Ch. B. Chiu, J. Pasupathy, and S. L. Wilson, Phys. Rev. D **33**, 1961 (1986).
9. Ch. B. Chiu, J. Pasupathy, and S. L. Wilson, Phys. Rev. D **36**, 1442 (1987).
10. Ch. B. Chiu, S. L. Wilson, J. Pasupathy, and J. P. Singh, Phys. Rev. D **36**, 1553 (1987).
11. W.-Y. P. Hwang and K.-C. Yang, Phys. Rev. D **49**, 460 (1994).
12. K.-C. Yang, W.-Y. P. Hwang, E. M. Henley, and L. S. Kisslinger, Phys. Rev. D **47**, 3001 (1993).
13. Shi-lin Zhu, W.-Y. P. Hwang, and Ze-sen Yang, Phys. Rev. D **57**, 1527 (1998).
14. T. M. Aliev, A. Özpineci, and M. Savci, Phys. Rev. D **66**, 016002 (2002); **67**, 039901(E) (2003).
15. T. M. Aliev, A. Özpineci, and M. Savci, Nucl. Phys. A **678**, 443 (2000).
16. T. M. Aliev, A. Özpineci, and M. Savci, Phys. Rev. D **65**, 096004 (2002).
17. T. M. Aliev, A. Özpineci, and M. Savci, Phys. Rev. D **65**, 056008 (2002).
18. T. M. Aliev, A. Özpineci, and M. Savci, Phys. Lett. B **516**, 299 (2001).
19. X. Jin and R. J. Furnstahl, Phys. Rev. C **49**, 1190 (1994).
20. X. Jin and M. Nielsen, Phys. Rev. C **51**, 347 (1995).
21. N. Yagisawa, T. Hatsuda, and A. Hayashigaki, Nucl. Phys. A **699**, 665 (2002).
22. G. Morpurgo, Physics (N.Y.) **2**, 95 (1965).
23. X. Jin, Phys. Rev. D **52**, 2964 (1995).
24. D. B. Leinweber, R. M. Woloshin, and T. Draper, Phys. Rev. D **43**, 1659 (1991).

Translated by A. Isaakyan

Physics of Atomic Nuclei, Vol. 68, No. 2, 2005, pp. 286–291. Translated from Yadernaya Fizika, Vol. 68, No. 2, 2005, pp. 311–316.
Original Russian Text Copyright © 2005 by Berezhnoy, Likhoded.

ELEMENTARY PARTICLES AND FIELDS
Theory

Exclusive Production of Charmed-Meson Pairs

A. V. Berezhnoy[1] and A. K. Likhoded[2]

Received April 21, 2004; in final form, August 25, 2004

Abstract—It is shown that data of the BELLE Collaboration on the exclusive production of charmed-meson pairs via the one-photon mechanism of e^+e^- annihilation can be adequately described within the constituent quark model. It is also shown that the cross section for the central production of two D mesons in the process $e^+e^- \to e^+e^-\gamma\gamma \to e^+e^-D\bar{D} + X$ is commensurate with the cross section for their production in one-photon annihilation. © *2005 Pleiades Publishing, Inc.*

1. INTRODUCTION

The exclusive production of meson pairs at high energies offers a unique possibility for studying the asymptotic behavior of the form factors for these mesons within perturbative QCD. Mesons involving a heavy quark are of particular interest because they can be considered on the basis of heavy-quark effective theory, which relates the production of such mesons to their decay [1]. The asymptotic behavior of the form factors can be described in terms of a factorized amplitude that involves both the valence-quark wave function $f(x,Q)$ and the hard-scattering amplitude [2]. To the leading order in the strong coupling α_s, the hard-scattering amplitude is described in terms of one-gluon exchange, while the wave function $f(x,Q)$ peaks at $x = \Lambda_{\mathrm{QCD}}/M$, where Λ_{QCD} is the scale of strong interactions and M is the meson mass. With increasing heavy-quark mass, the width of the distribution $f(x,Q)$ decreases, which makes it possible to use the approximate expression

$$f(x,Q) \sim \delta\left(x - \frac{m_q}{M}\right). \qquad (1)$$

This implies that the meson-momentum fraction carried by a constituent quark is proportional to its quark mass,

$$x_i \simeq m_i/M.$$

Within models like that proposed in [2], only a hard "tail" of the meson wave function is taken into account, whereas the preasymptotic terms caused by the "soft" component of the wave function are neglected. Nevertheless, such models can be employed as useful parametrizations that adequately describe both the threshold behavior and the asymptotic behavior for $Q^2 \to \infty$. At the same time, the inclusion of the quark binding energy in a meson does not lead to a substantial deviation from the above approximation [3] despite the fact that relation (1) does not hold in this case.

In the present study, we will analyze recent data of the BELLE Collaboration [4] on the production of $D^{*+}D^{*-}$ pairs in e^+e^- annihilation at $\sqrt{s} =$ 10.6 GeV. On the basis of the model employed for this analysis, we will also obtain predictions for the production of $D^{(*)}$-meson pairs in $\gamma\gamma$ collisions.

2. e^+e^- ANNIHILATION

The cross sections determined by the BELLE Collaboration for $D^{(*)+}D^{(*)-}$ production are [4]

$$\sigma(e^+e^- \to D^{*+}D^{*-}) = 0.65 \pm 0.04 \pm 0.07 \text{ pb},$$

$$\sigma(e^+e^- \to D^{+}D^{*-}) = 0.71 \pm 0.05 \pm 0.09 \text{ pb}.$$

This group also measured the respective angular distributions.

At an energy as high as 10.6 GeV, the meson form factor is described by the leading asymptotic contribution

$$F(Q^2) \simeq \alpha_s f_M^2/Q^2,$$

where f_M is the meson weak decay constant and $Q^2 = s = (k_{e^+} + k_{e^-})^2$ is the square of the total energy of e^+e^- collisions. However, it can be seen from the diagrams in Fig. 1 that, in the approximation used in this study, the virtuality of the gluon producing the quark–antiquark pair $q\bar{q}$ is somewhat lower,

$$q^2 \sim x_q^2 Q^2,$$

where x_q is the meson-momentum fraction carried by a light quark. In the presence of large preasymptotic contributions, this fact could reduce the predictive

---

[1] Institute of Nuclear Physics, Moscow State University, Vorob'evy gory, Moscow, 119899 Russia; e-mail: `aber@ttk.ru`

[2] Institute for High Energy Physics, Protvino, Moscow oblast, 142284 Russia; e-mail: `likhoded@mx.ihep.su`

power of our model. However, the results obtained in [3] suggest that this is not so in the case under study.

Returning to the model based on the valence-quark approximation, we recall that it describes adequately the threshold cross-section behavior $[(s/4 - M^2)^{3/2}]$ associated with the P-wave character of meson production. As $M \to \infty$, this model leads to the same cross-section ratios as heavy-quark effective theory; that is,

$$\sigma_{PP} : \sigma_{PV} : \sigma_{VV} = 1 : 4 : 7,$$

where P and V are the pseudoscalar and the vector, respectively [5]. The asymptotic behavior at high energies,

$$\sigma \sim \alpha^2 \alpha_s^2 / s^3,$$

is common to all three cases.

The distributions of product $D\bar{D}$ and $D\bar{D}^*$ pairs in the meson emission angle θ reckoned from the direction of colliding e^+e^- beams are given by

$$\frac{d\sigma(D\bar{D})}{d\cos\theta} \sim \sin^2\theta,$$

$$\frac{d\sigma(D\bar{D}^*)}{d\cos\theta} \sim 1 + \cos^2\theta.$$

The latter case is dominated by the contribution of the transverse component of the D^* meson because the production of longitudinally polarized mesons is forbidden by the laws of parity and angular-momentum conservation. To demonstrate this, we note that, in the reference frame comoving with the center of mass of a e^+e^- pair, the matrix element describing the production of a $D\bar{D}^*$ pair in the 1^- state is proportional to

$$\Big([\boldsymbol{\epsilon}_{D^*} \times \mathbf{p}] \cdot \boldsymbol{\epsilon}_q\Big)\varphi_D,$$

where $\boldsymbol{\epsilon}_{D^*}$ and $\boldsymbol{\epsilon}_q$ are, respectively, the D^*-meson and virtual-photon polarization vectors and $\mathbf{p}$ is the D^*-meson momentum. It follows that the contribution of the longitudinal component of the D^*-meson polarization vector,

$$\boldsymbol{\epsilon}_{\|} = \mathbf{n}(\mathbf{n} \cdot \boldsymbol{\epsilon}_{D^*})\frac{E}{M}$$

(where $\mathbf{n} = \mathbf{p}/|\mathbf{p}|$ and E and M are the D^*-meson energy and mass, respectively), is zero. The contribution of the longitudinal component could be generated in the two-photon annihilation of a e^+e^- pair into a $D\bar{D}^*$ pair; however, it was shown in [6] that this contribution is negligible. In the reference frame comoving with the center of mass of a e^+e^- pair, the P-wave production of two vector mesons $D^*\bar{D}^*$ can be described in terms of two independent symmetric structures,

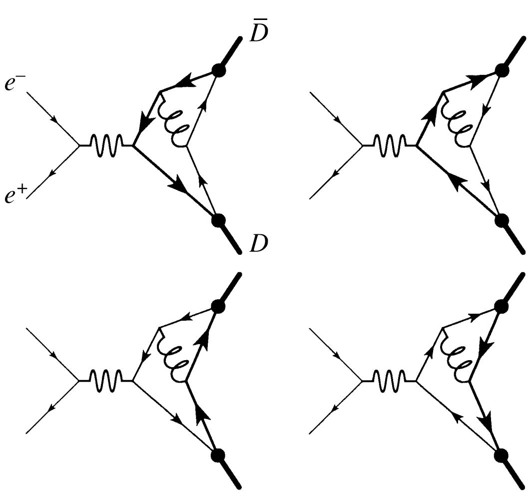

Fig. 1. Feynman diagrams for the production of charmed-meson pairs in e^+e^- annihilation.

$$M_1 \sim (\boldsymbol{\epsilon}_1 \cdot \mathbf{p})(\boldsymbol{\epsilon}_2 \cdot \boldsymbol{\epsilon}_q) + (\boldsymbol{\epsilon}_2 \cdot \mathbf{p})(\boldsymbol{\epsilon}_1 \cdot \boldsymbol{\epsilon}_q)$$

and

$$M_2 \sim (\boldsymbol{\epsilon}_1 \cdot \boldsymbol{\epsilon}_2)(\mathbf{p} \cdot \boldsymbol{\epsilon}_q).$$

The former matrix element corresponds to the $D_L^* D_T^*$ polarization state, whereas the latter involves all admissible polarization states. Within the model under consideration, relative contributions of these states depend on the ratio of constituent quark masses.

To obtain a good global fit to the BELLE data on the total cross sections and angular distributions, we choose the following values of the model parameters:

$$\alpha_s = 0.3, \quad f_D = 200 \text{ MeV},$$
$$m_q = 0.17 \text{ GeV}, \quad m_c = 1.5 \text{ GeV}.$$

As a result, the cross-section ratios appear to be (σ in pb)

$$\sigma(D^{*+}D^{*-}) : \sigma(D^+D^{*-} + D^-D^{*+}) : \sigma(D^+D^-)$$
$$= 0.73 : 0.58 : 0.02.$$

It can be seen that the cross section for the production of two pseudoscalar mesons is an order of magnitude smaller than that for the production of two vector mesons. The experimental angular distributions $d\sigma/d\cos\theta$ for $D^{*+}D^{*-}$ and D^+D^{*-} (D^-D^{*+}) pairs are shown in Fig. 2, along with the respective distributions predicted by our model. The best fit to the experimental data corresponds to the parameter values of $m_q = 0.17$ GeV and $m_c = 1.5$ GeV.

It should be noted that the proposed model of pair production is nothing but a rough approximation that

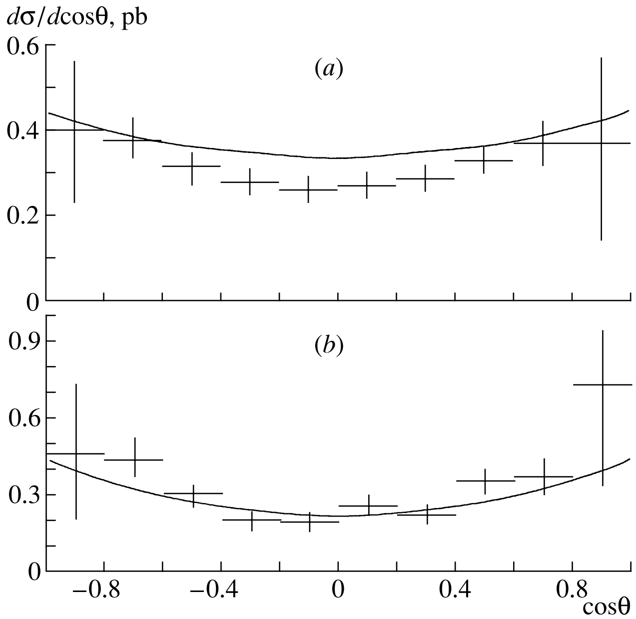

Fig. 2. Predicted distribution of the cross section with respect to $\cos\theta$ along with experimental data for (a) $e^+e^- \to D^{*+}D^{*-}$ and (b) $e^+e^- \to D^+D^{*-}$ (D^-D^{*+}). The parameter values were set to $m_c = 1.5$ GeV, $m_q = 0.17$ GeV, $f_D = 200$ MeV, and $\alpha_s = 0.3$.

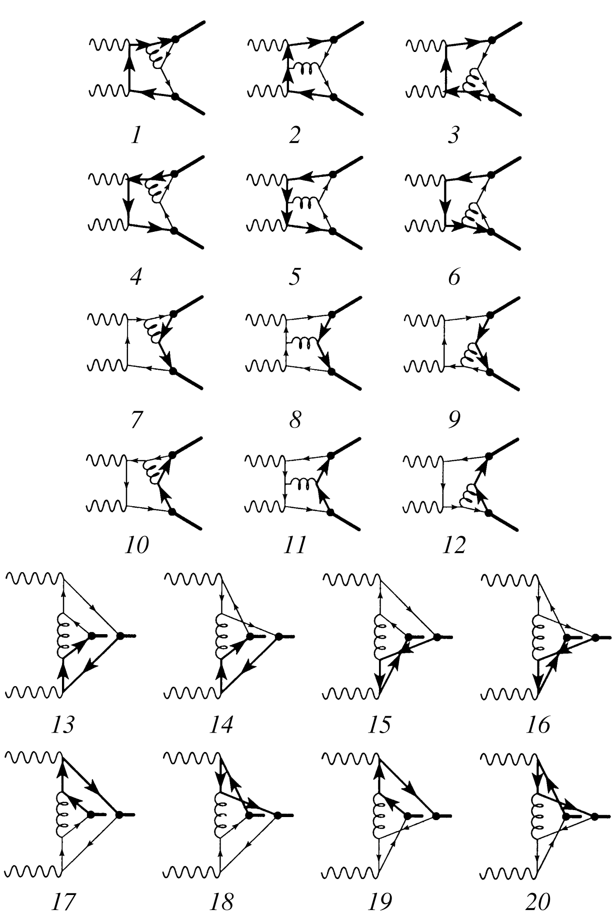

Fig. 3. Feynman diagrams for the production of charmed-meson pairs in photon–photon collisions.

includes only the hard "tail" of the meson wave function. The relative motion of quarks, which is described by the "soft" component of the wave function, is disregarded in our model. As a consequence, the total cross section for the production of two pseudoscalar mesons does not vanish in our predictions, in contrast to what one has in the model proposed in [1], where the motion of a light quark is described within heavy-quark effective theory. At the same time, the latter predicts a cross section that is an order of magnitude larger than its experimental counterpart. As has already been mentioned, the inclusion of the quark binding energy in a meson does not lead to significant deviations from the simplest approximation, as was shown in [3], despite the fact that the approximate relation (1) is not justified in that case.

3. TWO-PHOTON PRODUCTION OF $D^{(*)}\bar{D}^{(*)}$ PAIRS

The exclusive two-photon production of $D^{(*)}\bar{D}^{(*)}$ pairs was considered in [7] in the context of a comparison with predictions of heavy-quark effective theory. In the leading order in α_s, there are 20 Feynman diagrams for this process. It should be noted that the inclusive production of B_c mesons is described by similar diagrams [8]. As in [7], the diagrams for photon–photon production can be partitioned into three gauge-invariant groups. The first six diagrams describe the production of a pair of heavy quarks with subsequent hadronization via the one-gluon production of a pair of light quarks (diagrams *1–6* in Fig. 3). The next six diagrams are associated with the permutations $Q \leftrightarrow q$ (diagrams *7–12*). In the processes described by the third group of diagrams (diagrams *13–20*), the independent production of heavy and light quarks in the subprocesses $\gamma \to QQ$ and $\gamma \to q\bar{q}$ is followed by meson formation in their interactions via gluon exchange. The contribution of the diagrams of the third group is dominant at moderately low momentum transfers. Such contributions to the cross section for inclusive production violate the factorization theorem in this momentum region [8]. In particular, the cross section for inclusive production depends greatly on the light-quark charge e_q both near the threshold and at high energies. We obtained such a dependence on e_q in studying the energy dependence of the cross section for the two-photon production of $D^{(*)}\bar{D}^{(*)}$ pairs. Previously, this was indicated in [9], but only for asymptotically high energies. In what follows, we will continue analyzing the predictions of

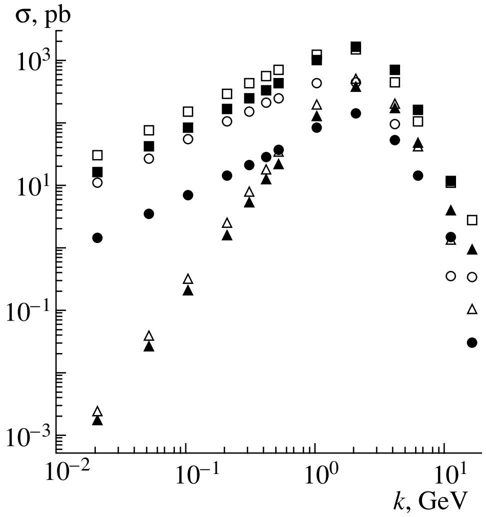

Fig. 4. Cross section for the production of neutral D mesons as a function of $k = \sqrt{s - s_{\rm thr}}$ (closed symbols), along with the analogous dependence for charged mesons (open symbols): (○, ●) σ_{PP}, (△, ▲) σ_{PV}, and (□, ■) σ_{VV}.

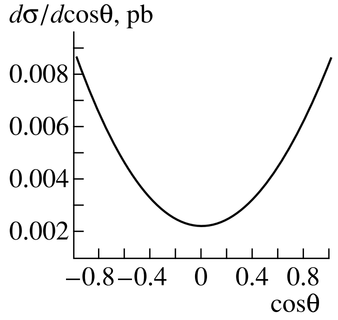

Fig. 5. Differential cross section for the production of D^+D^{*-} and D^-D^{*+} pairs in e^+e^- annihilation at $k = \sqrt{s - s_{\rm thr}} = 0.1$ GeV as a function of $\cos\theta$ (at small k, the production of other pairs of charmed mesons is isotropic).

our model, based on the diagrams in Fig. 3, for various kinematical domains.

We will now consider $D^{(*)}\bar{D}^{(*)}$ production near the threshold. It was noted above that, in the threshold region, $D^*\bar{D}^*$ and $D\bar{D}$ pairs are produced in the S wave (the dependence of the respective amplitudes on the relative momentum of the D mesons in the c.m. frame has the k^{2L+1} form). The S-wave production implies that the total angular momentum and parity of the two-photon system are 0^{++}. In contrast, $D^*\bar{D}$ pairs are produced in the P wave because the S-wave production is forbidden, in this case, by the Landau–Yang theorem. In the S-wave state, the total angular momentum and parity of the system are 1^+. The P-wave state of the $D^*\bar{D}$ system implies that the total angular momentum and parity of the $\gamma\gamma$ system are 0^-; therefore, the respective cross section for $D^*\bar{D}$ production in the threshold domain increases in proportion to k^3. It can be seen from Fig. 4 that, although the quantum numbers of the $D^{(*)}\bar{D}^{(*)}$ system are independent of the electric charge, the cross sections for the production of particles having different electric charges are different in magnitude, being, however, similar in energy dependence. The dependence of the angular distributions on the light-quark charge is even more pronounced.

Within our model, the production of $D^0\bar{D}^0$, $D^{*0}\bar{D}^0$, $D^0\bar{D}^{*0}$, D^+D^-, and $D^{*+}D^{*-}$ pairs in the threshold domain is virtually isotropic,

$$\frac{d\sigma}{d\cos\theta} \approx \text{const},$$

whereas production of a D^+D^{*-} pair has a peripheral character even at the threshold (see Fig. 5). However, it can be seen from Fig. 4 that the production of such pairs in the threshold region is suppressed.

It should also be noted that, in the threshold region, the total cross section for the production of neutral mesons is approximately three times larger than the cross section for the production of charged mesons.

At high energies, the dependence of the production cross section is typical of the peripheral production mechanism, displaying pronounced peaks at $\cos\theta$ equal to $+1$ and -1. This fact was also noted in [9], where the amplitude for the production of a pseudoscalar-meson pair was calculated analytically in the high-energy limit,

$$A^{PP} \sim \left[(e_Q - e_q)^2 \frac{1 + \beta^2\cos^2\theta}{1 - \beta^2\cos^2\theta} + 2e_Q^2\right],$$

where

$$\beta = \sqrt{1 - 4m^2/s}.$$

At large values of s, the cross sections for the production of charged and neutral mesons differ in asymptotic dependence on energy. All three cross sections for the production of charged mesons behave as $1/s^2$; at the same time, the different cross sections for the production of neutral mesons at asymptotically high energies are in the ratio

$$\sigma_{D^0\bar{D}^0} : \sigma_{D^{*0}\bar{D}^0} : \sigma_{D^{*0}\bar{D}^{*0}} \sim \frac{1}{s^3} : \frac{1}{s^4} : \frac{1}{s^2}.$$

It should be noted that the asymptotic regime is reached only for $\sqrt{s} > 20$ GeV; therefore, it is only of theoretical interest today. Moreover, logarithmic corrections generated in next-to-leading orders of perturbation theory can play a significant role at such energies.

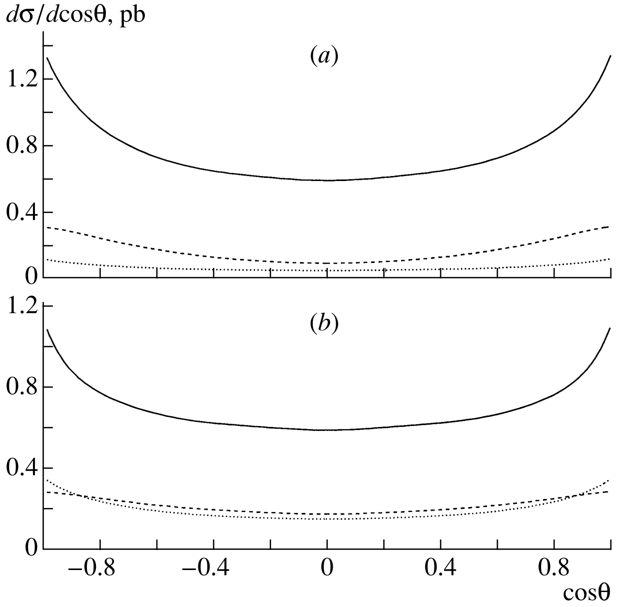

Fig. 6. Differential cross sections for the production of (*a*) charged- and (*b*) neutral-meson pairs in collisions of effective photons versus $\cos\theta$: (solid curves) results for a pair of vector mesons, (dashed curves) results for a pair involving a vector and a pseudoscalar meson, and (dotted curve) results for a pair of pseudoscalar mesons.

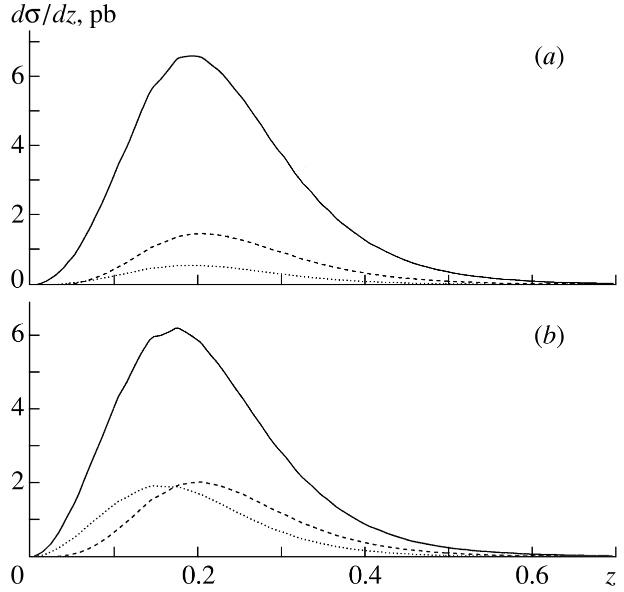

Fig. 7. Differential cross sections for the production of (*a*) charged- and (*b*) neutral-charmed-meson pairs in the interaction of effective photons versus $z = 2|\mathbf{p}_D|/\sqrt{s}$. The notation is identical to that in Fig. 6.

4. POSSIBILITY OF STUDYING TWO-PHOTON PRODUCTION OF $D^{(*)}\bar{D}^{(*)}$ PAIRS AT THE BELLE SETUP

It was shown in [6] that the contribution of two-photon annihilation

$$e^+e^- \to \gamma^*\gamma^* \to D\bar{D} \tag{2}$$

to the total cross section for the production of charmed-meson pairs is rather small. However, charmed-meson pairs can also be produced in collisions of effective (equivalent, or virtual) photons emitted by initial-state fermions,

$$e^+e^- \to e^+\gamma e^-\gamma \to D\bar{D} + e^+ + e^-. \tag{3}$$

The cross section for this reaction can be described within the “parton” model as

$$\sigma = \int\int \sigma_{\gamma\gamma}(\hat{s}) f^\gamma(x_1) f^\gamma(x_2) dx_1 dx_2,$$

where x_1 and x_2 are, respectively, the initial-positron- and initial-electron-momentum fractions carried away by colliding photons. In this model, the photon densities $f^\gamma(x)$ are given by the Weizsäcker–Williams formula

$$f^\gamma(x) = \frac{\alpha_{\text{em}}}{2\pi x}\left(\left(1-(1-x)^2\right) \ln\frac{Q^2_{\text{max}}}{Q^2_{\text{min}}} - m_e^2 x^2 \left(\frac{1}{Q_{\text{min}}} - \frac{1}{Q_{\text{max}}}\right) \right),$$

where m_e is the electron mass, $Q^2_{\text{min}} = m_e^2 x^2/(1-x)$, and $Q^2_{\text{max}} \simeq 1\ \text{GeV}^2$.

Since the amplitude for the process in (3) is not suppressed, in contrast to that for the process in (2), by the s-channel photon propagators, it is of interest to evaluate the cross section for the production of charmed-meson pairs in the interaction of effective photons. For the same parameter values as in the case of e^+e^- annihilation, we obtain (σ in pb)

$$\sigma(D^{*+}D^{*-}) : \sigma(D^+D^{*-}) : \sigma(D^+D^-) = 1.52 : 0.33 : 0.13,$$

$$\sigma(D^{*0}\bar{D}^{*0}) : \sigma(D^0\bar{D}^{*0}) : \sigma(D^0\bar{D}^0) = 1.39 : 0.43 : 0.40.$$

These results are quite unexpected. It can be seen that these cross sections are commensurate with the production cross section in e^+e^- annihilation. As can be seen from Fig. 6, the shapes of the angular distributions in the case under consideration are similar to those in the case of the production of charmed-meson pairs in e^+e^- annihilation. At the same time, the energy of mesons produced in the interaction of effective photons is lower. From the dependences of the cross sections on $z = 2|\mathbf{p}_D|/\sqrt{s}$ ($\mathbf{p}_D$ is the D-meson momentum in the reference frame comoving with the center of mass of the e^+e^- pair) in Fig. 7, it follows that the average value of z in this process is about 0.3, the corresponding momentum being estimated at 1 GeV.

It should also be noted that, in our model, the main contribution to the cross section comes from the production of two pairs of vector mesons.

5. CONCLUSION

Our analysis of the production of charmed-meson pairs in e^+e^- annihilation has revealed that the BELLE data at $\sqrt{s} = 10.6$ GeV are in good agreement with the predictions of the constituent quark model, where the hard component of the amplitude is calculated within perturbative QCD. In the case of e^+e^- annihilation, the production mechanism is the simplest: a $c\bar{c}$ pair is produced by a virtual photon, and hadronization is due to a light-quark pair, whose production can be described within perturbation theory. As a consequence, the production cross section is independent of the light-quark electric charge.

In contrast, the production processes in $\gamma\gamma$ collisions feature a strong dependence on the light-quark charge both at low and at high energies. The reason is that the main contribution to the cross section for $\gamma\gamma \to D\bar{D}$ comes from a set of diagrams rather than from a single one, the diagrams involving direct coupling of a photon to a light quark playing a significant role.

It has also been shown that the cross section for the central production of two D mesons in the reaction

$$e^+e^- \to e^+e^-\gamma\gamma \to e^+e^-D\bar{D} + X$$

is commensurate with the analogous cross section in the case of one-photon annihilation.

ACKNOWLEDGMENTS

This work was supported in part by the Russian Foundation for Basic Research (project no. 04-02-17530), the Ministry of Education of the Russian Federation (project no. E02-3.1-96), and the CDRF (project no. M0-011-0) and was performed within the program Russian Scientific Schools (project no. 1303.2003.2).

REFERENCES

1. A. G. Grozin and N. Neubert, Phys. Rev. D **55**, 272 (1997).
2. S. J. Brodsky and G. P. Lepage, Phys. Rev. D **22**, 2157 (1980).
3. Chueng-Ryong Ji and Alex Pang, Phys. Rev. D **55**, 1253 (1997).
4. BELLE Collab. (T. Uglov *et al.*), hep-ex/0401038; BELLE Collab. (K. Abe *et al.*), Surveys High Energy Phys. **18**, 221 (2003).
5. V. V. Kiselev, Int. J. Mod. Phys. A **10**, 465 (1995).
6. K. Y. Liu *et al.*, hep-ph/0311364.
7. A. V. Berezhnoy, V. V. Kiselev, and A. K. Likhoded, Yad. Fiz. **67**, 837 (2004) [Phys. At. Nucl. **67**, 815 (2004)].
8. A. V. Berezhnoy, M. V. Shevlyagin, and A. K. Likhoded, Phys. Lett. B **342**, 351 (1995).
9. M. S. Baek, S. Y. Choi, and H. S. Song, Phys. Rev. D **50**, 4363 (1994).

Translated by R. Rogalyov

Physics of Atomic Nuclei, Vol. 68, No. 2, 2005, pp. 292–305. Translated from Yadernaya Fizika, Vol. 68, No. 2, 2005, pp. 317–330.
Original Russian Text Copyright © 2005 by Loginov, Stibunov.

General Formulas for Invariant Functions Describing Generalized $\gamma N \to \gamma N$ Reactions within the Method of Effective Lagrangians

A. Yu. Loginov* **and V. N. Stibunov**

Institute of Nuclear Physics, Tomsk Polytechnic University, Tomsk, 634004 Russia

Received December 19, 2003; in final form, April 19, 2004

Abstract—The crossed channels of generalized $\gamma N \to \gamma N$ reactions are considered. The coefficients in the transformation from independent helicity amplitudes to invariant functions are calculated. Explicit expressions for the invariant functions are derived with allowance for the contribution from the Born diagrams in the s, u, and t channels and the diagrams for six resonances in the s and u channels. It is shown that the calculated invariant functions satisfy the crossing-symmetry requirements. © *2005 Pleiades Publishing, Inc.*

1. Photon–nucleon interaction is one of the fundamental processes in elementary-particle physics. At photon energies below 1 GeV, pion photoproduction, bremsstrahlung, and Compton scattering are the main channels of this process. In the present study, we consider generalized $\gamma N \to \gamma N$ reactions, which include three crossed channels: the Compton scattering of a photon on a nucleon, $\gamma N \to \gamma N$ (s channel); the Compton scattering of a photon on an antinucleon, $\gamma \bar{N} \to \gamma \bar{N}$ (u channel); and the annihilation of a nucleon–antinucleon pair into two photons, $N\bar{N} \to \gamma\gamma$ (t channel).

Some new experimental data were obtained in [1, 2] for Compton scattering on a proton and in [3, 4] for Compton scattering on a deuteron. At low photon energies, experiments of this type make it possible to perform precise measurements of static nucleon properties, such as an electric charge, a magnetic moment, and electric and magnetic polarizabilities. At photon energies above the pion-production threshold, the process involving the excitation of the $P_{33}(1232)$ resonance becomes dominant; as the photon energy increases further, processes involving the excitation of the Roper resonance $P_{11}(1430)$ and resonances of the second [$S_{11}(1500)$, $D_{13}(1505)$] and the third [$S_{31}(1620)$, $D_{33}(1700)$] energy region come into play. There are several approaches to describing Compton scattering: the use of dispersion relations [5, 6], the method of effective Lagrangians [7, 8], and chiral perturbation theory [9, 10]. In the present study, we use the method of effective Lagrangians to derive general analytic formulas for invariant functions describing generalized $\gamma N \to \gamma N$ reactions, taking into account the contribution of the Born diagrams in the s, u, and t channels and the diagrams for six resonances in the s and u channels. The availability of explicit expressions for invariant functions reduces considerably the machine time required for simulating the processes in question and is necessary for calculating the amplitudes for these processes on nuclei analytically.

This article is organized as follows. In Section 2, we present a general expression for the P- and T-invariant amplitude of $\gamma^- + 1/2^+ \to \gamma^- + 1/2^+$ reactions. In Section 3, we derive the coefficients in the transformation from independent helicity amplitudes for $\gamma^- + 1/2^+ \to \gamma^- + 1/2^+$ reactions to invariant functions. In Section 4, we discuss the Lagrangians that are used to construct Feynman diagrams—in particular, we dwell upon the question of gauge invariance and the question of coupling to a spin-3/2 fermion field. In Section 5, we consider the crossing-symmetry properties of the invariant functions and the crossing transformation of the amplitude from the s channel to the u and t channels. In Section 6, we present Feynman diagrams that are taken into account in writing the amplitude for Compton scattering and give a brief description of the method that we use to calculate the contributions of the Born diagrams in the s, u, and t channels and the contributions of the diagrams for the resonances in the s and u channels to the invariant functions. In the Appendix, we give explicit expressions for the Lagrangians used and for the results obtained with the aid of these Lagrangians for the contributions of the Born diagrams and diagrams for the resonances to the invariant functions.

2. The most convenient way to derive general expressions for the amplitude and invariant functions

---

*e-mail: `loginov@npi.tpu.ru`

is to consider $\gamma N \to \gamma N$ reactions in the s channel. The amplitudes for other channels can then be obtained by applying the crossing transformation to the amplitude for the s channel. In order to construct the amplitude for the s channel of $\gamma N \to \gamma N$ reactions, it is necessary to determine the number of independent invariant functions appearing in the expression for the amplitude. It is equal to the number of independent helicity amplitudes for $\gamma N \to \gamma N$ reactions with allowance for P and T invariance. The total number of helicity amplitudes for $\gamma^- + 1/2^+ \to \gamma^- + 1/2^+$ reactions is $2s_1(2s_2+1)2s_3(2s_4+1) = 16$. These amplitudes satisfy relations that follow from the P invariance of electromagnetic interaction; that is,

$$T(\lambda_3, \lambda_4; \lambda_1, \lambda_2) \tag{1}$$
$$= \eta(-1)^{(\lambda_1-\lambda_2)-(\lambda_3-\lambda_4)} T(-\lambda_3, -\lambda_4; -\lambda_1, -\lambda_2),$$

where $\eta = \eta_1\eta_2\eta_3\eta_4(-1)^{s_3+s_4-s_1-s_2}$, η_i and s_i being, respectively, the intrinsic parities and intrinsic spins of the particles involved in the reaction; λ_3 and λ_1 are the photon helicities in, respectively, the final and the initial state; and λ_4 and λ_2 are the nucleon helicities in, respectively, the final and the initial state. One can easily see that, owing to these relations, the number of independent helicity amplitudes decreases to eight. Further constraints on the number of independent helicity amplitudes follow from the T invariance of electromagnetic interaction. For elastic processes, T invariance leads to the following relations between the helicity amplitudes:

$$T(\lambda_3, \lambda_4; \lambda_1, \lambda_2) \tag{2}$$
$$= (-1)^{(\lambda_1-\lambda_2)-(\lambda_3-\lambda_4)} T(\lambda_1, \lambda_2; \lambda_3, \lambda_4).$$

As a result, the number of independent helicity amplitudes for Compton scattering decreases to six. For independent helicity amplitudes of Compton scattering, we chose here the following:

$$T\left(1, \frac{1}{2}; 1, \frac{1}{2}\right), \quad T\left(1, -\frac{1}{2}; 1, \frac{1}{2}\right), \tag{3}$$
$$T\left(-1, \frac{1}{2}; 1, \frac{1}{2}\right), \quad T\left(-1, -\frac{1}{2}; 1, \frac{1}{2}\right),$$
$$T\left(1, -\frac{1}{2}; 1, -\frac{1}{2}\right), \quad T\left(-1, \frac{1}{2}; 1, -\frac{1}{2}\right).$$

The remaining 10 helicity amplitudes can be expressed in terms of the independent helicity amplitudes (3) by using Eqs. (1) and (2).

Let us consider the general structure of the amplitude for the Compton scattering of a photon on a nucleon, $\gamma^- + 1/2^+ \to \gamma^- + 1/2^+$. We denote by k_1 and k_2 the 4-momenta of, respectively, the initial and the final photon; by p_1 and p_2 the 4-momenta of, respectively, the initial and the final nucleon; by $\epsilon(k_1)$ and $\epsilon(k_2)$ the polarization 4-vectors, of, respectively, the initial and the final photon; and by $u(p_1)$ and $u(p_2)$ the bispinors of, respectively, the initial and the final nucleon. In order to reveal the symmetry of the amplitude with respect to spatial reflection and time reversal, it is convenient to employ a symmetric and an antisymmetric combination of the photon 4-momenta:

$$K = (k_1 + k_2)/2, \quad Q = (k_2 - k_1)/2. \tag{4}$$

By adding, to K and Q, the symmetric 4-vector

$$P' = P - \frac{P \cdot K}{K^2} K,$$

where $P = (p_1 + p_2)/2$, and the pseudovector $N^\mu = i\epsilon^{\mu\nu\lambda\sigma} \times P'_\nu K_\lambda Q_\sigma$, we obtain four mutually orthogonal vectors in terms of which it is convenient to describe the gauge-invariant structure of the amplitude for $\gamma^- + 1/2^+ \to \gamma^- + 1/2^+$ reactions. The invariant variables s, t, and u are expressed in terms of the 4-vectors K, P, and Q as

$$s = (P+K)^2, \quad t = 4Q^2, \tag{5}$$
$$u = (P-K)^2, \quad s + t + u = 2M^2,$$

where M is the nucleon mass.

The general expression for the amplitude of $2 \to 2$ reactions involving arbitrary spins of participant particles has the form

$$T(p_2, p_1; P) = \sum_i f_i(s,t) R^i, \tag{6}$$

where $f_i(s,t)$ are invariant functions, which are dependent on the 4-momenta of initial and final particles only through the invariant variables s and t, and R^i are invariant linear combinations of the wave functions of all particles involved in the reaction. In the case of $\gamma^- + 1/2^+ \to \gamma^- + 1/2^+$ reactions, the number of independent invariant functions $f_i(s,t)$ is equal to six with allowance for P and T invariance. For R^i, we took here the independent invariant combinations

$$R^1 = \bar{u}(p_2)(P' \cdot \epsilon^*(k_2))(P' \cdot \epsilon(k_1)) P'^{-2} u(p_1), \tag{7}$$
$$R^2 = \bar{u}(p_2)(P' \cdot \epsilon^*(k_2))(P' \cdot \epsilon(k_1)) \widehat{K} P'^{-2} u(p_1),$$
$$R^3 = \bar{u}(p_2)(N \cdot \epsilon^*(k_2))(N \cdot \epsilon(k_1)) N^{-2} u(p_1),$$
$$R^4 = \bar{u}(p_2)(N \cdot \epsilon^*(k_2))(N \cdot \epsilon(k_1)) \widehat{K} N^{-2} u(p_1),$$
$$R^5 = \bar{u}(p_2)((P' \cdot \epsilon^*(k_2))(N \cdot \epsilon(k_1))$$
$$- (P' \cdot \epsilon(k_1))(N \cdot \epsilon^*(k_2)))\gamma_5 P'^{-2} K^{-2} u(p_1),$$
$$R^6 = \bar{u}(p_2)((P' \cdot \epsilon^*(k_2))(N \cdot \epsilon(k_1))$$
$$+ (P' \cdot \epsilon(k_1))(N \cdot \epsilon^*(k_2)))\gamma_5 \widehat{K} P'^{-2} K^{-2} u(p_1),$$

where $\widehat{K} = K_\mu \gamma^\mu$, $P'^{-2} = 1/P'^2$, $N^{-2} = 1/N^2$, and $K^{-2} = 1/K^2$. It can easily be seen that R^i are

P-invariant quantities. We will now show that R^i are also C-invariant quantities. Under the charge conjugation of the amplitude for $\gamma^- + 1/2^+ \to \gamma^- + 1/2^+$ reactions, the particle wave functions and 4-momenta are transformed as [11]

$$\epsilon(k_1) \to -\epsilon^*(k_2), \quad \epsilon(k_2) \to -\epsilon^*(k_1), \tag{8}$$
$$p_1 \to -p_2, \quad p_2 \to -p_1, \quad k_1 \to -k_2,$$
$$k_2 \to -k_1, \quad K \to -K, \quad P \to -P, \quad P' \to -P',$$
$$Q \to Q, \quad N \to N.$$

In addition, it is necessary to transpose R^i_{kl} in the Dirac indices k and l and multiply it from the left and from the right by the charge-conjugation matrix $C = \gamma^2\gamma^0$. The resulting transformation R^i_{kl} can be represented in the form

$$R^i_{kl}(\epsilon^*(k_2), k_2, p_2; \epsilon(k_1), k_1, p_1) \to C_{km} R^i_{nm} \tag{9}$$
$$\times (-\epsilon(k_1), -k_1, -p_1; -\epsilon^*(k_2), -k_2, -p_2) C_{nl}.$$

By using the properties of the charge-conjugation matrix [12, 13], we can readily show that, under the transformation in (9), all of the combinations in (7) go over to themselves—that is, they are C-invariant quantities. The invariant variables s, t, and u and, hence, the invariant amplitudes $f_i(s,t)$ remain unchanged under the transformations in (8). If use is made of the invariant combinations (7), the amplitude in (6) is P- and C-invariant; therefore, it is also T-invariant by virtue of the CPT theorem.

The invariant combinations R^i are also gauge-invariant, since all R^i vanish upon the substitution $\epsilon(k_1) \to k_1$ or $\epsilon(k_2) \to k_2$. To demonstrate this explicitly, we note that, since $k_1 = K - Q$ and $k_2 = K + Q$, we do indeed have

$$P' \cdot k_1 = P' \cdot (K - Q) = P' \cdot K - P' \cdot Q = 0, \tag{10}$$
$$P' \cdot k_2 = P' \cdot (K + Q) = P' \cdot K + P' \cdot Q = 0$$

by virtue of the orthogonality of the 4-vectors P', K, and Q. The scalar product of the 4-vectors N and k_1 and the scalar product of the 4-vectors N and k_2 also vanish,

$$N \cdot k_1 = i\epsilon^{\mu\nu\lambda\sigma} P'_\nu K_\lambda Q_\sigma k_{1\mu} \tag{11}$$
$$= i\epsilon^{\mu\nu\lambda\sigma} P'_\nu K_\lambda Q_\sigma (K_\mu - Q_\mu) = 0,$$
$$N \cdot k_2 = i\epsilon^{\mu\nu\lambda\sigma} P'_\nu K_\lambda Q_\sigma k_{2\mu}$$
$$= i\epsilon^{\mu\nu\lambda\sigma} P'_\nu K_\lambda Q_\sigma (K_\mu + Q_\mu) = 0,$$

since each of these scalar products is the convolution of tensors that are fully antisymmetric and symmetric in two tensor indices. From (10) and (11), it follows that R^i is a gauge-invariant quantity.

Finally, we will present a general expression for the P-, C-, T- and gauge-invariant helicity amplitude for $\gamma^- + 1/2^+ \to \gamma^- + 1/2^+$ reactions. We have

$$T(\lambda_3, \lambda_4, \lambda_1, \lambda_2) = f_1(s,t)\bar{u}(p_2, \lambda_4) \tag{12}$$
$$\times (P' \cdot \epsilon^*(k_2, \lambda_3))(P' \cdot \epsilon(k_1, \lambda_1)) P'^{-2} u(p_1, \lambda_2)$$
$$+ f_2(s,t)\bar{u}(p_2, \lambda_4)(P' \cdot \epsilon^*(k_2, \lambda_3))$$
$$\times (P' \cdot \epsilon(k_1, \lambda_1)) \widehat{K} P'^{-2} u(p_1, \lambda_2)$$
$$+ f_3(s,t)\bar{u}(p_2, \lambda_4)(N \cdot \epsilon^*(k_2, \lambda_3))$$
$$\times (N \cdot \epsilon(k_1, \lambda_1)) N^{-2} u(p_1, \lambda_2) + f_4(s,t)\bar{u}(p_2, \lambda_4)$$
$$\times (N \cdot \epsilon^*(k_2, \lambda_3))(N \cdot \epsilon(k_1, \lambda_1)) \widehat{K} N^{-2} u(p_1, \lambda_2)$$
$$+ f_5(s,t)\bar{u}(p_2, \lambda_4)((P' \cdot \epsilon^*(k_2, \lambda_3))(N \cdot \epsilon(k_1, \lambda_1))$$
$$- (P' \cdot \epsilon(k_1, \lambda_1))(N \cdot \epsilon^*(k_2, \lambda_3)))\gamma_5 P'^{-2}$$
$$\times K^{-2} u(p_1, \lambda_2) + f_6(s,t)\bar{u}(p_2, \lambda_4)$$
$$\times ((P' \cdot \epsilon^*(k_2, \lambda_3))(N \cdot \epsilon(k_1, \lambda_1))$$
$$+ (P' \cdot \epsilon(k_1, \lambda_1))(N \cdot \epsilon^*(k_2, \lambda_3)))\gamma_5 \widehat{K} P'^{-2}$$
$$\times K^{-2} u(p_1, \lambda_2).$$

In expression (12), the convention concerning the phase factor of a two-particle helicity state from [14] must be taken into account in defining helicity bispinors for nucleons.

3. Let us derive the transformation matrix relating the six independent helicity amplitudes in (3) to the six invariant functions f_i. Upon numbering the independent helicity amplitudes in (3) from one to six, we can write them explicitly. For this, it is necessary to substitute, into the general expression (12) for the helicity amplitude, the explicit expressions for the 4-vectors K, Q, P', and N; the explicit expressions for the helicity bispinors $u(p_1, \lambda_2)$ and $u(p_2, \lambda_4)$ of nucleons with allowance for the convention from [14]; and the explicit expressions for the polarization 4-vectors $\epsilon(k_1, \lambda_1)$ and $\epsilon(k_2, \lambda_3)$ of photons. As a result, we obtain a nonhomogeneous linear set of equations of the form

$$T_i(s,t) = \sum_{j=1}^{6} A_{ij} f_j(s,t), \tag{13}$$

where $T_i(s,t)$ are the independent helicity amplitudes given by (3). By using the Mathematica package for symbol calculus, one can show that the determinant of the matrix that specifies the set of Eqs. (13) does not vanish, which confirms the linear independence of the invariant combinations in (7). By means of the Mathematica package, the nonhomogeneous linear set of Eqs. (13) can be solved for the invariant functions $f_i(s,t)$; that is,

$$f_i(s,t) = \sum_{j=1}^{6} u_{ij} T_j(s,t). \tag{14}$$

Of 36 elements of the matrix $||u_{ij}||$, eight vanish. The remaining 28 nonzero matrix elements can be partitioned into four groups:

$$\begin{aligned} u_{11} &= -\frac{1}{2}u_{13} = u_{15} = -u_{31} = -\frac{1}{2}u_{33} \\ &= -u_{35} = Mu_{61} = -Mu_{65} = -\frac{M^2 \sec(\theta/2)}{s - M^2}, \\ u_{12} &= -2u_{14} = 2u_{16} = -u_{32} = -2u_{34} \\ &= 2u_{36} = -2u_{54} = -2u_{56} = \frac{2M\sqrt{s}\,\mathrm{cosec}(\theta/2)}{s - M^2}, \\ u_{21} &= -\frac{1}{2}u_{23} = u_{25} = -u_{41} = -\frac{1}{2}u_{43} \\ &= -u_{45} = \frac{M(M^2+s)\sec(\theta/2)}{(M^2 - s)^2}, \\ u_{22} &= -2u_{24} = 2u_{26} = -u_{42} = -2u_{44} \\ &= 2u_{46} = -\frac{4M^2\sqrt{s}\,\mathrm{cosec}(\theta/2)}{(M^2 - s)^2}, \\ u_{51} &= u_{52} = u_{53} = u_{55} = u_{62} = u_{63} \\ &= u_{64} = u_{66} = 0. \end{aligned} \tag{15}$$

In formulas (15), θ is the photon scattering angle in the c.m. frame of the s channel:

$$\cos\theta = 1 + \frac{2st}{(M^2 - s)^2}. \tag{16}$$

4. In calculating the invariant functions f_1–f_6, we will take into account here the contribution of the Born terms in the s, u, and t channels and the contribution of six resonances $P_{33}(1232)$, $P_{11}(1430)$, $S_{11}(1500)$, $D_{13}(1505)$, $S_{31}(1620)$, and $D_{33}(1700)$ in the s and u channels. In doing this, there arises the problem of choosing appropriate interaction Lagrangians corresponding to vertices of Feynman diagrams. In choosing interaction Lagrangians, we did not make here any simplifying assumptions. In other words, the interaction Lagrangians were written in the most general form compatible with the requirements of Hermitian conjugacy and P, T, and C invariance. In what is concerned with the gauge invariance of the Lagrangians used, we can say the following. The Lagrangians describing the interaction with a photon, which involve an electromagnetic field via the gauge-invariant tensor $F_{\mu\nu} = -i(k_\mu\epsilon_\nu - k_\nu\epsilon_\mu)$, are gauge-invariant themselves, irrespective of whether the particles involved are on or off the mass shell, since the tensor $F_{\mu\nu}$ vanishes identically under the substitution $\epsilon \to k$. With the exception of the Dirac part of the Lagrangian for photon–nucleon interaction [see formula (30) in the Appendix], almost all of the Lagrangians used in the present study belong to this type. The Dirac part in question is gauge-invariant only if both nucleons are on the mass shell, this being a corollary of the Dirac equation for a free nucleon. If one or both nucleons are off the mass shell, then the vertex corresponding to the Dirac part of the Lagrangian in (30) for photon–nucleon interaction is formally gauge-noninvariant. It can easily be shown, however, that the sum of two nucleon Born diagrams in the s and u channels is gauge-invariant, in just the same way as that for Compton scattering on an electron. Thus, all of the observables of the reactions in question are gauge-invariant quantities. For the Lagrangian describing the pion–nucleon interaction, we take here its pseudoscalar version. It should be noted that, in the case of Compton scattering, both nucleons of the t-channel Born diagram corresponding to pion–nucleon interaction are on the mass shell; therefore, the pseudovector version of the pion–nucleon interaction is equivalent in this case to the pseudoscalar version. In the case of Compton scattering, the pseudoscalar and the pseudovector coupling appear to be different only in considering loop diagrams, where one nucleon or both of them are off the mass shell. We note that the use of pseudovector coupling leads to extra degrees of the momentum in the numerator of the integrand, this impairing the convergence of the respective integral at high loop momenta. From the mathematical point of view, it is therefore preferable to use a pseudoscalar coupling in loop diagrams. In contrast to what occurs in the case of Compton scattering, one of the nucleons in the pion–nucleon–nucleon vertex of the Born diagrams for pion photoproduction on a nucleon is always off the mass shell, this violating the equivalence of the pseudoscalar and the pseudovector coupling even at the level of Born diagrams.

Let us consider the Lagrangian corresponding to a possible contact four-particle interaction of two photons and two nucleons. This Lagrangian is obtained via the minimal substitution $\partial_\mu \to \partial_\mu - ieA_\mu$ from the Pauli part of the Lagrangian for photon–nucleon interaction [see Eq. (30) below]; that is,

$$\mathcal{L}_{\text{cont}} = \frac{e^2}{2M} A^\mu \bar{N} \sigma_{\mu\nu} N A^\nu, \tag{17}$$

where A^μ is the electromagnetic-field 4-potential, N is the nucleon field, and $\sigma_{\mu\nu}$ is an antisymmetric matrix tensor that is defined as in [15]. It can be shown that, in the case of on-shell nucleons, the vertex corresponding to the Lagrangian in (17) does not vanish identically upon the gauge substitution $\epsilon^\mu \to k^\mu$, appearing to be a quantity proportional to $(s - M^2)$. Thus, the Lagrangian in (17) is not gauge-invariant within the approach of relativistic perturbation theory. We note that, in the three-dimensional form of the amplitude for Compton scattering in the c.m. frame, there are contact terms proportional to $\boldsymbol{\epsilon}_1 \cdot \boldsymbol{\epsilon}_2$ or $\boldsymbol{\epsilon}_1 \times \boldsymbol{\epsilon}_2$, but they arise as a three-dimensional reduction of noncontact relativistic diagrams.

Of six resonances whose contribution is taken into account in the direct and crossed channels, three have a spin of 3/2. The Rarita–Schwinger propagator corresponding to these resonances [see Eq. (42) in the Appendix] describes solely a transition between spin-3/2 states only if the respective spin-3/2 particle is on the mass shell. If the spin-3/2 particle is off the mass shell, then the Rarita–Schwinger propagator involves an unphysical sector corresponding to transitions between states such that at least one of them has a spin of 1/2. In order to eliminate the contribution of these undesirable transitions to analytic expressions corresponding to diagrams involving the exchange of a spin-3/2 resonance in the s or the u channel, it is necessary to impose a subsidiary condition on the Lagrangian for the $N^*N\gamma$ interaction. We will consider the interaction of a spin-3/2 particle with the electromagnetic-field tensor $F^{\mu\nu}$. In this case, the interaction Lagrangian has the form

$$\mathcal{L}_{\text{int}} = \bar{N}^{*\mu} O_{\mu\nu\sigma} N F^{\nu\sigma} + \text{h.c.}, \tag{18}$$

where $N^{*\mu}$ is a spin-3/2 field; here and below, the symbol h.c. stands for the Hermitian conjugate term, which is necessary for the Lagrangian to be an Hermitian operator. In order to suppress the contribution of transitions in the unphysical sector of the Rarita–Schwinger propagator, it is necessary to subject the vertex $O_{\mu\nu\sigma}$ to the condition [16]

$$\gamma^\mu O_{\mu\nu\sigma} = 0. \tag{19}$$

This condition can be realized in the following way. Suppose that, on the mass shell, the vertex $\Gamma_{\mu\nu\sigma}$ possesses all the required properties of relativistic invariance and C, P, and T invariance. We now introduce the vertex [16, 17]

$$O_{\mu\nu\sigma} = \Gamma_{\mu\nu\sigma} - \frac{1}{4}\gamma_\mu \gamma^\eta \Gamma_{\eta\nu\sigma}. \tag{20}$$

The vertex $O_{\mu\nu\sigma}$ obviously satisfies the condition in (19) and, on the mass shell, is equivalent to the vertex $\Gamma_{\mu\nu\sigma}$, since the Rarita–Schwinger spinors $N^{*\mu}$ satisfy the condition $\gamma_\mu N^{*\mu} = 0$. The vertices associated with all Lagrangians used in the present study to describe the interaction of spin-3/2 particles satisfy the condition in (19).

It should be noted that a different condition that completely eliminates the contribution of transitions in the unphysical sector of the Rarita–Schwinger propagator was proposed in [18, 19]. It consists in requiring that the interaction Lagrangian be invariant under a local gauge transformation of a spin-3/2 field: $N^{*\mu}(x) \to N^{*\mu}(x) + \partial_\mu \epsilon(x)$, where $\epsilon(x)$ is a spinor field. This invariance guarantees that the spin-3/2 field involved in the interaction has a correct number (equal to four) of degrees of freedom. In momentum space, this invariance results in that the $N^*N\gamma$-interaction vertex must satisfy the condition

$$P^\mu \Gamma_{\mu\nu\sigma} = 0, \tag{21}$$

where P^μ is the 4-momentum of the spin-3/2 particle involved. The use of the interaction Lagrangians satisfying the condition in (19) and those satisfying the condition in (21) leads to amplitudes differing by terms of a contact form [19].

The Lagrangians used to specify expressions for Feynman diagrams are given in the Appendix, along with explicit expressions for the propagators describing spin-1/2 and spin-3/2 particles.

5. Considering $\gamma N \to \gamma N$ as a generalized reaction that proceeds through three crossed channels, s, t, and u, we can establish the crossing-symmetry properties of the invariant amplitudes f_i. For an arbitrary generalized reaction, the crossing symmetry of invariant amplitudes arises in the case where, among four particles involved in the reaction, there are two identical particles, particles that belong to the same isomultiplet being treated as identical ones (this concerns, for example, nucleons or pions). In our case, there are two pairs of identical particles, two photons and two nucleons. The crossing within each of these particle pairs leads to an effective permutation of two invariant variables, $s \leftrightarrow u$, whereupon the amplitude resulting from the crossing of two photons must coincide with the original one by virtue of the generalized Pauli exclusion principle, while that which arises upon the crossing of two nucleons must differ from the original amplitude only in sign. It is the most straightforward to consider the crossing of two photons. In order to perform the crossing of two photons, it is necessary to make the following transformations in the original amplitude (12) [11]:

$$\begin{gathered} k_1 \to -k_2, \quad k_2 \to -k_1, \quad K \to -K, \\ P \to P, \quad P' \to P', \quad Q \to Q, \quad N \to -N, \\ s \to u, \quad u \to s, \quad t \to t, \\ \epsilon(k_1) \to -\epsilon^*(k_2), \quad \epsilon(k_2) \to -\epsilon^*(k_1). \end{gathered} \tag{22}$$

The invariant combinations R^i in (7) then transform as follows:

$$\begin{gathered} R^1 \to R^1, \quad R^2 \to -R^2, \quad R^3 \to R^3, \\ R^4 \to -R^4, \quad R^5 \to R^5, \quad R^6 \to R^6. \end{gathered} \tag{23}$$

By virtue of the generalized Pauli exclusion principle, the permutation of two identical photons must not lead to a change in the sign of the amplitude in (12);

therefore, the invariant functions f_1–f_6 transform as follow:

$$f_1(s,t) \to f_1(u,t), \quad f_2(s,t) \to -f_2(u,t), \quad (24)$$
$$f_3(s,t) \to f_3(u,t), \quad f_4(s,t) \to -f_4(u,t),$$
$$f_5(s,t) \to f_5(u,t), \quad f_6(s,t) \to f_6(u,t).$$

In order to reveal the symmetry properties of the invariant functions f_1–f_6 under the permutation $s \leftrightarrow u$, we can perform, on equal footing, the crossing of identical nucleons instead of the crossing of identical photons. Instead of (22), we will then have

$$p_1 \to -p_2, \quad p_2 \to -p_1, \quad K \to K, \quad (25)$$
$$P \to -P, \quad P' \to -P', \quad Q \to Q, \quad N \to -N,$$
$$s \to u, \quad u \to s, \quad t \to t,$$
$$u(p_1) \to u(-p_2) \equiv v(p_2),$$
$$u(p_2) \to u(-p_1) \equiv v(p_1),$$
$$\bar{u}_i(p_2) M_{ij}(p_2, p_1) u_j(p_1)$$
$$\to -\bar{v}_i(p_1) M_{ij}(-p_1, -p_2) v_j(p_2)$$
$$= \bar{u}_i(p_2) \widetilde{M}_{ij}(-p_1, -p_2) u_j(p_1),$$

where $\bar{u}_i(p_2) M_{ij}(p_2, p_1) u_j(p_1)$ is the reaction amplitude, in which we have explicitly indicated the bispinor indices i and j over which one performs summation and the nucleon 4-momenta p_1 and p_2. The tilde symbol denotes transposition in the bispinor indices. In the last transformation in (25), we have used the equalities $v(p) = C\widetilde{\bar{u}}(p)$ and $\bar{v}(p) = -\widetilde{u}(p) C$ and the properties of the charge-conjugation matrix $C = \gamma^2\gamma^0$ [12, 13]. It can easily be shown that the invariant spin combinations R^i (7) transform in just the same way as in (23), whence it again follows that the invariant functions f_i possess the crossing-symmetry properties (24).

The use of the crossing-symmetry properties (24) in calculating the invariant functions f_1–f_6 leads to a significant reduction of the volume of calculations. To demonstrate this, we note that, if one knows an analytic expression for the contribution of the nucleon Born diagrams or a resonance diagram in the s channel, $f_i^s(s,t)$, then the expression for the corresponding contribution in the u channel must have the form $f_i^u = \eta_i f_i^s(u,t) \equiv \eta_i f_i^s(2M^2 - s - t, t)$, where $\eta_1 = \eta_3 = \eta_5 = \eta_6 = 1$ and $\eta_2 = \eta_4 = -1$, no summation over the index i being performed. The crossing-symmetry properties (24) can also be considered a tool for verifying the mathematical correctness of rather complicated expressions for the invariant functions; however, the contribution of the u-channel diagrams must be calculated independently.

In calculating the invariant functions f_1–f_6, we have considered the s channel of $\gamma N \to \gamma N$ reactions. By means of the crossing transformation, one can go over from the reaction amplitude (12) for the s channel to the reaction amplitudes for the u and t channels. In order to go over from the reaction amplitude (12) for the s channel $\gamma(k_1)N(p_1) \to \gamma(k_2)N(p_2)$ to the reaction amplitude for the u channel $\gamma(k_1)\bar{N}(\bar{p}_1) \to \gamma(k_2)\bar{N}(\bar{p}_2)$, it is necessary to perform the following substitutions in (12):

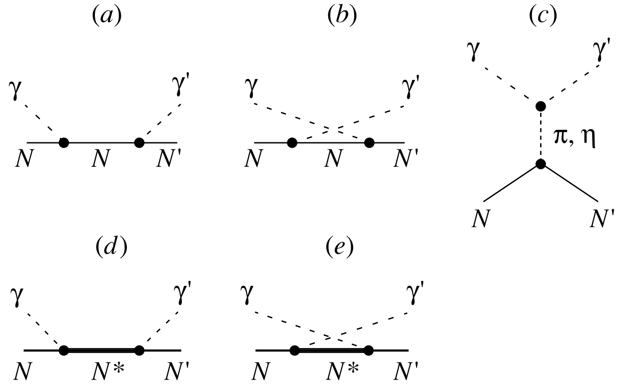

Diagrams whose contribution is taken into account in calculating the invariant functions f_1–f_6: (a, b, c) diagrams corresponding to the Born contributions in the s, u, and t channels and (d, e) diagrams corresponding to the resonance contributions in the s and u channels.

$$p_1 \to -\bar{p}_2, \quad p_2 \to -\bar{p}_1, \quad (26)$$
$$u(p_1) \to u(-\bar{p}_2) \equiv v(\bar{p}_2),$$
$$\bar{u}(p_2) \to \bar{u}(-\bar{p}_1) \equiv \bar{v}(\bar{p}_1).$$

Upon these substitutions, the 4-vectors K and Q remain unchanged, while the 4-vectors P, P', and N and the invariant variables s, t, and u are defined as

$$P = -\frac{1}{2}(\bar{p}_1 + \bar{p}_2), \quad P' = P - \frac{P \cdot K}{K^2} K, \quad (27)$$
$$N^\mu = i\epsilon^{\mu\nu\lambda\sigma} P'_\nu K_\lambda Q_\sigma,$$
$$s = (k_1 - \bar{p}_2)^2, \quad t = (k_1 - k_2)^2, \quad u = (\bar{p}_1 + k_1)^2.$$

In order to go over from the reaction amplitude (12) for the s channel to the reaction amplitude for the t channel $N(p)\bar{N}(\bar{p}) \to \gamma(k)\gamma(k')$, it is necessary to make the following substitutions in (12):

$$p_1 \to p, \quad p_2 \to -\bar{p}, \quad k_1 \to -k, \quad k_2 \to k', \quad (28)$$
$$u(p_1) \to u(p), \quad \bar{u}(p_2) \to \bar{u}(-\bar{p}) \equiv \bar{v}(\bar{p}),$$
$$\epsilon(k_1) \to \epsilon(-k) = -\epsilon^*(k), \quad \epsilon^*(k_2) \to \epsilon^*(k').$$

As a result, the 4-vectors K, Q, P, P', and N and the invariant variables s, t, and u are defined in the t channel as

$$K = \frac{1}{2}(k' - k), \quad Q = \frac{1}{2}(k + k'), \quad (29)$$
$$P = \frac{1}{2}(p - \bar{p}), \quad P' = P - \frac{P \cdot K}{K^2} K,$$

$$N^{\mu} = i\epsilon^{\mu\nu\lambda\sigma} P'_{\nu} K_{\lambda} Q_{\sigma}, \quad s = (p-k)^2,$$
$$t = (k+k')^2, \quad u = (\bar{p}-k)^2.$$

6. In calculating the invariant functions f_1–f_6, the amplitude of Compton scattering was written in accordance with Feynman rules for the diagrams in the figure. The vertices of the diagrams correspond to the Lagrangians presented in the Appendix. In the expression for the amplitude, use is made of the propagators for spin-1/2 and spin-3/2 resonances. These propagators are also given in the Appendix [see formulas (41), (42)].

By employing explicit expressions for the nucleon helicity bispinors and photon polarization 4-vectors [20], one can obtain, by means of the Mathematica package for symbol calculus, expressions for the six independent helicity amplitudes in (3) for Compton scattering. With the aid of the transformation matrix (15), which relates the independent helicity amplitudes (3) to the invariant functions f_1–f_6, one can then derive explicit expressions for the latter. The results of the calculations for the contribution of the Born diagrams in the s, u, and t channels and for the contributions of the diagrams for the $P_{33}(1232)$, $P_{11}(1430)$, $S_{11}(1500)$, $S_{31}(1620)$, $D_{33}(1700)$, and $D_{13}(1505)$ resonances in the s and u channels to the invariant functions for Compton scattering are given in the Appendix. The cases of Compton scattering on a proton and on a neutron have been considered. The invariant variables s and t have been taken for independent arguments of the invariant functions f_1–f_6. By means of a direct calculation at a few points of phase space, it has been verified that the analytic expressions for the contributions of the Born diagrams and the resonance diagrams satisfy the crossing-symmetry conditions (24), this being indicative of the absence of mathematical errors. The total expressions for the invariant functions describing Compton scattering on a proton and on a neutron can be obtained by summing the corresponding contributions of the Born diagrams and resonance diagrams. The invariant functions f_1–f_6 for Compton scattering that are subjected to the crossing transformations (26) and (28) can be used to construct the generalized-reaction amplitudes for the u channel $\gamma\bar{N} \to \gamma\bar{N}$ and the t channel $N\bar{N} \to \gamma\gamma$.

ACKNOWLEDGMENTS

This work was supported by the Russian Foundation for Basic Research (project nos. 01-02-17276, 03-02-06280) and the Ministry of Education of the Russian Federation (project no. E02-3.3-216).

APPENDIX

Presented below are the explicit expressions for the interaction Lagrangians employed in this study. In all of the formulas used for the Lagrangians, we adopt the following notation: $N^{*\mu}$ is the field of a spin-3/2 resonance, N^* is the field of a spin-1/2 resonance, N is the nucleon field, π_i is the pion field carrying the isotopic index i, η is the eta-meson field, A^{μ} is the electromagnetic-field 4-potential, and $F^{\mu\nu} = \partial^{\mu}A^{\nu} - \partial^{\nu}A^{\mu}$ is the gauge-invariant electromagnetic-field-strength tensor. The notation for masses is the following: M is the nucleon mass, μ is the pion mass, and μ_{η} is the eta-meson mass. The Dirac matrices γ_{μ} and γ_5, the antisymmetric matrix tensor $\sigma_{\mu\nu}$, and the metric tensor $g_{\mu\nu}$ are defined in just the same way as in [15]. In the isotopic part of the Lagrangians, τ_i is an isotopic Pauli matrix, while S_i is the isotopic matrix for the $3/2 \to 1/2$ transition [21].

The Lagrangian for photon–nucleon interaction has the form

$$\mathcal{L}_{NN\gamma} = \bar{N}\frac{1}{2}(F_1^S + F_1^V\tau_3)\widehat{A}N \tag{30}$$
$$- \frac{F^{\alpha\beta}}{4M}\bar{N}\sigma_{\alpha\beta}\frac{1}{2}(F_2^S + F_2^V\tau_3)N,$$

where $F_i^S = F_i^p + F_i^n$ and $F_i^V = F_i^p - F_i^n$ are, respectively, the isoscalar and isovector nucleon form factors; F_1^p and F_1^n are the proton and neutron Dirac form factors; and F_2^p and F_2^n are the proton and neutron Pauli form factors. In the present study, similar conventions are used for the form factors characterizing all isospin-1/2 resonances (P_{11}, S_{11}, D_{13}): the indices p and n label the form factors for the isodoublet components whose isospin projections onto the z axis are 1/2 and −1/2, respectively. The nucleon form factors are normalized at the photon point ($k^2 = 0$) according to the conditions $F_1^S = F_1^V = 1$, $F_2^S = \kappa^p + \kappa^n$, and $F_2^V = \kappa^p - \kappa^n$, where κ^p and κ^n are the anomalous magnetic moments of the proton and the neutron, respectively.

The interaction Lagrangians employed in calculating the t-channel Born diagrams for Compton scattering are given by

$$\mathcal{L}_{\pi\gamma\gamma} = \frac{1}{4}F^{\pi}\epsilon^{\mu\nu\alpha\beta}F_{\mu\nu}F_{\alpha\beta}\pi_0, \tag{31}$$

$$\mathcal{L}_{\pi NN} = \frac{2iMf}{\mu}\bar{N}\gamma_5\tau_i N\pi_i, \tag{32}$$

$$\mathcal{L}_{\eta\gamma\gamma} = \frac{1}{4}F^{\eta}\epsilon^{\mu\nu\alpha\beta}F_{\mu\nu}F_{\alpha\beta}\eta, \tag{33}$$

$$\mathcal{L}_{\eta NN} = \frac{2iMf_{\eta}}{\mu_{\eta}}\bar{N}\gamma_5 N\eta, \tag{34}$$

where F^{π}, F^{η}, f, and f_{η} are the corresponding coupling constants. The Lagrangians in (32) and (34) correspond to the pseudoscalar version of meson–nucleon coupling, while the Lagrangians in (31) and (33) have a manifest gauge-invariant structure.

The Lagrangian for the $NS_{11}\gamma$ interaction has the form

$$\mathcal{L}_{NS_{11}\gamma} = -\frac{F^{\alpha\beta}}{4M} \tag{35}$$
$$\times [\bar{N}\sigma_{\alpha\beta}\gamma_5(G^S_{NS_{11}\gamma} + \tau_3 G^V_{NS_{11}\gamma})N^*$$
$$- \bar{N}^*\sigma_{\alpha\beta}\gamma_5(G^S_{NS_{11}\gamma} + \tau_3 G^V_{NS_{11}\gamma})N],$$

where $G^S_{NS_{11}\gamma} = G^p_{NS_{11}\gamma} + G^n_{NS_{11}\gamma}$ and $G^V_{NS_{11}\gamma} = G^p_{NS_{11}\gamma} - G^n_{NS_{11}\gamma}$ are, respectively, the isoscalar and isovector form factors for $NS_{11}\gamma$ coupling.

The Lagrangian for the $NS_{31}\gamma$ interaction has the form

$$\mathcal{L}_{NS_{31}\gamma} = -\frac{G_{NS_{31}\gamma}}{2M}F^{\alpha\beta} \tag{36}$$
$$\times [\bar{N}\sigma_{\alpha\beta}\gamma_5 S_3 N^* - \bar{N}^*\sigma_{\alpha\beta}\gamma_5 S_3^{\dagger}N],$$

where $G_{NS_{31}\gamma}$ is the isovector form factor for the $NS_{31}\gamma$ interaction. In the present case, the isoscalar form factor is absent, since only an isovector photon can be absorbed or emitted in the process of $NS_{31}\gamma$ interaction. In the case of other isospin-3/2 resonances, the situation is similar.

The Lagrangian for the $NP_{11}\gamma$ interaction is given by

$$\mathcal{L}_{NP_{11}\gamma} = -\frac{F^{\alpha\beta}}{4M} \tag{37}$$
$$\times [\bar{N}\sigma_{\alpha\beta}(G^S_{NP_{11}\gamma} + \tau_3 G^V_{NP_{11}\gamma})N^*$$
$$+ \bar{N}^*\sigma_{\alpha\beta}(G^S_{NP_{11}\gamma} + \tau_3 G^V_{NP_{11}\gamma})N],$$

where $G^S_{NP_{11}\gamma} = G^p_{NP_{11}\gamma} + G^n_{NP_{11}\gamma}$ and $G^V_{NP_{11}\gamma} = G^p_{NP_{11}\gamma} - G^n_{NP_{11}\gamma}$ are, respectively, the isoscalar and the isovector form factor for the $NP_{11}\gamma$ interaction.

The Lagrangian for the $NP_{33}\gamma$ interaction has the form

$$\mathcal{L}_{NP_{33}\gamma} = \frac{G_{1NP_{33}\gamma}}{4M}\Big\{\bar{N}^{*\lambda}\Big[(g_{\lambda\alpha}\gamma_\beta - g_{\lambda\beta}\gamma_\alpha) \tag{38}$$
$$+ \frac{i}{2}\gamma_\lambda\sigma_{\alpha\beta}\Big]\gamma_5 S_3^{\dagger}N + \text{h.c.}\Big\}F^{\alpha\beta} - \frac{G_{2NP_{33}\gamma}}{8M^2}$$
$$\times \Big\{\bar{N}^{*\lambda}\Big[i\left(g_{\lambda\beta}\overleftrightarrow{\partial_\alpha} - g_{\lambda\alpha}\overleftrightarrow{\partial_\beta}\right)$$
$$- \frac{i}{4}\gamma_\lambda\left(\gamma_\beta\overleftrightarrow{\partial_\alpha} - \gamma_\alpha\overleftrightarrow{\partial_\beta}\right)\Big]\gamma_5 S_3^{\dagger}N + \text{h.c.}\Big\}F^{\alpha\beta}$$
$$+ \frac{G_{3NP_{33}\gamma}}{4M^2}\Big\{\Big[\bar{N}^{*\lambda}\left(-g_{\lambda\beta} + \frac{1}{4}\gamma_\lambda\gamma_\beta\right)i\gamma_5$$
$$\times S_3^{\dagger}N + \text{h.c.}\Big]\partial_\alpha F^{\alpha\beta}$$
$$+ \Big[\bar{N}^{*\lambda}\left(g_{\lambda\alpha} - \frac{1}{4}\gamma_\lambda\gamma_\alpha\right)i\gamma_5 S_3^{\dagger}N + \text{h.c.}\Big]\partial_\beta F^{\alpha\beta}\Big\},$$

where $G_{1NP_{33}\gamma}$, $G_{2NP_{33}\gamma}$, and $G_{3NP_{33}\gamma}$ are the isovector form factors for the $NP_{33}\gamma$ interaction. In formulas (38)–(40), the symbol $\overleftrightarrow{\partial}$ acts on the neighboring functions as follows: $u\overleftrightarrow{\partial}v = u(\partial v) - (\partial u)v$.

The Lagrangian for the $ND_{33}\gamma$ interaction has the form

$$\mathcal{L}_{ND_{33}\gamma} = \frac{G_{1ND_{33}\gamma}}{4M}\Big\{\bar{N}^{*\lambda}\Big[(g_{\lambda\alpha}\gamma_\beta - g_{\lambda\beta}\gamma_\alpha) \tag{39}$$
$$+ \frac{1}{2}\gamma_\lambda\sigma_{\alpha\beta}\Big]S_3^{\dagger}N + \text{h.c.}\Big\}F^{\alpha\beta} - \frac{G_{2ND_{33}\gamma}}{8M^2}$$
$$\times \Big\{\bar{N}^{*\lambda}\Big[i\left(g_{\lambda\beta}\overleftrightarrow{\partial_\alpha} - g_{\lambda\alpha}\overleftrightarrow{\partial_\beta}\right)$$
$$- \frac{i}{4}\gamma_\lambda\left(\gamma_\beta\overleftrightarrow{\partial_\alpha} - \gamma_\alpha\overleftrightarrow{\partial_\beta}\right)\Big]S_3^{\dagger}N + \text{h.c.}\Big\}F^{\alpha\beta}$$
$$+ \frac{G_{3ND_{33}\gamma}}{4M^2}\Big\{\Big[\bar{N}^{*\lambda}i\left(-g_{\lambda\beta} + \frac{1}{4}\gamma_\lambda\gamma_\beta\right)$$
$$\times S_3^{\dagger}N + \text{h.c.}\Big]\partial_\alpha F^{\alpha\beta}$$
$$+ \Big[\bar{N}^{*\lambda}i\left(g_{\lambda\alpha} - \frac{1}{4}\gamma_\lambda\gamma_\alpha\right)S_3^{\dagger}N + \text{h.c.}\Big]\partial_\beta F^{\alpha\beta}\Big\},$$

where $G_{1ND_{33}\gamma}$, $G_{2ND_{33}\gamma}$, and $G_{3ND_{33}\gamma}$ are the isovector form factors for the $ND_{33}\gamma$ interaction.

The Lagrangian for the $ND_{13}\gamma$ interaction is given by

$$\mathcal{L}_{ND_{13}\gamma} = \frac{1}{4M}\Big\{\bar{N}^{*\lambda}\Big[(g_{\lambda\alpha}\gamma_\beta - g_{\lambda\beta}\gamma_\alpha) \tag{40}$$
$$+ \frac{1}{2}\gamma_\lambda\sigma_{\alpha\beta}\Big]\frac{1}{2}[G^S_{1ND_{13}\gamma}$$
$$+ G^V_{1ND_{13}\gamma}\tau_3]N + \text{h.c.}\Big\}F^{\alpha\beta} - \frac{1}{8M^2}$$
$$\times \Big\{\bar{N}^{*\lambda}\Big[i\left(g_{\lambda\beta}\overleftrightarrow{\partial_\alpha} - g_{\lambda\alpha}\overleftrightarrow{\partial_\beta}\right)$$
$$- \frac{i}{4}\gamma_\lambda\left(\gamma_\beta\overleftrightarrow{\partial_\alpha} - \gamma_\alpha\overleftrightarrow{\partial_\beta}\right)\Big]\frac{1}{2}[G^S_{2ND_{13}\gamma}$$
$$+ G^V_{2ND_{13}\gamma}\tau_3]N + \text{h.c.}\Big\}F^{\alpha\beta}$$
$$+ \frac{1}{4M^2}\Big[\bar{N}^{*\lambda}i\left(-g_{\lambda\beta} + \frac{1}{4}\gamma_\lambda\gamma_\beta\right)\frac{1}{2}[G^S_{3ND_{13}\gamma}$$
$$+ G^V_{3ND_{13}\gamma}\tau_3]N + \text{h.c.}\Big]\partial_\alpha F^{\alpha\beta}$$

$$+ \frac{1}{4M^2}\left[\bar{N}^{*\lambda} i \left(g_{\lambda\alpha} - \frac{1}{4}\gamma_\lambda \gamma_\alpha\right) \frac{1}{2}[G^S_{3ND_{13}\gamma} + G^V_{3ND_{13}\gamma}\tau_3] N + \text{h.c.}\right] \partial_\beta F^{\alpha\beta},$$

where $G^S_{iND_{13}\gamma} = G^p_{iND_{13}\gamma} + G^n_{iND_{13}\gamma}$ and $G^V_{iND_{13}\gamma} = G^p_{iND_{13}\gamma} - G^n_{iND_{13}\gamma}$ are, respectively, the isoscalar and the isovector form factor for the $ND_{13}\gamma$ interaction. The Lagrangians in (35)–(40) are gauge-invariant, since the 4-potential A^μ appears in them through the gauge-invariant tensor $F^{\mu\nu}$. It should be noted that, in the Lagrangians given by (38)–(40), the contribution of the terms that are proportional to $\partial_\mu F^{\mu\nu}$ vanish for real photons ($k^2 = 0$, $\epsilon \cdot k = 0$). In the present study, the propagator for spin-1/2 resonances (S_{11}, S_{31}, P_{11}) is taken in the form

$$G(P^2; P) = \frac{\widehat{P} + M^*}{P^2 - M^{*2} + iM^*\Gamma(P^2)}. \tag{41}$$

For the spin-3/2 resonances (P_{33}, D_{33}, D_{13}), we employ the Rarita–Schwinger propagator

$$G^{\mu\nu}(P^2; P) = \frac{\widehat{P} + M^*}{P^2 - M^{*2} + iM^*\Gamma(P^2)} \times \left\{-g^{\mu\nu} + \frac{\gamma^\mu\gamma^\nu}{3} + \frac{2P^\mu P^\nu}{3M^{*2}} - \frac{P^\mu\gamma^\nu - \gamma^\mu P^\nu}{3M^*}\right\}. \tag{42}$$

In expressions (41) and (42), M^* and $\Gamma(P^2)$ are the mass and the width of the corresponding resonance whose 4-momentum is denoted by P. The resonance width $\Gamma(P^2)$ in (41) and (42) vanishes for $P^2 < (M + \mu)^2$—that is, in the resonance u-channel diagrams.

Below, we present explicit expressions for the contributions of the Born diagrams and the contributions of the diagrams for six resonances [$P_{33}(1232)$, $P_{11}(1430)$, $S_{11}(1500)$, $S_{31}(1620)$, $D_{33}(1700)$, $D_{13}(1505)$] to the invariant functions f_1–f_6 in the amplitude given by (12).

The contribution of the Born diagrams to the invariant functions f_1–f_6 for Compton scattering on a proton has the form

$$\left\{\frac{-2MtF_1^{p2}}{(M^2 - s)(M^2 - s - t)}, \frac{(2M^2 - 2s - t)F_1^{p2}}{(-M^2 + s)(-M^2 + s + t)}, \frac{(2F_1^p - F_2^p)F_2^p}{M}, \frac{(-2M^2 + 2s + t)(F_1^p - F_2^p)^2}{(M^2 - s)(M^2 - s - t)}, \right. \tag{43}$$

$$\frac{2M^2tF_1^{p2} + 2(M^4 - 2M^2(s + t) + s(s + t))F_1^pF_2^p - (M^2 - s)(M^2 - s - t)F_2^{p2}}{2M(M^2 - s)(M^2 - s - t)}$$

$$\left. + \frac{2fMtF^\pi}{\mu(t - \mu^2)} + \frac{2F^\eta Mtf_\eta}{\mu_\eta(t - \mu_\eta^2)}, \frac{-2M^2tF_1^{p2} + 2M^2tF_1^pF_2^p + (M^2 - s)(M^2 - s - t)F_2^{p2}}{2M^2(M^2 - s)(M^2 - s - t)}\right\}.$$

In the case of Compton scattering on a neutron, the following substitutions must be made in formulas (43):

$$F_1^p \to F_1^n, \quad F_2^p \to F_2^n, \quad f \to -f. \tag{44}$$

It should be noted that the t-channel Born diagram involving the exchange of a pion or an eta meson contributes to only one invariant function, f_5.

The contributions of P_{33} to the invariant functions $f_1 - f_6$ for Compton scattering (they have the same form for Compton scattering on a proton and on a neutron) are given by

$$\left\{-\frac{1}{576M^4D_{s\Delta}M_\Delta^2}(16M^2(M - M_\Delta) \right. \tag{45}$$

$$\times (M^4 - M^2s + 3(M^3 - Ms)M_\Delta$$

$$+ 3tM_\Delta^2)G^2_{1NP_{33}\gamma} - 16M(M^2(M^2 - s)s$$

$$+ (M^5 - Ms^2)M_\Delta - 3s(-M^2 + s + 2t)M_\Delta^2$$

$$+ 6M(-M^2 + s + t)M_\Delta^3)G_{1NP_{33}\gamma}G_{2NP_{33}\gamma}$$

$$+ (Ms(M^4 + 2M^2s - 3s^2) - 2s(-3M^4$$

$$+ 2M^2s + s^2)M_\Delta + 3M(5M^4 - 22M^2s$$

$$+ s(17s + 16t))M_\Delta^2 - 6(M^4 - 6M^2s + s(5s$$

$$+ 8t))M_\Delta^3)G^2_{2NP_{33}\gamma}) + \frac{1}{576M^4D_{u\Delta}M_\Delta^2}$$

$$\times (16M^2(M - M_\Delta)(M^2(M^2 - s - t)$$

$$+ 3M(M^2 - s - t)M_\Delta - 3tM_\Delta^2)G^2_{1NP_{33}\gamma}$$

$$- 16M(M^2(2M^4 - 3M^2(s + t) + (s + t)^2)$$

$$+ M(3M^4 - 4M^2(s + t) + (s + t)^2)M_\Delta$$

$$+ 3(2M^4 + s^2 - t^2 + M^2(t - 3s))M_\Delta^2$$

$$- 6(M^3 - Ms)M_\Delta^3)G_{1NP_{33}\gamma}G_{2NP_{33}\gamma}$$

$$+ (M(14M^6 - 27M^4(s + t) + 16M^2(s + t)^2$$

$$- 3(s+t)^3) + (20M^6 - 34M^4(s+t)$$
$$+ 16M^2(s+t)^2 - 2(s+t)^3)M_\Delta$$
$$- 3M(29M^4 + 17s^2 + 18st + t^2$$
$$- 2M^2(23s+7t))M_\Delta^2 + 6(9M^4 + 5s^2$$
$$+ 2st - 3t^2 + 2M^2(-7s+t))M_\Delta^3)G^2_{2NP_{33}\gamma}),$$

$$-\frac{1}{576M^4D_{s\Delta}M_\Delta^2}(16M^2(M^2(M^2+s)$$
$$+ 4M^3M_\Delta + 3(-3M^2+s+t)M_\Delta^2)G^2_{1NP_{33}\gamma}$$
$$- 8M(Ms(3M^2+s) + 2(M^4+3M^2s)M_\Delta$$
$$+ 3M(3M^2+s)M_\Delta^2 + 6(-5M^2+s$$
$$+ 2t)M_\Delta^3)G_{1NP_{33}\gamma}G_{2NP_{33}\gamma} + (s(M^4$$
$$+ 6M^2s+s^2) + 8Ms(M^2+s)M_\Delta$$
$$+ 3(5M^4 - 34M^2s + s(5s+16t))M_\Delta^2 + 24M$$
$$\times (M^2+s)M_\Delta^3)G^2_{2NP_{33}\gamma}) + \frac{1}{576M^4D_{u\Delta}M_\Delta^2}$$
$$\times (16(M^4(3M^2-s-t) + 4M^5M_\Delta - 3M^2$$
$$\times (M^2+s)M_\Delta^2)G^2_{1NP_{33}\gamma} - 8M(M(10M^4$$
$$- 7M^2(s+t) + (s+t)^2) + 2M^2(7M^2$$
$$- 3(s+t))M_\Delta + 3M(5M^2-s-t)M_\Delta^2$$
$$- 6(3M^2+s-t)M_\Delta^3)G_{1NP_{33}\gamma}G_{2NP_{33}\gamma}$$
$$+ (34M^6 - 37M^4(s+t) + 12M^2(s+t)^2$$
$$- (s+t)^3 + 8M(6M^4 - 5M^2(s+t)$$
$$+ (s+t)^2)M_\Delta - 3(43M^4 - 5s^2 + 6st$$
$$+ 11t^2 - 2M^2(7s+23t))M_\Delta^2$$
$$+ 24M(3M^2-s-t)M_\Delta^3)G^2_{2NP_{33}\gamma}),$$

$$\frac{1}{576M^4D_{s\Delta}M_\Delta^2}(16M^2(M+M_\Delta)(M^4$$
$$- M^2s - 3(M^3-Ms)M_\Delta + 3tM_\Delta^2)G^2_{1NP_{33}\gamma}$$
$$- 16M(M^2-s)^2(M-3M_\Delta)M_\Delta G_{1NP_{33}\gamma}$$
$$\times G_{2NP_{33}\gamma} + (M^2-s)^2(Ms + 2sM_\Delta$$
$$+ 15MM_\Delta^2 - 18M_\Delta^3)G^2_{2NP_{33}\gamma})$$
$$- \frac{1}{576M^4D_{u\Delta}M_\Delta^2}(16M^2(M+M_\Delta)$$
$$\times (M^2(M^2-s-t) + 3M(-M^2+s+t)M_\Delta$$
$$- 3tM_\Delta^2)G^2_{1NP_{33}\gamma} + 16M(-M^2+s+t)^2$$
$$\times (M-3M_\Delta)M_\Delta G_{1NP_{33}\gamma}G_{2NP_{33}\gamma} - (-M^2$$
$$+ s+t)^2(M(2M^2-s-t) + (4M^2$$
$$- 2(s+t))M_\Delta + 15MM_\Delta^2 - 18M_\Delta^3)G^2_{2NP_{33}\gamma}),$$

$$\frac{1}{576M^4D_{s\Delta}M_\Delta^2}(16M^2(M^2(M^2+s)$$
$$- 4M^3M_\Delta + 3(-3M^2+s+t)M_\Delta^2)G^2_{1NP_{33}\gamma}$$
$$- 8M(Ms(-M^2+s) + 2(M^4-M^2s)M_\Delta$$
$$- 3(M^3-Ms)M_\Delta^2 - 6(M^2-s)M_\Delta^3)G_{1NP_{33}\gamma}$$
$$\times G_{2NP_{33}\gamma} + (M^2-s)^2(s+15M_\Delta^2)G^2_{2NP_{33}\gamma})$$
$$- \frac{1}{576M^4D_{u\Delta}M_\Delta^2}(16(M^4(3M^2-s-t)$$
$$- 4M^5M_\Delta - 3M^2(M^2+s)M_\Delta^2)G^2_{1NP_{33}\gamma}$$
$$- 8M(M(2M^4 - 3M^2(s+t) + (s+t)^2)$$
$$+ 2M^2(-M^2+s+t)M_\Delta + 3M(M^2$$
$$- s-t)M_\Delta^2 + 6(M^2-s-t)M_\Delta^3)G_{1NP_{33}\gamma}$$
$$\times G_{2NP_{33}\gamma} + (-M^2+s+t)^2(2M^2$$
$$- s - t + 15M_\Delta^2)G^2_{2NP_{33}\gamma}),$$

$$-\frac{1}{288M^4D_{s\Delta}M_\Delta^2}(8M^2M_\Delta(2M^4$$
$$- 2M^2s + 3tM_\Delta^2)G^2_{1NP_{33}\gamma}$$
$$- 4M(M^2(M^2-s)s + M_\Delta(2M(M^2-s)s$$
$$+ 3M_\Delta(M^4 - M^2s + 2st + 2M(-M^2$$
$$+ s)M_\Delta)))G_{1NP_{33}\gamma}G_{2NP_{33}\gamma} + (M^2-s)$$
$$\times (Ms^2 + s(M^2+s)M_\Delta - 9MsM_\Delta^2$$
$$+ 3(M^2+s)M_\Delta^3)G^2_{2NP_{33}\gamma}) - \frac{1}{288M^4D_{u\Delta}M_\Delta^2}$$
$$\times (-8M^2M_\Delta(2M^2(M^2-s-t)$$
$$- 3tM_\Delta^2)G^2_{1NP_{33}\gamma} + 4M(M^2(M^2-s-t)$$
$$\times (2M^2-s-t) + M_\Delta(2M(M^2-s-t)$$
$$\times (2M^2-s-t) + 3M_\Delta(M^4 + 2t(s+t)$$
$$- M^2(s+5t) + 2M(-M^2+s+t)M_\Delta)))$$
$$\times G_{1NP_{33}\gamma}G_{2NP_{33}\gamma} - (M^2-s-t)$$
$$\times (M(-2M^2+s+t)^2 + (2M^2-s-t)$$
$$\times (3M^2-s-t)M_\Delta + 9M(-2M^2$$
$$+ s+t)M_\Delta^2 + (9M^2 - 3(s+t))M_\Delta^3)G^2_{2NP_{33}\gamma}),$$

$$-\frac{1}{576M^4D_{s\Delta}M_\Delta^2}(16M^2(M^4 - M^2s$$
$$+ 3(-M^2+s+t)M_\Delta^2)G^2_{1NP_{33}\gamma}$$
$$- 8M(M(M^2-s)s + 2(M^4-M^2s)M_\Delta$$
$$+ 3(M^3-Ms)M_\Delta^2 + 6(-M^2$$
$$+ s+t)M_\Delta^3)G_{1NP_{33}\gamma}G_{2NP_{33}\gamma} + (s(M^4-s^2)$$

$$
\begin{gathered}
+ 4M(M^2 - s)sM_\Delta - 9(M^4 - s^2)M_\Delta^2 \\
+ 12(M^3 - Ms)M_\Delta^3)G^2_{2NP_{33}\gamma}) \\
+ \frac{1}{576M^4 D_{u\Delta} M_\Delta^2}(16(M^4(M^2 - s - t) \\
- 3(M^4 - M^2 s)M_\Delta^2)G^2_{1NP_{33}\gamma} \\
- 8M(M(2M^4 - 3M^2(s+t) + (s+t)^2) \\
+ 2M^2(M^2 - s - t)M_\Delta + 3M(M^2 - s - t)M_\Delta^2 \\
- 6(M^2 - s)M_\Delta^3)G_{1NP_{33}\gamma}G_{2NP_{33}\gamma} + (6M^6 \\
- 11M^4(s+t) + 6M^2(s+t)^2 - (s+t)^3 \\
+ 4M(2M^4 - 3M^2(s+t) + (s+t)^2)M_\Delta \\
- 9(3M^4 - 4M^2(s+t) + (s+t)^2)M_\Delta^2 \\
+ 12M(M^2 - s - t)M_\Delta^3)G^2_{2NP_{33}\gamma})\Big\}.
\end{gathered}
$$

In formulas (45), M_Δ is the mass of the P_{33} resonance, while $D_{s\Delta} = s - M_\Delta^2 + iM_\Delta\Gamma_\Delta(s)$ and $D_{u\Delta} = u - M_\Delta^2 + iM_\Delta\Gamma_\Delta(u)$ are the denominators of the propagator for the P_{33} resonance in, respectively, the s and the u channel.

The contributions of P_{11} to the invariant functions f_1–f_6 for Compton scattering on a proton are

$$
\begin{gathered}
\Big\{ - \frac{(M^2 - s)G^{p2}_{NP_{11}\gamma}(M - M_{P_{11}})}{4M^2 D_{sP_{11}}} \qquad (46) \\
+ \frac{(M^2 - s - t)G^{p2}_{NP_{11}\gamma}(M - M_{P_{11}})}{4M^2 D_{uP_{11}}}, \\
- \frac{G^{p2}_{NP_{11}\gamma}(M^2 + s - 2MM_{P_{11}})}{4M^2 D_{sP_{11}}} \\
+ \frac{G^{p2}_{NP_{11}\gamma}(3M^2 - s - t - 2MM_{P_{11}})}{4M^2 D_{uP_{11}}}, \\
\frac{(M^2 - s)G^{p2}_{NP_{11}\gamma}(M + M_{P_{11}})}{4M^2 D_{sP_{11}}} \\
- \frac{(M^2 - s - t)G^{p2}_{NP_{11}\gamma}(M + M_{P_{11}})}{4M^2 D_{uP_{11}}}, \\
\frac{G^{p2}_{NP_{11}\gamma}(M^2 + s + 2MM_{P_{11}})}{4M^2 D_{sP_{11}}} \\
- \frac{G^{p2}_{NP_{11}\gamma}(3M^2 - s - t + 2MM_{P_{11}})}{4M^2 D_{uP_{11}}}, \\
\frac{(M^2 - s)G^{p2}_{NP_{11}\gamma}M_{P_{11}}}{4M^2 D_{sP_{11}}} \\
- \frac{(M^2 - s - t)G^{p2}_{NP_{11}\gamma}M_{P_{11}}}{4M^2 D_{uP_{11}}}, \\
- \frac{(M^2 - s)G^{p2}_{NP_{11}\gamma}}{4M^2 D_{sP_{11}}} + \frac{(M^2 - s - t)G^{p2}_{NP_{11}\gamma}}{4M^2 D_{uP_{11}}}\Big\}.
\end{gathered}
$$

In formulas (46), $M_{P_{11}}$ is the mass of the P_{11} resonance, while $D_{sP_{11}} = s - M_{P_{11}}^2 + iM_{P_{11}}\Gamma_{P_{11}}(s)$ and $D_{uP_{11}} = u - M_{P_{11}}^2 + iM_{P_{11}}\Gamma_{P_{11}}(u)$ are the denominators of the propagator for the P_{11} resonance in, respectively, the s and the u channel. In the case of Compton scattering on a neutron, the substitution $G^p_{NP_{11}\gamma} \to G^n_{NP_{11}\gamma}$ must be made in formulas (46).

The contributions of S_{11} to the invariant functions f_1–f_6 for Compton scattering on a proton are

$$
\begin{gathered}
\Big\{ - \frac{(M^2 - s)G^{p2}_{NS_{11}\gamma}(M + M_{S_{11}})}{4M^2 D_{sS_{11}}} \qquad (47) \\
+ \frac{(M^2 - s - t)G^{p2}_{NS_{11}\gamma}(M + M_{S_{11}})}{4M^2 D_{uS_{11}}}, \\
- \frac{G^{p2}_{NS_{11}\gamma}(M^2 + s + 2MM_{S_{11}})}{4M^2 D_{sS_{11}}} \\
+ \frac{G^{p2}_{NS_{11}\gamma}(3M^2 - s - t + 2MM_{S_{11}})}{4M^2 D_{uS_{11}}}, \\
\frac{(M^2 - s)G^{p2}_{NS_{11}\gamma}(M - M_{S_{11}})}{4M^2 D_{sS_{11}}} \\
- \frac{(M^2 - s - t)G^{p2}_{NS_{11}\gamma}(M - M_{S_{11}})}{4M^2 D_{uS_{11}}}, \\
\frac{G^{p2}_{NS_{11}\gamma}(M^2 + s - 2MM_{S_{11}})}{4M^2 D_{sS_{11}}} \\
- \frac{G^{p2}_{NS_{11}\gamma}(3M^2 - s - t - 2MM_{S_{11}})}{4M^2 D_{uS_{11}}}, \\
- \frac{(M^2 - s)G^{p2}_{NS_{11}\gamma}M_{S_{11}}}{4M^2 D_{sS_{11}}} \\
+ \frac{(M^2 - s - t)G^{p2}_{NS_{11}\gamma}M_{S_{11}}}{4M^2 D_{uS_{11}}}, \\
- \frac{(M^2 - s)G^{p2}_{NS_{11}\gamma}}{4M^2 D_{sS_{11}}} + \frac{(M^2 - s - t)G^{p2}_{NS_{11}\gamma}}{4M^2 D_{uS_{11}}}\Big\}.
\end{gathered}
$$

In formulas (47), $M_{S_{11}}$ is the mass of the S_{11} resonance, while $D_{sS_{11}} = s - M_{S_{11}}^2 + iM_{S_{11}}\Gamma_{S_{11}}(s)$ and $D_{uS_{11}} = u - M_{S_{11}}^2 + iM_{S_{11}}\Gamma_{S_{11}}(u)$ are the denominators of the propagator of the S_{11} resonance in, respectively, the s and the u channel. In the case of Compton scattering on a neutron, the substitution $G^p_{NS_{11}\gamma} \to G^n_{NS_{11}\gamma}$ must be made in formulas (47).

The contributions of S_{31} to the invariant functions f_1–f_6 for Compton scattering (they have the same form for Compton scattering on a proton and on a neutron) are

$$\begin{gathered}
\Bigg\{-\frac{2(M^2-s)G^2_{NS_{31}\gamma}(M+M_{S_{31}})}{3M^2D_{sS_{31}}} \\
+\frac{2(M^2-s-t)G^2_{NS_{31}\gamma}(M+M_{S_{31}})}{3M^2D_{uS_{31}}}, \\
-\frac{2G^2_{NS_{31}\gamma}(M^2+s+2MM_{S_{31}})}{3M^2D_{sS_{31}}} \\
+\frac{2G^2_{NS_{31}\gamma}(3M^2-s-t+2MM_{S_{31}})}{3M^2D_{uS_{31}}}, \\
\frac{2(M^2-s)G^2_{NS_{31}\gamma}(M-M_{S_{31}})}{3M^2D_{sS_{31}}} \\
-\frac{2(M^2-s-t)G^2_{NS_{31}\gamma}(M-M_{S_{31}})}{3M^2D_{uS_{31}}}, \\
\frac{2G^2_{NS_{31}\gamma}(M^2+s-2MM_{S_{31}})}{3M^2D_{sS_{31}}} \\
-\frac{2G^2_{NS_{31}\gamma}(3M^2-s-t-2MM_{S_{31}})}{3M^2D_{uS_{31}}}, \\
-\frac{2(M^2-s)G^2_{NS_{31}\gamma}M_{S_{31}}}{3M^2D_{sS_{31}}} \\
+\frac{2(M^2-s-t)G^2_{NS_{31}\gamma}M_{S_{31}}}{3M^2D_{uS_{31}}}, \\
-\frac{2(M^2-s)G^2_{NS_{31}\gamma}}{3M^2D_{sS_{31}}}+\frac{2(M^2-s-t)G^2_{NS_{31}\gamma}}{3M^2D_{uS_{31}}}\Bigg\}.
\end{gathered} \tag{48}$$

In formulas (48), $M_{S_{31}}$ is the mass of the S_{31} resonance, while $D_{sS_{31}} = s - M^2_{S_{31}} + iM_{S_{31}}\Gamma_{S_{31}}(s)$ and $D_{uS_{31}} = u - M^2_{S_{31}} + iM_{S_{31}}\Gamma_{S_{31}}(u)$ are the denominators of the propagator for the S_{31} resonance in, respectively, the s and the u channel.

The contributions of D_{33} to invariant functions f_1–f_6 for Compton scattering (they are identical for Compton scattering on a proton and on a neutron) are

$$\begin{gathered}
\Bigg\{\frac{1}{576M^4D_{sD_{33}}M^2_{D_{33}}}(16M^2(M+M_{D_{33}}) \\
\times(M^4+3M^2s-4s^2-3(M^3-Ms)M_{D_{33}} \\
+(-4M^2+4s+3t)M^2_{D_{33}})G^2_{1ND_{33}\gamma}-8M \\
\times(s(-3M^4+2M^2s+s^2)+2(M^5-Ms^2) \\
\times M_{D_{33}}+(M^4-6M^2s+s(5s+12t))M^2_{D_{33}} \\
-12M(M^2-s-t)M^3_{D_{33}})G_{1ND_{33}\gamma}G_{2ND_{33}\gamma} \\
+(Ms(M^4+2M^2s-3s^2)+2s(2M^2s \\
+s^2-3M^4)M_{D_{33}}+3M(5M^4-22M^2s \\
+s(17s+16t))M^2_{D_{33}}+6(M^4-6M^2s+s(5s \\
+8t))M^3_{D_{33}})G^2_{2ND_{33}\gamma})+\frac{1}{576M^4D_{uD_{33}}M^2_{D_{33}}} \\
\times(16M^2(M+M_{D_{33}})(9M^4-13M^2(s+t) \\
+4(s+t)^2+3M(s-M^2+t)M_{D_{33}} \\
+(4s+t-4M^2)M^2_{D_{33}})G^2_{1ND_{33}\gamma} \\
+8M(10M^6-17M^4(s+t)+8M^2(s+t)^2 \\
-(s+t)^3-2M(3M^4-4M^2(s+t) \\
+(s+t)^2)M_{D_{33}}+(9M^4+5s^2-2M^2(7s-5t) \\
-2st-7t^2)M^2_{D_{33}}+12(M^3-Ms)M^3_{D_{33}}) \\
\times G_{1ND_{33}\gamma}G_{2ND_{33}\gamma}+(M(14M^6-27M^4(s+t) \\
+16M^2(s+t)^2-3(s+t)^3)+2(-10M^6 \\
+17M^4(s+t)-8M^2(s+t)^2+(s+t)^3)M_{D_{33}} \\
-3M(29M^4+17s^2+18st+t^2-2M^2(23s \\
+7t))M^2_{D_{33}}-6(9M^4+5s^2+2st \\
-3t^2+2M^2(-7s+t))M^3_{D_{33}})G^2_{2ND_{33}\gamma}),
\end{gathered} \tag{49}$$

$$\begin{gathered}
\frac{1}{576M^4D_{sD_{33}}M^2_{D_{33}}}(16M^2(M^4+7M^2s \\
+2s^2-4(M^3-2Ms)M_{D_{33}}+(-15M^2 \\
+s+3t)M^2_{D_{33}}-8MM^3_{D_{33}})G^2_{1ND_{33}\gamma} \\
-16M(-2Ms(M^2+s)+(M^4+3M^2s)M_{D_{33}} \\
-4M^3M^2_{D_{33}}+3(-5M^2+s+2t)M^3_{D_{33}}) \\
\times G_{1ND_{33}\gamma}G_{2ND_{33}\gamma}+(s(M^4+6M^2s+s^2) \\
-8Ms(M^2+s)M_{D_{33}}+3(5M^4-34M^2s \\
+s(5s+16t))M^2_{D_{33}}-24M(M^2+s) \\
\times M^3_{D_{33}})G^2_{2ND_{33}\gamma})+\frac{1}{576M^4D_{uD_{33}}M^2_{D_{33}}} \\
\times(16M^2(23M^4-15M^2(s+t)+2(s+t)^2 \\
+4M(3M^2-2(s+t))M_{D_{33}}-(13M^2 \\
+s-2t)M^2_{D_{33}}-8MM^3_{D_{33}})G^2_{1ND_{33}\gamma} \\
+16M(2M(6M^4-5M^2(s+t) \\
+(s+t)^2)+M^2(-7M^2+3(s+t))M_{D_{33}} \\
+4M^3M^2_{D_{33}}+3(3M^2+s-t)M^3_{D_{33}}) \\
\times G_{1ND_{33}\gamma}G_{2ND_{33}\gamma}+(34M^6-37M^4(s+t) \\
+12M^2(s+t)^2-(s+t)^3-8M(6M^4 \\
-5M^2(s+t)+(s+t)^2)M_{D_{33}}-3(43M^4 \\
-5s^2+6st+11t^2-2M^2(7s+23t))M^2_{D_{33}} \\
-24M(3M^2-s-t)M^3_{D_{33}})G^2_{2ND_{33}\gamma}),
\end{gathered}$$

$$\begin{gathered}
\frac{1}{576M^4 D_{sD_{33}} M_{D_{33}}^2}(16M^2(M^5 - M^3 s \\
+ 2(M^4 - 3M^2 s + 2s^2)M_{D_{33}} + 3M(-M^2 + s \\
+ t)M_{D_{33}}^2 + (4M^2 - 4s - 3t)M_{D_{33}}^3)G_{1ND_{33}\gamma}^2 \\
- 8M(M^2 - s)^2(-s + 2MM_{D_{33}} \\
+ 7M_{D_{33}}^2)G_{1ND_{33}\gamma}G_{2ND_{33}\gamma} + (M^2 - s)^2 \\
\times (Ms - 2sM_{D_{33}} + 15MM_{D_{33}}^2 + 18M_{D_{33}}^3) \\
\times G_{2ND_{33}\gamma}^2) - \frac{1}{576M^4 D_{uD_{33}} M_{D_{33}}^2} \\
\times (16M^2(M^3(M^2 - s - t) - 2(3M^4 \\
- 5M^2(s + t) + 2(s + t)^2)M_{D_{33}} - 3(M^3 \\
- Ms)M_{D_{33}}^2 + (4M^2 - 4s - t)M_{D_{33}}^3)G_{1ND_{33}\gamma}^2 \\
- 8M(-M^2 + s + t)^2(2M^2 - s - t - 2MM_{D_{33}} \\
- 7M_{D_{33}}^2)G_{1ND_{33}\gamma}G_{2ND_{33}\gamma} - (-M^2 + s + t)^2 \\
\times (M(2M^2 - s - t) + 2(-2M^2 + s + t) \\
\times M_{D_{33}} + 15MM_{D_{33}}^2 + 18M_{D_{33}}^3)G_{2ND_{33}\gamma}^2),
\end{gathered}$$

$$\begin{gathered}
\frac{1}{576M^4 D_{sD_{33}} M_{D_{33}}^2}(16M^2(M^4 - M^2 s \\
+ 2s^2 + 4(M^3 - 2Ms)M_{D_{33}} + (-7M^2 + s \\
+ 3t)M_{D_{33}}^2 + 8MM_{D_{33}}^3)G_{1ND_{33}\gamma}^2 \\
- 16M(M^2 - s)M_{D_{33}}(M^2 + 2MM_{D_{33}} \\
- 3M_{D_{33}}^2)G_{1ND_{33}\gamma}G_{2ND_{33}\gamma} + (M^2 - s)^2 \\
\times (s + 15M_{D_{33}}^2)G_{2ND_{33}\gamma}^2) - \frac{1}{576M^4 D_{uD_{33}} M_{D_{33}}^2} \\
\times (16M^2(7M^4 - 7M^2(s + t) + 2(s + t)^2 \\
- 4M(3M^2 - 2(s + t))M_{D_{33}} - (5M^2 + s \\
- 2t)M_{D_{33}}^2 + 8MM_{D_{33}}^3)G_{1ND_{33}\gamma}^2 \\
+ 16M(M^2 - s - t)M_{D_{33}}(M^2 + 2MM_{D_{33}} \\
- 3M_{D_{33}}^2)G_{1ND_{33}\gamma}G_{2ND_{33}\gamma} + (s + t - M^2)^2 \\
\times (2M^2 - s - t + 15M_{D_{33}}^2)G_{2ND_{33}\gamma}^2),
\end{gathered}$$

$$\begin{gathered}
\frac{1}{288M^4 D_{sD_{33}} M_{D_{33}}^2}(8M^2(2Ms(s - M^2) \\
+ 2(M^4 - 3M^2 s + 2s^2)M_{D_{33}} + 2(M^3 - Ms) \\
\times M_{D_{33}}^2 + (4M^2 - 4s + 3t)M_{D_{33}}^3)G_{1ND_{33}\gamma}^2 \\
- 4M(s(M^4 - s^2) + 2Ms(-M^2 + s)M_{D_{33}} \\
+ (3M^4 - 4M^2 s + s(s + 6t))M_{D_{33}}^2 \\
+ 6(M^3 - Ms)M_{D_{33}}^3)G_{1ND_{33}\gamma}G_{2ND_{33}\gamma} \\
+ (Ms^2(s - M^2) + s(M^4 - s^2)M_{D_{33}} \\
+ 9M(M^2 - s)sM_{D_{33}}^2 + 3(M^4 - s^2)M_{D_{33}}^3) \\
\times G_{2ND_{33}\gamma}^2) + \frac{1}{288M^4 D_{uD_{33}} M_{D_{33}}^2} \\
\times (8M^2(2M(2M^4 - 3M^2(s + t) + (s + t)^2) \\
+ 2(3M^4 - 5M^2(s + t) + 2(s + t)^2)M_{D_{33}} \\
+ 2M(s + t - M^2)M_{D_{33}}^2 + (-4M^2 + 4s \\
+ 7t)M_{D_{33}}^3)G_{1ND_{33}\gamma}^2 + 4M(6M^6 \\
- 11M^4(s + t) + 6M^2(s + t)^2 - (s + t)^3 \\
- 2M(2M^4 - 3M^2(s + t) + (s + t)^2)M_{D_{33}} \\
+ (M^4 - s^2 - 12M^2 t + 4st + 5t^2)M_{D_{33}}^2 \\
+ 6M(M^2 - s - t)M_{D_{33}}^3)G_{1ND_{33}\gamma} \\
\times G_{2ND_{33}\gamma} + (M(M^2 - s - t)(s + t - 2M^2)^2 \\
+ (-6M^6 + 11M^4(s + t) - 6M^2(s + t)^2 \\
+ (s + t)^3)M_{D_{33}} - 9M(2M^4 - 3M^2(s + t) \\
+ (s + t)^2)M_{D_{33}}^2 - 3(3M^4 - 4M^2(s + t) \\
+ (s + t)^2)M_{D_{33}}^3)G_{2ND_{33}\gamma}^2),
\end{gathered}$$

$$\begin{gathered}
\frac{1}{576M^4 D_{sD_{33}} M_{D_{33}}^2}(16M^2(M^4 + M^2 s \\
- 2s^2 + (-5M^2 + 5s + 3t)M_{D_{33}}^2)G_{1ND_{33}\gamma}^2 \\
- 16M(Ms(-M^2 + s) + (M^4 - M^2 s)M_{D_{33}} \\
+ (-M^3 + Ms)M_{D_{33}}^2 + 3(-M^2 + s \\
+ t)M_{D_{33}}^3)G_{1ND_{33}\gamma}G_{2ND_{33}\gamma} + (s(M^4 - s^2) \\
+ 4Ms(-M^2 + s)M_{D_{33}} - 9(M^4 - s^2)M_{D_{33}}^2 \\
- 12(M^3 - Ms)M_{D_{33}}^3)G_{2ND_{33}\gamma}^2) \\
- \frac{1}{576M^4 D_{uD_{33}} M_{D_{33}}^2}(16M^2(5M^4 - 7M^2(s + t) \\
+ 2(s + t)^2 + (-5M^2 + 5s + 2t)M_{D_{33}}^2)G_{1ND_{33}\gamma}^2 \\
+ 16M(M(2M^4 - 3M^2(s + t) + (s + t)^2)M^2 \\
\times (-M^2 + s + t)M_{D_{33}} + M(M^2 - s - t)M_{D_{33}}^2 \\
+ 3(M^2 - s)M_{D_{33}}^3)G_{1ND_{33}\gamma}G_{2ND_{33}\gamma} + (6M^6 \\
- 11M^4(s + t) + 6M^2(s + t)^2 - (s + t)^3 \\
- 4M(2M^4 - 3M^2(s + t) + (s + t)^2)M_{D_{33}} \\
- 9(3M^4 - 4M^2(s + t) + (s + t)^2) \\
\times M_{D_{33}}^2 - 12M(M^2 - s - t)M_{D_{33}}^3)G_{2ND_{33}\gamma}^2)\Bigg\}.
\end{gathered}$$

In formulas (49), $M_{D_{33}}$ is the mass of the D_{33} resonance, while $D_{sD_{33}} = s - M_{D_{33}}^2 + iM_{D_{33}}\Gamma_{D_{33}}(s)$ and

$D_{uD_{33}} = u - M^2_{D_{33}} + iM_{D_{33}}\Gamma_{D_{33}}(u)$ are the denominators of the propagator for the D_{33} resonance in, respectively, the s and the u channel.

Since the D_{33} and D_{13} resonances have the same spin and parity of $3/2^-$ and differ only in isospin and mass, the contributions of D_{13} to the invariant functions f_1–f_6 for Compton scattering on a proton can be obtained from the corresponding formulas (49) for D_{33} by means of the substitutions

$$D_{sD_{33}} \to D_{sD_{13}}, \quad D_{uD_{33}} \to D_{uD_{13}}, \tag{50}$$
$$M_{D_{33}} \to M_{D_{13}},$$
$$G_{1ND_{33}\gamma} \to \sqrt{\frac{3}{2}}G^p_{1ND_{13}\gamma},$$
$$G_{2ND_{33}\gamma} \to \sqrt{\frac{3}{2}}G^p_{2ND_{13}\gamma},$$

where $D_{sD_{13}} = s - M^2_{D_{13}} + iM_{D_{13}}\Gamma_{D_{13}}(s)$ and $D_{uD_{13}} = u - M^2_{D_{13}} + iM_{D_{13}}\Gamma_{D_{13}}(u)$ are the denominators of the propagator for the D_{13} resonance in, respectively, the s and the u channel. For Compton scattering on a neutron, the last two rows in (50) must be replaced as follows:

$$G_{1ND_{33}\gamma} \to \sqrt{\frac{3}{2}}G^n_{1ND_{13}\gamma}, \tag{51}$$
$$G_{2ND_{33}\gamma} \to \sqrt{\frac{3}{2}}G^n_{2ND_{13}\gamma}.$$

REFERENCES

1. E. L. Hallin *et al.*, Phys. Rev. C **48**, 1497 (1993).
2. G. Blanpied *et al.*, Phys. Rev. Lett. **76**, 1023 (1996).
3. D. L. Hornidge *et al.*, Phys. Rev. Lett. **84**, 2334 (2000).
4. K. Kossert *et al.*, Phys. Rev. Lett. **88**, 162301 (2002).
5. A. I. L'vov, V. A. Petrun'kin, and M. Schumacher, Phys. Rev. C **55**, 359 (1997).
6. D. Drechsel, M. Gorchtein, B. Pasquini, and M. Vanderhaeghen, Phys. Rev. C **61**, 015204 (2000).
7. V. Pascalutsa and O. Sholten, Nucl. Phys. A **591**, 658 (1995).
8. S. Kondratyuk and O. Sholten, Phys. Rev. C **64**, 024005 (2001).
9. D. Babusci, G. Giordano, and G. Matone, Phys. Rev. C **55**, 1645 (1997).
10. J. A. McGovern, Phys. Rev. C **63**, 064608 (2001).
11. N. F. Nelipa, *Introduction to the Theory of Strongly Interacting Particles* (Atomizdat, Moscow, 1970) [in Russian].
12. V. B. Berestetskiĭ, E. M. Lifshitz, and L. P. Pitaevskiĭ, *Quantum Electrodynamics* (Nauka, Moscow, 1989; Pergamon Press, Oxford, 1982).
13. C. Itzykson and J.-B. Zuber, *Quantum Field Theory* (McGraw-Hill, New York, 1980; Mir, Moscow, 1984).
14. M. Jacob and G. C. Wick, Ann. Phys. (N.Y.) **7**, 404 (1959).
15. J. D. Bjorken and S. D. Drell, *Relativistic Quantum Theory* (McGraw-Hill, New York, 1965; Mir, Moscow, 1978).
16. R. D. Peccei, Phys. Rev. **181**, 1902 (1969).
17. H. Garcilazo and E. Moya de Guerra, Nucl. Phys. A **562**, 521 (1993).
18. V. Pascalutsa, Phys. Rev. D **58**, 096002 (1998).
19. V. Pascalutsa, Phys. Lett. B **503**, 85 (2001).
20. H. E. Haber, in *Proceedings of the Twenty-First SLAC Summer Institute on Particle Physics* (Stanford, California, 1993), p. 231.
21. T. E. O. Ericson and W. Weise, *Pions and Nuclei* (Clarendon Press, Oxford, 1988; Nauka, Moscow, 1991).

Translated by A. Isaakyan

Physics of Atomic Nuclei, Vol. 68, No. 2, 2005, pp. 306–314. Translated from Yadernaya Fizika, Vol. 68, No. 2, 2005, pp. 331–339.
Original Russian Text Copyright © 2005 by Zarzhitsky, Savrin.

ELEMENTARY PARTICLES AND FIELDS
Theory

Relativistic Description of $P\gamma^*\gamma$ Transition Form Factors within the Quasipotential Approach

A. A. Zarzhitsky and V. I. Savrin[*]

Institute of Nuclear Physics, Moscow State University, Vorob'evy gory, Moscow, 119899 Russia

Received December 8, 2003

Abstract—The possibility of a nonperturbative description of the $\pi^0\gamma^*\gamma$, $\eta\gamma^*\gamma$, and $\eta'\gamma^*\gamma$ transition form factors is investigated. The description is performed within the quasipotential approach in the lowest order approximation in the electromagnetic coupling constant. This makes it possible to obtain analytic expressions for these form factors in terms of the corresponding relativistic meson wave functions. The quasipotential wave functions chosen for pseudoscalar mesons in a natural way permit obtaining a quantitative description of present-day experimental data. A comparison of the parameters of the wave functions for π^0, η, and η' mesons demonstrates clearly the relativistic character of quark motion in light mesons. © *2005 Pleiades Publishing, Inc.*

1. INTRODUCTION

Investigation of electromagnetic hadron decays plays an important role in elementary-particle physics. Advances in QCD and the development of the fundamental concept of confinement related the physics of soft processes—that is, interactions at long distances—to this realm of investigations. Although the type of experiments that would be crucial for the problem of confinement has not been specified so far, measurement of phenomenological properties of hadrons—such as form factors, magnetic moments, and polarizations—can furnish required information. In other words, information about the distribution of various quark configurations in hadron matter can be quite accessible owing to the interaction of photons with the electric charges of quark fields. Such electromagnetic processes are relatively simple and admit theoretical interpretations that are less ambiguous than those in the case of purely hadron interactions. Thus, electromagnetic processes play the role of a testing ground for any theory describing the structure of strongly interacting particles.

The vector-meson-dominance model was one of the early models that were used to describe meson—photon transitions. According to this model, the hadron current is proportional to the fields of the vector mesons ρ, φ, and ω [1]; as a result, virtual mesons of these types mediate photon—hadron interactions.

Experimental data on $P\gamma^*\gamma$ transition form factors (here, γ^* and γ are, respectively, a virtual and a real photon, while P is a pseudoscalar meson) as functions of the momentum transfer squared Q^2 are usually approximated by the dipole formula

$$F_P(Q^2) = \frac{f_P}{1 + Q^2/\Lambda_P^2} \qquad (1)$$

(or by a superposition of dipole formulas), where f_P is the $P \to \gamma\gamma$ decay constant. The vector-meson-dominance model predicts that $\Lambda_P \simeq M_V$, where M_V is the vector-meson mass. As a matter of fact, this model is purely phenomenological, but it had been among basic ones for some time in the past.

Transition form factors cannot be calculated directly on the basis of QCD. However, they can be estimated by using perturbative QCD combined with sum rules and other theoretical methods.

A factorization procedure that separates perturbative effects at short distances from nonperturbative effects (at long distances) is one of the important concepts in methods based on QCD. The former have received adequate study and can be calculated on the basis of perturbative QCD, whereas the latter can be estimated only asymptotically in the limit of high momentum transfers. In calculations based on perturbative QCD, the transition form factor $F_P(Q^2)$ is represented as a combination of the hard-scattering amplitude and a soft nonperturbative wave function for the corresponding meson [2, 3].

In [4], the asymptotic behavior of the $\pi^0\gamma^*\gamma$ transition form factor in the limit of high Q^2 was calculated within perturbative QCD in the region of spacelike virtual-photon momentum $q^2 = -Q^2$. The result can be represented in the form

$$\lim_{Q^2\to\infty} Q^2 F_{\pi^0}(Q^2) = \sqrt{2} f_\pi,$$

---

[*] e-mail: `Savrin@theory.sinp.msu.ru`

where $f_\pi \simeq 0.128$ GeV is the pion-decay constant. It was also found that, in this limit, any meson wave function tends to an asymptotic wave function of a specific form [2, 5].

For $Q^2 \to \infty$, the $P\gamma^*\gamma$ transition form factors are predicted by perturbative QCD, whereas their behavior in the limit $Q^2 \to 0$ was investigated with the aid of current algebra and with allowance for an electromagnetic anomaly. For the neutral pion, this yields [2]

$$\lim_{Q^2\to 0} F_{\pi^0}(Q^2) \equiv f_0 = \frac{\sqrt{2}}{(2\pi)^2 f_\pi}$$

in the first order in m_q^2/M_0^2, where m_q is the u- or the d-quark mass and M_0 is the neutral-pion mass. In the above expression, f_0 is the $\pi^0 \to \gamma\gamma$ decay constant. Information about the behavior of $P\gamma^*\gamma$ transition form factors in the region of timelike virtual-photon momenta—in particular, in the limit $q^2 = Q^2 \to 0$—can be obtained by studying $P \to \ell\bar{\ell}\gamma$ Dalitz decays (here, ℓ and $\bar{\ell}$ are a lepton and an antilepton, respectively).

To describe effects to order m_q^2/Q^2 inclusive, use was made of the following interpolation between the two limits in question:

$$F_{\pi^0}(Q^2) = \frac{\sqrt{2} f_\pi}{Q^2 + (2\pi f_\pi)^2}. \qquad (2)$$

In order to calculate the long-distance effect in the soft nonperturbative region, the sum-rule method was employed in [5] with the aim of deriving the pion wave function in the experimentally accessible region of Q^2. It was shown that the proposed wave function describes some experimental data fairly well. However, this wave function suffers from large uncertainties because of the dependence on the strong coupling constant α_s.

By using small QCD corrections in calculating the $\pi^0\gamma^*\gamma$ transition form factor, it was further shown in [6, 7] that, in contrast to the results obtained with the asymptotic wave function, the data for this form factor with the wave function from [5] deviate significantly from experimental results. Approximately at that time, however, there appeared articles where the authors disregarded QCD corrections and took into account corrections to quark momenta. The results obtained in this way were equally satisfactory for the two wave functions.

Although methods based on perturbative QCD are often used to estimate and describe experimental data, the applicability of these methods at experimentally accessible momentum transfers (about a few gigaelectronvolts) has yet to be established conclusively within the theory of strong interactions.

In order to avoid such ambiguities in calculations within perturbative QCD, an alternative approach was developed in [8] on the basis of the sum-rule method. This approach was used to predict the $\pi^0\gamma^*\gamma$ transition form factors. In this case, predictions depend on the model of the hadron spectrum, which is chosen in a special way, and on the vacuum condensate, which is represented by a nonperturbative matrix element. Thus, it should be emphasized that, at the present time, a nonperturbative treatment of various exclusive processes is the subject of considerable interest in the theory.

In this study, we employ the quasipotential approach [9] to calculate the $\pi^0\gamma^*\gamma$, $\eta\gamma^*\gamma$, and $\eta'\gamma^*\gamma$ transition form factors. This approach, as well as the approach that is based on the Bethe–Salpeter equation [10] and which is similar to it, has already been used successfully a number of times to describe various meson decays [11]. For the time being, we will disregard radiative QCD corrections; as to electromagnetic interaction, we will take it into account in the lowest order of perturbation theory. The simplicity of this model makes it possible to obtain analytic expressions for relevant transition form factors in terms of relativistic meson wave functions, which include all soft nonperturbative contributions. It is shown that this model permits describing experimental data satisfactorily, the inclusion of the relativistic motion of quarks within mesons being essential. An expression for a transition form factor is derived from an analysis of the corresponding Dalitz decay, this being the most natural way for the quasipotential approach. After that, it is smoothly continued to the region of spacelike vitual-photon momenta, whereupon the asymptotic behavior of the form factor is studied for $Q^2 \to \infty$. A specific choice of the model quasipotential wave function enables one to describe form factors over the entire domain of Q^2, this function taking the form of the asymptotic wave function [2, 5] in the reference frame comoving with the fast meson.

2. FORM FACTOR FOR THE DECAY $P \to \gamma^*\gamma$

According to the quasipotential approach, the amplitude for the decay of a meson consisting of a quark and an antiquark to a lepton–antilepton pair and a photon is given by [12]

$$\mathcal{M}(\mathbf{p}, \mathbf{p}_\ell | P) = \int d^3\omega_{\mathbf{k}_q} T(\mathbf{p}, \mathbf{p}_\ell; \mathbf{k}_q | P, \varepsilon_P) \qquad (3)$$
$$\times \int d^3\omega_{\mathbf{k}'_q} \tilde{G}_q^{(0)}(\mathbf{k}_q; \mathbf{k}'_q | P, \varepsilon_P)$$
$$\otimes \int d^3\omega_{\mathbf{k}''_q} \left[\tilde{G}_q^{(-)}\right]^{-1} (\mathbf{k}'_q; \mathbf{k}''_q | P, \varepsilon_P) \tilde{\Phi}_P^{(-)}(\mathbf{k}''_q),$$

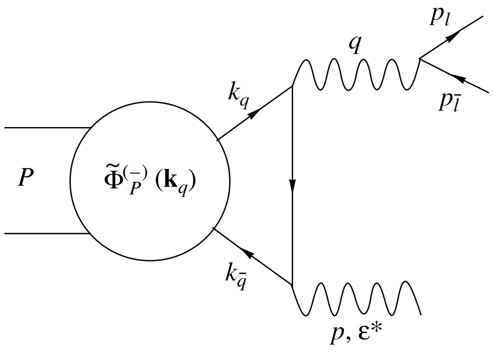

Fig. 1. Diagram illustrating the application of the quasipotential approach to quarkonium decay.

where $\mathbf{p}$ and $\mathbf{p}_\ell$ are the momenta of, respectively, the photon and one of the leptons; $\mathbf{k}_q$ is the quark momentum; $d^3\omega_{\mathbf{k}_q} = d\mathbf{k}_q / \left(2(2\pi)^3\sqrt{\mathbf{k}_q^2 + m_q^2}\right)$ is a momentum-volume element on the mass hyperboloid; P is the meson 4-momentum; $\varepsilon_P = (\lambda P)$ is the invariant meson energy, λ being a unit 4-vector ($\lambda^2 = 1$) (in considering particle decays, it is natural to set $\lambda = P/M$, in which case $\varepsilon_P = M$, where M is the meson mass); T is the off-energy-shell amplitude for the transition in which a quark–antiquark pair transforms into a lepton–antilepton pair, emitting a photon; $\tilde{G}_q^{(0)}$ and $\tilde{G}_q^{(-)}$ are the Green's functions for, respectively, a free and an interacting quark–antiquark system; and $\tilde{\Phi}_P^{(-)}$ is the single-time relativistic pseudoscalar-meson wave function. It should be noted that expression (3) involves, in addition to integration with respect to the momenta of the participant quarks, summation over their polarizations.

If one disregards intermediate-state quark–antiquark interaction (radiative QCD correction), formula (3) assumes a very simple form,

$$\mathcal{M}(\mathbf{p}, \mathbf{p}_\ell | P) = \int d^3\omega_{\mathbf{k}_q} T(\mathbf{p}, \mathbf{p}_\ell; \mathbf{k}_q | P, \varepsilon_P) \tilde{\Phi}_P^{(-)}(\mathbf{k}_q). \tag{4}$$

In the covariant formulation of the quasipotential approach—and we consider precisely this formulation—the 4-momenta involved satisfy the relations

$$\begin{aligned} &p + p_\ell + p_{\bar{\ell}} - (\varepsilon_p + \varepsilon_{p_\ell} + \varepsilon_{p_{\bar{\ell}}})\lambda \qquad (5) \\ &= k_q + k_{\bar{q}} - (\varepsilon_{k_q} + \varepsilon_{k_{\bar{q}}})\lambda = P - \varepsilon_P \lambda, \end{aligned}$$

where the indices $\bar{q}$ and $\bar{\ell}$ label 4-momenta associated with antiquarks and antileptons, respectively.

In the lowest order in the electromagnetic interaction within the quasipotential approach, the amplitude in (4) for the annihilation of a quark–antiquark system to a lepton–antilepton pair via photon emission takes the form

$$\begin{aligned} T(\mathbf{p}, \mathbf{p}_\ell; \mathbf{k}_q | P, \varepsilon_P) &= \frac{4\pi\alpha\sqrt{3}e_q^2}{Q^2} e\bar{v}_\ell^{(+)}(p_\ell) \qquad (6) \\ &\times \gamma^\mu v_\ell^{(+)}(p_{\bar{\ell}}) \otimes \Bigg[\bar{v}_q^{(-)}(k_{\bar{q}})\gamma_\mu \\ &\times \left\{\frac{\hat{p} - \hat{k}_q - (\varepsilon_p - \varepsilon_{k_q} + q^0)\hat{\lambda} - m_q}{2q^0(q^0 + \varepsilon_{k_{\bar{q}}} - \varepsilon_P + \varepsilon_p - i0)}\right. \\ &+ \left.\frac{\hat{p} - \hat{k}_q - (\varepsilon_p - \varepsilon_{k_q} - q^0)\hat{\lambda} - m_q}{2q^0(q^0 + \varepsilon_{k_q} - \varepsilon_p - i0)}\right\} \\ &\times \hat{e}^*(p) v_q^{(-)}(k_q) - \bar{v}_q^{(-)}(k_{\bar{q}})\hat{e}^*(p) \\ &\times \left\{\frac{\hat{p} + \hat{k}_q - (\varepsilon_p + \varepsilon_{k_q} + q'^0)\hat{\lambda} + m_q}{2q'^0(q'^0 + \varepsilon_{k_q} - \varepsilon_P + \varepsilon_p - i0)}\right. \\ &- \left.\frac{\hat{p} + \hat{k}_q - (\varepsilon_p + \varepsilon_{k_q} - q'^0)\hat{\lambda} + m_q}{2q'^0(q'^0 + \varepsilon_{k_{\bar{q}}} - \varepsilon_p - i0)}\right\}\gamma_\mu v_q^{(-)}(k_q)\Bigg], \end{aligned}$$

where $Q^2 = (p_\ell + p_{\bar{\ell}})^2$, $q^0 = \sqrt{\mathbf{q}^2 + m_q^2}$, $q'^0 = \sqrt{\mathbf{q}'^2 + m_q^2}$, and

$$\begin{aligned} \mathbf{q}^2 &= (\varepsilon_p - \varepsilon_{k_q})^2 - (p - k_q)^2, \qquad (7) \\ \mathbf{q}'^2 &= (\varepsilon_P - \varepsilon_p - \varepsilon_{k_q})^2 - (P - p - k_q)^2. \end{aligned}$$

In addition, we indicate that, here, $\sqrt{3}$ is the color factor and e_q is the quark charge and that we have assumed the equality of the u- and d-quark masses. In view of quark-flavor mixing within mesons, we must obviously set $e_q^2 = (e_u^2 - e_d^2)/\sqrt{2} = 1/(3\sqrt{2})$ for π^0 and $e_q^2 = (e_u^2 + e_d^2)/\sqrt{2} = 5/(9\sqrt{2})$ for η and η' (if we disregard the strange-quark admixture). In the approximation adopted here, the diagram corresponding to the amplitude in (4) is shown in Fig. 1. The most general form of the single-time wave function for a pseudoscalar bound state of a fermion and an antifermion is

$$\tilde{\Phi}_P^{(-)}(\mathbf{k}_q) = \frac{\bar{v}_q^{(+)}(k_q)\gamma^5 v_q^{(+)}(k_{\bar{q}})}{2\varepsilon_{k_{\bar{q}}}} \varphi_P(\mathbf{k}_q), \tag{8}$$

where $\varphi_P(\mathbf{k}_q)$ is its scalar part. Substituting (8) and (6) into (4), we obtain the decay amplitude in the form

$$\begin{aligned} &\mathcal{M}(\mathbf{p}, \mathbf{p}_\ell | P) \qquad (9) \\ &= \frac{4\pi\alpha}{Q^2} F_P(Q^2) i\epsilon_{\mu\nu\rho\sigma} e\bar{v}_\ell^{(+)}(p_\ell)\gamma^\mu v_\ell^{(+)}(p_{\bar{\ell}}) e^{*\nu} p^\rho P^\sigma. \end{aligned}$$

Going over to the meson rest frame ($\mathbf{P} = 0$) and performing integration with respect to angles in the

S state, we obtain

$$F_P(Q^2) = \frac{\sqrt{3}e_q^2 2m_q}{(2\pi)^2 p M_P}\int\limits_0^\infty \frac{dk_q k_q}{k_q^0} \tag{10}$$
$$\times \ln\left|\frac{\left(\sqrt{(p+k_q)^2+m_q^2}+k_q^0-M_P+p\right)}{\left(\sqrt{(p-k_q)^2+m_q^2}+k_q^0-M_P+p\right)}\right.$$
$$\left.\times\frac{\left(\sqrt{(p+k_q)^2+m_q^2}+k_q^0-p\right)}{\left(\sqrt{(p-k_q)^2+m_q^2}+k_q^0-p\right)}\right|\varphi_{M_P}(k_q),$$

where $\varphi_{M_P}(k_q)$ is the scalar part of the single-time wave function for an S-state pseudoscalar meson [see Eq. (8)] considered in its rest frame and M_P is the pseudoscalar-meson mass. In terms of the dimensionless variables $x = Q^2/M_P^2$ (for the case of the Dalitz decay, we have $4m_\ell^2/M_P^2 \le x \le 1$) and $y = 2k_q/M_P$, the photon momentum and energy reduce to $p = p^0 = (1-x)M_P/2$, while the expression for the form factor becomes

$$(1-x)F_P(x) = \frac{\sqrt{3}e_q^2 z_P}{(2\pi)^2}\int\limits_0^\infty \frac{ydy}{\sqrt{y^2+z_P^2}}\ln\left|\frac{\left(\sqrt{(y+1-x)^2+z_P^2}+\sqrt{y^2+z_P^2}-1\right)^2-x^2}{\left(\sqrt{(y-1+x)^2+z_P^2}+\sqrt{y^2+z_P^2}-1\right)^2-x^2}\right|\varphi_{M_P}(y), \tag{11}$$

where $z_P = 2m_q/M_P$. Within the quasipotential approach, the normalization condition for the wave function has the form

$$\int d^3\omega_{\mathbf{k}_q} 2\varepsilon_{k_q}|\varphi_P(\mathbf{k}_q)|^2 = 2\varepsilon_P. \tag{12}$$

In terms of the above variable, it reduces to

$$\int\limits_0^\infty dyy^2|\varphi_{M_P}(y)|^2 = \frac{(4\pi)^2}{M_P^2}. \tag{13}$$

3. BEHAVIOR OF THE $P\gamma^*\gamma$ TRANSITION FORM FACTOR IN THE SPACELIKE REGION

Above all, we are interested in the behavior of the integrand in expression (11) for the meson form factor as a function of the momenta of constituent quarks. In the timelike region ($x > 0$), such an analysis is not very convenient: the logarithmic function in the integrand has second-order discontinuities stemming from poles of the expression under the logarithm sign. These singularities have no effect on the divergence of the integral, since they are integrable logarithmic singularities. However, the presence of poles hinders the expansion of the integrand in a power series at small y. Moreover, it is difficult to perform experiments in the timelike region because of a small kinematical region of the processes in question, and all of the latest experimental data refer to the spacelike case—a transition to this case is accomplished by a mere substitution of $-x$ for x in (11). Considering the form factor in the spacelike region, we then deal with lepton–meson scattering rather than with a Dalitz decay—these two processes are related by crossing symmetry. As a result, we obtain

$$(1+x)F_P(x) = \frac{\sqrt{3}e_q^2 z_P}{(2\pi)^2}\int\limits_0^\infty \frac{ydy}{\sqrt{y^2+z_P^2}}\ln\frac{\left(\sqrt{(y+1+x)^2+z_P^2}+\sqrt{y^2+z_P^2}-1\right)^2-x^2}{\left(\sqrt{(y-1-x)^2+z_P^2}+\sqrt{y^2+z_P^2}-1\right)^2-x^2}\varphi_{M_P}(y). \tag{14}$$

Here, we have removed the modulus sign, since the expression under the logarithm sign is positive over the entire domain of integration and over the entire kinematical region $0 \le x < \infty$. Thus, we have obtained an analytic expression for the $P\gamma^*\gamma$ transition form factor in terms of the relativistic meson wave function $\varphi_{M_P}(y)$. Knowledge of this wave would enable us to calculate the form factor (14) explicitly. In the present study, we will consider two simple versions of the calculation of the form factor by formula (14), a calculation in the so-called static approximation and a calculation by the method of a trial wave function.

4. STATIC APPROXIMATION

The static approximation implies a slow motion of quarks within mesons—as a matter of fact, it is equivalent to the nonrelativistic approximation, $y \ll 1$. From the point of view of formula (14), this approximation would be valid if the wave function $\varphi_{M_P}(y)$

decreased very fast at large y. In that case, it is legitimate to expand the integrand (with the exception of φ_{M_P}) in y. Discarding all terms of order y^4 and higher order terms, we then have

$$F_P(x) = \frac{16\sqrt{3}e_q^2\tilde{\varphi}_{M_P}(0)}{M_P^{5/2}\sqrt{(1+x)^2+z_P^2}} \times \frac{\left(\sqrt{(1+x)^2+z_P^2}+z_P-1\right)}{\left(\sqrt{(1+x)^2+z_P^2}+z_P-1\right)^2-x^2}, \tag{15}$$

where we have introduced the value of the normalized (to unity) wave function at the origin of spatial coordinates,

$$\tilde{\varphi}_{M_P}(0) = \frac{M_P^{5/2}}{(4\pi)^2}\int\limits_0^\infty dy y^2 \varphi_{M_P}(y), \tag{16}$$

this quantity appearing here as an unknown parameter. In the same approximation, we can also calculate the $P \to \gamma\gamma$ decay constant as

$$f_P = \frac{16\sqrt{3}e_q^2\tilde{\varphi}_{M_P}(0)}{M_P^{5/2}\sqrt{1+z_P^2}\left(\sqrt{1+z_P^2}+z_P-1\right)}. \tag{17}$$

As a result, the form factor in (15) assumes the form

$$F_P(x) = \frac{f_P\sqrt{1+z_P^2}}{\sqrt{(1+x)^2+z_P^2}} \frac{\left(\sqrt{1+z_P^2}+z_P-1\right)\left(\sqrt{(1+x)^2+z_P^2}+z_P-1\right)}{\left(\sqrt{(1+x)^2+z_P^2}+z_P-1\right)^2-x^2}. \tag{18}$$

Thus, we have seen that, in the static approximation, we have a simple analytic formula describing the form factor and featuring one unknown parameter, z_P (or the quark mass m_q), since the decay constants f_P are known to a high precision from independent experiments.

It should be noted that formula (18) is not the nonrelativistic approximation in a literal sense, since we did not assume that the quark binding energy within mesons is small, so that the parameter z_P in this formula can deviate arbitrarily from unity. We only assumed that the momenta of the quarks are small against their masses. Of course, formula (18) differs from the simplest dipole approximation in (1), but one must choose the parameter z_P in order to find out how well it describes experimental data. This can be done by using an extrapolation of experimental data either for the slope parameter of the form factor in the vicinity of the point $Q^2 = 0$ or for the parameter Λ_P of the dipole formula for $Q^2 \to \infty$. Expanding the form factor (18) at small x, we obtain

$$F_P(x) \simeq f_P(1 - b_P x), \tag{19}$$

where

$$b_P = \frac{2\sqrt{1+z_P^2}+z_P-1}{(1+z_P^2)\left(\sqrt{1+z_P^2}+z_P-1\right)}. \tag{20}$$

Bearing in mind that the static approximation is applicable above all to heavy mesons, we begin our analysis by considering the η' meson. Attempts at experimentally determining the parameter b_P have been undertaken many times. We will rely on one of the latest studies of the CELLO Collaboration [13], where these parameter was estimated at $b_{\eta'} = 1.46$. As a result, we obtain $z_{\eta'} = 0.743$; that is, $m_q = 0.356$ GeV, which is quite in accord with our ideas of the constituent quark mass. Using this quark-mass value, we arrive at $b_\eta = 0.685$ and $b_{\pi^0} = 0.0540$, these values differing from the results of the CELLO Collaboration by a factor of about 1.5. This may suggest that the static approximation is not quite adequate to describing the form factors for the η and π^0 mesons. On the other hand, the slope parameter at the point $x = 0$ is “measured” by extrapolating experimental data; therefore, the accuracy of its determination is quite uncertain—it depends on the momentum-transfer region where the measurements were performed and on the extrapolation method.

Let us now consider the region of large x. The asymptotic behavior of the form factor is readily calculable and is coincident with the asymptotic behavior of the dipole formula (1):

$$\lim_{Q^2\to\infty} Q^2 F_P(Q^2) = f_P\Lambda_P^2. \tag{21}$$

Within the model considered here, we have

$$\Lambda_P^2 = \frac{\sqrt{1+z_P^2}\left(\sqrt{1+z_P^2}+z_P-1\right)M_P^2}{2z_P}. \tag{22}$$

As above, we will first consider the η'-meson form factor. From relatively recent data of the CLEO Collaboration [14], we have $\Lambda_{\eta'} = 0.859$ GeV; from (22), we therefore obtain $z_{\eta'} = 0.702$—that is, $m_q = 0.336$ GeV, which is in excellent agreement with the quark mass extracted from the slope parameter of the form factor at $Q^2 = 0$. From here, one can conclude that the η'-meson form factor is fully described within the static approximation. Using the same quark-mass value for the other two mesons, we arrive at $\Lambda_\eta = 0.591$ GeV and $\Lambda_{\pi^0} = 0.290$ GeV, which deviates from the experimental extrapolation (especially in the case of the π^0 meson) significantly (by more than a factor of 2.5). The only conclusion to be drawn from this is that the static approximation is inappropriate for describing light mesons, so that it is necessary to take into account the relativistic motion of quarks within them.

5. DESCRIPTION OF A TRIAL QUASIPOTENTIAL WAVE FUNCTION

In order to perform a more accurate comparison of the behavior of the form factor with experimental data, it is necessary to calculate the integral in (14) with a wave function $\varphi_{M_P}(y)$ that, unfortunately, is unknown at the present time. In principle, one could find it by solving the quasipotential equation for the wave function. For want of a complete understanding of the quark-confinement phenomenon, however, we had to employ a phenomenological approach to specifying the quasipotential of quark–quark interaction. Since one cannot avoid the use of free parameters, it is therefore more reasonable to introduce, from the outset, a trial wave function that decreases rather fast at high quark momenta and which satisfies the normalization condition (12).

Since the wave function for a pseudoscalar meson moving with an arbitrary momentum, $\varphi_P(\mathbf{k}_q)$, is a Lorentz-invariant quantity, one can represent it in the S state, taking into account symmetry with respect to the momenta of the quark and the antiquark, as

$$\varphi_P(\mathbf{k}_q) = \varphi_{M_P}\left(\frac{P(k_q + k_{\bar{q}})}{M_P}\right); \tag{23}$$

that is, it depends on only one invariant combination in the form of the scalar product of 4-momenta, since, in the quasipotential approach, the momenta of the particles themselves lie on the mass hyperboloids: $k_q^2 = k_{\bar{q}}^2 = m_q^2$ and $P^2 = M_P^2$. Now, the simplest way to choose a trial wave function is to take it in the form of an exponentially decreasing function of the invariant variable introduced above; that is,

$$\varphi_{M_P}\left(\frac{P(k_q + k_{\bar{q}})}{M_P}\right) = A_P \exp\left\{-\frac{a_P P(k_q + k_{\bar{q}})}{M_P^2}\right\}, \tag{24}$$

where a_P is the dimensionless slope parameter. It is the only parameter introduced here since the parameter A_P is determined by the normalization condition (12). In the meson rest frame, we eventually have

$$\varphi_{M_P}(y) = A_P \exp\left\{-\frac{2a_P k_q^0}{M_P}\right\} \tag{25}$$

$$= A_P \exp\left\{-a_P\sqrt{y^2 + z_P^2}\right\},$$

where $k_q^0 = \sqrt{\mathbf{k}_q^2 + m_q^2}$. Obviously, the parameter a_P controls the quark-momentum distribution within a meson. Small values of this parameter ($a_P \ll 1$) correspond to the case where the main contribution comes from high values of the quark momenta. On the contrary, low momenta are dominant at $a_P \gg 1$.

It is interesting to find out which form the trial wave function introduced above takes in the reference frame comoving with a fast meson, $P^0 \to \infty$. In this limit, we readily find, upon disregarding the masses, that

$$k_q^0 = \sqrt{\mathbf{k}_q^2 + m_q^2} = xP^0 + \frac{k_T^2}{2xP^0} \tag{26}$$

and

$$k_{\bar{q}}^0 = \sqrt{(\mathbf{P} - \mathbf{k}_q)^2 + m_q^2} \tag{27}$$

$$= (1-x)P^0 + \frac{k_T^2}{2(1-x)P^0},$$

where $\mathbf{k}_T$ is the transverse component of the quark momentum and $x = k_{||}/P^0$. As a result, the wave function

$$\varphi_P(\mathbf{k}_q) \equiv \varphi_{M_P}(x, \mathbf{k}_T) = A_P \exp\left\{-\frac{a_P k_T^2}{2M_P x(1-x)}\right\} \tag{28}$$

coincides with the asymptotic wave function used in [2, 5].

The chosen trial wave function (25) makes it possible to perform some calculations in an analytic form. For example, its substitution into the normalization condition (12) yields

$$A_P = \frac{4\pi}{M_P z_P}\sqrt{\frac{2a_P}{K_2(2a_P z_P)}}, \tag{29}$$

where K_2 is a second-order Bessel function of the second kind. From (14), it follows that

$$\lim_{Q^2\to\infty} Q^2 F_P(Q^2) = \frac{2\sqrt{3}e_q^2 M_P^2 z_P A_P}{(2\pi)^2} \tag{30}$$

$$\times \int\limits_0^\infty \frac{y\,dy}{\sqrt{y^2 + z_P^2}} \ln\frac{\sqrt{y^2 + z_P^2} + y}{z_P}$$

$$\times \exp(-a_P\sqrt{y^2 + z_P^2}) = \frac{2\sqrt{6}e_q^2 M_P}{\pi}$$

$$\times \frac{K_0(a_P z_P)}{\sqrt{a_P K_2(2a_P z_P)}} = f_P \Lambda_P^2,$$

Parameters of pseudoscalar-meson wave functions and corresponding form-factor parameters

	π^0		η		η'	
	calculation	experiment	calculation	experiment	calculation	experiment
z_P	6.21		1.53		0.88	
a_P	0.08		2.0		18.8	
c_P	1.716		0.039		0.004	
$f_P\,[\mathrm{GeV}^{-1}]$	0.27	0.27	0.26	0.26	0.34	0.34
$\Lambda_P\,[\mathrm{GeV}]$	0.70	0.77 ± 0.02	0.76	0.77 ± 0.02	0.92	0.84 ± 0.02
b_P	6.1×10^{-3}	$(3.3 \pm 0.3) \times 10^{-2}$	0.32	0.43 ± 0.06	1.0	1.5 ± 0.2

where K_0 is a zero-order Bessel function of the second kind. By virtue of the above comments, the limit of this formula for $a_P \to \infty$ corresponds to the static approximation. On the contrary, the limit $a_P \to 0$ corresponds to the ultrarelativistic motion of the quarks. It turns out that experimental data cannot be described satisfactorily on the basis of formula (30) in this asymptotic regions. This means that values of the parameter a_P lie somewhere in the intermediate region; therefore, it is necessary to calculate the relevant integrals numerically.

6. RESULTS OF THE NUMERICAL CALCULATION

In the preceding sections, we tried to establish analytically special features in the behavior of the $P\gamma^*\gamma$ electromagnetic-transition form factors for the π^0, η, and η' mesons. In doing this, we were able to reveal a significant difference in the applicability of two limiting cases (the static and the ultrarelativistic one) to this group of mesons. In order to obtain deeper insight into this difference in the behavior of the form factors and to perform a detailed comparison of our results with experimental data, it is desirable to calculate $F_P(x)$ over the entire region Q^2 where measurements have been performed. For this purpose, we have calculated, in the present study, relevant integrals numerically, taking a trial wave function in the more general form

$$\varphi_{M_P}(y) = A_P \exp\left(-a_P\sqrt{y^2 + c_P^2}\right), \qquad (31)$$

which involves two unknown parameters, a_P and c_P. All of the above comments concerning the wave function in (25) remain in force for (31) as well, and the new free parameter c_P, which we introduced in (31), affects the behavior of $\varphi_{M_P}(y)$ more subtly than a_P.

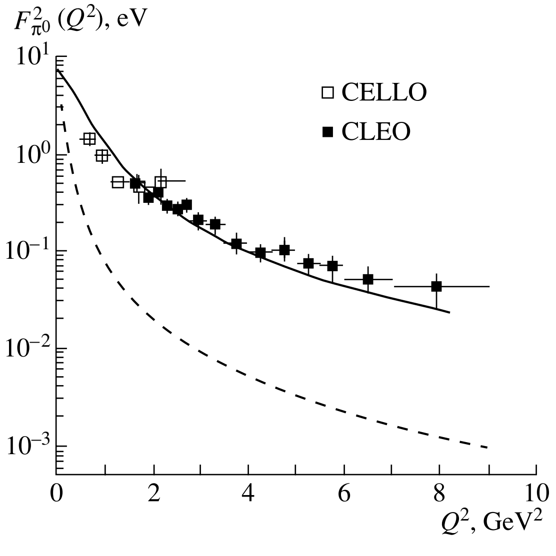

Fig. 2. $\pi^0\gamma^*\gamma$ transition form factor as a function of momentum transfer squared according to calculations in the static approximation (dashed curve) and according to calculations with a trial relativistic wave function (solid curve).

A comparison of our theoretical results with experimental data is given in the table.

All of the results for z_P correspond to the quark-mass value of $m_q = m_u = m_d = 420$ MeV. The values of all free parameters were obtained by fitting the form-factor values at the origin to the corresponding constants of meson decays into two photons under the fixed normalization condition (13) for the wave function (31).

Data on Λ_P and b_P were averaged over the results from [13–16]. Experimental data directly on form-factor values were borrowed from [13, 14]. The graphical results for π^0, η, and η' are given in Figs. 2, 3, and 4, respectively.

The solid curves in the figures represent the results of the numerical calculation of the integral for the form factor with the trial wave function (31). The dashed curves show the results for the static case

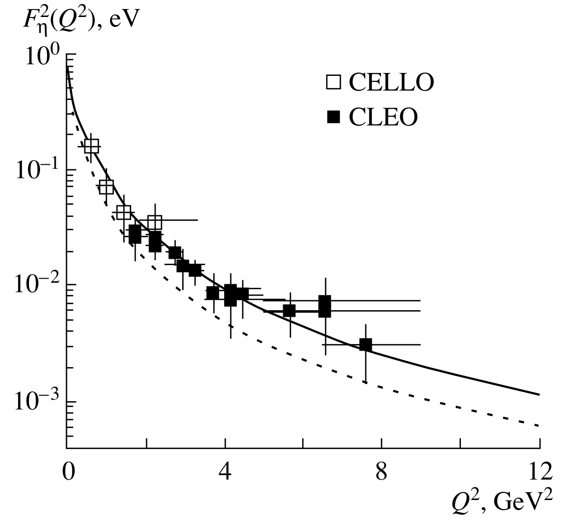

Fig. 3. As in Fig. 2, but for the $\eta\gamma^*\gamma$ transition form factor.

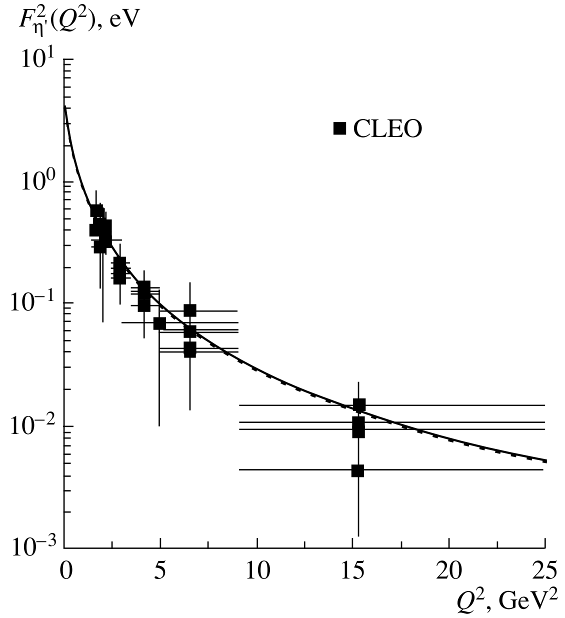

Fig. 4. As in Fig. 2, but for the $\eta'\gamma^*\gamma$ transition form factor.

with the parameter z_P corresponding to the numerical calculations for a given meson.

From a comparison of two descriptions—that in the static case and that which was obtained with a trial wave function that makes it possible to take into account the contribution from the whole region of quark momenta—one can draw the following conclusions. First, a large discrepancy between the results in the static approximation and experimental data for the π^0 meson is indicative of high characteristic (mean) momenta of its constituent quarks. Second, perfect agreement between the two descriptions for the η' meson gives sufficient grounds to state that characteristic quark momenta are low in that case. In all probability, the η meson represents an intermediate case. The values in the table for the slope parameter a_P of the wave function clearly illustrate these conclusions.

7. CONCLUSION

The problem of describing the $\pi^0\gamma^*\gamma$, $\eta\gamma^*\gamma$, and $\eta'\gamma^*\gamma$ transition form factors has been considered with the aim of obtaining deeper insight into the regularities of the internal motion of quarks within mesons. Figures 2, 3, and 4 shows graphical results for the π^0, η, and η' mesons, respectively. The best description of the form factors with the trial wave function in (31) is represented by the solid curves. One can see that agreement with experimental data is quite satisfactory. Moreover, it is not poorer than that which is provided by the most successful modern models, which employ more exotic assumptions (see [14]). Our results corroborate the traditional idea that the higher the binding energy of quarks in a hadron, the higher the characteristic kinetic energy of its constituent quarks. This statement does not follow directly from any modern model that attempts to describe strong interactions; therefore, such a clear-cut corroboration of it is an important result.

Thus, results that agree with modern experimental data have been obtained by a more economical method on the basis of a relatively simple quasipotential model (see Fig. 1). This gives every reason to believe that, at the present-day accuracy of measurements, a modification to the wave function and the inclusion of QCD corrections can hardly lead to significant changes. At the same time, the quasipotential approach makes it possible to obtain more detailed information about meson wave functions and to take into account, in the future, radiative QCD corrections.

ACKNOWLEDGMENTS

This study benefited greatly from joint work with N.B. Skachkov and from his enlightening comments.

REFERENCES

1. L. G. Landsberg, Phys. Rep. **128**, 301 (1985).
2. S. J. Brodsky and G. P. Lepage, Phys. Rev. D **22**, 2157 (1980).
3. V. V. Anisovich, D. I. Melikhov, and V. A. Nikonov, Phys. Rev. D **55**, 2918 (1997).
4. S. J. Brodsky and G. P. Lepage, Phys. Rev. D **24**, 1808 (1981).
5. V. L. Chernyak and A. R. Zhitnitsky, Phys. Rep. **112**, 173 (1984).

6. R. Jakob and P. Kroll, Phys. Lett. B **315**, 463 (1993).
7. R. Jakob, P. Kroll, and M. Raulfs, J. Phys. G **22**, 45 (1996).
8. I. V. Musatov and A. V. Radyushkin, Phys. Rev. D **56**, 2713 (1997).
9. A. A. Logunov and A. N. Tavkhelidze, Nuovo Cimento **29**, 380 (1963).
10. V. I. Savrin and N. B. Skachkov, *High Energy Physics and Field Theory Problems* (Inst. High Energy Phys., Protvino, 1982), Vol. 2, p. 229 [in Russian]; V. I. Savrin and N. B. Skachkov, Teor. Mat. Fiz. **54**, 372 (1983); G. A. Kozlov, S. P. Kuleshov, V. V. Sanadze, *et al.*, Z. Phys. C **21**, 63 (1983); R. N. Faustov, V. O. Galkin, and A. Yu. Mishurov, Phys. Lett. B **356**, 516 (1995).
11. L. Bergström and H. Snellman, Z. Phys. C **8**, 363 (1981); H.-W. Huang, J.-H. Liu, and J. Tang, Phys. Rev. D **56**, 368 (1997).
12. V. A. Matveev, V. I. Savrin, A. N. Sisakyan, and A. N. Tavkhelidze, Teor. Mat. Fiz. **132**, 267 (2002).
13. CELLO Collab. (H. J. Behrend *et al.*), Z. Phys. C **49**, 401 (1991).
14. CLEO Collab. (V. Savinov *et al.*), hep-ex/9507005.
15. Lepton-G Collab. (R. I. Dzhelyadin *et al.*), Phys. Lett. B **88B**, 379 (1979); **94**, 548 (1980).
16. TPC/2γ Collab. (H. Aihara *et al.*), Phys. Rev. Lett. **64**, 172 (1990).

Translated by A. Isaakyan

Physics of Atomic Nuclei, Vol. 68, No. 2, 2005, pp. 315–325. Translated from Yadernaya Fizika, Vol. 68, No. 2, 2005, pp. 340–350.

Determination of the Glueball Mass with Allowance for the Relativistic Character of Interaction

M. Dineykhan[*], **S. A. Zhaugasheva**, and **T. A. Kozhamkulov**

Kazakh National University, Almaty, Kazakhstan

Received April 2, 2004

Abstract—Nonperturbative corrections to an interaction Hamiltonian that are associated with relativistic motion and a large coupling constant are determined on the basis of an investigation of the asymptotic behavior of the polarization loop for charged scalar particles in an external gauge field. The mass spectrum of a bound state is determined analytically. The mechanism responsible for the emergence of the constituent mass of particles that form a bound state is explained. It is shown that the contribution of the vector potential and the contribution of the potential associated with a nonperturbative character of interaction cancel each other and that the slope of the Regge trajectory is determined in terms of the string tension.

1. INTRODUCTION

The development of the idea of gauge invariance [1] led to the emergence of QCD, which describes the interaction of color objects. Gross and Wilczek [2] and Politzer [3] showed that the coupling constants for quark–gluon interaction are small at short distances, but that they grow with increasing spatial scale. At the present time, this has been confirmed by numerous experimental data—in particular, by data on the deep-inelastic scattering of electrons on protons and neutrons. According to [2, 3], the strength of attraction between quarks is modest at short distances, and the Coulomb law is valid in this case; at long distances, the attraction must be much stronger and ensure quark confinement. Thus, the interaction of color quarks goes over from the confining to the deconfining phase, depending on the distance. The phenomenological potential quark model [4–7], which describes well the spectra and the properties of charmonia [7] and bottomonia [8–11], satisfies this condition best of all. However, the phenomenological potential quark model does not follow from the underlying principles of QCD.

Throughout the past three decades, theorists have attempted to deduce an effective quark-interaction Hamiltonian that would explain the conditions of confinement and deconfinement for composite objects on the basis of the underlying principles of QCD (for details, see [11]). There exist a great many potential quark models that are constructed on the basis of various physical assumptions. By and large, these models describe the physics of hadrons consisting of heavy quarks. In studying the properties of hadrons consisting of light quarks, it is necessary, however, to consider that the interaction there has a relativistic and a nonperturbative character. There is no generally accepted recipe for taking into account the nonperturbative character of interaction within phenomenological quark models. At the same time, it is well known that the problems of strong coupling—that is, the description of the properties of bound states at a large coupling constant—are essentially relativistic; possibly, they can be solved only within quantum field theory.

Within relativistic quantum field theory, the main features of a bound state are generally determined on the basis of the position of the pole of the amplitude for the transition characterized by the corresponding quantum numbers. It is precisely in the transition amplitude that there arises a nonperturbative character of interaction due to a large coupling constant. This character is determined by an integral equation of the Bethe–Salpeter type. In specifying the nonperturbative character of interaction within conventional quantum field theory, one usually faces the problem of solving an integral equation with an arbitrary kernel. Of course, it is very difficult to find a solution to such an equation. At the same time, the mechanism according to which only nonlocal interactions between constituent particles can lead to the formation of a bound state has been widely discussed (see, for example, [12]). In view of this, it is of great interest to investigate the quark-hadronization mechanism with allowance for a nonperturbative character of interaction. Thus, the relativistic character of interaction is taken into account within perturbation theory—that is, only the contributions of various classes of

---

[*] e-mail: `diney@physics.kz`

diagrams are summed. However, this is possible only in the case of a rather small coupling constant. In describing the properties of bound states at a large coupling constant, summation of the contributions of specific types of diagrams does not reflect the true character of the interaction; moreover, perturbation-theory series do not converge in this case. For this reason, allowances for a nonperturbative and a relativistic character of the interaction require a dedicated consideration in describing the properties of bound states.

A unique method for taking into account a nonperturbative character of interaction in describing the properties of a relativistic bound state was proposed in [13], where use was made of the Fock–Feynman–Schwinger representation. Later on, this method was refined in [14, 15] and was successfully applied in [16] to describing the mass spectrum of hadrons and glueballs. Here, we report on one of the direct continuations of those studies. The representation of the polarization-loop function in the form of a path integral is a key point of this approach, whereby, the main task here is reduced to calculating the integral in question. Of course, the path integral cannot be calculated in a general form; therefore, this is usually done under some specific physical assumptions. In the present study, we propose one of the alternative versions of the calculation of the path integral and determine, for the interaction potential, an analytic form that corresponds to a nonperturbative character of the interaction.

The ensuing exposition is organized as follows. In Section 2, we present some details of a determination of bound-state masses in terms of the polarization-loop function. In Section 3, we calculate nonperturbative corrections to the interaction Hamiltonian. In Section 4, we derive the mass spectrum of a two-gluon bound state for various forms of potential. In the Conclusion, we summarize our basic results. In the Appendix, we expound on some details of the calculations.

2. MODEL DESCRIBING THE MASS SPECTRUM OF A BOUND STATE

In this section, we will describe one of the alternative methods for determining the bound-state mass with allowance for a nonperturbative and a relativistic character of interaction.

The problem of determining the mass of the system is one of the fundamental problems that arise in describing the mechanism of bound-state interaction. We will now consider the interaction of two charged scalar particles in an external gauge field. We will assume that the system of these particles forms a bound state. We will determine the mass of the bound state, relying on an investigation of the asymptotic behavior of the polarization-loop function for a charged scalar particle in an external gauge field. This function can be written in the form

$$\Pi(x-y) = \left\langle G_{m_1}(x,y|A) G^*_{m_2}(y,x|A)\right\rangle_A . \quad (2.1)$$

Here, averaging is performed over the external gauge field $A_\alpha(x)$. The Green's function $G_m(y,x|A)$ for a scalar particle in an external gauge field can be determined from the equation

$$\left[\left(i\frac{\partial}{\partial x_\alpha} + \frac{g}{c\hbar}A_\alpha(x)\right)^2 + \frac{c^2m^2}{\hbar^2}\right] G(x,y|A) = \delta(x-y), \quad (2.2)$$

where m is the scalar-particle mass and g is the coupling constant. In averaging over the external gauge field $A_\alpha(x)$, we will restrict ourselves to the lowest order terms—that is, we take into account only a two-point Gaussian correlation function,

$$\left\langle \exp\left\{ i\int dx A_\alpha(x) J_\alpha(x)\right\}\right\rangle_A \quad (2.3)$$
$$= \exp\left\{-\frac{1}{2}\int\int dx dy J_\alpha(x) D_{\alpha\beta}(x-y) J_\beta(y)\right\},$$

where $J_\alpha(x)$ is a real current. The gauge-field propagator has the form

$$D_{\alpha\beta}(x-y) = \langle A_\alpha(x) A_\beta(y)\rangle_A = \delta_{\alpha\beta} D(x-y). \quad (2.4)$$

The bound-state mass is generally determined in terms of the polarization-loop function $\Pi(x-y)$ as

$$M = -\lim_{|x-y|\to\infty} \frac{\ln \Pi(x-y)}{|x-y|}. \quad (2.5)$$

It can be seen from (2.1) that, in order to obtain the loop function, it is first necessary to determine the Green's function.

A solution to Eq. (2.2) can be represented in the form of a path integral as (for details, see [17])

$$G(x,y|A) \quad (2.6)$$
$$= \int_0^\infty \frac{ds}{(4s\pi)^2} \exp\left\{-sm^2 - \frac{(x-y)^2}{4s}\right\}$$
$$\times \int d\sigma_\beta \exp\left\{ ig\int_0^1 d\xi \frac{\partial Z_\alpha(\xi)}{\partial\xi} A_\alpha(\xi)\right\},$$

where we have introduced the notation

$$Z_\alpha(\xi) = (x-y)_\alpha \xi + y_\alpha - 2\sqrt{s} B_\alpha(\xi), \quad (2.7)$$

$$d\sigma_\beta = N\delta B_\beta \exp\left\{-\frac{1}{2}\int\limits_0^1 d\xi B'^2(\xi)\right\},$$

N being a normalization factor; the normalization conditions are taken to be

$$B_\alpha(0) = B_\alpha(1) = 0, \quad \int d\sigma_\beta = 1.$$

Substituting (2.6) into (2.1) and performing averaging over the external gauge field according to (2.3), we obtain the loop function in the form

$$\Pi(x) = \int\limits_0^\infty\int\limits_0^\infty \frac{d\mu_1 d\mu_2}{(8x\pi^2)^2} \tag{2.8}$$
$$\times \exp\left\{-\frac{1}{2}x\left(\frac{m_1^2}{\mu_1}+\mu_1\right) - \frac{x}{2}\left(\frac{m_2^2}{\mu_2}+\mu_2\right)\right\}J(\mu_1,\mu_2),$$

where the path integral is

$$J(\mu_1,\mu_2) = N_1N_2\int\int \delta r_1\delta r_2 \tag{2.9}$$
$$\times \exp\left\{-\frac{1}{2}\int\limits_0^x d\tau\left(\mu_1 {r'_1}^2(\tau) + \mu_2 {r'_2}^2(\tau)\right)\right\}$$
$$\times \exp\left\{-W_{1,1} + 2W_{1,2} - W_{2,2}\right\},$$

the notation here being

$$W_{i,j} = \frac{g^2}{2}(-1)^{i+j}\int\limits_0^x\int\limits_0^x d\tau_1 d\tau_2 Z'^{(i)}_\alpha(\tau_1) \tag{2.10}$$
$$\times D_{\alpha\beta}\left(Z^{(i)}(\tau_1) - Z^{(j)}(\tau_2)\right)Z'^{(j)}_\beta(\tau_2).$$

The path integral in (2.9) is similar to the Feynman path integral in nonrelativistic quantum mechanics [18] for the motion of two particles whose masses are μ_1 and μ_2. The interaction between these particles is described by expression (2.10), which involves both potential and nonpotential interactions. In particular, the terms $W_{1,1}$ and $W_{2,2}$ specify nonpotential interactions, while the term $W_{1,2}$ is responsible for a potential interaction of a nonlocal character. From (2.5), it follows that, upon determining the loop function, one can determine the bound-state as well. However, the path integral appearing in (2.8) and (2.9) cannot be calculated in a general form. According to (2.5), it is necessary to determine the asymptotic behavior of the loop function. Suppose that, in the limit $|x-y| \to \infty$, the path integral specified by (2.9) is defined as

$$\lim_{|x|\to\infty} J(\mu_1,\mu_2) \Longrightarrow \exp\{-xE(\mu_1,\mu_2)\}, \tag{2.11}$$

where $E(\mu)$ is a quantity that depends on μ_1 and μ_2 and on the coupling constant g. In this approximation, the integral in (2.9) is calculated by the saddle-point method. As a result, we find for the bound-state mass from (2.5) that

$$M = \sqrt{m_1^2 - 2\mu^2E'(\mu)} \tag{2.12}$$
$$+ \sqrt{m_2^2 - 2\mu^2E'(\mu)} + \mu E'(\mu) + E(\mu)$$

and determine the parameter μ from the equation

$$\frac{1}{\mu} = \frac{1}{\mu_1} + \frac{1}{\mu_2} \tag{2.13}$$
$$= \frac{1}{\sqrt{m_1^2 - 2\mu^2E'(\mu)}} + \frac{1}{\sqrt{m_2^2 - 2\mu^2E'(\mu)}},$$

where we have used the notation

$$E'(\mu) = \partial E(\mu)/\partial\mu.$$

The parameters μ_1 and μ_2 will be considered as the masses of constituent particles in a bound state. These masses differ from the free-state masses m_1 and m_2. In describing the mass spectrum of a relativistic bound state, one usually introduces the constituent mass of constituent particles [4–10], which differs from the mass of the original free particle. In particular, a description of the mass spectrum of hadrons consisting of quarks usually involves introducing the valence-quark and current-quark masses, which differ from each other.

If a bound state is formed by two gluons, it follows from (2.13) that the constituent gluon mass is not equal to zero. In this case, a two-gluon bound state can be identified with a Pomeron, which is widely used in describing the mechanism of inelastic particle scattering.

3. NONPERTURBATIVE CORRECTION TO THE INTERACTION HAMILTONIAN

In a standard calculation that takes into account a nonperturbative character of interactions, one usually retains only the lowest degree of the ratio v/c, but our approach includes the ultrarelativistic limit—that is, we determine the form of interaction by summing an infinite series in powers of v/c.

Let us now proceed to determine the structure of the interaction Hamiltonian. Taking into account Eq. (2.7) and employing the Fourier transform of the gluon propagator (2.4), we recast the expression for $W_{i,j}$ into the form

$$W_{i,j} = \frac{g^2}{2}(-1)^{i+j} \tag{3.1}$$

$$\times \int\limits_0^x \int\limits_0^x d\tau_1 d\tau_2 \left(\mathbf{n} + \frac{1}{c}\mathbf{r}'_i(\tau_1)\right) \cdot \left(\mathbf{n} + \frac{1}{c}\mathbf{r}'_j(\tau_2)\right)$$

$$\times \int \frac{d\mathbf{q}}{(2\pi)^3} \int\limits_{-\infty}^{\infty} \frac{ds}{2\pi} \widetilde{D}\left(\mathbf{q}^2 + \frac{s^2}{c^2}\right)$$

$$\times \exp\left\{ is(\tau_1 - \tau_2) + \frac{is}{c}\left(r_i^{(4)}(\tau_1) - r_j^{(4)}(\tau_2)\right) + i\mathbf{q} \cdot (\mathbf{r}_i(\tau_1) - \mathbf{r}_j(\tau_2)) \right\},$$

where $\mathbf{n} = \mathbf{r}/r$ with $\mathbf{r} = \mathbf{r}_1(\tau) - \mathbf{r}_2(\tau)$ and $r = |\mathbf{r}|$, while $\widetilde{D}$ is the Fourier transform of the function D. Constituent particles interact via the exchange of gauge fields; therefore, we represent the propagator in the standard form,

$$\widetilde{D}\left(\mathbf{q}^2 + \frac{s^2}{c^2}\right) \simeq \left(\mathbf{q}^2 + \frac{s^2}{c^2}\right)^{-1} \tag{3.2}$$

$$= \int\limits_0^{\infty} d\eta \exp\left\{-\eta\left(\mathbf{q}^2 + \frac{s^2}{c^2}\right)\right\}.$$

According to (3.1), we find for the interaction potential after integration with respect to $\mathbf{q}$ that

$$W_{i,j} = \frac{2}{3} g^2 (-1)^{i+j} \tag{3.3}$$

$$\times \int\limits_0^t \int\limits_0^t d\tau_1 d\tau_2 \int\limits_{-\infty}^{\infty} \frac{ds}{2\pi} \int\limits_0^{\infty} \frac{d\eta}{(2\sqrt{\pi\eta})^3}$$

$$\times \exp\left\{-\frac{\mathbf{r}^2}{4\eta}\right\} \sum_{k=0}^{\infty} \sum_{n=0}^{k} \frac{(-1)^{n+k}}{n!(k-n)!} \eta^n r^{(4)(k-n)}$$

$$\times \left(\frac{is}{c}\right)^{n+k} e^{is\tau} \Theta_{ij},$$

where we have introduced the notation

$$\tau = (\tau_1 - \tau_2), \quad \mathbf{r} = \mathbf{r}_i(\tau_1) - \mathbf{r}_j(\tau_2), \tag{3.4}$$

$$r^{(4)} = r_i^{(4)}(\tau_1) - r_j^{(4)}(\tau_2),$$

$$\Theta_{ij} = 1 + \frac{\mathbf{n}}{c} \cdot \left(\mathbf{r}'_i(\tau_1) + \mathbf{r}'_j(\tau_2)\right) + \frac{\mathbf{r}'_i(\tau_1) \cdot \mathbf{r}'_j(\tau_2)}{c^2}.$$

Here, τ_1 and τ_2 are treated as the proper times of the relative motion of constituent particles 1 and 2, respectively. Further, we assume that, at the initial instant of time, the constituent particles are at rest and interact with each other only via an electric or a chromoelectric field. We will now investigate the asymptotic behavior of the polarization-loop function. From (2.11), it follows that, in the asymptotic limit $x \to \infty$ (or $t \to \infty$), $W_{i,j}$ must depend on t linearly. On the other hand, the Euclidean time $r^{(4)}$ depends on the proper time τ of the constituent particle. In view of this, we choose the τ dependence of $r^{(4)}$ in the form

$$r^{(4)} = c(\tau_1 - \tau_2)u \equiv c\tau u, \tag{3.5}$$

where u is a new variable. Taking into account Eqs. (3.4) and (3.5) and performing integration with respect to s and u, we find from (3.3), after some simple algebra, that

$$W_{i,j} = (-1)^{i+j} \frac{g^2}{6\pi} \tag{3.6}$$

$$\times \int\limits_0^t \int\limits_0^t d\tau_1 d\tau_2 \frac{\delta(\tau_1 - \tau_2)}{|\mathbf{r}_i(\tau_1) - \mathbf{r}_j(\tau_2)|}$$

$$+ (-1)^{i+j} \frac{g^2}{6\pi} \sum_{k=1}^{\infty} \frac{(-1)^k}{(2k)!c^{2k}} \int\limits_0^t d\tau \frac{\partial^{2k}}{\partial\tau^{2k}}$$

$$\times |\mathbf{r}_i(\tau) - \mathbf{r}_j(\tau)|^{2k-1} \equiv W_{i,j}^{(1)} + W_{i,j}^{(2)}.$$

Let us now consider each term in (3.6) individually. The first term $W_{i,j}^{(1)}$ corresponds to the one-photon-exchange (one-gluon-exchange) contribution, which involves both a diagonal and an off-diagonal interaction, the diagonal ($i = j$) interaction determining a mass renormalization,

$$-W_{1,1}^{(1)} + 2W_{1,2}^{(1)} - W_{2,2}^{(1)} \tag{3.7}$$

$$= \int\limits_0^t d\tau \left\{-\frac{4}{3}\frac{\alpha_s}{r(\tau)} + V(0)\right\},$$

where

$$r(\tau) = |\mathbf{r}_1(\tau) - \mathbf{r}_2(\tau)|, \tag{3.8}$$

$$V(0) = \frac{4}{3}\alpha_s \int \frac{d\mathbf{q}}{(2\pi)^2} \frac{1}{\mathbf{q}^2}.$$

The term $V(0)$ corresponds to the usual renormalization of the mass operator in the nonrelativistic limit, and we will consider this term as a constant parameter in the ensuing calculations. Within phenomenological potential models, one resorts to an ad hoc introduction of a new parameter [19, 20],

$$V_0 = -2\sqrt{\lambda}\exp\{-(\gamma - 1/2)\},$$

$$\gamma = 0.577215665,$$

which makes it possible to ensure perfect agreement with experimental data. This parameter can be associated with a nonpotential character of the interaction. From (3.6), one can see that the second term $W_{i,j}^{(2)}$ generates only an off-diagonal contribution

$(i \neq j)$, the diagonal $(i = j)$ contribution being equal to zero.

We will now determine nonperturbative corrections. The parameter τ will be treated as the proper time of the relative motion of constituent particles. The quantity

$$\mathbf{v}(\tau) = \frac{\partial}{\partial \tau}(\mathbf{r}(\tau)) \tag{3.9}$$

then determines the relative velocity of constituent particles.

Let us first consider the case where the velocity of the relative motion is constant:

$$\partial \mathbf{v}(\tau)/\partial \tau = 0. \tag{3.10}$$

In this case, the contribution of the nonperturbative correction to the interaction Hamiltonian is represented as the sum in (3.6),

$$I = \sum_{k=1}^{\infty} \frac{(-1)^k}{(2k)!c^{2k}} \frac{\partial^{2k}}{\partial \tau^{2k}} \left(r^{2k-1}(\tau) \right), \tag{3.11}$$

where $r = |\mathbf{r}|$. In order to perform summation, we will first calculate the partial derivatives of the radius vector:

$$\mathbf{v} = \frac{\partial \mathbf{r}}{\partial \tau}, \quad \frac{\partial r}{\partial \tau} = (\mathbf{n} \cdot \mathbf{v}), \tag{3.12}$$
$$\mathbf{n} = \frac{\mathbf{r}}{r}, \quad \mathbf{v}' = \frac{\partial \mathbf{v}}{\partial \tau} = 0.$$

In this approximation, we find for various values of k that

$$\begin{array}{ll} k = 1 & \dfrac{\partial^2 r}{\partial \tau^2} = \dfrac{[\mathbf{r}, \mathbf{v}]^2}{r^3} = \dfrac{\hat{\ell}^2}{r^3}, \\ k = 2 & \dfrac{\partial^4 r^3}{\partial \tau^4} = \dfrac{9\hat{\ell}^4}{r^5}, \\ \vdots & \vdots \\ k = n & \dfrac{\partial^{2n} r^{2n-1}}{\partial \tau^{2n}} = \dfrac{\hat{\ell}^{2n}}{r^{2n+1}} \prod\limits_{j=1}^{n} (2j-1)^2, \end{array} \tag{3.13}$$

where

$$\hat{\ell} = [\mathbf{r}, \mathbf{v}] \tag{3.14}$$

is the orbital-angular-momentum operator. Using the relation

$$\prod_{j=1}^{k} (2j-1)^2 = \left[\frac{(2k-1)!}{2^{k-1}(k-1)!} \right]^2 \tag{3.15}$$
$$= \frac{\Gamma^2(2k)}{\Gamma^2(k) \cdot 2^{2(k-1)}}$$

with allowance for the identity

$$\Gamma(2k) = \frac{2^{2k-1}}{\sqrt{\pi}} \Gamma(k) \Gamma(k + 1/2) \tag{3.16}$$

and taking into account Eq. (3.13), we recast the original series in (3.11) into the form

$$I = \sum_{k=1}^{\infty} \frac{(-1)^k}{(2k)!c^{2k}} \frac{\hat{\ell}^{2k}}{r^{2k+1}} \frac{\Gamma^2(2k)}{\Gamma^2(k) \cdot 2^{2(k-1)}} \tag{3.17}$$
$$= \frac{1}{\sqrt{\pi} r} \sum_{k=1}^{\infty} \frac{(-1)^k A^k}{(k)!} \Gamma(k + 1/2),$$

where we have introduced the notation

$$A = \hat{\ell}^2/(c^2 r^2). \tag{3.18}$$

By using the integral representation for the function $\Gamma(k + 1/2)$, we ultimately find from (3.17) that

$$I = \frac{1}{\sqrt{\pi} r} \sum_{k=1}^{\infty} \frac{(-1)^k A^k}{(k)!} \int_0^{\infty} dx \frac{x^k}{\sqrt{x}} e^{-x} \tag{3.19}$$
$$= \frac{1}{\sqrt{\pi} r} \int_0^{\infty} \frac{dx}{\sqrt{x}} e^{-x} (e^{-Ax} - 1)$$
$$= \frac{1}{r} \left[\frac{1}{\sqrt{1 + \ell(\ell+1)/(c^2 r^2)}} - 1 \right].$$

Taking into account (3.7), (3.11), and (3.19) and using (3.6), we then obtain the interaction Hamiltonian with allowance for the nonperturbative correction. The result is

$$H = H^0 + \triangle H^0_{\text{nonper}}, \tag{3.20}$$

where H^0 is the nonrelativistic Hamiltonian and $\triangle H^0_{\text{nonper}}$ is the nonperturbative correction,

$$H^0 = \frac{1}{2\mu} \mathbf{P}^2 - \frac{4}{3} \frac{\alpha_s}{r} + V(0), \tag{3.21}$$
$$\triangle H^0_{\text{nonper}} = -\frac{4}{3} \frac{\alpha_s}{r} \left[\frac{1}{\sqrt{1 + \ell(\ell+1)/(c^2 r^2)}} - 1 \right].$$

Thus, we have obtained a nonperturbative correction to the interaction Hamiltonian, this correction being associated with the relativistic nature of the system. We have established that, in the nonrelativistic limit $(c \to \infty)$, there is no such correction. We assumed, among other things, that our system consists of quarks and antiquarks that move at a constant velocity with respect to each other. Similar results were obtained in [16].

4. CALCULATION OF THE GLUEBALL MASS SPECTRUM

4.1. Mass Spectrum of a Glueball Consisting of Scalar Gluons

In this subsection, we will consider a two-gluon bound state of mass $\mu_1 \equiv \mu_2 = 2\mu$. Since a gluon occurs only in a bound state, the interaction Hamiltonian is chosen in such a way as to satisfy the gluon-confinement condition. The Schrödinger equation for such a system then has the form

$$\left[\frac{1}{2\mu}\mathbf{P}^2+\sigma_{\rm ad}r\right]\Psi=E(\mu)\Psi, \qquad (4.1)$$

where $\sigma_{\rm ad}$ is the string-tension parameter. In order to determine the eigenvalue and wave function from (4.1), we will apply the oscillator-representation method. Before proceeding to determine the energy spectrum and the wave functions for the Schrödinger equation by the oscillator-representation method [21, 22], it is advisable to recall that this method is based on the ideas and methods of the quantum theory of a scalar field. One of the substantial distinctions between quantum field theory and quantum mechanics is that quantized fields, which form a set of an infinite number of oscillators for the ground state or the vacuum, retain their oscillator nature in quantum-field interactions. In quantum mechanics, the behavior of eigenfunctions for the majority of potentials differs from the Gaussian behavior of an oscillator wave function. In order to apply the methods and ideas of quantum field theory to solving quantum-mechanical problems, it is necessary to perform a change of variables in the original Schrödinger equation in such a way that the sought wave function would have Gaussian behavior at long distances and that the transformed equation could be identified with a radial Schrödinger equation in a space of higher dimension. It should be noted that, for the first time, this idea was discussed by Fock in solving the problem of the hydrogen spectrum by means of a transformation to four-dimensional momentum space [23].

In accordance with the aforesaid, we make the change of variables (for details, see [24])

$$r=q^{2\rho}, \qquad (4.2)$$

$$\Psi\Rightarrow\Psi(q^2)=q^{2\rho\ell}\Phi(q^2),$$

where the parameter ρ controls the behavior of the wave function at long distances. We use here the atomic system of units ($\hbar=c=1$). The resulting Schrödinger equation obtained from (4.1) after some standard simplifications has the form

$$\Bigg\{-\frac{1}{2}\left(\frac{\partial^2}{\partial q^2}+\frac{d-1}{q}\frac{\partial}{\partial q}\right) \qquad (4.3)$$

$$+4\rho^2\mu\sigma_{\rm ad}q^{2(3\rho-1)}-4\rho^2\mu Eq^{2(2\rho-1)}\Bigg\}\Phi(q^2)=0,$$

where

$$d=2+2\rho+4\rho\ell \qquad (4.4)$$

is the dimensionality of the auxiliary space. Thus, we have obtained, upon the above change of variables, a modified Schrödinger equation in d-dimensional space R^d. From (4.3) and (4.4), it follows that the orbital quantum number ℓ appears in the definition of the dimensionality d of the above auxiliary space. By means of this trick, we can determine all of the features in which we are interested (namely, the spectrum and the wave function), solving the modified Schrödinger equation only for the ground state in the auxiliary d-dimensional space R^d.

The ground-state wave function $\Psi_m(q^2)$ in R^d depends only on the variable q^2. Therefore, we identify the operator

$$\frac{\partial^2}{\partial q^2}+\frac{d-1}{q}\frac{\partial}{\partial q}\equiv\triangle_q \qquad (4.5)$$

with the Laplacian $\triangle_q$ in the auxiliary space R^d as applied to the ground-state wave function, which depends only on the radius q. On the basis of the modified Schrödinger equation

$$H\Phi(q)=\varepsilon(E)\Phi(q), \qquad (4.6)$$

we find in accordance with (4.3) that the energy spectrum $\varepsilon(E)$ in R^d is equal to zero,

$$\varepsilon(E)=0. \qquad (4.7)$$

We will consider this relation as the condition for determining the energy spectrum E of the Hamiltonian from (4.3). Following the oscillator-representation method, we express canonical variables in terms of the creation (a^+) and annihilation (a) operators in the space R^d as

$$q_j=\frac{a_j+a_j^+}{\sqrt{2\omega}},\quad P_j=\sqrt{\frac{\omega}{2}}\frac{a_j-a_j^+}{i}, \qquad (4.8)$$

$$j=1,...,d,\qquad [a_i,a_j^+]=\delta_{i,j},$$

where ω is the oscillator frequency, which is unknown at the present stage. Substituting (4.8) into (4.3) and introducing normal ordering with respect to the creation operators a^+ and the annihilation operators a, we obtain

$$H=H_0+\varepsilon_0(E)+H_I, \qquad (4.9)$$

where H_0 is the free-oscillator Hamiltonian

$$H_0=\omega(a_j^+a_j), \qquad (4.10)$$

while ε_0 is the ground-state energy in the zero-order approximation of the oscillator-representation method. The interaction Hamiltonian H_I can also be represented in a normal form with respect to the creation operators a^+ and the annihilation operators a. It should be noted that the interaction Hamiltonian does not involve terms that are quadratic in the canonical variables; that is,

$$H_I = \int \left(\frac{dk}{2\pi}\right)^d \widetilde{W}(k^2) \exp\left\{-\frac{k^2}{4\omega}\right\} : e_2^{-i(kq)} :, \tag{4.11}$$

where

$$W(q^2) = \int \left(\frac{dk}{2\pi}\right)^d \widetilde{W}(k^2) e^{-i(kq)}. \tag{4.12}$$

Here, $: * :$ is the normal-ordering symbol, and we have used the notation

$$e_2^{-x} = e^{-x} - 1 + x - x^2/2$$

and

$$W(q^2) = 4\rho^2 \mu \sigma_{\rm ad} q^{2(3\rho-1)} - 4E\rho^2 \mu q^{2(2\rho-1)}. \tag{4.13}$$

Some details of the procedure used here to reduce the Hamiltonian to a normally ordered form are given in the Appendix (see also [24]).

The contribution of the interaction Hamiltonian H_I is considered as a small perturbation. Upon expressing the canonical variables of a quantum field theory in terms of creation and annihilation operators and representing the respective interaction Hamiltonian in a normal form, the requirement that the interaction Hamiltonian not involve field operators raised to the second power is essentially equivalent in quantum field theory to renormalizing the coupling constant and the wave function [25–27]. Moreover, this procedure enables one to take into account the main contribution through a mass renormalization and the vacuum energy. In other words, all quadratic forms are fully included in the free-oscillator Hamiltonian. This requirement makes it possible to formulate, according to the oscillator-representation method, the condition

$$\partial \varepsilon_0(E)/\partial \omega = 0 \tag{4.14}$$

for determining the oscillator frequency ω, which specifies the main quantum contribution. Taking into account relation (4.9), we can then calculate the energy E on the basis of Eqs. (4.7) and (4.14).

Within the oscillator representation, it was repeatedly verified for various potentials [28–30] that the first-order correction associated with the interaction Hamiltonian is identically equal to zero and that the second-order correction is less than 1%. Therefore, we consider only the zero-order approximation.

We now present ultimate results for the ground-state energy in the zero-order approximation of the oscillator representation:

$$\varepsilon_0(E) = \frac{d\omega}{4} + \frac{4\rho^2 \mu \sigma_{\rm ad}}{\omega^{3\rho-1}} \frac{\Gamma(d/2 + 3\rho - 1)}{\Gamma(d/2)} - \frac{4E\rho^2 \mu}{\omega^{2\rho-1}} \frac{\Gamma(d/2 + 2\rho - 1)}{\Gamma(d/2)}. \tag{4.15}$$

According to (4.14)—that is, the oscillator-representation condition—the oscillator frequency ω is given by

$$\omega^\rho = \left[4\rho^2 \mu \sigma_{\rm ad} \frac{\Gamma(d/2 + 3\rho - 1)}{\Gamma(d/2)}\right]^{1/3}. \tag{4.16}$$

Taking into account (4.15) and (4.16), we find the energy spectrum E from (4.7) as a function of the parameter μ:

$$E(\mu) = \frac{3}{2\mu^{1/3}} \frac{1}{\Gamma(d/2 + 2\rho - 1)} \times \left[\frac{\sigma_{\rm ad}^2 \Gamma(d/2 + 1) \Gamma^2(d/2 + 3\rho - 1)}{4\rho^2}\right]^{1/3}. \tag{4.17}$$

The variational parameter ρ is usually found from equations that minimize the energy $E(\mu)$; that is,

$$\begin{gathered} \Psi(2 + 2\rho\ell + \rho)(1 + 2\ell) \\ + 2\Psi(2\rho\ell + 4\rho)(4 + 2\ell) - 2/\rho \\ - 3\Psi(2\rho\ell + 3\rho)(3 + 2\ell) = 0, \end{gathered} \tag{4.18}$$

where the function Ψ is

$$\Psi(x) = \frac{\partial}{\partial x} \ln \Gamma(x). \tag{4.19}$$

We now proceed to determine the glueball masses. According to (2.13), the parameter μ for the bound state of gluons is found from the equation

$$2 + \frac{dE(\mu)}{d\mu} = 0. \tag{4.20}$$

Taking into account (4.17) and using (4.20), we then obtain

$$\mu = \left[\frac{\sigma_{\rm ad}^2 \Gamma(d/2 + 1) \Gamma^2(d/2 + 3\rho - 1)}{256\rho^2 \Gamma^3(d/2 + 2\rho - 1)}\right]^{1/4}. \tag{4.21}$$

After some simplifications, we find that the glueball mass is

$$M = 2\sqrt{\sigma_{\rm ad}} \left[\frac{\Gamma(2 + \rho + 2\rho\ell) \Gamma^2(4\rho + 2\rho\ell)}{\rho^2 \Gamma^3(3\rho + 2\rho\ell)}\right]^{1/4}, \tag{4.22}$$

and that the constituent gluon mass is

$$\mu_G = \frac{\sqrt{\sigma_{\rm ad}}}{2} \left[\frac{\Gamma(2 + \rho + 2\rho\ell) \Gamma^2(4\rho + 2\rho\ell)}{\rho^2 \Gamma^3(3\rho + 2\rho\ell)}\right]^{1/4}. \tag{4.23}$$

From (4.22) and (4.23), it can be seen that, at specific values of the orbital quantum number ℓ, the glueball (Pomeron) mass and the constituent gluon mass are

Table 1. Mass spectrum of the glueball and the gluon in a bound state without allowance for spin interaction

l	ρ	μ_G, GeV	M, GeV
0	0.57241	0.5279	2.1116(2.11)
1	0.57392	0.69306	2.77224 (2.77)
2	0.57493	0.82612	3.304487 (3.30)
3	0.57513	0.94063	3.762514

Note: Here and in Tables 2 and 3, the results reported in [16] are given in parentheses.

Table 2. Mass spectrum of the glueball and the gluon in a bound state with allowance for one-gluon exchange

α_s	ρ	μ, GeV	μ_G, GeV	M, GeV
0	0.5735	0.26398	0.52795	2.1116 (2.11)
0.1	0.6300	0.28568	0.57135	1.95543
0.2	0.700	0.31561	0.63121	1.78442 (1.776)
0.3	0.795	0.35950	0.71899	1.59448 (1.587)
0.39	0.885	0.41961	0.83921	1.39809 (1.39)

functions of the string-tension parameter $\sigma_{\rm ad}$. Table 1 gives numerical results obtained at the value

$$\sigma_{\rm ad} = 9\sigma_f/4, \quad \sigma_f = 0.18\ \text{GeV}^2. \tag{4.24}$$

Also given in Table 1 are the results reported in [16], our results being in good agreement with them.

4.2. Contribution of One-Gluon Exchange to the Glueball Mass

As is well known, gluons interact with one another; therefore, we address here the problem of determining the contribution of one-gluon exchange to the glueball mass. The Schrödinger equation for a bound state of a two-gluon system with allowance for one-gluon exchange has the form

$$\left[\frac{1}{2\mu}\mathbf{P}^2 + \sigma_{\rm ad} r - \frac{4}{3}\frac{\alpha_s}{r}\right]\Psi = E(\mu)\Psi, \tag{4.25}$$

where α_s is the coupling constant for strong interaction. Relying on Eq. (4.25) and employing the oscillator-representation method, we first determine the energy spectrum $E(\mu)$ as a function of μ. After a change of variables, we find from (4.25) that the modified Schrödinger equation in R^d space takes the form

$$\left[\frac{1}{2}\mathbf{P}_q^2 + 4\rho^2\mu\sigma_{\rm ad}q^{2(3\rho-1)} \right. \tag{4.26}$$
$$\left. - \frac{16}{3}\alpha_s\rho^2\mu q^{2(\rho-1)} - 4\rho^2\mu E(\mu)q^{2(2\rho-1)}\right]\Phi(q^2) = 0.$$

After some standard simplifications that were described above, the ground-state energy in the zero-order approximation of the oscillator-representation method can be reduced to the form

$$\varepsilon_0(E) = \frac{d\omega}{4} + \frac{4\rho^2\mu\sigma_{\rm ad}}{\omega^{3\rho-1}}\frac{\Gamma(d/2+3\rho-1)}{\Gamma(d/2)} \tag{4.27}$$
$$- \frac{4\rho^2\mu E}{\omega^{2\rho-1}}\frac{\Gamma(d/2+2\rho-1)}{\Gamma(d/2)}$$
$$- \frac{16\alpha_s\rho^2\mu}{3\omega^{\rho-1}}\frac{\Gamma(d/2+\rho-1)}{\Gamma(d/2)}.$$

In this case, we restrict our consideration to the case of the ground state; that is, we set $\ell = 0$. After some simplifications, we then find for $E(\mu)$ that

$$E(\mu) = \min_\rho\left\{\frac{Z^2}{8\rho^2\mu}\frac{\Gamma(2+\rho)}{\Gamma(3\rho)} \right. \tag{4.28}$$
$$\left. + \frac{\sigma_{\rm ad}}{Z}\frac{\Gamma(4\rho)}{\Gamma(3\rho)} - \frac{4\alpha_s Z}{3}\frac{\Gamma(2\rho)}{\Gamma(3\rho)}\right\}.$$

Here, the parameter $Z = \omega^\rho$ is determined from the equation

$$Z^3 - Z^2\frac{16\rho^2\mu\alpha_s\Gamma(2\rho)}{\Gamma(2+\rho)} - \frac{4\rho^2\mu\sigma_{\rm ad}\Gamma(4\rho)}{\Gamma(2+\rho)} = 0, \tag{4.29}$$

which was obtained from the oscillator-representation condition. Taking into account Eqs. (4.28) and (4.29), we determine the parameter μ from Eq. (4.20). From Eq. (2.12), we then find that the glueball mass is

$$M = 2\mu + E(\mu), \tag{4.30}$$

and that the constituent gluon mass is

$$\mu_G = 2\mu. \tag{4.31}$$

The respective numerical result is given in Table 2.

4.3. Mass Spectrum of the Glueball with Allowance for a Nonperturbative Character of the Interaction Potential

We now proceed to calculate the mass spectrum of a two-gluon bound state with allowance for one-gluon exchange and a nonperturbative character of the interaction. According to (3.20), the total interaction Hamiltonian has the form

$$H = \frac{1}{2\mu}\mathbf{P}^2 + \sigma_{\rm ad} r \tag{4.32}$$

$$-\frac{4}{3}\frac{\alpha_s}{r} - \frac{4}{3}\frac{\alpha_s}{r}\left[\frac{1}{\sqrt{1+\ell(\ell+1)/r^2}} - 1\right].$$

The eigenvalues of this Hamiltonian are also determined by the oscillator-representation method. After a change of variables, the modified Schrödinger equation for this case assumes the form

$$\left\{\frac{1}{2}\mathbf{P}_q^2 + 4\rho^2\mu\sigma_{\rm ad}q^{2(3\rho-1)} - 4\rho^2\mu E q^{2(2\rho-1)} - \frac{16}{3} \times \frac{q^{2(\rho-1)}\rho^2\mu\alpha_s}{\sqrt{1+\ell(\ell+1)/q^{4\rho}}}\right\}\Phi(q^2) = 0. \tag{4.33}$$

After some simplifications (the details are given in the Appendix), we obtain the following result for the ground-state energy in the zero-order approximation:

$$\varepsilon_0(E) = \frac{d\omega}{4} + \frac{4\rho^2\mu\sigma_{\rm ad}}{\omega^{3\rho-1}}\frac{\Gamma(d/2+3\rho-1)}{\Gamma(d/2)} - \frac{4\rho^2\mu E}{\omega^{2\rho-1}}\frac{\Gamma(d/2+2\rho-1)}{\Gamma(d/2)} - \frac{16\alpha_s\rho^2\mu\omega^{d/2}}{3\Gamma(d/2)}\int\limits_0^\infty du\frac{u^{d/2+2\rho-2}e^{-\omega u}}{\sqrt{u^{2\rho}+\ell(\ell+1)}}. \tag{4.34}$$

Taking into account relation (4.34) and using Eqs. (4.7) and (4.14), we obtain the energy spectrum of the original Hamiltonian in the form

$$E(\mu) = \min_\rho\left\{\frac{Z^2}{8\rho^2\mu}\frac{\Gamma(2+\rho+2\ell\rho)}{\Gamma(3\rho+2\ell\rho)} + \frac{\sigma_{\rm ad}}{Z}\frac{\Gamma(4\rho+2\ell\rho)}{\Gamma(3\rho+2\ell\rho)} - \frac{4\alpha_s}{3\rho}\frac{Z}{\Gamma(3\rho+2\ell\rho)}\int\limits_0^\infty dt\frac{t^{2+2\ell}\exp\left(-t^{1/\rho}\right)}{\sqrt{t^2+Z^2\ell(\ell+1)}}\right\}, \tag{4.35}$$

where the parameter Z can be found from the equation

$$Z^3 - \frac{4\rho^2\mu\sigma_{\rm ad}\Gamma(4\rho+2\ell\rho)}{\Gamma(2+\rho+2\ell\rho)} - \frac{16Z^2\rho^2\mu\alpha_s}{3\Gamma(2+\rho+2\ell\rho)}\int\limits_0^\infty dt\frac{t^{2+2\ell}\exp\left(-t^{1/\rho}\right)}{\sqrt{t^2+Z^2\ell(\ell+1)}} \times \left[3\rho+2\rho\ell-t^{1/\rho}\right] = 0. \tag{4.36}$$

Taking into account relations (4.35) and (4.36), we determine the glueball mass and the constituent gluon mass from Eqs. (4.30) and (4.31). The respective numerical results are given in Table 3.

Table 3. Mass spectrum of the glueball and the gluon in a bound state with allowance for a nonperturbative character of the interaction

α_s	ρ	μ, GeV	μ_G, GeV	M, GeV
$l = 1$				
0	0.574	0.3465	0.6931	2.772 (2.77)
0.1	0.58	0.3553	0.7106	2.684
0.2	0.59	0.3644	0.7288	2.594 (2.56)
0.3	0.595	0.3739	0.7478	2.5002 (2.45)
0.39	0.60	0.3827	0.7654	2.418 (2.36)
$l = 2$				
0	0.5745	0.4131	0.8261	3.304 (3.30)
0.1	0.575	0.4184	0.8373	3.239
0.2	0.58	0.4245	0.8489	3.173 (3.14)
0.3	0.58	0.4302	0.8603	3.106 (3.05)
0.39	0.585	0.4354	0.8707	3.045 (2.97)
$l = 3$				
0	0.5751	0.4703	0.9406	3.762
0.1	0.5752	0.4744	0.9488	3.710
0.2	0.5755	0.4784	0.9556	3.656
0.3	0.5765	0.4824	0.9647	3.603
0.39	0.585	0.486	0.9719	3.555

4.4. Determination of the Slope of the Regge Trajectory for the Glueball

In this subsection, we will determine the slope of the Regge trajectory for a two-gluon bound state. At high values of the orbital quantum number, $\ell \gg 1$, the contributions of the potentials corresponding to one-gluon exchange and a nonperturbative interaction cancel each other. As to the interaction between the constituent particles, it is determined by the confining potential. The glueball mass spectrum is given by (4.22). From this relation, we determine the dependence of the glueball mass on ℓ for $\ell \gg 1$, employing the asymptotic formula for the Euler gamma function,

$$\Gamma(az+b) \sim \sqrt{2\pi}e^{-az}(az)^{az+b-1/2}. \tag{4.37}$$

As a result, we obtain

$$M^2 = 8\sigma_{\rm ad}\ell. \tag{4.38}$$

This result is in good agreement with experimental data (for details, see [14]). From Tables 1, 2, and 3, one can see that, with increasing coupling constant α_s, the bound-state mass decreases, while the constituent mass of the particles forming the bound state increases.

5. CONCLUSION

On the basis of studying the asymptotic behavior of the polarization loop for charged scalar particles in an external gauge field, we have determined a relativistic correction to the interaction Hamiltonian. We have proposed a scheme for summing an infinite power series in the ratio v/c. A nonperturbative correction to the interaction Hamiltonian has been obtained. This correction vanishes in the limit $c \to \infty$.

The mass spectrum of a bound state has been determined analytically. The mechanism responsible for the formation of the constituent mass forming the bound state in question has been explained. It has been shown that the constituent masses of these particles differ from the free-state mass—in particular, a gluon becomes massive when it forms a bound state.

On the basis of our analytic calculations, we have determined the mass spectrum of glueballs (Pomerons) and the constituent gluon mass. At high values of the orbital quantum number, the vector potential is completely annihilated, and the interaction between gluons is determined by the scalar confining potential. Within conventional potential quark models, this behavior of the interaction is ensured through the introduction of quark–gluon hybrids. The slope of the respective Regge trajectory has been determined. At high values of the orbital quantum number—that is, in the limit $\ell \Rightarrow \infty$—the contribution of the vector potential and the contribution of the potential associated with a nonperturbative character of the interaction cancel each other, and the slope of the Regge trajectory is determined in terms of the string tension. These results faithfully reproduce experimental data.

APPENDIX

The representation of canonical variables in a normally ordered form is an important element of the calculations on the basis of the oscillator-representation method [22]. In view of this, we will specify below such representations for various potentials:

(a) For a growing potential, we have

$$q^{2n} = (-1)^n \frac{d^n}{dx^n} e^{-xq^2}\Big|_{x=0} = (-1)^n \qquad \text{(A.1)}$$

$$\times \frac{d^n}{dx^n} \int \left(\frac{d\eta}{\sqrt{\pi}}\right)^d e^{-\eta^2(1+x/\omega)} : e^{-2i\sqrt{x}(q\eta)} : \Big|_{x=0}$$

$$= \frac{1}{\omega^n} \frac{\Gamma\left(\frac{d}{2}+n\right)}{\Gamma\left(\frac{d}{2}\right)} + :q^2: \frac{n}{\omega^{n-1}} \frac{\Gamma\left(\frac{d}{2}+n\right)}{\Gamma\left(\frac{d}{2}+1\right)}$$

$$+ \frac{(-1)^n}{\omega^n} \frac{d^n}{dx^n} \int \left(\frac{d\eta}{\sqrt{\pi}}\right)^d$$

$$\times e^{-\eta^2(1+x)} : e_2^{-2i\sqrt{x\omega}(q\eta)} : \Big|_{x=0},$$

where $n = 1, 2, \ldots$ is a positive integer.

(b) For a decreasing potential, the respective result is

$$q^{2\tau} = \int_0^\infty \frac{dx}{\Gamma(-\tau)} x^{-1-\tau} e^{-xq^2} \qquad \text{(A.2)}$$

$$= \int_0^\infty dx \frac{x^{-1-\tau}}{\Gamma(-\tau)} \int \left(\frac{d\eta}{\sqrt{\pi}}\right)^d$$

$$\times e^{-\eta^2(1+x/\omega)} : e^{-2i\sqrt{x}(q\eta)} :$$

$$= \frac{1}{\omega^\tau} \frac{\Gamma\left(\frac{d}{2}+\tau\right)}{\Gamma\left(\frac{d}{2}\right)} + :q^2: \frac{\tau}{\omega^{\tau-1}} \frac{\Gamma\left(\frac{d}{2}+\tau\right)}{\Gamma\left(\frac{d}{2}+1\right)}$$

$$+ \frac{1}{\omega^\tau} \int_0^\infty \frac{dx}{\Gamma(-\tau)} x^{-1-\tau} \int \left(\frac{d\eta}{\sqrt{\pi}}\right)^d$$

$$\times e^{-\eta^2(1+x)} : e_2^{-2i\sqrt{x\omega}(q\eta)} : .$$

In particular, we find from (A.1) that, at $n = 1, 2, 3$,

$$q^2 = \frac{d}{2\omega} + :q^2:, \qquad \text{(A.3)}$$

$$q^4 = \frac{d(d+2)}{4\omega^2} + \frac{d+2}{\omega} :q^2: + :q^4:,$$

$$q^6 = \frac{d(d+2)(d+4)}{8\omega^3} + \frac{3(d+2)(d+4)}{4\omega^2} :q^2:$$

$$+ \frac{3(d+4)}{2\omega} :q^4: + :q^6: .$$

Let us now derive a number of useful relations for creation and annihilation operators. These relations are frequently encountered in calculating matrix elements for various physical processes within the oscillator-representation method.

Suppose that the operators a_j^+ and a_j satisfy the commutation relations (4.8). For these operators, we then have the standard identity

$$e^{i\mathbf{k}\cdot\mathbf{a}} e^{i\mathbf{p}\cdot\mathbf{a}^+} = e^{i\mathbf{p}\cdot\mathbf{a}^+} e^{i\mathbf{k}\cdot\mathbf{a}} e^{-(kp)}, \qquad \text{(A.4)}$$

where $\mathbf{k}$ and $\mathbf{p}$ are vector in d-dimensional space.

Let us consider the expression

$$Y_j(\mathbf{k}) = e^{i\mathbf{k}\cdot\mathbf{a}} a_j^+ e^{-i\mathbf{k}\cdot\mathbf{a}}. \qquad \text{(A.5)}$$

At $\mathbf{k} = 0$, we find from (A.5) that

$$Y_j(0) = a_j^+. \qquad \text{(A.6)}$$

Taking into account (A.6) and using (A.5), we obtain an expression for $dY_j(\mathbf{k})/dk_l$ in the form

$$\frac{dY_j(\mathbf{k})}{dk_l} = e^{i\mathbf{k}\cdot\mathbf{a}} i \left[a_l, a_j^+\right] e^{-i\mathbf{k}\cdot\mathbf{a}} = i\delta_{jl}. \tag{A.7}$$

Performing integration with respect to k_l and taking into account (A.6), we arrive at

$$Y_j(\mathbf{k}) = e^{i\mathbf{k}\cdot\mathbf{a}} a_j^+ e^{-i\mathbf{k}\cdot\mathbf{a}} = a_j^+ + ik_j. \tag{A.8}$$

In a similar way, one can derive the relations

$$\begin{aligned} e^{-i\mathbf{p}\cdot\mathbf{a}^+} a_j e^{i\mathbf{p}\cdot\mathbf{a}^+} &= a_j + ip_j, \\ e^{\alpha\mathbf{a}^+\cdot\mathbf{a}} a_j e^{-\alpha\mathbf{a}^+\cdot\mathbf{a}} &= a_j e^{-\alpha}, \\ e^{\alpha\mathbf{a}^+\cdot\mathbf{a}} a_j^+ e^{-\alpha\mathbf{a}^+\cdot\mathbf{a}} &= a_j^+ e^{\alpha}. \end{aligned} \tag{A.9}$$

Using these representations, we have derived expressions for the ground-state energy $\varepsilon_0(E)$ and the interaction Hamiltonian H_I.

REFERENCES

1. N. P. Konopleva and V. N. Popov, *Gauge Fields* 2nd ed. (Atomizdat, Moscow, 1980; Harwood, Chur, 1981).
2. D. J. Gross and F. Wilczek, Phys. Rev. Lett. **30**, 1343 (1973); Phys. Rev. D **8**, 3633 (1973).
3. H. D. Politzer, Phys. Rev. Lett. **30**, 1346 (1973).
4. E. Eichten *et al.*, Phys. Rev. Lett. **34**, 369 (1975).
5. D. Gromes, Nucl. Phys. B **131**, 80 (1977); Z. Phys. C **22**, 265 (1984).
6. J. L. Richardson, Phys. Lett. B **82B**, 272 (1979).
7. C. Quigg and J. L. Rosner, Phys. Rep. **56**, 167 (1979).
8. A. Martin, Phys. Lett. B **100B**, 511 (1981).
9. A. A. Bykov, I. M. Dremin, and A. V. Leonidov, Usp. Fiz. Nauk **143**, 3 (1984) [Sov. Phys. Usp. **27**, 321 (1984)].
10. W. Lucha, F. F. Schöberl, and D. Gromes, Phys. Rep. **200**, 127 (1991).
11. G. S. Bali, K. Schilling, and A. Wachter, Phys. Rev. D **56**, 2566 (1997); hep-lat/9703019; G. S. Bali and P. Boyle, Phys. Rev. D **59**, 114504 (1999); hep-lat/9809180.
12. G. V. Efimov and S. N. Nedelko, Phys. Rev. D **51**, 176 (1995); **54**, 4483 (1996).
13. H. G. Dosch, Phys. Lett. B **190**, 177 (1987); H. G. Dosch and Yu. A. Simonov, Phys. Lett. B **205**, 339 (1988); Yu. A. Simonov, Nucl. Phys. B **307**, 512 (1988).
14. Yu. A. Simonov, Phys. Lett. B **249**, 514 (1990); Preprint TPI-MINN-90/19-T.
15. A. Yu. Dubin, A. B. Kaidalov, and Yu. A. Simonov, Yad. Fiz. **56** (12), 213 (1993) [Phys. At. Nucl. **56**, 1745 (1993)].
16. A. B. Kaidalov and Yu. A. Simonov, Yad. Fiz. **63**, 1507 (2000) [Phys. At. Nucl. **63**, 1428 (2000)].
17. M. Dineykhan, G. V. Efimov, and Kh. Namsrai, Fortschr. Phys. **39**, 259 (1991).
18. R. P. Feynman and A. P. Hibbs, *Quantum Mechanics and Path Integrals* (McGraw-Hill, New York, 1965).
19. S. Godfrey and N. Isgur, Phys. Rev. D **32**, 189 (1985).
20. N. Isgur and M. Wise, Phys. Lett. B **232**, 113 (1989); **237**, 527 (1990).
21. M. Dineykhan and G. V. Efimov, Fiz. Élem. Chastits At. Yadra **26**, 651 (1995) [Phys. Part. Nucl. **26**, 275 (1995)].
22. M. Dineykhan, G. V. Efimov, G. Ganbold, and S. N. Nedelko, *Oscillator Representation in Quantum Physics, Lecture Notes in Physics* (Springer-Verlag, Berlin, 1995), Vol. 26.
23. V. A. Fock, *Elements of Quantum Mechanics* (Nauka, Moscow, 1976).
24. M. Dineykhan and G. V. Efimov, Rep. Math. Phys. **36**, 287 (1995); Yad. Fiz. **59**, 862 (1996) [Phys. At. Nucl. **59**, 824 (1996)].
25. E. S. Fradkin, Nucl. Phys. **49**, 624 (1963).
26. K. Hayashi, M. Hirayama, T. Muta, *et al.*, Fortschr. Phys. **15**, 625 (1967).
27. A. Salam, *Nonpolynomial Lagrangians: Renormalization and Gravity* (Gordon and Breach, New York, 1971).
28. M. Dineykhan and R. G. Nazmitdinov, Yad. Fiz. **62**, 143 (1999) [Phys. At. Nucl. **62**, 138 (1999)].
29. M. Dineykhan, Z. Phys. D **41**, 77 (1997).
30. M. Dineĭkhan, S. A. Zhaugasheva, and R. G. Nazmitdinov, Zh. Éksp. Teor. Fiz. **119**, 1210 (2001) [JETP **92**, 1049 (2001)].

Translated by A. Isaakyan

Physics of Atomic Nuclei, Vol. 68, No. 2, 2005, pp. 326–331. From Yadernaya Fizika, Vol. 68, No. 2, 2005, pp. 351–356.
Original English Text Copyright © 2005 by Ioffe, Shushpanov, Zyablyuk.

ELEMENTARY PARTICLES AND FIELDS
Theory

Formation of Antideuterons in Heavy-Ion Collisions*

B. L. Ioffe**, **I. A. Shushpanov*****, and **K. N. Zyablyuk******

Institute of Theoretical and Experimental Physics,
Bol'shaya Cheremushkinskaya ul. 25, Moscow, 117259 Russia

Received March 16, 2004; in final form, August 12, 2004

Abstract—The antideuteron production rate at high-energy heavy-ion collisions is calculated based on the concept of $\bar{d}$ formation by antinucleons which move in the mean field of the fireball constituents (mainly pions). The explicit formula is presented for the coalescence parameter B_2 in terms of deuteron binding energy and fireball volume. © *2005 Pleiades Publishing, Inc.*

1. INTRODUCTION

Recent measurements have reported the production of antideuterons in heavy-ion collisions [1–3]. The theoretical description of this interesting effect is complicated, because the antideuterons are produced at the intermediate stage of fireball evolution, when the hadrons are already formed and may be considered as a hadronic gas, but the particle collisions are still important. In other words, they are produced at the "dense-gas" stage of fireball evolution.

Here, we present the theoretical picture of this stage and calculate the $\bar{d}$ production. The basic ideas of our approach are the following. The dominant mechanism of $\bar{d}$ production is the formation of antideuterons through the fusion reaction $\bar{p}+\bar{n}\to\bar{d}$. The fusion reaction is not possible if all participating particles are on the mass shell. However, in the fireball at the dense-gas stage of its evolution, $\bar{p}$, $\bar{n}$, $\bar{d}$ are not on the mass shell, since they interact with surrounding matter. The interaction with the fireball constituents leads to the appearance of the mass shift and widths of all particles propagating in the medium (or width broadening for unstable ones), analogous to refraction and attenuation indices in the case of photon propagation. The fusion reaction rate is strongly enhanced in comparison with the main process of $\bar{d}$ production in vacuum $\bar{p}+\bar{n}\to\bar{d}+\pi$. Another important ingredient of the theoretical picture is the balance of the antideuteron formation and disintegration rates. This balance is achieved because of a large number of produced pions and high rate of $\pi+\bar{d}$ collisions leading to $\bar{d}$ disintegration. The balance does not imply a statistical equilibrium, but rather a stationary process, like a balance in the isotope concentrations in a radiative chain. The formation rate $\bar{p}+\bar{n}\to\bar{d}$ vanishes when the $\bar{d}$ size increases, i.e., its binding energy $\varepsilon\to 0$. This fact explicitly manifests itself in our calculations. The previous theoretical investigations of the problem were performed in statistical models [4, 5], in the model of (anti)nucleon sources in the fireball [6], and in the Wigner function approach (see [7, 8] and references therein). In all these approaches, the interaction of nucleons, forming d (or $\bar{p}$ and $\bar{n}$ forming $\bar{d}$) with the fireball constituents, as well as $\bar{d}$ (d) disintegration, was not taken into account (in [4, 5], the results do not depend on ε).

According to the dominant coalescence mechanism, it is convenient to characterize $\bar{d}$ production in heavy-ion collisions by the coalescence parameter

$$B_2 = E_{\bar{d}}\frac{d^3N_{\bar{d}}}{d^3p_{\bar{d}}}\left(E_{\bar{p}}\frac{d^3N_{\bar{p}}}{d^3p_{\bar{p}}}E_{\bar{n}}\frac{d^3N_{\bar{n}}}{d^3p_{\bar{n}}}\right)^{-1}, \qquad (1)$$

where we can set $d^3N_{\bar{p}}/d^3p_{\bar{p}} = d^3N_{\bar{n}}/d^3p_{\bar{n}}$, $p_{\bar{p}} = p_{\bar{n}} = p_{\bar{d}}/2$. In what follows, we will consider only the central heavy-ion collisions at energies of the order of $\sqrt{s} = 4.8A$ GeV or higher.

2. THEORY

Consider the dense-gas stage of fireball evolution, which follows after the so-called "chemical freeze-out" stage [9, 10]. Assume that particle propagations at this stage may be described classically using kinetic equations. We use the notation $q_i(x,p)$, $i=\bar{p}$, $\bar{n}$, $\bar{d}$, π, …, for the double densities in coordinate and momentum spaces, $n_i(x) = \int q_i(x,p)d^3p$ being the densities ($q_i(x,p)$ are Lorentz invariant). Let us work

---

*This article was submitted by the authors in English.

**e-mail: `ioffe@vitep1.itep.ru`

***e-mail: `shushpan@heron.itep.ru`

****e-mail: `zyablyuk@heron.itep.ru`

1063-7788/05/6802-0326$26.00 © 2005 Pleiades Publishing, Inc.

in the c.m.s. of colliding ions. The kinetic equation for $q_{\bar d}(p_{\bar d}, x)$ reads

$$\frac{m_{\bar d}}{E_{\bar d}}\frac{\partial q_{\bar d}(p_{\bar d}, x)}{\partial x_\mu}u^{\bar d}_\mu = \frac{\partial q_{\bar d}}{\partial t} + \mathbf{v}_{\bar d}\nabla q_{\bar d} \qquad (2)$$
$$= \int d^3p_{\bar p}\,d^3p_{\bar n}\,q_{\bar p}(p_{\bar p})q_{\bar n}(p_{\bar n})\sigma_{\bar p\bar n\to\bar d}v^{\rm rel}_{\bar p\bar n}$$
$$\times\,\delta^3(p_{\bar p}+p_{\bar n}-p_{\bar d}) - q_{\bar d}(p_{\bar d})$$
$$\times\left[\int d^3p_\pi q_\pi(p_\pi)\sigma_{\pi\bar d}v^{\rm rel}_{\pi\bar d} + \ldots\right],$$

where $u^{\bar d}_\mu = (1, \mathbf{v}_{\bar d})/\sqrt{1-v^2_{\bar d}}$ is the $\bar d$ 4-velocity, the ellipsis means similar terms for collisions of $\bar d$ with other constituents of the fireball (p, n, etc.), and $v^{\rm rel}_{\bar p\bar n}$ and $v^{\rm rel}_{\pi\bar d}$ are the relative $\bar p$, $\bar n$ and π, $\bar d$ velocities: $v^{\rm rel}_{\bar p\bar n} = \sqrt{(\mathbf{v}_{\bar p}-\mathbf{v}_{\bar n})^2 - [\mathbf{v}_p\times\mathbf{v}_n]^2}$, etc. The terms when $\bar d$ appears or disappears in the momentum interval $p_{\bar d} + \Delta p_{\bar d}$ due to elastic collisions are small and can be neglected. The necessary applicability condition of (2) is $\lambda = p_i^{-1} \ll d$, where d is the mean distance between fireball constituents.

The cross section $\sigma_{\bar p\bar n\to\bar d} = \sigma_{pn\to d}$ is equal to

$$\sigma_{pn\to d} = \frac{3}{4}\frac{\pi}{4}\frac{g^2}{E_pE_nE_d}\frac{1}{v^{\rm rel}_{pn}}\delta(E_p+E_n-E_d), \qquad (3)$$

where E_p, E_n, and E_d are p, n, and d total energies, 3/4 is the spin factor, and g is the coupling constant of low-energy effective pnd interaction (in the d c.m.s.). The value of g^2 was found by Landau [11] from the requirement of coincidence (at the deuteron pole) of the pn-scattering amplitude in effective theory with the amplitude in the Bethe–Peierls theory of low-energy pn scattering [12]. In the limit of zero range of nuclear forces, g^2 is

$$g^2 = 128\pi m_N\sqrt{m_N\varepsilon}, \qquad (4)$$

where m_N is the nucleon mass and $\varepsilon = 2.2$ MeV is the deuteron binding energy. The account of nonzero range r_0 increases g^2 by a factor of $(1-\sqrt{m_N\varepsilon}r_0)^{-1} \approx 1.6$ [12, 13].

The mass of the particle moving in the medium is shifted in comparison with its vacuum value. Similarly, due to interaction with constituents of the medium, the width Γ appears (or width broadening, if the particle has its proper width). The mass shift $\Delta m(E)$ and $\Gamma(E)$ are expressed through the forward scattering amplitude $f(E)$ of the particle on the medium constituent (see [14, 15] and references therein):

$$\Delta m(E) = -2\pi\frac{n}{m}{\rm Re}f(E), \qquad (5)$$

$$\Gamma(E) = 4\pi\frac{n}{m}{\rm Im}f(E) = \frac{np}{m}\sigma(E), \qquad (6)$$

where E, p, and m are particle energy, momentum, and mass, and n is the density of the constituent in the medium. Equations (5), (6) apply in the system where the constituents are at rest. In the case of moving constituents, the corresponding Lorentz boost must be done. (By definition, Δm and Γ are Lorentz invariant; for details, see [16].)

Therefore, $\bar p$, $\bar n$, and $\bar d$ in the reaction $\bar p + \bar n \to \bar d$ can be considered as Breit–Wigner resonances with varying masses distributed according to the Breit–Wigner formula. In the process of fireball expansion, these Breit–Wigner resonances smoothly evolve to their stable counterparts. So we integrate the first term on the right-hand side of (2) after substituting (3) over the masses m' of the Breit–Wigner resonances:

$$I = \int dm'_{\bar p}dm'_{\bar n}dm'_{\bar d}\frac{\Gamma_{\bar p}/2\pi}{(m'_{\bar p}-m_{\bar p})^2+\Gamma^2_{\bar p}/4} \qquad (7)$$
$$\times\,\frac{\Gamma_{\bar n}/2\pi}{(m'_{\bar n}-m_{\bar n})^2+\Gamma^2_{\bar n}/4}\,\frac{\tilde\Gamma_{\bar d}/2\pi}{(m'_{\bar d}-m_{\bar d})^2+\tilde\Gamma^2_{\bar d}/4}$$
$$\times\,\frac{3\pi}{16}\frac{g^2}{E'_{\bar d}}\int\frac{d^3p_{\bar p}}{E'_{\bar p}}\frac{d^3p_{\bar n}}{E'_{\bar n}}q_{\bar p}(p_{\bar p})q_{\bar n}(p_{\bar n})$$
$$\times\,\delta^3(p_{\bar p}+p_{\bar n}-p_{\bar d})\delta(E'_{\bar p}+E'_{\bar n}-E'_{\bar d}),$$

where $E'_{\bar p} = \sqrt{p^2_{\bar p}+m'^2_{\bar p}}$, etc. We assume that the widths $\Gamma \ll m$ are much smaller than the typical momenta in $\bar p$, $\bar n$ distributions. Then the distributions $q_{\bar p}(p_{\bar p}) = q_{\bar n}(p_{\bar n})$ can be taken outside the integral sign at the values $p_{\bar p} = p_{\bar n} = p_{\bar d}/2$. The result of calculation is given by

$$I = \frac{3\pi^2}{16E_{\bar d}}g^2\sqrt{\frac{\Gamma_{\bar p}+\Gamma_{\bar n}+\tilde\Gamma_{\bar d}}{m_N}}q^2_{\bar p}(p_{\bar p}) \qquad (8)$$

[the mean mass shift $\Delta\bar m \equiv \bar m_{\bar d} - m_{\bar p} - m_{\bar n} \sim 30$ MeV is small in comparison with the width $\Gamma \sim 300$ MeV and neglected in (8)]. Later, we assume $\Gamma_{\bar p} = \Gamma_{\bar n} \equiv \Gamma$. $\tilde\Gamma_{\bar d}$ generally is not equal to the antideuteron width $\Gamma_{\bar d} \approx 2\Gamma \sim 600$ MeV. The $\bar p\bar n$ system with $\bar d$ quantum numbers at high excitations will not evolve to $\bar d$ in the process of fireball expansion, but may decay in other ways. One may expect $\tilde\Gamma_{\bar d} < \Gamma_{\bar d}$. We shall keep the ratio $a \equiv \tilde\Gamma_{\bar d}/\Gamma_{\bar d}$ as a free parameter in the calculations. However, the results weakly depend on this ratio: the variation within the limits $0 < a < 1$ may change the coalescence parameter (1) by at most $\sqrt{2}$ times, but in real cases about 20%. This uncertainty is within the accuracy of the whole method, estimated at 50%.

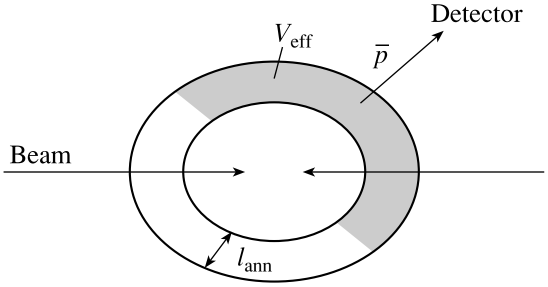

Fireball at the dense-gas stage. The effective volume $V_{\rm eff}$ is half of the outer shell of thickness $l_{\rm ann}$, from which the antiprotons reach the detector.

The contributions of direct processes $\bar p + \bar p \to \bar d + \pi^-$, $\bar n + \bar n \to \bar d + \pi^+$, and $\bar p + \bar n \to \bar d + \pi^0$ are small, all together about 20% in comparison with (8). If these processes were essential, the coalescence parameter B_2 (1) would be meaningless, since the antideuteron distribution $d^3N_{\bar d}/d^3p_{\bar d}$ is given by a complicated integral over the antinucleon distributions in this case.

At large $p_{\bar p\perp}$, the $\bar p$ spectrum decreases steeply, so the approximation $p_{\bar p} = p_{\bar d}/2$ becomes inaccurate. The case of large $p_{\bar p\perp} > 1$ GeV is not considered here.

After using (6) and performing Lorentz boost to the heavy-ion c.m. frame, the term in square brackets in (2) can be brought to the form $(m_d/E_{\bar d})\Gamma_{\bar d}$, where

$$\Gamma_{\bar d} = \sum_i \int d^3p_i q_i(p_i) v^{\rm rel}_{i\bar d}\sigma_{i\bar d}(\bar d \text{ at rest}) \tag{9}$$

and the summation runs over all medium constituents.

Suppose that the rate of antideuteron collisions with other constituents of the fireball resulting in antideuteron disintegration is much larger than the rate of fireball expansion. This happens during collisions of heavy nuclei at high energies, when the fireball size is large because of the large number of produced pions. In this case, one may expect a balance: the first term on the right-hand side of (2) is equal to the second one and

$$q_{\bar d}(p_{\bar d}) = \frac{I}{\Gamma_{\bar d}(m_{\bar d}/E_{\bar d})} \tag{10}$$
$$= \frac{3\pi^2}{32m_N}\sqrt{\frac{1+a}{2\Gamma m_N}}g^2q^2_{\bar p}(p_{\bar p}).$$

The momentum distribution $d^3N_{\bar d}/d^3p_{\bar d}$ entering into (1) is obtained from (10) by integration over the fireball volume

$$\frac{d^3N_{\bar d}(p_{\bar d})}{d^3p_{\bar d}} = \int d^3x q_{\bar d}(p_{\bar d}, x). \tag{11}$$

Using (1), (10), (11), and (4) (with r_0 correction), we find for the coalescence parameter

$$B_2^{\rm th} = \frac{24\pi^3}{E_{\bar p}} \times 1.6\sqrt{\frac{(1+a)\varepsilon}{2\Gamma}} \tag{12}$$
$$\times \frac{\int d^3x q^2_{\bar p}(p_{\bar p}, x)}{\left[\int d^3x q_{\bar p}(p_{\bar p}, x)\right]^2}.$$

Since the x dependence of $q_{\bar p}(p_{\bar p}, x)$ is not known, we replace (12) by

$$B_2^{\rm th} = \frac{24\pi^3}{E_{\bar p}} \times 1.6\sqrt{\frac{(1+a)\varepsilon}{2\Gamma}}\frac{2}{V}\frac{\overline{n^2}_{\bar p}}{(\bar n_{\bar p})^2}, \tag{13}$$

where V is the fireball volume, and $\bar n_p$ and $\overline{n^2}_p$ are the mean and mean square $\bar p$ densities in the fireball. (The coordinate dependence of $\sqrt{\Gamma}$ is neglected.) $B_2^{\rm th}$ is Lorenz invariant, as it should be. The volume V may be understood as a mean value of the fireball volume at a stage where, on one hand, hadrons are already formed, i.e., mean distances between them are larger than the confinement radius $R_c \sim 1/m_\rho \sim (1/4)$ fm, but, on the other hand, hadron interactions are still essential. The antinucleon distributions $n_{\bar p}(\mathbf{r})$, $n_{\bar n}(\mathbf{r})$ inside the fireball are nonuniform: at the dense-gas stage and before it, the antinucleons strongly annihilate in the internal part of the fireball and to a much less extent in its external layer of thickness of order $\bar p(\bar n)$ annihilation length $l_{\rm ann}$ (this effect was considered in [6]). For this reason, $\overline{n^2}_p/\bar n_p^2$ may be remarkably larger than 1. For the same reason, the antinucleons and antideuterons from the backside of the fireball (relative to the observer) are absorbed in the fireball and cannot reach the detector (see figure). Therefore, only one-half of the fireball volume contributes to the number of recorded $\bar p$, $\bar n$, and $\bar d$. The corresponding factor approximately equal to 2 is taken into account in (13).

In fact, the fireball evolution after the balance may reduce the antideuteron number as $N_{\bar d} \to N_{\bar d}e^{-\Gamma_{\bar d}\Delta t}$, where Δt is a typical time required for the antideuteron to leave the interaction region. (Such ≈ 50% reduction of K^- mesons was observed in [17].) However, this effect does not change the coalescence parameter B_2. Indeed, in this case, B_2 should be multiplied by the factor $e^{-\Gamma_{\bar d}\Delta t}/(e^{-\Gamma_{\bar p}\Delta t})^2$; the time Δt is the same for both antideuteron and antiproton under consideration, because they move with equal velocities. But since $\Gamma_{\bar d} = 2\Gamma_{\bar p}$ with good accuracy [we checked it explicitly by Eq. (9)], this factor is close to unity regardless of the evolution details.

The width Γ may be calculated if the spectrum and densities of the fireball constituents at the hadronic gas stage are known. At a high energy of heavy-ion collisions (SPS, RHIC), the main contributions to $\Gamma_{\bar{p}}$, $\Gamma_{\bar{n}}$, $\Gamma_{\bar{d}}$ come from the collisions of $\bar{p}$, $\bar{n}$, $\bar{d}$ with pions. Therefore, $\Gamma_{\bar{p}}$, $\Gamma_{\bar{n}}$, $\Gamma_{\bar{d}}$ essentially depend on the pionic density in the fireball, the dependence of Γ on the densities of other fireball constituents being much weaker. The dependence of Γ on the spectrum of the fireball constituents is also weak, since the main contribution to $\Gamma_{\bar{p}}$ ($\Gamma_{\bar{n}}$, $\Gamma_{\bar{d}}$) arises from the collisions at high energies in the c.m.s. of $\bar{p}(\bar{n},\bar{d})+\pi$, where the cross sections are approximately constant. For this reason, without a serious error, for the calculation of Γ we can take the spectra from the experimental data, i.e., corresponding to the final stage of fireball evolution. Moreover, since the widths enter as $\sqrt{\Gamma}$ in (13), the errors are reduced twice. If Γ is known, then, by comparison with the data, the parameter $V^{-1}(\overline{n^2}_{\bar{p}}/\bar{n}^2_{\bar{p}})$ can be found, which would allow one to check various models of fireball evolution.

3. COMPARISON WITH THE DATA

Consider the NA44 experiment at SPS (CERN): Pb + Pb collisions at $\sqrt{s}=17A$ GeV [1]. Antideuterons were observed at $0.6<p_{\bar{d}t}<1.6$ GeV and in the rapidity interval from 1.9 to 2.1 in the laboratory system, which corresponds to $\bar{p}_{\bar{p}t}=0.55$ GeV, $(E_{\bar{p}})_{\text{c.m.}}=1.5$ GeV. The spectra and particle yields under such collisions are given in [18]. The number of active nucleons participating in collision ("wounded" nucleons), N_N, and the number of produced pions are presented in [19]: $N_N=362$, $N_\pi=1890$, $Q_\pi=N_\pi/N_N=5.2$ (see also [20] for a review of the data on heavy-ion collisions).

We accept the following model for the dense-gas stage of fireball evolution [15]. (A related model had been suggested long ago [21, 22]: it may be called the Fermi–Pomeranchuk model). Neglect for a moment contributions of all particles except for nucleons and pions. Assume that any participant—nucleon or pion—occupies the volume v_N or v_π, respectively. Then

$$n_N=\frac{N_N}{V}=\frac{n_N^0}{1+Q_\pi\beta}, \qquad (14)$$
$$n_\pi=\frac{N_\pi}{V}=\frac{n_N^0 Q_\pi}{1+Q_\pi\beta},$$

where $n_N^0=1/v_N$, $\beta=v_\pi/v_N$. For numerical estimations, we take $n_N^0=0.26\text{ fm}^{-3}$, 1.5 times the standard nucleus density, and $\beta=(r_\pi/r_N)^3\approx0.55$, where $r_\pi=0.66$ fm and $r_N=0.81$ fm are pion and nucleon electric radii. It must be stressed that n_N^0 is the only essential uncertain parameter in our approach. Even if Q_π at the dense-gas stage differs from the ones at the final stage, the arising error is essentially compensated by the appearance of Q_π in both the numerator and the denominator in (14). (As was already mentioned, the nucleon contribution to Γ is small.)

Check first the applicability conditions of our approach. We have $n=n_N+n_\pi\approx0.42\text{ fm}^{-3}$ and the mean distance between the fireball constituents is $d=1/n^{1/3}=1.3$ fm. Evidently, the condition $\lambda_{\bar{p}}=1/p_{\bar{p}}\ll d$ is well satisfied. The calculation of Γ according to (9) ($\Gamma=\Gamma_{\bar{d}}/2$) gives $\Gamma\approx300$ MeV. (Only inelastic cross sections were taken into account; the pion contribution comprises about 75%, and the nucleon one about 25%. The Glauber screening correction, reducing Γ, is not taken into account. Note that the value of Γ is close to the momentum integration interval in the Wigner function approach, $\Delta P\approx200-300$ MeV, found in [8].) Check now the balance condition—that the deuteron disintegration rate exceeds the fireball expansion rate. The former is given by $2\Gamma(m_N/E_{\bar{p}})$. The estimate for the escape rate (or fireball expansion) is $w\sim(1/4)\text{ fm}^{-1}$. We have $2\Gamma(m_N/E_p)\approx2.0\text{ fm}^{-1}\gg0.25\text{ fm}^{-1}$. So, this condition is also fulfilled. Even more, the balance condition would be fulfilled at much lower hadronic densities than that chosen above, up to $n_N^0\approx0.05\text{ fm}^3$, i.e., up to densities not much higher than that supposed for thermal freeze-out [10, 23, 24]. However, such low densities would lead to much lower values of B_2 than the ones obtained in experiments. Equation (6) is legitimate if $\text{Im}f(E)\ll d$ [14, 15]. Since $\text{Im}f\approx1$ fm, this condition is not well satisfied. For this reason, the value of Γ presented above has a large (maybe 50%) uncertainty and, probably, is overestimated (the effect of screening). This fact, however, does not influence too much the value B_2^{th}, since $\sqrt{\Gamma}$ enters (12). One may expect that, because of their slightly larger velocities in comparison with nucleons, pions form a halo around the fireball. This effect also may lead to an overestimation of Γ.

For the parameters used above, the fireball volume turns out to be $V=6.2\times10^3\text{ fm}^3$ (15% correction for other particles, except for pions and nucleons, was taken into account). This value is about 2 times larger than the ones found in [9] at chemical freeze-out and about 2 times smaller than at thermal freeze-out [23, 24]. (Note that the dense-gas stage is an intermediate between these two.) In the case of a sphere, its radius is equal to $R=11.4$ fm. If we assume that antiprotons are mainly concentrated in the outer shell of the fireball of thickness $l_{\text{ann}}\approx3$ fm, then $\overline{n^2}/\bar{n}^2\approx2$ and we get for the coalescence parameter

$$B_2^{\text{th}}=3.0\times10^{-4}\text{ GeV}^2 \qquad (15)$$

(we set $\tilde{\Gamma}_{\bar{d}} = \Gamma$, or $a = 1/2$). Experimentally [1], for the average value of the most central 10% of events, it was found that $B_2^{\rm exp} = (4.4 \pm 1.3) \times 10^{-4}$ GeV^2. However, $B_2^{\rm exp}$ strongly depends on centrality: the results for 0–5% centrality are about 1.5 times lower. Bearing in mind all uncertainties, theoretical and experimental, we believe that the NA44 data for the coalescence parameter are in agreement with theoretical expectation.

Turn now to the STAR experiment at RHIC: Au + Au collisions at $\sqrt{s} = 130A$ GeV [2]. Antideuterons were measured at $0.5 < p_t < 0.8$ GeV, and in the rapidity interval $|\Delta y_{\rm c.m.}| < 0.3$, 18% of central collisions were collected. We take $\bar{E}_{\bar{p},{\rm c.m.}} = 1.05$ GeV. The number of wounded nucleons in the 18% of central Au + Au collisions can be estimated as $N_N = 320$ [25]. The multiplicity of negative hadrons $\bar{h}$ (mainly, pions) was measured in [26] at pseudorapidity $\eta = 0$ only, and an increase in $d\bar{h}/d\eta|_{\eta=0}$ of 52% as compared with the SPS data at $\sqrt{s} = 17A$ GeV was found. But it is known that $d\bar{h}/d\eta/_{\eta=0}$ increases faster with energy than the total multiplicity. We estimate $Q_\pi = N_\pi/N_N \approx 7 \pm 1$. (A value close to the one presented above can be found from the data compilation [27].) At $N_N = 320$ with account of 20% correction for K mesons and hyperons, $V = 7.2 \times 10^3$ fm^3. The coalescence parameter is equal to

$$B_2^{\rm th} = 3.8 \times 10^{-4}\ {\rm GeV}^2 \tag{16}$$

($\Gamma = 320$ MeV, $\overline{n^2}/(\bar{n})^2$ was set to 2). Experimentally, STAR found $B_2^{\rm exp} = (4.5 \pm 0.3 \pm 1.0) \times 10^{-4}$ GeV^2.

The main uncertainty of $B_2^{\rm th}$ comes from the fireball volume V which was calculated by (14). The width Γ depends on the hadronic density; i.e., for a fixed number of hadrons, it also depends on the fireball volume. So, $B_2^{\rm th} \sim 1/\sqrt{V}$, which suppresses this uncertainty twice. We expect the accuracy of our estimates (15), (16) to be about 50%.

In the E864 experiment [3] at AGS, the antideuterons were observed in Au + Pt collisions at $\sqrt{s} = 4.8A$ GeV and 10% of central collisions were selected. From the data we take $p_{\bar{p}t} = 0.17$ GeV, $\overline{E}_{\bar{p},{\rm c.m.}} = 0.99$ GeV. The number of wounded nucleons and the π/N ratio are $N_N = 350$ and $Q_\pi = 1.6$ (see [20] and references therein). In the same way as before, we find $V = 2.8 \times 10^3$ fm^3, $\Gamma = 220$ MeV, $l_{\rm ann} = 1.2$ fm. In this case, the validity conditions of our approach are at the edge of their applicability. So, the theoretical expectations for B_2 are valid only in order of magnitude:

$$B_2^{\rm th} \sim 1.5 \times 10^{-3}\ {\rm GeV}^2 \tag{17}$$

in comparison with $B_2^{\rm exp} = (4.1 \pm 2.9 \pm 2.3) \times 10^{-3}$ GeV^2.

4. SUMMARY

The coalescence parameter B_2 for the antideuteron production in heavy-ion collisions was calculated. It was supposed that the $\bar{d}$ production proceeds at the stage when the fireball may be treated as a dense gas of interacting hadrons. The $\bar{d}$ production is described as the formation process $\bar{p} + \bar{n} \to \bar{d}$, where $\bar{p}$, $\bar{n}$, $\bar{d}$ are moving in the mean field of the fireball constituents (mainly pions). It was shown that, in the case of a large N_π/N_N ratio, one may expect a balance: the number of produced antideuterons is equal to the number of disintegrated $\bar{d}$ due to collisions with pions. The balance condition determines the $\bar{d}$ production rate and the value of coalescence parameter B_2. The latter is expressed in terms of deuteron binding energy and mean fireball volume at this stage. The comparison with data demonstrates that $\bar{d}$ production proceeds at the stage intermediate between chemical and thermal freeze-out—the dense-gas stage of fireball evolution. The theoretical values of B_2 are in satisfactory agreement with experimental data at SPS, RHIC, and AGS, but more data for various nuclei and various energies of collision and $\bar{d}$ energies would be very desirable. Comparison of the data with theory would allow one to check various models of fireball evolution.

ACKNOWLEDGMENTS

We are grateful to G. Brown, L. McLerran, E. Shuryak for discussions and S. Kiselev, Yu. Kiselev, A. Smirnitsky, and N. Rabin for information about experimental data. This work was supported in part by INTAS, grant no. 2000-587, and the Russian Foundation for Basic Research, project no. 03-02-16209.

REFERENCES

1. I. G. Bearden *et al.*, Phys. Rev. Lett. **85**, 2681 (2000).
2. C. Adler *et al.*, Phys. Rev. Lett. **87**, 262301 (2001).
3. T. A. Armstrong *et al.*, Phys. Rev. Lett. **85**, 2685 (2000).
4. A. Z. Mekjian, Phys. Rev. C **17**, 1051 (1978).
5. L. P. Csernai and J. I. Kapusta, Phys. Rep. **131**, 223 (1986).
6. S. Mrowczynski, Phys. Lett. B **308**, 216 (1993).
7. M. Gyulassy, K. Frankel, and E. A. Rambler, Nucl. Phys. A **402**, 596 (1983).
8. J. L. Nagle, B. S. Kumar, D. Kusnezov, *et al.*, Phys. Rev. C **53**, 367 (1996).
9. P. Braun-Munziger, I. Heppe, and J. Stachel, Phys. Lett. B **465**, 15 (1999).

10. E. V. Shuryak and G. E. Brown, Nucl. Phys. A **717**, 322 (2003).
11. L. D. Landau, Zh. Éksp. Teor. Fiz. **39**, 1856 (1960) [Sov. Phys. JETP **12**, 1294 (1960)].
12. H. A. Bethe and R. E. Peierls, Proc. R. Soc. London, Ser. A **149**, 176 (1935).
13. H. A. Bethe and P. Morrison, *Elementary Nuclear Theory,* 2nd ed. (Wiley, New York, 1956; IL, Moscow, 1958).
14. V. L. Eletsky and B. L. Ioffe, Phys. Rev. Lett. **78**, 1010 (1997).
15. V. L. Eletsky, B. L. Ioffe, and J. I. Kapusta, Eur. Phys. J. A **3**, 381 (1998).
16. V. L. Eletsky and B. L. Ioffe, Phys. Lett. B **401**, 327 (1997).
17. S. Pal, C. M. Ko, and Zi-wei Lin, Phys. Rev. C **64**, 042201(R) (2001).
18. M. van Leeuwen, Nucl. Phys. A **715**, 161 (2003).
19. S. V. Afanasiev *et al.*, Phys. Rev. C **66**, 054902 (2002).
20. W. Cassing and E. L. Bratkovskaya, Phys. Rep. **308**, 65 (1999).
21. E. Fermi, Prog. Theor. Phys. **5**, 570 (1950).
22. I. Pomeranchuk, Dokl. Akad. Nauk SSSR **78**, 889 (1951).
23. H. Appelshaser *et al.*, Eur. Phys. J. C **2**, 611 (1998).
24. J. Stachel, Nucl. Phys. A **654**, 119 (1999).
25. C. Adler *et al.*, Phys. Rev. Lett. **89**, 202301 (2002).
26. C. Adler *et al.*, Phys. Rev. Lett. **87**, 112303 (2001).
27. P. Braun-Munziger *et al.*, Phys. Lett. B **518**, 41 (2001).

Physics of Atomic Nuclei, Vol. 68, No. 2, 2005, pp. 332–339. Translated from Yadernaya Fizika, Vol. 68, No. 2, 2005, pp. 357–365.
Original Russian Text Copyright © 2005 by Vardanyan, Lokhtin, Sarycheva, Snigirev, Teplov.

ELEMENTARY PARTICLES AND FIELDS
Theory

Modification of the Jet Fragmentation Function for Ultrarelativistic Collisions of Nuclei and Its Determination in the Channel Involving the Production of a Leading Neutral Pion

I. N. Vardanyan, I. P. Lokhtin*, L. I. Sarycheva, A. M. Snigirev, and C. Yu. Teplov

Institute of Nuclear Physics, Moscow State University, Vorob'evy gory, Moscow, 119899 Russia

Received March 2, 2004

Abstract—The modification of the jet fragmentation function due to the parton-energy loss in dense quark–gluon matter is studied in channels involving the production of leading particles. The "softening" effect for the jet fragmentation function is shown to be determined by the angular distribution of gluons emitted in matter. This effect anticorrelates with the "suppression" of the total yield of jets owing to the energy loss of jet partons outside the jet cone. The possibility of measuring the jet fragmentation function by using leading electromagnetic clusters in heavy-ion collisions at the LHC energies is analyzed.

1. INTRODUCTION

Jet production is one of the important tools for studying the properties of superdense strongly interacting matter, quark–gluon plasma, which is expected to be produced in heavy-ion collisions in experiments at the RHIC and LHC colliders. Parton energy losses (far more pronounced in quark–gluon plasma than in "cold" nuclear matter) may result in observable effects (for an overview, see [1] and references therein). In particular, some authors [2–9] studied the possibility of the "softening" of the jet fragmentation function and, as a consequence, the suppression of the yield of hadrons having high transverse momenta p_T in nucleus–nucleus collisions in relation to the model of independent binary nucleon–nucleon collisions. The latest RHIC data on the inclusive production of high-p_T charged and neutral hadrons in the STAR [10], PHENIX [11], PHOBOS [12], and BRAHMS [13] experiments confirm the existence of such a suppression and agree with the hypothesis that hard partons lose energy in quark–gluon plasma [14]. However, an event-by-event reconstruction of jets and their properties was not performed in those experiments; therefore, the assumption that all high-p_T particles are jet-fragmentation products is not well justified (see, for example, [15]). A new regime of heavy-ion-collision physics, where hard and semihard production processes will probably dominate over soft effects and where statistics are expected to be sufficiently high for a systematic analysis of various aspects of "QCD physics" in a medium of initial energy density significantly exceeding the critical value for the quark–hadron phase transition [16], will become possible at the LHC energies. An adequate reconstruction of hadronic jets and electromagnetic clusters in a wide acceptance of hadronic and electromagnetic calorimeters will become possible, in particular, under conditions of the CMS (Compact Muon Solenoid) experiment [16–18]. Thus, the identification of leading particles in jets (that is, particles that carry the maximum fraction of the jet momentum) will enable a direct measurement of the jet fragmentation function. A comparison of the jet fragmentation functions in AA and pp collisions (or in central and peripheral AA collisions) will furnish information about the modification of the jet fragmentation function in matter.

The angular distribution of emitted gluons, which determines the gluon-energy fraction leaving the jet cone [19–23], is an important point in studying the jet fragmentation function. The coherent gluon radiation from hard partons (the QCD analog of the Landau–Pomeranchuk–Migdal effect in QED) results in a strong angular dependence of the energy loss by radiation; this radiation softens the particle distribution in the jet, increases the multiplicity of the secondary particles, and—to a lesser extent—affects the total jet energy. As a matter of fact, the energy loss of hard partons by collisions does not depend on the angular dimension of the jet cone, because the main part of thermal particles knocked out of the medium by elastic collisions travel in directions virtually orthogonal to the jet axis [19], thus reducing its energy. In addition, the total energy loss of a jet

---

[*] e-mail: `igor@lav01.sinp.msu.ru`

will also be sensitive to such experimental restrictions on the detection of low-p_T particles as the minimum energy threshold for the signal in the calorimeter and the impact of the strong magnetic field (4 T for CMS).

The objective of this study is to analyze the possibility of measuring the jet fragmentation function modified in matter by means of leading particles in ultrarelativistic heavy-ion collisions. In Section 2, we present the main expressions for the jet fragmentation function and for the integral factor of jet suppression. In Section 3, we describe the model used in our calculations and discuss results obtained on the basis of this model. In Section 4, we study the possibility of measuring the modified jet fragmentation function under conditions of the CMS experiment: we describe the algorithms developed for reconstructing jets and electromagnetic clusters in heavy-ion collisions and compare the results obtained by calculating the modification of the jet fragmentation function at the particle level with the results of a Monte Carlo simulation. In the Conclusion, we formulate the main results of this study.

2. JET FRAGMENTATION FUNCTION AND ITS MODIFICATION IN MATTER

We recall that, in the leading order of perturbative QCD, the cross section for the production of a jet in nucleon–nucleon collisions that is characterized by a transverse momentum p_T and a rapidity y has the form

$$\frac{d\sigma^{\rm jet(k)}}{dp_T^2dy} = \sum_{ij}\int dx_i dx_j f_a^i(x_i, Q^2) \qquad (1)$$

$$\times f_b^j(x_j, Q^2)\frac{d\hat{\sigma}}{d\hat{t}}(ij \to kl)\delta(\xi - 1),$$

where $x_i = p_i/p_a$ and $x_j = p_j/p_b$ are the initial nucleon-momentum fractions carried by partons (the indices a and b label nucleons, while the indices i and j label partons); $f_a^i(x_i, Q^2)$ and $f_b^j(x_j, Q^2)$ are the parton structure functions of nucleons; $\hat{s}$, $\hat{t}$, and $\hat{u}$ are the Mandelstam variables for the hard parton subprocesses; $d\hat{\sigma}(ij \to kl)/d\hat{t}$ is the Born cross section for the hard scattering subprocess $ij \to kl$; $Q^2 = p_T^2 = (\hat{t}\hat{u})/\hat{s}$; $\xi = (\exp{(y)}/x_i + \exp{(-y)}/x_j)p_T/\sqrt{s}$ is the parton-momentum fraction carried by the jet for parton k; and $\sqrt{s} = \sqrt{\hat{s}/(x_i x_j)}$ is the energy of colliding nucleons in their c.m. frame. The inclusive cross section for the generation of a hadron h having a rapidity y_h and a transverse momentum p_T^h is given by the product of the jet-formation cross section and the $k \to h$ fragmentation function $D_k^h(z', p_T^2)$,

$$\frac{d\sigma^{h(k)}}{d(p_T^h)^2dy^hdz'} = \frac{d\sigma^{\mathrm{jet}(k)}}{dp_T^2dy}\frac{1}{z'^2}D_k^h(z', p_T^2), \qquad (2)$$

where $y^h = y$ and $z' = p^h/p^k = p_T^h/p_T$ is the parton-momentum fraction carried by the final hadron.

The parton structure functions $f_a^i(x_i, Q^2)$ are measured in deep-inelastic-scattering experiments—for example, at HERA [24]—and in e^+e^- annihilation at PETRA, PEP, and LEP [25]. The gluon fragmentation functions are determined from the data on hadron collisions [26].

In nucleus–nucleus collisions, the hard-parton energy losses induced by a medium can modify the yield of high-p_T hadrons and jets (other effects, like nuclear shadowing or higher order corrections in α_s are assumed to be insignificant for rather hard jets and hadrons, $x_{i,j} \gtrsim 0.2$ [27]). In AA collisions at an impact parameter b, the yield of k-type jets of angular cone dimension θ_0 in the central rapidity region that have a transverse momentum $p_T^{\rm jet}$ can be calculated as

$$\frac{dN_{AA}^{\mathrm{jet}(k)}}{d(p_T^{\rm jet})^2dy}(\theta_0, b) = \int\limits_0^{2\pi} d\psi \int\limits_0^{r_{\max}} rdrT_A(r_1) \qquad (3)$$

$$\times T_A(r_2)\frac{d\sigma^{\mathrm{jet}(k)}(p_T^{\rm jet} + \Delta p_T^{\rm jet}(r, \psi, \theta_0))}{dp_T^2dy},$$

where $r_{1,2}(b, r, \psi)$ are the distances from the centers of the nuclei to the jet-production vertex $V(r\cos\psi, r\sin\psi)$; $r_{\max}(b, \psi) \le R_A$ is the maximum possible transverse distance from the axis of the nuclear collision to V, R_A being the radius of nucleus A; and $T_A(r_{1,2})$ is the nuclear-thickness function (a detailed description of the nuclear geometry used can be found in [27]). The effective shift $\Delta p_T^{\rm jet}(r, \psi, \theta_0)$ of the jet-momentum spectrum depends on the jet-cone dimension θ_0.

Further, it is assumed that the fragmentation functions in a hadronic medium have the same form as in a vacuum (corrections to the parton fragmentation functions in a thermal medium were considered in [28, 29]). Here, we consider only the fragmentation of leading partons and neglect the fragmentation of emitted gluons, because we study leading particles in a jet. The yield with high-p_T hadrons (from jets) can be estimated as

$$\frac{dN_{AA}^{h(k)}}{d(p_T^h)^2dydz'}(b) = \int\limits_0^{2\pi} d\psi \int\limits_0^{r_{\max}} rdrT_A(r_1) \qquad (4)$$

$$\times T_A(r_2)\frac{d\sigma^{\mathrm{jet}(k)}(p_T + \Delta p_T(r, \psi))}{dp_T^2dy}\frac{1}{z'^2}D_k^h(z', p_T^2),$$

where the shift Δp_T of the hadron-momentum spectrum is not equal in general (owing to an abrupt power-law decrease in the p_T spectrum) to the average energy loss of partons in a medium [3].

The integral jet-suppression factor Q can be defined as the ratio of the number of jets that underwent energy losses to the number of jets that did not lose energy; that is,

$$Q^{\text{jet}}(p_{T\,\min}^{\text{jet}}) = \int\limits_{p_{T\,\min}^{\text{jet}}} d(p_T^{\text{jet}})^2 dy \tag{5}$$

$$\times \frac{dN_{AA}^{\text{jet}(k)}}{d(p_T^{\text{jet}})^2 dy} \Bigg/ \int\limits_{p_{T\,\min}^{\text{jet}}} d(p_T^{\text{jet}})^2 dy \frac{dN_{AA}^{\text{jet}(k)}}{d(p_T^{\text{jet}})^2 dy}$$

$$\times (\Delta p_T^{\text{jet}} = 0),$$

where the jet fragmentation function has the form

$$D(z) = \int\limits_{zp_{T\,\min}^{\text{jet}}} d(p_T^h)^2 dydz' \frac{dN_{AA}^{h(k)}}{d(p_T^h)^2 dydz'} \tag{6}$$

$$\times \delta(z - p_T^h/p_T^{\text{jet}}) \Bigg/ \int\limits_{p_{T\,\min}^{\text{jet}}} d(p_T^{\text{jet}})^2 dy \frac{dN_{AA}^{\text{jet}(k)}}{d(p_T^{\text{jet}})^2 dy}$$

and approximately coincides with $D_k^h(z, (p_{T\,\min}^{\text{jet}})^2)$ in the case without an energy loss if the jet type is specified. We note that $z \equiv p_T^h/p_T^{\text{jet}} (= z' p_T/p_T^{\text{jet}})$ is an observable quantity that depends on the jet-cone size θ_0. Hereafter, we will use the relation

$$\frac{D(z > z_0)}{D(z > z_0, \Delta p_T = 0)} \tag{7}$$

$$\equiv \frac{\int\limits_{z_0}^{1} dz D(z)}{\int\limits_{z_0}^{1} dz D(z, \Delta p_T = 0)} = \frac{Q^h(p_{T\,\min}^{\text{jet}}, z_0)}{Q^{\text{jet}}(p_{T\,\min}^{\text{jet}})},$$

where the integral hadron-suppression factor

$$Q^h(p_{T\,\min}^{\text{jet}}, z_0) = \int\limits_{z_0}^{1} dz \int\limits_{zp_{T\,\min}^{\text{jet}}} d(p_T^h)^2 dydz' \tag{8}$$

$$\times \frac{dN_{AA}^{h(k)}}{d(p_T^h)^2 dydz'} \delta(z - p_T^h/p_T^{\text{jet}}) \Bigg/ \int\limits_{z_0}^{1} dz$$

$$\times \int\limits_{zp_{T\,\min}^{\text{jet}}} d(p_T^h)^2 dydz' \frac{dN_{AA}^{h(k)}}{d(p_T^h)^2 dydz'} (\Delta p_T = 0)$$

$$\times \delta(z - p_T^h/p_T^{\text{jet}})$$

differs from the differential suppression factor, which is usually defined in the literature as [3, 6–18]

$$\bar{Q}^h(p_T^h) = \int dydz' \frac{dN_{AA}^{h(k)}}{d(p_T^h)^2 dydz'} \Bigg/ \int dydz' \tag{9}$$

$$\times \frac{dN_{AA}^{h(k)}}{d(p_T^h)^2 dydz'} (\Delta p_T = 0).$$

3. MODEL AND NUMERICAL RESULTS

We used the PYTHIA 6.2 [30] generator, with the CTEQ5M structure functions, to simulate the initial jet distribution in nucleon–nucleon collisions at the LHC energy of $\sqrt{s} = 5.5$ TeV. After that, we performed an event-by-event Monte Carlo simulation of the rescattering and energy loss of jet partons in quark–gluon plasma (see [19, 27] for a detailed description of the model used). In this model, energy losses by collisions and radiation are associated with each scattering event in an expanding medium, interference effects being included in gluon radiation by modifying the emission spectrum dE/dl as a function of decreasing temperature. The basic kinetic integral equation for the energy loss ΔE as a function of the initial energy E and the total range L has the form

$$\Delta E(L, E) = \int\limits_0^L dl \frac{dP(l)}{dl} \lambda(l) \frac{dE(l, E)}{dl}, \tag{10}$$

$$\frac{dP(l)}{dl} = \frac{1}{\lambda(l)} \exp\left(-l/\lambda(l)\right),$$

where l is the current transverse (with respect to the nuclear-collision axis) parton coordinate; dP/dl is the scattering-probability density in a medium; dE/dl is the energy loss per unit length; and $\lambda = 1/(\sigma\rho)$ is the parton range in a medium, $\rho \propto T^3$ and σ being, respectively, the medium density at temperature T and the integrated cross section for parton interaction in this medium. This numerical simulation of the range of hard jet partons in quark–gluon plasma makes it possible to obtain distributions with respect to any kinematical features of jets and leading particles of the jet in the final state. In addition, we can also simulate various scenarios of the spacetime evolution of the medium.

In our calculations, we used the collision part of the energy loss in the form [19, 27]

$$\frac{dE}{dl}^{\text{col}} = \frac{1}{4T\lambda\sigma} \int\limits_{\mu_{\text{D}}^2}^{3TE/2} dt \frac{d\sigma}{dt} t \tag{11}$$

and the dominant contribution to the differential cross section,

$$\frac{d\sigma}{dt} \cong C\frac{2\pi\alpha_s^2(t)}{t^2}, \tag{12}$$

$$\alpha_s = \frac{12\pi}{(33 - 2N_f)\ln\left(t/\Lambda^2_{\mathrm{QCD}}\right)},$$

for the scattering of a hard parton of energy E on a thermal parton of energy (or effective mass) $m_0 \sim 3T \ll E$. Here, $C = 9/4$, 1, and 4/9 for, respectively, gg, gq, and qq scattering; α_s is the QCD running coupling constant for N_f active quark flavors; and Λ_{QCD} is the QCD scale parameter, which is on the order of the critical temperature, $\Lambda_{\mathrm{QCD}} \simeq T_c \simeq 200$ MeV. The integrated cross section σ is regularized at the lower limit by the square of the Debye screening mass, $\mu^2_{\mathrm{D}}(T)$.

The energy spectrum of coherent gluon radiation induced by the medium and the corresponding dominant part of the energy loss by radiation per unit length were calculated here within the Baier–Dokshitzer–Mueller–Schiff model [20] as

$$\frac{dE^{\mathrm{rad}}}{dl} = \frac{2\alpha_s(\mu^2_{\mathrm{D}})C_R}{\pi L} \tag{13}$$

$$\times \int\limits_{\omega_{\min}}^{E} d\omega \left[1 - y + \frac{y^2}{2}\right] \ln\left|\cos\left(\omega_1\tau_1\right)\right|,$$

$$\omega_1 = \sqrt{i\left(1 - y + \frac{C_R}{3}y^2\right)\bar{\kappa}\ln\frac{16}{\bar{\kappa}}}, \tag{14}$$

$$\bar{\kappa} = \frac{\mu^2_{\mathrm{D}}\lambda_g}{\omega(1-y)},$$

where $\tau_1 = L/(2\lambda_g)$, $y = \omega/E$ is the hard-parton-energy fraction carried by the emitted gluon, and $C_R = 4/3$ is the quark color factor. A similar expression can be obtained for a gluon jet by substituting $C_R = 3$ and by replacing the bracketed expression in (13) by the result found in [20] for gluons. Integration in (13) is performed from the minimum gluon energy in the Landau–Pomeranchuk–Migdal coherent regime, $\omega_{\min} = E_{\mathrm{LPM}} = \mu^2_{\mathrm{D}}\lambda_g$ (λ_g is the gluon range), to the maximum possible energy, which is equal to the initial energy of the hard parton, E. We note that, although gluon radiation is a dominant mechanism of the parton energy loss in relation to losses by collisions, the relative contribution of the latter for a jet of finite angular size increases as this size increases, since the angular distributions of the losses for the two different mechanisms are different [19].

In the ensuing calculations, we describe the evolution of a dense medium within one-dimensional scaling (Lorentz-invariant) fluid dynamics, in which case particle production occurs on a hypersurface of the same proper time τ [31]. For the sake of definiteness, we used the initial conditions for the formation of the gluon-rich plasma that are expected for central Pb–Pb collisions at LHC [32]: $\tau_0 \approx 0.1$ fm/c, $T_0 \approx 1$ GeV, $N_f = 0$, and $\rho_g \approx 1.95T^3$. For noncentral collisions, we assume that the initial energy density is proportional to the ratio of the nuclear-overlap function to the effective cross-sectional area of nuclear overlap [27].

In each ith event of scattering on an accompanying medium constituent (that is, that which moves at the same longitudinal velocity), a fast parton loses energy both by collisions and by radiation, $\Delta e_i = t_i/(2m_0) + \omega_i$, where t_i and ω_i are simulated according to Eqs. (11) and (13), while the distribution with respect to the coordinates of the jet-production vertex was simulated in accordance with Eq. (3). In each event the energy of the initial parton is then reduced by $\Delta p_T(r,\psi) = \sum_i \Delta e_i$, while the jet energy loss is $\Delta p_T^{\mathrm{jet}}(r,\psi,\theta_0) = \varepsilon\Delta p_T(r,\psi)$, where ε is the hard-parton-energy-loss fraction that is carried outside the jet cone and which is considered as a phenomenological parameter. We note that the use of this parametrization simplifies the simulation considerably, because a complete calculation of the angular spectrum of gluon radiation is a complicated task [19–23]. In principle, the parameter ε is determined by the jet-cone size θ_0; the corresponding dependences were studied numerically in [20, 22], where the authors considered ε values in the interval between 0 and 1 (although ε can even exceed unity at small θ_0 [20, 22]).

In this study, only neutral pions are considered as leading particles in a jet, but similar numerical results are expected for charged hadrons as well. However, a complete tracking in heavy-ion collisions at LHC is a very complicated (albeit solvable) problem from the methodological point of view, whereas the reconstruction of jets and electromagnetic clusters by using calorimeter systems seems quite feasible now [16, 18] (see the next section). At a rather high transverse momentum of π^0 (not less than 15 GeV for CMS), both photons from π^0 decay hit the same crystal of the electromagnetic calorimeter, in which case the traditional procedure for reconstructing π^0 on the basis of the invariant-mass spectrum of the photon pairs is inapplicable. However, such an electromagnetic cluster can be identified as a leading neutral pion in a jet if it belongs to a hard jet and carries away a significant part of its energy.

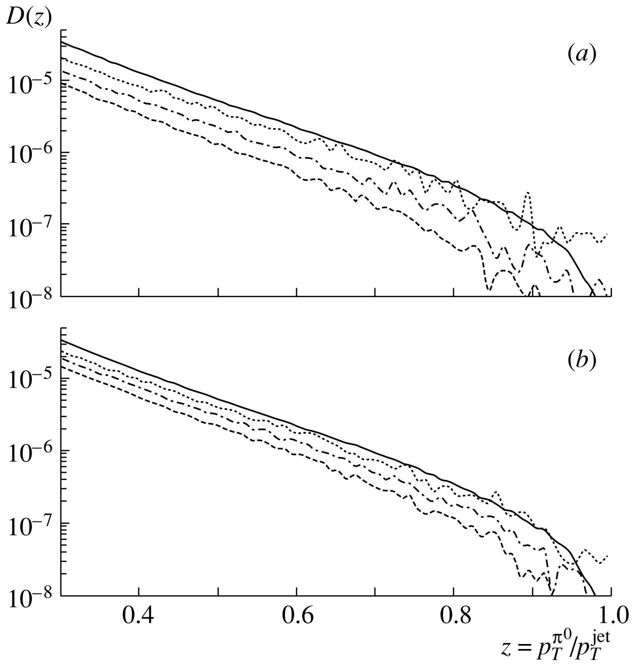

Fig. 1. Jet fragmentation function for a leading neutral pion in (*a*) central Pb–Pb collisions and (*b*) those integrated over all values of the impact parameter ($E_T^{\rm jet} > 100$ GeV, $|\eta^{\rm jet}| < 3$). The solid curves represent the results in the absence of the parton energy loss, while the remaining curves correspond to the presence of parton energy losses: $\varepsilon =$ (dashed curves) 0, (dashed-dotted curves) 0.3, and (dotted curves) 0.7.

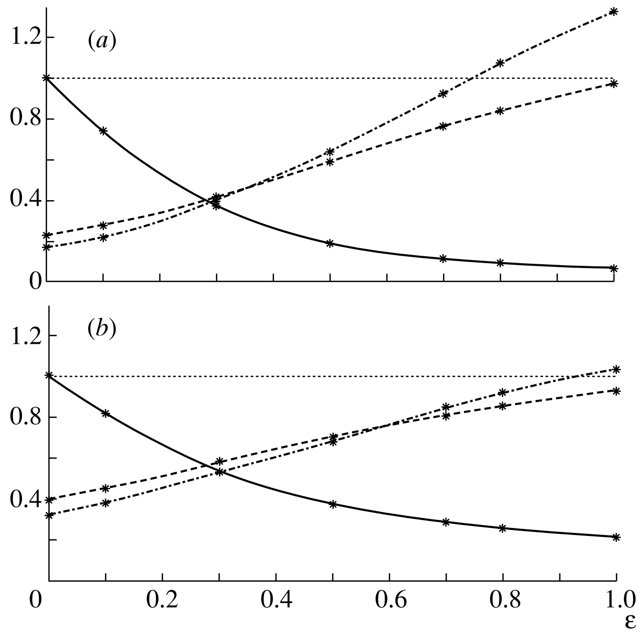

Fig. 2. Jet suppression factor $Q^{\rm jet}$ (solid curves) and ratio of the jet fragmentation functions for the cases with and without an energy loss, $D(z > z_0)/D(z > z_0, \Delta p_T = 0)$, for $z_0 =$ (dashed curves) 0.5 and (dashed-dotted curves) 0.7 in (*a*) central Pb–Pb collisions and (*b*) those integrated over all impact-parameter values ($E_T^{\rm jet} > 100$ GeV, $|\eta^{\rm jet}| < 3$).

Figure 1 displays the calculated jet fragmentation functions (6) for leading π^0 in the cases with and without parton energy losses in (*a*) central Pb–Pb collisions and (*b*) those integrated over all values of the impact parameter. For a minimum threshold used for the energy of a reconstructed jet, $E_{T\,\min}^{\rm jet} = 100$ GeV, the statistics estimated within the geometric acceptance of the CMS facility, $|\eta^{\rm jet}| < 3$, are on the order of 10^7 jets over a month of LHC operation with lead beams. Figure 2 demonstrates the ε dependence of the jet suppression factor $Q^{\rm jet}$ and of the ratio (7) of the jet fragmentation functions for the cases with and without energy losses, $D(z > z_0)/D(z > z_0, \Delta p_T = 0)$, for the fixed values of $z_0 = 0.5$ and 0.7. We note that, in the absence of energy losses, the fraction of events where a leading neutral pion carries more than 50% (70%) of the jet transverse momentum is 7×10^{-3} (1×10^{-3}) of the total number of jets characterized by $E_T > 100$ GeV. If the parameter ε is close to zero (radiation at small angles is dominant), the softening of the jet fragmentation function is maximal, which is clear from Fig. 1, while the jet suppression factor $Q^{\rm jet}$ (5) is close to unity (that is, there is virtually no jet-yield suppression). An increase in the parameter ε (that is, an increase in the contribution from large-angle radiation and collision losses) leads to an increase in the jet suppression effect and to the respective decrease in $Q^{\rm jet}$, while the softening of the jet fragmentation function becomes weaker (especially for large values of z). In Fig. 2, we can see a typical anticorrelation between the suppression of the jet yield and the softening of the jet fragmentation function [the ratio in (7) can even exceed unity for rather large values of ε and z]. The physical reason for this anticorrelation, which is determined primarily by the hard-parton-energy fraction carried outside the jet cone, is that an increase in ε leads to a decrease in the jet final transverse momentum $p_T^{\rm jet} = p_T^{\rm jet}(\Delta p_T^{\rm jet} = 0) - \varepsilon \Delta p_T$ [which is the denominator in the definition of $z \equiv p_T^h/p_T^{\rm jet}$ in the jet fragmentation function (6)], but it does not change the numerator in the definition of z. As a result, the softening of the jet fragmentation function becomes weaker, while the integral jet-suppression factor (5) decreases. It is interesting to note that the jet-suppression effect is expected to be commensurate with the effect of the softening of the jet fragmentation function at a value of $\varepsilon \sim 0.3$.

4. RECONSTRUCTION OF JETS AND ELECTROMAGNETIC CLUSTERS AND POSSIBILITY OF MEASURING THE JET FRAGMENTATION FACTOR AT LHC

In this section, we will illustrate the possibility of measuring the jet fragmentation function and its modifications in ultrarelativistic collisions of nuclei by considering the example of the CMS calorimeter system [17, 18]. The central part of the CMS facility covers the pseudorapidity range $|\eta| < 1.5$, the cell dimensions of the electromagnetic and hadron calorimeters in the η–φ space being $\Delta\eta \times \Delta\varphi = 0.0174 \times 0.0174$ and $\Delta\eta \times \Delta\varphi = 0.0872 \times 0.0872$, respectively.

An adequate reconstruction of jets in heavy-ion collisions characterized by a high multiplicity and the reconstruction of electromagnetic clusters in such jets are important conditions for measuring the jet fragmentation function. The developed algorithms for seeking jets and electromagnetic clusters can solve this problem.

4.1. Jet Reconstruction

The developed algorithm is based on the search for jet clusters above the average energy and on an event-by-event background subtraction. Each event is processed by applying the following sequence of operations:

(1) Within each η ring, we first calculate the average transverse energy $\overline{E_T^{\text{tower}}(\eta)}$ of a tower and the respective variance, $\sigma_T^{\text{tower}}(\eta) = \sqrt{\overline{(E_T^{\text{tower}}(\eta))^2} - \left(\overline{E_T^{\text{tower}}(\eta)}\right)^2}$. The tower size corresponds to the cell size of the hadron calorimeter.

(2) We then rescale the energy of each tower according to the expression $E_T^{\text{tower}\,*} = E_T^{\text{tower}} - \overline{E_T^{\text{tower}}} - \sigma_T^{\text{tower}}$, where E_T^{tower} is the initial transverse energy of a tower. If the transverse energy of a tower becomes negative after this subtraction, we assign the value zero to this energy.

(3) We find jets by using a standard cone iteration algorithm that gathers the corrected tower energy around the tower characterized by the maximum energy deposition in a given cone $R = \sqrt{\Delta\varphi^2 + \Delta\eta^2}$ ($R = 0.5$ in our case).

(4) We rescale the average energy and the variance for each tower by using only those towers that do not belong to any jet found previously (this rescaling employs the initial energy values).

(5) The average energy of each tower is once again rescaled according to the expression $E_T^{\text{tower}\,*} = E_T^{\text{tower}} - \overline{E_T^{\text{tower}}} - \sigma_T^{\text{tower}}$ (if the rescaled transverse energy of the tower becomes negative upon this subtraction, it is assigned the value zero).

(6) The final jet reconstruction is performed by using the iteration cone algorithm with the new energy values for each tower.

We performed a GEANT simulation of the response of the CMS calorimeter system. Signal jets were generated by the PYTHIA 6.2 generator [30]. Events of central Pb–Pb collisions simulated by the HIJING generator of nucleus–nucleus interactions [33] with the charged-particle density per unit rapidity $dN^{\pm}/dy(y = 0) = 5000$ were used as a background. We obtained the following basic results:

(i) The reconstruction efficiency for jets of energy in the region $E_T^{\text{jet}} > 100$ GeV (the ratio of the number of reconstructed jets to the total number of generated jets) is close to 100%, the fraction of spurious jets being not greater than 1% of the total number of reconstructed jets.

(ii) The mean reconstructed jet energy $E_T^{\text{jet}}(\text{reco})$ is a linear function of the mean generated jet energy $E_T^{\text{jet}}(\text{MC})$, the shape of this dependence being identical in the presence and in the absence of the background from Pb–Pb events (that is, pp collisions can be used for a comparison with Pb–Pb collisions). The energy resolution [approximately 17% for $E_T^{\text{jet}}(\text{MC}) = 100$ GeV] in Pb–Pb events is poorer than in pp events by a factor of about 1.3.

(iii) The attainable precision of the space resolution of jets is rather high; it is less than the size of a hadron-calorimeter tower [$\delta\eta \sim \delta\varphi \sim 0.03$ for $E_T^{\text{jet}}(\text{MC}) = 100$ GeV in the Pb–Pb events].

4.2. Reconstruction of Electromagnetic Clusters

The developed algorithm is based on the search for electromagnetic clusters above the average energy and on an event-by-event background subtraction. Each event is processed by applying the following sequence of operations:

(1) We first find the average energy $\langle E\rangle_i$ and the variance D_i within each ith crystal ring in η.

(2) We then subtract, from the energy in each jth crystal of the ith ring, E_{ij}, the average energy and the variance, $E'_{ij} = E_{ij} - \langle E\rangle_i - D_i$. If the value of E'_{ij} appears to be negative, it is replaced by $E'_{ij} = 0$.

(3) We find the crystal of maximum energy after the initial background subtraction, E'_{ij}, and assume it to be the center of an electromagnetic cluster.

(4) At the stage of the reconstruction of the electromagnetic-cluster energy, we consider the 5×5

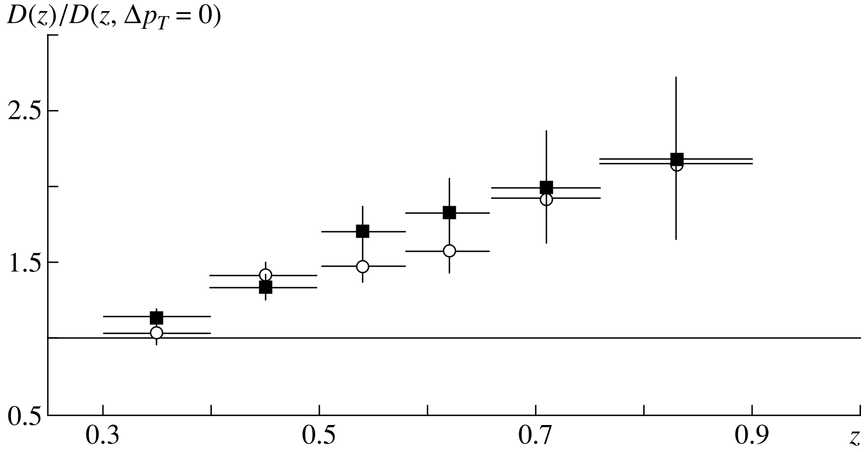

Fig. 3. Modification factor for the jet fragmentation function, $D(z)/D(z, \Delta p_T = 0)$, in central Pb–Pb collisions for $\varepsilon = 1$: (■) result at the particle level and (○) result at the level of reconstructed responses.

cell centered at the above crystal of maximum energy. For crystal rings in η that involve the 5×5 cell selected above, we recalculate the average energy $\langle E \rangle_i''$ and the dispersion D_i'', omitting the crystals inside the 5×5 cell.

(5) From the energy of each jth crystal of the cell from the ith ring, E_{ij}, we subtract the average energy and dispersion, $E_{ij}'' = E_{ij} - \langle E \rangle_i'' - D_i''$. If a negative value is obtained for E_{ij}'', it is taken to be zero.

(6) The sum of the energies E_{ij}'' over the 25 crystals of the 5×5 cell is taken to be the energy of the electromagnetic cluster.

We simulated the responses of the CMS calorimeters for the same conditions as in the jet case (see Subsection 4.1).

We considered photons, individual neutral pions, and leading neutral pions in a jet of transverse energy above 20 GeV.

The results are the following:

(i) The efficiency of the search for electromagnetic clusters is about 100% for individual particles and about 90% for a leading neutral pion in a jet.

(ii) The energy resolution is about 5% in all three cases.

(iii) In all cases, the spatial resolution (the precision in determining the centers of electromagnetic clusters) is $\sigma_\eta \sim 0.03$ and $\sigma_\varphi \sim 0.01$, this being on the same order of magnitude as the size of the electromagnetic-calorimeter crystals.

4.3. Simulation of the Jet Fragmentation Function

We compared the factor characterizing the in-medium modification of the jet fragmentation function for central Pb–Pb interaction, $D(z)/D(z, \Delta p_T = 0)$. We estimated it (a) at the particle level within the model described in Section 3 and (b) at the level of reconstructed responses of the CMS calorimeter system. Since the calculation of the angular distribution of gluons emitted in a medium is a complicated problem, which is not fully solved, we considered, for the sake of simplicity, the case where gluons emitted in a medium do not contribute to the energy measured within the jet cone $R = 0.5$ (that is, the case of $\varepsilon = 1$). Figure 3 presents the ratio $D(z)/D(z, \Delta p_T = 0)$. We note that, for $\varepsilon = 1$ and for rather high z (not less than 0.3), this ratio is greater than unity (that is, the jet fragmentation function undergoes "hardening" rather than "softening") owing mainly to a decrease in the effective virtuality at which the jet fragmentation function is determined in a medium. It is clear that the modification factor calculated at the particle level agrees within the statistical errors with the modification factor calculated in reconstructing electromagnetic clusters.

5. CONCLUSION

We have studied the possibility of measuring the jet fragmentation function in ultrarelativistic heavy-ion collisions by using leading neutral pions in a jet. Within the developed model, we calculated the modified jet fragmentation function in heavy-ion collisions at the LHC energy, allowing for the rescattering and energy loss of jet partons in quark–gluon plasma. An analysis of the spectra of leading particles in a jet has enabled us to predict the anticorrelation between the softening of the jet fragmentation function and the suppression of the total jet yield owing to the energy loss of jet partons outside the jet cone. The use of a typical anticorrelation of these two effects has made it possible to compare the relative contributions of various mechanisms of losses of the jet energy (by radiation and collisions) carried outside the jet angular cone, and this will be of importance in analyzing actual experiments.

We have shown that the algorithms developed for reconstructing jets and electromagnetic clusters in high-multiplicity events create preconditions for adequately solving the problem of measuring the jet fragmentation function in heavy-ion collisions at LHC.

ACKNOWLEDGMENTS

We are grateful to U.A. Wiedemann, Yu. Dokshitzer, P. Epes, O.L. Kodolov, S.V. Petrushanko, and B.G. Zakharov for stimulating discussions.

This work was supported by the Russian Foundation for Basic Research (project no. 04-02-16333).

REFERENCES

1. R. Baier, D. Schiff, and B. G. Zakharov, Annu. Rev. Nucl. Part. Sci. **50**, 37 (2000).
2. M. Gyulassy and X.-N. Wang, Phys. Rev. Lett. **68**, 1480 (1992).
3. R. Baier, Yu. L. Dokshitzer, A. H. Mueller, and D. Schiff, J. High-Energy Phys. **0109**, 033 (2001).
4. M. Gyulassy, P. Levai, and I. Vitev, Phys. Lett. B **538**, 282 (2002).
5. E. Wang and X.-N. Wang, Phys. Rev. Lett. **89**, 162301 (2002).
6. C. A. Salgado and U. A. Wiedemann, Phys. Rev. Lett. **89**, 092303 (2002).
7. B. Müller, Phys. Rev. C **67**, 061901 (2003).
8. C. A. Salgado and U. A. Wiedemann, Phys. Rev. D **68**, 014008 (2003).
9. I. P. Lokhtin and A. M. Snigirev, Phys. Lett. B **567**, 39 (2003).
10. STAR Collab. (C. Adler *et al.*), Nucl. Phys. A **698**, 64 (2002); Phys. Rev. Lett. **89**, 202301 (2002).
11. PHENIX Collab. (K. Adcox *et al.*), Nucl. Phys. A **698**, 511 (2002); Phys. Rev. Lett. **88**, 022301 (2002).
12. PHOBOS Collab. (B. B. Back *et al.*), Nucl. Phys. A **698**, 655 (2002).
13. BRAHMS Collab. (I. G. Bearden *et al.*), Nucl. Phys. A **698**, 29 (2002).
14. X.-N. Wang, Phys. Lett. B **579**, 299 (2004).
15. E. V. Shuryak, Phys. Rev. C **66**, 027902 (2002).
16. A. Accardi *et al.*, hep-ph/0310274.
17. CMS Collab., Technical Proposal, CERN/LHCC 94-38.
18. G. Baur *et al.*, CERN CMS Note 2000/060.
19. I. P. Lokhtin and A. M. Snigirev, Phys. Lett. B **440**, 163 (1998).
20. R. Baier, Yu. L. Dokshitzer, A. H. Mueller, and D. Schiff, Phys. Rev. C **60**, 064902 (1999); **64**, 057902 (2001).
21. B. G. Zakharov, Pis'ma Zh. Éksp. Teor. Fiz. **70**, 181 (1999) [JETP Lett. **70**, 176 (1999)].
22. U. A. Wiedemann and M. Gyulassy, Nucl. Phys. B **560**, 345 (1999); U. A. Wiedemann, Nucl. Phys. B **588**, 303 (2000); Nucl. Phys. A **690**, 731 (2001).
23. M. Gyulassy, P. Levai, and I. Vitev, Nucl. Phys. B **571**, 197 (2000); Phys. Rev. Lett. **85**, 5535 (2000); Nucl. Phys. B **594**, 371 (2001).
24. H1 Collab. (C. Adloff *et al.*), Nucl. Phys. B **497**, 3 (1997); ZEUS Collab. (J. Breitweg *et al.*), Eur. Phys. J. C **7**, 609 (1999).
25. L. Bourhis, M. Fontanaz, J.-Ph. Guillet, and M. Werlen, Eur. Phys. J. C **19**, 89 (2001).
26. UA1 Collab. (G. Bocquet *et al.*), Phys. Lett. B **366**, 434 (1996).
27. I. P. Lokhin and A. M. Snigirev, Yad. Fiz. **64**, 1563 (2001) [Phys. At. Nucl. **64**, 1487 (2001)].
28. B. G. Zakharov, Pis'ma Zh. Éksp. Teor. Fiz. **76**, 236 (2002) [JETP Lett. **76**, 201 (2002)].
29. J. A. Osborne, E. Wang, and X.-N. Wang, Phys. Rev. D **67**, 094022 (2003).
30. T. Sjostrand, Comput. Phys. Commun. **135**, 238 (2001).
31. J. D. Bjorken, Phys. Rev. D **27**, 140 (1983).
32. K. J. Eskola, K. Kajantie, and K. Tuominen, Phys. Lett. B **497**, 39 (2001); K. J. Eskola, P. V. Ruuskanen, S. S. Rasanen, and K. Tuominen, Nucl. Phys. A **696**, 715 (2001).
33. M. Gyulassy and X.-N. Wang, Comput. Phys. Commun. **83**, 307 (1994).

Translated by M. Kobrinsky

Physics of Atomic Nuclei, Vol. 68, No. 2, 2005, pp. 340–347. From Yadernaya Fizika, Vol. 68, No. 2, 2005, pp. 366–373.
Original English Text Copyright © 2005 by Andreev, Bityukov, Krasnikov.

ELEMENTARY PARTICLES AND FIELDS
Theory

Sleptons at Post-WMAP Benchmark Points at LHC(CMS)*

Yu. M. Andreev[1], **S. I. Bityukov****, and **N. V. Krasnikov**[1]

Institute for High Energy Physics, Protvino, Moscow oblast, 142281 Russia

Received April 26, 2004

Abstract—We study the possibility of detecting sleptons at post-WMAP benchmark points at LHC(CMS). We find that, at $L_{\rm tot} = 30$ fb^{-1}, it would be possible to detect sleptons at points B, C, D, G. We also investigate the production and decays of right and left sleptons separately. We find that, at $L_{\rm tot} = 30$ fb^{-1}, it would be possible to detect right sleptons with a mass up to 200 GeV and left ones with a mass up to 300 GeV. © *2005 Pleiades Publishing, Inc.*

1. INTRODUCTION

One of the supergoals of the Large Hadron Collider (LHC) [1] is the discovery of the supersymmetry (SUSY). In particular, it is very important to investigate the possibility of discovering nonstrongly interacting superparticles (sleptons, higgsino, gaugino). In [2–4], the slepton discovery potential was investigated for direct slepton production via the Drell–Yan mechanism and a "generic" LHC detector. In [4], the production of sleptons from chargino and neutralino decays was considered. In [5], the LHC slepton discovery potential was investigated within the minimal supersymmetric model (MSSM) in the minimal supergravity (mSUGRA) scenario ($\tan\beta = 2$ case) for the Compact Muon Solenoid (CMS) detector. In [6, 7], the LHC(CMS) slepton discovery potential and the possibility of discovering lepton-number violation in sleptons decays were investigated for direct production of right and left sleptons within MSSM.

In this paper, we investigate the possibility of discovering sleptons at LHC(CMS) for post-WMAP supersymmetric benchmark scenarios [8]. These benchmark points take into account WMAP and other cosmological data, as well as the LEP and $b \to s\gamma$ constraints. We also reanalyze the LHC(CMS) discovery potential for the case of direct production of right and left sleptons in the MSSM with arbitrary relation between the mass of the lightest stable superparticle (LSP) and the slepton mass. One of the important "technical" differences between this paper and the previous studies is that we use PYTHIA program [9] for both simulation of background and signal supersymmetric events, whereas in [5–7] the PYTHIA program was used for the simulation of background events and the ISAJET program [10] for simulation of supersymmetric events. As in [5–7], we use the CMS fast detector simulation program CMSJET [11]. We find that, at total luminosity $L_{\rm tot} = 30$ fb^{-1}, it would be possible to detect sleptons at post-WMAP points B, C, D, G. We also find that, at $L_{\rm tot} = 30$ fb^{-1}, it would be possible to detect right sleptons with a mass up to 200 GeV and left ones with a mass up to 300 GeV.

The organization of the paper is the following. In Section 2, we review the main features of the mSUGRA model [12] and describe post-WMAP benchmark points for SUSY proposed in [8]. In Section 3, we describe sleptons production mechanisms and sleptons decays relevant to this study. Section 4 is devoted to a discussion of the background and cuts used to suppress the background. In Section 5, we present the results of our numerical calculations. Section 6 contains concluding remarks.

2. POST-WMAP BENCHMARKS

In the MSSM, SUSY is broken at some high scale M by generic soft terms, so in general all soft SUSY-breaking terms are arbitrary, which complicates the analysis and spoils the predictive power of the theory. In the mSUGRA model [12], the universality of different soft parameters at Grand Unified Theory (GUT) scale $M_{\rm GUT} \approx 2 \times 10^{16}$ GeV is postulated. Namely, all the spin-zero particle masses (squarks, sleptons, Higgses) are postulated to be equal to the universal value m_0 at the GUT scale. All gaugino particle masses are postulated to be equal to the universal value $m_{1/2}$ at the GUT scale. Also, the coefficients in front of quadratic and cubic soft SUSY-breaking

---

*This article was submitted by the authors in English.

[1] Institute for Nuclear Research, Russian Academy of Sciences, pr. Shestidesyatiletiya Oktyabrya 7a, Moscow, 117312 Russia.

**e-mail: `bityukov@mx.ihep.su;Serguei.Bitioukov@cern.ch`

1063-7788/05/6802-0340$26.00 © 2005 Pleiades Publishing, Inc.

Table 1. The mSUGRA parameters and some sparticle masses for proposed post-WMAP benchmarks (all masses in GeV), as calculated in ISASUGRA 7.67

Point	$m_{1/2}$	m_0	$\tan\beta$	sgn(μ)	A_0	$\tilde{\chi}_1^0$	$\tilde{\chi}_2^0$	$\tilde{e}_L, \tilde{\mu}_L$	$\tilde{e}_R, \tilde{\mu}_R$	$\tilde{\nu}_e, \tilde{\nu}_\mu$	$\tilde{\tau}_1$	$\tilde{\tau}_2$	$\tilde{\nu}_\tau$
A	600	107	5	+	0	242	471	425	251	412	249	425	411
B	250	57	10	+	0	95	180	188	117	167	109	191	167
C	400	80	10	+	0	158	305	290	174	274	167	291	273
D	525	101	10	–	0	212	415	376	224	362	217	376	360
E	300	1532	10	+	0	112	184	1543	1534	1539	1521	1534	1532
F	1000	3440	10	+	0	421	610	3499	3454	3492	3427	3485	3478
G	375	113	20	+	0	148	286	285	185	270	157	290	266
H	935	244	20	+	0	388	750	679	426	665	391	674	657
I	350	181	35	+	0	138	266	304	227	290	150	312	278
J	750	299	35	+	0	309	598	591	410	579	312	579	558
K	1300	1001	39.6	–	0	554	1064	1324	1109	1315	896	1251	1239
L	450	303	45	+	0	181	351	434	348	423	194	420	387
M	1840	1125	45.6	+	0	794	1513	1660	1312	1648	796	1504	1492

terms are postulated to be equal. The renormalization group equations are used to relate GUT and electroweak scales. The equations for the determination of the nontrivial minimum of the electroweak potential are used to decrease the number of unknown parameters by two. So the mSUGRA model depends on five unknown parameters. At present, a more or less standard choice of free parameters in the mSUGRA model includes $m_0, m_{1/2}, \tan\beta, A$, and sign($\mu$) [12]. All sparticle masses depend on these parameters. For instance, the slepton masses of the first two generations are determined by the formulas [12]

$$m^2_{\tilde{l}_R} = m_0^2 + 0.15 m^2_{1/2} - \sin^2\theta_{\rm W} M_Z^2 \cos(2\beta), \quad (1)$$

$$m^2_{\tilde{l}_L} = m_0^2 + 0.52 m^2_{1/2} - (1 - 2\sin^2\theta_{\rm W}) M_Z^2 \cos(2\beta)/2, \quad (2)$$

$$m^2_{\tilde{\nu}} = m_0^2 + 0.52 m^2_{1/2} + \cos^2\theta_{\rm W} M_Z^2 \cos(2\beta)/2. \quad (3)$$

Charged left sleptons are the heaviest sleptons, whereas the right sleptons are the lightest sleptons. For gaugino masses, the following approximate formulas are used:

$$M_{\tilde{\chi}_1^0} \approx 0.45 m_{1/2}, \quad (4)$$

$$M_{\tilde{\chi}_2^0} \approx M_{\tilde{\chi}_1^\pm} \approx 2 M_{\tilde{\chi}_1^0}, \quad (5)$$

$$M_{\tilde{\chi}_2^0} \approx (0.25\text{—}0.35) M_{\tilde{g}}. \quad (6)$$

In the mSUGRA model, the $\tilde{\chi}_1^0$ gaugino is LSP.

As has been mentioned before in the mSUGRA model, sparticle masses depend on five unknown parameters, which complicates numerical analysis of the LHC SUSY discovery potential. In [13], benchmark sets of supersymmetric parameters (13 post-LEP points) within mSUGRA model were suggested for further careful analysis. The suggested points take into account the constraints from LEP, Tevatron, $b \to s\gamma$, $g_\mu - 2$, and cosmology. Recently, in [8], upgraded benchmark sets (post-WMAP benchmarks) were proposed. These post-WMAP benchmarks take into account new WMAP data on dark matter density of the Universe. The mSUGRA model parameters and some sparticle masses for these post-WMAP benchmark points are given in Table 1 (see Table 2 in [8]).

3. SLEPTON PRODUCTION AND DECAYS

When sleptons are heavy relative to $\tilde{\chi}_1^\pm, \tilde{\chi}_1^0$, sleptons are produced at the LHC only through the Drell—Yan mechanism (direct slepton production), via $q\bar{q}$ annihilation with neutral or charged boson exchange in the s channel, namely, $pp \to \tilde{l}_L\tilde{l}_L, \tilde{l}_R\tilde{l}_R, \tilde{\nu}\tilde{\nu}, \tilde{\nu}\tilde{l}$,

$\tilde{l}_L\tilde{l}_R$. The left sleptons decay to charginos and neutralinos via the following (kinematically accessible) decays:

$$\tilde{l}^{\pm}_L \to l^{\pm} + \tilde{\chi}^0_{1,2}, \qquad (7)$$

$$\tilde{l}^{\pm}_L \to \nu_l + \tilde{\chi}^{\pm}, \qquad (8)$$

$$\tilde{\nu} \to \nu_l + \tilde{\chi}^0_{1,2}, \qquad (9)$$

$$\tilde{\nu} \to l^{\pm} + \tilde{\chi}^{\mp}_1. \qquad (10)$$

For right sleptons, only decays to neutralino are possible and they decay mainly to LSP:

$$\tilde{l}^{\pm}_R \to l^{\pm} + \tilde{\chi}^0_1. \qquad (11)$$

Note that an account of the mixing between left and right charged sleptons slightly complicates the situation and allows decays (7), (8) for eigenstates of $\tilde{l}_L$ and $\tilde{l}_R$. If decays to second neutralino or first chargino are kinematically possible, the most interesting decays of $\tilde{\chi}^{\pm}_1, \tilde{\chi}^0_2$ are the following:

$$\tilde{\chi}^0_2 \to \tilde{\chi}^0_1 + l^+l^-, \qquad (12)$$

$$\tilde{\chi}^0_2 \to \tilde{\chi}^0_1 + \nu\bar{\nu}, \qquad (13)$$

$$\tilde{\chi}^0_2 \to \tilde{\chi}^0_1 + Z^0, \qquad (14)$$

$$\tilde{\chi}^{\pm}_1 \to \tilde{\chi}^0_1 + l^{\pm} + \nu, \qquad (15)$$

$$\tilde{\chi}^{\pm}_1 \to \tilde{\chi}^0_1 + W^{\pm}. \qquad (16)$$

If sleptons are light relative to $\tilde{\chi}^{\pm}_1, \tilde{\chi}^0_1$, sleptons can be produced besides the Drell–Yan mechanism from chargino and neutralino decays ($\tilde{\chi}^{\pm}_1, \tilde{\chi}^0_2$ indirect production), namely,

$$\tilde{\chi}^0_2 \to \tilde{l}^{\pm}_{L,R} l^{\mp}, \qquad (17)$$

$$\tilde{\chi}^0_2 \to \tilde{\nu}\nu, \qquad (18)$$

$$\tilde{\chi}^{\pm}_1 \to \tilde{\nu} l^{\pm}, \qquad (19)$$

$$\tilde{\chi}^{\pm}_1 \to \tilde{l}^{\pm}\nu. \qquad (20)$$

4. SIGNATURE AND BACKGROUND

The slepton production and decays described in the previous section lead to the signature with the simplest event topology: two leptons + $E_T^{\rm miss}$ + no jets. This signature arises for both direct and indirect slepton-pair production. In the case of indirectly produced sleptons, event topology not only with two leptons but also with single, three, and four leptons is possible. Besides indirect slepton production from decays of squarks and gluinos through charginos, neutralinos can lead to the following event topology: two leptons + $E_T^{\rm miss}$ + ($n \geq 1$) jets.

Table 2. The parameters of the cuts used

Cut	$p_T^{\rm lept,0}$, GeV	$E_T^{\rm miss,0}$, GeV	$\Delta\Phi^0_{ll}$, deg	$E_T^{\rm jet,0}$, GeV	δM_Z, GeV	$\Delta\Phi^0$, deg
1	20	50	130	30	10	160
2	20	50	–	30	10	160
3	50	140	140	60	10	150
4	50	100	130	30	10	150
5	100	200	130	60	10	150
6	60	150	130	45	10	150
7	80	120	140	70	10	145
8	75	170	160	100	10	160
9	30	75	130	45	10	150
10	40	90	130	50	10	150

Table 3. The SM background cross sections after cuts

Cut	1	2	3	4	5	6	7	8	9	10
σ_B, fb	288	775	3.6	6.7	0.68	1.9	3.3	3.0	101	24

Table 4. Slepton discovery points at $L_{\rm tot} = 30$ fb^{-1}

Point	Cut	N_S	N_B	S
B	4	180	212	10.5
C	3	84	112	6.8
D	3	61	110	5.2
G	6	49	57	5.5

In this paper, we use the event topology two leptons + $E_T^{\rm miss}$ + no jets to detect sleptons at LHC(CMS). Our simulations are made at the particle level with parametrized detector responses based on a detailed detector simulation. The CMS detector simulation program CMSJET 4.704 [11] is used. It incorporates the full ECAL and HCAL granularity. The energy resolutions for electrons (photons), hadrons, and jets are parametrized. Transverse and longitudinal profiles are also included according to parametrizations.

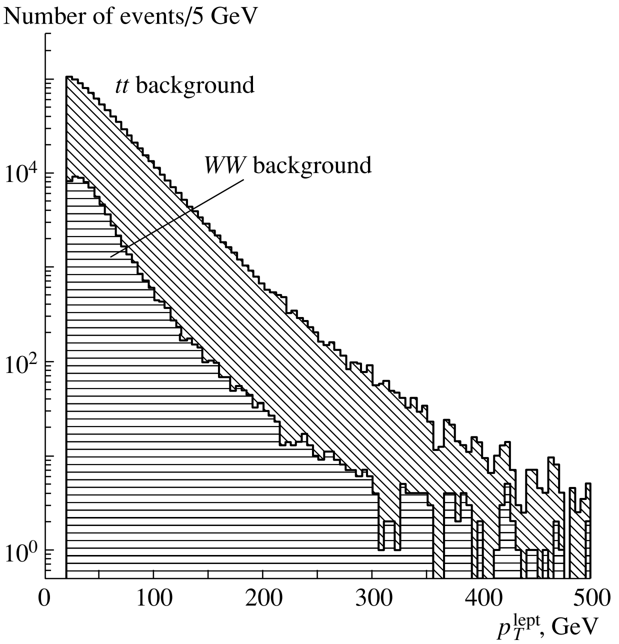

Fig. 1. Lepton p_T^{lept} distributions for main SM background (WW, $t\bar{t}$) before any cuts ($L_{\text{tot}} = 10\ \text{fb}^{-1}$).

All the SUSY processes except the particle spectrum are generated with PYTHIA 6.215 [9]. Sparticle masses for updated post-WMAP benchmark points were taken from [8]. The Standard Model (SM) backgrounds are also generated with PYTHIA 6.215. In our calculations, we used the CTEQ 5L parton distribution set. The signature used for the search for sleptons at LHC is two same-flavor opposite-sign leptons + E_T^{miss} + no jets [2–7]. Our cuts are the following:

For leptons:

p_T cut on leptons ($p_T^{\text{lept}} \geq p_T^{\text{lept},0}$) and lepton isolation within $\Delta R < 0.3$ cone with ISOL < 0.1 (CMSJET default);

effective mass of two opposite-sign leptons of the same flavor: outside $M_Z \pm \delta M_Z$ band ($\delta M_Z =$ 10 GeV);

$\Delta\Phi(l^+l^-) < \Delta\Phi_{ll}^0$ cut.

For E_T^{miss}:

$E_T^{\text{miss}} > E_T^{\text{miss},0}$ cut;

$\Delta\Phi$ (E_T^{miss}, ll) $> \Delta\Phi^0$ cut for relative azimuthal angle between two same-flavor opposite-sign leptons.

For jets:

jet veto cut: $N_{\text{jet}} = 0$ for some $E_T^{\text{jet}} > E_T^{\text{jet},0}$ threshold in pseudorapidity interval $|\eta_{\text{jet}}| < 4.5$.

Such type of cuts is the standard one and it was used previously [2–7].

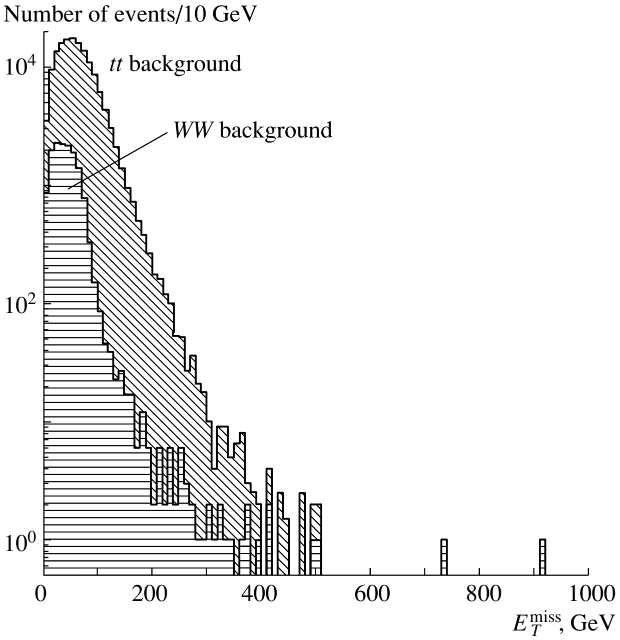

Fig. 2. E_T^{miss} distributions for main SM background (WW, $t\bar{t}$) events with two isolated leptons $p_T^{\text{lept}} > 20$ GeV ($L_{\text{tot}} = 10\ \text{fb}^{-1}$).

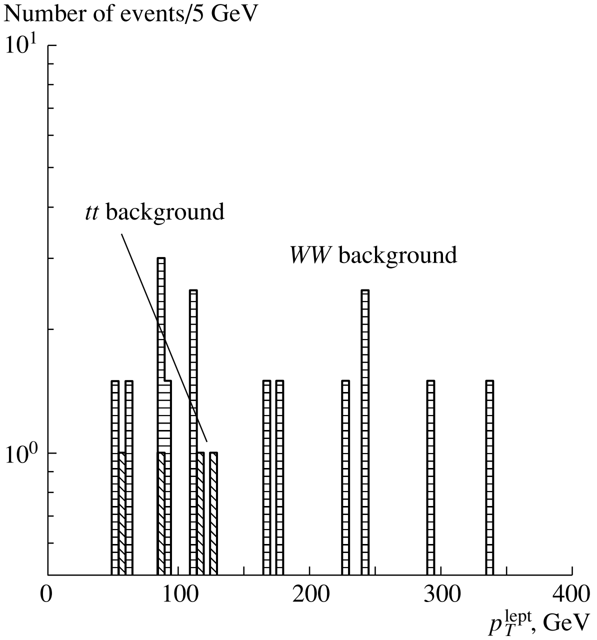

Fig. 3. Lepton p_T^{lept} distributions for main SM background (WW, $t\bar{t}$) for cut 3 ($L_{\text{tot}} = 10\ \text{fb}^{-1}$).

In this paper, we use a set of ten cuts (see Table 2). The main SM backgrounds are WW, WZ, $Wt\bar{b}$, $t\bar{t}$, $\tau\bar{\tau}$, $b\bar{b}$. The distributions of the SM background on p_T^{lept} and E_T^{miss} are presented in Figs. 1–4. The

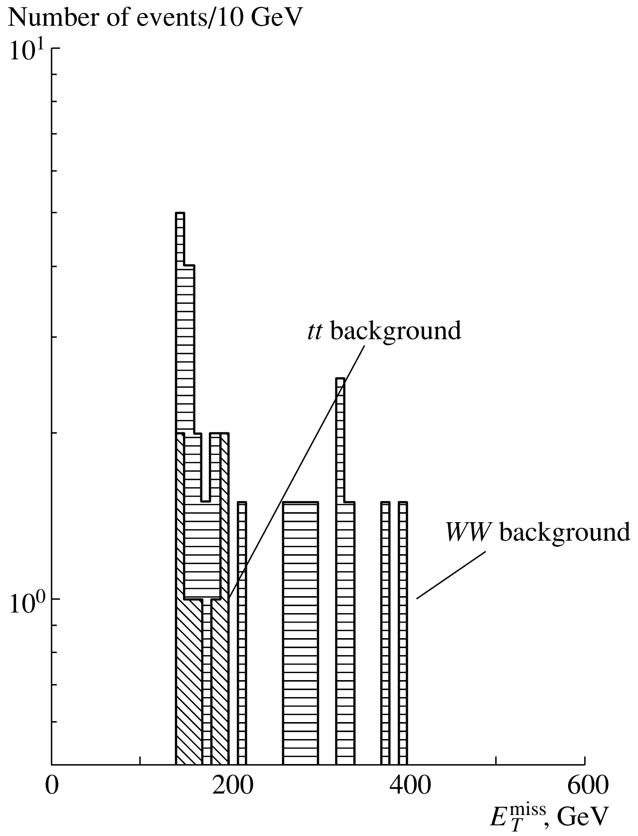

Fig. 4. E_T^{miss} distributions for main SM background (WW, $t\bar{t}$) events for cut 3 ($L_{\text{tot}} = 10$ fb^{-1}).

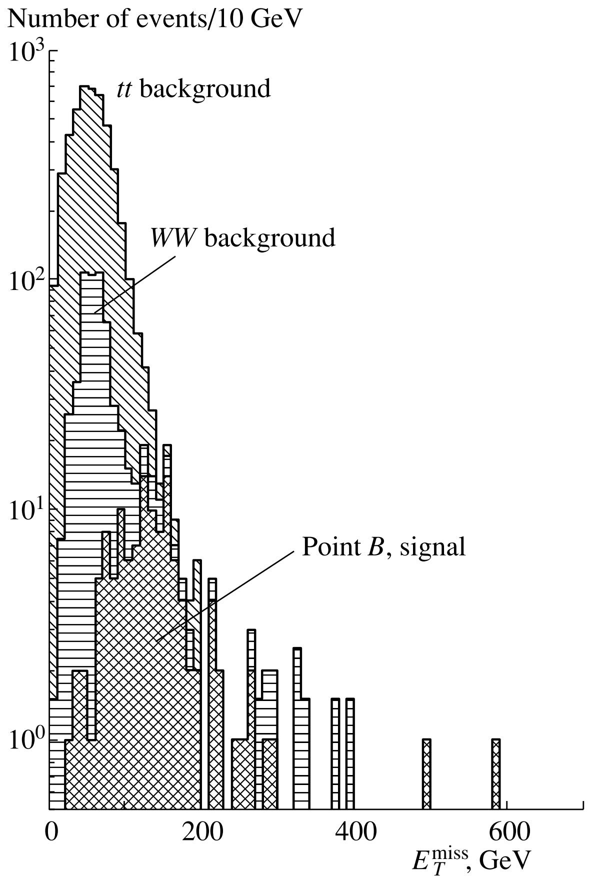

Fig. 5. E_T^{miss} distributions for main SM background (WW, $t\bar{t}$) and signal at point B for events with two isolated leptons $p_T^{\text{lept}} > 50$ GeV for cut 3 before cuts on E_T^{miss} and $\Delta\Phi^0$ ($L_{\text{tot}} = 10$ fb^{-1}).

contribution of WW background is 40–80% depending on the cut number. There are also internal SUSY backgrounds which arise through $\tilde{q}\tilde{q}$, $\tilde{g}\tilde{g}$, and $\tilde{q}\tilde{g}$ productions and subsequent cascade decays with jets outside acceptance or below threshold. SUSY backgrounds depend on SUSY masses and, as a rule, they are small compared to SM backgrounds. Note that, when we are interested in a new physics discovery (the first stage of any data analysis), we have to compare the calculated number of standard background events N_B with new physics signal events $N_{\text{new physics}} = N_{\text{slept}} + N_{\text{SUSY},B}$, so SUSY background events increase the discovery potential of new physics.

SM background cross sections after cuts are given in Table 3.

5. RESULTS

For post-WMAP points (A–M), our results are the following. We found that, at $L_{\text{tot}} = 10$ fb^{-1}, it would be possible to discover sleptons only at point B.[2] For cut 3, we found that $N_S = 45$, $N_B = 38$, $S = 5.9$. For $L_{\text{tot}} = 30$ fb^{-1}, it is possible to discover sleptons at points B, C, D, G (see Table 4).[3]

At $L_{\text{tot}} = 100$ fb^{-1}, the slepton discovery points are A, B, C, D, G, and I.[4] We also investigated the slepton discovery potential for post-LEP benchmark points [13] and found that the LHC(CMS) slepton discovery potential for post-LEP points coincides with the slepton discovery potential for post-WMAP points.

---

[2] In our calculations, we used the approximate formula for the significance $S = 2N_S/\left(\sqrt{N_B} + \sqrt{N_S + N_B}\right)$ (here, N_S and N_B are the numbers of signal and background events, respectively), which is an appropriate characteristic for future experiments (see [14, 15]).

[3] See also Figs. 5 and 6 for an illustration of the dependence of the background and the signal on the cut parameters.

[4] We did not take into account pileup effects; therefore, the results for high luminosity $L_{\text{tot}} = 100$ fb^{-1} are rather preliminary. We think that the use of “hard” cuts 3–8 allows us to minimize the influence of pileup effects on the significance.

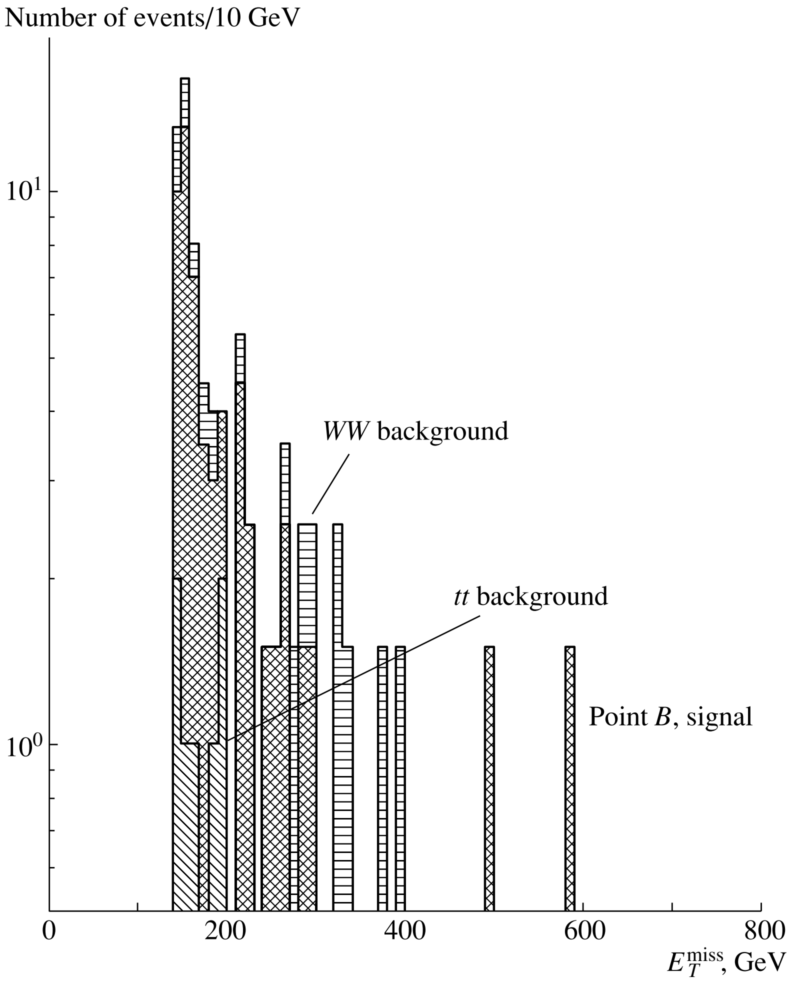

Fig. 6. E_T^{miss} distributions for main SM background (WW, $t\bar{t}$) and signal at point B for cut 3 ($L_{\text{tot}} = 10$ fb^{-1}).

In this paper, we also studied the production and decays of right and left sleptons separately.[5] In this study, we assumed that sleptons decay mainly into LSP and leptons:

$$\tilde{l}_R^- \to l^- + \tilde{\chi}_1^0, \tag{21}$$

$$\tilde{l}_L^\pm \to l^\pm + \tilde{\chi}_1^0. \tag{22}$$

Of course, in real life, we expect that the decays of other sparticles will also contribute to the signature: two leptons $+ E_T^{\text{miss}} +$ no jets. But if we are interested in new physics signal discovery, an additional contribution only increases the new physics discovery potential of this signature.

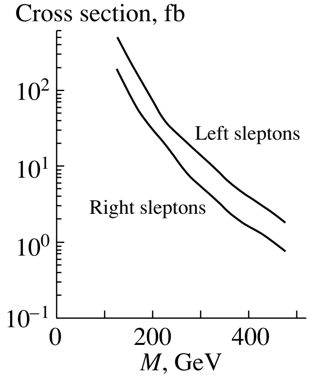

Fig. 7. Cross section $\sigma(pp \to \tilde{l}_R\tilde{l}_R)$ for various values of the right slepton masses and cross section $\sigma(pp \to \tilde{l}_L\tilde{l}_L)$ for various values of the left slepton masses at LHC.

We made simulations for LSP mass m_{LSP} equal to $0.2m_{\tilde{l}}$, $0.4m_{\tilde{l}}$, $0.6m_{\tilde{l}}$, and $0.8m_{\tilde{l}}$.[6] The dependence of

---

[5] To be precise, we considered the production and decays of the first- and second-generation sleptons $\tilde{e}_R, \tilde{e}_L, \tilde{\nu}_{e_L}, \tilde{\mu}_R, \tilde{\mu}_L, \tilde{\nu}_{\mu_L}$. An account of the third-generation sleptons with the masses equal to the masses of the first- and second-generation sleptons is not essential since Br($\tau \to$ leptons) ≈ 0.35.

[6] We assume that $m_{\tilde{e}_R} = m_{\tilde{\mu}_R}$ and $m_{\tilde{e}_L} = m_{\tilde{\mu}_L}$.

Table 5. The left and right slepton LHC(CMS) 5σ discovery potential for different luminosities

L, fb^{-1}	$m_{\mathrm{LSP}}/m_{\tilde{e}}$	$m_{\tilde{e}}$, GeV							
		100	150	200	250	300	350	400	450
		Left sleptons							
10	0.8	−	−	−	−	−	−	−	−
	0.6	+	−	−	−	−	−	−	−
	0.4	+	+	−	−	−	−	−	−
	0.2	+	+	+	−	−	−	−	−
30	0.8	−	−	−	−	−	−	−	−
	0.6	+	+	+	−	−	−	−	−
	0.4	+	+	+	+	+	−	−	−
	0.2	+	+	+	+	+	−	−	−
100	0.8	−	−	−	−	−	−	−	−
	0.6	+	+	+	+	+	−	−	−
	0.4	+	+	+	+	+	+	−	−
	0.2	+	+	+	+	+	+	+	−
		Right sleptons							
10	0.8	−	−	−	−	−	−	−	
	0.6	−	−	−	−	−	−	−	
	0.4	−	−	−	−	−	−	−	
	0.2	+	−	−	−	−	−	−	
30	0.8	−	−	−	−	−	−	−	
	0.6	−	−	−	−	−	−	−	
	0.4	+	−	−	−	−	−	−	
	0.2	+	+	+	−	−	−	−	
100	0.8	−	−	−	−	−	−	−	
	0.6	+	−	−	−	−	−	−	
	0.4	+	+	+	+	−	−	−	
	0.2	+	+	+	+	+	−	−	

the cross section for the production of right and left sleptons for the case of two flavor degenerate right and left charged sleptons is presented in Fig. 7. Our results are given in Table 5.

As follows from our results, the slepton discovery potential depends on the LSP mass. For $m_{\mathrm{LSP}} = 0.2\ m_{\tilde{l}}$, it would be possible to detect right sleptons with a mass up to 200 GeV and left ones with a mass up to 300 GeV. For instance, for a right slepton with mass $m_{\tilde{l}_R} = 200$ GeV and LSP with mass $m_{\mathrm{LSP}} = 40$ GeV, we found that $N_S = 70$, $N_B = 108$, $S = 5.9$ (cut 3, $L_{\mathrm{tot}} = 30\ \mathrm{fb}^{-1}$). For a left slepton with mass $m_{\tilde{l}_L} = 300$ GeV and LSP with mass $m_{\mathrm{LSP}} = 120$ GeV, we found that $N_S = 140$, $N_B = 108$, $S = 10.7$ (cut 3, $L_{\mathrm{tot}} = 30\ \mathrm{fb}^{-1}$).

6. CONCLUSION

In this paper, we studied the possibility of detecting sleptons at LHC(CMS). For post-WMAP benchmark points, we found that it is possible to discover sleptons at point B, points B, C, D, G, and points A, B, C, D, G, I for total luminosities $L_{\mathrm{tot}} = 10, 30$, and $100\ \mathrm{fb}^{-1}$, respectively. We also investigated the possibility of detecting sleptons for the case when they decay predominantly to leptons and LSP.[7] For $L_{\mathrm{tot}} = 30\ \mathrm{fb}^{-1}$, we found that it is possible to discover right sleptons with masses up to 200 GeV and left sleptons with masses up to 300 GeV.

ACKNOWLEDGMENTS

We are indebted to V.A. Matveev for valuable comments.

This work was supported by the Russian Foundation for Basic Research, project nos. 03-02-16933 and 04-02-16020.

REFERENCES

1. N. V. Krasnikov and V. A. Matveev, Preprint INR-1104/2003; hep-ph/0309200.
2. F. del Aguila and L. Ametller, Phys. Lett. B **261**, 326 (1991).
3. H. Baer, C. H. Chen, F. Paige, and X. Tata, Phys. Rev. D **49**, 3283 (1994).
4. H. Baer, C. H. Chen, F. Paige, and X. Tata, Phys. Rev. D **53**, 6241 (1996); hep-ph/9512383.
5. D. Denegri, L. Rurua, and N. Stepanov, CMS Note TN/96-059 (1996).
6. N. V. Krasnikov, Pis'ma Zh. Éksp. Teor. Fiz. **65**, 139 (1997) [JETP Lett. **65**, 148 (1997)]; hep-ph/9611282.
7. S. I. Bityukov and N. V. Krasnikov, Yad. Fiz. **62**, 1288 (1999) [Phys. At. Nucl. **62**, 1213 (1999)]; hep-ph/9806504.
8. M. Battaglia *et al.*, Eur. Phys. J. C **33**, 273 (2004); hep-ph/0306219.

---

[7] For right sleptons, they do indeed decay predominantly to leptons and LSP, while, for left-handed sleptons, cascade decays may be dominant in the case of $m_{\tilde{l}} > m_{\tilde{\chi}_2^0}$.

9. T. Sjostrand *et al.*, Comput. Phys. Commun. **135**, 238 (2001).
10. H. Baer, F. E. Paige, S. D. Protopopescu, and X. Tata, hep-ph/0001086.
11. S. Abdullin, A. Khanov, and N. Stepanov, CMS Note TN/94-180.
12. Reviews and original references can be found in: R. Barbieri, Riv. Nuovo Cimento **11**, 1 (1988); D. V. Nanopoulos, Phys. Rep. **145**, 1 (1987); H. P. Nilles, Phys. Rep. **110**, 1 (1984); N. V. Krasnikov and V. A. Matveev, Fiz. Élem. Chastits At. Yadra **28**, 441 (1997) [Phys. Part. Nucl. **28**, 180 (1997)]; hep-ph/9703204.
13. M. Battaglia *et al.*, eConf. C010630, E3015 (2001); hep-ph/0112013.
14. S. I. Bityukov and N. V. Krasnikov, Mod. Phys. Lett. A **13**, 3235 (1998); Nucl. Instrum. Methods Phys. Res. A **452**, 518 (2000).
15. V. Bartsch and G. Quast, CMS-IN-2003/039.

Physics of Atomic Nuclei, Vol. 68, No. 2, 2005, pp. 348–350. Translated from Yadernaya Fizika, Vol. 68, No. 2, 2005, pp. 374–376.

LETTERS TO THE EDITOR

On Neutron Generation in Beryllium Plasma under the Effect of a Fast-Electron Beam

V. I. Kukulin[*], **V. T. Voronchev, and B. M. Kuzhevsky**

Institute of Nuclear Physics, Moscow State University, Vorob'evy gory, Moscow, 119899 Russia

Received June 9, 2004

1. The overwhelming majority of present-day neutron sources belong to the type of solid-state generators where neutrons are produced in solid-state targets via nuclear reactions induced by fast ions or energetic bremsstrahlung photons. Plasma neutron sources, whose operation is based on initiating reactions in a relatively cold plasma upon irradiation with a particle beam, have not yet received adequate study. At the same time, reactions in plasmas possess important special features, the main of these being the suppression of the channel of ionization losses—that is, of the useless loss of the charged-particle energy by medium ionization. This leads to an increase in the projectile-particle range and to the enhancement of the yield of nuclear reactions in plasma targets. For example, it was shown in [1, 2] that plasma sources of neutrons can ensure sizable fluxes; therefore, they can be applied in solving a number of scientific and technological problems.

Employing electron beams in creating neutron sources may prove to be efficient, at least from the economic point of view. At present, relatively cheap and reliable facilities for producing intense beams of fast electrons have been developed, the efficiency of the input-energy transformation into the beam energy being there as high as 85 to 90%. In neutron sources, an electron beam can perform two functions. First, it is able to transform the target into a plasma state; second, it can initiate nuclear processes in the target that are accompanied by neutron generation. These are the electrodisintegration of target nuclei via $(e, e'n)$ reactions and secondary photonuclear reactions (γ, n) induced by bremsstrahlung photons. Photonuclear reactions have already been employed in experimental neutron sources. As to electrodisintegration processes, the question of whether their application will be promising has so far received very little study. However, the traditional opinion is that, in all probability, their role cannot be significant because of the smallness of the cross sections for $(e, e'n)$ reactions.

In this article, we state, however, that, under some conditions, there are grounds to revise this pessimistic conclusion. We show that, if use is made of intense electron beams and if the composition of the target is chosen appropriately, the flux of neutrons from electrodisintegration processes can become as great as 2×10^{13} neutron/s.

2. Beryllium-9 may be a promising material for manufacturing targets for neutron sources. The ^{9}Be nucleus is characterized by the lowest neutron-separation energy of $E_{\text{sep}} = 1.67$ MeV. In addition, it has a nonspherical charge distribution and a pronounced cluster structure $n + 2\alpha$ [3], where the valence-neutron wave function extends over large distances. Back in the early experiments reported in [4, 5], it was demonstrated that, even at comparatively weak electron beams ($I = 10{-}100$ μA and $E < 3$ MeV), the yield of neutrons from a thick beryllium target can be quite sizable, reaching a level equivalent in activity to 0.5–1 Ci. These studies have so far remained nearly the only source of experimental information about the electrodisintegration of ^{9}Be at low energies. Therefore, there presently arises the interesting and important question of assessing the expected level of neutron generation in beryllium for the case where use is made of modern high-intensity electron beams.

In order to answer this question, we consider the electrodisintegration of ^{9}Be in the plasma formed upon the evaporation of a solid-state target under the effect of a beam. We assume that the medium is fully ionized and that the velocity distribution of ions in it is Maxwellian. It is also reasonable to assume that, in such plasma formed under the effect of fast electrons, the electron temperature T_e exceeds the ion temperature T_i. For typical values, we take $T_e =$ 1 keV and $T_i = 100$ eV; by and large, they correspond to the state of such a medium. Further, we set the ion density n_i to 10^{23} cm^{-3}, which corresponds to the occurrence of reactions before the beginning of hydrodynamic plasma expansion.

---

[*] e-mail: `kukulin@nucl-th.sinp.msu.ru`

1063-7788/05/6802-0348$26.00 © 2005 Pleiades Publishing, Inc.

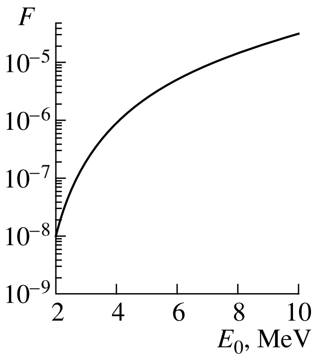

Fig. 1. Probability F of the electrodisintegration reaction $^9\mathrm{Be}(e,e'n)2\alpha$ in a plasma as a function of the initial electron energy E_0.

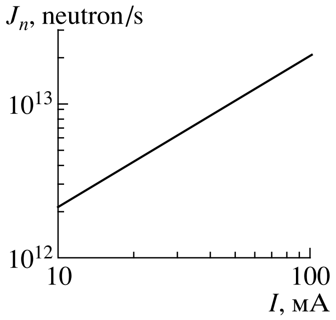

Fig. 2. Neutron flux from a beryllium plasma at various values of the current of a 10-MeV electron beam.

The probability F that a fast electron entering a plasma at an initial energy E_0 initiates the electrodisintegration reaction $^9\mathrm{Be}(e,e'n)2\alpha$ within the time of deceleration to the threshold energy of $E_{\mathrm{sep}} = 1.67$ MeV is

$$F = 1 - \exp\left[\int\limits_{E_{\mathrm{sep}}}^{E_0} \frac{dE_e n_i \sigma(E_e) v_e}{\langle dE_e/dt\rangle_{\mathrm{Coul}} + \langle dE_e/dt\rangle_{\mathrm{brem}}}\right],$$

where σ is the cross section for the reaction $^9\mathrm{Be}(e,e'n)$ and E_e and v_e are, respectively, the kinetic energy and the velocity of the electron, which are related by the relativistic equation $v_e = c\sqrt{1-[m_ec^2/(m_ec^2+E_e)]^2}$. The terms $\langle dE_e/dt\rangle_{\mathrm{Coul}}$ and $\langle dE_e/dt\rangle_{\mathrm{brem}}$ represent the electron energy losses by, respectively, Coulomb recoil [6] and bremsstrahlung [7] in elastic $ee(i)$ scattering. Formula (1) does not take into account the effect of thermal motion of plasma ions, but we can disregard this process since we consider the case of a relatively cold plasma ($T_i \ll E_e$).

The calculations were performed for initial electron energies in the range between 2 and 10 MeV. The cross sections for the reaction $^9\mathrm{Be}(e,e'n)$ were set to the experimental values from [5] for $E \leq 3$ MeV and were determined by means of an extrapolation procedure for high energies in the range $E = 3$–10 MeV. In order to test the reliability of this extrapolation, we rescaled these cross sections to the cross sections for the photodisintegration reaction $^9\mathrm{Be}(\gamma,n)$, which has been well studied. It turned out that the (γ,n) data extracted in this way are in satisfactory agreement with the results of direct measurements from [8, 9].

The calculated reaction probability F is given in Fig. 1. One can see that F grows fast with increasing energy of electrons in the beam and reaches a value of 3.37×10^{-5} at an energy as low as 10 MeV, the thermalization of electrons occurring within a very short time interval of about 1 ns. It has also been found that a variation in the plasma temperature within the range 0.1–5 keV has virtually no effect on the results. This unexpected circumstance has a simple explanation. The point is that the deceleration of an electron depends on the relative velocity of colliding particles, which, in the case being considered, is determined by the energy of the electron beam, since even its minimum energy E_{sep} is much higher than $T_{e(i)}$.

We will now estimate the neutron flux J_n from a beryllium plasma. It is obvious that $J_n = FJ_e$, where F is the calculated probability of the relevant $(e,e'n)$ reaction and J_e is the electron flux in the beam. We consider a beam characterized by a current in the range $I = 10$–100 mA and an electron energy of 10 MeV. Considering that a current of 1 mA corresponds to a flux of 6.24×10^{15} electrons per second, we obtain J_n [neutron/s] = $2.10 \times 10^{11} I$ [mA]. This relation is shown in Fig. 2. Thus, the expected integrated neutron flux appears to be at a high level of $2 \times (10^{12}$–$10^{13})$ neutron/s. It can easily be found that, in the pulsed electron-gun-operation mode characterized by a mean current of $\bar{I} = 100$ mA/s and a pulse duration of $\tau = 1$ μs, the number of neutrons per pulse may amount to 2×10^{19}.

3. This neutron yield is ensured by the single-step reaction $^9\mathrm{Be}(e,e'n)$ alone. However, there exist additional neutron-generation channels in a beryllium plasma. These are the cascade reactions like $(e',e''n)$, $(e'',e'''n)$, etc.; the disintegration reaction $^9\mathrm{Be}(\gamma,n)$ induced by bremsstrahlung photons; the neutron-multiplication reaction $^9\mathrm{Be}(n,2n)$; and neutron knockout by the fast beryllium-breakup products, $^9\mathrm{Be}(\alpha,\alpha n)$. For a 10-MeV electron beam, an upper limit on the enhancement of neutron generation due to cascade processes is about 85%. Moreover, the role of photodisintegration may prove to be significant, since, over a broad interval of photon energies from the threshold, the cross section for the reaction ^{9}Be(γ, n) is quite sizable, about 0.5 to 1 mb [8, 9]. Finally, the multiplication processes must also lead to an additional enhancement, whose degree has yet to be established.

All of this suggests that the irradiation of a beryllium target with an intense electron beam can induce neutron-flux generation at the level of the intensities of the fluxes expected from sources that are being created in a number of large physics centers worldwide. In view of this, we believe that the results presented here provide a serious argument in favor of performing thorough experimental and theoretical investigations into the interaction of intense electron beams with beryllium targets.

REFERENCES

1. E. P. Kruglyakov *et al.*, in *Proceedings of the 30th EPS Conference on Controlled Fusion and Plasma Physics, St. Petersburg, July 2003*, ECA 27A, P-2. 189 (2003).
2. V. T. Voronchev *et al.*, Nucl. Instrum. Methods Phys. Res. A **525**, 626 (2004).
3. V. T. Voronchev *et al.*, Yad. Fiz. **57**, 1964 (1994) [Phys. At. Nucl. **57**, 1890 (1994)]; Few-Body Syst. **18**, 191 (1995).
4. G. B. Collins *et al.*, Phys. Rev. **56**, 876 (1939).
5. M. L. Wiedenbeck, Phys. Rev. **69**, 235 (1946).
6. D. V. Sivukhin, Vopr. Teor. Plazmy **4**, 81 (1964).
7. S. V. Starodubtsev and A. M. Romanov, *Propagation of Charged Particles through Matter* (Akad. Nauk UzSSR, Tashkent, 1962), p. 196.
8. B. S. Dolbilkin *et al.*, Yad. Fiz. **9**, 914 (1969) [Sov. J. Nucl. Phys. **9**, 534 (1969)].
9. H. Utsunomiya *et al.*, Phys. Rev. C **63**, 018801 (2001).

Translated by A. Isaakyan

Physics of Atomic Nuclei, Vol. 68, No. 2, 2005, pp. 351–352. From Yadernaya Fizika, Vol. 68, No. 2, 2005, pp. 377–378.

LETTERS TO THE EDITOR

Time-Integrated Method for Measurement of *CP* Asymmetries $A_{\rm mix}$ and $A_{\rm dir}$ in $B_d \to \pi^+\pi^-$ Decay*

V. N. Roinishvili

Institute of Physics, Georgian Academy of Sciences, Tbilisi, Georgia; Joint Institute for Nuclear Research, Dubna, Moscow oblast, 141980 Russia

Received June 7, 2004

1. INTRODUCTION

CP violation in B_d^0 decay leads to a difference between the rates of B_d^0 and $\bar{B}_d^0$ decay into a CP eigenstate f (for details, see, e.g., [1]). In terms of the normalized proper time $\tau = \Gamma t$ and the mixing parameter $x_d = \Delta m/\Gamma$ (t is the proper time of flight of B_d, Γ is the decay width, and Δm is the mass difference between the B_d^0 mass eigenstates), the time-dependent CP asymmetry can be written as

$$A(\tau) = \frac{N(B_d^0 \to f;\tau) - N(\bar{B}_d^0 \to f;\tau)}{N(B_d^0 \to f;\tau) + N(\bar{B}_d^0 \to f;\tau)} \qquad (1)$$
$$= A_{\rm dir}\cos(x_d\tau) + A_{\rm mix}\sin(x_d\tau),$$

where $A_{\rm dir}$ is the asymmetry arising directly from the decay amplitudes and $A_{\rm mix}$ is the asymmetry from interference effects between B_d^0–$\bar{B}_d^0$ mixing and decay processes, respectively. For $f \equiv J/\psi K_s$, $A_{\rm dir}$ is expected to be very small and $A_{\rm mix} = \sin(2\beta)$, where β is the angle in the unitarity triangle of the CKM matrix. For $f \equiv \pi^+\pi^-$, the asymmetry $A_{\rm dir}$ is not negligible anymore and both terms in (1) are significant.

Equation (1) can be solved by experimentally fitting the measured time-dependent asymmetry $A(\tau)$ with two free parameters $A_{\rm mix}$ and $A_{\rm dir}$. The asymmetries $A_{\rm mix}$ and $A_{\rm dir}$ can also be obtained using time-integrated measurements proposed here in a properly chosen wide τ range.

2. THE METHOD

From (1), the time-integrated asymmetry in the range $\tau_l \le \tau \le \infty$ (in practice, the lower limit of integration τ_l should be taken greater than 0 in order to select B particles with reduced background)

$$A(\tau \ge \tau_l) = A_{\rm mix} Is(\tau_l) + A_{\rm dir} Ic(\tau_l), \qquad (2)$$

where $Is(\tau_l)$ denotes $e^{\tau_l}\int_{\tau_l}^{\infty} e^{-\tau}\sin(x_d\tau)d\tau$ and $Ic(\tau_l)$ denotes $e^{\tau_l}\int_{\tau_l}^{\infty} e^{-\tau}\cos(x_d\tau)d\tau$.

For

$$\tau_l \equiv \tau_m = \frac{\arctan(1/x_d)}{x_d} \qquad (3)$$
$$(\tau_m = 1.37 \text{ for } x_d = 0.7),$$

the second integral in (2) vanishes: $Ic(\tau_m) = 0$. This range $\tau_m \le \tau \le \infty$ is adequate for $A_{\rm mix}$ measurement, since

$$A(\tau \ge \tau_m) = A_{\rm mix} Is(\tau_m) \qquad (4)$$

contains only one free parameter $A_{\rm mix}$. The direct asymmetry $A_{\rm dir}$ can then be measured using the full available range of τ [with fixed $A_{\rm mix}$ obtained from (4)] by the expression

$$A(\tau \ge \tau_l) = A_{\rm mix}^{\rm fix} Is(\tau_l) + A_{\rm dir} Ic(\tau_l), \qquad (5)$$

which again contains only one free parameter $A_{\rm dir}$.

3. CONCLUSION AND REMARK

The time-integrated method proposed here may be useful for current experiments at e^+e^- colliders and at Fermilab and for future experiments at LHC–LHCb since it is less sensitive to the precision of τ measurements and, contrary to the time-dependent measurements, the value of $A_{\rm mix}$ defined from (4) is not correlated with the value of $A_{\rm dir}$.

The method also gives a way to measure CP asymmetries in experiments without particle identification at hadron colliders. In such experiments, it is impossible to separate kinematically $B_d^0 \to \pi^+\pi^-$

---

*This article was submitted by the author in English.

events from $B_s^0 \to K^+K^-$ ones. But asymmetries which could arise from $B_s^0 \to K^+K^-$ decays will be very much diluted for time-integrated asymmetries because of the large value of the mixing parameter for B_s^0: $x_s > 20$ (dilution factor is $\sim x_s/(1 + x_s^2)$). The detailed study of application of the method to the CMS at LHC (as an example) is given elsewhere [2].

REFERENCES

1. *B Decays at the LHC,* Ed. by P. Ball, R. Fleischer, G. F. Tartarelli, *et al.*, hep-ph/0003238.
2. V. Roinishvili, in *Physics Program with the CMS Detector, the Fifth Annual RDMS CMS Collaboration Meeting, ITEP, Moscow, Russia, Nov. 22–24, 2000*; Preprint No. 2003-29, IHEP (Protvino, 2003).

Physics of Atomic Nuclei, Vol. 68, No. 2, 2005, pp. 353–355. Translated from Yadernaya Fizika, Vol. 68, No. 2, 2005, pp. 379–381.
Original Russian Text Copyright © 2005 by the Editorial Board.

FUTURE PUBLICATIONS

Observation of a Narrow Baryon Resonance Decaying through the pK_S^0 Channel in 70-GeV/c pA Interactions at the CVD-2 Facility

A. N. Aleev, N. S. Amaglobeli[†], E. N. Ardashev, V. P. Balandin, S. G. Basiladze, S. F. Berezhnev, G. A. Bogdanova, I. V. Boguslavsky, M. V. Vasiliev, A. M. Vishnevskaya, V. Yu. Volkov, A. P. Vorobiev, A. G. Boronin, S. N. Golovnia, S. A. Golubkov, A. V. Gorkov, S. A. Gorokhov, I. M. Gramenitsky, N. I. Grishin, Ya. V. Grishkevich, N. N. Egorov, V. B. Ezhov, G. G. Ermakov, P. F. Ermolov, N. K. Zhidkov, L. L. Zakamsky, V. N. Zapolsky, V. V. Zmushko, D. S. Zotkin, S. A. Zotkin, E. G. Zverev, D. E. Karманov, A. A. Kiriakov, V. V. Kozlov, Yu. F. Kozlov, E. S. Kokoulina, N. V. Korotkov, I. G. Kosarev, V. A. Kramarenko, A. V. Kubarovsky, E. N. Kuznetsov, N. A. Kouzmin, V. A. Kuzmin, L. L. Kurchaninov, G. I. Lanshchikov, A. N. Larichev, M. S. Levitsky, A. K. Leflat, S. I. Lyutov, S. V. Maiorov, M. M. Merkin, A. A. Minaenko, G. Ya. Mitrofanov, A. M. Moiseev[†], V. S. Murzin, V. A. Nikitin, P. P. Nomokonov, A. A. Oleinik, S. V. Orfanitsky, V. V. Parakhin, V. S. Petrov, L. V. Pilavova, A. V. Pleskach, V. V. Popov, R. E. Rudenko, I. A. Pyfanov, V. N. Riadovikov, V. A. Senko, A. I. Sidorov, M. M. Soldatov, L. A. Tikhonova, T. P. Topuria, N. F. Furmanec, A. G. Kholodenko, Yu. P. Tsupa, N. A. Shalanda, M. D. Shafranov, A. I. Yukaev, and V. I. Yakimchuk
(CVD Collaboration)

The data from the CVD experiment that were obtained at the IHEP accelerator in 70-GeV/c pA interactions are analyzed with the aim of seeking an exotic Θ^+ baryon that decays through the pK_S^0 channel. The reaction $pA \to pK_S^0 + X$ characterized by a bounded multiplicity of secondary charged particles is taken for this analysis. A resonance of mass $M = 1526 \pm 3(\text{stat.}) \pm 3(\text{syst.})$ MeV/c^2 and width $\Gamma < 24$ MeV/c^2 is observed in the invariant-mass spectrum of the pK_S^0 system at a statistical significance of 5.6σ. The mass and the width of this resonance correspond to the recently found positive-strangeness Θ^+ baryon, which was predicted as an exotic baryon consisting of five quarks (pentaquark), $uudd\bar{s}$. The total cross section for the production of a Θ^+ baryon in pN interactions is estimated at a value within the range 30–120 μb for $x_{\text{F}} \geq 0$. An analysis of the A dependence of the cross section for Θ^+-baryon production does not reveal a significant deviation from the A dependence for inelastic events ($\sim A^{0.7}$).

Some Features of the Production of Baryons with Heavy Quarks in e^+e^- Collisions

S. P. Baranov and V. L. Slad

The production of various baryons with heavy quarks in e^+e^- annihilation is considered. On the basis of exact formulas that we obtained previously within full perturbation theory, new numerical calculations of cross sections are performed, and simple approximate expressions are then constructed for the results of these calculations. The dependence of the total cross sections on the masses of constituent quarks is discussed. The application of the Peterson fragmentation function and a fragmentation function of the Regge type to describing differential cross sections is analyzed.

Employing a Spheroidal Global Potential to Estimate the Quadrupole Deformation of Nuclei

B. S. Ishkhanov and V. N. Orlin

A spheroidal global shell potential is constructed on the basis of an optical model whose global parameters are extracted from experimental data on nucleon–nucleus scattering. This potential is used to estimate the quadrupole deformation of a large number of light, intermediate, and heavy nuclei in the mass-number range $10 \lesssim A \lesssim 240$. The results are compared with the results of similar calculations for the Nilsson potential and with the estimates of the quadrupole deformation that follow from data on the static quadrupole moments of the nuclei considered in the present study.

1063-7788/05/6802-0353$26.00 © 2005 Pleiades Publishing, Inc.

Photonuclear Data and Contemporary Physics of Giant Resonances

S. P. Kamerdzhiev and S. F. Kovalev

The results of the development (renaissance) of giant-resonance physics are discussed briefly from the point of view of their application to creating a database of photonuclear processes. It is indicated that, among recommendations from the existing databases, the part that is used within this methodology does not correspond to the current state of the art. The most reliable experimental data on the $M1$ resonance are parametrized for seven spherical nuclei, and it is shown that the width of this resonance is severalfold—sometimes, an order of magnitude—smaller than the value of $\Gamma_0 = 4$ MeV, which is recommended for all nuclei. The need for microscopically taking into account more complicated configurations than those included within the RPA or QRPA—or, more precisely, coupling to phonons—is demonstrated by proving that this changes the functional dependence of damping on temperature in relation to that used previously and is necessary for explaining the properties of the pygmy dipole resonance in the region of the nucleon binding energy. The calculations of the mean energies of this resonance in the Ca and Sn isotopes within the microscopic generalized theory of finite Fermi systems revealed that the inclusion of coupling to phonons reduces this energy considerably, rendering it closer to the experimental value. The idea of creating a database of photonuclear processes for unstable nuclei, including fission fragments, by relying on the generalized theory of finite Fermi systems is discussed in view of the fact that information necessary for fitting the parameters of phenomenological theories is absent or scanty for these nuclei.

Spectroscopic Factors and Barrier Penetrability in Cluster Radioactivity

S. N. Kuklin, G. G. Adamian, and N. V. Antonenko

The model of cold cluster decay is presented within the concept of a dinuclear system. The calculated barrier penetrabilities and experimental half-lives are used to extract spectroscopic factors. The effect of the deformations of the light cluster and the residual nucleus on the nucleus–nucleus potential and decay properties is demonstrated. The half-lives of neutron-deficient actinides and medium-mass nuclei are predicted. The interplay between spontaneous fission and cluster radioactivity is discussed.

Is It Still Interesting to Seek Lepton-Flavor Violation in the Rare Decays of K Mesons?

L. G. Landsberg

Further possibilities of experiments to seek lepton-flavor violation in kaon decays at present and future intermediate-energy accelerators are considered. It is shown that such investigations are complementary to searches for muonic lepton-flavor-violation processes and can possess, in some models featuring partly conserved quantum numbers of the generations, a very high and even record sensitivity. Searches for lepton-flavor-violation processes in kaon decays should be considered as a very important and independent part of the general program of searches for the violation of lepton flavors in processes involving charged leptons.

Investigation of Anomalous Constants of Four-Boson Interaction in Collisions of High-Energy Photons

I. B. Marfin and T. V. Shishkina

The production of two and three bosons in $\gamma\gamma$ collisions at high energies makes it possible to study the anomalous constants of four-boson interaction. Three anomalous constants appearing in the cross section for the production of a W^+W^- pair are considered at the TESLA energies ($\sqrt{s} \sim 1$ TeV). A full analysis of the anomalous contributions to the cross section for the process and to the respective angular distribution is performed.

Electroproduction of $D^{*\pm}$ Mesons at High Energies

V. A. Saleev and D. V. Vasin

A comparative analysis of the predictions of the collinear parton model and the k_T-factorization approach is performed for the case of the D^*-meson electroproduction at the HERA ep collider. It is shown that, owing to effectively taking into account, in noncollinear distributions, next-order corrections in the strong coupling constant α_s, the k_T-factorization approach increases, in contrast to the predictions of the collinear parton model, the absolute value of the cross sections for charmed-meson electroproduction approximately by a factor of 1.5 to 2. As a result, the agreement with experimental data is improved. This is not so only for the pseudorapidity spectrum, where the shape of the spectrum differs considerably from the experimental one and depends greatly on the choice of parametrization of the noncollinear gluon distribution within the proton.

Character of Coulomb Shifts of Nuclear Scattering Resonances

N. Sh. Takibaev

Relations determining the shift of energies and widths of scattering resonances are obtained within the method of evolution in the coupling constant. These relations generalize the known relations for the shift of levels in a discrete spectrum. The problem of determining the Coulomb shifts of low-energy resonances appearing in the cross section for the scattering of some light nuclei is solved. Examples that are of importance for nuclear astrophysics and the problem of the production of chemical elements are considered. The character of Coulomb shifts is studied within simple nuclear models. Respective numerical estimates are given, which agree satisfactorily with experimental data.

Quark–Antiquark Composite Systems: The Bethe–Salpeter Equation in the Spectral-Integration Technique in the Case of Different Quark Masses

A. V. Anisovich, V. V. Anisovich, V. N. Markov, M. A. Matveev, and A. V. Sarantsev

The Bethe–Salpeter equations for quark–antiquark composite systems involving different quark masses, such as $q\bar{s}$ (with $q = u,d$), $q\bar{Q}$, and $s\bar{Q}$ $(Q = c,b)$, are written in terms of spectral integrals. For mesons characterized by a mass M, a spin J, and a radial quantum number n, the equations are written for the (n, M^2) trajectories with fixed J. Mixing between states with different quark spins S and angular momenta L is also discussed.